

Supplementary Materials for

Architecture of the cytoplasmic face of the nuclear pore

Christopher J. Bley,[#] Si Nie,[#] George W. Mobbs,[#] Stefan Petrovic,[#] Anna T. Gres,[#]
Xiaoyu Liu,[#] Somnath Mukherjee, Sho Harvey, Ferdinand M. Huber, Daniel H. Lin,
Bonnie Brown, Aaron W. Tang, Emily J. Rundlet, Ana R. Correia, Shane Chen,
Saroj G. Regmi, Taylor A. Stevens, Claudia A. Jette, Mary Dasso, Alina Patke,
Alexander F. Palazzo, Anthony A. Kossiakoff, André Hoelz*

[#]these authors contributed equally to this work

*Corresponding author. Email: hoelz@caltech.edu (A.H.)

This PDF file includes:

Material and Methods
Supplementary Text Figs.
S1 to S89
Tables S1 to S18
References

Other Supplementary Materials for this manuscript include the following:

MDAR Reproducibility Checklist

Materials and Methods

Materials and reagents

A detailed summary of materials and reagents is provided in [Table S1](#).

Bacterial expression constructs

C. thermophilum cDNA was generated using a previously established protocol (102). Briefly, *C. thermophilum* (DSM-1495; gift of Ed Hurt, University of Heidelberg, Germany) mycelium was grown in combined-carbon source media (CCM). After harvesting, washing, and drying, the mycelium was frozen in liquid nitrogen and lysed in a Retsch mill. Total RNA was isolated using the SV Total RNA Isolation System (Promega). cDNA was generated using Superscript III Reverse Transcriptase (Invitrogen) and an oligo d(T₂₀) primer prior to purification with a QIAquick PCR Purification Kit (QIAGEN). The generation of cDNAs encoding Nsp1, Dbp5, Nup145N, Nup42, Nic96, Nup120, Nup37, Elys, Nup85, Sec13, Nup145C, Nup84, and Nup133 was previously reported (11, 38, 63). NUP98 cDNA was a gift of Beatriz Fontoura (UT Southwestern Medical Center, USA) (103), and cDNAs encoding NUP42 and NUP155 were a gift of Susan Wente (Vanderbilt University, USA) (104). NUP62 and NUP88 cDNAs were obtained commercially (Open Biosystems). To improve bacterial expression of NUP88, the sequence encoding residues 1 to 493 was replaced with a synthetic codon-optimized DNA fragment (GenScript). The generation of cDNAs encoding NUP358 (76), NUP214 (54), DDX19 (55), GLE1 (63), and RAE1 (57) was previously described.

DNA fragments were amplified by PCR using *C. thermophilum* and *H. sapiens* cDNA and cloned into either a modified pET28a vector encoding an N-terminal His₆-tag followed by a PreScission protease cleavage site (pET28a-PreS) (105), a modified pET28a vector (Novagen) encoding an N-terminal His₆-tag followed by a small ubiquitin-like modifier (SUMO) with or without an uncleavable C-terminal His₆-tag (pET28a-SUMO) (106), a modified pET-Duet1 vector (Novagen) encoding an N-terminal His₆-SUMO-tag in the first expression site and an untagged protein in the second site (pET-Duet1-SUMO), a modified pET-Duet1 vector encoding N-terminal SUMO-tags in both expression sites (pET-Duet1-SUMO2), a modified pET-MCN vector (107) encoding an N-terminal His₆-tag followed by a PreScission protease cleavage site (pET-MCN-PreS), a modified pET-MCN vector encoding an N-terminal His₆-tag followed by SUMO (pET-MCN-SUMO) (11), an unmodified pET24a vector (Novagen) encoding an uncleavable N-terminal His₆-tagged protein, or pGEX-6P1 vector (GE Healthcare) encoding an N-terminal GST-tag followed by a PreScission protease cleavage site. pET28a-SUMO-Avi and pET-Duet1-SUMO-Avi expression constructs were generated by subsequently cloning an Avi-tag-encoding DNA cassette into the BamHI site. pET28a-His₆-PreS-Avi-SUMO constructs were generated by first cloning DNA encoding proteins to pET28a-SUMO using the BamHI and XhoI restriction sites, and subsequently subcloning the SUMO-insert cassette using NdeI and BamHI restriction sites into the previously described pET28a-PreS-Avi vector (27). The variable complementarity determining region (CDR) of synthetic antibodies (sAB) was cloned into the pRH2.2 vector (Sidhu lab, University of Toronto, Canada), using the HindIII and Sall restriction sites (108). Mutants were generated by QuikChange mutagenesis using PfuUltra II Fusion HotStart DNA Polymerase (Agilent Technologies) and confirmed by DNA sequencing. Details of bacterial expression constructs are summarized in [Table S2](#).

Bacterial protein expression

Bacterial protein expression was carried out in *E. coli* BL21-CodonPlus(DE3)-RIL cells in Luria-Bertani (LB) media and induced at an OD 600 of 0.8 with 0.5 mM isopropyl- β -D-thiogalactopyranoside (IPTG). Seleno-L-methionine (SeMet)-labeled proteins were expressed by a methionine pathway inhibition protocol, as previously described (109). For details of the expression times and temperatures, see [Table S2](#). Cells were harvested by centrifugation and re-suspended in a buffer containing 20 mM TRIS (pH 8.0), 300 mM NaCl (for cells expressing

GST-tagged proteins) or 500 mM NaCl (for cells expressing His₆-tagged proteins), 5 mM 2-mercaptoethanol (β -ME), supplemented with complete EDTA-free protease inhibitor cocktail (Roche), 2 μ M bovine lung aprotinin (Sigma), and 1 mM phenylmethylsulfonyl fluoride (PMSF, Gold Biotechnology). For purification, the cell suspensions of all proteins and protein complexes were supplemented with 1 mg DNase I and lysed using a cell disruptor (Avestin). Cell lysates were cleared by centrifugation at 30,000 $\times g$ for 1 hour. The supernatants were filtered through a 0.45 μ m filter (Millipore) and purified using standard chromatography methods.

Baculoviral protein expression

The baculoviral expression constructs of RAE1 and RAE1•NUP98^{GLEBS} were described previously (57). Briefly, a DNA fragment encompassing the entire coding region of RAE1 was cloned into a pFastbac-Dual vector (Gibco), using SmaI and KpnI restriction sites, expressing RAE1 with a non-cleavable C-terminal His₇-tag. A DNA fragment encoding NUP98^{GLEBS} (residues 157-213) with an N-terminal tobacco etch virus (TEV) protease cleavable N-terminal GST-tag was cloned into the pFastbac-Dual vector that harbored RAE1 in the second expression site, using BamHI and EcoRI restriction sites. For *C. thermophilum* Gle2, a DNA fragment encompassing the entire coding region of the protein was cloned into the pFastBac-HTB vector (Gibco), using BamHI and XhoI restriction sites, expressing Gle2 with a TEV-cleavable N-terminal His₆-tag. Details of Baculoviral expression constructs are summarized in [Table S3](#). Baculoviral stocks were generated using the Bac-to-Bac baculovirus expression system (Gibco) according to the manufacturer's guidelines. Briefly, pFastBac vectors were transformed into DH10Bac cells, bacmids were then extracted by precipitation in 50% (v/v) isopropanol after cell lysis using the QIAprep miniprep kit (QIAGEN). P0 virus was generated by transfection of 10 μ l bacmid DNA with 20 μ l CellFectin-II (Gibco) into 4 ml of 0.6×10^6 /ml *S. frugiperda* Sf9 cells grown in Sf-900 III SFM medium (Gibco) incubated at 27 °C for 5-6 days until ~25% viability. P1 virus was generated by infecting 40 ml of 1.5×10^6 /ml Sf9 cells in suspension with 135 μ l of P0 virus and incubating at 27 °C for 3-4 days until ~60% viability. Protein expression was carried out in 1 L cultures of 2.5×10^6 /ml *T. ni* Hi5 cells grown in suspension and infected with 1% (v/v) P1 virus to give an approximate multiplicity of infection (MOI) of 1. Hi5 cells were grown in ESF 921 insect cell culture medium (Expression systems) at 27 °C, supplemented after 24 hours with 1.5% (v/v) production boost additive (Expression systems). The cells were harvested 2-3 days post infection at ~80% viability through centrifugation and re-suspended in a buffer, containing 20 mM TRIS (pH 8.0), 500 mM NaCl, and 5 mM β -ME, supplemented with Complete EDTA-free protease inhibitor cocktail, 2 μ M bovine lung aprotinin, and 1 mM PMSF. For purification, the cell suspensions were supplemented with 1 mg DNase I and lysed using a cell disruptor (Avestin), and 2 \times 30 second cycles of sonication. Cell lysates were cleared by centrifugation at 30,000 $\times g$ for 1 hour. The supernatants were filtered through a 5 μ m filter (Millipore) and purified using standard chromatography methods.

Protein purification

A detailed summary of the chromatography steps and associated buffer conditions for all protein purifications is provided in [Table S5](#). The purification and reconstitution of protein complexes and sABs are detailed below.

Purification of sABs. The expression of sABs was carried out in *E. coli* BL21-Gold cells (Agilent Technologies) and induced at an OD 600 of 1.0 with 0.5 mM IPTG and grown at 37 °C for 3 hours. The lysate was incubated at 65 °C for 30 minutes and then cooled on ice for 15 minutes before centrifugation at 30,000 $\times g$ for 1 hour. The supernatant was filtered through a 0.45 μ m filter (Millipore) and loaded onto a 5 ml HiTrap MabSelect SuRe column (GE Healthcare), equilibrated in a buffer containing 20 mM TRIS (pH 8.0) and 500 mM NaCl and eluted using a linear gradient of an elution buffer containing 0.1 M acetic acid. The eluted fractions were dialyzed against a buffer containing 20 mM TRIS (pH 8.0) and 100 mM NaCl and

concentrated to ~10 mg/ml for biochemical interaction experiments, complex reconstitution, and crystallization.

Reconstitution of RAE1•NUP98^{GLEBS-APD}. Purified RAE1 was mixed with a 1.2-fold molar excess of NUP98^{GLEBS-APD} and incubated on ice for 30 minutes. The mixture was then loaded onto a Superdex 75 10/300 GL gel filtration column (GE Healthcare), equilibrated in buffer containing 20 mM TRIS (pH 8.0), 150 mM NaCl, and 5 mM DTT. Peak fractions containing a stoichiometric RAE1•NUP98^{GLEBS-APD} complex were pooled and concentrated to ~10 mg/ml for biochemical studies.

Reconstitution of NUP62•NUP88•NUP214•DDX19(ADP)•RAE1•NUP98^{GLEBS-APD} (CFNC). Purified NUP62•NUP88•NUP214 was mixed with a 1.5-fold molar excess of purified DDX19(ADP) and RAE1•NUP98^{GLEBS-APD} and incubated on ice for 30 minutes. The mixture was then loaded onto a Superose 6 10/300 GL gel filtration column (GE Healthcare), equilibrated in a buffer containing 20 mM TRIS (pH 8.0), 100 mM NaCl, 5 mM DTT, and 5% (v/v) glycerol. Peak fractions containing CFNC were pooled and concentrated to ~7 mg/ml for biochemical studies.

Reconstitution of NUP88^{NTD}•NUP98^{APD}. Purified NUP88^{NTD} was mixed with a 1.2-fold molar excess of NUP98^{APD} and incubated on ice for 1 hour. The mixture was then loaded onto a HiLoad Superdex 200 16/60 PG gel filtration column (GE Healthcare), equilibrated in a buffer containing 20 mM TRIS (pH 8.0), 100 mM NaCl, and 5 mM DTT. Peak fractions containing a stoichiometric NUP88^{NTD}•NUP98^{APD} complex were pooled and concentrated to ~20 mg/ml for biochemical studies and crystallization.

Purification of NUP358^{NTD}•sAB-14. Purified NUP358^{NTD} was mixed with a 1.5-fold molar excess of sAB14 and incubated on ice for 1 hour. The mixture was then loaded onto a HiLoad Superdex 200 16/60 PG gel filtration column equilibrated in buffer containing 20 mM TRIS (pH 8.0), 100 mM NaCl, and 5 mM DTT. Peak fractions containing a stoichiometric NUP358^{NTD}•sAB-14 complex were pooled and concentrated to ~10 mg/ml for biochemical studies and crystallization.

Purification of NUP358/NUP50 RanBDs in complex with Ran(GMPPNP). Ran nucleotide exchanged from bound GDP to the non-hydrolysable GTP analogue 5'-guanosine- $[\beta,\gamma]$ -imido]-triphosphate (GMPPNP) was achieved by incubating Ran(GDP) with a two-fold excess of GMPPNP and 2.5 units of alkaline phosphatase (Roche) per mg protein overnight at 4 °C in buffer containing 20 mM potassium phosphate (pH 7.4), 200 mM ammonium sulfate, 0.1 mM ZnCl₂, and 1 mM DTT, as previously described (110). After nucleotide exchange, protein was buffer exchanged using a 5 ml HiTrap Desalting column (GE Healthcare), equilibrated in a buffer containing 20 mM TRIS (pH 8.0), 100 mM NaCl, 5 mM DTT, and 2 mM MgCl₂. The purified RanBD protein was mixed with a 1.5-fold molar excess of Ran(GMPPNP) and incubated on ice for 1 hour. The mixture was injected onto a 5 ml HiTrap QHP column (GE Healthcare) and eluted via a NaCl gradient (100-400 mM). The complex-containing fractions were pooled, concentrated, and further purified by size-exclusion chromatography using a Superdex 200 16/60 PG gel filtration column equilibrated in a buffer containing 20 mM TRIS (pH 8.0), 100 mM NaCl, 5 mM DTT, and 2 mM MgCl₂. For Nup358^{RanBD-II} and Nup50^{RanBD}, the HiTrap QHP column step was omitted. Peak fractions containing stoichiometric RanBD•Ran(GMPPNP) complex were pooled and concentrated to ~15 mg/ml for biochemical studies and crystallization.

Reconstitution of Nup82•Nup159•Nsp1•Dpb5•Gle2•Nup145N^{GLEBS-APD} (CFNC). Purified Nup82•Nup159•Nsp1 was mixed with a 1.5-fold molar excess of purified Dpb5 and Gle2•Nup145N^{GLEBS-APD} and incubated on ice for 1 hour before injection onto a Superose 6 10/300 GL gel filtration column equilibrated in a buffer containing 20 mM TRIS (pH 8.0), 100 mM NaCl, 5 mM DTT, and 5% (v/v) glycerol. Peak fractions containing stoichiometric CFNC were pooled and concentrated to ~10 mg/ml for biochemical studies.

Reconstitution of Nup120•Nup37•Elys•Nup85•Sec13-Nup145C (CNC-hexamer). Purified Nup120•Nup37•Elys•Nup85 hetero-tetramer was mixed with a 1.2-fold molar excess of purified Sec13-Nup145C, incubated for 1 hour on ice, and injected onto a Superose 6 10/300 GL gel filtration column equilibrated in a buffer containing 20 mM TRIS (pH 8.0), 100 mM NaCl, 5 mM DTT, and 5% (v/v) glycerol. Peak fractions containing stoichiometric CNC-hexamer were pooled and concentrated to ~10 mg/ml for biochemical studies and further reconstitutions.

Reconstitution of Nup120•Nup37^{ΔCTE}•Elys•Nup85•Sec13-Nup145C (CNC-hexamer^{Δ37CTE}). Purified Nup120•Nup37^{ΔCTE}•Elys•Nup85 hetero-tetramer was mixed with a 1.2-fold molar excess of purified Sec13-Nup145C and incubated for 1 hour on ice. The mixture was loaded onto a Superose 6 10/300 GL gel filtration column equilibrated in a buffer containing 20 mM TRIS (pH 8.0), 100 mM NaCl, 5 mM DTT, and 5% (v/v) glycerol. Peak fractions containing stoichiometric CNC-hexamer^{Δ37CTE} were pooled and concentrated to ~10 mg/ml for biochemical studies and further reconstitutions.

Reconstitution of Nup120•Nup37•Elys•Nup85•Sec13-Nup145C^{ΔNTE} (CNC-hexamer^{Δ145CNTE}). Purified Nup120•Nup37•Elys•Nup85 hetero-tetramer was mixed with a 1.2-fold molar excess of purified Sec13-Nup145C^{ΔNTE} and incubated for 1 hour on ice. The mixture was loaded onto a Superose 6 10/300 GL gel filtration column equilibrated in a buffer containing 20 mM TRIS (pH 8.0), 100 mM NaCl, 5 mM DTT, and 5% (v/v) glycerol. Peak fractions containing stoichiometric CNC-hexamer^{Δ145CNTE} were pooled and concentrated to ~10 mg/ml for biochemical studies and further reconstitutions.

Reconstitution of Nup120•Nup37^{ΔCTE}•Elys•Nup85•Sec13-Nup145C^{ΔNTE} (CNC-hexamer^{Δ37CTEΔ145CNTE}). Purified Nup120•Nup37^{ΔCTE}•Elys•Nup85 hetero-tetramer was mixed with a 1.2-fold molar excess of purified Sec13-Nup145C^{ΔNTE} and incubated for 1 hour on ice. The mixture was loaded onto a Superose 6 10/300 GL gel filtration column equilibrated in a buffer containing 20 mM TRIS (pH 8.0), 100 mM NaCl, 5 mM DTT, and 5% (v/v) glycerol. Peak fractions containing stoichiometric CNC-hexamer^{Δ37CTEΔ145CNTE} were pooled and concentrated to ~10 mg/ml for biochemical studies and further reconstitutions.

Reconstitution of Nup120•Nup37•Elys•Nup85•Sec13-Nup145C•Nup84•Nup133^{ΔNTE} (CNC). Purified Nup120•Nup37•Elys•Nup85•Sec13-Nup145C (CNC-hexamer) was mixed with a 1.2-fold molar excess of purified Nup84•Nup133^{ΔNTE} hetero-dimer, incubated for 1 hour on ice, and injected onto a Superose 6 10/300 GL gel filtration column, equilibrated in a buffer containing 20 mM TRIS (pH 8.0), 100 mM NaCl, 5 mM DTT, and 5% (v/v) glycerol. Peak fractions containing stoichiometric CNC were pooled and concentrated to ~10 mg/ml for biochemical studies and further reconstitutions. CNC variants lacking either Nup37^{CTE}, Nup145C^{NTE}, or both were reconstituted using the corresponding CNC-hexamer variants.

Reconstitution of Nup82^{NTD}•Nup145N^{APD}•Nup159^{TAIL}. Purified Nup82^{NTD}•Nup159^{TAIL} heterodimer was mixed with a 1.5-fold molar excess of purified Nup145N^{APD}, incubated for 1 hour on ice, and injected onto a HiLoad Superdex 200 16/60 PG gel filtration column, equilibrated in a buffer containing 20 mM TRIS (pH 8.0), 100 mM NaCl, and 5 mM DTT. Peak fractions containing a stoichiometric Nup82^{NTD}•Nup145N^{APD}•Nup159^{TAIL} were pooled and concentrated to ~30 mg/ml for biochemical studies.

Reconstitution of Nup159^{NTD}•Dbp5. Purified Dbp5 was mixed with a 1.5-fold molar excess of Nup159^{NTD} and incubated on ice for 1 hour. The mixture was then loaded onto a HiLoad Superdex 200 16/60 PG gel filtration column, equilibrated in a buffer containing 20 mM TRIS (pH 8.0), 100 mM NaCl, and 5 mM DTT. Peak fractions containing a stoichiometric Nup159^{NTD}•Dbp5 were pooled and concentrated to ~20 mg/ml for biochemical studies.

Reconstitution of Gle2•Nup145^{GLEBS-APD}. Purified Gle2 was mixed with a 1.5-fold molar excess of Nup145N^{GLEBS-APD} and incubated on ice for 1 hour. The mixture was then loaded onto a

HiLoad Superdex 75 16/60 PG gel filtration column, equilibrated in a buffer containing 20 mM TRIS (pH 8.0), 100 mM NaCl, and 5 mM DTT. Peak fractions containing a stoichiometric Gle2•Nup145N^{GLEBS-APD} were pooled and concentrated to ~10 mg/ml for biochemical studies.

Reconstitution of Gle2•Nup145N^{GLEBS}. Purified Gle2 was mixed with a 1.5-fold molar excess of Nup145N^{GLEBS} and incubated on ice for 1 hour. The mixture was then loaded onto a HiLoad Superdex 75 16/60 PG gel filtration column equilibrated in a buffer containing 20 mM TRIS (pH 8.0), 100 mM NaCl, and 5 mM DTT. Peak fractions containing a stoichiometric Gle2•Nup145N^{GLEBS} were pooled and concentrated to ~20 mg/ml for biochemical studies.

Multi-angle light scattering coupled to analytical size-exclusion chromatography (SEC-MALS)

Purified proteins and complex formation were characterized by inline multi-angle light scattering following separation on Superdex 200 10/300 GL, Superdex 200 Increase 10/300 GL, or Superose 6 10/300 GL columns (111). *C. thermophilum* proteins and complexes were primarily analyzed in a buffer containing 20 mM TRIS (pH 8.0), 100 mM NaCl, 5 mM DTT, and 5% (v/v) glycerol. The stability of the CFNC-hub interactions with Nup37^{CTE} and Nup145C^{NTE} was assessed in a series of buffers containing 20 mM TRIS (pH 8.0), 5 mM DTT, 5% (v/v) glycerol, and increasing NaCl concentrations (100 mM, 200 mM, 300 mM, 500 mM, or 1000 mM). Reconstitution of the human CFNC hexamer was also tested in a buffer containing 20 mM TRIS (pH 8.0), 100 mM NaCl, 5 mM DTT, and 5% (v/v) glycerol. Whereas the human CFNC pairwise interaction network was conducted in a buffer containing 20 mM TRIS (pH 8.0), 100 mM NaCl, and 5 mM DTT. The oligomerization behavior of NUP358^{NTD}, NUP358^{OE}, and the NUP358^{NTD-OE} LIQIML mutant was analyzed in a 20 mM TRIS (pH 8.0), 5 mM DTT buffer, containing either 100 mM or 350 mM NaCl. Because of solubility restrictions, NUP358^{NTD-OE} was analyzed exclusively in a buffer containing 350 mM NaCl. The chromatography system was connected in series with an 18-angle light scattering detector (DAWN HELEOS II, Wyatt Technology), a dynamic light scattering detector (DynaPro Nanostar, Wyatt Technology), and a refractive index detector (Optilab t-REX, Wyatt Technology). Data were collected every 1 second at a flow rate of 0.5 ml/min (Superdex 200 10/300 GL, Superdex 200 Increase 10/300 GL) or 0.4 ml/min (Superose 6 10/300 GL) at 25 °C and analyzed using ASTRA 6 software, yielding molar mass and mass distribution (polydispersity) of the samples. For interaction studies, proteins were mixed and incubated on ice for 30 minutes prior to being applied to the gel filtration column. Protein-containing fractions were analyzed by SDS-PAGE followed by Coomassie brilliant blue staining. Theoretical and experimental masses of all proteins and complexes measured by SEC-MALS are listed in [Table S6](#).

Liquid-liquid phase separation (LLPS) protein-protein interaction assay

Proteins were labeled under conditions that were selective for the N-terminal amino group, as previously described (38). Prior to labeling, purified protein complexes at concentrations of 10-20 μM were dialyzed in a buffer containing 100 mM sodium bicarbonate (pH 8.0), 100 mM NaCl, 5% (v/v) glycerol, and 5 mM DTT. For the labeling reactions three fluorescent dyes were utilized, Bodipy (boron-dipyrromethene) NHS ester (succinimidyl ester; Invitrogen), Coumarin (7-hydroxycoumarin-3-carboxylic acid) NHS ester (Sigma-Aldrich), or Alexa Fluor 647 NHS ester (Invitrogen), each dissolved in dimethyl sulfoxide (DMSO; Sigma-Aldrich) and added at equimolar ratios to the dialyzed protein samples, then incubated for 50 minutes at room temperature. Subsequently, the labeling reaction was quenched by buffer exchange using a 5 ml HiTrap Desalting column, equilibrated in a buffer containing 25 mM TRIS (pH 8.0), 100 mM NaCl, 5% (v/v) glycerol, and 5 mM DTT. Fluorescently labeled proteins were concentrated to 10-20 mg/ml for use in LLPS interaction assays. CNC-hexamer variants were labeled with Bodipy, the CFNC and its subcomplexes Dbp5•Nup159^{NTD}, Nup82^{NTD}•Nup145N^{APD}•Nup159^{TAIL}, Gle2•Nup145N^{GLEBS}, and CFNC-hub were labeled with Alexa Fluor 647, and Gle1•Nup42^{GBM}, Gle1^{NTD}, and Gle1^{CTD}•Nup42^{GBM} were labeled with Coumarin.

LLPS droplet formation was analyzed by fluorescence microscopy with a Carl Zeiss AxioImagerZ.1 microscope equipped with a Hamamatsu C10600 Orca-R2 camera and a 63×oil immersion objective. Fluorescently labeled proteins were mixed directly on a glass coverslip in a total volume of 10 μ l in a buffer containing 25 mM TRIS (pH 8.0), 100 mM NaCl, 5% (v/v) glycerol, and 5 mM DTT. CNC-LLPS formation was triggered by combining Bodipy-labeled CNC-hexamer with a 1.2-fold molar excess of unlabeled Nup84•Nup133 with final concentrations of 8 μ M and 9.6 μ M, respectively. In a stepwise manner, the Alexa Fluor 647- and Coumarin-labeled cytoplasmic filament nups were added to the CNC-LLPS in 1.2-fold molar excess with final concentrations of 9.6 μ M. In a subset of experiments, IP₆ was added at a 200 μ M final concentration. These LLPS mixtures were incubated for 10 minutes at room temperature prior to imaging. Analogously, an SDS-PAGE analysis of proteins present in the LLPS condensate was conducted with unlabeled proteins. The CNC-hexamer at a final concentration of 8 μ M was mixed with a 1.1-fold molar excess of Nup84•Nup133 and the cytoplasmic filament nups in a total volume of 40 μ l. These mixtures were incubated on ice for 10 minutes prior to centrifugation at 20,000 $\times g$ for 10 minutes. The pellet was resuspended in 55 μ l 1.5 \times SDS-PAGE loading dye, while the soluble fraction was transferred to a fresh tube, to which 15 μ l 4 \times SDS-PAGE loading dye was added. Subsequently, the pellet and soluble fractions were analyzed by SDS-PAGE and visualized by Coomassie brilliant blue staining.

Biotinylation of Avi-tagged protein

Biotinylation was carried out with 40 μ M purified Avi-tagged proteins in a buffer containing 50 mM bicine (pH 8.3), 100 mM biotin, 10 mM ATP, 10 mM magnesium acetate, and 30 μ g biotin ligase (BirA) at 30 °C for 2 hours in a total volume of 2 ml. After labeling, proteins were buffer exchanged using a 5 ml HiTrap Desalting column equilibrated in a buffer containing 20 mM TRIS (pH 8.0), 100 mM NaCl, and 5 mM DTT. The extent of biotinylation and efficiency of capture were tested by incubating 10 μ g protein with 50 μ l of Streptavidin MagneSphere Paramagnetic Particles (Promega), followed by a single washing step with 50 μ l buffer containing 20 mM TRIS (pH 8.0), 100 mM NaCl, and 5 mM DTT. The bound proteins were resolved by SDS-PAGE and visualizing by Coomassie brilliant blue staining.

Streptavidin pulldowns of CFNC-hub with Nup37 and Nup145C assembly sensors

Streptavidin magnetic beads were prebound with biotinylated Nup37^{CTE} or Nup145C^{NTE} bait by incubating 50 μ l of resuspended streptavidin beads with 10 μ M bait in 50 μ l buffer containing 20 mM TRIS (pH 8.0), 300 mM NaCl, and 4 mM β -ME for 30 minutes at room temperature. Bait-bound streptavidin beads were washed three times with 50 μ l buffer, discarding the supernatant. Beads were incubated on ice for 30 minutes, with 30 μ l of clarified lysate for the individually expressed Nup82, Nup159 and Nsp1 coiled-coil segments either in isolation, or 10 μ l of each lysate mixed together, then diluted to a total volume of 75 μ l with buffer. Beads were washed twice with 50 μ l buffer discarding the supernatant and then resuspended in 50 μ l buffer and supplemented with SDS loading dye. Competition experiments were performed by mixing 150 μ M unlabeled Nup37^{CTE} or Nup145C^{NTE} into lysate before incubation with bait-bound streptavidin magnetic beads. Competitor protein was added with an ~10-fold excess relative to prey. Bound proteins were analyzed by SDS-PAGE and visualized by Coomassie brilliant blue staining.

In vitro RNA transcription and purification

U₂₀ single stranded ssRNA (5'-GGGUUUUUUUUUUUUUUUUUUUUUU-3'), A₂₀ ssRNA (5'-GGGAA AAAAAAAAAAAAAAAAAA-3'), double stranded dsRNA (5'-GGCCGGGCCCGGTTCCGCCGGG CCCGGCC-3'), CTE1/2 RNA (5'-GUGACAUUUUUCACUAACCUAAGACAGGAGGGCCGUC AGAGCUACUGCCUAAUCCAAGACGGUAAAAGUGAUAAAAAUGUAUCAC-3'), and RNA encoding the placental alkaline phosphatase signal sequence coding region (ALPP^{SSCR},

5'-GGACCAUGCUGGGGCCUGCAUGCUGCUGCUGCUGCUGCUGCUGGGCCUGAGGCUA CAGCCUCGA-3') were prepared by *in vitro* transcription using T7 RNA polymerase in a 1 ml run-off transcription reaction containing 40 mM TRIS (pH 8.0), 20 mM MgCl₂, 2 mM spermidine-HCl, 10 mM DTT, 7.5 mM of each NTP, 15 U inorganic pyrophosphatase from baker's yeast (Sigma-Aldrich), 20 U SUPERase-In (Invitrogen) RNase inhibitor, and 25 µg PCR generated template. After a 4-hour incubation at 37 °C, the RNA was resolved on a 0.5×TBE (44.5 mM TRIS-borate (pH 8.3), 1 mM EDTA), 10% denaturing polyacrylamide-urea gel and visualized by UV shadowing. For purification, the RNA band was excised and passively eluted overnight at 4 °C in a buffer containing 25 mM TRIS (pH 8.0), 300 mM sodium acetate, and 0.5 mM EDTA (pH 8.0), followed by extraction with an acid-phenol:chloroform:isoamyl alcohol (125:134:1) mixture (Invitrogen) and ethanol precipitation. Pelleted RNA was resuspended in a 10 mM TRIS (pH 8.5) buffer. The RNA concentration was measured by UV absorbance at 260 nm.

Radioactive 5'-end labeling of RNA and DNA

Prior to radiolabeling, 600 ng RNA was dephosphorylated with 5 U calf intestinal alkaline phosphatase (New England Biolabs) and 10 U SUPERase-In (Invitrogen) for 1 hour at 37 °C in 1×NEB Buffer 4 (New England Biolabs) containing 50 mM potassium acetate, 20 mM TRIS-acetate, and 10 mM magnesium acetate (pH 7.9). Following dephosphorylation, RNA was extracted twice with an acid-phenol:chloroform:isoamyl alcohol (125:134:1) mixture. After ethanol precipitation, the pelleted RNA was resuspended in 25 µl of a 10 mM TRIS (pH 8.5) buffer. Radioactive ³²P 5'-end labeling of 600 ng of dephosphorylated RNA or DNA oligonucleotides was carried out in a 30 µl reaction mixture volume, composed of 1×PNK buffer (New England Biolabs) containing 70 mM TRIS-HCl (pH 7.6), 10 mM MgCl₂, and 5 mM DTT, supplemented with 0.5 µl γ-³²P-ATP (3,000 Ci/mmol, 10 µCi/µl; Perkin Elmer), 5 U T4 polynucleotide kinase (New England Biolabs), and 10 U SUPERase-In, and incubated for 1 hour at 37 °C. Free nucleotide was removed with a 0.5 ml Zeba Spin Desalting Column (Thermo Scientific), following the manufacturer's protocol. For future experiments, radiolabeled RNAs and DNAs were stored at -80 °C at a concentration of ~5 ng/µl.

Electrophoretic mobility shift assay (EMSA)

Prior to use, U₂₀ ssRNA, A₂₀ ssRNA, dsRNA, CTE1/2 RNA, and ALPP^{SSCR} RNA and ssDNA were diluted in 10 mM TRIS (pH 8.0) heated to 80 °C for 2 minutes and snap cooled on ice and diluted into EMSA buffer containing 20 mM TRIS (pH 8.0), 100 mM NaCl, 1 mM MgCl₂, and 5 mM DTT. A DNA oligonucleotide encoding U1 3' box (5'-ACTTTCTGGAGTTTCAAAAACAGACTGT ACGCCA-3') was used as a ssDNA probe, which was hybridized with a complimentary oligonucleotide (5'-TGGCGTACAGTCTGTTTTGAACTCCAGAAAGT-3') to form a dsDNA probe, as previously described (112). dsDNA was prepared by heating to 80 °C and slowly cooled on the benchtop. Protein was serially diluted in EMSA buffer and mixed with an equal volume of 25 nM RNA/DNA or 2.5 nM RNA/DNA for unlabeled and ³²P radiolabeled probes, respectively. DDX19 binding reactions were supplemented with 5% (v/v) glycerol. The protein-RNA/DNA mixture was incubated on ice for 30 minutes and resolved on a pre-run 0.25×TBE, 5% polyacrylamide gel run at a constant voltage of 10 V/cm for 35 minutes. Unlabeled gels were incubated with SYBR Gold (Invitrogen) stain (1:10,000 dilution in 0.5×TBE) for 3 minutes and imaged on a FluorChem HD2 imager. Radioactive ³²P-end labeled gels were dried, exposed to storage phosphor screen and imaged on a Typhoon FLA 9000 (GE Healthcare).

RAE1•NUP98^{GLEBS} and Gle2•Nup145N^{GLEBS} gel shifts were performed as previously described for RAE1•NUP98^{GLEBS} with minor modifications (57). Protein was serially diluted in 20 mM TRIS (pH 8.5), 150 mM NaCl, and 1 mM DTT and mixed with an equal volume of nucleic acid diluted in the same buffer. The protein-RNA/DNA mixture was incubated 5 minutes at room temperature before being loaded on a pre-run 0.5×TBE (pH 8.5), 6% polyacrylamide native gel

run at a constant voltage of 3 V/cm for 3 hours at 4 °C. The gel was stained with SYBR Gold for 3 minutes and imaged.

Generation of high affinity synthetic antibodies (sABs) by phage display

sABs were obtained by phage display selection using library E and a biotinylated NUP358¹⁴⁵⁻⁶⁷³ bait, following published protocols (77, 113). In the first round, 1 ml of phage library E containing 10^{12} - 10^{13} virions was added to streptavidin magnetic beads pre-coated with 200 nM of biotinylated NUP358¹⁴⁵⁻⁶⁷³ and incubated for 30 minutes. Beads containing bound virions after extensive washing were used to infect freshly grown log-phase *E. coli* XL1-Blue cells (Agilent Technologies). Phages were amplified overnight in 2×YT media with 50 µg/ml ampicillin and 10^9 plaque-forming units/ml M13-KO7 helper phage (New England Biolabs). To increase the stringency of selection, three additional rounds of sorting were performed, using the amplified pool of virions of the preceding round as the input and decreasing the NUP358¹⁴⁵⁻⁶⁷³ concentration to 100 nM, 50 nM and 10 nM in the second, third, and fourth rounds, respectively. Sorting from the second to fourth rounds was done on a Kingfisher instrument. From the second round onward, a 0.1 M glycine (pH 2.7) buffer was used to elute the bound phage from immobilized NUP358¹⁴⁵⁻⁶⁷³. To eliminate potential streptavidin binders, the amplified phage pool after each round was negatively selected against streptavidin magnetic beads before using as input for the next round. After four rounds of selection, the enrichment ratio, defined as phage titer of the NUP358¹⁴⁵⁻⁶⁷³ specific binders over the background, was >50.

A single-point competitive phage ELISA was used to rapidly estimate the affinities of the obtained sABs in phage format (114). Colonies of *E. coli* XL1-Blue harboring phagemids were inoculated directly into 500 µl of 2×YT media supplemented with 100 µg/ml ampicillin and M13-KO7 helper phage. The cultures were grown at 37 °C for 16-20 hours in a 96 deep-well block plate shaken at 280 rpm. 25 nM biotinylated NUP358¹⁴⁵⁻⁶⁷³ was immobilized on ELISA plates (Greiner Bio-One) coated with neutravidin (ThermoFisher) and blocked with 0.5% (w/v) bovine serum albumin (BSA, Sigma-Aldrich) in TRIS-buffered saline (TBS) buffer containing 50 mM TRIS (pH 7.5) and 150 mM NaCl. Culture supernatants containing sAB-phage were diluted ten-fold in TBS-T buffer (TBS buffer supplemented with 0.05% (v/v) Tween-20) in the absence or presence of 50 nM NUP358¹⁴⁵⁻⁶⁷³ protein as soluble competitor in a 96-well plate. After 15-minute incubation at room temperature, the mixtures were transferred to ELISA plates, containing the immobilized NUP358¹⁴⁵⁻⁶⁷³. The ELISA plates were incubated with the phage-competitor mixture for another 15 minutes and then washed with TBS-T buffer. The washed ELISA plates were incubated with a mouse monoclonal HRP conjugated anti-M13 phage coat protein antibody (Invitrogen, 1:5,000 dilution in TBS-T buffer) for 30 minutes. After a final TBS-T buffer wash, the plates were developed with 3,3',5,5'-tetramethylbenzidine (TMB) substrate (Pierce), quenched with 1.0 M HCl, and the absorbance determined spectrophotometrically at 450 nm (A_{450}). For each clone, the ratio of A_{450} in the presence or absence of 50 nM competitor gives the fraction of Fab-phage un-complexed with soluble competitor (competition ratio). DNA of the clones with high ELISA signal and low competition ratio were sequenced to identify the number of unique binders. For Nup358¹⁴⁵⁻⁶⁷³, 62 unique binders were obtained. Binders were ranked on basis of high ELISA signal and low competition ratio then reformatted as sAB in the expression vector pRH2.2 to generate untagged antibody constructs for subsequent expression and purification.

Crystallization and structure determination

Crystallization trials for all proteins were conducted using hanging drop vapor diffusion at 21 °C with drops containing 1 µl of protein and 1 µl of reservoir solution. Details regarding protein crystallization and cryoprotection conditions are supplied in Table S7. X-ray diffraction data were collected at 100 K, on GM/CA-CAT beamlines 23ID-B and 23ID-D at the Advanced Photon Source (APS), and beamline BL12-2 at the Stanford Synchrotron Radiation Source (SSRL). X-ray diffraction data were either processed in HKL2000 (115), or integrated with XDS (116) or DIALS

(117) and scaled with AIMLESS (118). Initial phases were calculated in PHASER (119) or SHARP (120) by single anomalous dispersion (SAD), using anomalous X-ray diffraction data collected at the peak wavelength. The positions of the anomalous scatterers were determined using SHELXD (121) or HYSS (122). The inclusion of additional native and anomalous inflection and high energy remote wavelength X-ray diffraction data in subsequent phase calculations was systematically assessed for their ability to help in the identification of anomalous scatterer positions and to improve the obtained electron density maps. Solvent flattening and NCS averaging were performed in RESOLVE (123) or DM (124), yielding improved phases and electron density maps of excellent quality. Initial models were improved by iterative rounds of model building and refinement using Coot (125) and PHENIX (126), respectively. The final coordinates of all crystal structures exhibit excellent stereochemistry and geometry, as determined by MolProbity (127). Details of data processing and refinement statistics are provided in [Tables S8 to S17](#).

Crystal structure determination of NUP358¹⁴⁵⁻⁶⁷³. NUP358¹⁴⁵⁻⁶⁷³ was crystallized at 21 °C with the hanging drop method using 1 µl of protein solution (20 mg/ml) and 1 µl of reservoir solution, composed of 0.1 M HEPES (pH 7.0), 0.8 M succinic acid (pH 7.0), and 1% (w/v) PEG 2,000 MME. Crystals were cryoprotected by exchange into reservoir solution containing 20% (v/v) ethylene glycol, prior to plunge freezing in liquid nitrogen. Native data were integrated with DIALS (117) and scaled with AIMLESS (118) to 3.8 Å resolution. Anomalous SeMet X-ray diffraction data were collected at three wavelengths, corresponding to the selenium peak, inflection and high energy remote energies, and processed in HKL2000 to 4.2 Å resolution (115). Initial phases were calculated in SHARP (120) by multiple isomorphous replacement with anomalous scattering (MIRAS), identifying 20 selenium sites with 3 molecules in the asymmetric unit (ASU). Density modification in DM with solvent flattening, non-crystallographic symmetry (NCS) averaging, and histogram matching, yielded an electron density map of sufficient quality for *de novo* building of a complete initial model. Iterative rounds of model building and refinement were performed using the 3.8 Å resolution native X-ray diffraction data in Coot (125) and PHENIX (126), respectively. Refinement was performed with NCS restraints, manually assigned for three sections, encompassing residues 148-215, 228-502, and 512-672. The unambiguous assignment of the sequence register was achieved by anomalous difference Fourier map calculations using anomalous X-ray diffraction data, obtained from a series of SeMet-labeled crystals, each harboring methionine substitutions (I169M, I372M, I385M, I401M, I481M, I599M, I615M and I652M). The final structure possessed excellent stereochemistry and geometry and was refined to 3.8 Å resolution with R_{work} and R_{free} values of 20.8% and 24.2%, respectively. For data processing and refinement statistics, see [Tables S8 and S9](#).

Crystal structure determination of NUP358^{NTD}•sAB-14. Despite extensive efforts, NUP358^{NTD} did not yield well diffracting crystals. This hurdle was overcome by systematically employing high affinity, conformation specific, synthetic antibodies (sABs) as crystallization chaperones. Crystals of NUP358^{NTD}•sAB-14 were obtained at 21 °C with the hanging drop method using 1 µl of protein solution (5 mg/ml) and 1 µl of reservoir solution, composed of 0.1 M sodium citrate (pH 4.6), 0.15 M sodium acetate, and 3% (w/v) PEG 4,000. Crystals were cryoprotected by exchange into reservoir solution containing 25% (v/v) ethylene glycol, prior to plunge freezing in liquid nitrogen. Native data was integrated with XDS (116) and scaled with AIMLESS (118) to 3.95 Å resolution. The NUP358^{NTD}•sAB-14 structure was determined by molecular replacement with PHASER (119), using the coordinates of NUP358^{TPR} (PDB ID 4GA0) (76), sAB-158 (PDB ID 5CWS) (11) and NUP358¹⁴⁵⁻⁶⁷³ as search models, identifying two NUP358^{NTD}•sAB-14 complexes per ASU. Model building was aided by a single isomorphous replacement anomalous scattering (SIRAS) experimental map, combining SeMet-peak SAD measurements with native X-ray diffraction data. Refinement was performed using torsion NCS restraints with PHENIX (126). The unambiguous assignment of the NUP358^{NTD} sequence register was further aided by anomalous difference Fourier map calculations from seventeen distinct

SeMet mutant NUP358^{NTD} crystals, introducing eighteen additional selenium sites (T92M, Q137M, D140M, D152M, D171M, I322M, L401M, I427M, I453M, I539M, I559M, I599M, I615M, I626M, I652M, V668M, D693M and N709M), providing a sequence register marker for every α -helix in NUP358^{NTD}, apart from the TPR sub-domain, for which we had previously determined a 0.95 Å resolution structure (76). The final structure possessed excellent stereochemistry and geometry and was refined to 3.95 Å resolution with R_{work} and R_{free} values of 19.2% and 24.1%, respectively. For data processing and refinement statistics, see [Tables S10 to S12](#).

Crystal structure determination of NUP358^{NTD}•sAB-14 ANE1 mutants. Structures of NUP358^{NTD}•sAB-14 harboring the ANE1 T585M, T653I or I656V mutant were individually determined. The three NUP358^{NTD}•sAB-14 ANE1 mutant complexes were crystallized at 21 °C with the hanging drop method using 1 μ l of protein solution (5 mg/ml) and 1 μ l of reservoir solution, composed of 0.1 M sodium citrate (pH 4.6), 0.15 M sodium acetate, and 3.5% (w/v) PEG 4,000. Crystals were cryoprotected by exchange into reservoir solution containing 20% (v/v) ethylene glycol, prior to plunge freezing in liquid nitrogen. Native X-ray diffraction data were integrated with XDS (116) and scaled with AIMLESS (118) to 4.7 Å, 6.7 Å, and 6.7 Å resolution for the NUP358^{NTD}•sAB-14 T585M, T653I, and I656V ANE1 mutant, respectively. All three NUP358^{NTD}•sAB-14 ANE1 mutant structures were determined by molecular replacement with PHASER (119), using the coordinates of wildtype NUP358^{NTD}•sAB-14 as a search model, identifying two complexes per ASU. Refinement was performed using torsion NCS restraints with PHENIX (126). The final structures possessed excellent stereochemistry and geometry and were refined to R_{work}/R_{free} values of 20.4/25.4% (T585M), 21.7/26.3% (T653I), and 20.5/25.4% (I656V). For data processing and refinement statistics, see [Table S10](#).

Crystal structure determination of NUP358^{OE}. NUP358^{OE} was crystallized at 21 °C with the hanging drop method using 1 μ l of protein solution (20 mg/ml) and 1 μ l of reservoir solution, composed of 2.0 M ammonium sulfate and 0.1 M citric acid (pH 3.5). Crystals were cryoprotected by gradual exchange into reservoir solution containing 20% (v/v) ethylene glycol in 5% steps, prior to plunge freezing in liquid nitrogen. The NUP358^{OE} structure was solved in PHASER (119) using highly redundant 1.45 Å resolution anomalous sulfur-SAD X-ray diffraction data, identifying 19 sulfur sites and four molecules per ASU. An initial model was built *de novo* into the experimental electron density map and was iteratively refined using 1.1 Å resolution native X-ray diffraction data in PHENIX (126). The final structure possessed ideal stereochemistry and geometry and was refined to 1.1 Å resolution with R_{work} and R_{free} values of 15.5% and 16.7%, respectively. For data processing and refinement statistics, see [Table S13](#).

Crystal structure determination of NUP358^{ZnF}•Ran(GDP) complexes. NUP358^{ZnF} is composed of eight ZnF modules, ZnF1 does not bind to Ran and ZnF5 and ZnF6 are identical in sequence. Initially, we determined the crystal structures of ZnF2, ZnF3, ZnF4, ZnF5/6, ZnF7, and ZnF8 in complex with Ran(GDP), containing an N-terminal His₆-thrombin cleavage site. Purified NUP358^{ZnF} was mixed with equimolar Ran(GDP) and co-crystallized in similar conditions, containing 0.1 M Bis-TRIS (pH 6.4-7.0) and 17-22% (w/v) PEG 3,350. Crystals were cryoprotected by exchange into reservoir solution containing 20% (v/v) glycerol, prior to plunge freezing in liquid nitrogen. X-ray diffraction data were collected at the zinc edge, with data integrated using XDS (116) or DIALS (117) and scaled with AIMLESS (118) to resolutions in the range of 1.8-2.45 Å. The NUP358^{ZnF}•Ran(GDP) structures were all solved by zinc-SAD using PHASER (119). In the NUP358^{ZnF2}•Ran(GDP) structure, the N-terminal His₆-thrombin-tag occupied Ran's nucleotide-state independent hydrophobic surface pocket. To structurally characterize NUP358^{ZnF2} interactions at this pocket, we re-crystallized NUP358^{ZnF2} with Ran(GDP), using a Ran construct lacking the N-terminal His₆-thrombin-tag, in a reservoir solution, containing 0.1 M Bis-TRIS (pH 6.4) and 17% (w/v) PEG 3,350. All six NUP358^{ZnF}•Ran(GDP) structures were iteratively refined using torsion NCS restraints in PHENIX (126). The final structures possess excellent refinement statistics and exhibit excellent geometry. For data

processing and refinement statistics, see [Table S14](#).

Crystal structure determination of NUP153^{ZnF}•Ran(GDP) complexes. NUP153^{ZnF} is composed of four ZnF modules. We determined NUP153 ZnF1, ZnF2, ZnF3, and ZnF4 in complex with Ran(GDP) containing a thrombin cleavable N-terminal His₆-tag. Purified NUP153^{ZnF} was mixed with equimolar Ran(GDP) and co-crystallized in similar conditions, containing 0.1 M Bis-TRIS (pH 7.5) and 19% (w/v) PEG 3,350. Crystals were cryoprotected by exchange into reservoir solution, containing 20% (v/v) glycerol, prior to plunge freezing in liquid nitrogen. Anomalous X-ray diffraction data were collected at the zinc edge, integrated using XDS (116) and scaled with AIMLESS (118) to resolutions between 1.6-1.9 Å. The NUP153^{ZnF}•Ran(GDP) structures were all solved by zinc-SAD using PHASER (119). As previously observed with NUP358^{ZnF2}•Ran(GDP), all four NUP153^{ZnF}•Ran(GDP) structures determined exhibited a His₆-thrombin-tag bound to Ran's nucleotide-state independent hydrophobic surface pocket. To structurally characterize NUP153^{ZnF} interactions with this pocket, we re-crystallized all four NUP153^{ZnF} domains in complex with Ran(GDP), using a Ran construct lacking the N-terminal thrombin cleavable His₆-tag, in reservoir solution, containing 0.1 M Bis-TRIS (pH 6.0-7.0) and 21% (w/v) PEG 3,350. Crystals were cryoprotected by exchange into reservoir solution containing 20% (v/v) glycerol, prior to plunge freezing in liquid nitrogen. The structures were determined by molecular replacement with the equivalent NUP153^{ZnF}•Ran(GDP) structure containing the His₆-thrombin-tag as a search model using PHASER (119). We report two NUP153^{ZnF3}•Ran(GDP) structures, one at 2.05 Å resolution with data completeness of 93.2%, where specific flexible regions of the structure could not be modeled accurately, and a complete 2.4 Å resolution dataset with additional electron density features. All five NUP153^{ZnF}•Ran(GDP) structures were iteratively refined using torsion NCS restraints in PHENIX (126). The final structures exhibit excellent refinement statistics and stereochemistry. For data processing and refinement statistics, see [Table S15](#).

Structure determination of NUP50^{RanBD}•Ran(GMPPNP) complex. SeMet-labeled Nup50^{RBD} was complexed with nucleotide exchanged Ran(GMPPNP) and crystallized at 21 °C with the hanging drop method using 1 µl of protein solution (20 mg/ml) and 1 µl of reservoir solution, containing 0.1 M HEPES (pH 7.5), 0.2 M ammonium sulfate, and 20% (w/v) PEG 3,350. Crystals were cryoprotected by exchanging the crystallization buffer with reservoir solution containing 20% (v/v) ethylene glycol, prior to plunge freezing in liquid nitrogen. Anomalous X-ray diffraction data was collected at the selenium edge and processed to 2.45 Å resolution with XDS (116) and AIMLESS (118). The NUP50^{RBD}•Ran(GMPPNP) structure was solved by selenium-SAD using PHASER (119), identifying 14 selenium sites and two complexes per ASU. Refinement was performed using torsion NCS restraints with PHENIX (126). The final structure possessed excellent stereochemistry and geometry and was refined to 2.45 Å resolution with R_{work} and R_{free} values of 21.2% and 23.9%, respectively. For data processing and refinement statistics, see [Table S16](#).

Crystal structure determination of NUP358^{RanBD}•Ran(GMPPNP) complexes. NUP358 contains four RanBD domains NUP358^{RanBD-I}, NUP358^{RanBD-II}, NUP358^{RanBD-III}, and NUP358^{RanBD-IV}. Crystals of NUP358^{RanBD-I}•Ran(GMPPNP) were grown in a reservoir solution containing 0.2 M potassium sodium tartrate tetrahydrate and 20% (w/v) PEG 3,350, and were cryoprotected by transfer in reservoir solution supplemented with 20% (v/v) glycerol. Crystals of NUP358^{RanBD-II}•Ran(GMPPNP) were grown in 125 mM magnesium formate and 15% (w/v) PEG 3,350, and were cryoprotected by transfer in reservoir solution supplemented with 20% (v/v) ethylene glycol. Crystals of NUP358^{RanBD-III}•Ran(GMPPNP) were grown in 0.2 M sodium formate and 20% (w/v) PEG 3,350, and were cryoprotected by transfer in reservoir solution supplemented with 25% (v/v) ethylene glycol. All crystals were frozen by plunge freezing in liquid nitrogen. Despite extensive efforts NUP358^{RanBD-IV} initially failed to yield well diffracting crystals. A sequence alignment of all NUP358 RanBD identified a poorly conserved 8-residue surface loop

in NUP358^{RanBD-IV} (residues 2962-2969; WHTMKNY) that was mutated to the corresponding region of NUP358^{RanBD-III} (residues 2359-2366; QNYDNKQV). The modified NUP358^{RanBD-IV}•Ran(GMPPNP) complex crystallized in a reservoir solution, containing 0.1 M HEPES (pH 7.0), 0.1 M ammonium sulfate, and 20% (w/v) PEG 3,350. Crystals were cryoprotected by transfer in reservoir solution supplemented with 20% (v/v) ethylene glycol, prior to plunge freezing in liquid nitrogen. Native X-ray diffraction data was processed with XDS/AIMLESS (116, 118) for RanBD-I and RanBD-IV at 2.4 Å and 2.7 Å resolution, and with DIALS/AIMLESS (117, 118) for RanBD-II and RanBD-III at 2.4 Å and 2.7 Å resolution, respectively. The NUP358^{RanBD}•Ran(GMPPNP) structures were determined by molecular replacement using the coordinates of NUP50^{RanBD}•Ran(GMPPNP) as a search model in PHASER (119). Refinement was performed using torsion NCS restraints with PHENIX (126). The final structures possess excellent refinement statistics and exhibit excellent geometry. For data processing and refinement statistics, see [Table S16](#).

Crystal structure determination of NUP88^{NTD}•NUP98^{APD}. NUP88^{NTD}•NUP98^{APD} was crystallized at 21 °C by the hanging drop method using 1 µl of protein solution (15 mg/ml) and 1 µl of reservoir solution, consisting of 0.1 M TRIS (pH 8.3), 0.22 M NaCl, and 20% (w/v) PEG 4,000. Crystals were cryoprotected by exchanging the crystallization buffer with paratone-N, prior to plunge freezing in liquid nitrogen. X-ray diffraction data were collected at beamline 23ID-B at the Advanced Photon Source (APS). Native data was integrated with XDS (116) and scaled with AIMLESS (118) to 2.0 Å resolution. The NUP88^{NTD}•NUP98^{APD} structure was determined by molecular replacement using the coordinates of the *C. thermophilum* Nup82^{NTD} (PDB ID 5CWW) (11) and human NUP98^{APD} (PDB ID 1KO6) (13) as search models in PHASER (119). Refinement was performed using torsion NCS restraints in PHENIX (126). The final model possessed excellent stereochemistry and geometry and was refined to 2.0 Å resolution with R_{work} and R_{free} values of 17.5% and 20.8%, respectively. For data processing and refinement statistics, see [Table S17](#).

Quantitative docking of NUP358^{NTD} into intact human NPC cryo-ET maps

The open and closed conformations of the NUP358^{NTD} structure were each independently quantitatively docked in the full map of the ~12 Å cryo-ET reconstruction of the intact human NPC (EMD-14322) (46). We used the UCSF Chimera fitmap tool to generate 1 million random placements of densities simulated from the NUP358^{NTD} crystal structures conservatively low pass filtered close to the resolution of the cryo-ET map, at 15 Å (128). Placements were limited to an asymmetric unit of the C8 symmetry-averaged cryo-ET map from which nuclear envelope membrane regions had been eliminated by segmentation with the UCSF Chimera Segger tool (128), and a volume overlap cutoff of 20% was employed to limit the random placements to the cryo-ET map density. To prevent missing any unique placements, we assessed the number of random initial placements in our docking procedure and established 1 million random initial placements as at least 100-fold saturating. To evaluate the docking within a statistical framework, we performed an analysis similar to previous approaches in docking residue-level resolution structures into lower resolution cryo-ET maps (30). After local rigid body optimization of the randomly placed simulated volumes' fit to the cryo-ET map, calculated correlations about the mean (Pearson correlations) were Fisher z-transformed and normalized. The hereby obtained distribution of Fisher z-transformed Pearson correlations was modeled by a normal distribution. Because correct placements are rare events relative to the bulk of random placements, we used the Fisher z-score distribution as a null distribution from which to calculate one-tailed p-values for the top-scoring placements.

Five copies of the NUP358^{NTD} open conformation were identified as top scoring placements per human NPC spoke, for a total of 40 copies per NPC. Whereas the 1st, 3rd, 4th, and 5th highest scoring solutions corresponded to NUP358^{NTD} copies that wrap around the stalk of the Y-shaped CNCs, the 2nd highest scoring solution identified the dome NUP358^{NTD} copy that

sits on top of the other four NUP358^{NTD} copies. All docking solutions identified for the NUP358^{NTD} closed conformation fell below the Pearson correlation score and p-value of the accepted NUP358^{NTD} open conformation placements. Importantly, visual inspection of the top scoring placements in both the human NPC cryo-ET map (fig. S56) and a higher resolution ~7Å region of the cryo-ET map of the *X. laevis* NPC cytoplasmic face protomer (45), which displays emergent secondary structure features (figs. S58 and S59), corroborates the placement of the open over the closed NUP358^{NTD} conformation by clearly establishing the correspondence of the cryo-ET and cryo-EM density with the open conformation of the NUP358 N-terminal TPR sub-domain (residues 1-145).

This analysis, enabled by our novel residue level resolution crystal structures, allowed us to rectify an incorrect assignment of density previously referred to as the 'U-domain' and the 'bridge domain' of the 'NUP358 complex' (45) to the dome copy of NUP358^{NTD} and the distal copy of NUP93^{SOL}, respectively. Considering the unusual triple α -helical solenoid architecture of NUP358^{NTD}, it is unsurprising that *de novo* atomic model building and chain tracing in a distorted anisotropic map led to incorrect density interpretation (fig. S59).

For reference, we performed an equivalent quantitative docking analysis of the NUP358^{NTD} open conformation, whose simulated volume was low pass filtered to 25 Å, into a previously available ~23 Å cryo-ET map of an intact human NPC (44) (fig. S57A). NUP358^{NTD} placements from the docking in the ~12 Å cryo-ET map corresponded to top scoring solutions (1st, 3rd, 4th, and 5th), except for the placement at the proximal inner position, which was scored 53rd highest. Overall, the confidence of placement estimated by p-values was lower for the NUP358^{NTD} open conformation docked in the ~23 Å cryo-ET map than the NUP358^{NTD} open conformation docked in the ~12 Å cryo-ET map. As for the ~12 Å cryo-ET map, all docking solutions identified for the NUP358^{NTD} closed conformation in the ~23 Å cryo-ET map fell below the Pearson correlation score and p-value of the NUP358^{NTD} open conformation placements (fig. S57B).

Placement of remaining cytoplasmic filament nups into the intact human NPC cryo-ET map

After quantitatively docking five NUP358^{NTD} copies into the unexplained density cluster I of the ~12 Å cryo-ET map of the intact human NPC, we attempted to explain leftover unexplained density cluster II by quantitatively docking the following cytoplasmic filament nup complex structures into a ~12 Å cryo-ET map of the intact human NPC from which the hereto explained density corresponding to NUP358^{NTD} and the symmetric core nups, whose docking is outlined in the accompanying manuscript (42), had been subtracted: NUP88^{NTD}•NUP98^{APD}, NUP214^{NTD}•DDX19 (PDB ID 3FMO) (55), GLE1^{CTD}•NUP42^{GBM} (PDB ID 6B4F) (63), RAE1•NUP98^{GLEBS} (PDB ID 3MMY) (57), NUP358^{RanBD-II}•Ran(GMPPNP), NUP358^{ZnF3}•Ran(GTP), and NUP358^{CTD} (PDB ID 4I9Y) (129). As in the quantitative docking of NUP358^{NTD}, we used the UCSF Chimera fitmap tool to perform 1 million random initial placements of densities simulated from the crystal structures and low pass filtered to 15 Å in the subtracted cryo-ET map, followed by local rigid-body fitting and correlation-based scoring. However, due to their small size and featureless globular shape, the available cytoplasmic filament structures could not be confidently assigned to specific locations in the leftover cryo-ET density. Instead, we proceeded to interpret unexplained density cluster II and the rest of the leftover cryo-ET density by manually docking and locally rigid-body fitting cytoplasmic filament structures.

First, we explained the two nearly perpendicular segments of tube-shaped density by manually placing individual coiled-coil segments of a poly-alanine model derived from the *X. laevis* NUP54•NUP58•NUP62 (PDB ID 5C3L) (10) and *C. thermophilum* Nup49•Nup57•Nsp1•Nic96 (PDB ID 5CWS) (11) complexes, in lieu of an experimental structure of the CFNC-hub. Second, based on shape complementarity and the distance restraint imposed by its interaction with NUP214^{TAIL}, we placed the NUP88^{NTD}•NUP98^{APD} into the disk-shaped

density at the base of the long tube-like density assigned to the N-terminal segment of the CFNC-hub coiled-coil and adjacent to the NUP75 arm of the proximal CNC. Third, we placed the NUP214^{NTD}•DDX19 crystal structure into the dumbbell-shaped density that protrudes into the central transport channel, thus tentatively explaining all the density in the unexplained density cluster II. Last, we identified unexplained density between the cytoplasmic bridge NUP155 and the cytoplasmic face of the nuclear envelope that could accommodate the GLE1^{CTD}•NUP42^{GBM} crystal structure (PDB ID 6B4F) (fig. S88) (63). The placement is supported by the proximity of a mutually exclusive binding site for NUP98^{R3} and GLE1^{NTD} on the bridge NUP155 surface (63). All docked structures were locally rigid body fit into the cryo-ET density, but the accuracy of the orientation is inherently limited by the lack of shape features in the structures and the resolution of the cryo-ET map.

Estimation of the root-mean square length of flexible NUP93 linker

The linker spanning the region between the NUP205-binding NUP93^{R2} region and the CFNC-hub-binding NUP93^{R1} region is ~45 residues in length and predicted to be devoid of secondary structure. To estimate the expected distance at which the NUP93^{R1} region is found, we calculated the root-mean square (r.m.s) end-to-end length of a linear polymer chain according to the Gaussian chain model developed by Flory, with a characteristic ratio parameter of ~3, typical for unstructured polypeptide linkers (130, 131).

Placement of ELYS into the ~12 Å cryo-ET map of the intact human NPC

Due to the small size and lack of distinct shape features, the quantitative docking of the *M. musculus* ELYS^{NTD} domain (PDB ID 4I0O) (25) into the ~12 Å cryo-ET map of the intact human NPC after all the hereto explained density has been subtracted did not result in high confidence placements (fig. S89B). Nevertheless, we identified unexplained density in the shape of a crescent with a disk at the base in the nuclear outer rings alongside NUP160. We assigned ELYS^{NTD} β-propeller domains in the disk-like shape, seemingly interfacing with the nuclear envelope at the base of proximal and distal NUP160 copies (fig. S89C). The crescent-like densities are consistent with the α-solenoid ELYS domain (residues 495-1018) (fig. S89D). The anchoring of 32 copies of ELYS by binding to NUP160 in the nuclear outer ring of the human NPC is supported by biochemical and *in vivo* evidence of interaction between ELYS and NUP160 homologs from different species (24, 25, 132).

Docking into the anisotropic single particle cryo-EM map of the *X. laevis* cytoplasmic outer ring

As in the accompanying manuscript, the anisotropic 5.5-7.9 Å composite single particle cryo-EM map of the *X. laevis* cytoplasmic outer ring protomer (EMD-0909) (45) was superposed to the ~12 Å cryo-ET map of the intact human NPC (EMD-14322) (fig. S58) (46). A cytoplasmic outer ring protomer composite structure was then further refined by rigid-body fitting the individual nup and nup complex structures into the 5.5-7.9 Å composite single particle cryo-EM map of the *X. laevis* cytoplasmic outer ring protomer. The map did not include regions corresponding to the proximal copy of NUP93^{SOL}•NUP53^{R2} and NUP214^{NTD}•DDX19, presumably due to omission by the masking applied during map processing.

Docking into the dilated ~37 Å *in situ* cryo-ET map of the human NPC

As in the accompanying manuscript, the anisotropic 5.5-7.9 Å composite single particle cryo-EM map of the *X. laevis* cytoplasmic outer ring protomer (EMD-0909) (45) was superposed to the ~12 Å cryo-ET map of the intact human NPC (EMD-14322) (46). A cytoplasmic outer ring protomer composite structure was then further refined by rigid-body fitting the individual nup and nup complex structures into the 5.5-7.9 Å composite single particle cryo-EM map of the *X. laevis* cytoplasmic outer ring protomer. The map did not include regions corresponding to the proximal copy of NUP93^{SOL}•NUP53^{R2} and NUP214^{NTD}•DDX19, presumably due to omission by the masking applied during map processing.

Plasmid construction for AID-tagged NUP358 and NUP160

The CRISPR/Cas9 gene-editing technique was utilized to tag the N-terminus of NUP358 and the C-terminus of NUP160 at the endogenous loci. HCT116 and DLD1 cells were selected for their amenability to subcellular imaging and stable diploid karyotype (133, 134). Two gRNA plasmids were generated per construct and integrated into pX330 vectors, as previously described (135). Guide RNAs were selected using CRISPR Design Tools (135). For AID-tagged NUP358, the guide RNA primers: 5'-caccgCCACCCCGTCGCCTCGAC-3', 5'-aacGTCGAGGCGACGGG GTGGc-3', 5'-caccgAGCAAGGCTGACGTGGAG-3', 5'-aacCT CCACCAGCCTTGCTc-3' were used. To induce the desired DNA sequence into CRISPR/Cas9-cleaved genomic regions via homology-mediated recombination, the donor vector, pCassette-Hyg-P2A-microAID-NUP358 was built from pCassette (136). Briefly, the homology arms are amplified from genomic DNA extract from HCT116 and DLD1 cells. The DNA sequences of hygromycin, P2A, and micro-AID degren encoding residues 71-114 from plant AID sequence were cloned into pCassette vector between Asc1 and Sbf1 restriction sites. For AID-tagged NUP160, the gRNA plasmids were generated, as previously described (94). The donor vector pCassette-NUP160-NeonGreen-AID-P2A-Hyg was built from pCassette (94). The sequences of homology arms were amplified from genomic DNA extracted from DLD1 cells. The DNA sequence of NeonGreen fluorescent protein, hygromycin, P2A, and three copies of reduced AID tag (65-132 amino acids) were used. All PCR reactions were performed using Platinum SuperFi DNA Polymerase (ThermoFisher).

Construction of cell lines

Ten thousand cells per well were plated in 24-well plates one day before transfection. Plasmids for transfection were purified using the NucleoSpin buffer set (Clontech) and Nucleic acid miniprep columns (VitaScientific). Plasmids were not linearized before transfection. Cells were transfected with 500 ng of donor and sgRNA plasmids in ratio 1:1 using ViaFect (Promega) transfection reagent according to the manufacturer's instructions. Cells were seeded on 100 mm cell culture dishes with the selective antibiotics (hygromycin 200 µg/ml) in complete medium after 72 hours post-transfection and cultured until clones were visualized on a plate. Clones were picked and propagated in regular complete media without selective antibiotics. *AID::NUP358* HCT116, *AID::NUP358* DLD1, and *NUP160::NG-AID* DLD1 cell lines were generated by CRISPR/Cas9. The insertion of the microAID tag was verified by genomic PCR using oligos: 5'-TGTGGT CTTTTTCATTATGCAGTTC-3' and 5'-AACTGGCCCCAAATACCCAG-3'. The insertion of plant E3 ubiquitin ligase, TIR1, in the *AID::NUP358* HCT116, *AID::NUP358* DLD1, and *NUP160::NG-AID* DLD1 cell lines was confirmed, as previously described (136). Briefly, using CRISPR/Cas9, C-terminus of RCC1 was tagged with sequences encoding infra-red fluorescent protein (iRFP670) and TIR1-9Myc, separated by a P2A sequence. The fusion protein is cleaved during translation to yield RCC1^{iRFP670} and TIR1-9myc. Localization and expression of targeted NUP358 and NUP160 were validated using immunofluorescence microscopy and western blot.

Cell culture and synchronization

AID::NUP358 HCT116 cells were grown in McCoy's 5A medium containing 10% fetal bovine serum (FBS), 100 U/ml penicillin, and 100 µg/ml streptomycin. *AID::NUP358* DLD1 and *NUP160::NG-AID* DLD1 cells were grown in Dulbecco's Modified Eagle Medium (DMEM) containing 10% FBS, 100 U/ml penicillin, and 100 µg/ml streptomycin. Cells were cultured in 100 mm cell culture dishes at 37 °C in 5% CO₂/95% humidified incubator. Cell cultures were passaged every 3-4 days using a 0.25% trypsin and 0.05% EDTA solution in phosphate buffered saline (PBS), containing 137 mM NaCl, 2.7 mM KCl, 8 mM sodium hydrogen phosphate and 2 mM potassium dihydrogen phosphate. For NUP358 and NUP160 depletion, the media was supplemented with 1 mM 3-indoleacetic acid (auxin; Sigma-Aldrich), added from a 250 mM auxin-solution in PBS. For synchronization, *AID::NUP358* HCT116 cells were seeded in 24-well plates and grown to ~25% confluency. Nocodazole (Sigma-Aldrich) was then supplemented to the cells with a final concentration of 50 ng/ml. Following 12 hours of incubation,

nocodazole-containing medium was replaced with fresh 37 °C prewarmed medium. Cell populations at this point were mitotically enriched.

Immunofluorescence microscopy

For NUP358 variants localization analysis, different NUP358 variants were cloned into a modified pcDNA3.1 vector (Invitrogen) containing an N-terminal 3×HA-tag using BamHI and NotI restriction sites. For a summary of all mammalian expression constructs, see [Table S4](#). *AID::NUP358* HCT116 cells were grown on Poly-L-lysine coated slides until ~50% confluency. Transfection was performed with Lipofectamine 2000 transfection reagent (Invitrogen) according to the manufacturer's instructions. After 10 hours, the media was removed, and cells are washed in PBS, and fixed in PBS supplemented with 2% (w/v) paraformaldehyde (PFA) for 5 minutes at room temperature. After two washes with PBS, the cells were permeabilized with PBS containing 0.1% (v/v) TritonX-100 (Sigma-Aldrich) for 10 minutes at room temperature. The cells were then washed in PBS and blocked in PBS supplemented with 10% (v/v) FBS for 20 minutes at room temperature. For nuclear envelope staining, the cells were incubated with a 1:1,000 dilution of the monoclonal antibody mAb414 in PBS buffer, supplemented with 0.1% (w/v) saponin and 10% (v/v) FBS for 1 hour at room temperature, followed by three washes with PBS supplemented with 10% (v/v) FBS for 10 minutes at room temperature. Secondary antibody incubation was performed with a 1:3,000 dilution of Alexa Fluor 568-labeled goat anti-mouse antibody (Invitrogen) in PBS, supplemented with 0.1% (w/v) saponin and 10% (v/v) FBS for 1 hour at room temperature, followed by three washes with PBS supplemented with 10% (v/v) FBS for 10 minutes at room temperature. For detection of the HA-tagged proteins, the cells were incubated with a mouse monoclonal anti-HA Fluor488 conjugate antibody (Invitrogen) at 1:2,000 dilution for 16 hours at 4°C, followed by three washes with PBS supplemented with 10% (v/v) FBS for 10 minutes at room temperature. The cells were mounted onto coverslips with ProLong Gold Antifade reagent with DAPI (Invitrogen). Slides were examined by fluorescence microscopy on a Carl Zeiss AxioImagerZ.1 equipped with an AxioCamMRm camera. For localization analysis in the absence of endogenous NUP358, NUP358 depletion was induced by an additional 3-hour incubation with 1mM auxin-containing media, prior to fixation.

For validation of auxin-induced NUP358 depletion, synchronized *AID::NUP358* HCT116 or unsynchronized *AID::NUP358* DLD1 cells were treated with 1 mM auxin at 37 °C. The localization of NUP358 was examined by immunofluorescence after 0, 1, 2, 3, 4, 5, 6, 7, 8, 9, 10, and 24 hours, with a rabbit polyclonal anti-NUP358 antibody (Bethyl Laboratories; 1:500 dilution). Secondary antibody incubation was performed with an Alexa Fluor 488-labeled donkey anti-rabbit antibody (Invitrogen, 1:3,000 dilution). For nuclear envelope staining, the cells were incubated with a 1:1,000 dilution of the monoclonal antibody mAb414 in PBS buffer, supplemented with 0.1% (w/v) saponin and 10% (v/v) FBS for 1 hour at room temperature, followed by three washes with PBS supplemented with 10% (v/v) FBS for 10 minutes at room temperature. Cell handling, fixation, permeabilization, mounting, and fluorescence microscopy analysis were carried out as described above.

For validation of auxin-induced NUP160 depletion, unsynchronized *NUP160::NG-AID* DLD1 cells were treated with 1 mM auxin at 37 °C. The localization of NUP160 was examined by immunofluorescence after 0, 1, 2, 3, 4, 5, 6, 7, 8, 9, 10, and 24 hours, with a rabbit polyclonal anti-NUP160 antibody (St John's Lab; 1:500 dilution). Secondary antibody incubation was performed with an Alexa Fluor 488-labeled donkey anti-rabbit antibody (Invitrogen, 1:3,000 dilution). For nuclear envelope staining, the cells were incubated with a 1:1,000 dilution of the monoclonal antibody mAb414 in PBS buffer, supplemented with 0.1% (w/v) saponin and 10% (v/v) FBS for 1 hour at room temperature, followed by three washes with PBS supplemented with 10% (v/v) FBS for 10 minutes at room temperature. Cell handling, fixation, permeabilization, mounting, and fluorescence microscopy analysis were carried out as described above, apart from NUP160 antibody staining, for which fixing and permeabilization were carried out in a single

15-minute incubation step with -20 °C 100% (v/v) methanol.

The localization of different endogenous nups upon NUP358 depletion was also examined by immunofluorescence microscopy. The synchronized *AID::NUP358* HCT116 cells were treated with 1 mM auxin and fixed after 0, 2, 4, 6, 8, 10, and 24 hours. Cell handling, fixation, permeabilization, and mounting were carried out as described above. The immunofluorescence microscopy analysis was performed with a rabbit polyclonal anti-NUP358 antibody (Bethyl Laboratories; 1:500 dilution), a rabbit polyclonal anti-NUP214 antibody (Abcam; 1:1,000 dilution), a mouse monoclonal anti-NUP88 antibody (Santa Cruz; 1:250 dilution), a rat monoclonal anti-NUP98 antibody (Abcam; 1:500 dilution), a rabbit polyclonal anti-GLE1 antibody (Abcam; 1:500 dilution), a mouse monoclonal mAb414 antibody (BioLegend; 1:1,000 dilution), a rabbit polyclonal anti-NUP160 antibody (St John's Lab; 1:500 dilution), a rabbit polyclonal anti-NUP96 antibody (Bethyl; 1:500 dilution), a rabbit polyclonal anti-NUP133 antibody (Bethyl; 1:500 dilution), and a mouse monoclonal anti-NUP93 antibody (Santa Cruz; 1:200 dilution). Secondary antibody incubation was performed with an Alexa Fluor 488-labeled donkey anti-rabbit antibody (Invitrogen, 1:3,000 dilution), an Alexa Fluor 568-labeled goat anti-mouse antibody (Invitrogen, 1:3,000 dilution), or an Alexa Fluor 488-labeled goat anti-rat antibody (Invitrogen, 1:3,000 dilution).

Cell fractionation

Synchronized *AID::NUP358* HCT116 cells were treated with 1 mM auxin at 37 °C and after 0, 2, 4, 6, 8, 10 and 24 hours cells were trypsinized, washed twice with cold PBS, and harvested by centrifugation at 400 × *g* for 5 minutes at 4 °C. 5×10⁵ cells were pelleted and resuspended in 35 μL lysis buffer, containing 10 mM TRIS (pH 8.0), 320 mM sucrose, 3 mM calcium chloride, 2 mM magnesium acetate, 0.1 mM EDTA, 0.05% Triton X-100, 1 mM DTT, and Complete protease inhibitor cocktail for 15 minutes on ice and spun at 500 × *g* for 5 minutes at 4 °C. The supernatant was kept as the cytoplasmic fraction and then spun at 30,000 × *g* for 15 minutes to clarify, diluted with SDS-PAGE loading dye. Pelleted nuclei were washed with a buffer containing 10 mM TRIS (pH 8.0), 320 mM sucrose, 3 mM calcium chloride, 2 mM magnesium acetate, 0.1 mM EDTA, 1 mM DTT, and Complete protease inhibitor cocktail and spun at 500 × *g* for 5 minutes at 4 °C. The supernatant was aspirated, and the pelleted nuclei were resuspended in SDS-PAGE loading dye. Cytoplasmic and nuclear fractions were boiled at 95 °C for 10 minutes before SDS-PAGE analysis.

Reporter expression analysis

The generation of cDNAs encoding insulin, green fluorescence protein (GFP), and histone 1B (H1B) was previously described (89). The cDNAs encoding anti-inflammatory cytokine interleukin-10 (IL-10), pro-inflammatory cytokine IL-6, tumor necrosis factor alpha (TNF α), membrane-bound alkaline phosphatase placental (ALPP), and large ribosomal subunit protein 26 (RPL26) were obtained commercially (DNASU, Arizona State University; Horizon Discovery Biosciences). DNA fragments encompassing the entire coding regions of insulin, GFP, H1B, IL-10, IL-6, TNF α , ALPP, and RPL26 were amplified by PCR and cloned into a modified pcDNA3.1 vector (Invitrogen) containing a C-terminal 3×FLAG-tag using the KpnI restriction site (137). To avoid transfection differences arising from auxin treatment, we transfected reporter constructs prior to auxin induced degradation of NUP358. Specifically, four hours after release from mitotic arrest synchronized *AID::NUP358* HCT116 cells were transfected with reporter constructs using Lipofectamine 2000, according to the manufacturer's instructions. After 10 hours, the cells were treated with 1 mM auxin in fresh media at 37 °C. After 0, 2, 4, 6, 8, 10, or 24 hours, cells were trypsinized, washed twice with cold PBS, and harvested by centrifugation at 400 × *g* for 5 minutes at 4 °C. Cell pellets were resuspended in 2×SDS-PAGE loading dye and boiled at 95 °C for 10 minutes prior to loading on an SDS-PAGE gel. The relative expression of reporter from auxin treated or untreated cells was quantitated at the 10-hour time point. Bands

were quantitated in Fiji and plotted as a percentage against untreated cells (138). The statistical analysis was carried out using three sets of independent experiments for every analyzed sample. Error bars represent standard error.

Western blot analysis

Expression levels of 3×HA-NUP358, and C-terminal 3×FLAG tagged reporter constructs were assessed by western blot analysis. To collect the whole cell lysates, the transfected cells were trypsinized, washed twice with cold PBS, and harvested by centrifugation at 400 × *g* for 5 minutes at 4 °C. Cell pellets were resuspended in 2×SDS-PAGE loading dye and boiled at 95 °C for 10 minutes prior to loading on an SDS-PAGE gel. Western blot analyses were performed with a mouse monoclonal anti- α -tubulin (Sigma-Aldrich; 1:5,000 dilution), a mouse monoclonal anti-HA (Covance, 1:4,000 dilution), and a mouse monoclonal anti-FLAG (Sigma-Aldrich, 1:4,000 dilution) antibodies, then visualized with and a goat anti-mouse antibody fused to an IR800 fluorescent protein (Licor, 1:5,000 dilution). The imaging was carried out with an IR imager (Li-Cor Odyssey) using the 800 nm channels in a single scan at 169 μ m resolution and a scan intensity of 5. Antibodies were diluted in Superblock-PBS blocking buffer (Thermo Fisher) and washes were carried out in PBS supplemented with 0.05% (v/v) Tween-20 (PBS-T).

For validation of auxin-induced NUP358/NUP160 depletion, the expression levels of NUP358/NUP160 were also examined by western blot analysis. The synchronized *AID::NUP358* HCT116 cells, and unsynchronized *AID::NUP358 DLD1* or *NUP160::NG-AID DLD1* cells were treated with 1 mM auxin at 37 °C. After 0, 1, 2, 3, 4, 5, 6, 7, 8, 9, 10, and 24 hours, the whole cell lysates were collected, as described above. The primary antibodies, including a rabbit polyclonal anti-NUP358 (Bethyl Laboratories; 1:1,000 dilution), a rabbit polyclonal anti-NUP160 (St John's Lab; 1:500 dilution), a mouse monoclonal mAb414 (BioLegend; 1:3,000 dilution), a mouse polyclonal anti-NUP93 (Santa Cruz; 1:200 dilution), a rabbit polyclonal anti-NUP96 (Bethyl; 1: 1,000 dilution), and a mouse monoclonal anti- α -tubulin (Sigma-Aldrich; 1:5,000 dilution), were used. Then a goat anti-mouse or anti-rabbit fused to an IR800 fluorescent protein (Licor, 1:5,000 dilution) secondary antibodies were used.

Both cytoplasmic and nuclear fractions were sampled from auxin treated synchronized *AID::NUP358* HCT116 cells at different times, as described above. The expression levels of different nups were examined by western blot, using a rabbit polyclonal anti-NUP358 (Bethyl Laboratories; 1:1,000 dilution), a rabbit polyclonal anti-NUP214 (Abcam; 1:2,000 dilution), a mouse monoclonal anti-NUP88 (Santa Cruz; 1:500 dilution), a rat monoclonal anti-NUP98 (Abcam; 1:1,000 dilution), a rabbit anti-GLE1 (Abcam; 1:1,000 dilution), a mouse monoclonal mAb414 (BioLegend; 1:3,000 dilution), a rabbit polyclonal anti-NUP160 (St John's Lab; 1:500 dilution), a rabbit polyclonal anti-NUP96 (Bethyl; 1: 1,000 dilution), a rabbit polyclonal anti-NUP133 (Bethyl; 1:1,000 dilution), a rabbit polyclonal anti-NUP43 (gift of Valerie Doye, CRNS Paris, France; 1:1,000 dilution), a rabbit polyclonal anti-ELYS (gift of Iain Mattaj, EMBL Heidelberg, Germany; 1:3,000 dilution), a rabbit polyclonal anti-NUP205 (gift of Ulrike Kutay, ETH Zurich, Switzerland; 1:2,000 dilution), a mouse polyclonal anti-NUP93 (Santa Cruz; 1:200 dilution), a rabbit polyclonal anti-LaminA/C (Abcam; 1:5,000 dilution), a rabbit polyclonal anti-TBP (Abcam; 1:1,000 dilution), and a mouse monoclonal anti- α -tubulin (Sigma-Aldrich; 1:5,000 dilution) antibodies, visualized with goat anti-mouse, goat anti-rabbit, and goat anti-rat secondary antibodies fused to an IR800 fluorescent protein (Licor, 1:5,000 dilution). Antibodies were diluted in Superblock-PBS and washes were carried out in PBS-T.

Pulse-chase RNA export assay

For NUP358/NUP160 depletion, the media of synchronized *AID::NUP358* HCT116, and unsynchronized *AID::NUP358 DLD1* or *NUP160::NG-AID DLD1* cells was supplemented with 1 mM auxin, added from a 250 mM auxin-solution in PBS. Control cells were supplemented with PBS buffer only. After 3 hours, the media was exchanged for DMEM-10% (v/v) FBS,

supplemented with 0.5 mM 5-ethynyl uridine (5-EU; Invitrogen) and 1 mM auxin. After 1-hour pulse-labeling of newly synthesized RNA, the media was exchanged for fresh DMEM-10% (v/v) FBS, supplemented with auxin, and either fixed immediately, using a 4% (w/v) PFA solution in PBS, or fixed after an additional 1-, 2-, 3-, 4-, or 5-hour chase. The fixed cells were washed with PBS and permeabilized using 0.1% (v/v) Triton X-100 for 15 minutes at room temperature. 5-EU labeling of cells was visualized according to the manufacturer's instructions (Invitrogen, Click-iT RNA imaging kits). Briefly, the samples were incubated for 30 minutes at room temperature with a 1×Click-iT reaction cocktail, containing Alexa Fluor 594 azide and copper sulfate. After removal of the reaction cocktail, cells were washed once with Click-iT reaction rinse buffer. After this step, samples were processed further for NUP358 or NUP160 antibody staining. The statistical analysis was carried out using three sets of independent images with at least 200 cells each for every analyzed sample. Error bars represent standard error.

Thermosolubility pelleting assay

10 µg of purified NUP358^{NTD}, wildtype or harboring ANE1 mutations, were incubated in a total volume of 50 µl for 20 minutes at 30-43 °C, increased in 1 °C increments. An additional titration was performed for NUP358^{NTD} ANE1 W681C and wildtype protein from 15-33 °C, increased in 3 °C increments. Soluble and pellet fractions were separated by centrifugation at 30,000 × *g* for 15 minutes at 4 °C, resolved by SDS-PAGE, and visualized by Coomassie brilliant blue staining. Bands were quantitated in Fiji and plotted as a percentage of the soluble fraction per temperature point (138).

Illustrations and figures

Gel filtration profiles and MALS graphs were generated in IGOR (WaveMetrics) and assembled in Illustrator (Adobe). Sequence alignments were generated using ClustalX (139) and colored with ALSCRIPT (140). Electrostatic potentials were calculated with APBS (Adaptive Poisson-Blotzmann Solver) software (141). Structure figures were generated with PyMOL (www.pymol.org).

Supplementary Text

Modular architecture of the evolutionarily conserved 6-protein cytoplasmic filament nup complex

Although pair-wise interactions between selected CF nups had previously been reported, comprehensive knowledge on the entire CF nup interaction network has remained unavailable to date (11, 47-64). We had previously found that nups from the thermophilic fungus *C. thermophilum* exhibit superior biochemical stability, allowing us to overcome long-standing technical challenges and elucidate the interaction network of the seventeen symmetric core nups (38). We therefore first sought to establish the protein-protein interaction network and complex stoichiometry of the eight evolutionarily conserved *C. thermophilum* CF nups Nup82, Nup159, Nsp1, Nup145N, Gle2, Dbp5, Gle1, and Nup42 (Fig. 1B and fig. S1) (2). Most CF nups contain both structured and unstructured regions that can harbor multiple distinct binding sites and FG repeats (Fig. 1B). We established expression and purification protocols for the *C. thermophilum* CF nups, omitting FG-repeat regions as well as an unstructured linker region in Nup145N to improve solubility, and analyzed their binding by size-exclusion chromatography coupled with multiangle light scattering (SEC-MALS) (figs. S1 to S3 and tables S1 to S5).

Nup82 and Nup159 both contain N-terminal β -propeller domains and C-terminal tripartite coiled-coil segments (CCS1-3), which have previously been shown to complex with the similarly built C-terminal coiled-coil region of Nsp1 (49, 142). Another complex has previously been shown to be formed between the Gle2 β -propeller and the Gle2-binding sequence (GLEBS) motif of Nup145N (48, 57). Mixing of the Nup82•Nup159•Nsp1 and Gle2•Nup145N complexes with the DEAD-box RNA helicase Dbp5 resulted in the stoichiometric hetero-hexameric CFNC (Fig. 1, C and D and fig. S4A and table S6). To further map CF nup interactions within this complex, we systematically removed individual fragments and domains from the CFNC and probed for remaining interactions (fig. S4). Consistent with previous characterizations of isolated CF nup dimers and trimers (11, 47-64), this analysis established that the Nup82 N-terminal β -propeller domain binds an α -helical TAIL segment in Nup159 and the Nup145N autoproteolytic domain (APD), which in turn recruits Gle2 (Fig. 1C and fig. S4). Analogously, the Nup159 N-terminal β -propeller domain provides the binding site for Dbp5 (Fig. 1C and fig. S4). These results suggested that the CFNC must be held together by the C-terminal coiled-coil regions of Nup82, Nup159, and Nsp1. Indeed, when the CFNC is divided into four distinct stable subcomplexes, the Nup82•Nup159•Nsp1 C-terminal coiled-coil hetero-trimer, Nup82^{NTD}•Nup159^{TAIL}•Nup145N^{APD}, Nup159^{NTD}•Dbp5, and Gle2•Nup145N^{GLEBS}, their mixing did not result in any additional interactions and the four subcomplexes did not bind each other, demonstrating that the entire CFNC is held together by interactions in the Nup82•Nup159•Nsp1 C-terminal coiled-coil heterotrimer (fig. S5). In addition to the CFNC, Nsp1 is also an essential part of the hetero-trimeric CNT, where it forms a parallel array of three coiled-coil segments together with Nup49 and Nup57 (10, 11). Given these similarities, we wondered whether the coiled-coil segments of Nup82•Nup159•Nsp1 also formed a parallel coiled-coil domain. Indeed, we were able to reconstitute separate stoichiometric complexes of the CCS1 and the CCS2-3 coiled-coil regions of Nup82•Nup159•Nsp1, consistent with the CCS1-3 coiled-coil regions of Nup82, Nup159, and Nsp1 forming a CFNC-hub similar to the CNT (fig. S6).

Having characterized the protein-protein interactions within the CFNC, we next tested whether the reconstituted complex was capable of binding to the hetero-octameric CNC (Nup120•Nup37•Elys•Nup85•Sec13•Nup145C•Nup84•Nup133^{ANTE}), its neighbor in the intact NPC (fig. S7). Indeed, the reconstituted CFNC and CNC formed a stoichiometric 1:1 complex that was dependent on the CFNC-hub (fig. S8). Because the structurally related CNT is recruited to NPCs through a 39-residue α -helical assembly sensor supplied by Nic96 (11), we next asked whether the CNC harbors equivalent assembly sensors for the CFNC-hub. Among the CNC subunits, Nup133, Nup145C, Nup85, and Nup37 each have N- or C-terminal primarily

unstructured extensions (NTEs, CTEs) that could potentially contain assembly sensors and were tested for binding to the CFNC-hub. This systematic analysis identified Nup37^{CTE} and Nup145C^{NTE} as binding partners (fig. S9). Deletion of the CTE from Nup37 abolished its binding to the CFNC-hub, showing that Nup37^{CTE} is both necessary and sufficient for binding (fig. S10). Moreover, removal of Nup37^{CTE} from the intact CNC substantially reduced its interactions with the CFNC (fig. S11A). While the removal of Nup145C^{NTE} alone from the CNC had no detectable effect, simultaneous elimination of both Nup37^{CTE} and Nup145C^{NTE} almost completely abolished the interaction with CFNC (fig. S11, B and C). Preferential CFNC-hub recruitment by Nup37^{CTE} persisted when the CNC was dissected into its three subcomplexes, with weak and stoichiometric interactions formed with Sec13•Nup145C and Nup120•Nup37•Elys•Nup85, respectively (fig. S12). Vestigial CFNC binding to a CNC lacking both Nup37^{CTE} and Nup145C^{NTE} was mapped to a weak CNC-interaction with Gle2-Nup145N^{GLEBS} (fig. S13).

In the CNT•Nic96 crystal structure, the 39-residue Nic96 assembly sensor forms two ~10-residue α -helical segments joined by an ~15-residue linker, with the C-terminal helix being necessary and sufficient for CNT binding (11). Secondary structure predictions for both Nup37^{CTE} and Nup145C^{NTE} suggest comparable arrangements of two shorter α -helices separated by a linker from a longer α -helix. Moreover, Nup145C^{NTE} interactions have previously been mapped to an equivalent region, encompassing the C-terminal helix followed by a short unstructured segment (62). Through systematic truncation of Nup37^{CTE}, we mapped its minimal CFNC-hub binding site to the predicted C-terminal helix and a short unstructured region (fig S14). This demonstrates that the predicted C-terminal α -helix in both Nup37^{CTE} and Nup145C^{NTE} assembly sensors is necessary and sufficient for CFNC-hub binding, whereas the N-terminal helices likely adopt an organizational role in stabilizing a specific tertiary structure of the three coiled-coil segments, as previously observed for the CNT-Nic96 interaction (11).

Next, we asked whether Nup145C^{NTE} and Nup37^{CTE} function as *bona fide* assembly sensors for the CFNC-hub by recognizing intact hetero-trimeric coiled-coils but not isolated CFNC-hub constituents. Pulldown experiments probing Nup37^{CTE} or Nup145C^{NTE} with bacterial lysates containing individual CFNC-hub components or a mixture of all three, revealed that both fragments bound exclusively to the assembled hetero-trimeric CFNC-hub, but failed to recognize individual component nups (fig. S15, A and B). Moreover, splitting the CFNC-hub into CCS1 and CCS2-3 portions revealed that both Nup37^{CTE} and Nup145C^{NTE} bind preferentially to CCS2-3, albeit weaker than to the intact CFNC-hub CCS1-3 (figs. S6 and S15C).

Because our SEC-MALS analysis indicated that the CNC only binds to a single CFNC copy, we investigated whether Nup37^{CTE} and Nup145C^{NTE} can simultaneously bind to the CFNC-hub. We found that Nup37^{CTE} and Nup145C^{NTE} bind the CFNC-hub in a mutually exclusive manner, via a hydrophobic interface stable in a high salt (1 M NaCl) buffer (figs. S15D and S16). In fact, Nup37^{CTE} outcompetes Nup145C^{NTE} for CFNC-hub binding, consistent with both our intact CNC and CFNC interaction experiments (figs. S12 and S17). Although we conducted our SEC-MALS analyses at the highest feasible concentrations, we acknowledge the apparent discrepancy arising from the detection of a single CFNC binding to an intact CNC that harbored two assembly sensor binding sites, yet at permissible concentrations Nup145C^{NTE} interactions are unstable.

In addition to the hetero-hexameric CFNC analyzed thus far, Gle1 and Nup42 locate to the cytoplasmic face of the NPC, where they are involved in the export and remodeling of mRNPs (63). Gle1 can interact with Dbp5 in an IP₆-dependent manner and also binds Nup42 at its Gle1-binding motif (GBM) (53, 58, 63, 65). To further characterize nup complex interactions at the cytoplasmic NPC side, we tested for incorporation of Gle1•Nup42^{GBM} into the CFNC or CNC. Despite binding only weakly to its known interaction partner Dbp5 in isolation, Gle1•Nup42^{GBM} formed a stable, stoichiometric, hetero-octameric complex with the CFNC that cannot be mapped to any of its sub-complexes, indicating a distributed binding site (Fig. 1E and figs. S18 to S21).

Furthermore, Gle1•Nup42^{GBM} alone does not interact with the CNC, but it can be incorporated into the CNC•CFNC complex, forming a stoichiometric ~1.2 MDa 16-protein nup assembly (Fig. 1F and figs. S22 and S23A). Because the Gle1-Dbp5 interaction is IP₆-dependent (53, 65), we carried out all SEC-MALS interaction experiments involving Gle1•Nup42^{GBM} in the presence of IP₆. However, when Gle1•Nup42^{GBM}, CNC, and CFNC were mixed in the absence of IP₆, the resulting complex displayed a molecular mass of ~2.0 MDa, consistent with the formation of a stoichiometric dimer of the 16-protein complex (fig. S23B). We systematically mapped this biochemical behavior and identified a novel interaction between Gle1^{CTD}•Nup42^{GBM} and the CNC, establishing that the CNC-CF nup interaction network can be remodeled by IP₆ (figs. S23 to S25).

For the Y-shaped CNC, we had previously observed liquid-liquid phase separation (LLPS) when subcomplexes representing its upper arms (Nup120•Nup37•Elys•Nup85•Sec13•Nup145C, CNC-hexamer) and base (Nup84•Nup133) were mixed (38). This LLPS formation depended on the N-terminal extension (NTE) of Nup133, which mediates head-to-tail *trans*-interactions between CNCs (21). In fact, interaction analyses involving CNCs by SEC-MALS require prevention of LLPS formation by removal of Nup133^{NTE} and are also limited by an inherent CNC solubility limit of 8 μM. To rule out having missed interactions between coat and CF nups in our SEC-MALS analyses because of these limitations, we re-tested binding behaviors by measuring the incorporation of the respective CF nup complexes into a CNC LLPS condensate. Importantly, these interaction analyses performed at higher concentrations corroborated all of our SEC-MALS findings (Fig. 1, G and H, and fig. S26).

Given the special importance of the CF nups for human disease, we next tested whether the molecular architecture of the CFNC is evolutionarily conserved from *C. thermophilum* to humans. The human CFNC is comprised of NUP88 (*ctNup82*), NUP214 (*ctNup159*), NUP62 (*ctNsp1*), DDX19 (*ctDbp5*), RAE1 (*ctGle2*), and NUP98 (*ctNup145N*). Apart from a rearrangement of the FG-repeat and coiled-coil regions in NUP214, the domain organization of the human CFNC nups is identical to that of the *C. thermophilum* orthologs (Fig. 2, A and B and fig. S27). As in *C. thermophilum*, we developed expression and purification protocols omitting FG-repeat and unstructured regions and analyzed CFNC nup interactions by SEC-MALS. Indeed, mixing of the NUP88•NUP214•NUP62 hetero-trimer with RAE1•NUP98 and DDX19 resulted in a monodisperse stoichiometric ~337 kDa *H. sapiens* CFNC hetero-hexamer (Fig. 2C and figs. S28 and S29). To establish whether the *hsCFNC* adopts the same modular architecture as in *C. thermophilum*, we dissected the human CF nups to generate CFNC sub-complexes and carried out a systematic pairwise SEC-MALS interaction analysis (Fig. 2D and figs. S30 to S39). Showing complete evolutionary conservation, the human CFNC could be divided into the same four subcomplexes we found in our analysis of the *C. thermophilum* CF nups: NUP88^{NTD}•NUP98^{APD}•NUP214^{TAIL}, NUP214^{NTD}•DDX19, RAE1•NUP98^{GLEBS}, and the NUP88•NUP214•NUP62 coiled-coil complex (*hsCFNC-hub*) (Fig. 2D and figs. S30 to S39). Because the identified Nup37 and Nup145C coat nup assembly sensors for the intact CFNC in *C. thermophilum* each contain ~60-residue regions with three short α-helices, we conducted secondary structure predictions of all ten human coat nups. This analysis confirmed the presence of extended unstructured regions in NUP96, NUP107, and NUP133, yet analogous assembly sensor motifs could not be identified.

Together, our data establish that the CF nups form an evolutionarily conserved six-protein complex that is held together by an extensive parallel coiled-coil hub generated by the C-terminal regions of Nup82/NUP88, Nup159/NUP214 and Nsp1/NUP62, which shares architectural similarities with the heterotrimeric Nsp1/NUP62•Nup49/NUP58•Nup57/NUP54 CNT (11). The Nup82/NUP88 N-terminal β-propeller domain is attached by an interaction between the C-terminal α-helical TAIL fragment of Nup159/NUP214 and provides a binding site for the Nup145N/NUP98 APD, which in turn recruits Gle2/RAE1 to the NPC. Analogously, the Nup159/NUP214 N-terminal β-propeller domain provides a binding site for the DEAD-box helicase Dbp5/DDX19. In

C. thermophilum, the CFNC-hub is anchored to the CNC by two distinct assembly sensors in Nup37^{CTE} and Nup145C^{NTE}, similar to the anchoring of the CNT by the Nic96^{R1}/NUP93^{R1} assembly sensor in the inner ring. In contrast, the human CNC lacks comparable assembly sensor motifs, suggesting alternative mechanisms for anchoring CF nups at the cytoplasmic face of the human NPC.

RNA interactions of human cytoplasmic filament nups

Taking advantage of our complete set of purified human CF nup domains and sub-complexes, we carried out a comprehensive electrophoretic mobility shift assay (EMSA) screen to systematically assess binding against a consistent set of ss/dsRNA probes (Fig. 2F). We selected a 12 bp GC-rich stem loop capped by a UUCG tetraloop dsRNA and U₂₀ ssRNA as generic probes. Positive RNA interactions were subsequently validated by titrating the protein concentration in EMSAs to establish approximate apparent binding constants (K_{Ds}) (fig. S40). Additionally, to establish whether the observed binding was RNA-specific, we tested all CF nups for binding to ss/dsDNA using a U1 3'-box ssDNA oligonucleotide in the absence and presence of a complimentary ssDNA oligonucleotide.

First, we assayed the CFNC nups for nucleic acid binding. Both RAE1•NUP98^{GLEBS} and DDX19 bound ss/dsRNA, as previously shown (fig. S40, B and C) (50, 57). We discovered moderate binding of NUP88^{NTD} and GLE1^{CTD}•NUP42^{GBM} to ssRNA (Fig. 2H and fig. S40A). In the context of the NUP88^{NTD}•NUP98^{APD}•NUP214^{TAIL} complex, NUP88^{NTD} binding was specifically enhanced to ssRNA, exhibiting a $K_D \approx 150$ nM compared to $K_{Ds} > 5$ μ M for dsRNA and ss/dsDNA probes (fig. S40A). In contrast, GLE1^{CTD}•NUP42^{GBM} bound both ssRNA and ssDNA weakly with $K_{Ds} > 2$ μ M. We found that the orthologous *C. thermophilum* Nup82^{NTD}•Nup145C^{APD}•Nup159^{TAIL}, Gle1^{CTD}•Nup42^{GBM}, and Gle2•Nup145C^{GLEBS} complexes bound ssRNA, demonstrating that RNA binding is an evolutionarily conserved feature of CFNC nups (Fig. 2H and fig. S40D).

Next, we analyzed the RNA-binding properties of the metazoan-specific NUP358, taking advantage of structurally well-defined domain boundaries for the N-terminal domain (NTD), oligomerization element (OE), four distinct Ran-binding domains (RanBDs), a zinc-finger domain (ZFD) comprising eight C4-type zinc-finger motifs (ZnF) arranged in tandem, and the C-terminal prolyl isomerase domain (CTD) (see below) (71, 72, 110, 129). Previously, NUP358^{ZFD} was shown to bind to a 63 nt RNA fragment encoding the signal sequence coding region (SSCR) of insulin, an interaction that was abolished in the presence of Ran(GDP/GTP) (89). Using our four nucleic acid probes, we did not detect RNA binding for NUP358^{OE}, NUP358^{ZFD}, or NUP358^{CTD} at the assayed concentrations (Fig. 2F). However, we detected moderate RNA and DNA binding for NUP358^{NTD} (Fig. 2G and fig. S40G). Because the previously identified insulin SSCR RNA binding partner for NUP358 was sensitive to degradation, we systematically tested RNAs encoding the SSCRs of other secretory proteins. This analysis identified the 63 nt placental alkaline phosphatase (ALPP) SSCR RNA as most amenable to biochemical studies (fig. S40I). Whereas we only observed an insubstantial shift of ALPP^{SSCR} RNA with NUP358^{ZFD}, NUP358^{NTD} robustly bound to ALPP^{SSCR} RNA with a $K_D \approx 150$ nM, ~4-fold tighter than our generic ssRNA or dsRNA probes (fig. S40I). Unexpectedly, we also found that the four NUP358^{RanBD}•Ran(GMPPNP) complexes preferentially bound ssRNA, with a $K_D \approx 500$ nM, over dsRNA and ss/dsDNA (Fig. 2G and fig. S40E). To test whether RNA binding is a general property of RanBDs when bound to Ran, we assayed the related nuclear basket NUP50^{RanBD}•Ran(GMPPNP) complex, but detected weaker binding to RNA and DNA (fig. S40, E and F).

Together, our systematic CF nup analysis confirmed previously established RNA binding sites in DDX19, p15•TAP, and RAE1•NUP98^{GLEBS}, whilst uncovering novel sites in NUP88^{NTD}•NUP214^{TAIL}•NUP98^{APD}, GLE1^{CTD}•NUP42^{GBM}, NUP358^{NTD}, and the four NUP358 RanBD•Ran(GMPPNP) complexes.

Ran interactions with human asymmetric nups

Nucleocytoplasmic transport depends on Karyopherin transport factors (Kaps) and a gradient in the state of the small GTPase Ran from the Ran(GDP)-high cytoplasm to the Ran(GTP)-high nucleus (2, 7, 9). Import Kap•cargo complexes assembled in the cytoplasm enter the central transport channel of the NPC and are disassembled upon arrival in the nucleus by Kap binding to Ran(GTP), which triggers the release of the bound cargo. Conversely, Ran(GTP) is an obligate component of nuclear export Kap•cargo complexes, which are disassembled upon activation of Ran's GTPase activity at the cytoplasmic face of the NPC (7). Multiple Ran binding sites are distributed among the asymmetric nups at the cytoplasmic and nuclear sides of the NPC in the form of distinct Ran-binding domains (RanBDs) and Zn²⁺-finger (ZnF) modules. On the cytoplasmic face, NUP358 contains four dispersed RanBDs and a central zinc finger domain (ZFD) with a tandem array of eight ZnFs (Fig. 3A) (80). On the nuclear side, NUP153 and NUP50 contain a central ZFD with four ZnFs and a solitary C-terminal RanBD, respectively (fig. S51) (81, 82).

Testing the Ran(GDP/GTP)-binding activity of all 17 domains by SEC-MALS, we confirmed that all domains bound to Ran as expected except for NUP358^{ZnF1} (Fig. 3, I and J, and figs. S51 to S55). Consistent with previous reports, the RanBDs of NUP358 and NUP50 only bound Ran(GTP), whereas the ZnFs in NUP358 and NUP153 bound Ran in both nucleotide states but showed a preference for Ran(GDP) (figs. S52 and S54) (80, 83-85). To clarify the molecular basis for the differential binding behaviors, we determined the co-crystal structures of all 16 domains bound to Ran in their preferred nucleotide-bound state at 1.8 Å-2.45 Å resolutions (tables S14 to S16 and figs. S51 and S55).

All eleven NUP358/NUP153 ZnFs form small, ~36-residue spherical domains stabilized by a central Zn²⁺ ion coordinated by the sulfhydryl groups of four conserved cysteines (Fig. 3K and fig. S51). The primary interface between the ZnFs and Ran(GDP) is a flat hydrophobic composite surface formed by Ran's switch-I and -II regions, as previously described (Fig. 3K and fig. S51) (84, 85). However, an additional ZnF-Ran interaction was also observed in all structures, which was formed between a phenylalanine or leucine in a ~10-residue unstructured extension N-terminal to the ZnF module and a nucleotide state-independent hydrophobic pocket on the Ran surface (Fig. 3K, fig. S51, and Movie 3). Removal of this extension from ZnFs eliminated Ran(GTP)-binding, showing that the secondary interaction we observed is responsible for the weak Ran(GTP)-binding capacity of NUP358/NUP153 ZnFs (fig. S52). Structural elucidation of the ZnF-Ran interfaces also showed that NUP358^{ZnF1} harbors sequence variations at important sites, explaining its weakened Ran(GDP) binding we observed biochemically (figs. S51 and S52). Furthermore, the NUP358 ZnF structures revealed an absence of conserved residues mediating canonical RNA binding, providing a molecular explanation for the surprising lack of RNA binding we observed biochemically contrary to previous reports (Fig. 2F and fig. S53) (89, 143, 144).

The crystal structures of the five NUP358/NUP50 RanBD•Ran(GMPPNP) complexes show that they have the same architecture as previously observed for the NUP358^{RanBD-I}•Ran complex (Fig. 3L and fig. S55 and table S16) (110). In addition to the previously described interactions between the pleckstrin-homology-fold of RanBDs and Ran(GMPPNP), we observed an extensive positively charged surface patch in all five RanBDs that sequesters Ran's acidic C-terminal DEDDDL motif and is necessary for tight binding (145). Ran's C-terminal α -helix binds to a conserved groove on the surface of all five RanBDs, but shows some plasticity in the exact molecular interactions (fig. S55E). Interestingly, the same hydrophobic Ran pocket bound by ZnF N-terminal extensions (NTEs) in the ZnF•Ran(GDP) complex structures is occupied by a proline or leucine residue in the ~20-residue NTEs of all four NUP358 RanBDs, but not the NUP50 RanBD (fig. S55C and Movie 4).

Together, our data establish that the human CF and nuclear basket nups NUP358, NUP153, and NUP50 harbor a total of 16 distinct Ran binding sites that, considering their

stoichiometry in the NPC, could together recruit up to several hundred Ran molecules. Considering the substantial size difference between metazoan and *S. cerevisiae* cells, it is conceivable that additional Ran binding sites provided by the metazoan-specific asymmetric nups NUP358 and NUP153 help ensure high enough Ran-concentrations in the NPC vicinity to enable nucleocytoplasmic transport, as has been previously suggested (85).

Structural and biochemical analysis of NUP88^{NTD}•NUP98^{APD}•NUP214^{TAIL}

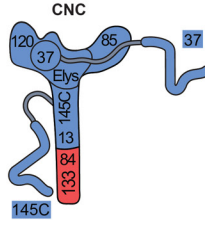
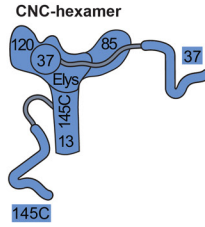
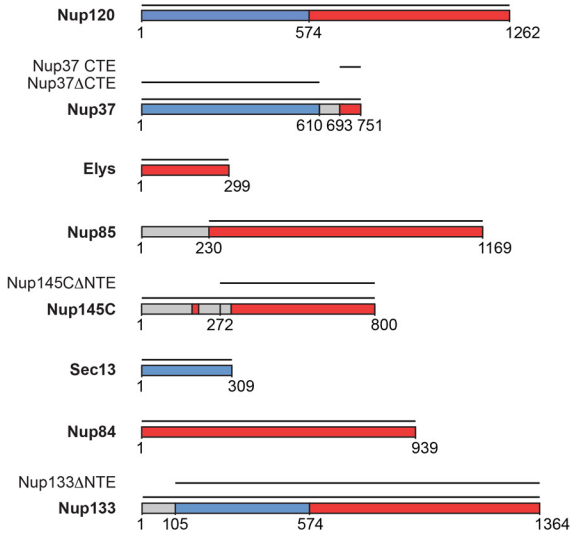
NUP88^{NTD} forms a seven-bladed β -propeller domain, which is extensively decorated by a series of extended loops and insertions, with NUP98^{APD} bound to the fourth and fifth blades (fig. S74, A and B). NUP88^{NTD} and NUP98^{APD} form a bipartite interaction through a cross-handshake exchange of loops. NUP98^{APD} extends the K/R loop to present residue K814 to hydrogen bond with the NUP88^{NTD} 4D5A loop backbone carbonyls of N273 and G308 (Fig. 6H). The tight K814 coordination forms a robust interaction, which is dependent on the conformation of NUP88^{NTD} 4D5A loop. Indeed, severing requires an aggressive combination mutant of four 4D5A loop residues (E275A, M299A, N306A, and Y307A; EMNY) (fig. S74, D and E). The FGL loop of NUP88^{NTD} reaches over to bind into a hydrophobic groove of NUP98^{APD} (Fig. 6H). Removal of the FGL loop leads to weakened interactions between NUP88^{NTD} and NUP98^{APD} (fig. S74F). Despite low sequence homology, the overall architecture of the NUP88^{NTD}•NUP98^{APD} complex is conserved from fungi to humans, although the orientation of NUP98^{APD} relative to NUP88^{NTD} varies between the co-crystal structures of human and fungal orthologs by as much as $\sim 20^\circ$ (figs. S75 to S77, and Movie 5) (11, 59).

Because the NUP214^{TAIL}-NUP88^{NTD} interaction was crystallographically intractable, we mapped a minimal NUP88^{NTD}-binding region spanning NUP214 residues 938-955 by systematic truncation (figs. S78 and S79). NUP214^{TAIL} forms a hydrophobic interaction with NUP88^{NTD} at the 6CD insertion, which was abolished by a combined NUP88^{NTD} LLL mutation (L424A, L428A, and L438A), analogous to a mutation we had previously shown to abolish the interaction between the *S. cerevisiae* orthologs Nup159^{TAIL} and Nup82^{NTD} (fig. S79E) (59). Interestingly, this NUP88 LLL mutation straddles a naturally occurring D434Y mutation in NUP88 linked to a fatal disorder called fetal akinesia deformation sequence (FADS), which is associated with congenital malformations and impaired fetal movement (fig. S80) (93). Given its location, the D434Y mutation is expected to interfere with the NUP214^{TAIL} interaction.

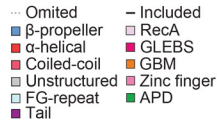
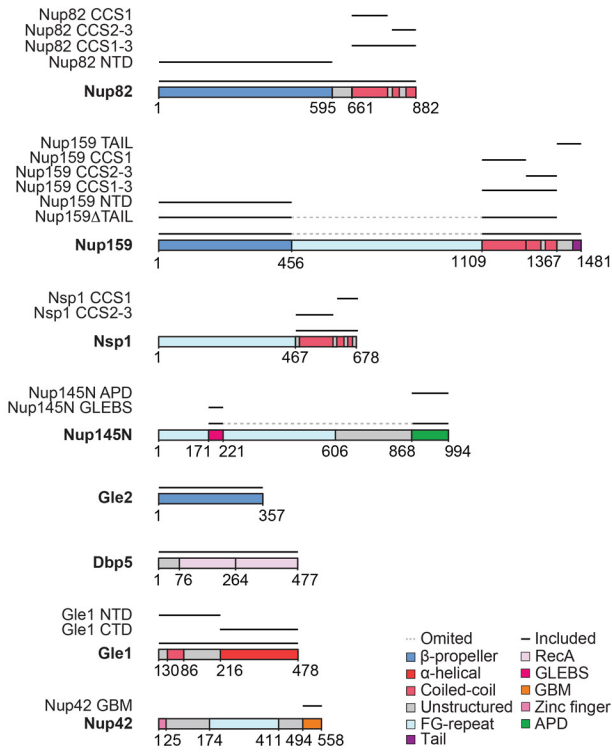
Complementing our earlier NUP358^{NTD} surface mutagenesis, we also performed structure-driven mutagenesis of NUP88^{NTD} to identify the NUP358^{NTD} binding site, focusing on acidic surface residues expected to bind to the basic NUP358^{NTD} concave surface. Indeed, we identified several alanine substitutions of acidic residues at the tip of the 6CD insertion and in the adjacent 5C5D extended loop that abolished NUP358^{NTD} binding (fig. S81).

Combined, our structural and biochemical data reveal the molecular details of the interactions between NUP88, NUP214, and NUP98, uncovering that despite the divergence of individual nup sequences, their shape, mode of interaction, and the overall architecture of the nup complex they give rise to are evolutionarily conserved from fungi to humans.

Coat nups



Cytoplasmic filament nups



CFNC-hub

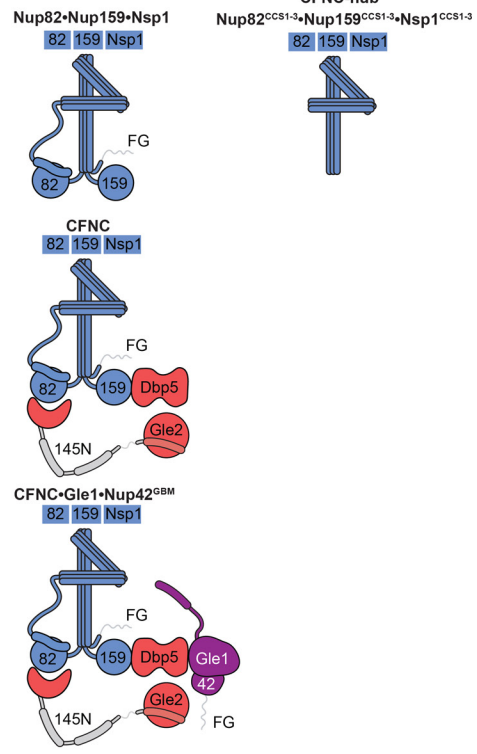
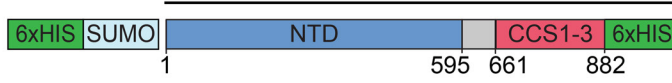


Fig. S1. *C. thermophilum* nucleoporin fragments. Domain architectures of the *C. thermophilum* coat and cytoplasmic filament nups. Domains are drawn as horizontal boxes with residue numbers indicated and their observed or predicted folds colored according to the legend. The black lines indicate the fragments used throughout the text. Dashed lines indicate regions excluded from expression constructs. As a reference, schematics of nup complexes are shown on the right.

A

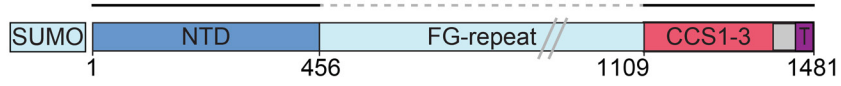
pET-28-SUMO

● Nup82

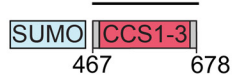


pET-Duet

● Nup159



● Nsp1



B

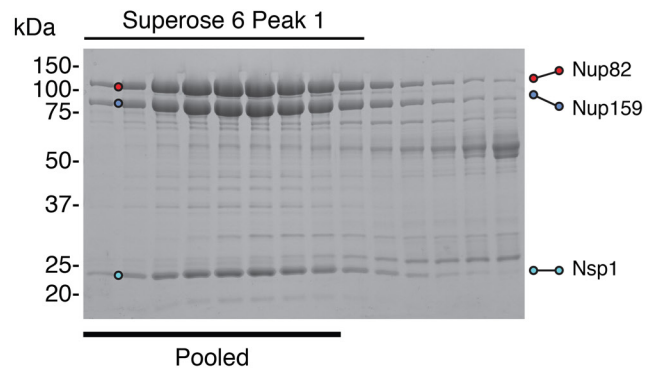
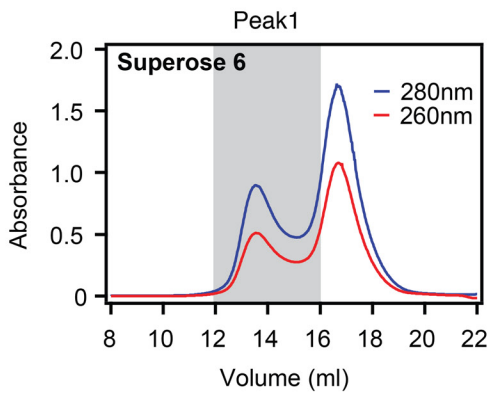
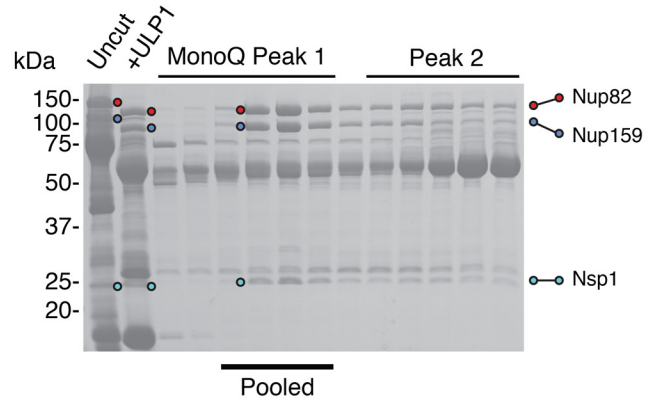
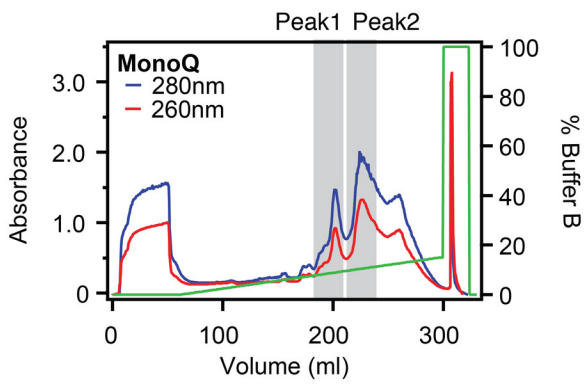
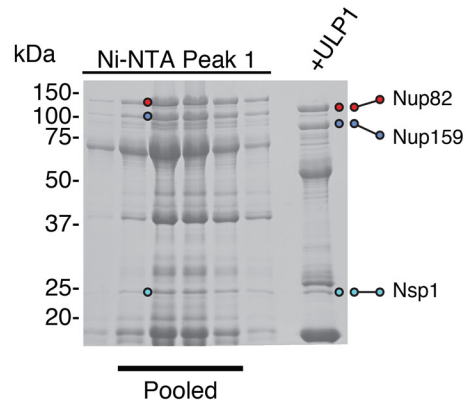
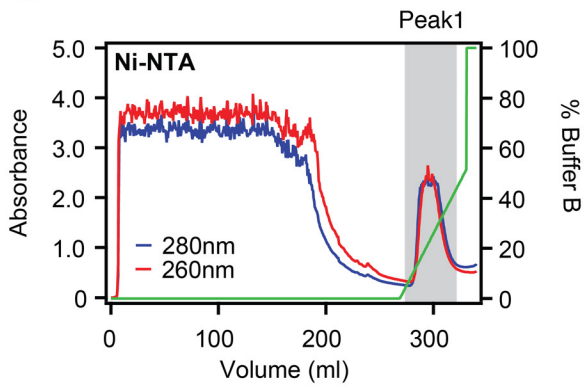


Fig. S2. Purification of the *C. thermophilum* Nup82•Nup159•Nsp1 hetero-trimer. (A) Domain boundaries of the purified nups are shown with black lines indicating the construct boundaries of Nup82, Nup159, and Nsp1 in our bacterial expression constructs. The dashed line indicates a central FG-repeat region in Nup159 that was excluded. (B) Nup82•Nup159•Nsp1 hetero-trimer purification. Sequential chromatography purification steps are shown from top to bottom with the employed columns indicated. The gray boxes indicate fractions that were resolved on SDS-PAGE gels and visualized by Coomassie staining. Pooled fractions are indicated with a black bar below the SDS-PAGE gels. For details of the buffer conditions see [Table S5](#).

Reconstitution and biochemical dissection of the cytoplasmic filament nup complex (CFNC)

Strong interaction
No interaction

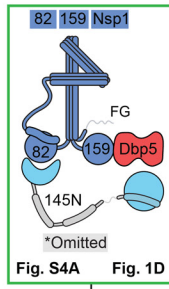
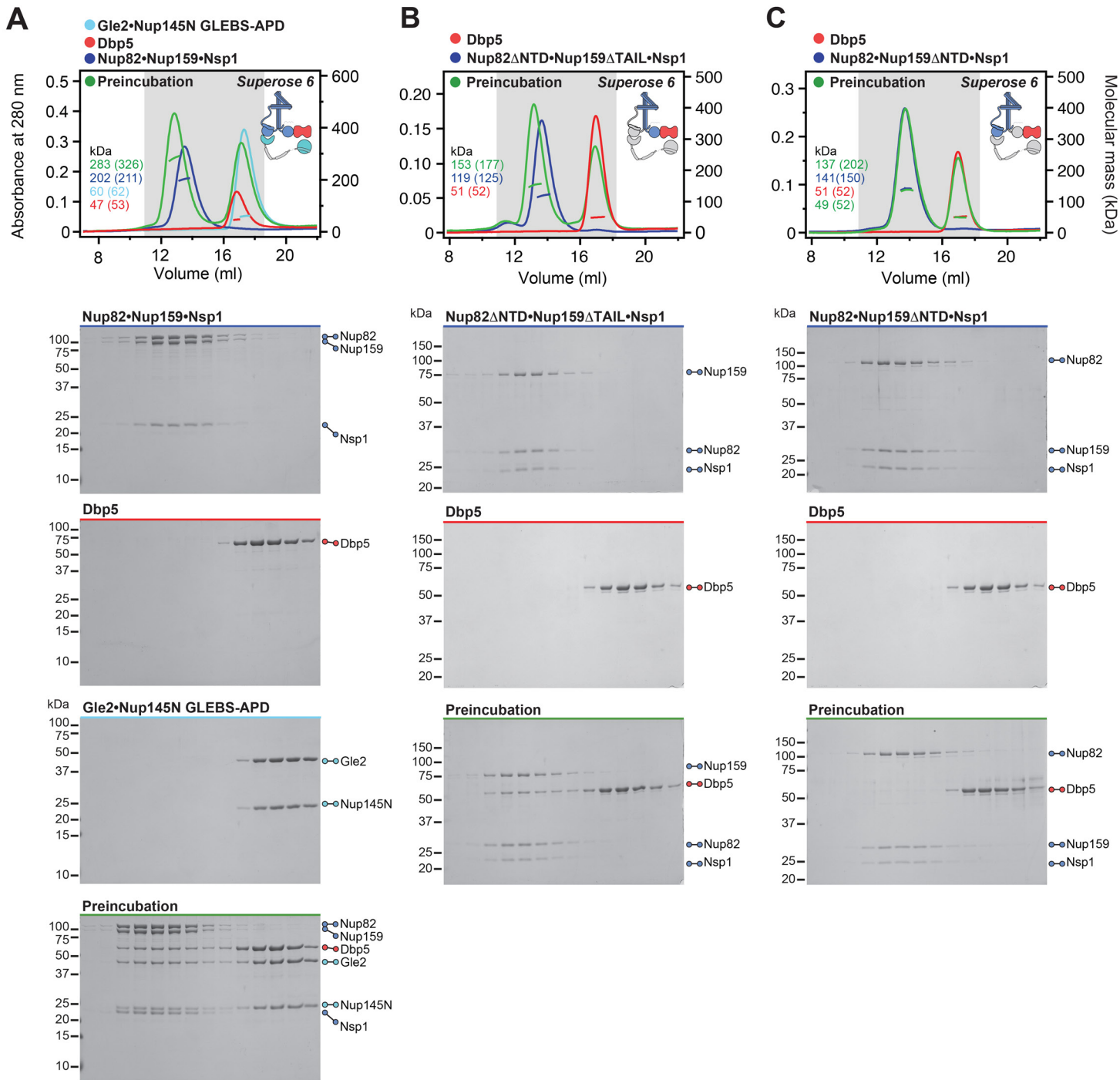


Fig. S3. Biochemical dissection of the CFNC architecture. Summary of the SEC-MALS interaction analyses of the indicated figure panels. Each box in the flow chart represents a SEC-MALS interaction experiment, involving individually purified CFNC sub-complexes that were tested for their ability to form stoichiometric complexes, colored by the experimental outcome; strong interaction (green), no interaction (red). The inset schematics are colored to indicate the CFNC sub-complexes of each SEC-MALS interaction experiment.



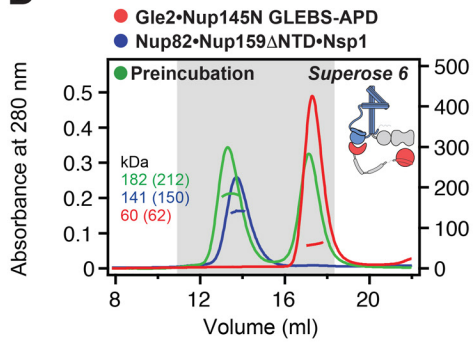
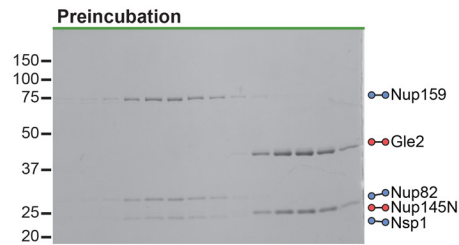
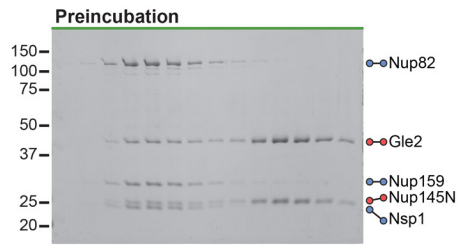
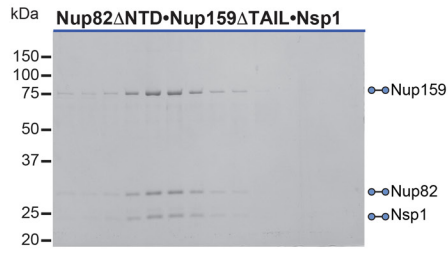
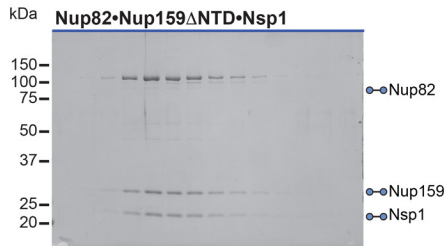
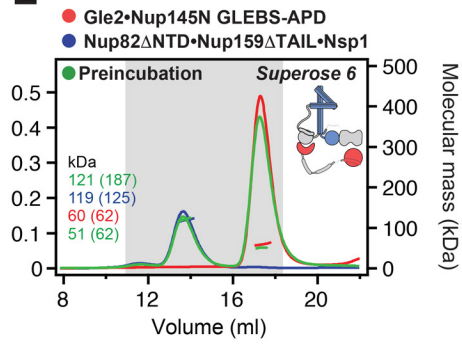
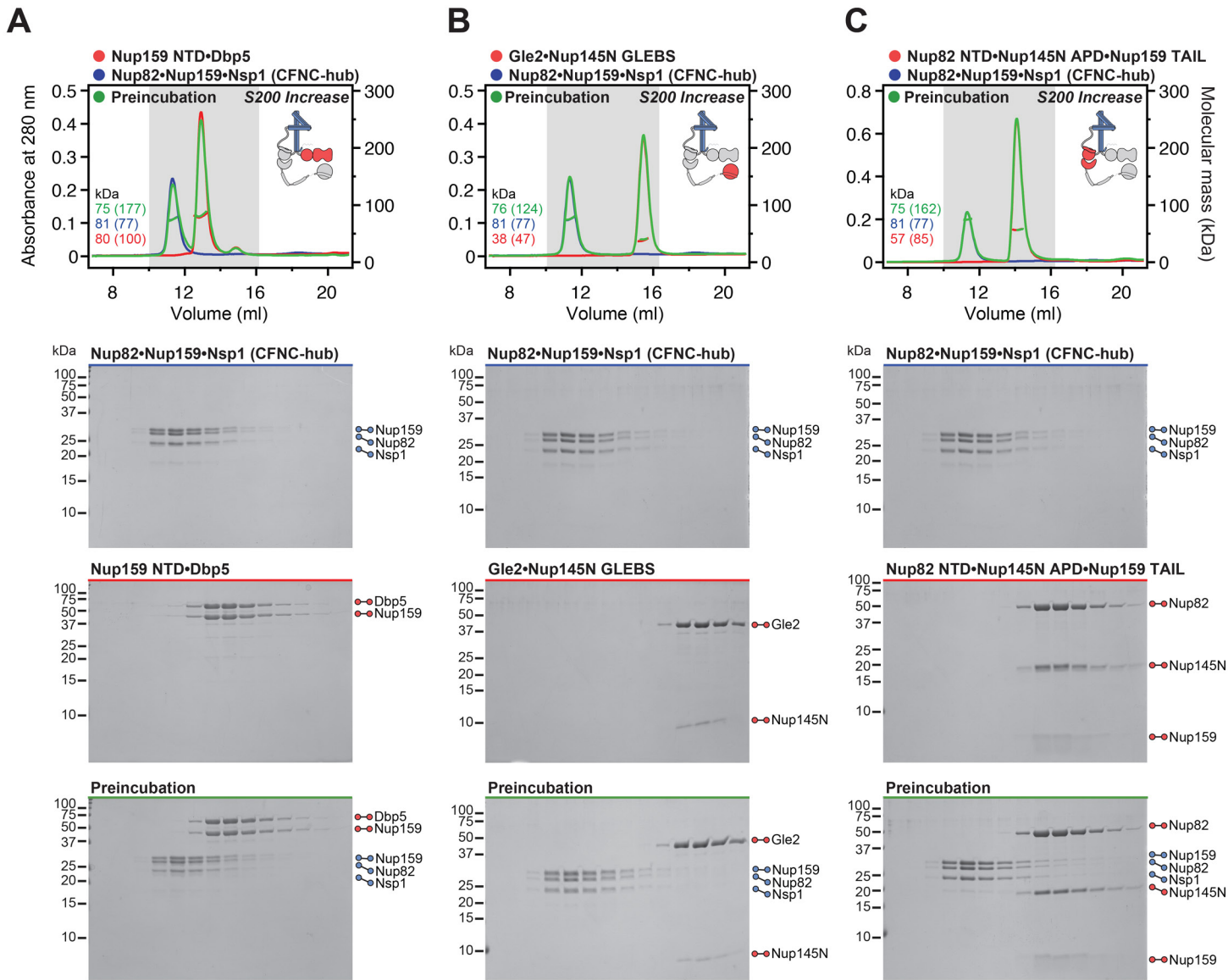
D**E**

Fig. S4. Reconstitution of the CFNC and elucidation of the Dbp5 and Gle2•Nup145N binding sites. (A) SEC-MALS interaction analysis showing the biochemical reconstitution of the ~290 kDa hetero-hexameric CFNC from Nup82•Nup159•Nsp1, Gle2•Nup145N, and Dbp5 (corresponding to Fig. 1D). (B, C) SEC-MALS interaction analyses probing the interaction of Dbp5 with (B) Nup82^{ΔNTD}•Nup159^{ΔTAIL}•Nsp1 and (C) Nup82•Nup159^{ΔNTD}•Nsp1 truncated CFNC variants. (D, E) SEC-MALS interaction analyses probing the interaction of Gle2•Nup145N^{GLEBS-APD} with (D) Nup82•Nup159^{ΔNTD}•Nsp1 and (E) Nup82^{ΔNTD}•Nup159^{ΔTAIL}•Nsp1 truncated CFNC variants. SEC-MALS profiles of nup complexes are shown individually (red, blue, and cyan) and after preincubation (green). SEC profiles were obtained using a Superose 6 10/300 GL column. Measured molecular masses are indicated, with the respective theoretical masses shown in parentheses. Inset schematics display tested protein samples colored to match the corresponding chromatogram trace. Gray boxes indicate fractions resolved on SDS-PAGE gels and visualized by Coomassie brilliant blue staining.



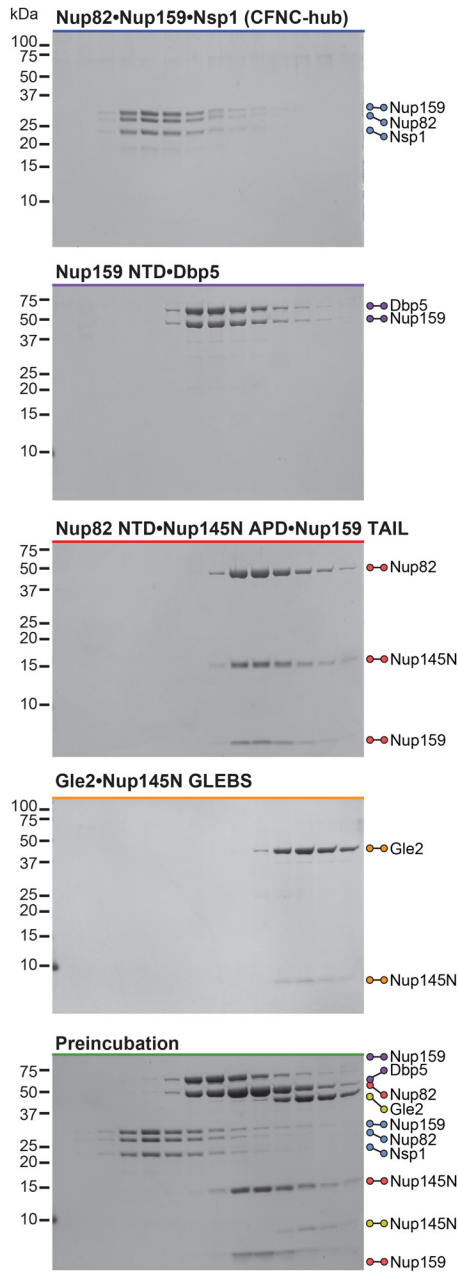
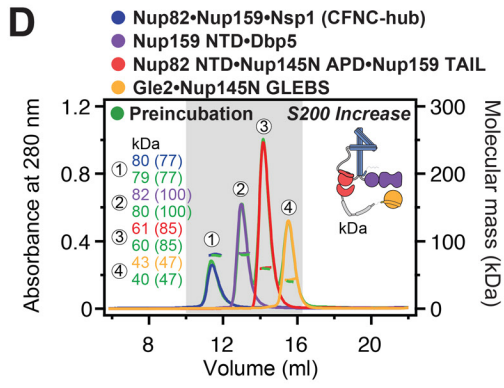


Fig. S5. Biochemical dissection of the CFNC into four distinct non-interacting sub-complexes. SEC-MALS interaction analysis of the Nup82•Nup159•Nsp1 CCS1-3 (CFNC-hub) with (A) Nup159^{NTD}•Dbp5, (B) Gle2•Nup145N^{GLEBS}, (C) Nup82^{NTD}•Nup145N^{APD}•Nup159^{TAIL}, and (D) a mixture of all four subcomplexes. SEC-MALS profiles of nup complexes are shown individually (red, blue, purple and orange) and after preincubation (green). SEC profiles were obtained using a Superdex 200 Increase 10/300 GL column. Measured molecular masses are indicated, with the respective theoretical masses shown in parentheses. Inset schematics display tested protein samples colored to match the corresponding chromatogram trace. Gray boxes indicate fractions resolved on SDS-PAGE gels and visualized by Coomassie brilliant blue staining.

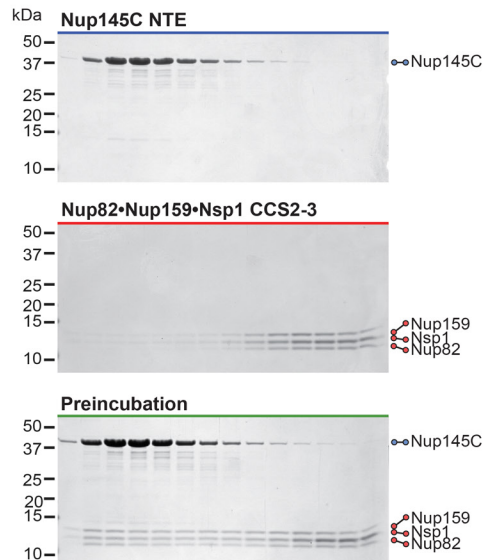
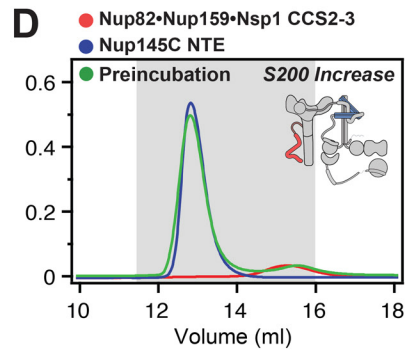
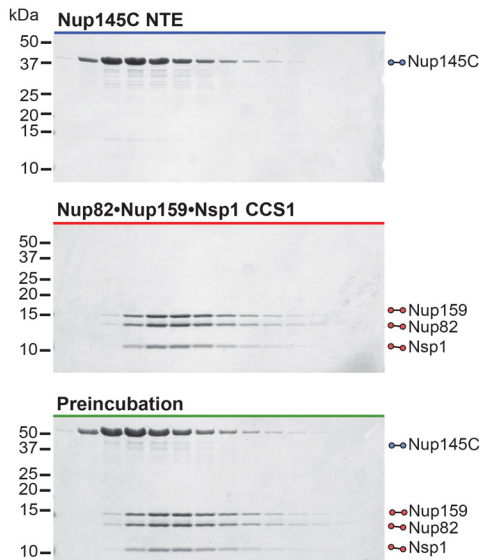
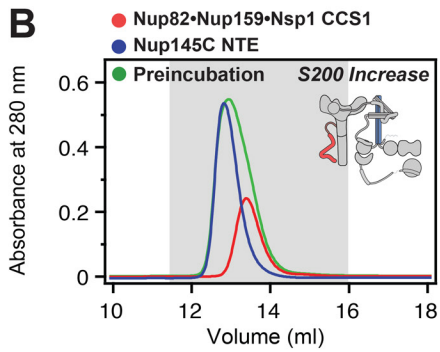
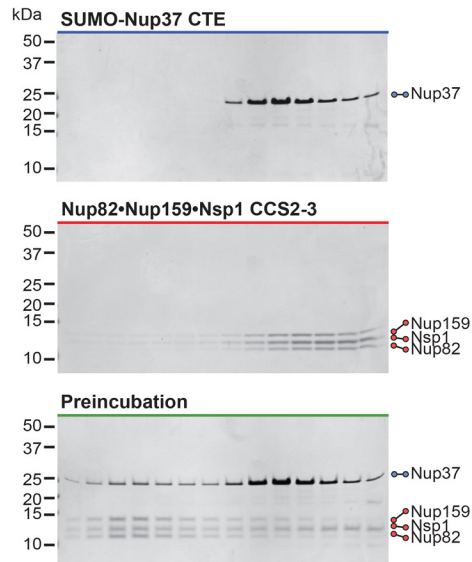
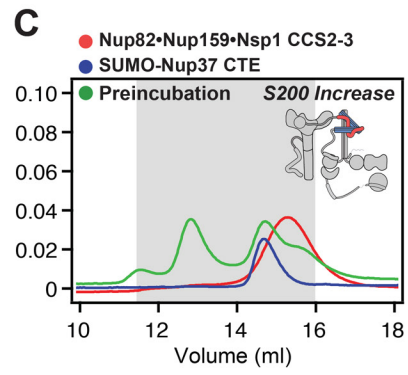
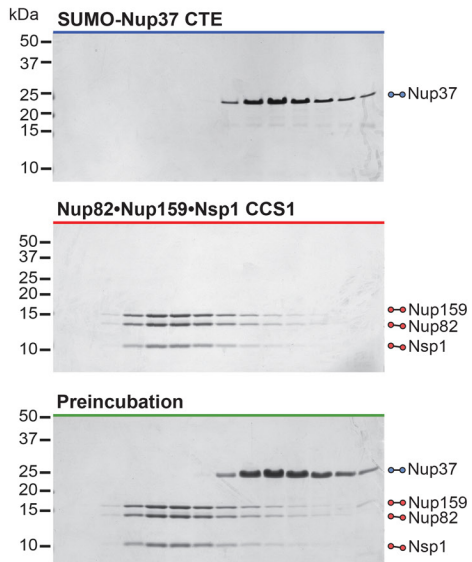
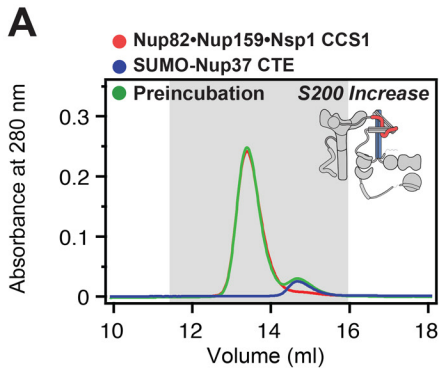


Fig. S6. Biochemical analysis of the Nup37/Nup145C-CFNC-hub interaction. (A, B) SEC interaction analyses of Nup82•Nup159•Nsp1 CCS1 with (A) SUMO-Nup37^{CTE} and (B) Nup145C^{NTE}, showing that neither form a stable complex. (C, D) SEC interaction analyses of Nup82•Nup159•Nsp1 CCS2-3 with (C) SUMO-Nup37^{CTE} and (D) Nup145C^{NTE}, demonstrating that both form stable interactions. SEC profiles of nup complexes are shown individually (red, blue) and after preincubation (green). SEC profiles were obtained using a Superdex 200 Increase 10/300 GL column. Inset schematics display tested protein samples colored to match the corresponding chromatogram trace. Gray boxes indicate fractions resolved on SDS-PAGE gels and visualized by Coomassie brilliant blue staining.

Reconstitution and biochemical dissection
of the CNC-CFNC complex

- Strong interaction
- Weak interaction
- No interaction

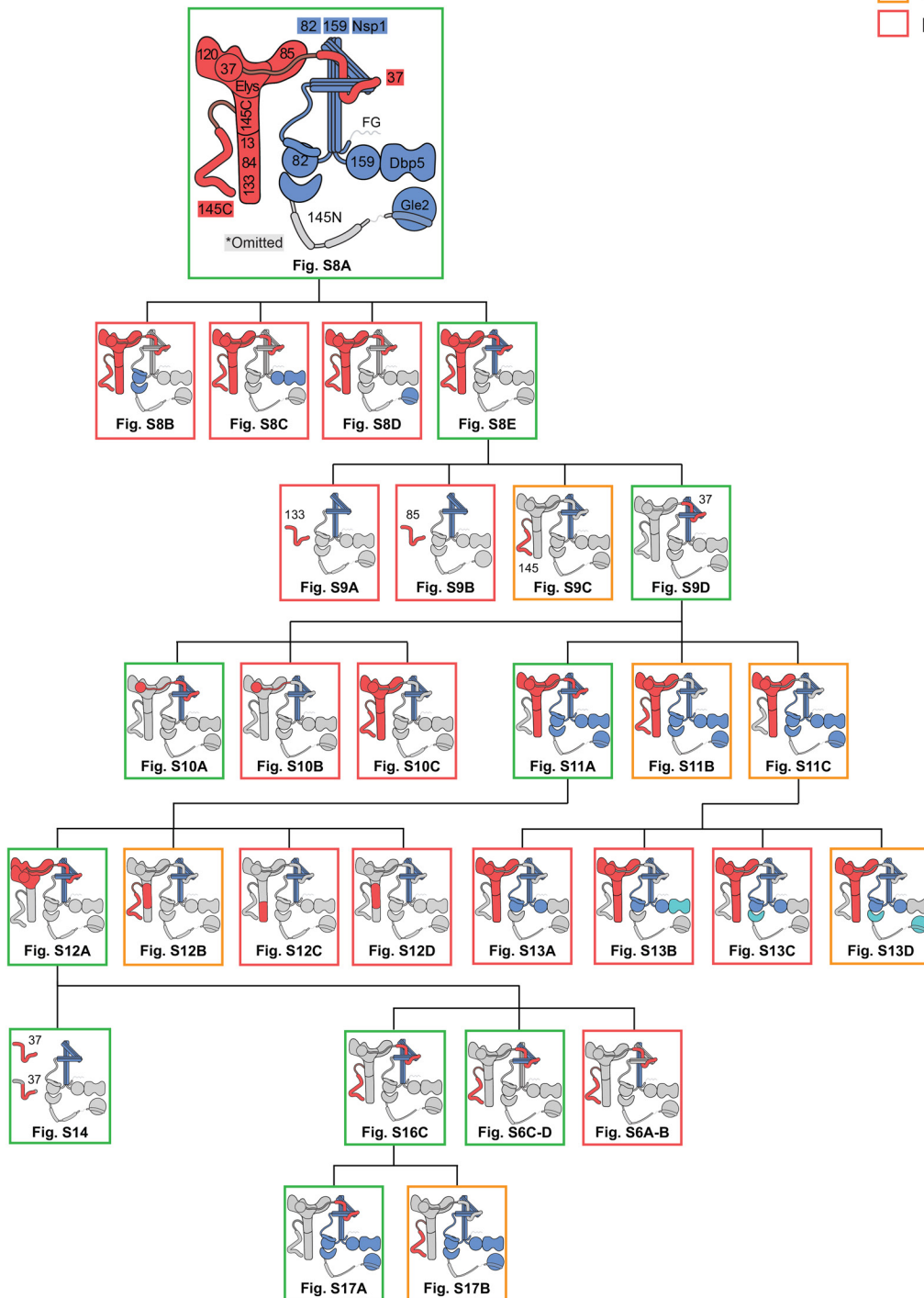
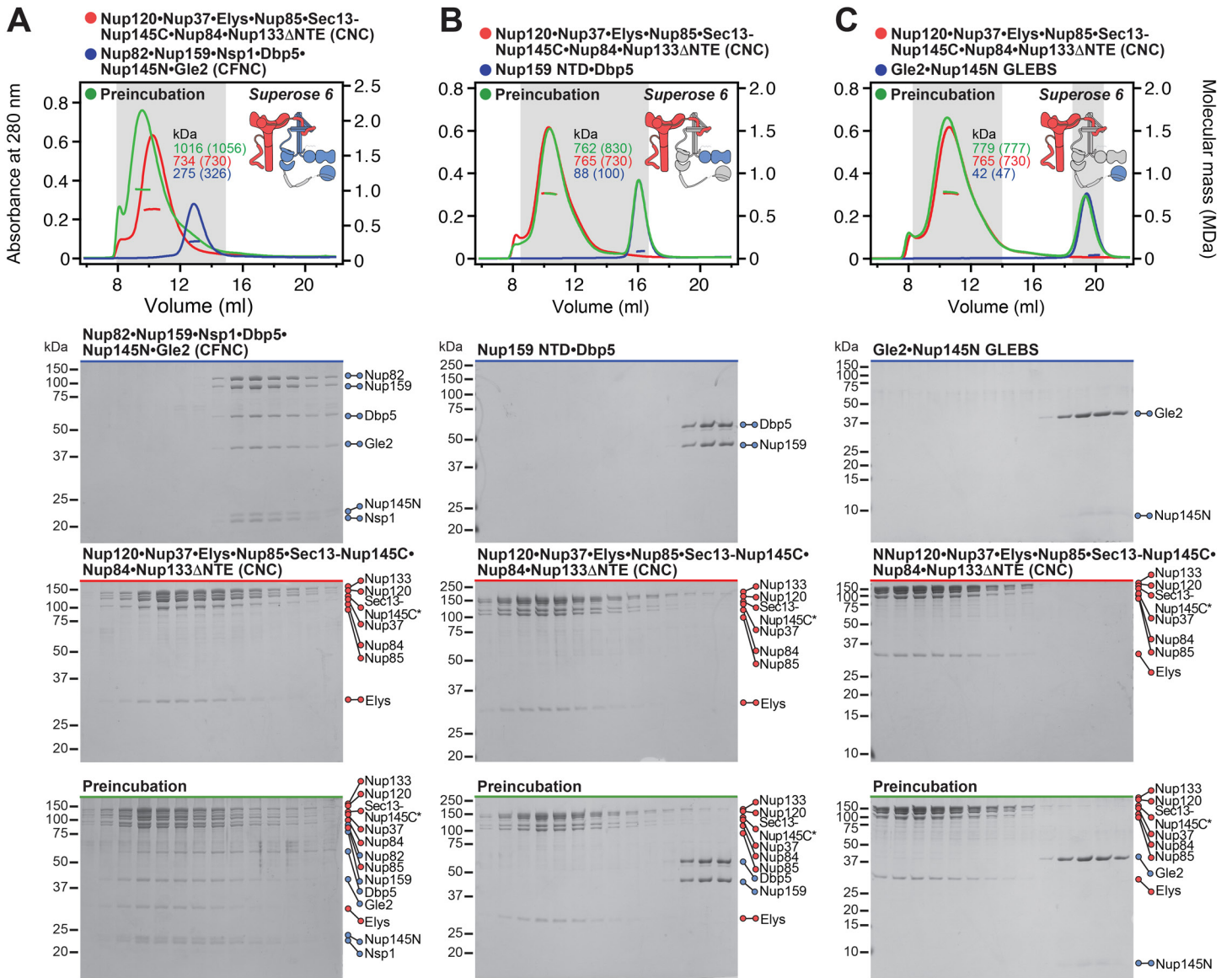


Fig. S7. Reconstitution and dissection strategy for the 14-protein CNC•CFNC complex. Flow chart detailing reconstitution and biochemical dissection of the 14-protein *C. thermophilum* CNC•CFNC complex. Each box in the flow chart represents a SEC-MALS interaction experiment, involving individually purified CNC and CFNC sub-complexes that were tested for their ability to form stoichiometric complexes, colored by the experimental outcome; strong interaction (green), weak interaction (orange), no interaction (red). The inset schematics are colored to indicate the CNC and CFNC sub-complexes of each SEC-MALS interaction experiment, gray regions stipulate proteins omitted from each analysis.



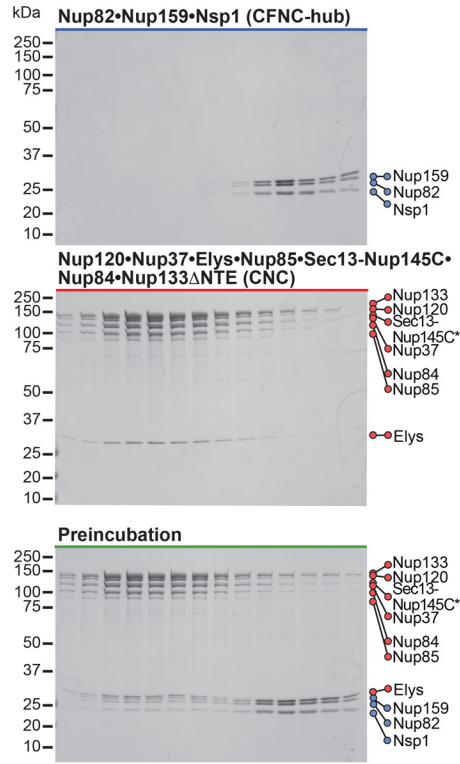
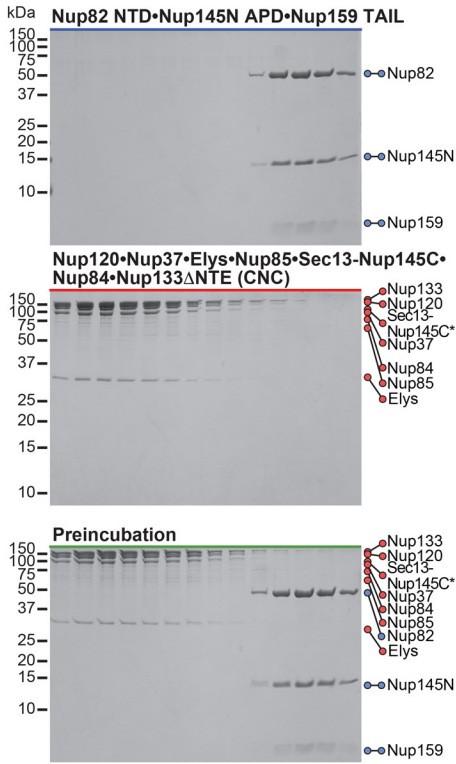
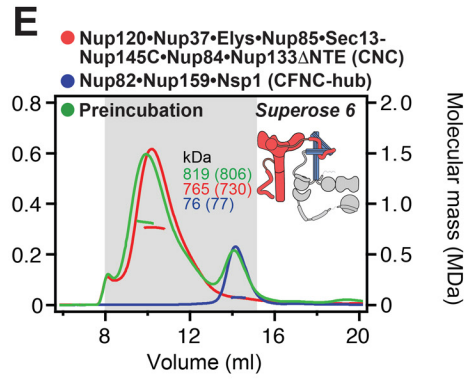
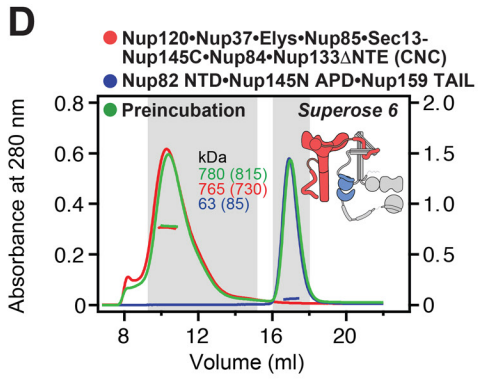
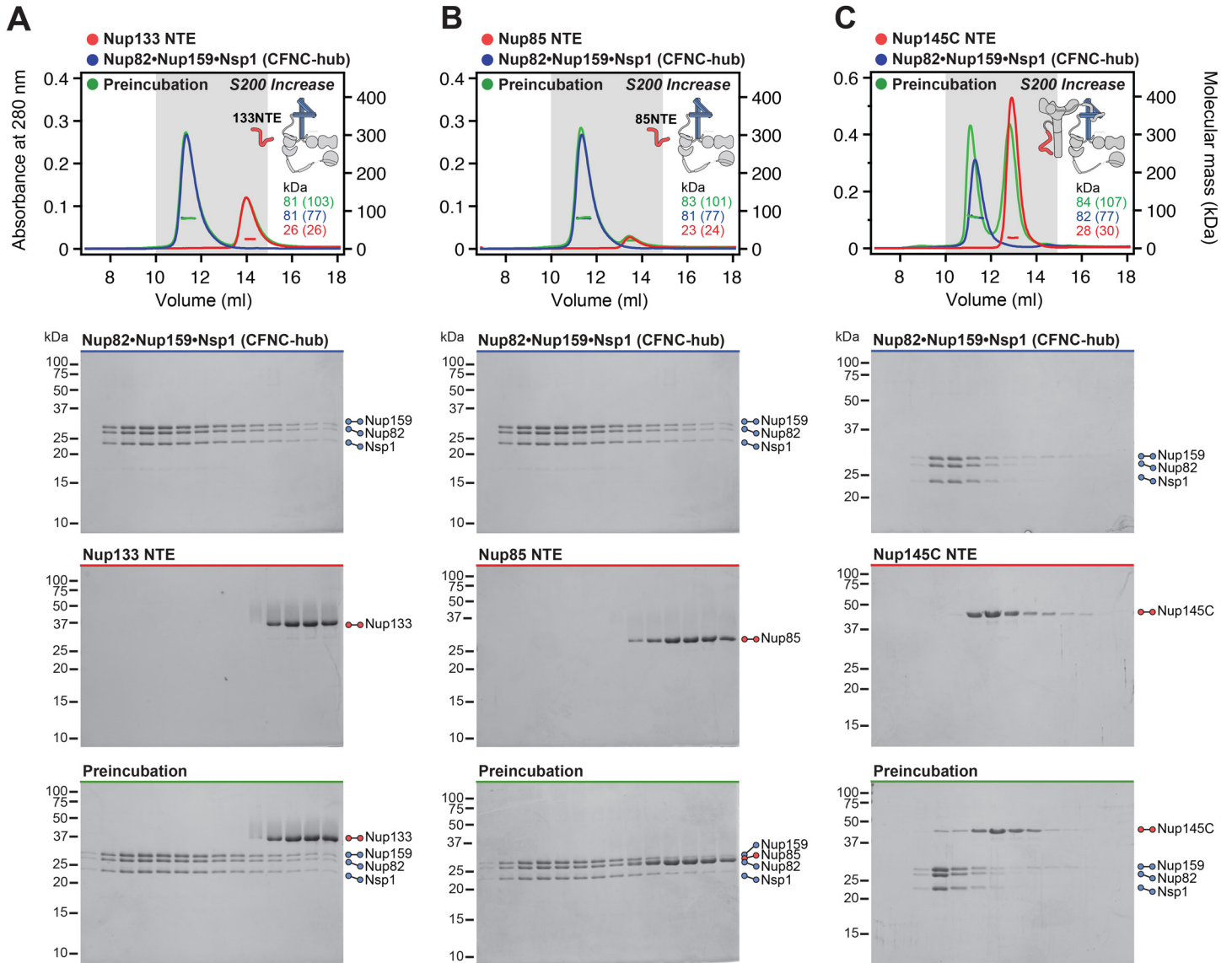


Fig. S8. Reconstitution and dissection of the 14-protein CNC-CFNC interaction. (A) SEC-MALS interaction analysis of the Nup120•Nup37•Elys•Nup85•Sec13-Nup145C•Nup84•Nup133^{ΔNTE} (CNC) with the intact CFNC, demonstrating the formation of a ~1,016 kDa monodisperse, stoichiometric 14-protein CNC•CFNC complex. (B-E) SEC-MALS interaction analysis of the intact CNC with (B) Nup159^{NTD}•Dbp5, (C) Gle2•Nup145N^{GLEBS}, (D) Nup82^{NTD}•Nup145N^{APD}•Nup159^{TAIL}, and (E) CFNC-hub, showing that of the four distinct CFNC subcomplexes only the CFNC-hub forms a stable interaction with the CNC. SEC-MALS profiles of nup complexes are shown individually (red, blue) and after preincubation (green). SEC profiles were obtained using a Superose 6 10/300 GL column. Measured molecular masses are indicated, with the respective theoretical masses shown in parentheses. Inset schematics display tested protein samples colored to match the corresponding chromatogram trace. Gray boxes indicate fractions resolved on SDS-PAGE gels and visualized by Coomassie brilliant blue staining.



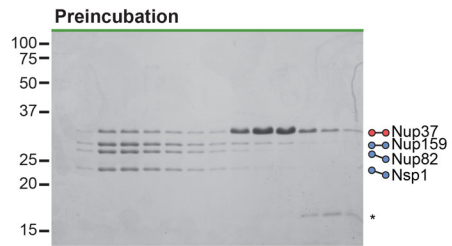
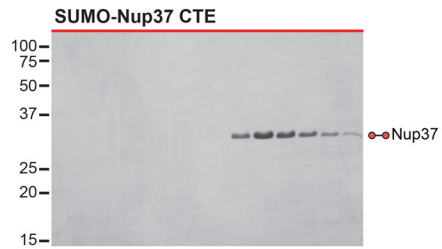
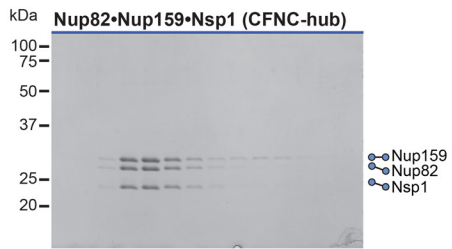
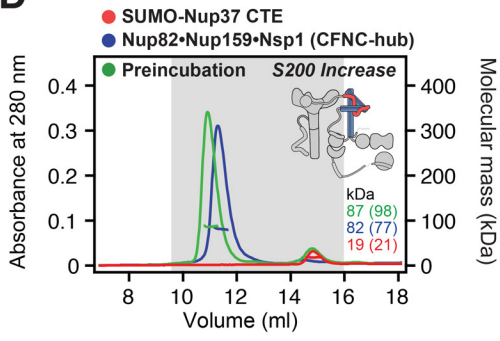
D

Fig. S9. Anchoring of the CFNC-hub to the CNC is mediated by Nup145C^{NTE} and Nup37^{CTE}. SEC-MALS interaction analyses of CFNC-hub with (A) Nup133^{NTE}, (B) Nup85^{NTE}, (C) Nup145C^{NTE}, and (D) SUMO-Nup37^{CTE}, showing that Nup145C and Nup37 bind to the CFNC-hub. SEC-MALS profiles of nup complexes are shown individually (red, blue) and after preincubation (green). SEC profiles were obtained using a Superdex 200 Increase 10/300 GL column. Measured molecular masses are indicated, with the respective theoretical masses shown in parentheses. Inset schematics display tested protein samples colored to match the corresponding chromatogram trace. Gray boxes indicate fractions resolved on SDS-PAGE gels and visualized by Coomassie brilliant blue staining.

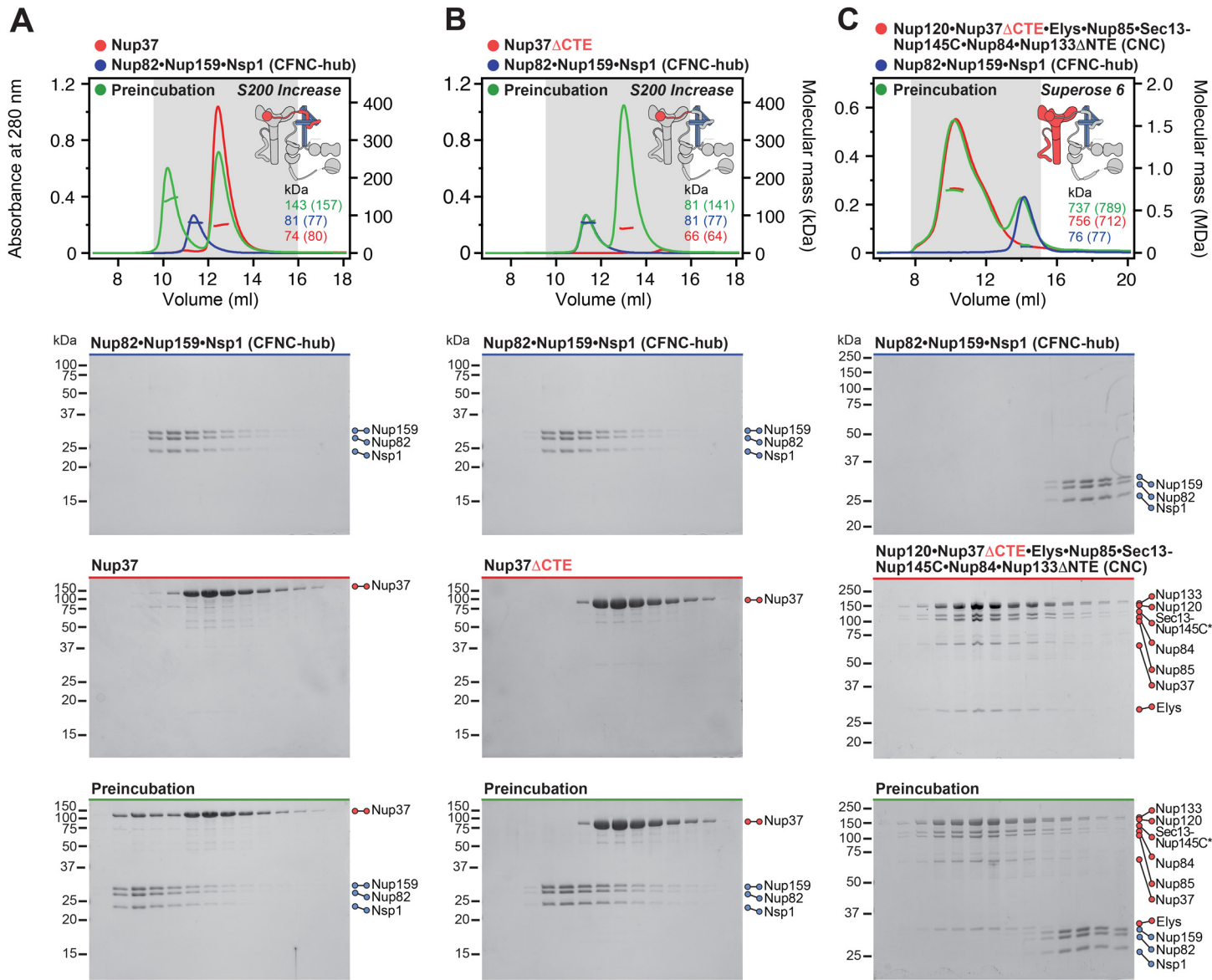


Fig. S10. Nup37^{CTE} is necessary and sufficient for CFNC-hub binding. SEC-MALS interaction analysis of CFNC-hub with (A) Nup37, (B) Nup37^{ΔCTE}, (C) Nup120•Nup37^{ΔCTE}•Elys•Nup85•Sec13-Nup145C•Nup84•Nup133^{ANTE} (CNC^{Δ37CTE}). SEC-MALS profiles of nup complexes are shown individually (red, blue) and after preincubation (green). SEC profiles were obtained using (A, B) Superose 6 10/300 GL and (C) Superdex 200 10/300 GL columns. Measured molecular masses are indicated, with the respective theoretical masses shown in parentheses. Inset schematics display tested protein samples colored to match the corresponding chromatogram trace. Gray boxes indicate fractions resolved on SDS-PAGE gels and visualized by Coomassie brilliant blue staining.

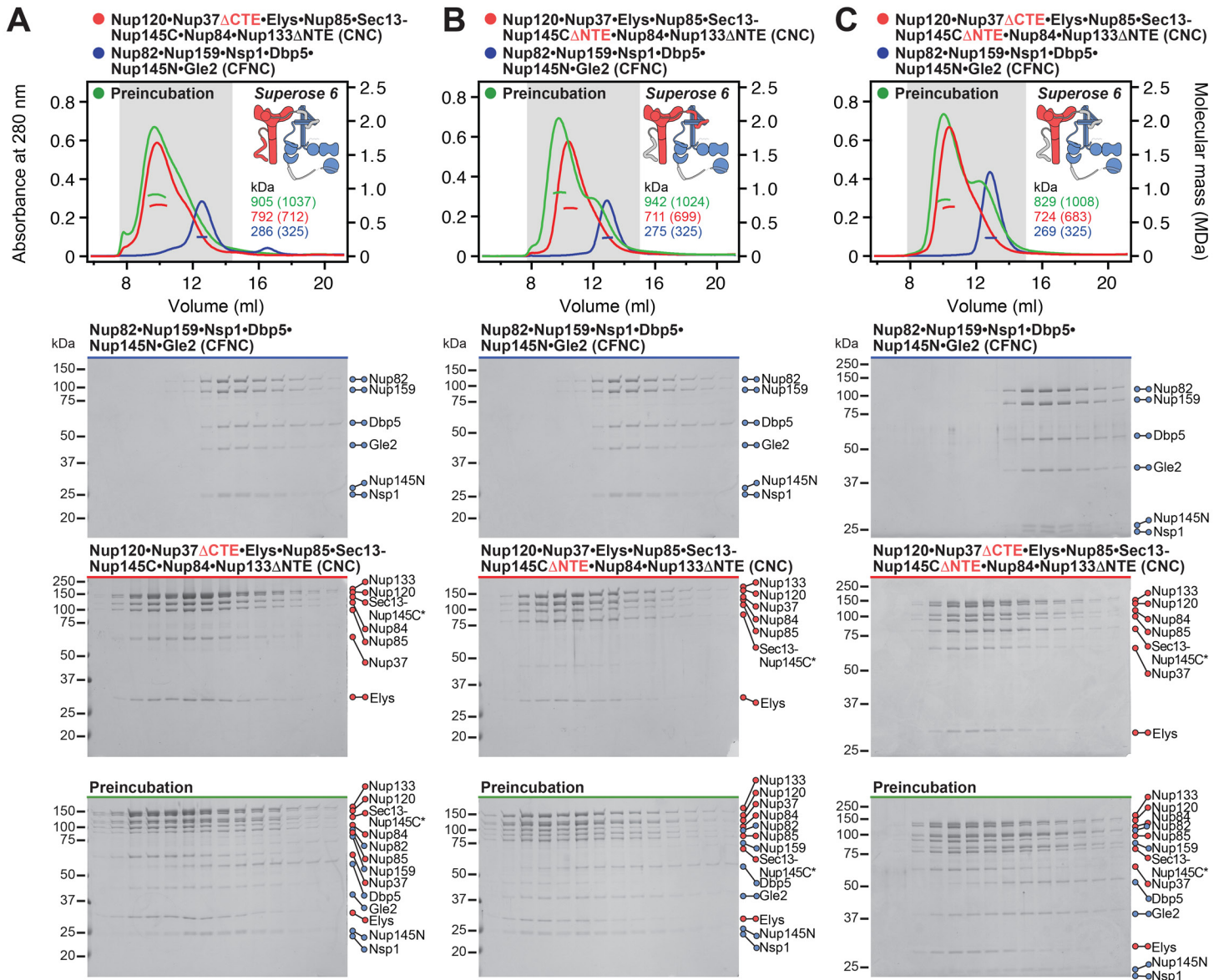
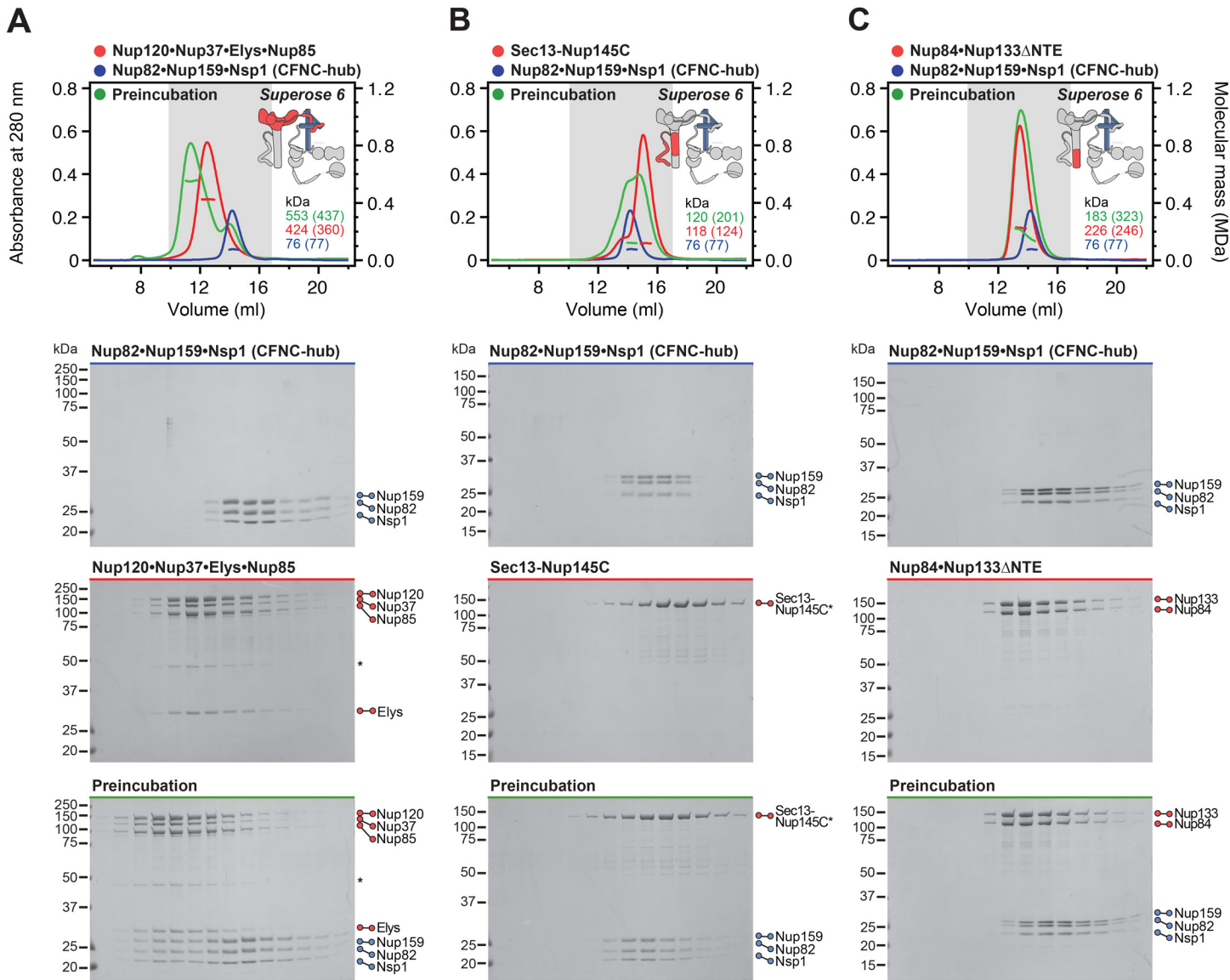


Fig. S11. Each intact CNC contains two distinct CFNC binding sites. SEC-MALS interaction analysis of intact CFNC with (A) CNC $\Delta^{37\text{CTE}}$, (B) CNC $\Delta^{145\text{CNTE}}$, and (C) CNC $\Delta^{37\text{CTE}\Delta^{145\text{CNTE}}}$, showing that the simultaneous removal of both Nup37 CTE and Nup145C NTE disrupts the CFNC interaction, whereas their individual removal only weakens the CNC-CFNC interaction. The mildly sub-stoichiometric Dbp5 incorporation in the CNC-CFNC complex results from the concentration limitation of the CNC. SEC-MALS profiles of nup complexes are shown individually (red, blue) and after preincubation (green). SEC profiles were obtained using a Superose 6 10/300 GL column. Measured molecular masses are indicated, with the respective theoretical masses shown in parentheses. Inset schematics display tested protein samples colored to match the corresponding chromatogram trace. Gray boxes indicate fractions resolved on SDS-PAGE gels and visualized by Coomassie brilliant blue staining.



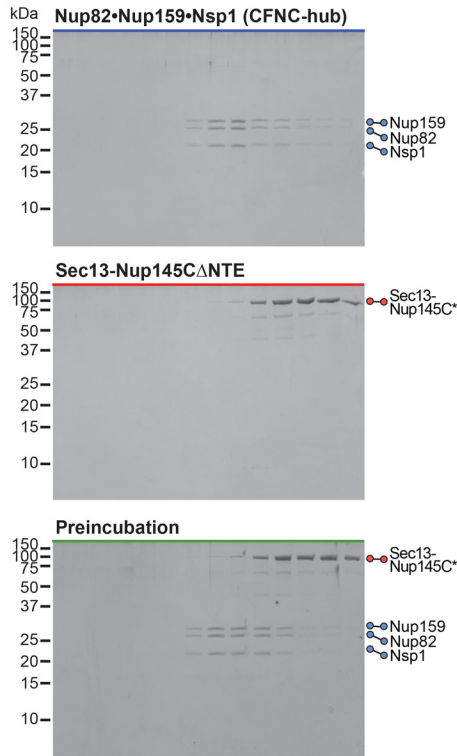
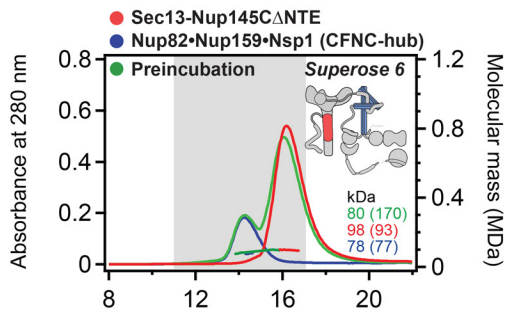
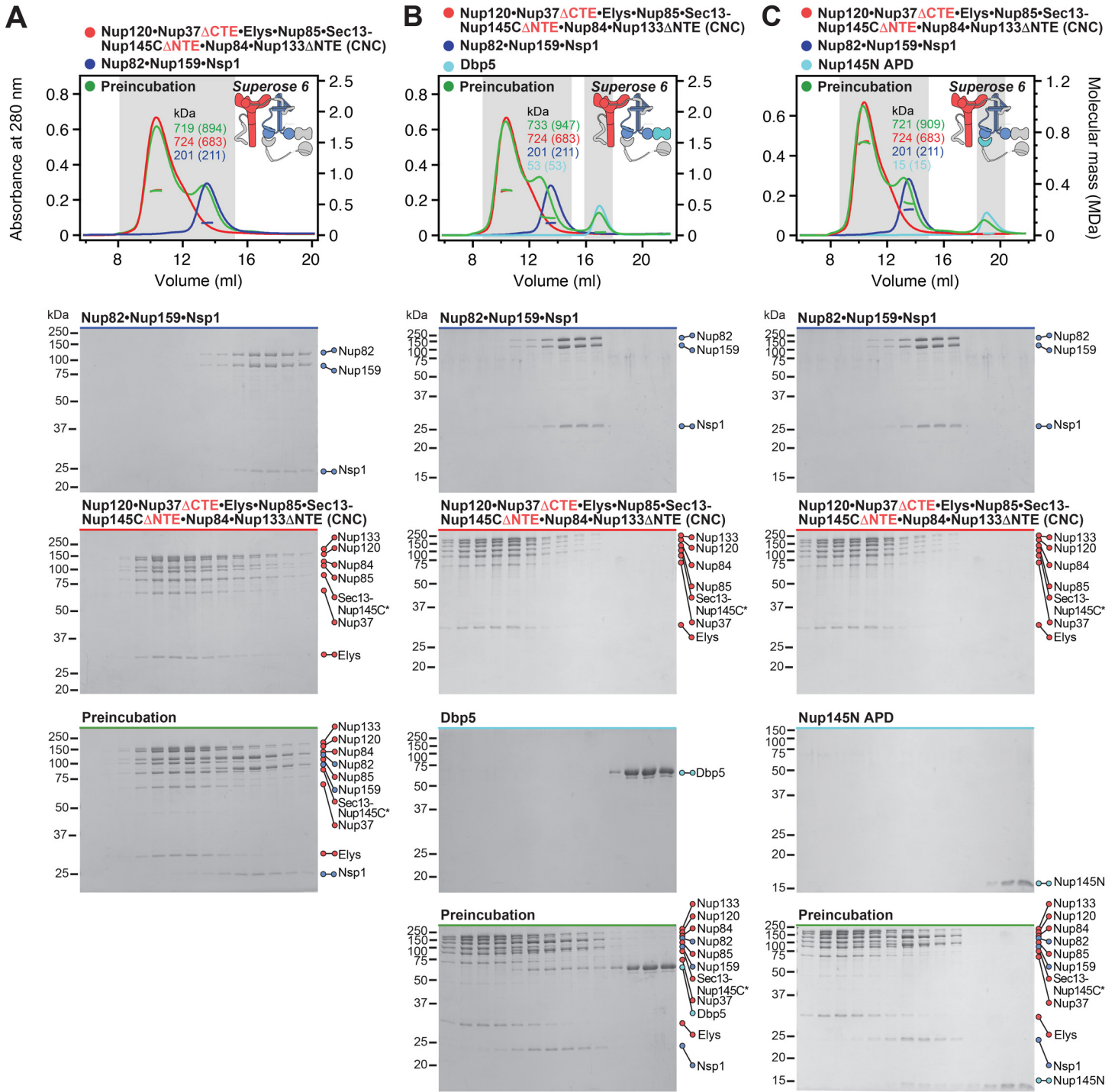
D

Fig. S12. Two CNC sub-complexes bind the CFNC-hub. SEC-MALS interaction analysis of CFNC-hub with (A) Nup120•Nup37•Elys•Nup85, (B) Sec13-Nup145C, (C) Nup84•Nup133^{ANTE}, and (D) Sec13-Nup145C^{ANTE}. SEC-MALS profiles of nup complexes are shown individually (red, blue) and after preincubation (green). SEC profiles were obtained using a Superose 6 10/300 GL column. Measured molecular masses are indicated, with the respective theoretical masses shown in parentheses. Inset schematics display tested protein samples colored to match the corresponding chromatogram trace. Gray boxes indicate fractions resolved on SDS-PAGE gels and visualized by Coomassie brilliant blue staining.



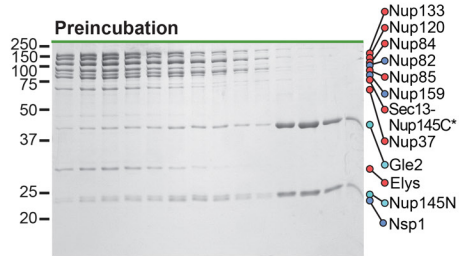
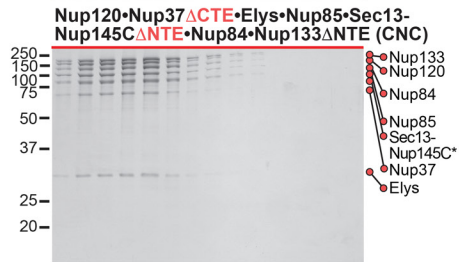
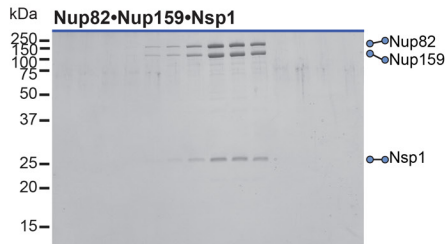
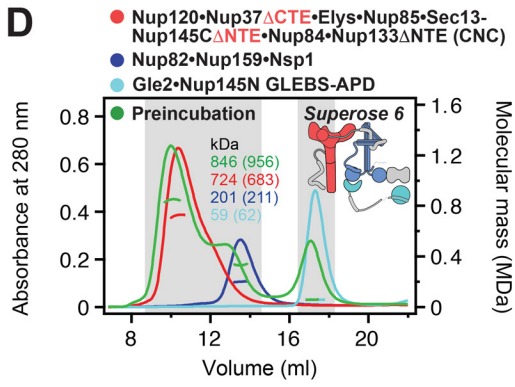


Fig. S13. Gle2•Nup145N contributes weakly to the CNC-CFNC interaction. SEC-MALS interaction analysis of CNC $\Delta^{37\text{CTE}}\Delta^{145\text{CNTE}}$ with (A) Nup82•Nup159•Nsp1, (B) Nup82•Nup159•Nsp1 and Dbp5, (C) Nup82•Nup159•Nsp1 and Nup145N^{APD}, and (D) Nup82•Nup159•Nsp1 and Gle2•Nup145N^{GLEBS-APD}, showing that in the absence of both Nup37^{CTE} and Nup145^{NTTE} CFNC binding sites, residual CNC binding is Gle2•Nup145N^{GLEBS}-dependent. SEC-MALS profiles of nup complexes are shown individually (red, blue, cyan) and after preincubation (green). SEC profiles were obtained using a Superose 6 10/300 GL column. Measured molecular masses are indicated, with the respective theoretical masses shown in parentheses. Inset schematics display tested protein samples colored to match the corresponding chromatogram trace. Gray boxes indicate fractions resolved on SDS-PAGE gels and visualized by Coomassie brilliant blue staining.

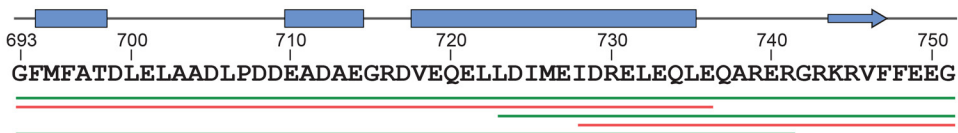
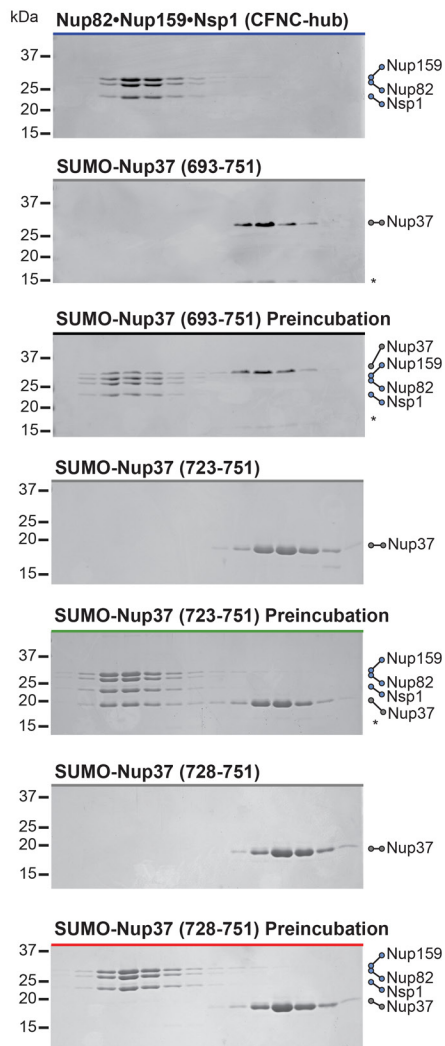
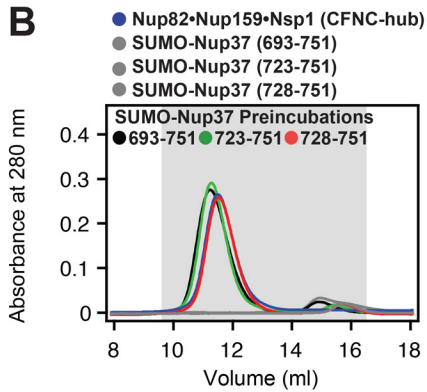
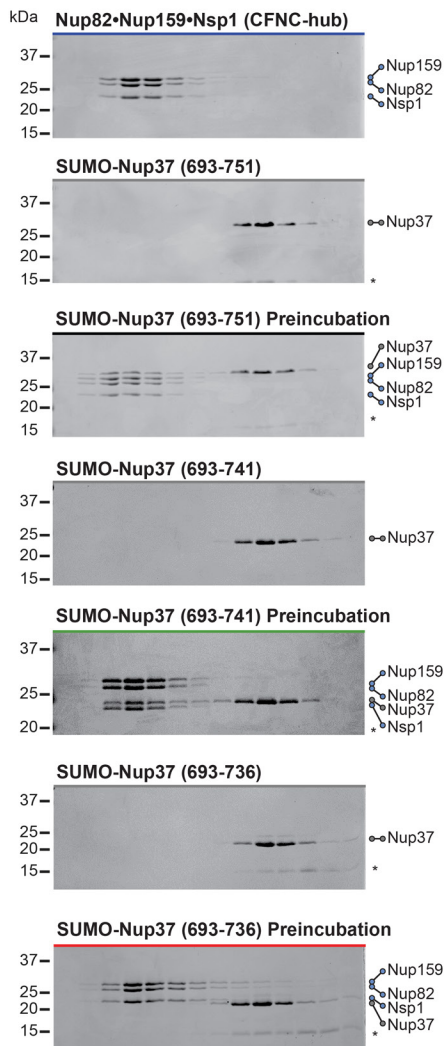
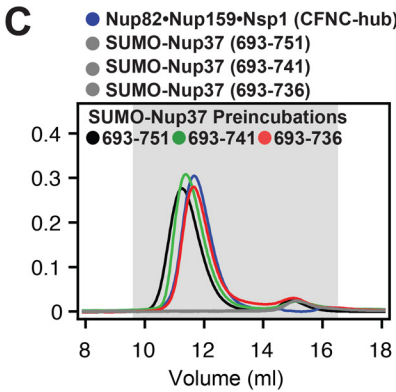
A**Nup37****B****C**

Fig. S14. Identification of a minimal Nup37^{CTE} CFNC-hub binding region. (A) Primary sequence of Nup37^{CTE} with predicted secondary structure elements. Colored lines indicate Nup37^{CTE} N- and C-terminal truncation fragments that were systematically tested for their ability to interact with the CFNC-hub, colored in green and red to indicate binding and no binding, respectively. Secondary structure predictions were conducted using Jpred4 (141). (B-C) SEC interaction analyses of CFNC-hub with (B) N-terminal SUMO-Nup37^{CTE} truncations, or (C) C-terminal SUMO-Nup37^{CTE} truncations, mapping a minimal binding site to residues 723-741. SEC profiles of nup complexes are shown individually (blue, gray) and after preincubation (black, red and green). SEC profiles were obtained using a Superdex 200 10/300 GL column. Gray boxes indicate fractions resolved on SDS-PAGE gels and visualized by Coomassie brilliant blue staining.

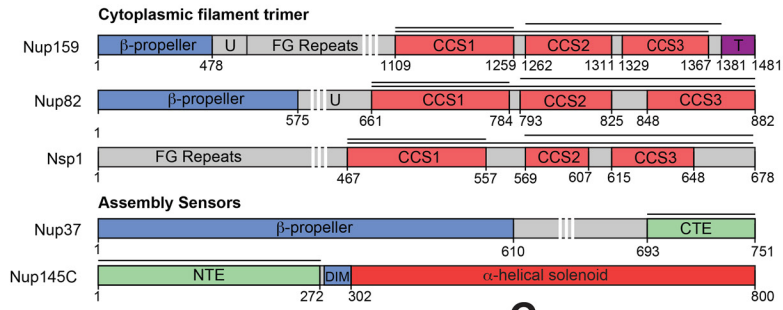
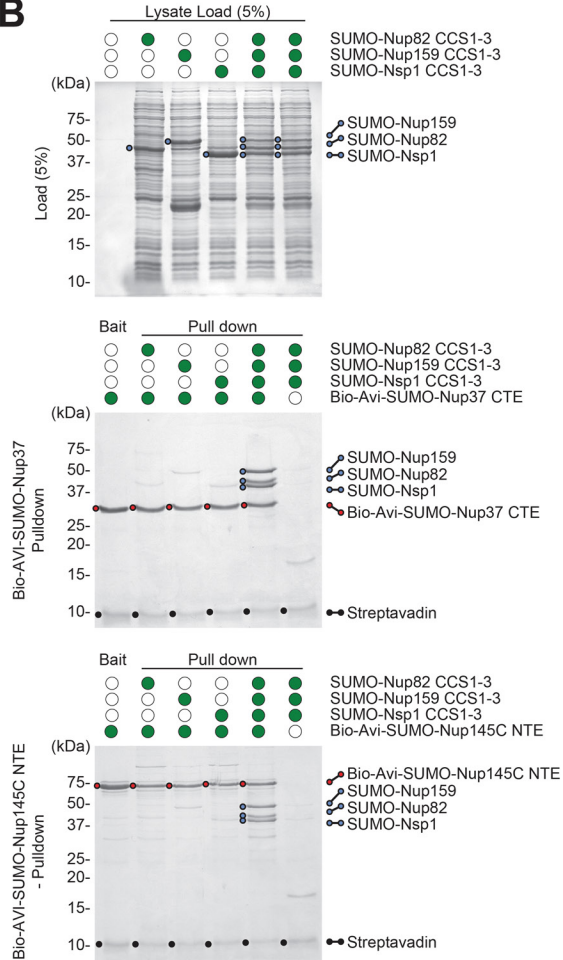
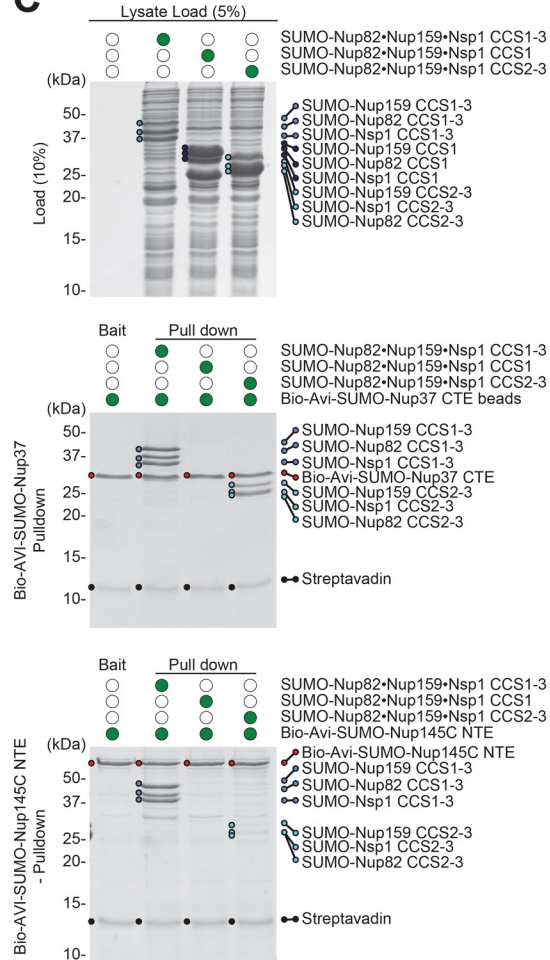
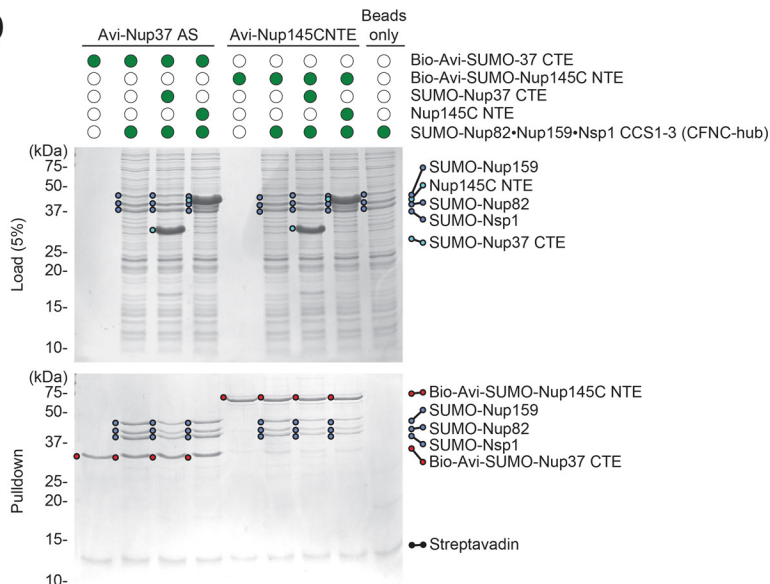
A**B****C****D**

Fig. S15. Nup37^{CTE} and Nup145C^{NTE} encode assembly sensors for the CFNC-hub. (A) Domain architectures of Nup159, Nup82, Nsp1, Nup37, and Nup145C. Domains are drawn as horizontal boxes with residue numbers indicated and their observed or predicted folds colored. The black lines indicate the fragments used in the pull-down analysis. (B-D) Streptavidin pulldowns using Bio-Avi-SUMO-Nup37^{CTE} or Bio-Avi-SUMO-Nup145C^{NTE} baits with (B) bacterial lysates, containing either Nup82, Nup159, and Nsp1 CCS1-3 fragments individually or a mixture of all three, demonstrating exclusive binding to the hetero-trimeric CFNC-hub, (C) bacterial lysates containing either the Nup82•Nup159•Nsp1 CCS1-3 (CFNC-hub), or hetero-trimeric CCS1 and CCS2-3 segments, demonstrating binding to CCS2-3 albeit to a lesser extent, and (D) bacterial lysates containing CFNC-hub and a ~10 fold excess of purified SUMO-Nup37^{CTE} or Nup145C^{NTE} competitor, demonstrating mutually exclusive binding events. SDS-PAGE gels are visualized by Coomassie brilliant blue staining.

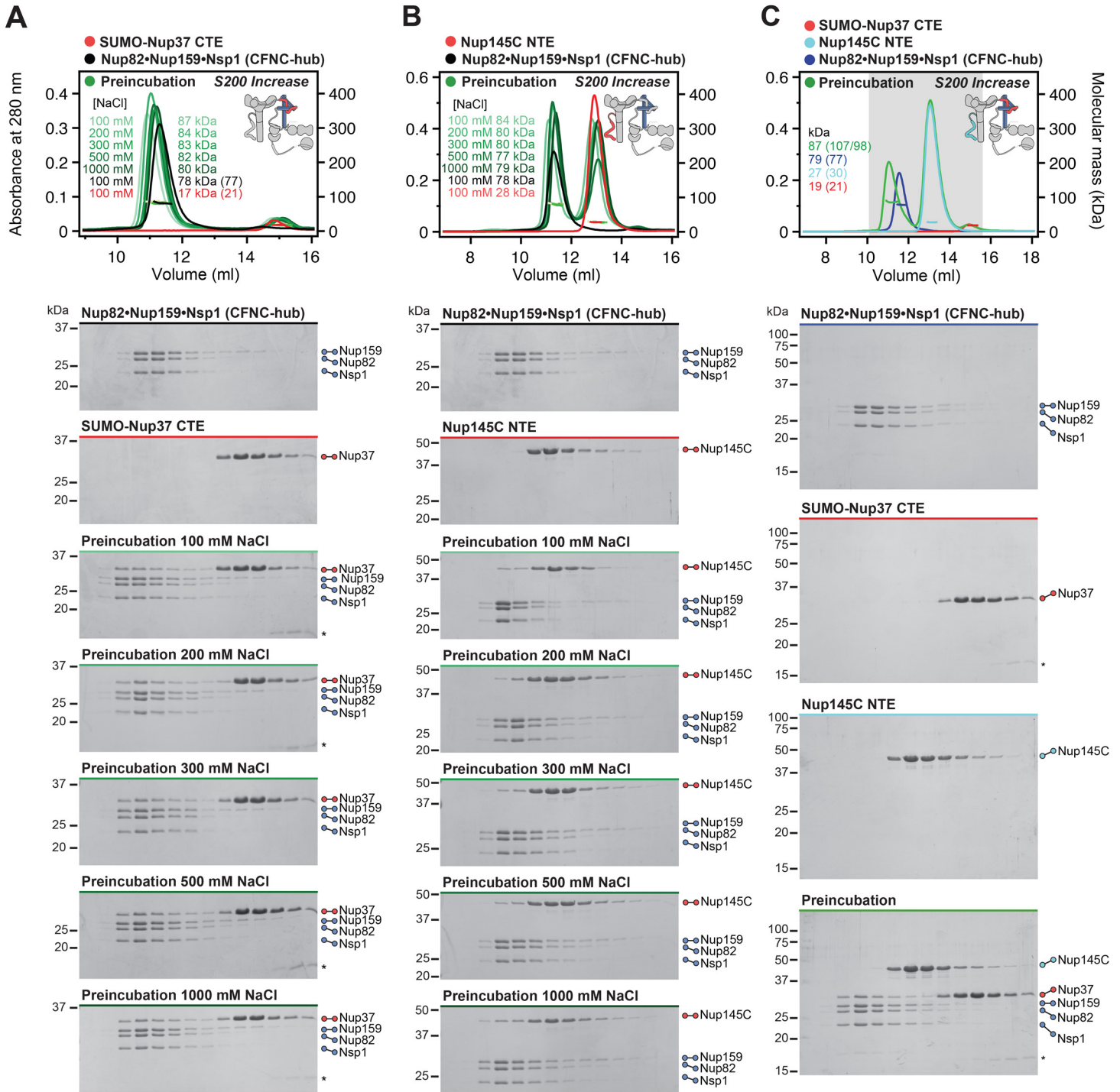


Fig. S16. Nup37^{CTE} and Nup145C^{NTE} bind CFNC-hub in a mutually exclusive fashion. SEC-MALS interaction analysis of the CFNC-hub with (A) SUMO-Nup37^{CTE} and (B) Nup145C^{NTE} across increasing buffer NaCl concentrations, establishing the hydrophobic nature of both interactions. (C) SEC-MALS competition analysis of SUMO-Nup37^{CTE} and Nup145C^{NTE} binding to CFNC-hub, establishing mutually exclusive overlapping binding sites. SEC-MALS profiles of nup complexes are shown individually (red, blue, cyan, and black) and after preincubation (green). SEC profiles were obtained using a Superdex 200 Increase 10/300 GL column. Measured molecular masses are indicated, with the respective theoretical masses shown in parentheses. Inset schematics display tested protein samples colored to match the corresponding chromatogram trace. Gray boxes indicate fractions resolved on SDS-PAGE gels and visualized by Coomassie brilliant blue staining.

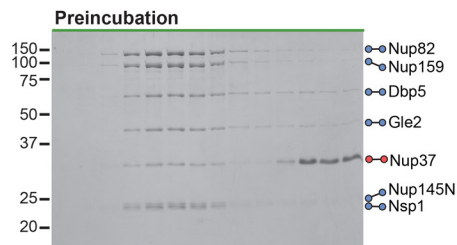
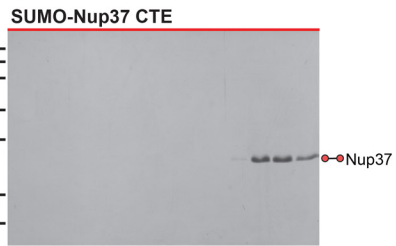
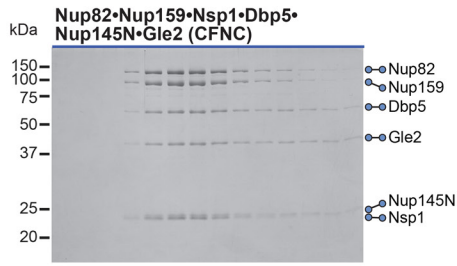
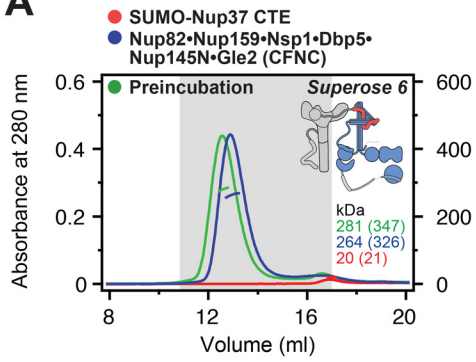
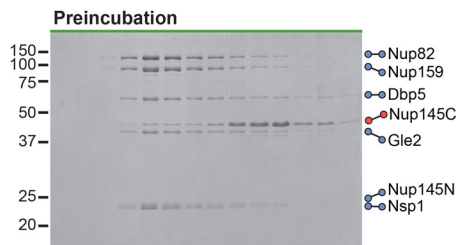
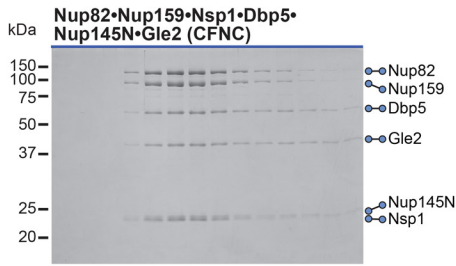
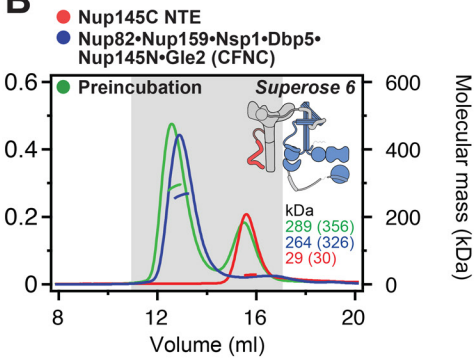
A**B**

Fig. S17. Nup37^{CTE} and Nup145C^{NTE} bind the intact CFNC hetero-hexamer. SEC-MALS interaction analysis of CFNC with (A) SUMO-Nup37^{CTE} and (B) Nup145C^{NTE}. SEC-MALS profiles of nup complexes are shown individually (red, blue) and after preincubation (green). SEC profiles were obtained using a Superose 6 10/300 GL column. Measured molecular masses are indicated, with the respective theoretical masses shown in parentheses. Inset schematics display tested protein samples colored to match the corresponding chromatogram trace. Gray boxes indicate fractions resolved on SDS-PAGE gels and visualized by Coomassie brilliant blue staining.

Reconstitution and biochemical dissection of CFNC-Gle1•Nup42^{GBM} complex

- Strong interaction
- Weak interaction
- No interaction

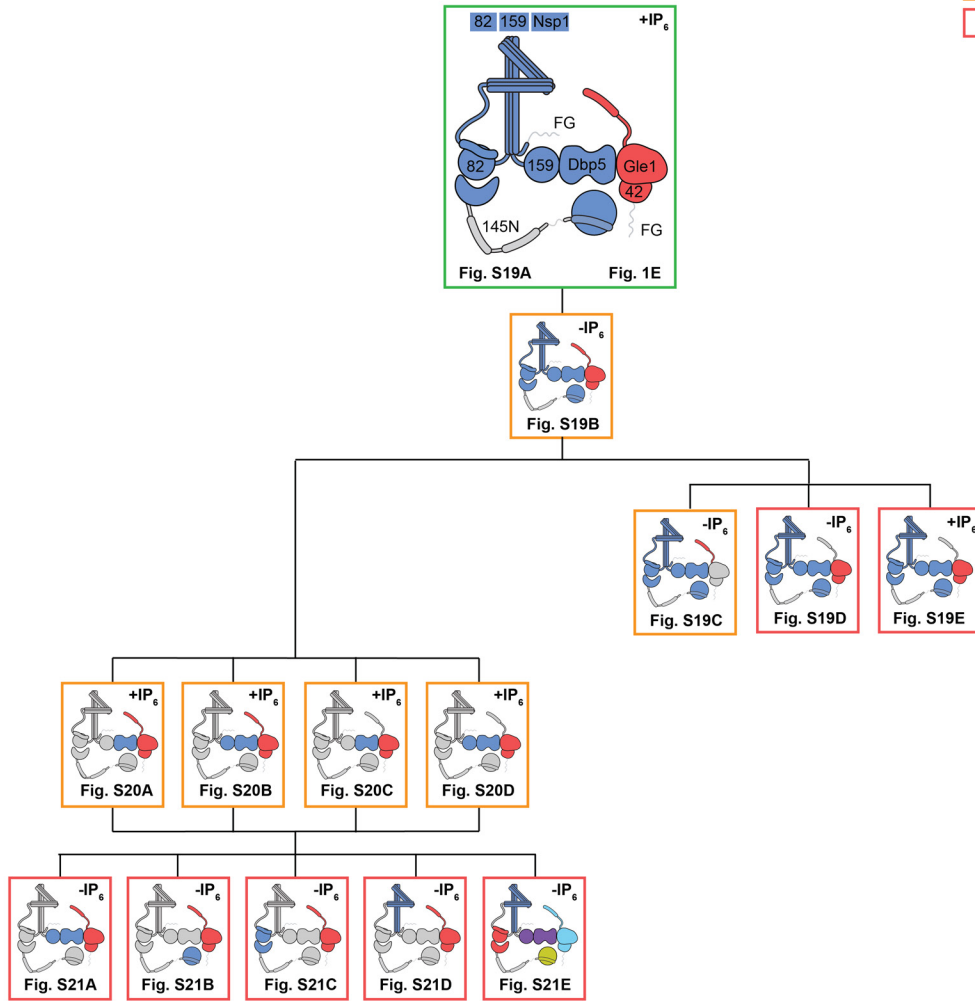
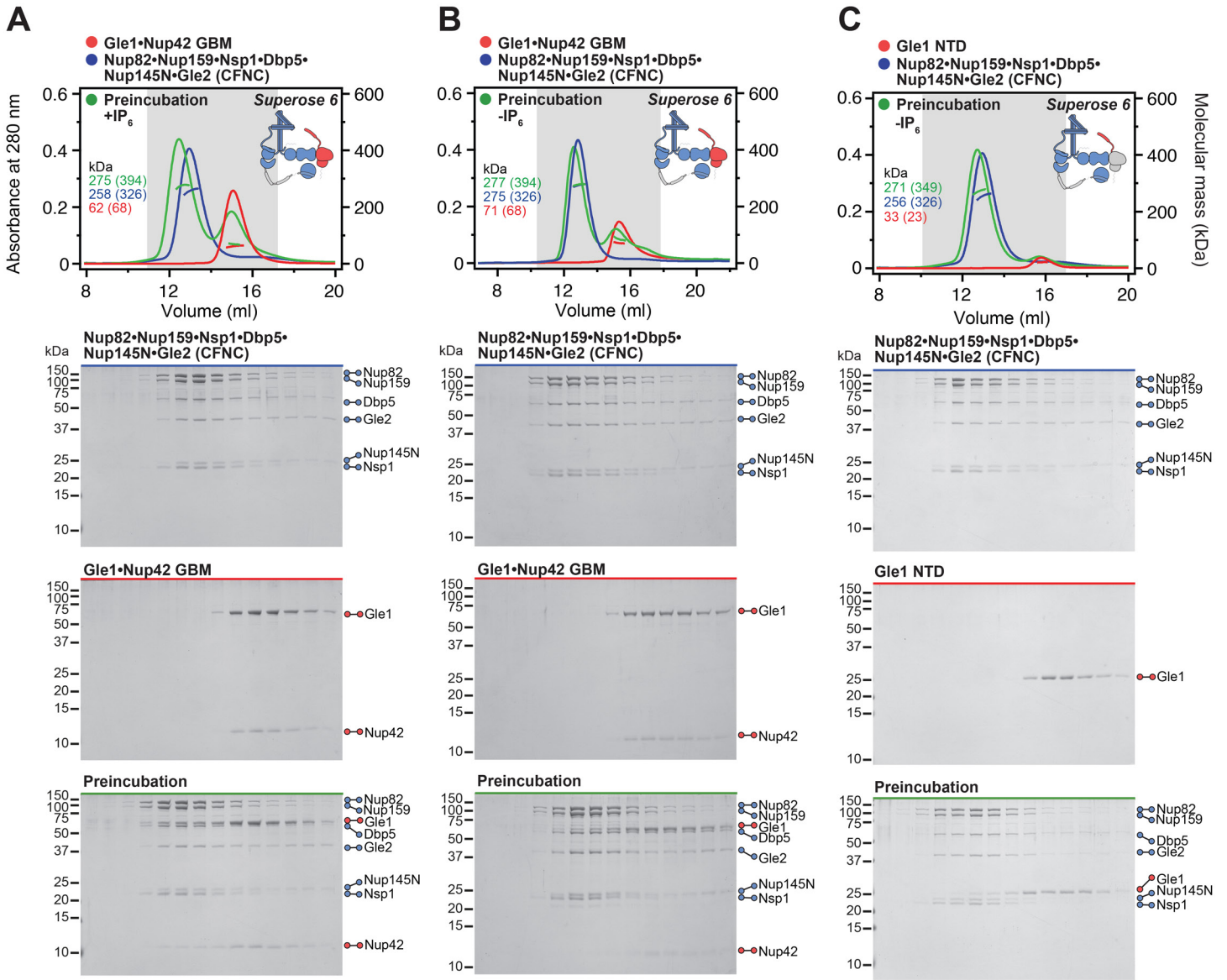


Fig. S18. Reconstitution and dissection strategy for the CFNC•Gle1•Nup42^{GBM} hetero-octamer. Summary of the SEC-MALS interaction analyses of the indicated figure panels. Each box in the flow chart represents a SEC-MALS interaction experiment, involving individually purified Gle1•Nup42^{GBM} and CFNC sub-complexes that were tested for their ability to form stoichiometric complexes, colored by the experimental outcome; strong interaction (green), weak interaction (orange), no interaction (red). The inset schematics are colored to indicate the individually purified Gle1•Nup42^{GBM} and CFNC sub-complexes of each SEC-MALS interaction experiment. Gray regions stipulate proteins omitted from each analysis and the presence and absence of IP₆ in the interaction analyses are indicated.



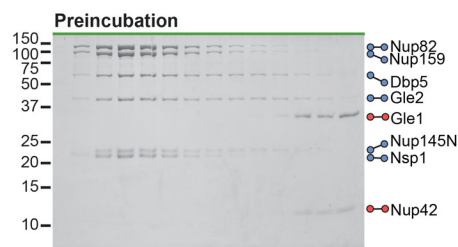
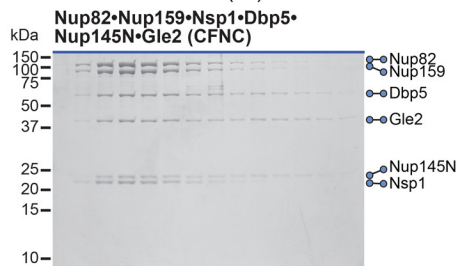
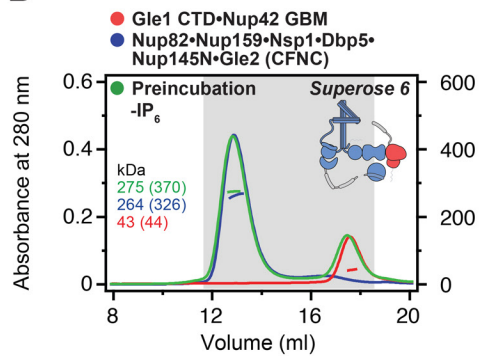
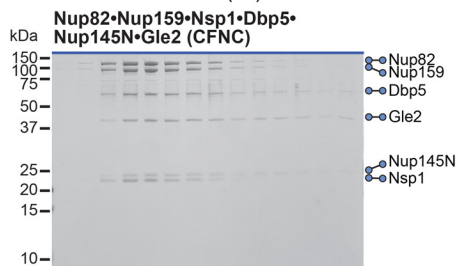
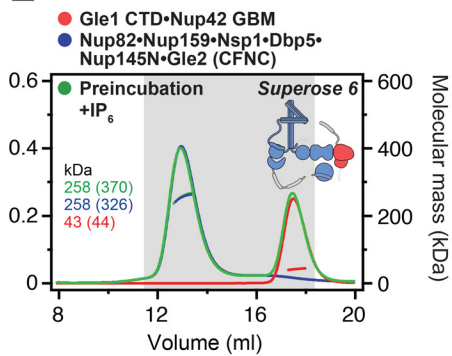
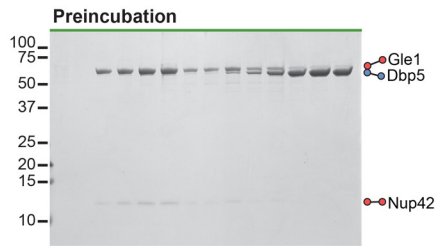
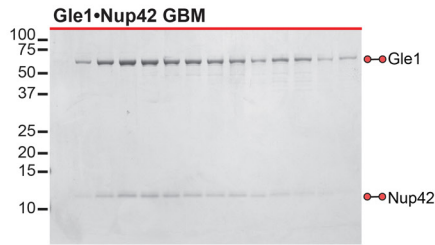
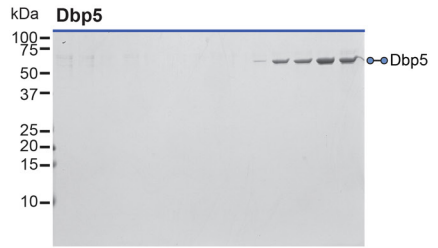
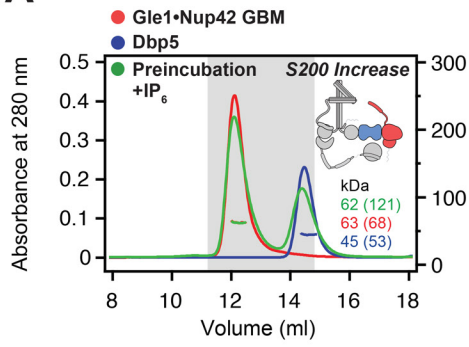
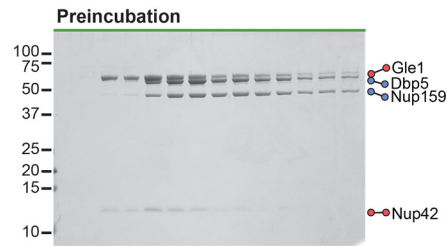
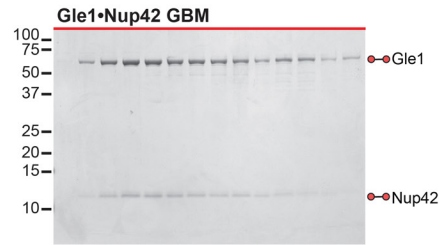
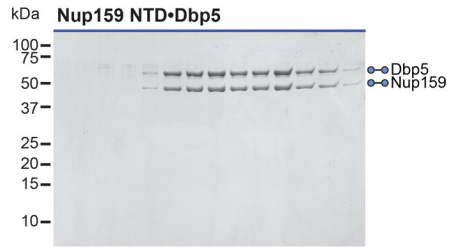
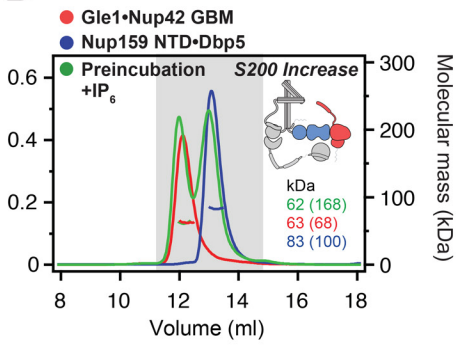
D**E**

Fig. S19. Gle1•Nup42^{GBM} binds the CFNC via a distributed binding site. (A, B) SEC-MALS interaction analysis of Gle1•Nup42^{GBM} and CFNC in the (A) presence and (B) absence of IP₆, demonstrating that formation of a stable stoichiometric CFNC•Gle1•Nup42^{GBM} hetero-octamer is IP₆-dependent (corresponding to Fig. 1E). (C, D) SEC-MALS interaction analyses of CFNC in the absence of IP₆ with (C) Gle1^{NTD} and (D) Gle1^{CTD}•Nup42^{GBM}, demonstrating that Gle1^{NTD} contributes to CFNC binding. (E) SEC-MALS interaction analysis of CFNC in the presence of IP₆ with Gle1^{CTD}•Nup42^{GBM}, showing that Gle1^{CTD} is insufficient for CFNC binding. SEC-MALS profiles of nup complexes are shown individually (red and blue) and after preincubation (green). SEC profiles were obtained using a Superose 6 10/300 GL column. Measured molecular masses are indicated, with the respective theoretical masses shown in parentheses. Inset schematics display tested protein samples colored to match the corresponding chromatogram trace. Gray boxes indicate fractions resolved on SDS-PAGE gels and visualized by Coomassie brilliant blue staining.

A**B**

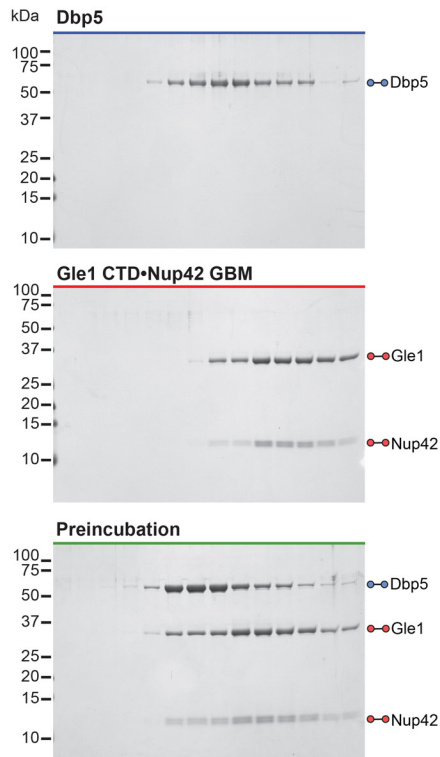
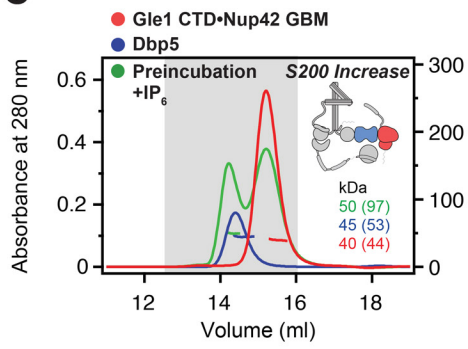
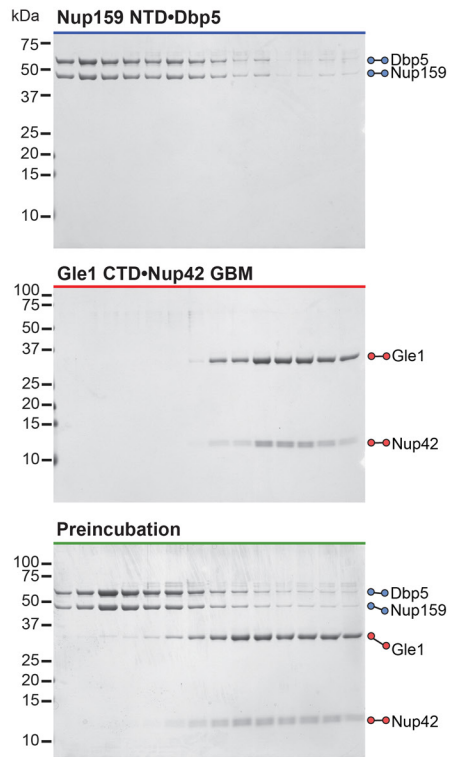
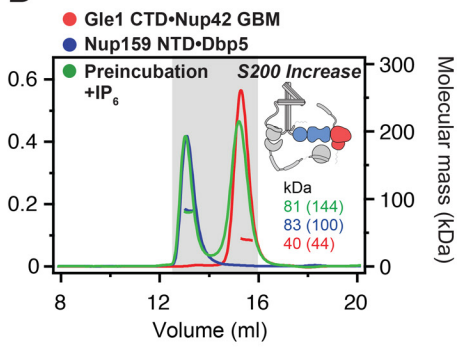
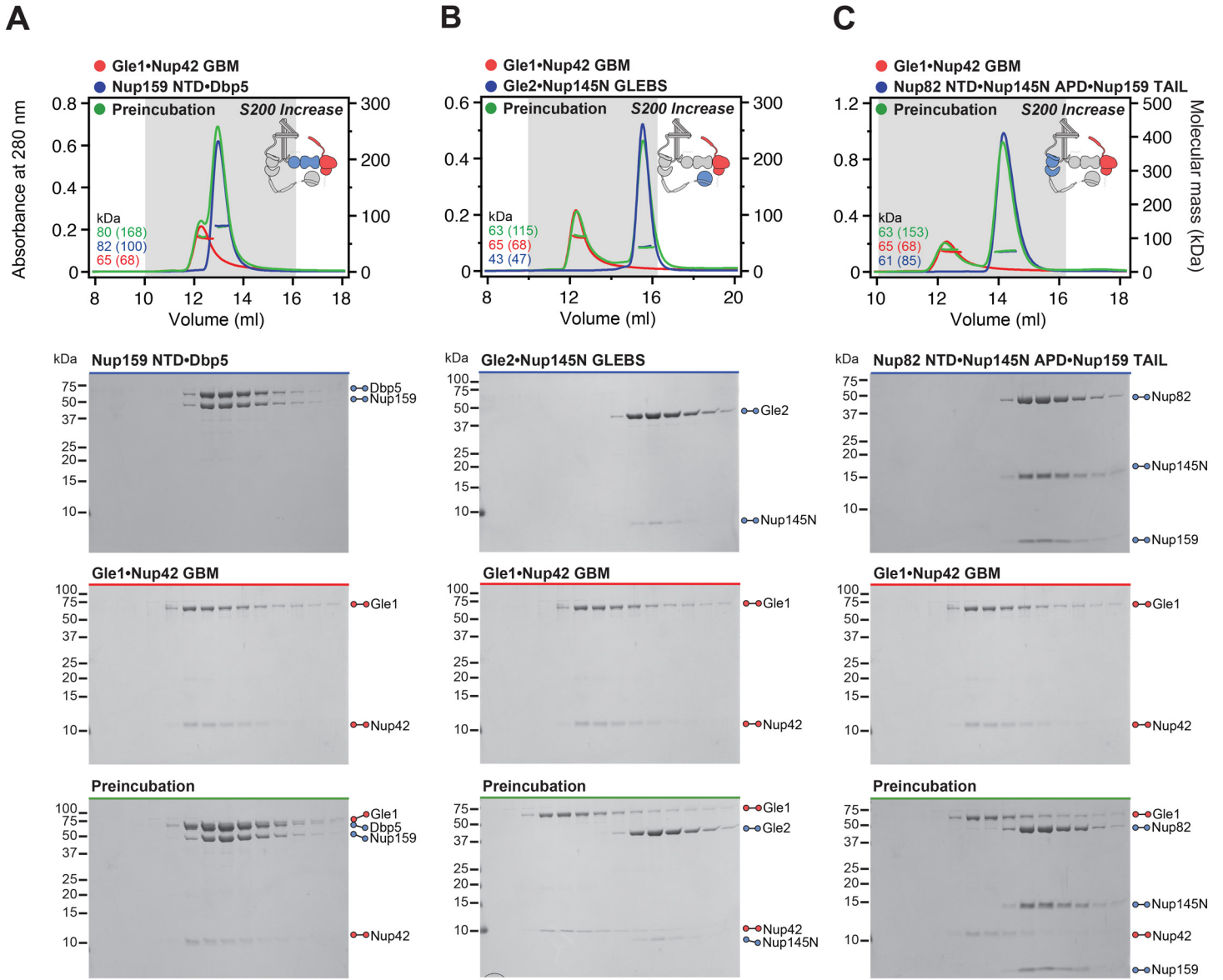
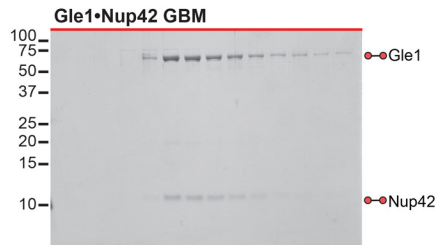
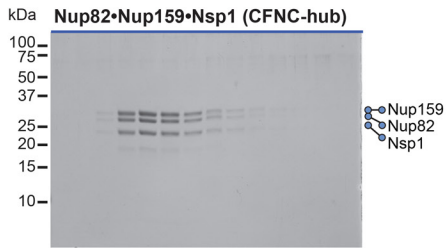
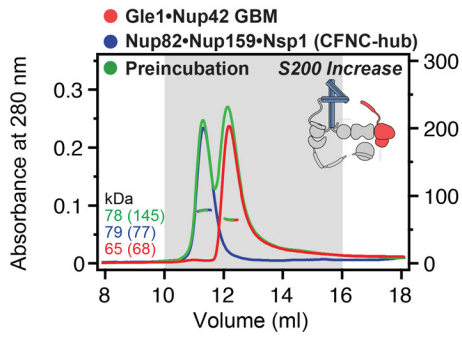
C**D**

Fig. S20. Both Nup159^{NTD} and Gle1^{NTD} are dispensable for the Gle1•Nup42^{GBM}-Dbp5 interaction. (A, B) SEC-MALS interaction analyses of Gle1•Nup42^{GBM} in the presence of IP₆ with (A) Dbp5 and (B) Nup159^{NTD}•Dbp5, showing that Nup159^{NTD} is dispensable for the Gle1•Nup42^{GBM}-Dbp5 interaction. (C, D) SEC-MALS interaction analyses of Gle1^{CTD}•Nup42^{GBM} in the presence of IP₆ with (C) Dbp5 and (D) Nup159^{NTD}•Dbp5, showing that Gle1^{NTD} is dispensable for the Gle1•Nup42^{GBM}-Dbp5 interaction. SEC-MALS profiles of nup complexes are shown individually (red, blue) and after preincubation (green). SEC profiles were obtained using a Superdex 200 Increase 10/300 GL column. Measured molecular masses are indicated, with the respective theoretical masses shown in parentheses. Inset schematics display tested protein samples colored to match the corresponding chromatogram trace. Gray boxes indicate fractions resolved on SDS-PAGE gels and visualized by Coomassie brilliant blue staining.



D



E

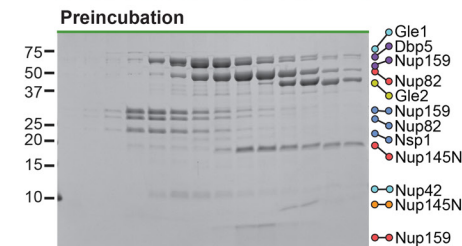
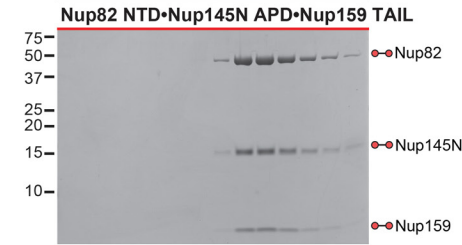
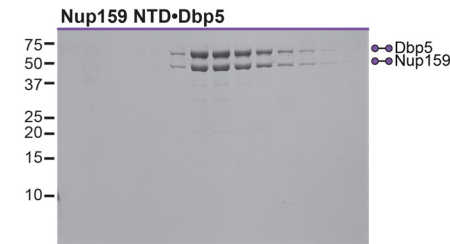
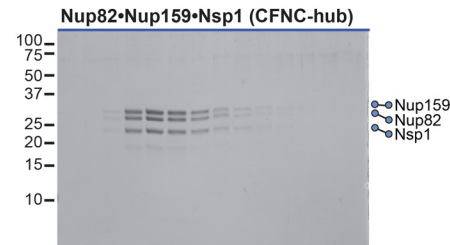
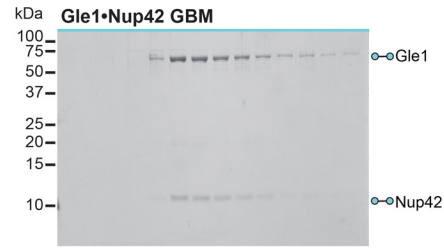
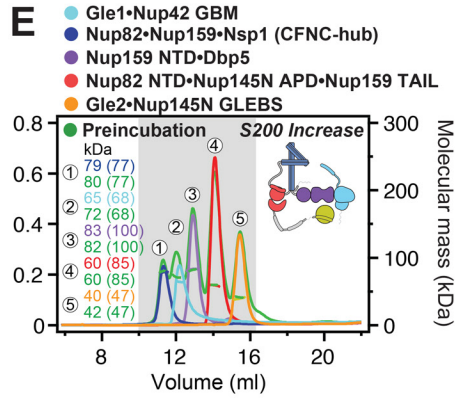


Fig. S21. A distributed CFNC binding site mediates the Gle1•Nup42^{GBM} interaction. (A-E) SEC-MALS interaction analyses of Gle1•Nup42^{GBM} in the absence of IP₆ with (A) Nup159^{NTD}•Dbp5, (B) Gle2•Nup145N^{GLEBS}, (C) Nup82^{NTD}•Nup145N^{APD}•Nup159^{TAIL}, (D) CFNC-hub, and (E) a mixture of all four CFNC subcomplexes, demonstrating that none of the four CFNC sub-complexes recapitulates the binding of intact CFNC. SEC-MALS profiles of nup complexes are shown individually (red, blue, purple and yellow) and after preincubation (green). SEC profiles were obtained using a Superdex 200 Increase 10/300 GL column. Measured molecular masses are indicated, with the respective theoretical masses shown in parentheses. Inset schematics display tested protein samples colored to match the corresponding chromatogram trace. Gray boxes indicate fractions resolved on SDS-PAGE gels and visualized by Coomassie brilliant blue staining.

Reconstitution and biochemical dissection
 CNC•CFNC•Gle1•Nup42^{GBM}

- Strong interaction
- Weak interaction
- No interaction

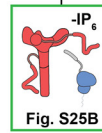
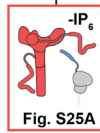
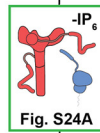
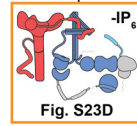
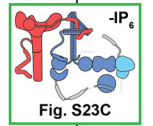
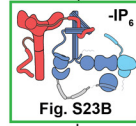
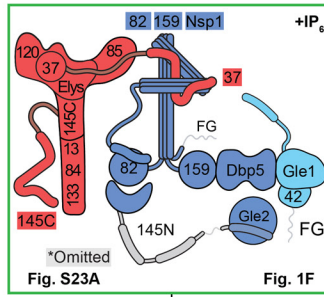
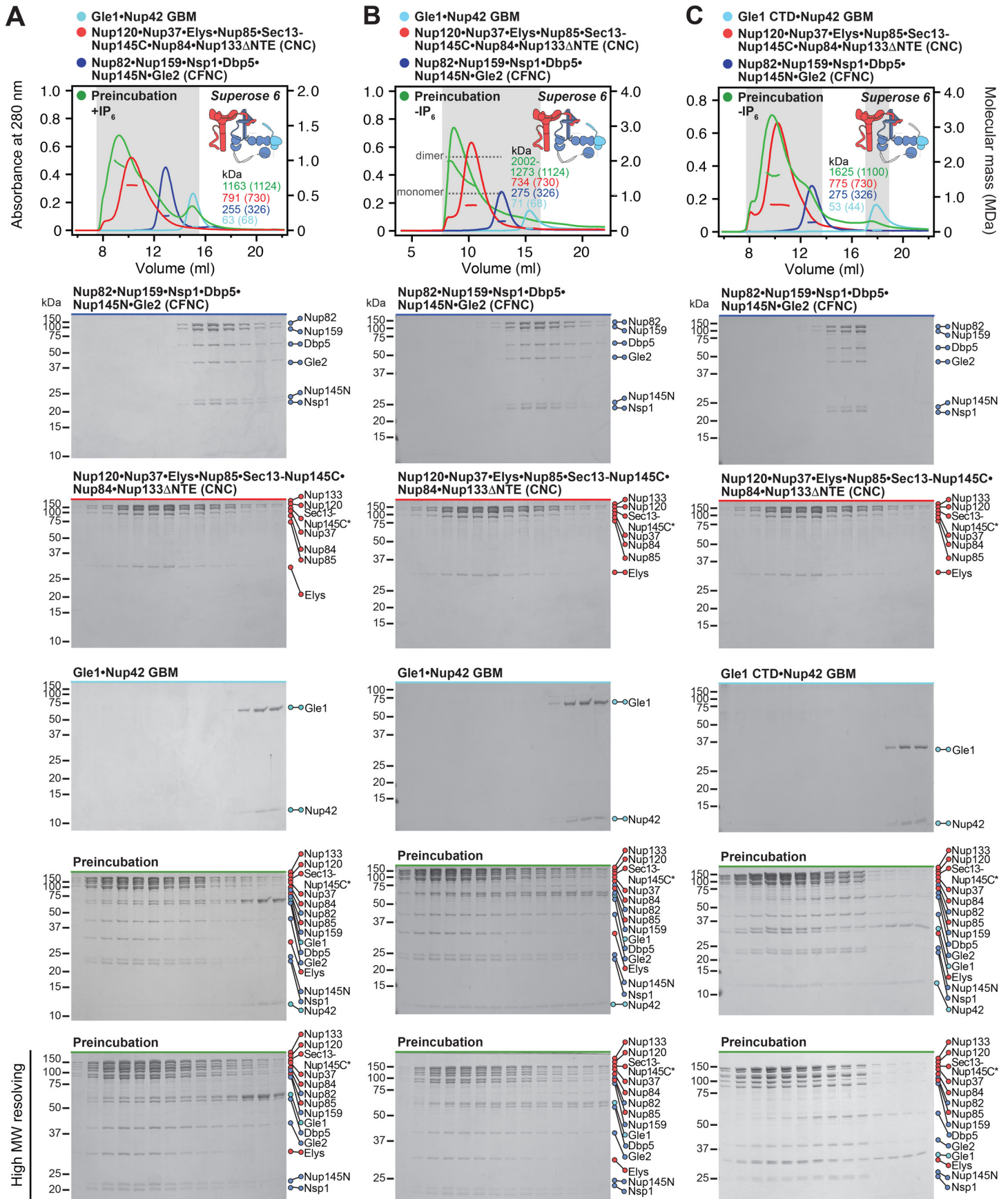


Fig. S22. Reconstitution and dissection strategy for the 16-protein CNC•CFNC•Gle1•Nup42^{GBM}. Summary of the SEC-MALS interaction analyses of the indicated figure panels. Each box in the flow chart represents a SEC-MALS interaction experiment, involving individually purified Gle1•Nup42^{GBM}, CFNC, and CNC sub-complexes that were tested for their ability to form stoichiometric complexes, colored by the experimental outcome; strong interaction (green), weak interaction (orange), no interaction (red). The inset schematics are colored to indicate the individually purified Gle1•Nup42^{GBM}, CFNC, and CNC sub-complexes of each SEC-MALS interaction experiment. Gray regions stipulate proteins omitted from each analysis and the presence and absence of IP₆ in the interaction analyses are indicated.



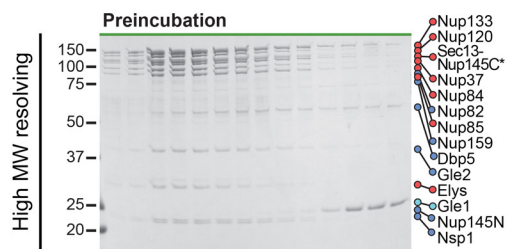
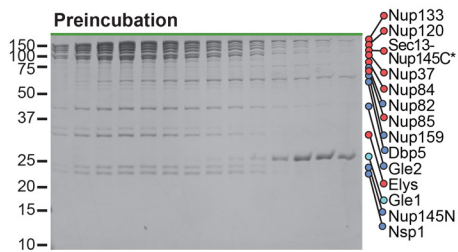
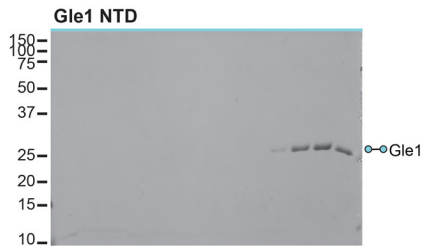
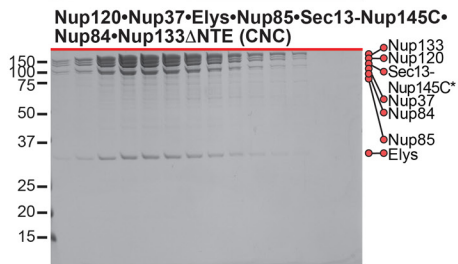
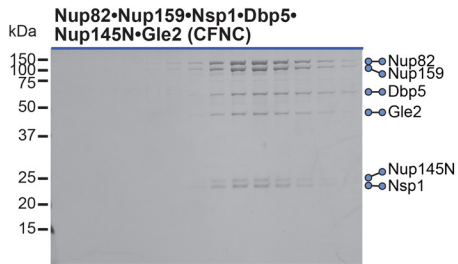
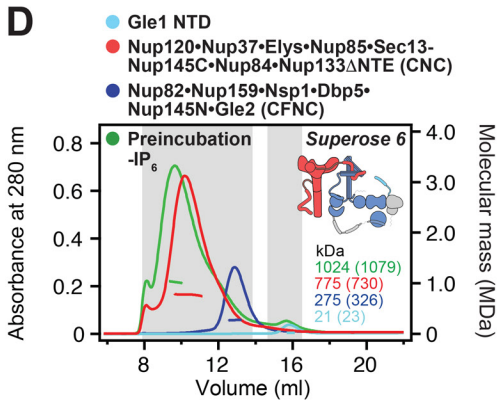


Fig. S23. Reconstitution of a 16-protein coat-cytoplasmic filament nup complex. (A) SEC-MALS interaction analysis of CNC, CFNC, and Gle1•Nup42^{GBM} in the presence of IP₆, demonstrating the formation of an ~1,163 kDa monodisperse, stoichiometric 16-protein CNC•CFNC complex (corresponding to Fig. 1F). (B) SEC-MALS interaction analysis of CNC, CFNC, and Gle1•Nup42^{GBM} in the absence of IP₆, demonstrating the formation of a peak corresponding to a monomeric and a dimeric assembly state of the 16-protein CNC•CFNC complex with molecular masses ranging from ~2,002 to ~1,273 kDa. (C, D) SEC-MALS analysis of the CNC•CFNC interaction with (C) Gle1^{CTD}•Nup42^{GBM} and (D) Gle1^{NTD} in the absence of IP₆, demonstrating Gle1^{CTD}•Nup42^{GBM} incorporation into the CNC-CFNC complex and partial dimer formation, whereas the Gle1^{NTD} exhibits barely detectable binding. SEC-MALS profiles of nup complexes are shown individually (red, blue and cyan) and after preincubation (green). SEC profiles were obtained using a Superose 6 10/300 GL column. Measured molecular masses are indicated, with the respective theoretical masses shown in parentheses. Inset schematics display tested protein samples colored to match the corresponding chromatogram trace. Gray boxes indicate fractions resolved on SDS-PAGE gels and visualized by Coomassie brilliant blue staining.

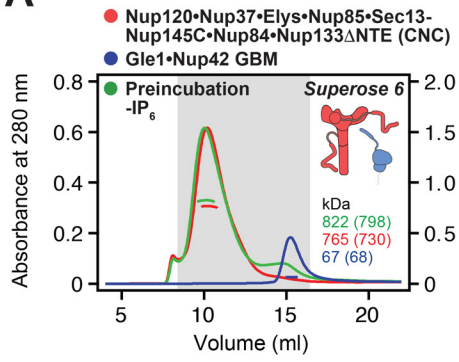
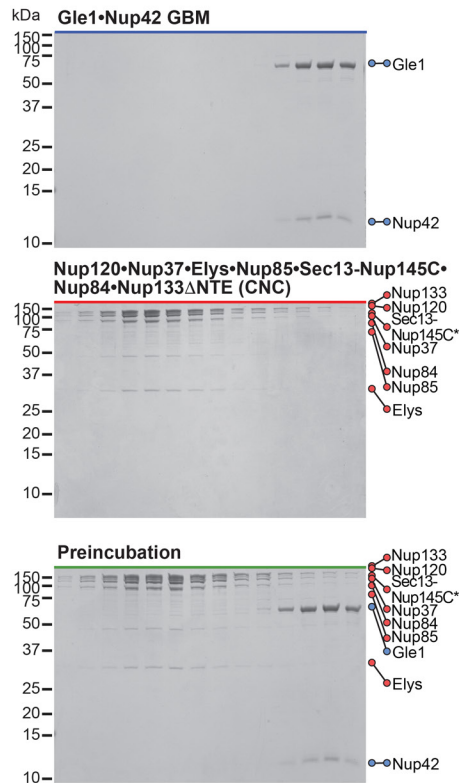
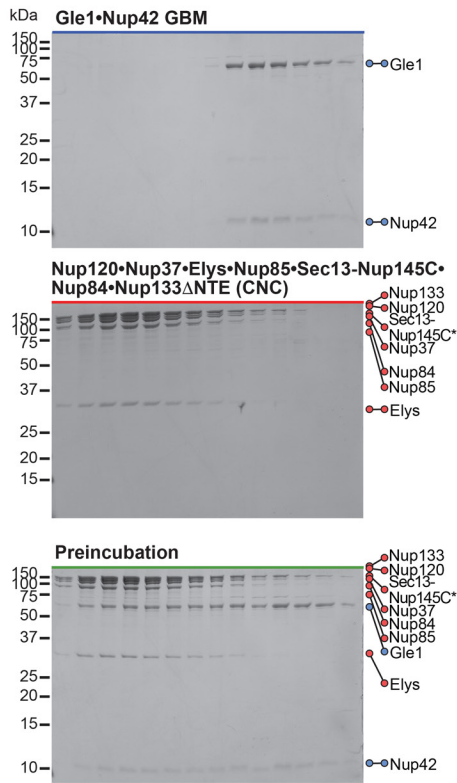
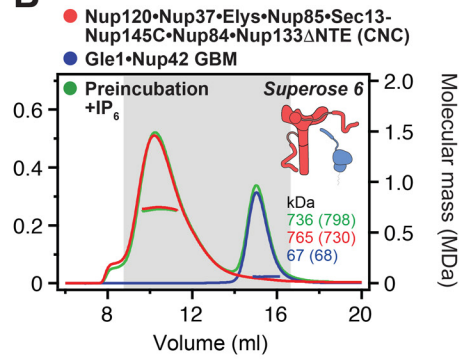
A**B**

Fig. S24. Gle1•Nup42^{GBM} binds to the CNC in an IP₆-dependent fashion. (A, B) SEC-MALS analyses of the interaction between Gle1•Nup42^{GBM} and CNC (A) in the absence and (B) presence of IP₆, demonstrating the formation of a stoichiometric monodisperse ~822 kDa Gle1•Nup42^{GBM}•CNC complex exclusively in the absence of IP₆. SEC-MALS profiles of nup complexes are shown individually (red, blue) and after preincubation (green). SEC profiles were obtained using a Superose 6 10/300 GL column. Measured molecular masses are indicated, with the respective theoretical masses shown in parentheses. Inset schematics display tested protein samples colored to match the corresponding chromatogram trace. Gray boxes indicate fractions resolved on SDS-PAGE gels and visualized by Coomassie brilliant blue staining.

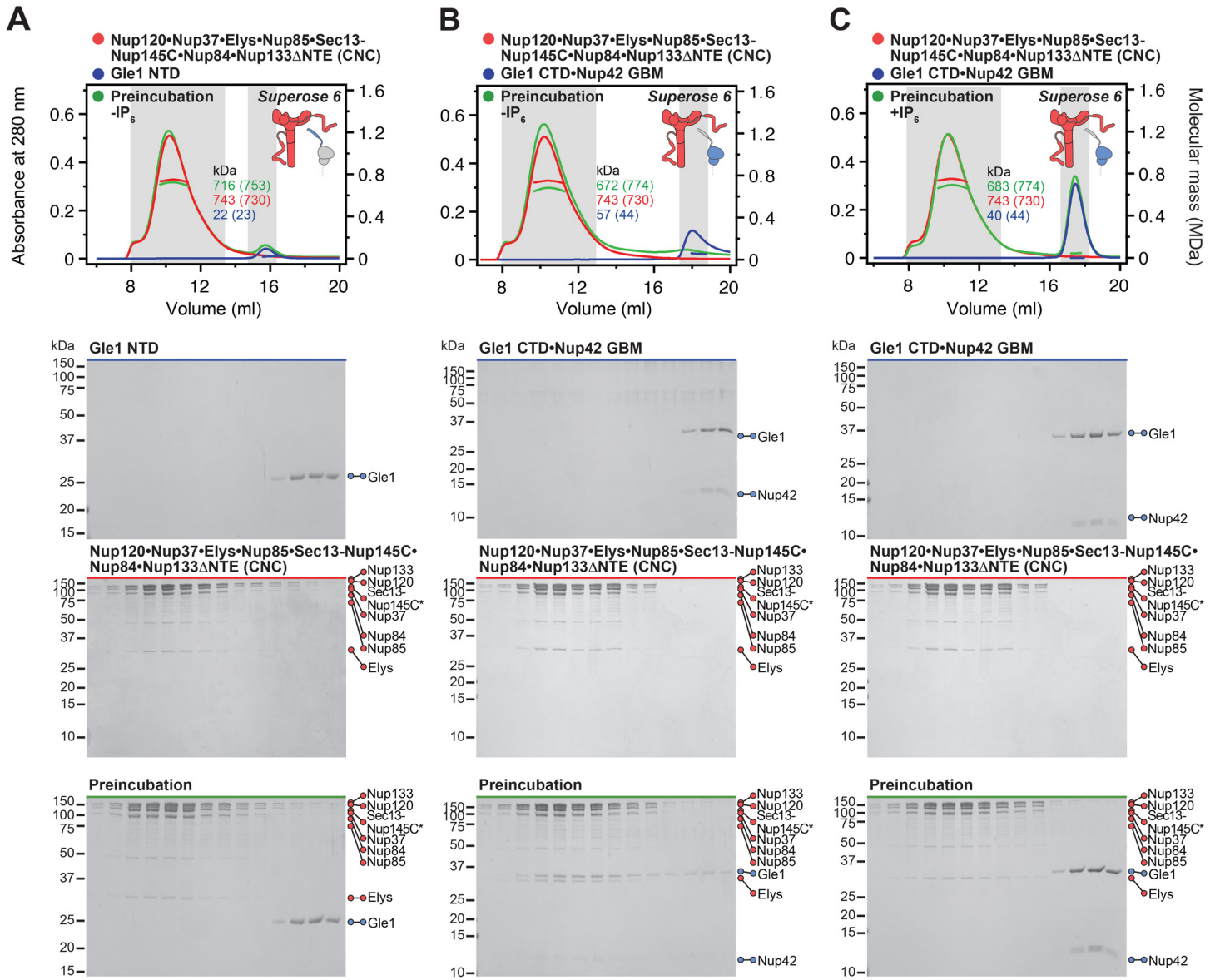


Fig. S25. Gle1^{NTD} is dispensable for the Gle1•Nup42^{GBM}-CNC interaction. (A, B) SEC-MALS interaction analyses of the CNC in the absence of IP₆ with (A) Gle1^{NTD} and (B) Gle1^{CTD}•Nup42^{GBM}, showing that Gle1^{CTD}•Nup42^{GBM} binds the CNC, whereas no binding is detected for Gle1^{NTD}. (C) SEC-MALS interaction analysis of the CNC in the presence of IP₆ with Gle1^{CTD}•Nup42^{GBM}, demonstrating that the presence of IP₆ prevents binding of Gle1^{CTD}•Nup42^{GBM} to CNC. SEC-MALS profiles of nup complexes are shown individually (red, blue) and after preincubation (green). SEC profiles were obtained using a Superose 6 10/300 GL column. Measured molecular masses are indicated, with the respective theoretical masses shown in parentheses. Inset schematics display tested protein samples colored to match the corresponding chromatogram trace. Gray boxes indicate fractions resolved on SDS-PAGE gels and visualized by Coomassie brilliant blue staining.

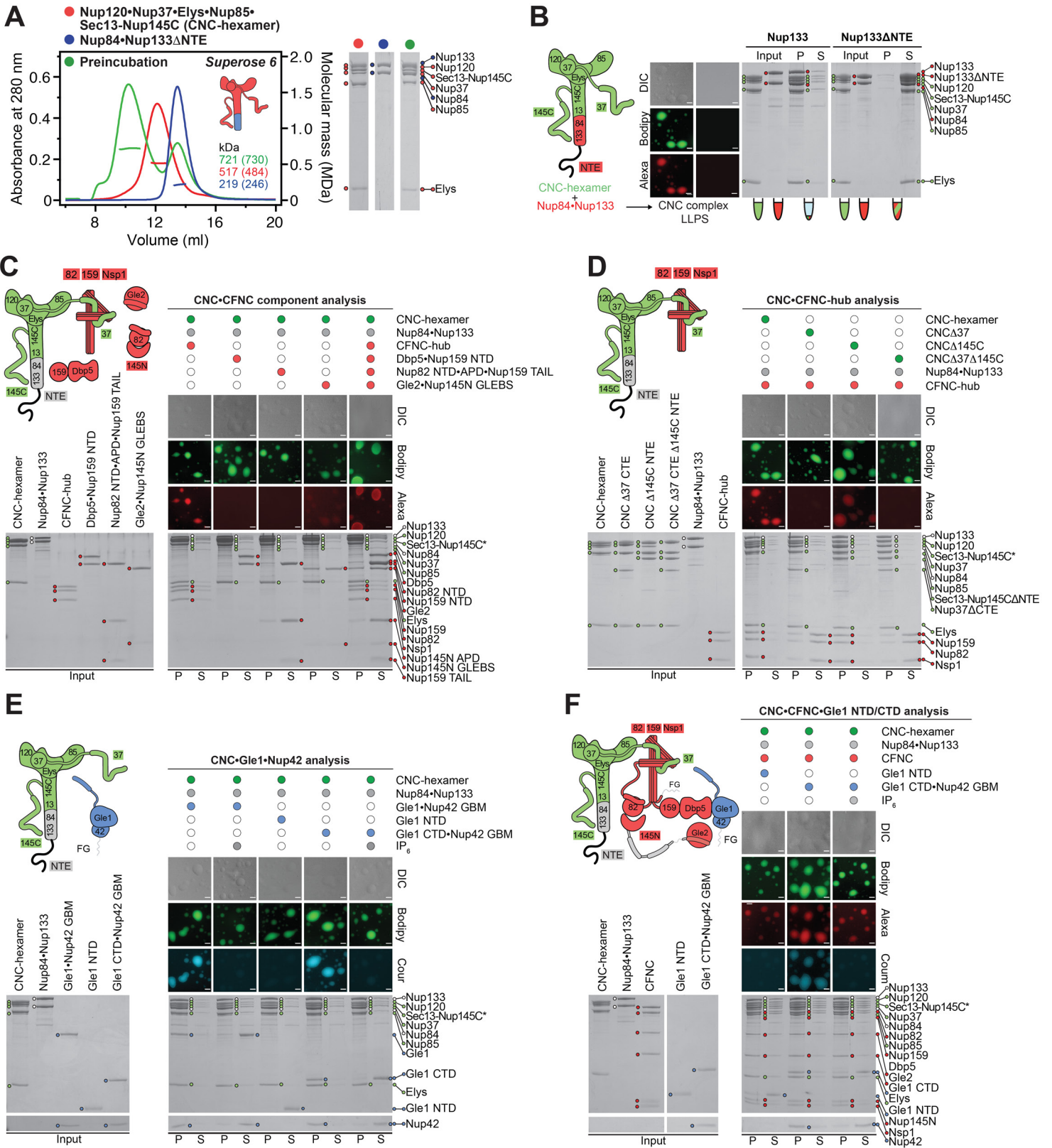


Fig. S26. Liquid-liquid phase separation analysis of coat-cytoplasmic filament nup interactions. (A) SEC-MALS interaction analysis of Nup120•Nup37•Elys•Nup85•Sec13-Nup145C (CNC-hexamer; red) with Nup84•Nup133^{ANTE} (blue), and their preincubation (green), showing the formation of a stoichiometric monodisperse CNC complex in the absence of Nup133^{NTE}. SEC profiles were obtained using a Superose 6 10/300 GL column. Measured molecular masses are indicated, with the respective theoretical masses shown in parentheses. SDS-PAGE gels strips of the peak fractions are shown. (B) Mixing CNC-hexamer (green) with Nup84•Nup133 (red) results in formation of liquid-liquid phase separation (LLPS) condensates, dependent on the presence of Nup133^{NTE}. (C) LLPS interaction assay, assessing the incorporation of the four CFNC subcomplexes (CFNC-hub, Dbp5•Nup159^{NTD}, Nup82^{NTD}•Nup145N^{APD}•Nup159^{TAIL}, and Gle2•Nup145N^{GLEBS}) into the CNC-LLPS condensate, identifying that only CFNC-hub enters. (D) LLPS interaction assay, assessing CFNC-hub incorporation into LLPS condensates, generated by CNC variants lacking either Nup37^{CTE}, Nup145C^{NTE}, or both assembly sensors, demonstrating that CFNC-hub entry is dependent on both assembly sensors. (E) LLPS interaction assay, assessing the incorporation of Gle1•Nup42^{GBM}, Gle1^{NTD}, and Gle1^{CTD}•Nup42^{GBM}, into the CNC-LLPS condensate. Whereas Gle1^{NTD} fails to incorporate, both Gle1•Nup42^{GBM} and Gle1^{CTD}•Nup42^{GBM} enter the condensate, but only in the absence of IP₆. (F) LLPS interaction assay, assessing Gle1^{NTD} and Gle1^{CTD}•Nup42^{GBM} incorporation into CNC-CFNC-LLPS condensates. As for the CNC-LLPS, Gle1^{NTD} fails to incorporate, whereas the condensate incorporation of Gle1^{CTD}•Nup42^{GBM} occurs only in the absence of IP₆. These results establish that the CFNC-CNC interaction is mediated by the Nup37^{CTE} and Nup145C^{NTE} assembly sensors and show that Gle1•Nup42^{GBM} incorporation requires both Gle1^{NTD} and Gle1^{CTD}•Nup42^{GMB} in the presence of IP₆. The fluorescence microscopy analyses utilized dye labeled proteins, CNC-hexamer and its variants (Bodipy; green), CFNC and its sub-complexes (Alexa Fluor 647; red), and Gle1•Nup42^{GBM} and its fragments (Coumarin; cyan). Pelleted CNC condensate phase (P) and soluble (S) fractions were analyzed by SDS-PAGE and visualized by Coomassie brilliant blue staining. All experiments were repeated at least three times. Scale bars are 10 μ m.

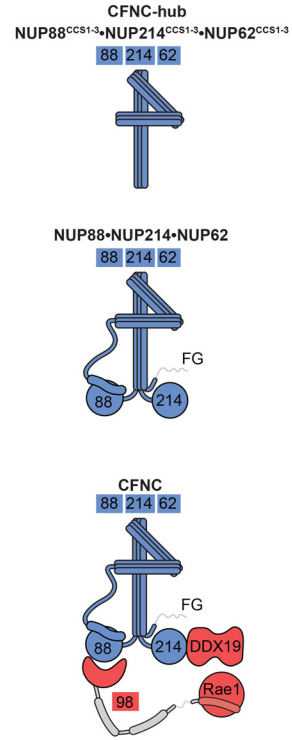
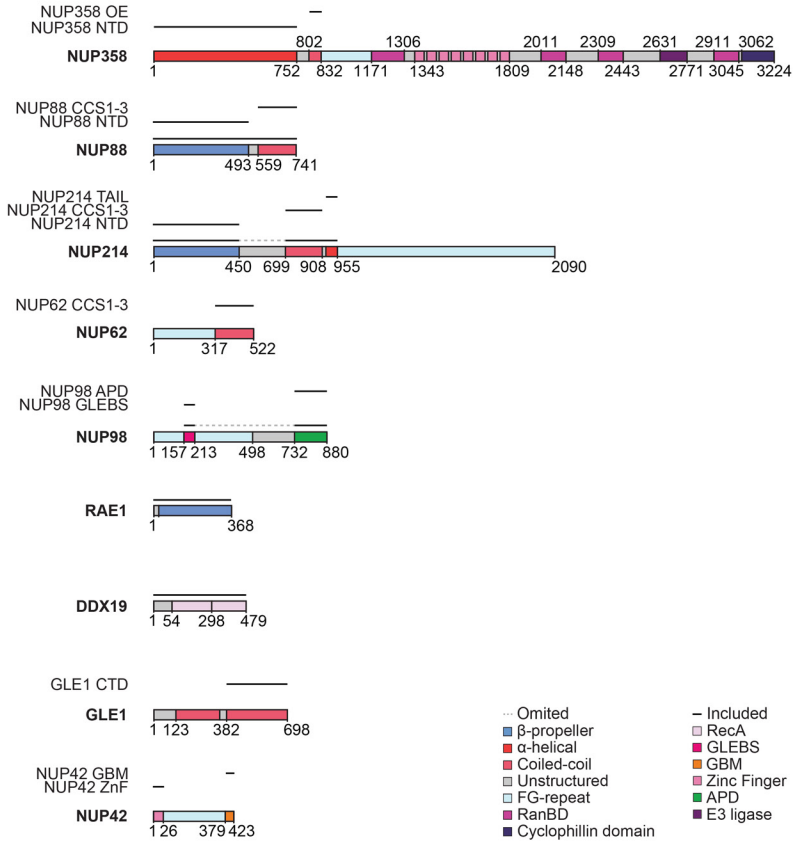


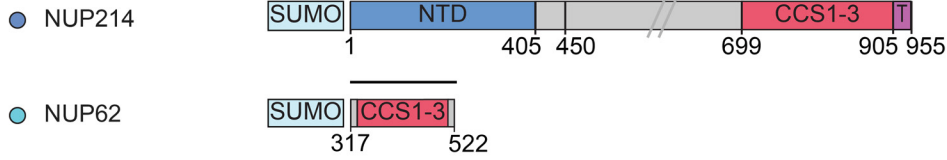
Fig. S27. *H. sapiens* nucleoporin fragments. Domain architectures of the human cytoplasmic filament nups. Domains are drawn as horizontal boxes with residue numbers indicated and their observed or predicted folds colored according to the legend. The black lines indicate the fragments used throughout the text. Dashed lines indicate regions excluded from expression constructs. As a reference, schematics of nup complexes are shown on the right.

A

pET-28-SUMO



pET-Duet



B

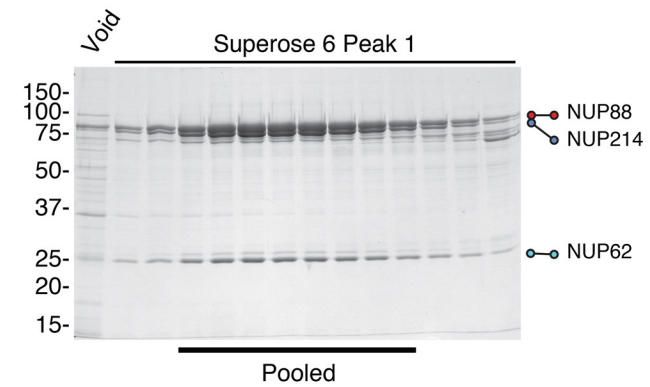
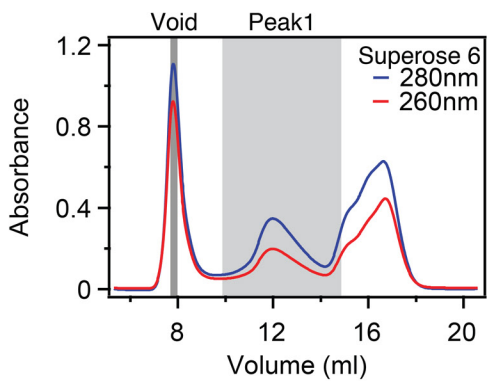
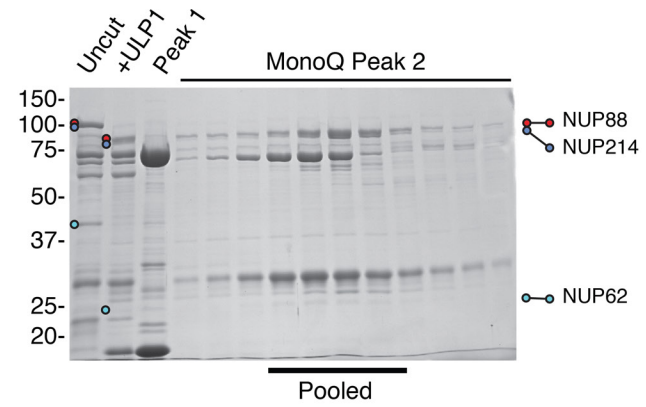
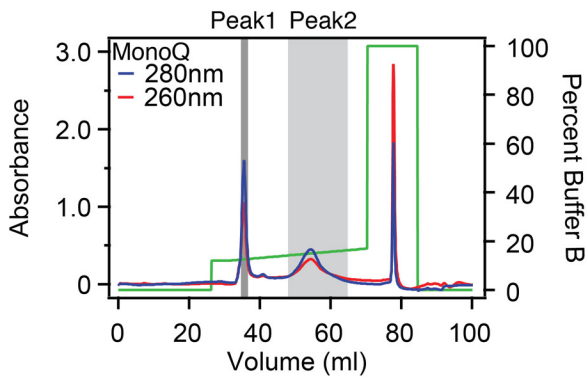
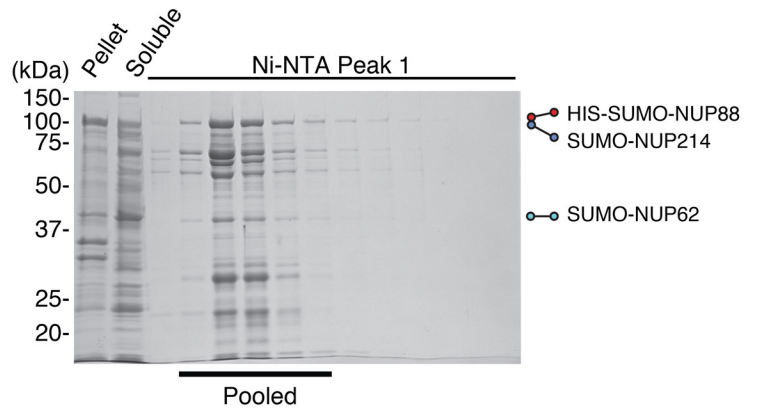
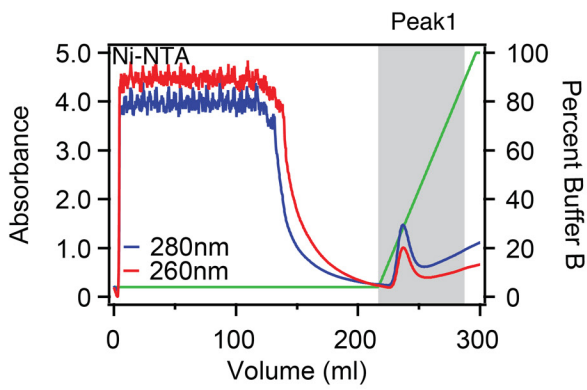


Fig. S28. Purification of the human NUP88•NUP214•NUP62 hetero-trimer. (A) Domain boundaries of the purified nups are shown with black lines indicating the construct boundaries of NUP88, NUP214, and NUP62 in our bacterial expression constructs. The dashed line indicates a central unstructured region in NUP214 that was excluded. (B) NUP88•NUP214•NUP62 hetero-trimer purification. Sequential chromatography purification steps are shown from top to bottom with the employed columns indicated. The gray boxes indicate fractions that were resolved on SDS-PAGE gels and visualized by Coomassie staining. Pooled fractions are indicated with a black bar below the SDS-PAGE gels. For details of the buffer conditions see [Table S5](#).

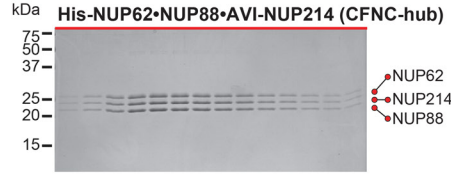
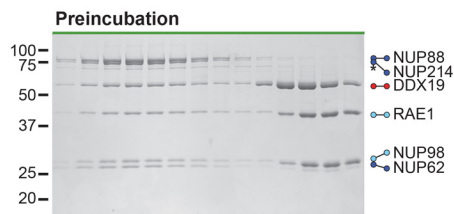
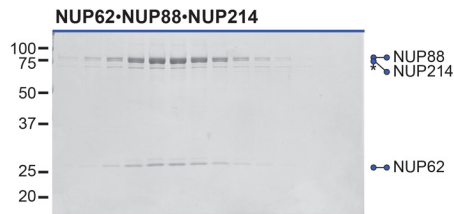
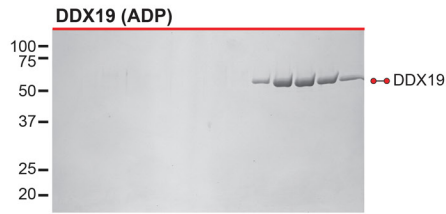
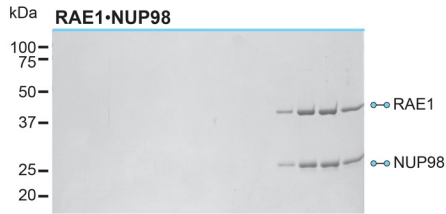
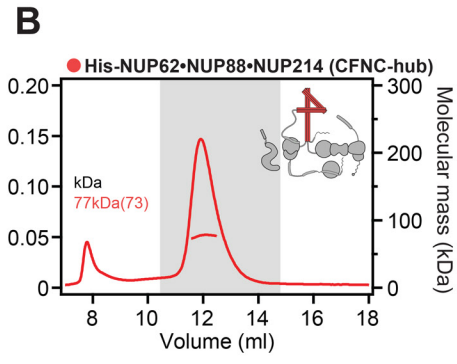
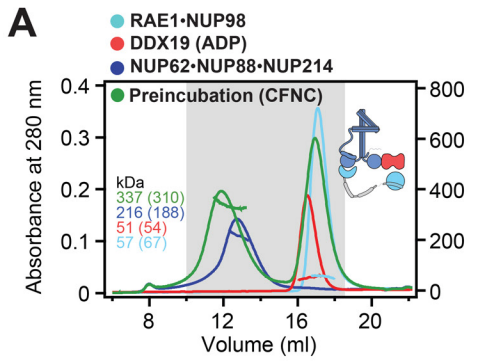
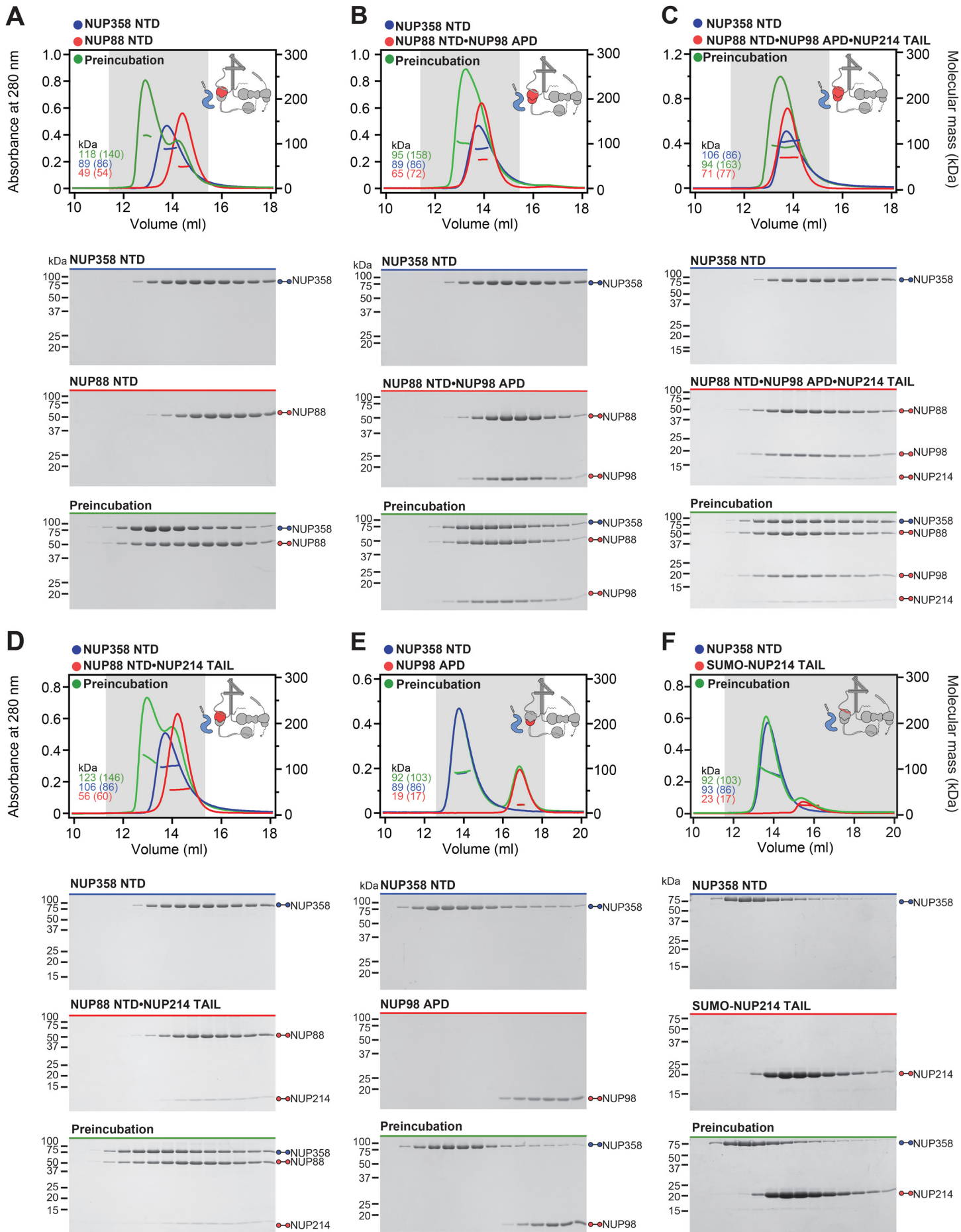
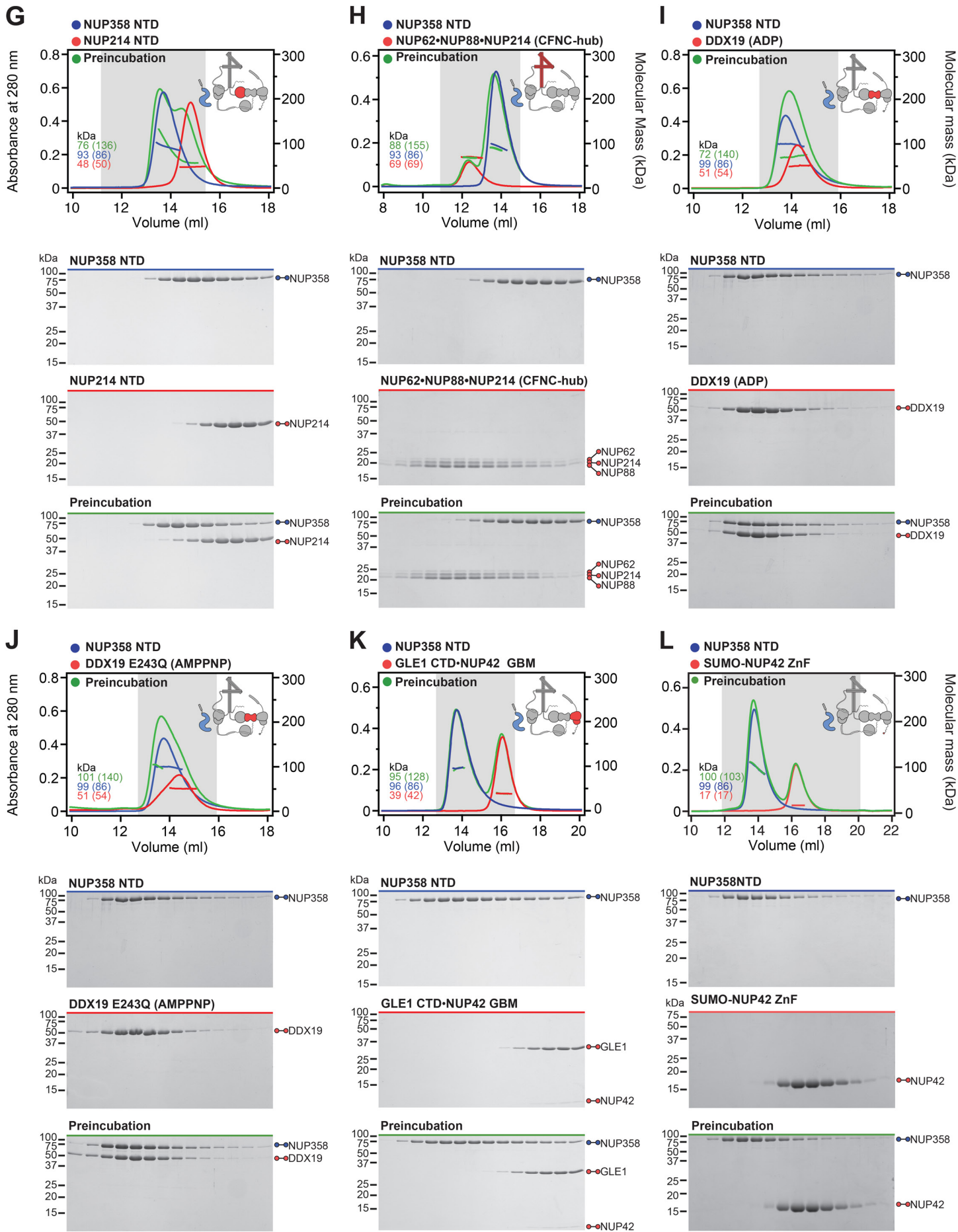


Fig. S29. Reconstitution of the evolutionarily conserved human CFNC hetero-hexamer. (A) SEC-MALS interaction analysis showing the biochemical reconstitution of the ~330 kDa hetero-hexameric CFNC (green) from NUP62•NUP88•NUP214 (blue), RAE1•NUP98 (cyan), and DDX19(ADP) (red) (corresponding to [Fig. 2C](#)). SEC profiles were obtained on a Superose 6 10/300 GL column. (B) SEC-MALS analysis of the hetero-trimeric NUP62•NUP88•NUP214 CCS1-3 complex (CFNC-hub). SEC profile was obtained on a Superdex 200 10/300 GL column. Measured molecular masses are indicated, with the respective theoretical masses shown in parentheses. The inset schematics are colored to indicate the CFNC sub-complexes of each SEC-MALS interaction experiment, with gray domains and regions omitted from the experiment. Gray boxes indicate fractions resolved on SDS-PAGE gels and visualized by Coomassie brilliant blue staining.





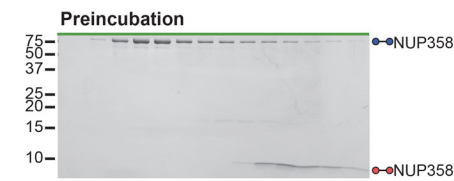
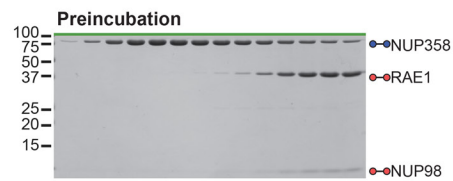
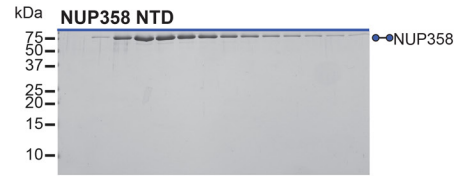
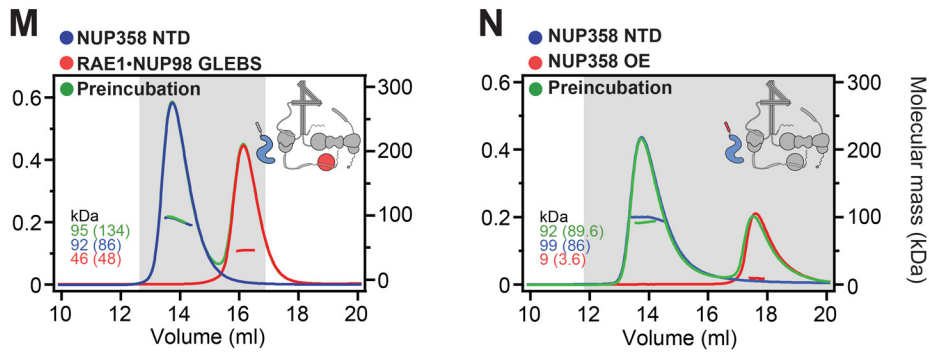
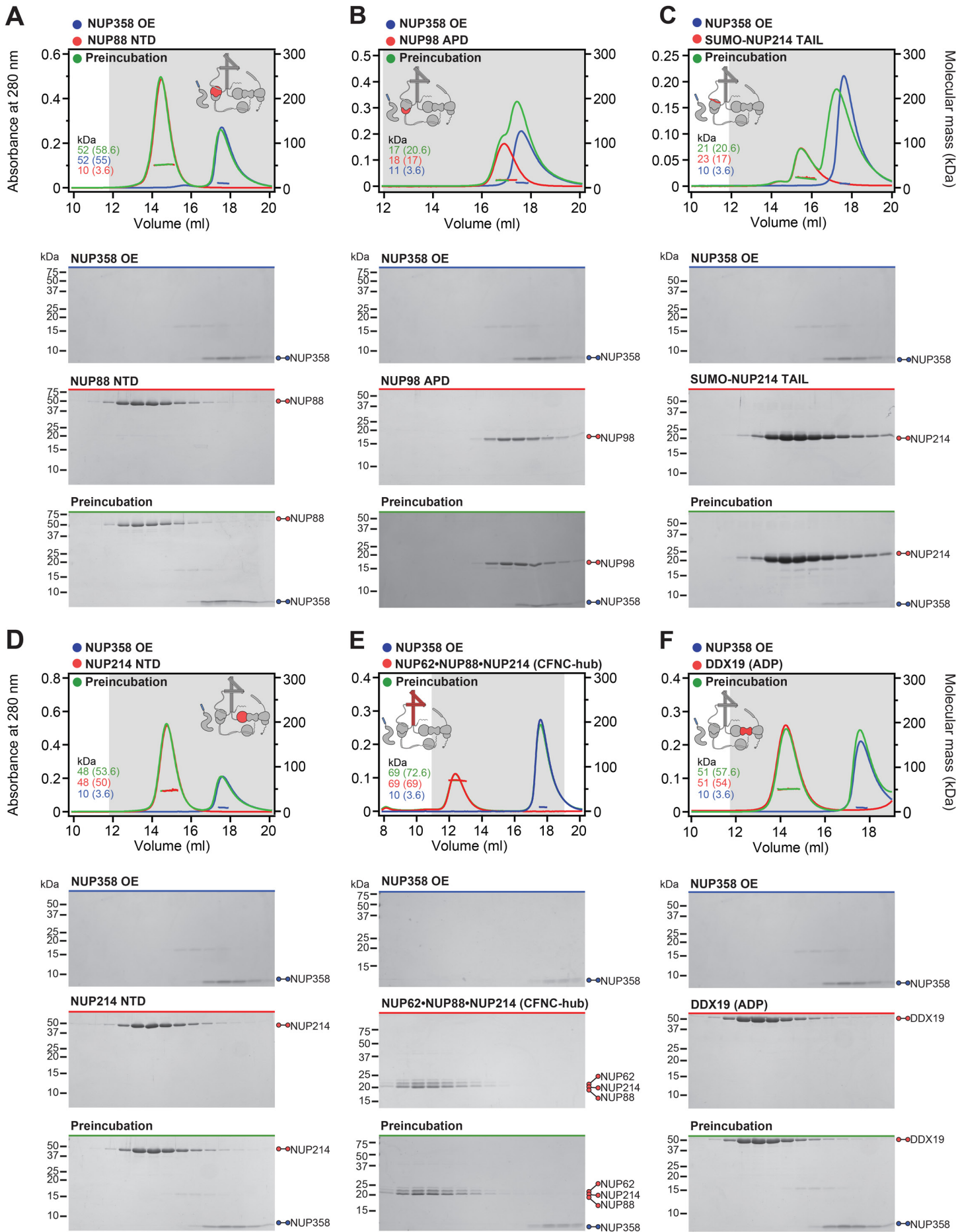


Fig. S30. Systematic interaction analyses of NUP358^{NTD} with human CF nup fragments. SEC-MALS interaction analyses of NUP358^{NTD} with (A) Nup88^{NTD}, (B) NUP88^{NTD}•NUP98^{APD}, (C) NUP88^{NTD}•NUP98^{APD}•NUP214^{TAIL}, (D) NUP88^{NTD}•NUP214^{TAIL}, (E) NUP98^{APD}, (F) SUMO-NUP214^{TAIL}, (G) NUP214^{NTD}, (H) CFNC-hub, (I) DDX19 (ADP), (J) DDX19 E243Q (AMPPNP), (K) GLE1^{CTD}•NUP42, (L) SUMO-NUP42^{ZnF}, (M) RAE1•NUP98^{GLEBS}, and (N) NUP358^{OE}. Interactions were observed between Nup358^{NTD} and Nup88^{NTD}, Nup88^{NTD}-Nup98^{APD}, and Nup88^{NTD}-Nup98^{APD}-Nup214^{TAIL}. SEC-MALS profiles of nup complexes are shown individually (red and blue) and after preincubation (green). SEC profiles were obtained using a Superdex 200 10/300 GL column. Measured molecular masses are indicated, with the respective theoretical masses shown in parentheses. Inset schematics display tested protein samples colored to match the corresponding chromatogram trace. Gray boxes indicate fractions resolved on SDS-PAGE gels and visualized by Coomassie brilliant blue staining.



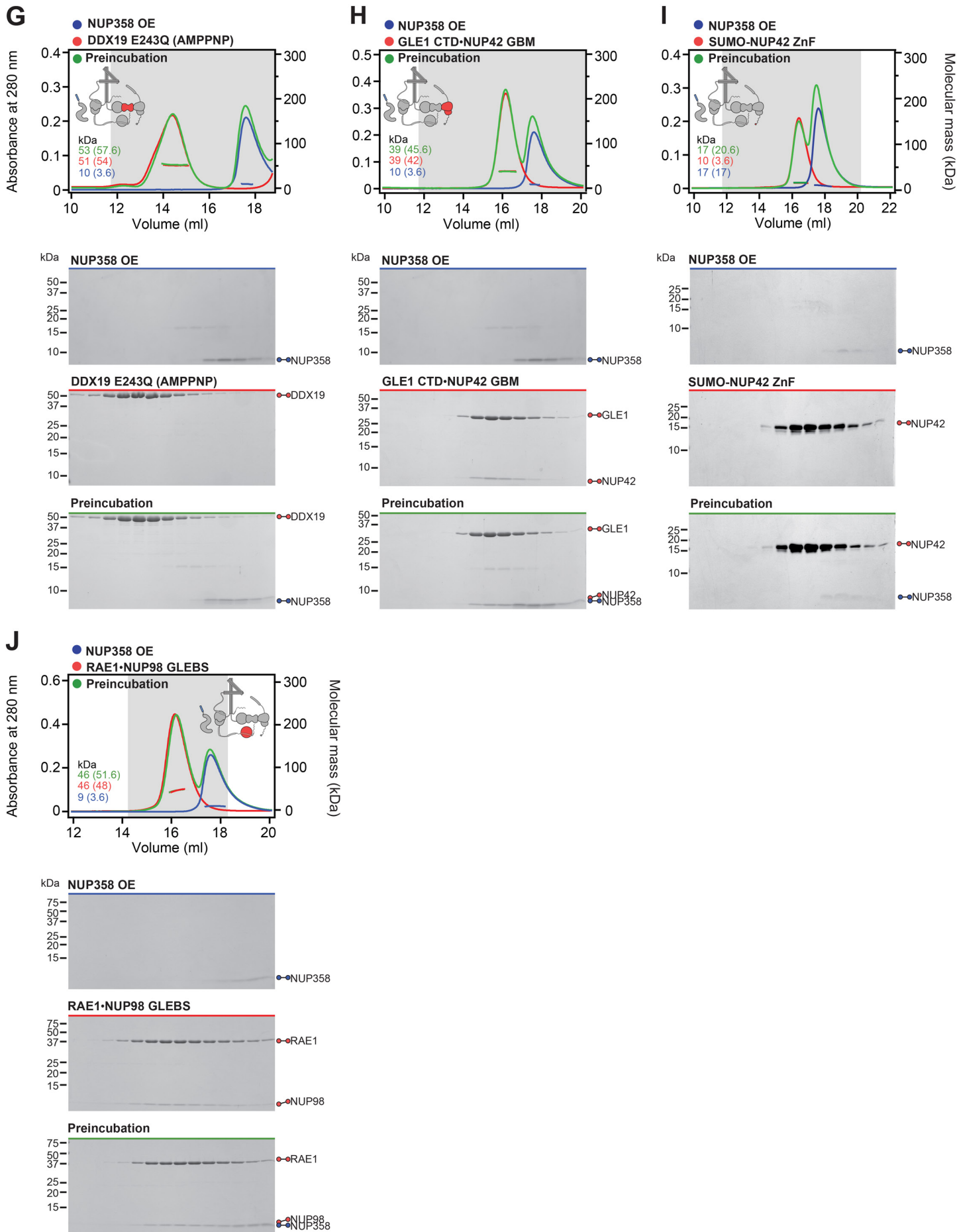
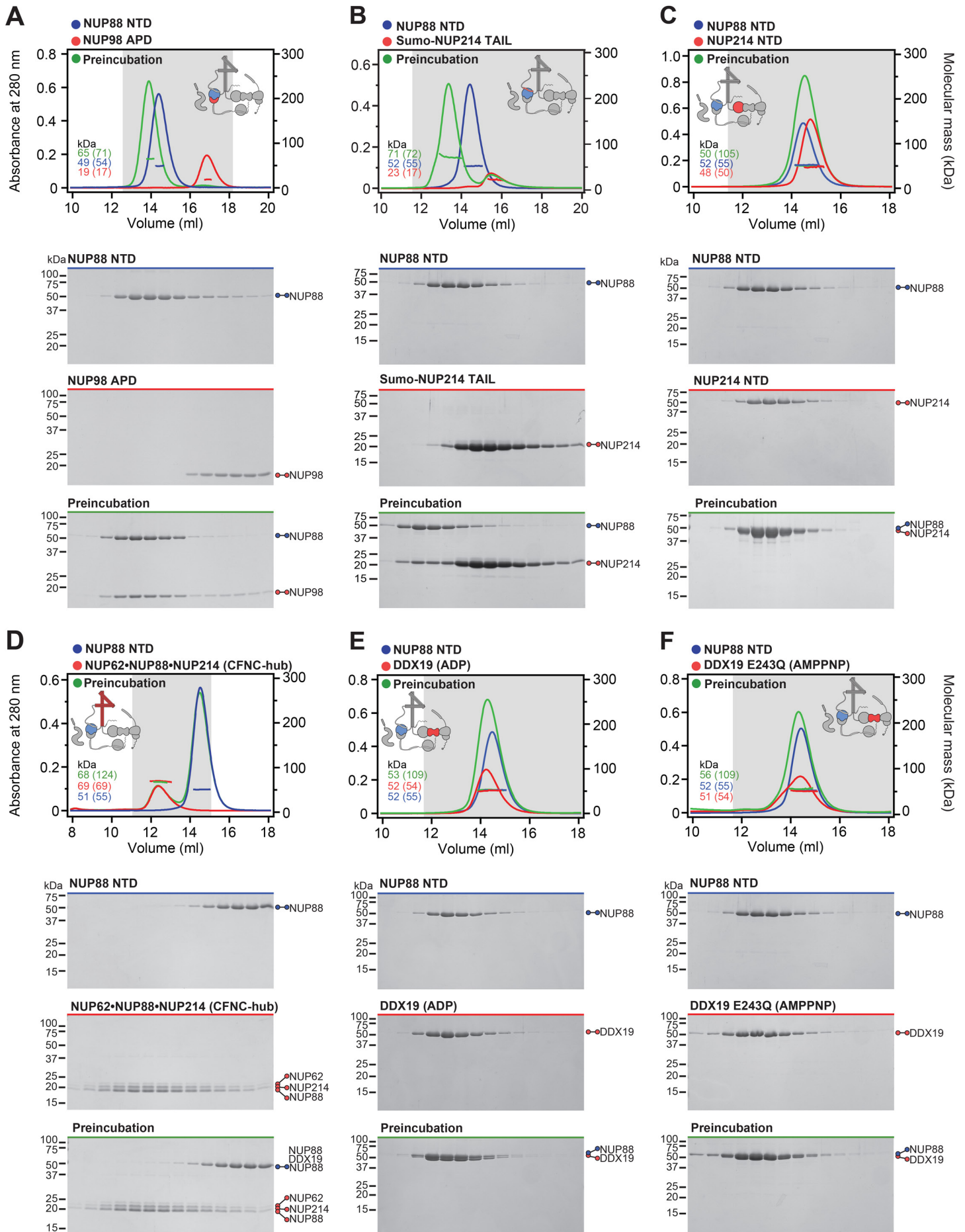


Fig. S31. Systematic interaction analyses of NUP358^{OE} with human CF nup fragments. SEC-MALS interaction analyses of NUP358^{OE} with (A) Nup88^{NTD}, (B) NUP98^{APD}, (C) SUMO-NUP214^{TAIL}, (D) NUP214^{NTD}, (E) CFNC-hub, (F) DDX19(ADP), (G) DDX19(AMPPNP) E243Q, (H) GLE1^{CTD}•NUP42, (I) SUMO-NUP42^{ZnF}, and (J) RAE1•NUP98^{GLEBS}. SEC-MALS profiles of nup complexes are shown individually (red and blue) and after preincubation (green). SEC profiles were obtained using a Superdex 200 10/300 GL column. Measured molecular masses are indicated, with the respective theoretical masses shown in parentheses. Inset schematics display tested protein samples colored to match the corresponding chromatogram trace. Gray boxes indicate fractions resolved on SDS-PAGE gels and visualized by Coomassie brilliant blue staining.



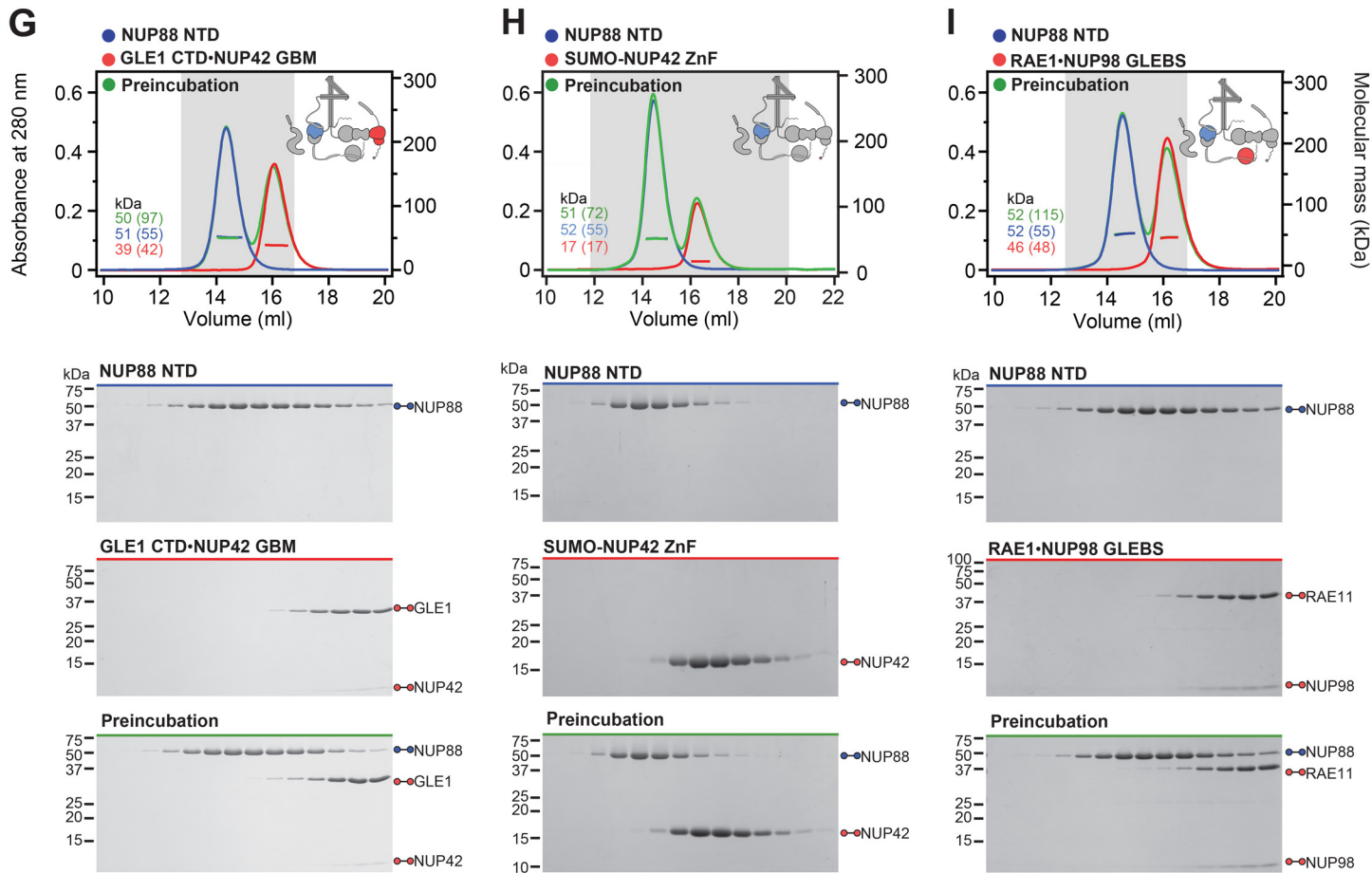
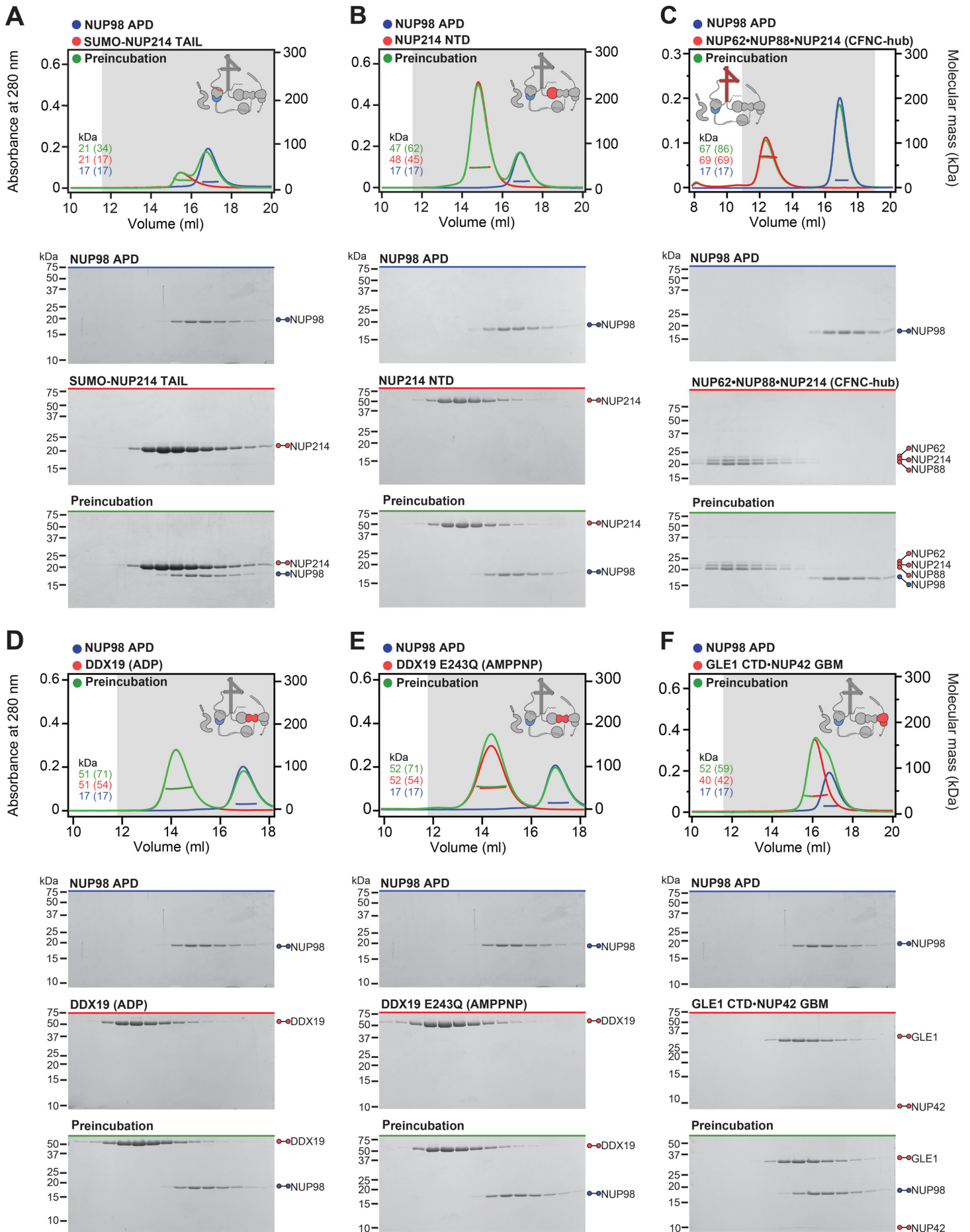


Fig. S32 Systematic interaction analyses of NUP88^{NTD} with human CF nup fragments. SEC-MALS interaction analyses of NUP88^{NTD} with (A) NUP98^{APD}, (B) SUMO-NUP214^{TAIL}, (C) NUP214^{NTD}, (D) CFNC-hub, (E) DDX19(ADP), (F) DDX19(AMPPNP) E243Q, (G) GLE1^{CTD}•NUP42, (H) SUMO-NUP42^{ZnF}, and (I) RAE1•NUP98^{GLEBS}. SEC-MALS profiles of nup complexes are shown individually (red and blue) and after preincubation (green). SEC profiles were obtained using a Superdex 200 10/300 GL column. Measured molecular masses are indicated, with the respective theoretical masses shown in parentheses. Inset schematics display tested protein samples colored to match the corresponding chromatogram trace. Gray boxes indicate fractions resolved on SDS-PAGE gels and visualized by Coomassie brilliant blue staining.



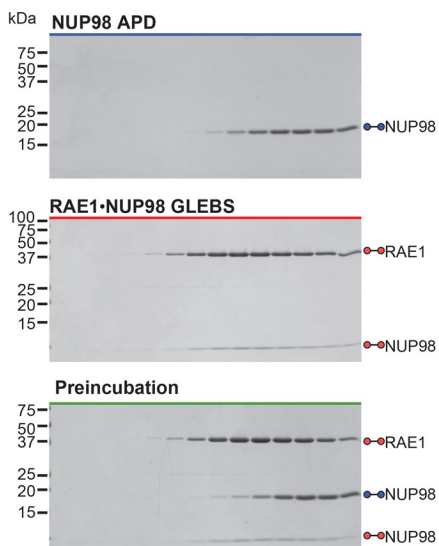
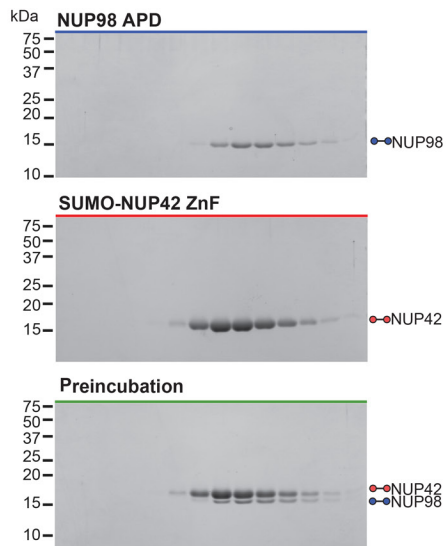
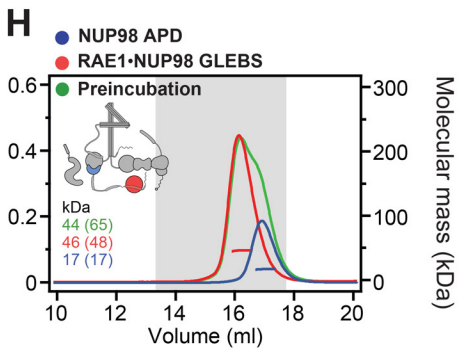
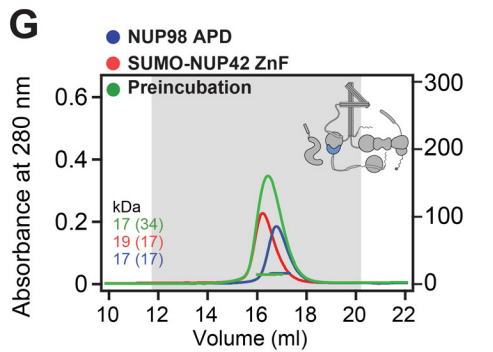
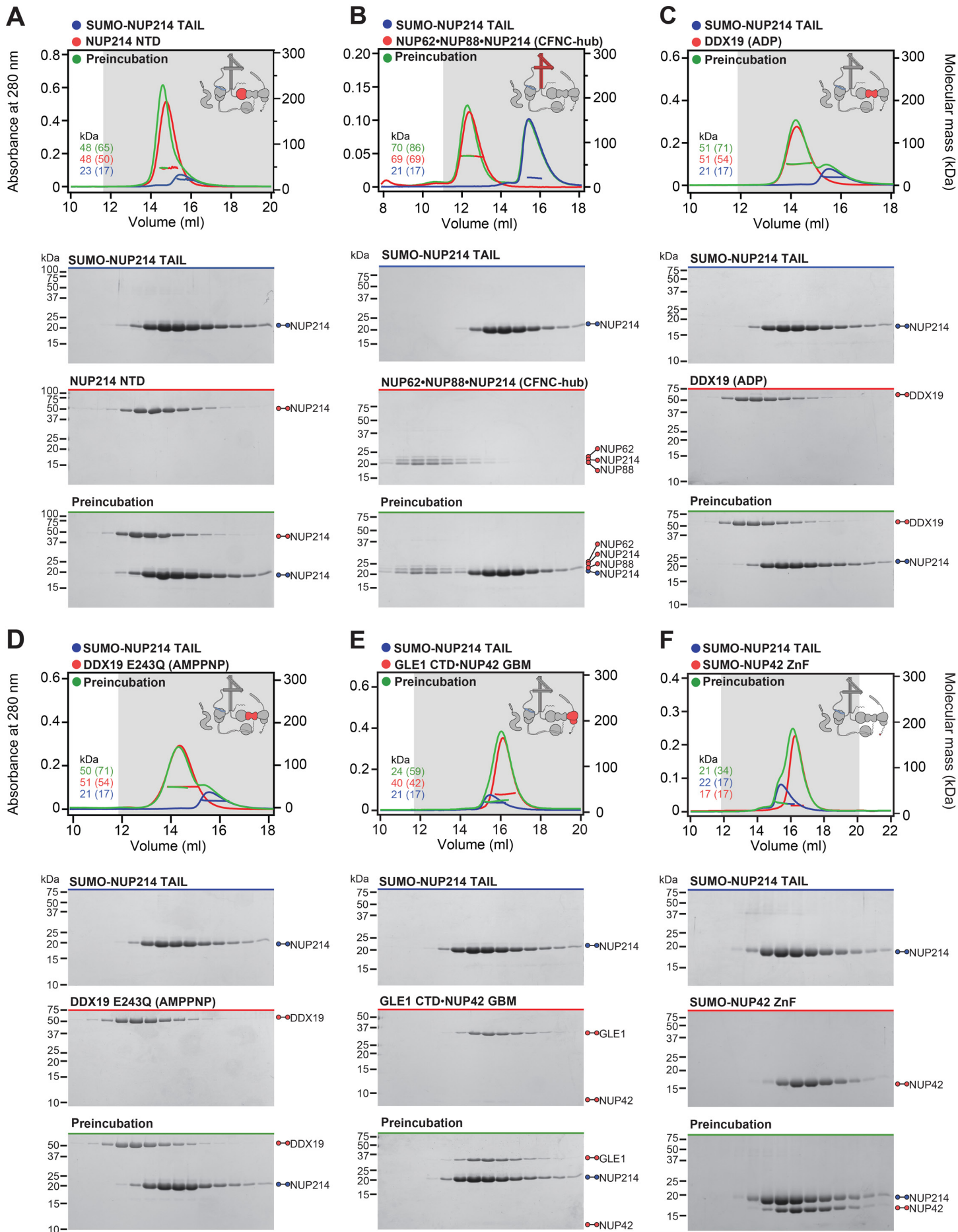


Fig. S33 Systematic interaction analyses of NUP98^{APD} with human CF nup fragments. SEC-MALS interaction analyses of NUP98^{APD} with (A) SUMO-NUP214^{TAIL}, (B) NUP214^{NTD}, (C) CFNC-hub, (D) DDX19(ADP), (E) DDX19(AMPPNP) E243Q, (F) GLE1^{CTD}•NUP42, (G) SUMO-NUP42^{ZnF}, and (H) RAE1•NUP98^{GLEBS}. SEC-MALS profiles of nup complexes are shown individually (red and blue) and after preincubation (green). SEC profiles were obtained using a Superdex 200 10/300 GL column. Measured molecular masses are indicated, with the respective theoretical masses shown in parentheses. Inset schematics display tested protein samples colored to match the corresponding chromatogram trace. Gray boxes indicate fractions resolved on SDS-PAGE gels and visualized by Coomassie brilliant blue staining.



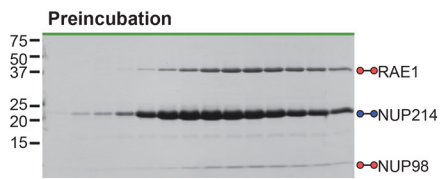
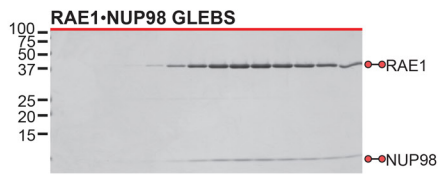
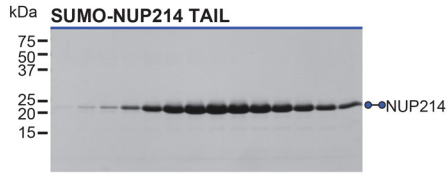
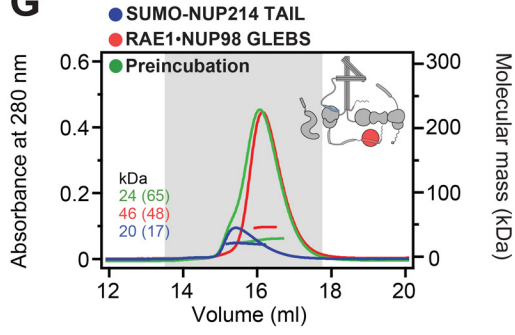
G

Fig. S34. Systematic interaction analyses of NUP214^{TAIL} with human CF nup fragments. SEC-MALS interaction analyses of SUMO-NUP214^{TAIL} with (A) NUP214^{NTD}, (B) CFNC-hub, (C) DDX19(ADP), (D) DDX19(AMPPNP) E243Q, (E) GLE1^{CTD}•NUP42, (F) SUMO-NUP42^{ZnF}, and (G) RAE1•NUP98^{GLEBS}. SEC-MALS profiles of nup complexes are shown individually (red and blue) and after preincubation (green). SEC profiles were obtained using a Superdex 200 10/300 GL column. Measured molecular masses are indicated, with the respective theoretical masses shown in parentheses. Inset schematics display tested protein samples colored to match the corresponding chromatogram trace. Gray boxes indicate fractions resolved on SDS-PAGE gels and visualized by Coomassie brilliant blue staining.

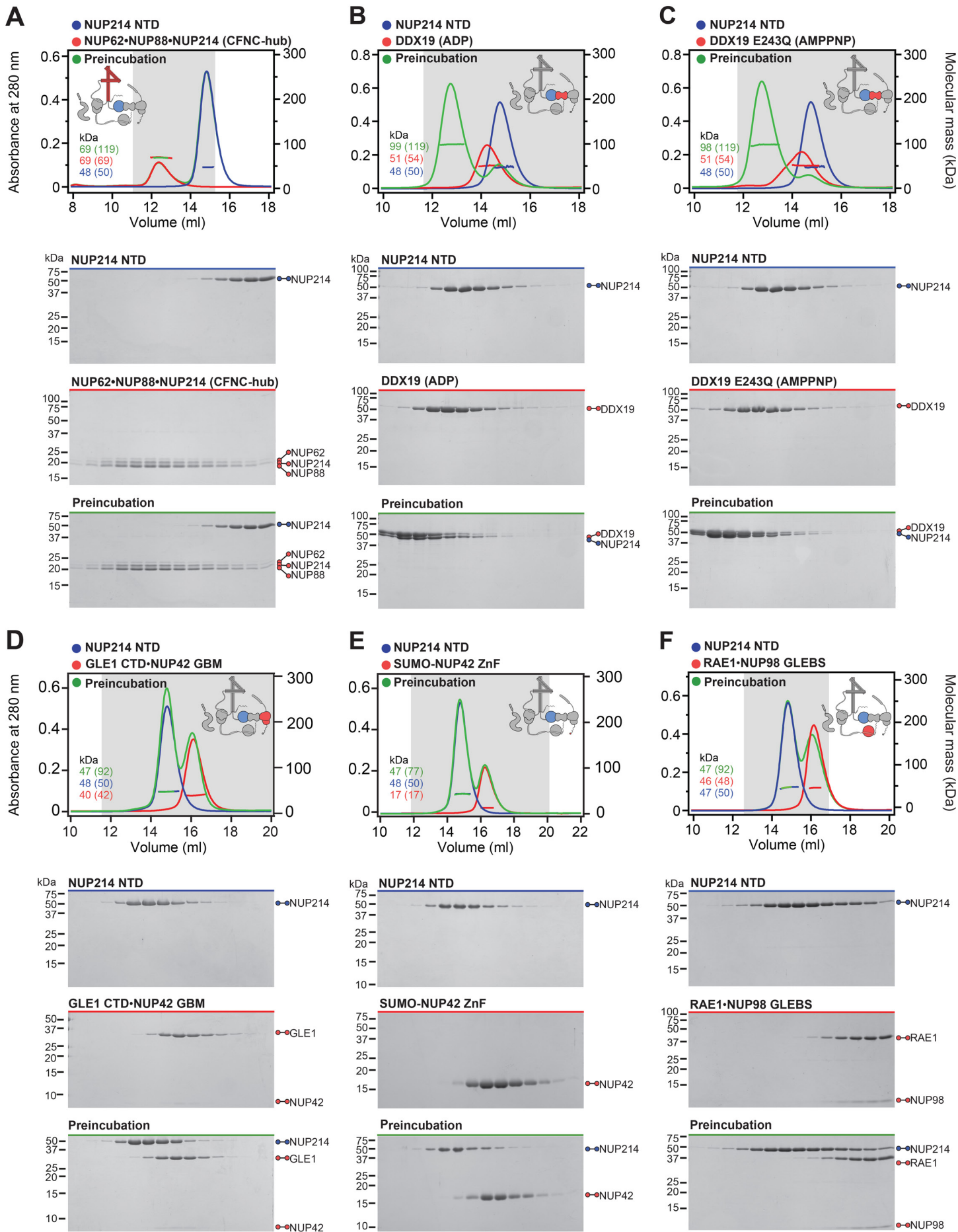


Fig. S35. Systematic interaction analyses of NUP214^{TAIL} with human CF nup fragments. SEC-MALS interaction analyses of NUP214^{NTD} with (A) CFNC-hub, (B) DDX19(ADP), (C) DDX19(AMPPNP) E243Q, (D) GLE1^{CTD}•NUP42, (E) SUMO-NUP42^{ZnF}, and (F) RAE1•NUP98^{GLEBS}. SEC-MALS profiles of nup complexes are shown individually (red and blue) and after preincubation (green). SEC profiles were obtained using a Superdex 200 10/300 GL column. Measured molecular masses are indicated, with the respective theoretical masses shown in parentheses. Inset schematics display tested protein samples colored to match the corresponding chromatogram trace. Gray boxes indicate fractions resolved on SDS-PAGE gels and visualized by Coomassie brilliant blue staining.

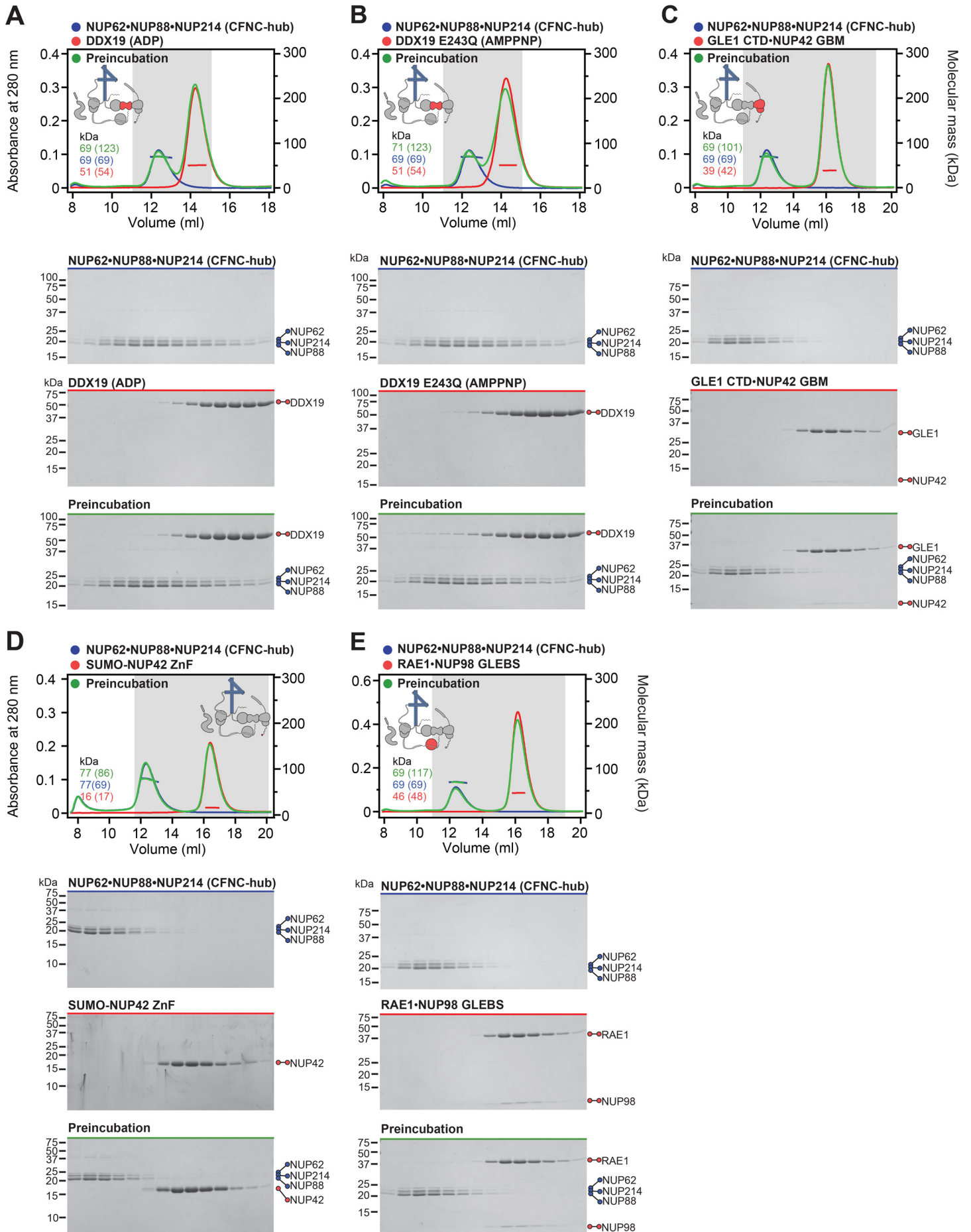


Fig. S36. Systematic interaction analyses of NUP214^{TAIL} with human CF nup fragments. SEC-MALS interaction analyses of CFNC-hub with (A) DDX19 (ADP), (B) DDX19(AMPPNP) E243Q, (C) GLE1^{CTD}•NUP42, (D) SUMO-NUP42^{ZnF}, and (E) RAE1•NUP98^{GLEBS}. SEC-MALS profiles of nups complexes are shown individually (red and blue) and after preincubation (green). SEC profiles were obtained using a Superdex 200 10/300 GL column. Measured molecular masses are indicated, with the respective theoretical masses shown in parentheses. Inset schematics display tested protein samples colored to match the corresponding chromatogram trace. Gray boxes indicate fractions resolved on SDS-PAGE gels and visualized by Coomassie brilliant blue staining.

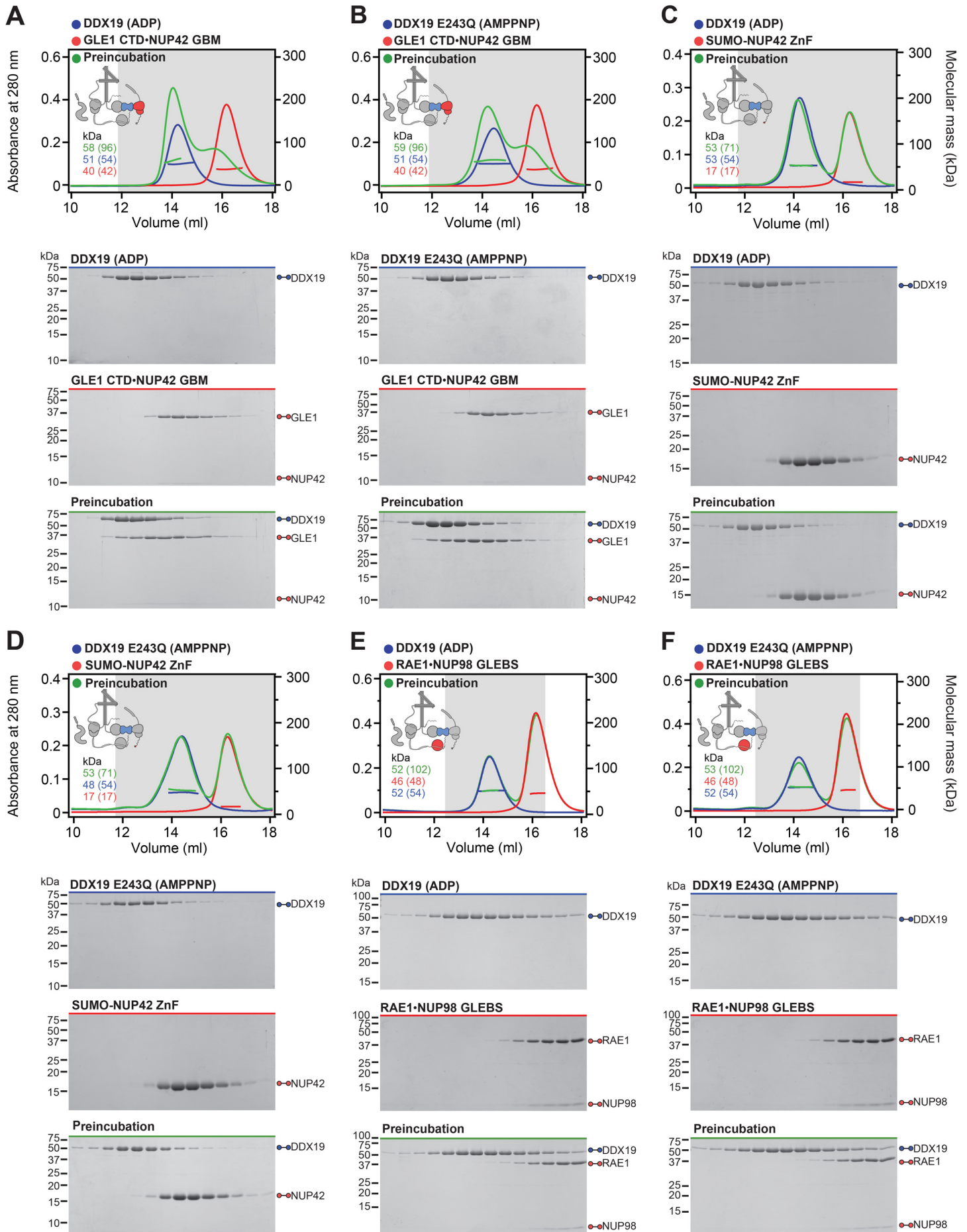


Fig. S37. Systematic interaction analyses of DDX19 with human CF nup fragments. SEC-MALS interaction analyses of DDX19 (ADP) or DDX19(AMPPNP) E243Q with (A, B) GLE1^{CTD}•NUP42, (C, D) SUMO-NUP42^{ZnF}, and (E, F) RAE1•NUP98^{GLEBS}. SEC-MALS profiles of nup complexes are shown individually (red and blue) and after preincubation (green). SEC profiles were obtained using a Superdex 200 10/300 GL column. Measured molecular masses are indicated, with the respective theoretical masses shown in parentheses. Inset schematics display tested protein samples colored to match the corresponding chromatogram trace. Gray boxes indicate fractions resolved on SDS-PAGE gels and visualized by Coomassie brilliant blue staining.

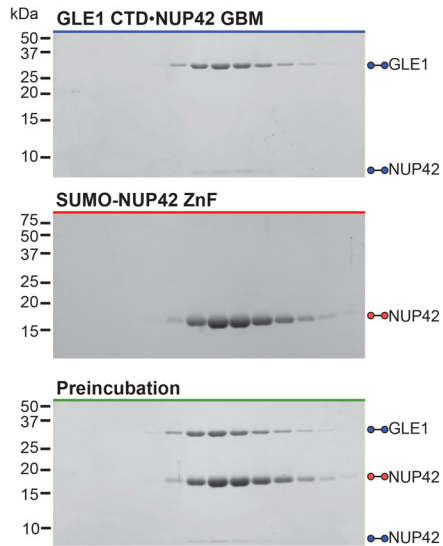
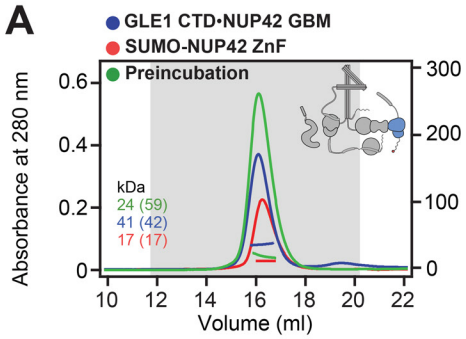
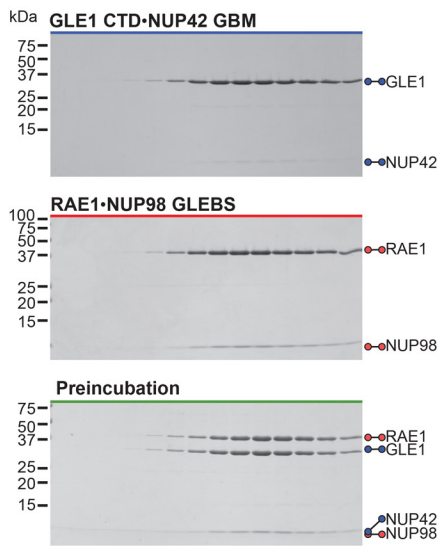
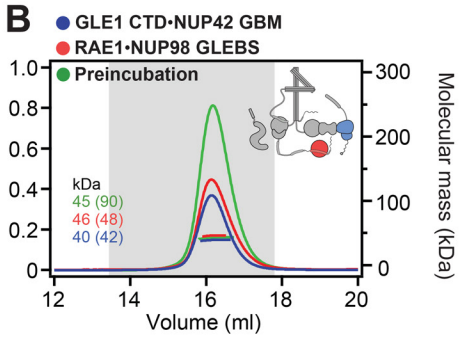
A**B**

Fig. S38. Systematic interaction analyses of GLE1^{CTD}•NUP42 with human CF nup fragments. SEC-MALS interaction analyses of GLE1^{CTD}•NUP42 with (A) SUMO-NUP42^{ZnF}, and (B) RAE1•NUP98^{GLEBS}. SEC-MALS profiles of nup complexes are shown individually (red and blue) and after preincubation (green). SEC profiles were obtained using a Superdex 200 10/300 GL column. Measured molecular masses are indicated, with the respective theoretical masses shown in parentheses. Inset schematics display tested protein samples colored to match the corresponding chromatogram trace. Gray boxes indicate fractions resolved on SDS-PAGE gels and visualized by Coomassie brilliant blue staining.

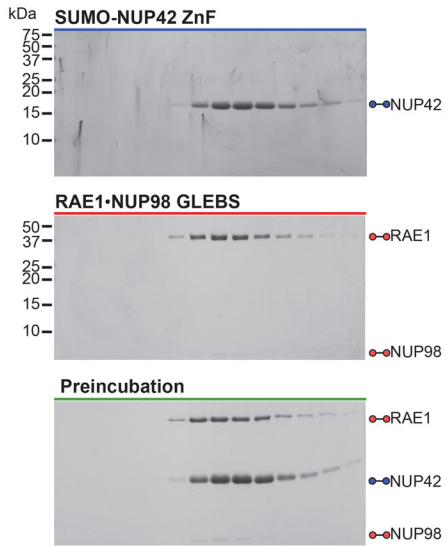
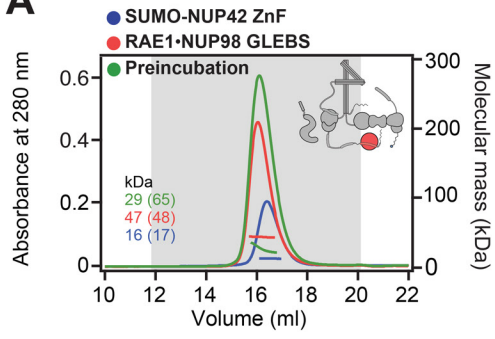
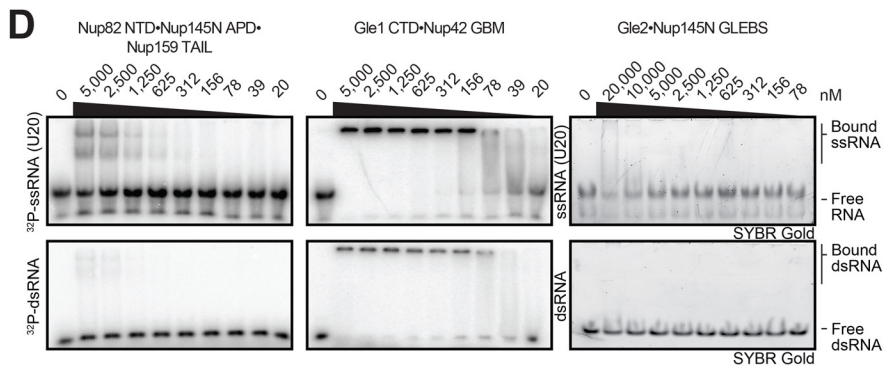
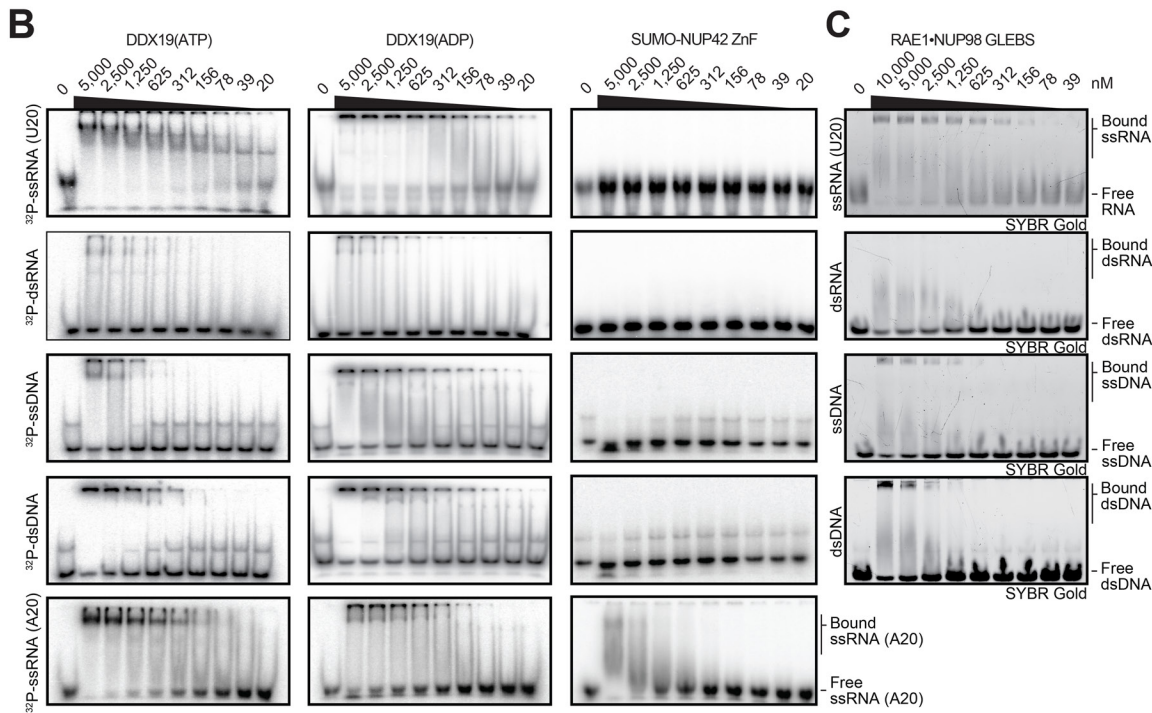
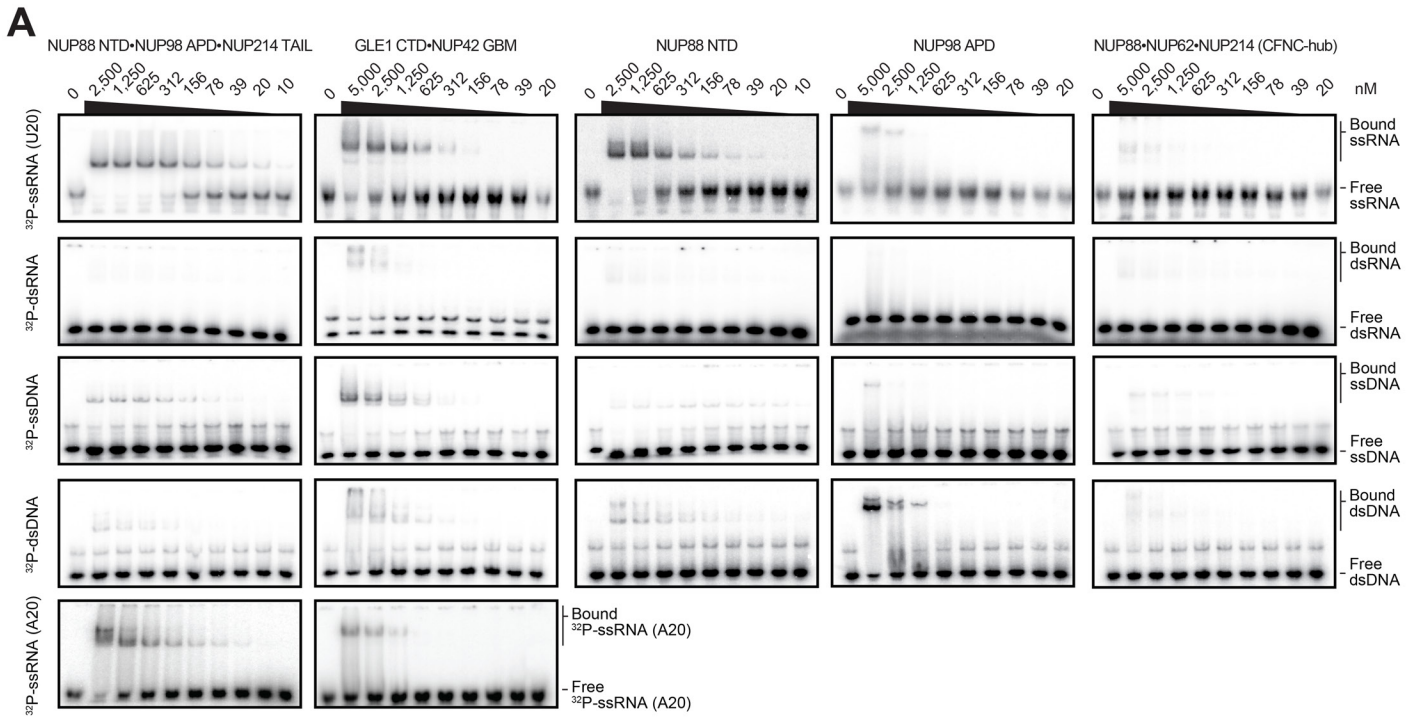
A

Fig. S39. Systematic interaction analyses of NUP42^{ZnF} and RAE1•NUP98^{GLEBS} with human CF nup fragments. SEC-MALS interaction analysis of SUMO-NUP42^{ZnF} with (A) RAE1•NUP98^{GLEBS}. SEC-MALS profiles of SUMO-NUP42^{ZnF} and RAE1•NUP98^{GLEBS} are shown individually (blue and red, respectively) and after preincubation (green). SEC profiles were obtained using a Superdex 200 10/300 GL column. Measured molecular masses are indicated, with the respective theoretical masses shown in parentheses. Inset schematics display tested protein samples colored to match the corresponding chromatogram trace. Gray boxes indicate fractions resolved on SDS-PAGE gels and visualized by Coomassie brilliant blue staining.



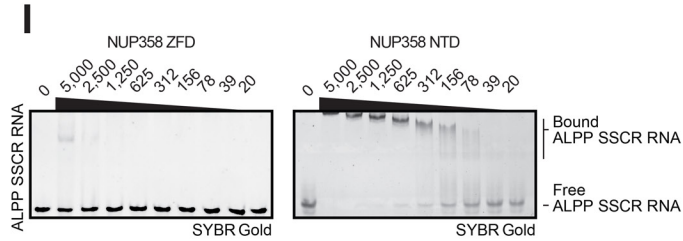
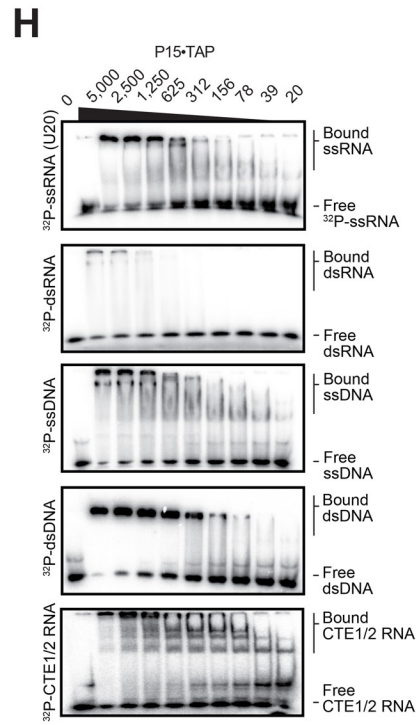
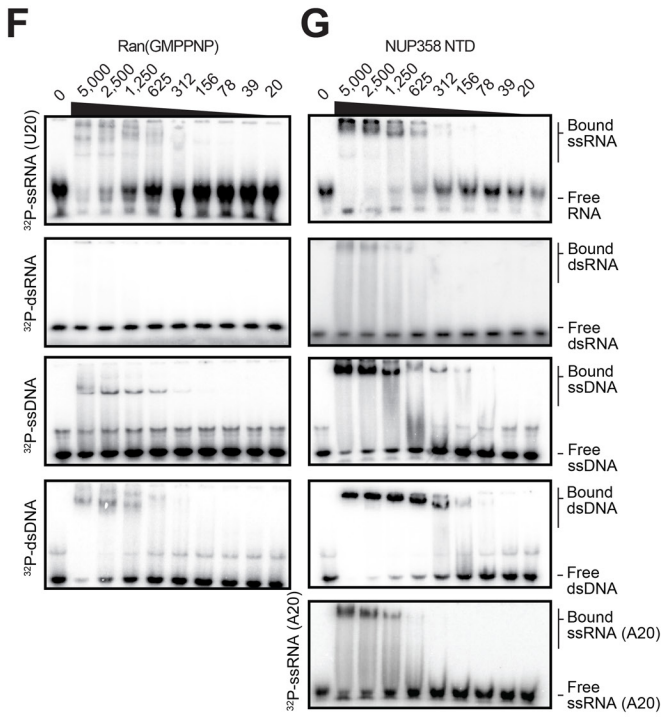
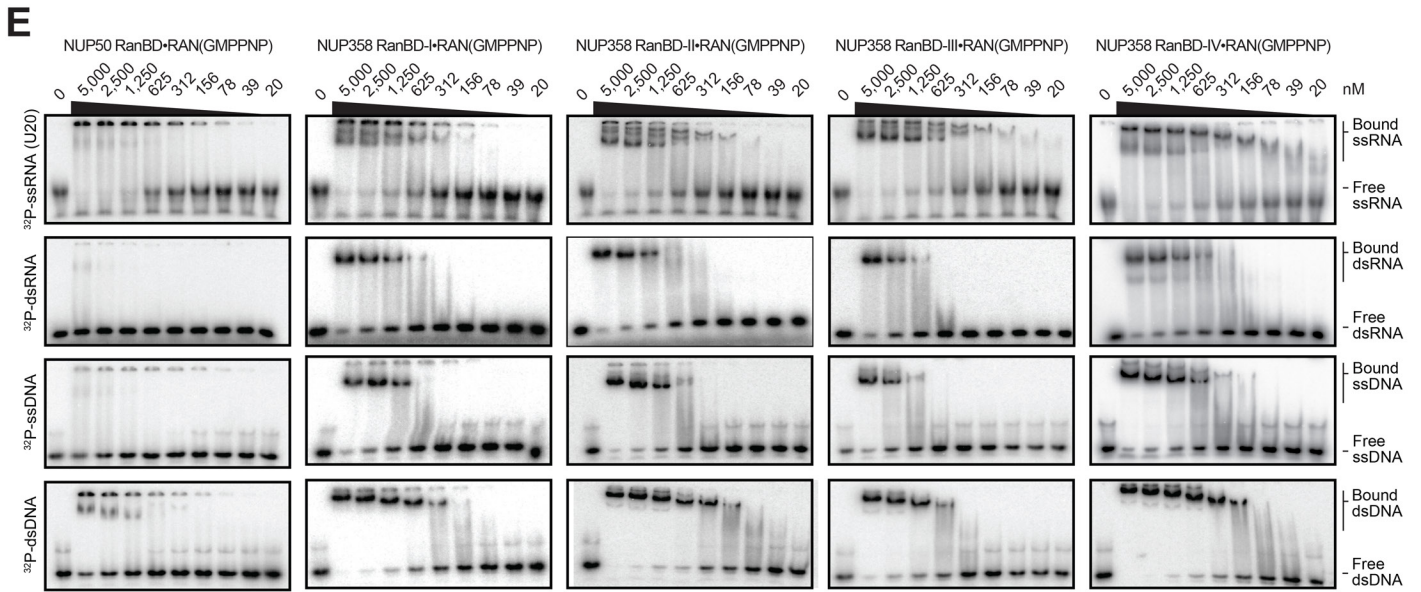


Fig. S40. Evolutionary conservation of cytoplasmic filament nup RNA binding properties. Cytoplasmic filament nup domains and complexes were assayed for binding to single stranded (ss) and double stranded (ds) RNA and DNA probes by electrophoretic mobility shift assay (EMSA); ssRNA (U₂₀), dsRNA (28-nt hairpin), ssDNA (34-nt DNA oligonucleotide), dsDNA (34-bp hybridized DNA oligonucleotides) and ssRNA (A₂₀). Final concentrations of protein and complexes are indicated. EMSA titration of **(A-C)** human CFNC nup domains and subcomplexes, **(D)** *C. thermophilum* CFNC subcomplexes, **(E)** NUP358 and NUP50 RanBDs pre-complexed with Ran(GMPPNP), **(F)** Ran(GMPPMP), and **(G)** NUP358^{NTD}. **(H)** EMSA titration of mRNA export complex P15•TAP with ss/ds RNA and DNA and CTE1/2 RNA, a commonly used viral RNA probe for P15•TAP. **(I)** EMSA titrations of NUP358^{NTD} and NUP358^{ZFD} with ALPP^{SSCR} RNA.

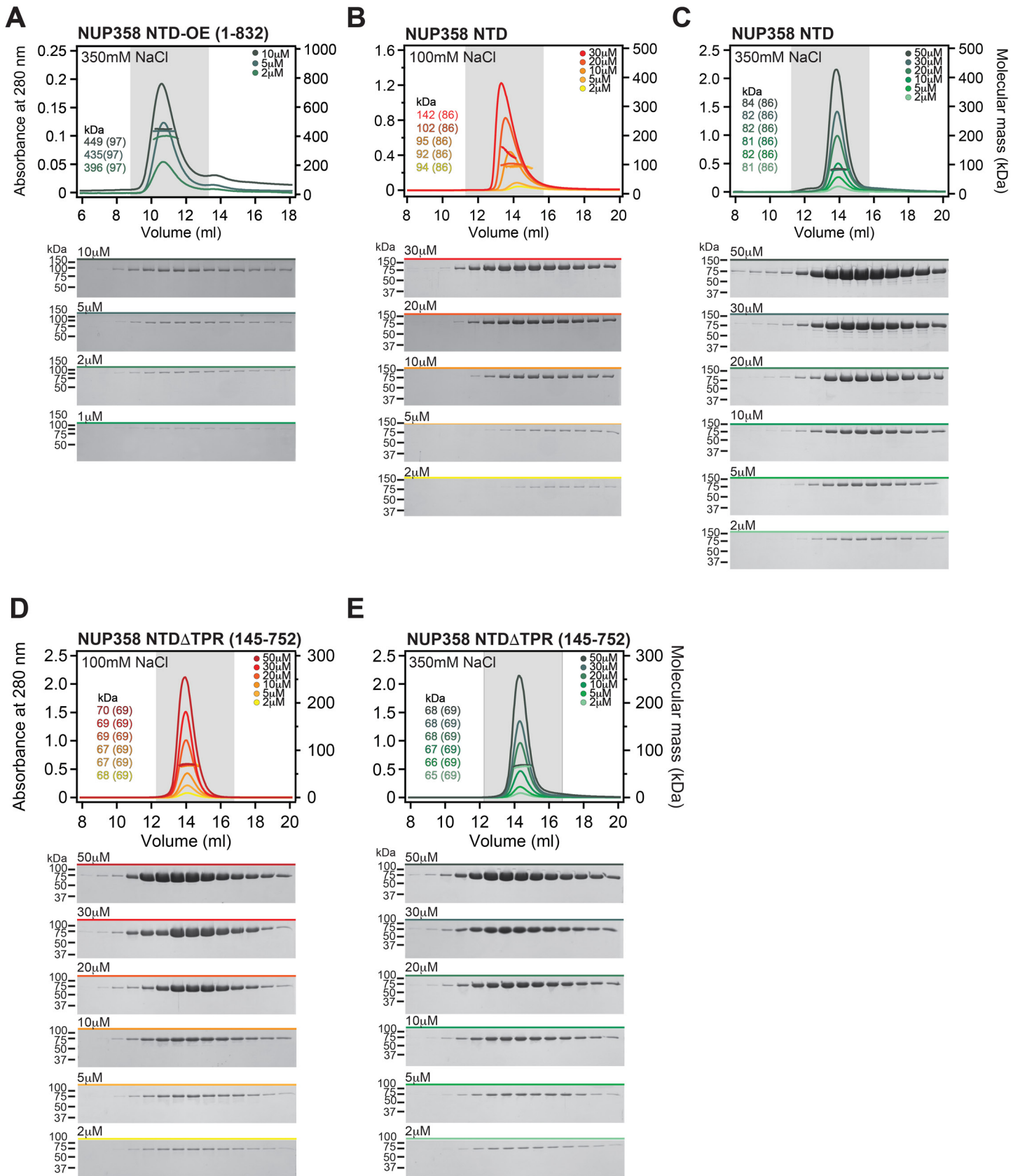


Fig. S41. Biochemical analysis of oligomerization properties of NUP358 fragments. (A) SEC-MALS analysis of NUP358^{NTD-OE} at the indicated increasing protein concentrations. The measured molecular masses increase from ~400 kDa to ~450 kDa, indicating the formation of a concentration-dependent oligomer, ranging from a homo-tetramer or -pentamer. (B, C) SEC-MALS oligomerization analyses of NUP358^{NTD} at the indicated increasing protein concentrations and buffer conditions. NUP358^{NTD} forms a concentration-dependent monomer-dimer mixture that is interrupted by 350 mM NaCl. (D, E) SEC-MALS oligomerization analyses of NUP358^{NTD Δ TPR} at the indicated increasing protein concentrations and buffer conditions. NUP358^{NTD Δ TPR} is monomeric in all buffer conditions tested, establishing that NUP358^{TPR} contributes to NUP358^{NTD} dimerization. Measured molecular masses are indicated, with the respective theoretical masses shown in parentheses. Gray boxes indicate fractions resolved on SDS-PAGE gels and visualized by Coomassie brilliant blue staining.

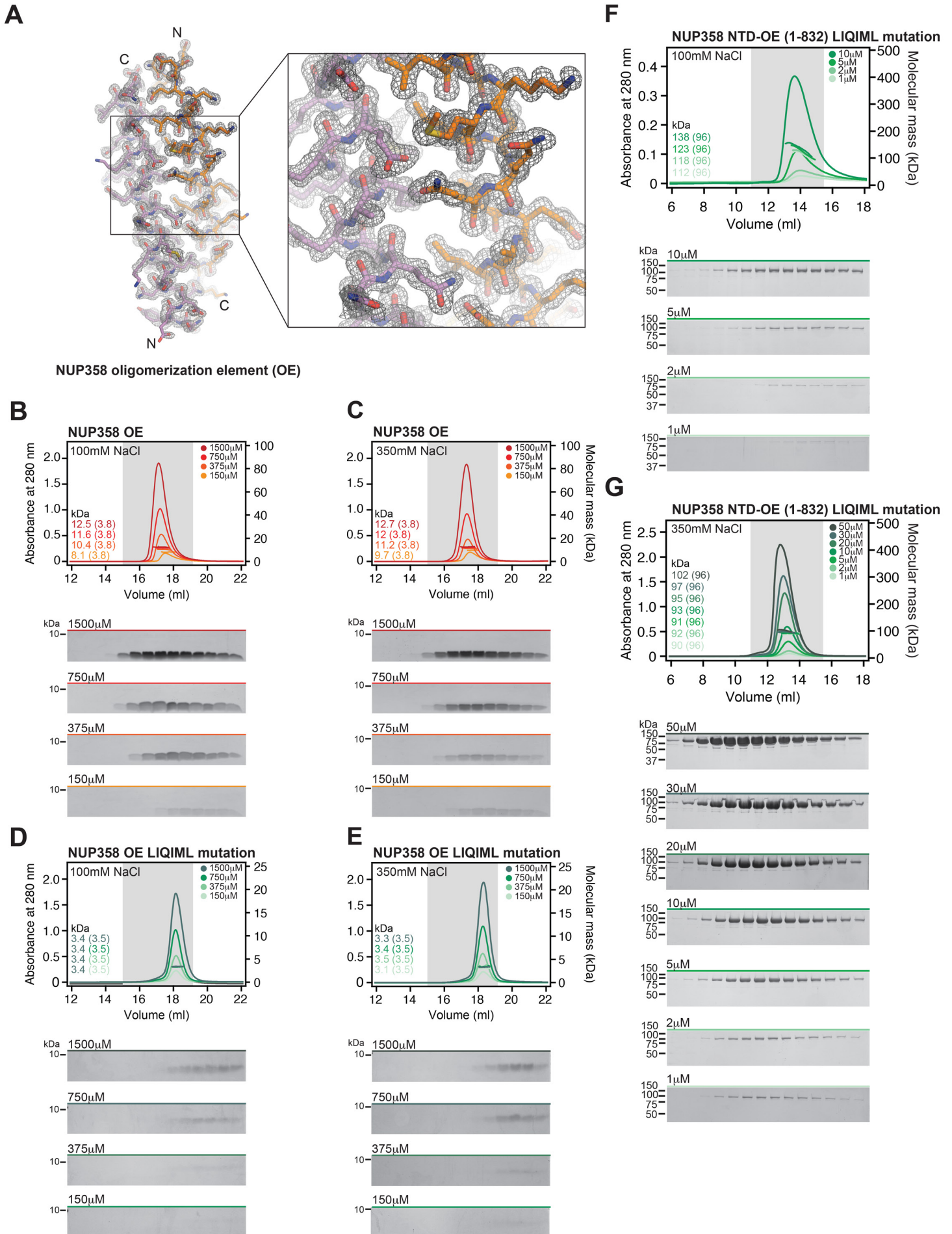


Fig. S42. Structural and biochemical characterization of NUP358^{OE}. (A) Experimental electron density map after density modification of NUP358^{OE} phased with the sulfur-SAD anomalous X-ray diffraction data, contoured at 1.0 σ . (B, C) SEC-MALS oligomerization analysis of NUP358^{OE}, at the indicated increasing protein concentrations and buffer conditions. NUP358^{OE} forms oligomeric states ranging from homo-dimer to -tetramer independent of the buffer condition. (D, E) SEC-MALS oligomerization analysis of NUP358^{OE} LIQIML mutant (L811A, I814A, Q817A, I821A, M825A, and L828A), at the indicated increasing protein concentrations and buffer conditions. The measured molecular masses at all proteins concentrations and both buffer conditions correspond to a monomeric species, demonstrating that the LIQIML mutation abolishes the oligomeric behavior of NUP358^{OE}. (F, G) SEC-MALS oligomerization analysis of NUP358^{NTD-OE} LIQIML mutant, at the indicated increasing protein concentrations and buffer conditions. The LIQIML mutation abolishes the homo-tetramer or -pentamer formation, yielding a dynamic monomer-dimer equilibrium, as observed for NUP358^{NTD}. In the 350 mM NaCl buffer, the NUP358^{NTD-OE} LIQIML mutant is a monodisperse monomer at all protein concentrations tested. SEC profiles were obtained using a Superdex 200 10/300 GL column. Measured molecular masses are indicated, with the respective theoretical masses shown in parentheses. Gray boxes indicate fractions resolved on SDS-PAGE gels and visualized by Coomassie brilliant blue staining.

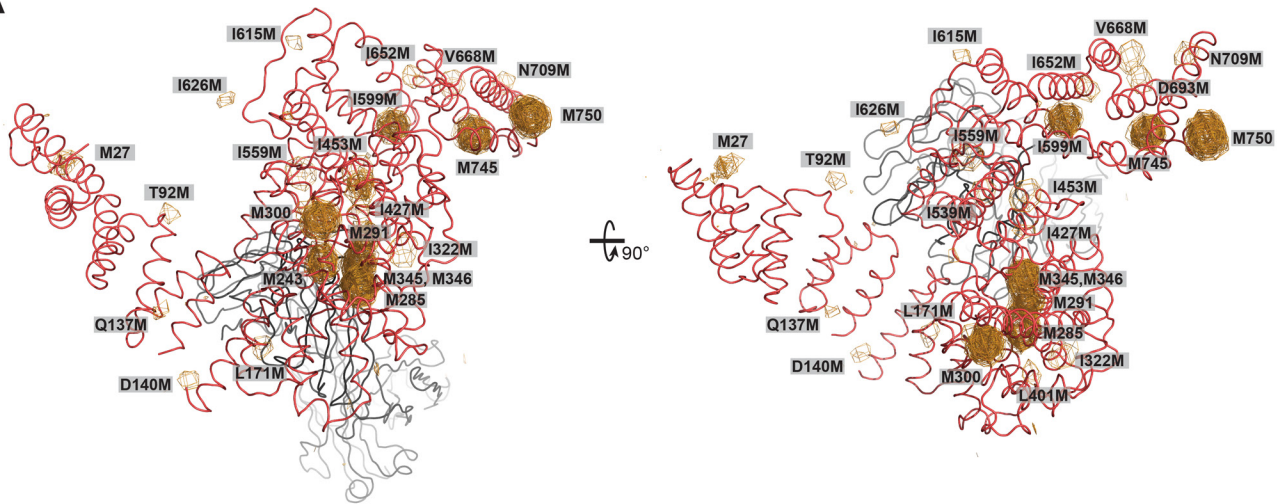
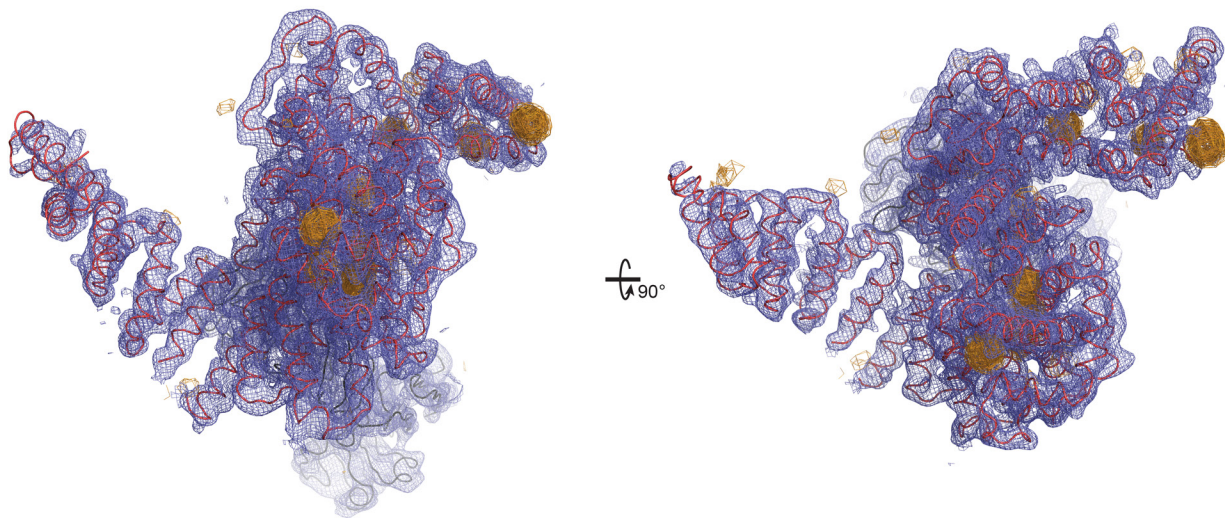
A**B**

Fig. 43. Determination of the NUP358^{NTD}•sAB-14 crystal structure and sequence assignment. (A) The NUP358^{NTD}•sAB-14 structure is shown in coil representation and overlaid with anomalous difference Fourier maps (contoured at 3.5 σ), calculated from SeMet-SAD X-ray diffraction data obtained from SeMet-labeled crystals of 17 different methionine mutants. Together with the endogenous methionines of the wildtype complex, this analysis identified a total of 26 selenium positions, providing a marker for the unambiguous assignment of the NUP358^{NTD} sequence register. A 90°-rotated view is shown on the right. For clarity, the second NUP358^{NTD}•sAB-14 copy in the asymmetric unit is omitted. (B) Final 2|Fo|-|Fc| electron density map contoured at 1.0 σ .

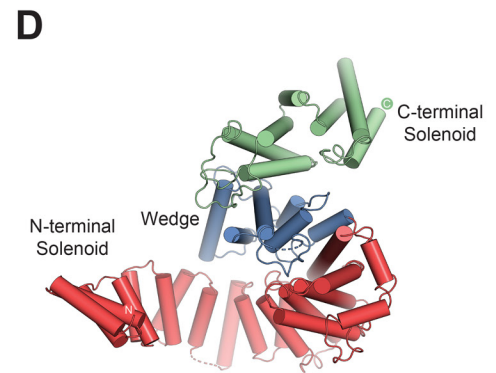
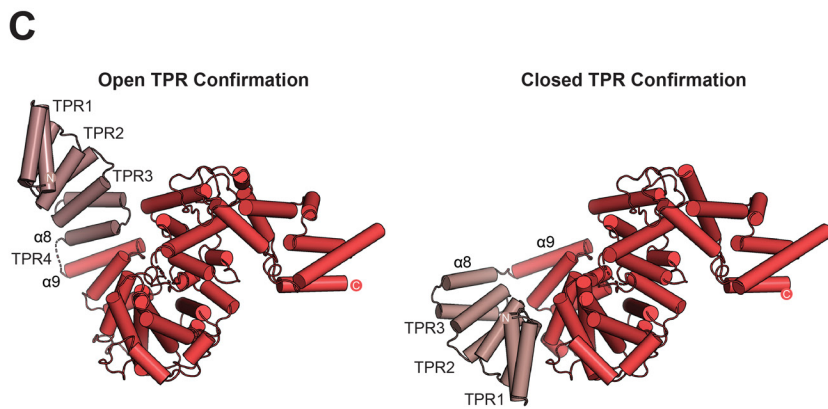
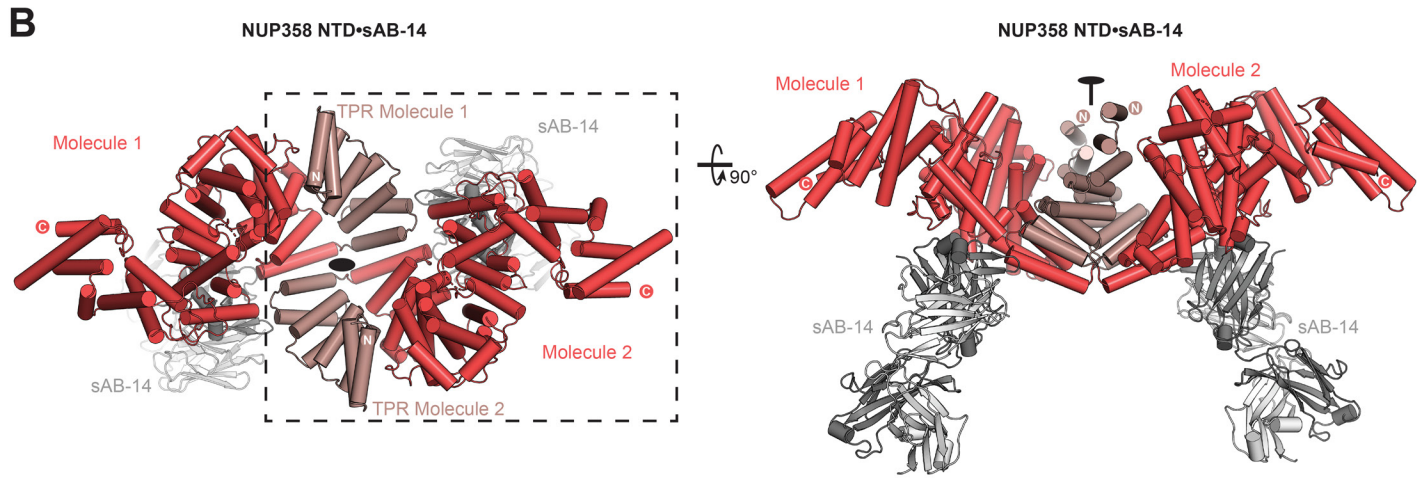
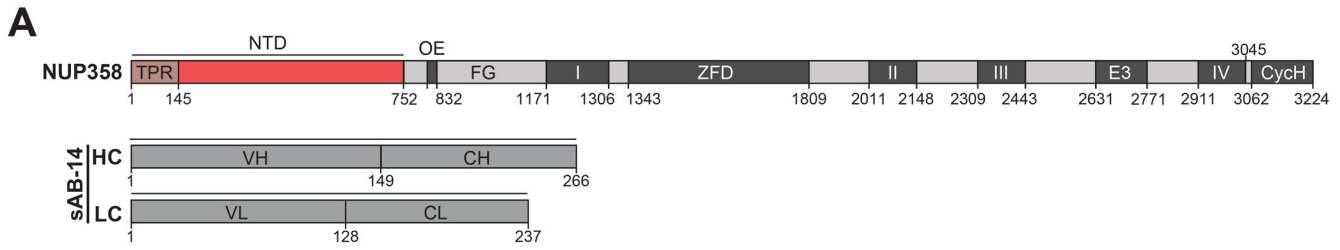
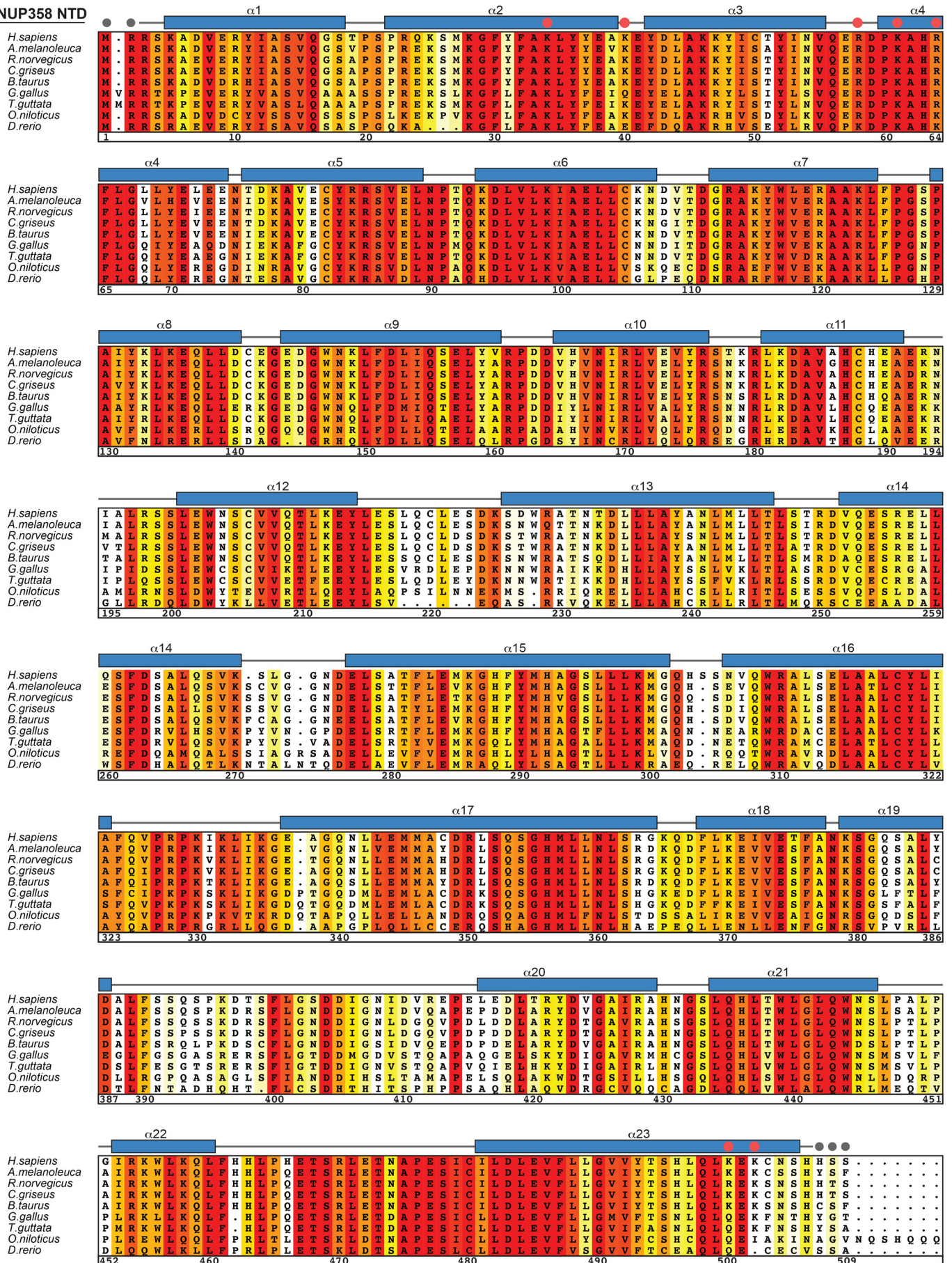
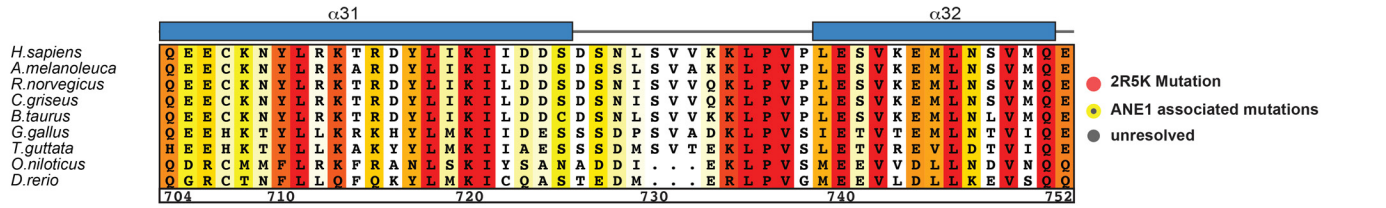
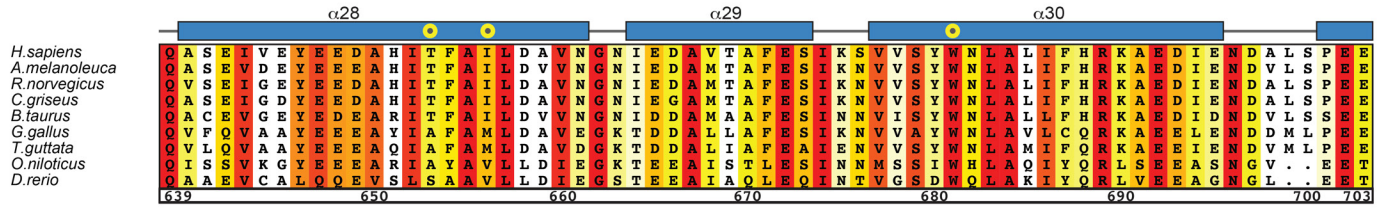
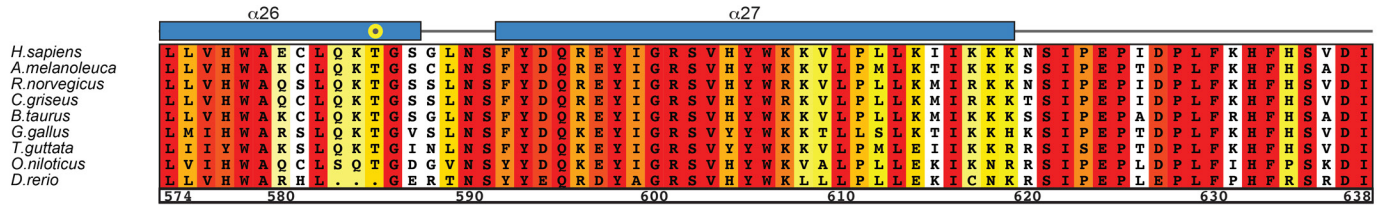
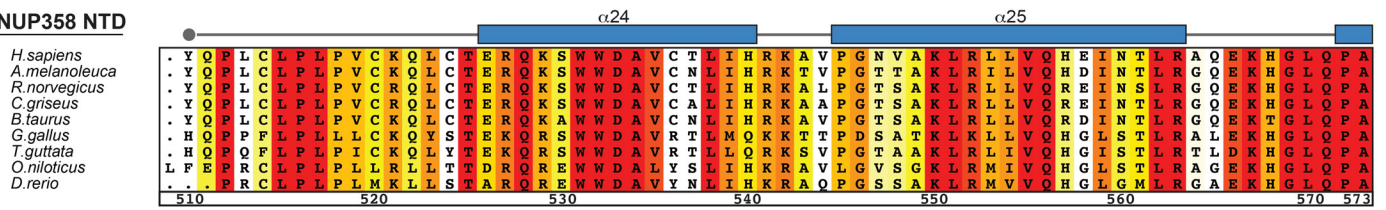


Fig. S44. Crystal structure of NUP358^{NTD} bound by sAB-14. (A) Domain structure of NUP358 and sAB-14 light and heavy chains drawn as horizontal boxes with residue numbers indicated. Black lines indicate the boundaries of the crystallized fragments. (B) Cartoon representation of the NUP358^{NTD}•sAB-14 co-crystal structure dyad of the P6₅22 lattice, illustrating the swap of the N-terminal TPR subdomain between symmetry related NUP358^{NTD} molecules. A 90°-rotated view highlights sAB-14 binding to the convex surface of NUP358^{NTD}. (C) Comparison of open and closed conformations of NUP358^{NTD}. The crystallographic dimer reveals two alternative conformations of NUP358^{NTD}, in which NUP358^{TPR} either forms a continuous solenoid (open), or folds back, separating TPR4 and forming electrostatic interactions with HEAT repeats 5-7 of the N-terminal solenoid (closed). The open conformation adopts an overall S-shaped architecture, whereas the closed conformation is a compact particle. (D) Cartoon representation colored to indicate the three α -helical solenoids that compose the NUP358^{NTD} giving rise to an overall S-shape molecule; N-terminal α -helical solenoid (red), α -helical wedge (blue), C-terminal α -helical solenoid (green).

NUP358 NTD



NUP358 NTD



● 2R5K Mutation
● ANE1 associated mutations
● unresolved

Fig. S45. Multispecies sequence alignment of NUP358^{NTD}. Sequences of nine metazoan species were aligned and colored according to similarity using the BLOSUM62 matrix from white (less than 40% similarity), through yellow (60% similarity), to red (100% identity). The numbering is according to the *H. sapiens* protein. The secondary structure is indicated above the sequences as rectangles (α -helices) and lines (unstructured regions), residues unresolved in the crystal structure are indicated by gray dots. Yellow dots indicate residues found in sequence variants associated with acute necrotizing encephalopathy 1 (ANE1). Red dots indicate the seven residues that are substituted by alanine in the 2R5K mutation that abolishes the NUP88^{NTD} and ALPP^{SSCR} RNA interactions.

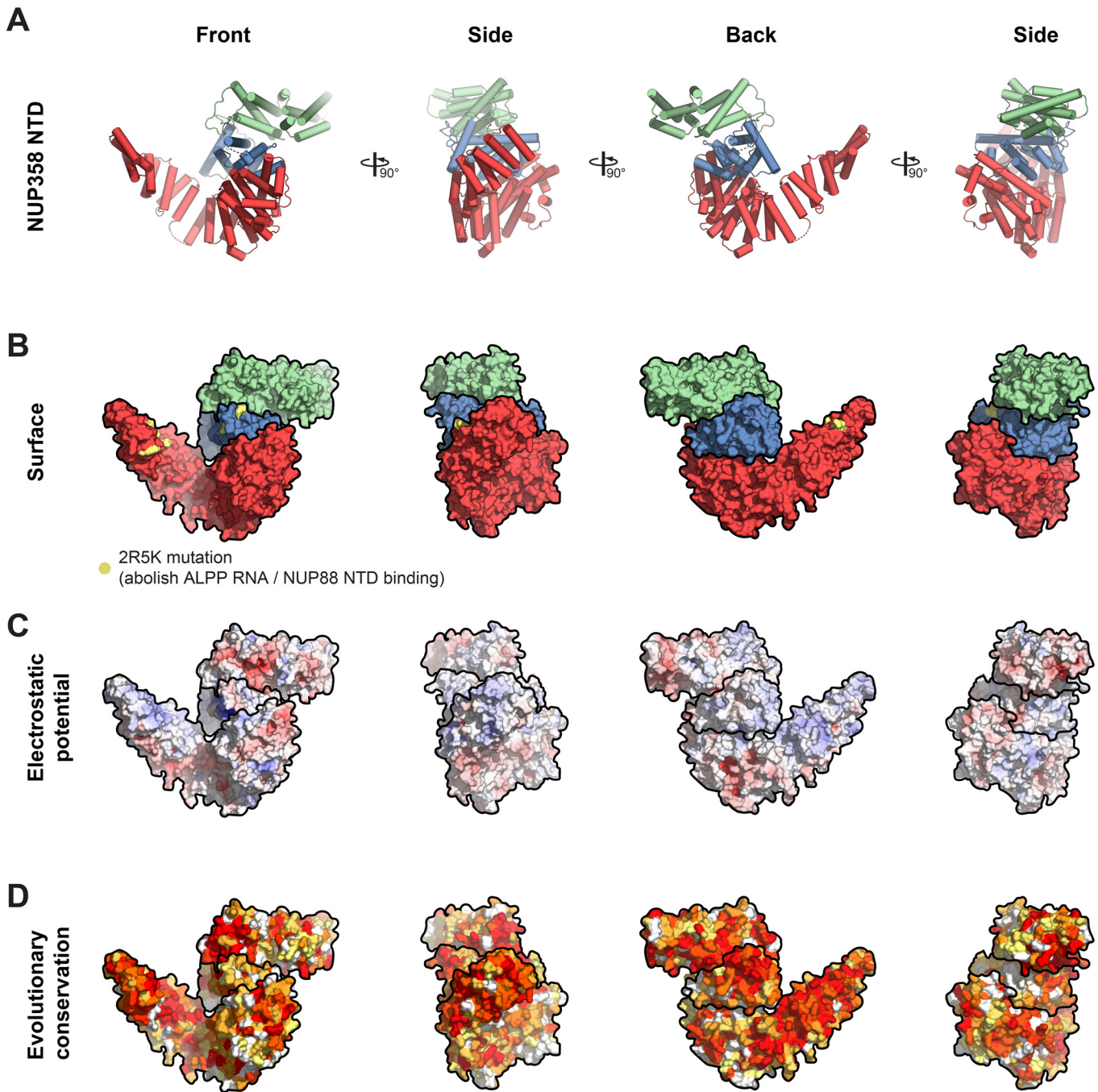


Fig. S46. Surface properties of NUP358^{NTD}. (A) Cartoon representation of NUP358^{NTD} with N-terminal α -helical solenoid in red, α -helical wedge domain in blue, and C-terminal α -helical solenoid in green. (B) Surface representation of NUP358^{NTD} colored as in (A). Residues mutated to alanine in the 2R5K mutation are indicated in yellow (C) Surface representation colored according to electrostatic potential from red ($-10 k_B T/e$) to blue ($+10 k_B T/e$). (D) Surface representation colored according to sequence conservation based on alignment in [fig. S45](#). The NUP358^{NTD} structure is shown from four different orientations related by 90° rotations around the vertical axis.

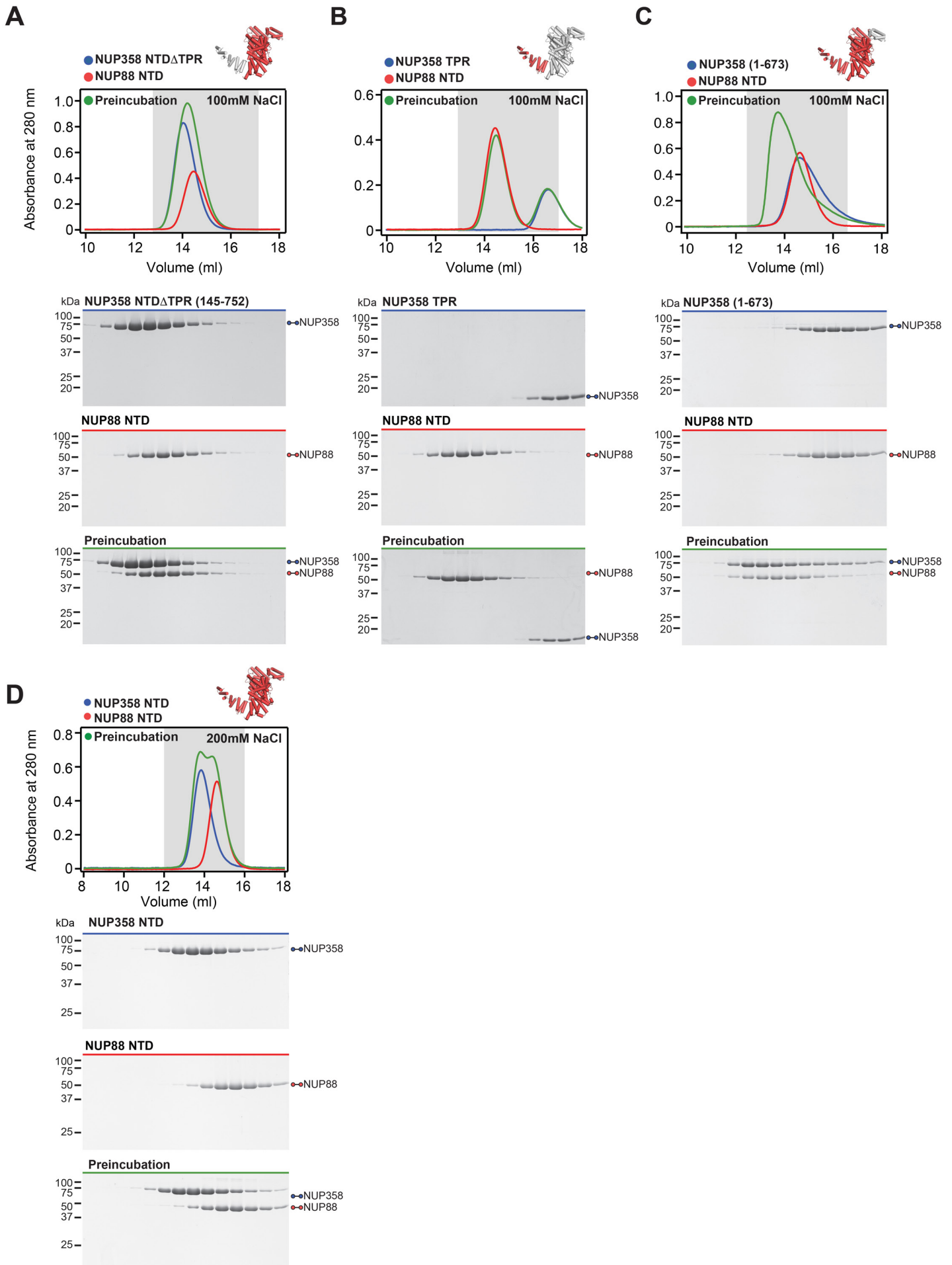


Fig. S47. Biochemical characterization of the NUP358^{NTD}-NUP88^{NTD} interaction. (A-C) SEC interaction analyses of NUP88^{NTD} with (A) NUP358^{NTD Δ TPR}, (B) NUP358^{TPR}, and (C) NUP358¹⁻⁶⁷³, demonstrating that NUP358^{TPR} is necessary but insufficient for NUP88^{NTD} binding. (D) SEC analysis of NUP88^{NTD} with NUP358^{NTD} in a buffer containing 200 mM NaCl, revealing the salt-sensitive nature of the interaction. SEC profiles of NUP358^{NTD} variants (blue) and NUP88^{NTD} (red) are shown individually and after their preincubation (green). SEC profiles were obtained using a Superdex 200 10/300 GL column. Gray boxes indicate fractions resolved on SDS-PAGE gels and visualized by Coomassie brilliant blue staining.

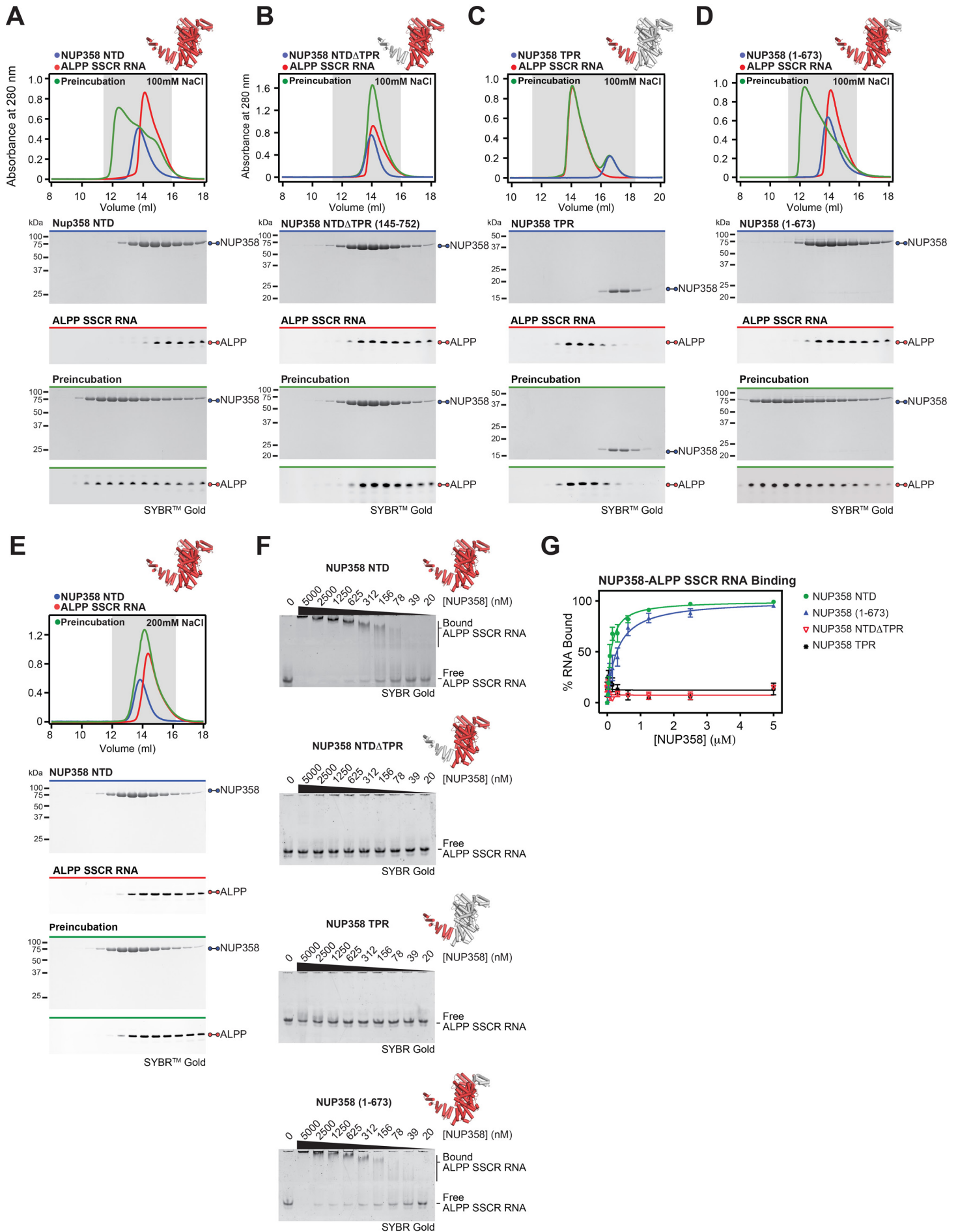


Fig. S48. Biochemical characterization of the NUP358^{NTD}-ALPP^{SSCR} RNA interaction. (A-D) SEC interaction analyses of ALPP^{SSCR} RNA with (A) NUP358^{NTD}, (B) NUP358^{NTD Δ TPR}, (C) NUP358^{TPR}, and (D) NUP358¹⁻⁶⁷³, demonstrating that NUP358^{TPR} is necessary but insufficient for ALPP^{SSCR} RNA binding. (E) SEC analysis of ALPP^{SSCR} RNA with NUP358^{NTD} in a buffer containing 200 mM NaCl, revealing the salt-sensitive nature of the interaction. SEC profiles of NUP358 variants (blue) and ALPP^{SSCR} RNA (red) are shown individually and after their preincubation (green). SEC profiles were obtained using a Superdex 200 10/300 GL column. Gray boxes indicate fractions resolved on SDS-PAGE and 0.5X TBE urea-PAGE denaturing gels and visualized by Coomassie brilliant blue and SYBR Gold staining, respectively. (F) EMSA titrations against ALPP^{SSCR} RNA are shown for each NUP358 variant used in (A-D), corroborating the SEC interaction results. (G) Quantitation of RNA binding of three independent experiment and plotted against protein concentration. Error bars represent standard error.

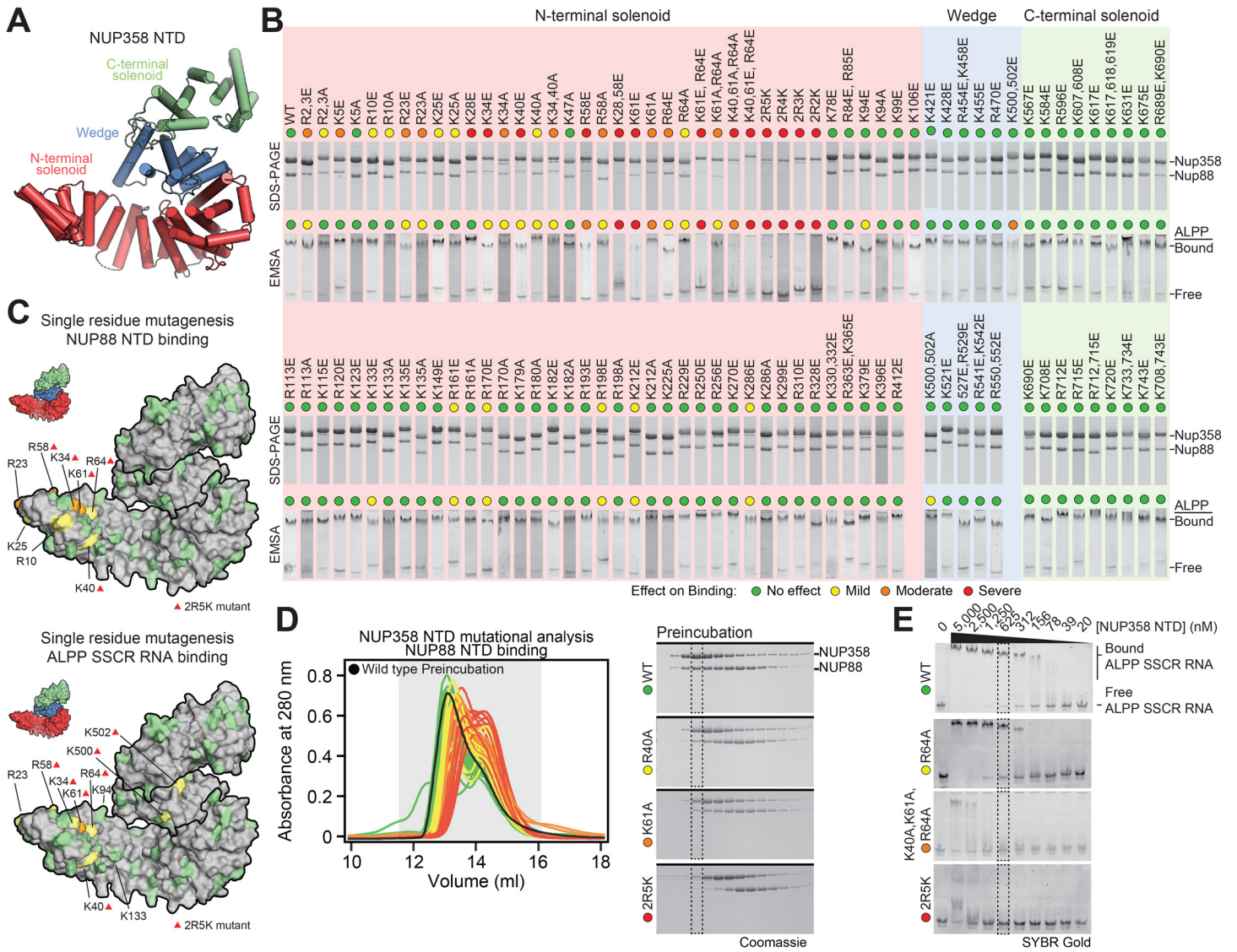


Fig. S49. Identification of NUP88^{NTD} and ALPP^{SSCR} RNA binding sites on the NUP358^{NTD} surface. (A) Cartoon representation of NUP358^{NTD}. (B) 106 NUP358^{NTD} surface mutants were tested for their interaction with NUP88^{NTD} and ALPP^{SSCR} RNA by SEC and EMSA, respectively. SDS-PAGE gel strips from each NUP358^{NTD} mutant, corresponding to the peak fraction from the wildtype SEC interaction, were visualized by Coomassie brilliant blue staining. EMSA gel strips for each NUP358^{NTD} mutant at 625 nM concentration, were visualized by SYBR Gold staining. The colored dots indicate the effect on binding of the mutations. (C) Surface representations of NUP358^{NTD} with saturating mutagenesis residues colored according to their effect on NUP88^{NTD} and ALPP^{SSCR} RNA binding. Red triangles indicate residues of the 2R5K combination mutant, which abolishes the interactions with both NUP88^{NTD} and ALPP^{SSCR} RNA. (D) SEC profiles of NUP88^{NTD} interactions with NUP358^{NTD} mutants are overlaid and colored according to their effect on NUP88^{NTD} binding. Gray boxes indicate fractions resolved on SDS-PAGE gels for representative interactions in each category of binding. (E) Full EMSA titrations are shown for representative interactions in each category of binding. Dashed lines indicate SDS-PAGE and EMSA lanes shown in panel (B). Combination mutations are referred to as 2R5K (K34A, K40A, R58A, K61A, R64A, K500A, and K502A), 2R4K (K40A, R58A, K61A, R64A, K500A, and K502A), 2R3K (K34A, K40A, R58A, K61A, and R64A), and 2R2K (K40A, R58A, K61A, and R64A).

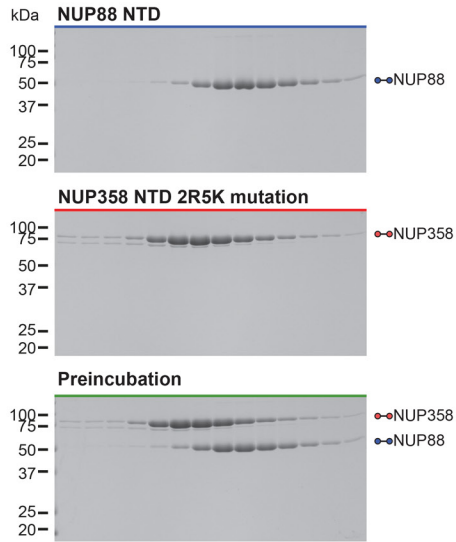
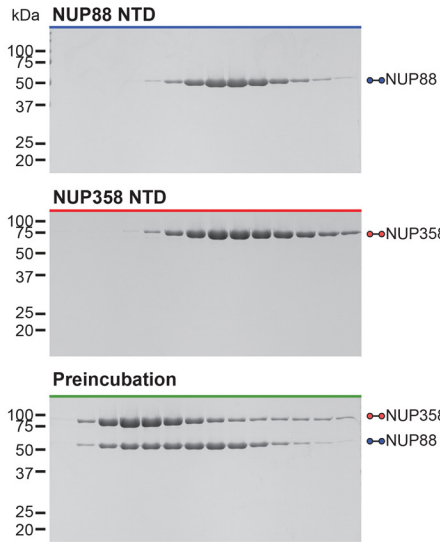
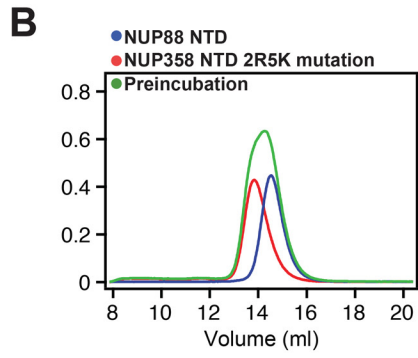
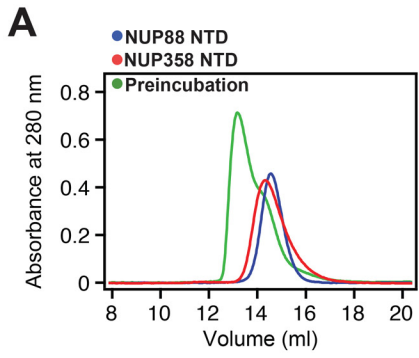


Fig. S50. NUP358^{NTD} 2R5K combination mutant abolishes NUP88^{NTD} binding. (A, B) SEC interaction analysis of NUP88^{NTD} with (A) NUP358^{NTD} and (B) the NUP358^{NTD} 2R5K combination mutant (K34A, K40A, R58A, K61A, R64A, K500A, and K502A). The 2R5K combination mutation abolishes the NUP358^{NTD}-NUP88^{NTD} interaction. SEC profiles of NUP358^{NTD} variants (blue) and NUP88^{NTD} (red) are shown individually and after their preincubation (green). SEC profiles were obtained using a Superdex 200 10/300 GL column. Gray boxes indicate fractions resolved on SDS-PAGE gels and visualized by Coomassie brilliant blue staining.

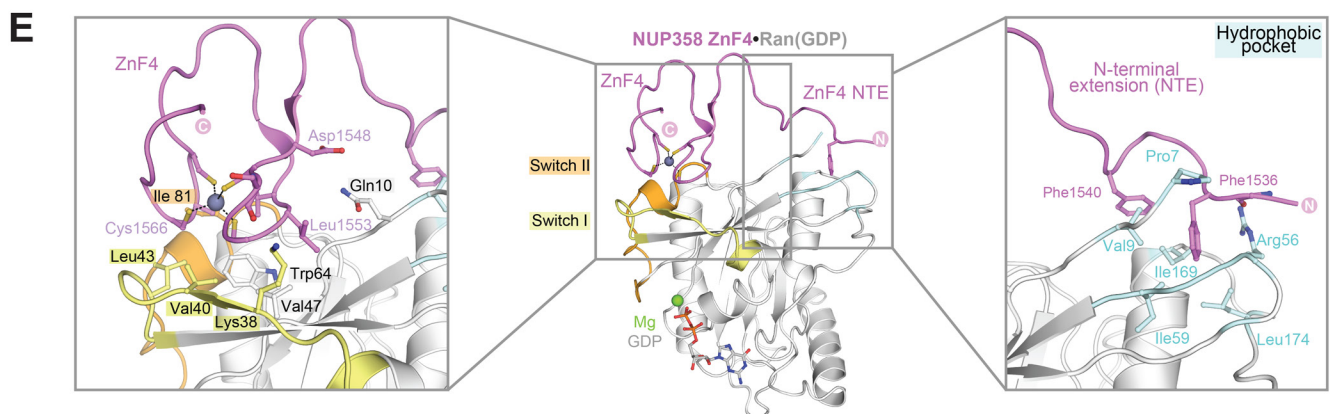
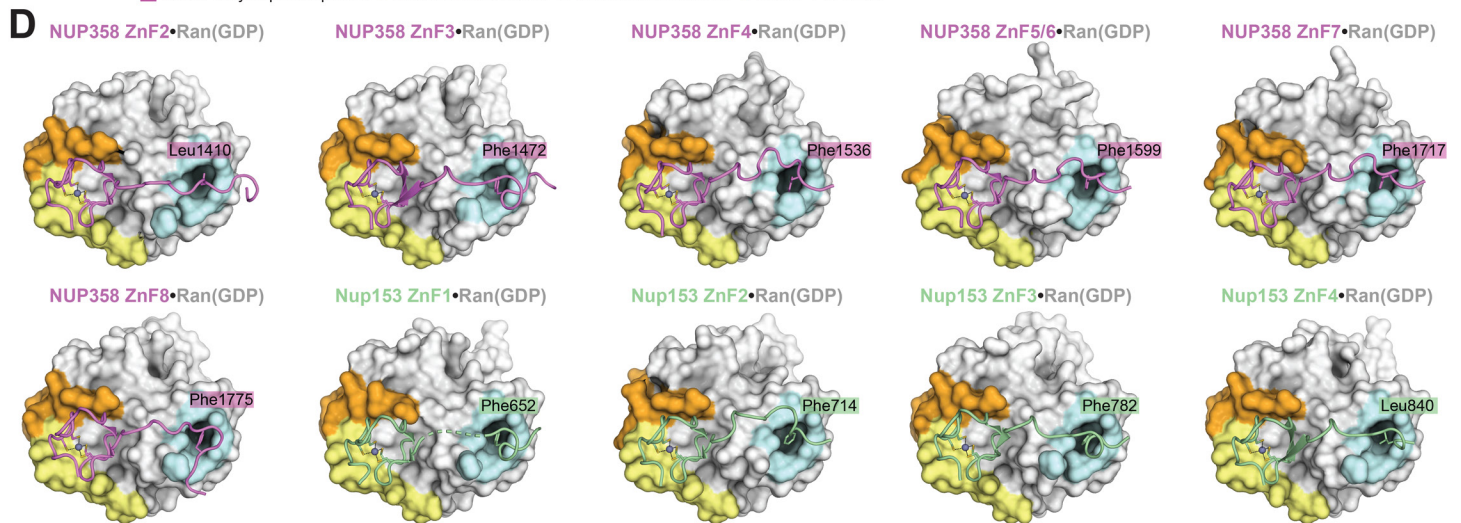
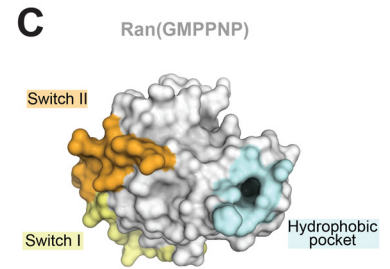
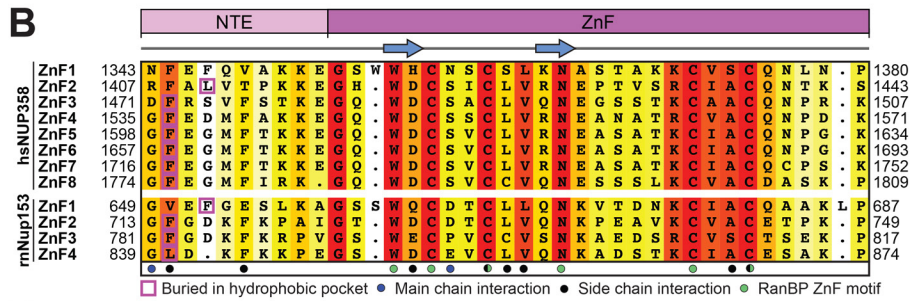
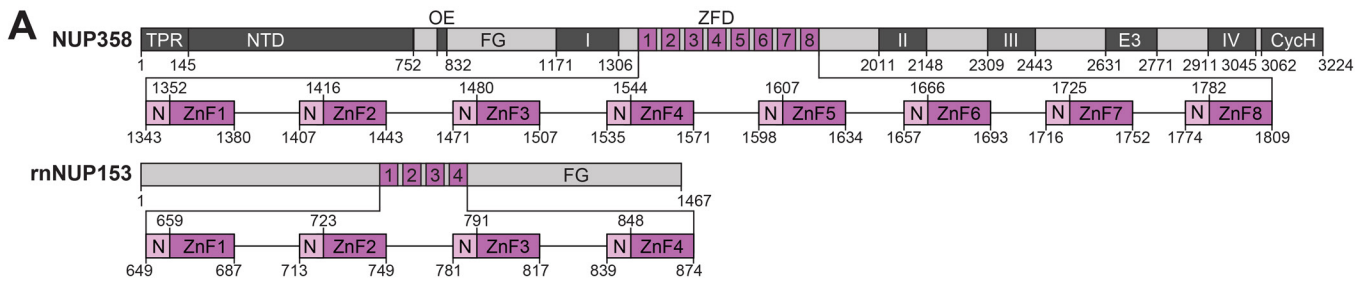


Fig. S51. Crystal structures of NUP358^{ZnF}•Ran(GDP) and NUP153^{ZnF}•Ran(GDP) complexes. (A) Domain structures of NUP358 and NUP153 drawn as horizontal boxes with residue numbers indicated. (B) Sequence alignment of the eight NUP358 and four *R. norvegicus* rnNUP153 ZnFs colored according to the BLOSUM62 weighting algorithm from white (less than 40% similarity), through yellow (60% similarity), to red (100% identity). (C) Surface representation of Ran(GMPPNP) from the NUP358^{RanBD-IV}•Ran crystal structure, highlighting the switch I (yellow), switch II (orange), and the nucleotide-independent hydrophobic pocket (cyan). (D) Co-crystal structures of six NUP358^{ZnF}•Ran(GDP) and four rnNUP153^{ZnF}•Ran(GDP) complexes are shown. The ZnFs and Ran(GDP) are shown in cartoon and surface representation, respectively. In all structures, a hydrophobic residue of each NTE occupies Ran's nucleotide-independent hydrophobic pocket. (E) Magnified views of NUP358^{ZnF4}•Ran(GDP) illustrating Ran's interactions with the ZnF motif and NTE.

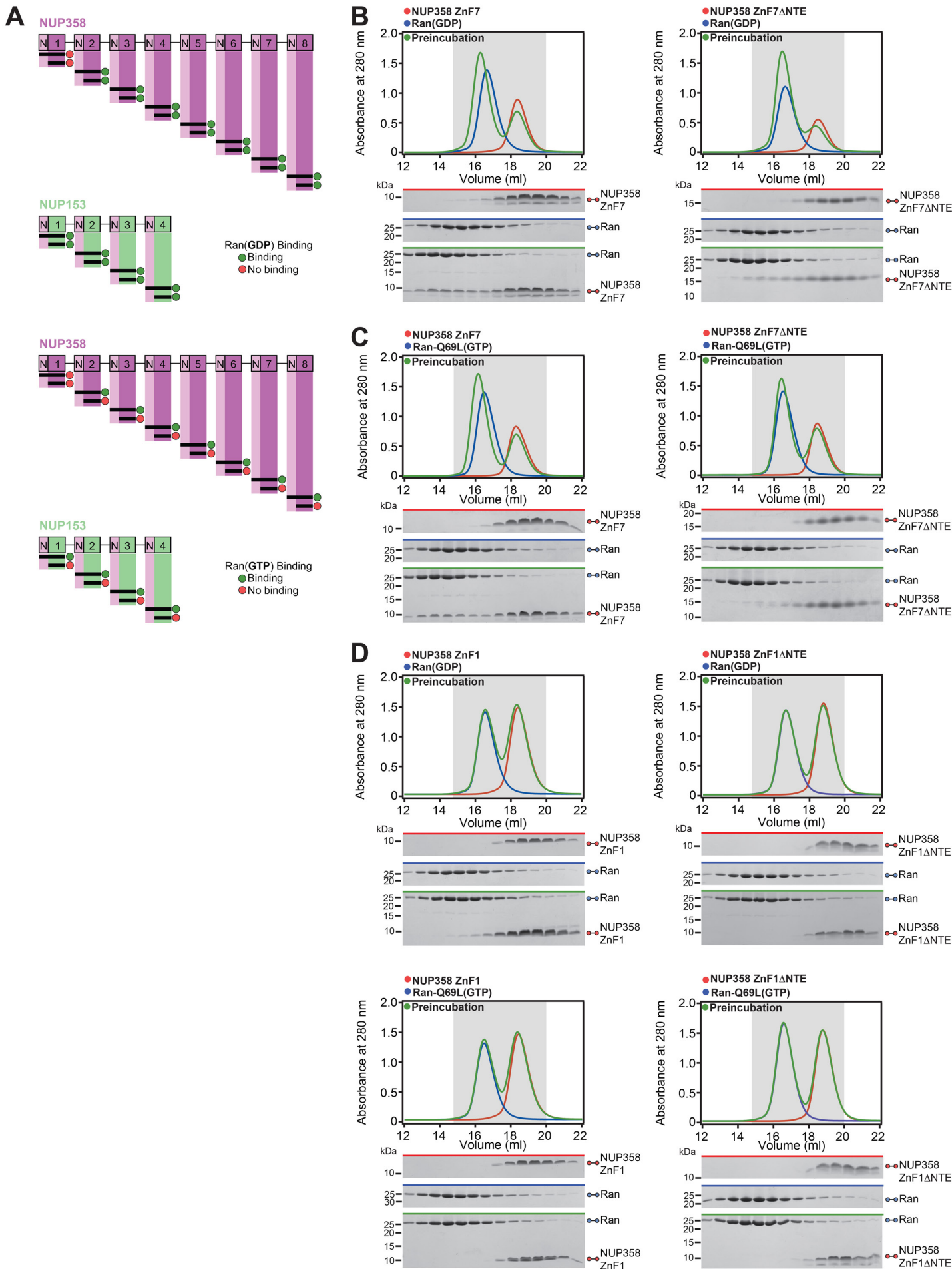


Fig. S52. Biochemical analysis of the Ran interaction with NUP358/NUP153 ZnF modules. (A) Summary of the Ran(GDP) binding properties of the twelve NUP358/NUP153 ZnF modules. Apart from NUP358^{ZnF1}, for which no binding is detected, the remaining eleven ZnF modules bind Ran(GDP) irrespective of the presence of the NTE. (B) Representative SEC interaction analysis of RAN(GDP) with NUP358^{ZnF7} in the absence or presence of the NTE. (C) Summary of the Ran(GTP) binding properties of the twelve NUP358/NUP153 ZnF modules. Apart from NUP358^{ZnF1}, for which no binding is detected, Ran(GTP) binding of the remaining eleven ZnF modules is dependent on the presence of the NTE. (D) SEC interaction analyses of NUP358^{ZnF1} with Ran(GDP) and Ran(GTP), showing no binding irrespective of the presence of the NTE.

A

RanBP2-type ZnFs

| | | NTE | | ZnF | | | | | | | | | | | | | | | | | | | | | | | | | | | | | | | | | | | | | | | | | |
|-------------------|-------------|------|------|-----|---|---|---|---|---|---|---|---|---|---|---|---|---|---|---|---|---|---|---|---|---|---|---|---|---|---|---|---|---|---|---|---|---|---|---|-----|---|-----|------|------|------|
| | | | | ← | | | | | | | | | | | | | | → | | | | | | | | | | | | | | | | | | | | | | | | | | | |
| Ran (GDP) binding | NUP358 | ZnF1 | 1343 | N | F | E | F | Q | V | A | K | K | E | G | S | W | W | H | C | N | . | . | S | C | S | L | K | N | A | S | T | A | K | K | C | V | S | C | Q | N | L | N | P | 1380 | |
| | | ZnF2 | 1407 | R | F | A | L | V | T | P | K | K | E | G | H | . | W | D | C | S | . | . | I | C | L | V | R | N | E | P | T | V | S | R | K | I | A | C | Q | N | T | K | S | 1443 | |
| | | ZnF3 | 1471 | D | F | R | S | V | F | S | T | K | K | E | G | Q | . | W | D | C | S | . | . | A | C | L | V | Q | N | E | G | S | S | T | K | C | A | A | C | Q | N | P | R | K | 1507 |
| | | ZnF4 | 1535 | G | F | E | D | M | F | A | K | K | E | G | Q | . | W | D | C | S | . | . | S | C | L | V | R | N | E | A | N | A | T | R | C | V | A | C | Q | N | P | D | K | 1571 | |
| | | ZnF5 | 1598 | G | F | E | G | M | F | T | K | K | E | G | Q | . | W | D | C | S | . | . | V | C | L | V | R | N | E | A | S | A | T | K | C | I | A | C | Q | N | P | G | K | 1634 | |
| | | ZnF6 | 1657 | G | F | E | G | M | F | T | K | K | E | G | Q | . | W | D | C | S | . | . | V | C | L | V | R | N | E | A | S | A | T | K | C | I | A | C | Q | N | P | G | K | 1693 | |
| | | ZnF7 | 1716 | G | F | E | G | M | F | T | K | K | E | G | Q | . | W | D | C | S | . | . | V | C | L | V | R | N | E | A | S | A | T | K | C | I | A | C | Q | C | P | S | K | 1752 | |
| | | ZnF8 | 1774 | G | F | E | G | M | F | I | R | K | . | G | Q | . | W | D | C | S | . | . | V | C | V | Q | N | E | S | S | L | K | C | V | A | C | Q | D | A | S | K | P | 1809 | | |
| Ran Binding | NUP153 | ZnF1 | 649 | G | I | G | F | G | E | S | L | K | A | G | S | W | Q | C | D | . | . | T | C | L | L | Q | N | K | V | T | D | N | K | C | I | A | C | Q | A | A | K | L | 686 | | |
| | | ZnF2 | 714 | G | F | G | D | K | F | K | P | V | I | G | T | . | W | D | C | D | . | . | T | C | L | V | Q | N | K | P | E | A | I | K | C | V | A | C | E | T | P | K | P | 750 | |
| | | ZnF3 | 785 | G | F | G | D | K | F | K | R | P | I | G | S | . | W | D | C | S | . | . | V | C | C | V | S | N | N | A | E | D | N | K | C | V | S | C | M | S | E | K | P | 821 | |
| | | ZnF4 | 844 | . | G | L | E | K | F | K | K | P | E | G | S | . | W | D | C | E | . | . | L | C | L | V | Q | N | K | A | D | S | T | K | L | A | C | E | S | A | K | P | 879 | | |
| RNA Binding | TAF15 | 345 | G | F | Q | G | R | G | D | P | K | S | G | D | W | V | C | P | N | P | S | C | G | N | M | N | F | A | R | R | N | S | C | N | Q | C | N | E | P | R | P | 384 | | | |
| | FUS | 414 | G | G | G | G | G | Q | Q | R | A | G | D | . | W | K | C | P | N | P | T | C | E | N | M | N | F | A | R | R | N | S | C | N | Q | C | K | A | P | K | P | 452 | | | |
| | EWS | 510 | S | G | G | G | N | V | Q | H | R | A | G | D | . | W | Q | C | P | N | P | T | C | E | N | Q | N | F | A | R | R | T | S | C | N | Q | C | K | A | P | K | P | 548 | | |
| | ZRANB2 ZnF1 | 1 | . | M | S | T | K | N | F | R | S | D | G | D | . | W | I | C | P | D | K | K | C | G | N | V | N | F | A | R | R | T | S | C | N | Q | C | G | R | E | K | T | 39 | | |
| | ZRANB2 ZnF2 | 56 | L | A | E | K | S | R | G | L | F | S | A | N | D | W | Q | C | K | . | . | T | C | S | N | V | N | F | A | R | R | S | E | C | N | M | C | N | T | P | K | Y | 93 | | |
| | TEX13A | 368 | Q | O | R | P | P | V | R | R | P | D | . | W | D | C | P | . | . | T | C | S | N | A | V | N | F | S | R | R | D | T | C | N | F | D | C | G | K | G | I | W | 404 | | |
| RBM10 | 215 | H | Y | S | D | P | K | P | K | I | N | E | D | . | W | L | C | N | . | . | K | C | G | V | Q | N | F | K | R | R | E | K | C | F | K | C | G | V | P | K | S | 241 | | | |
| RBM5 | 174 | H | Y | S | N | P | R | P | K | F | . | E | D | . | W | L | C | N | . | . | K | C | L | N | F | R | K | R | L | K | C | F | R | C | G | A | D | K | F | 209 | | | | | |
| Protein Binding | RBCK1 | 184 | G | Q | P | D | A | V | P | E | P | P | P | V | G | W | Q | C | P | . | . | G | C | T | F | I | N | K | P | T | R | P | G | C | E | M | C | C | R | A | R | P | 221 | | |
| | MDM2 | 290 | S | F | E | E | D | P | E | I | S | L | A | D | Y | W | K | C | T | . | . | S | C | N | E | M | N | P | P | L | P | S | H | C | N | R | C | W | A | L | R | E | 327 | | |
| | MDM4 | 291 | S | D | D | T | D | V | E | V | T | S | E | D | E | W | Q | C | T | . | . | E | C | K | K | F | N | S | P | S | K | R | Y | C | F | R | C | W | A | L | R | K | 328 | | |
| | TAB2 | 655 | P | K | T | Q | D | T | E | D | D | E | G | A | Q | W | N | C | T | . | . | A | C | T | F | L | N | H | P | A | L | I | R | C | E | Q | C | E | M | P | R | H | 692 | | |

W x C x (2-4) C x x x N x x x x x x C x x C

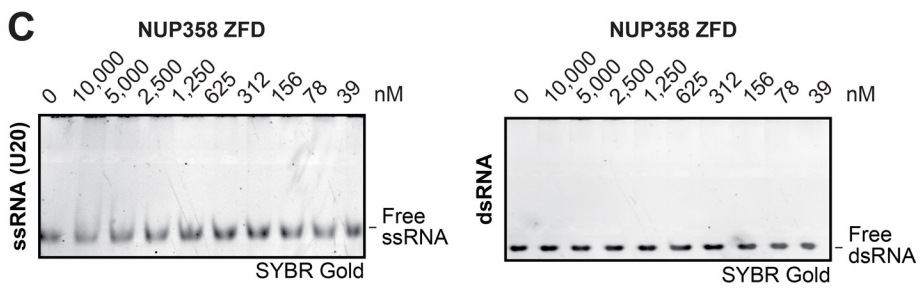
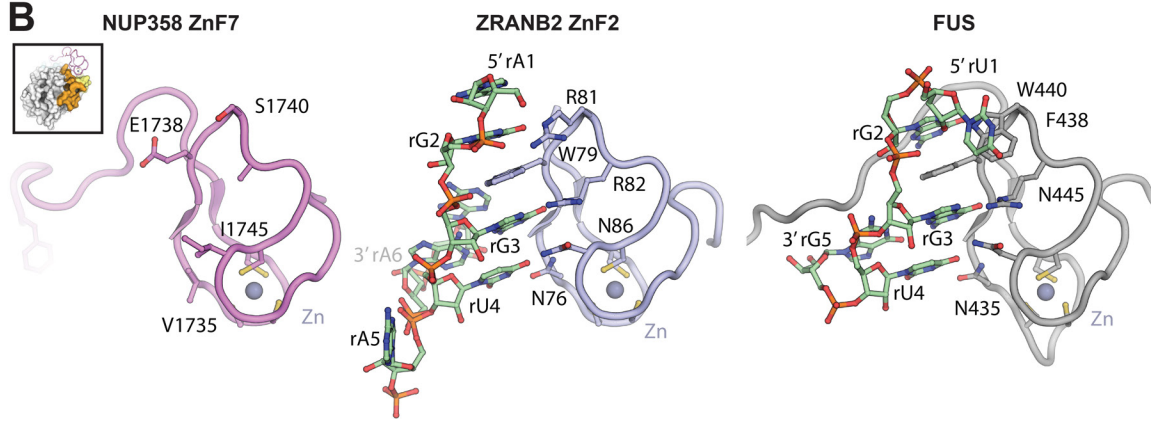


Fig. S53. NUP358 ZFD does not bind to single- or double-stranded RNA. (A) Sequence alignment of the twelve NUP358/NUP153 ZnF modules with representative members of the RanBP2 ZnF family with established RNA or protein binding properties, colored according to the BLOSUM62 weighting algorithm from white (less than 40% similarity) through yellow (60% similarity) to red (100% identity). Essential RNA binding residues are highlighted by a black box. RanBP2-type zinc finger motif residues are indicated by green dots. (B) Structures of NUP358^{ZnF7}, ZRANB2^{ZnF}•ssRNA (PDB ID 3G9Y) (143), and FUS^{ZnF}•ssRNA (PDB ID 6G99) (144) are shown, illustrating the absence of residues required for RNA binding. Inset indicates NUP358^{ZnF7} orientation in comparison to Ran(GDP). (C) EMSA titration of NUP358^{ZFD} with ssRNA and dsRNA visualized with SYBR Gold stain, demonstrating the absence of RNA binding properties.

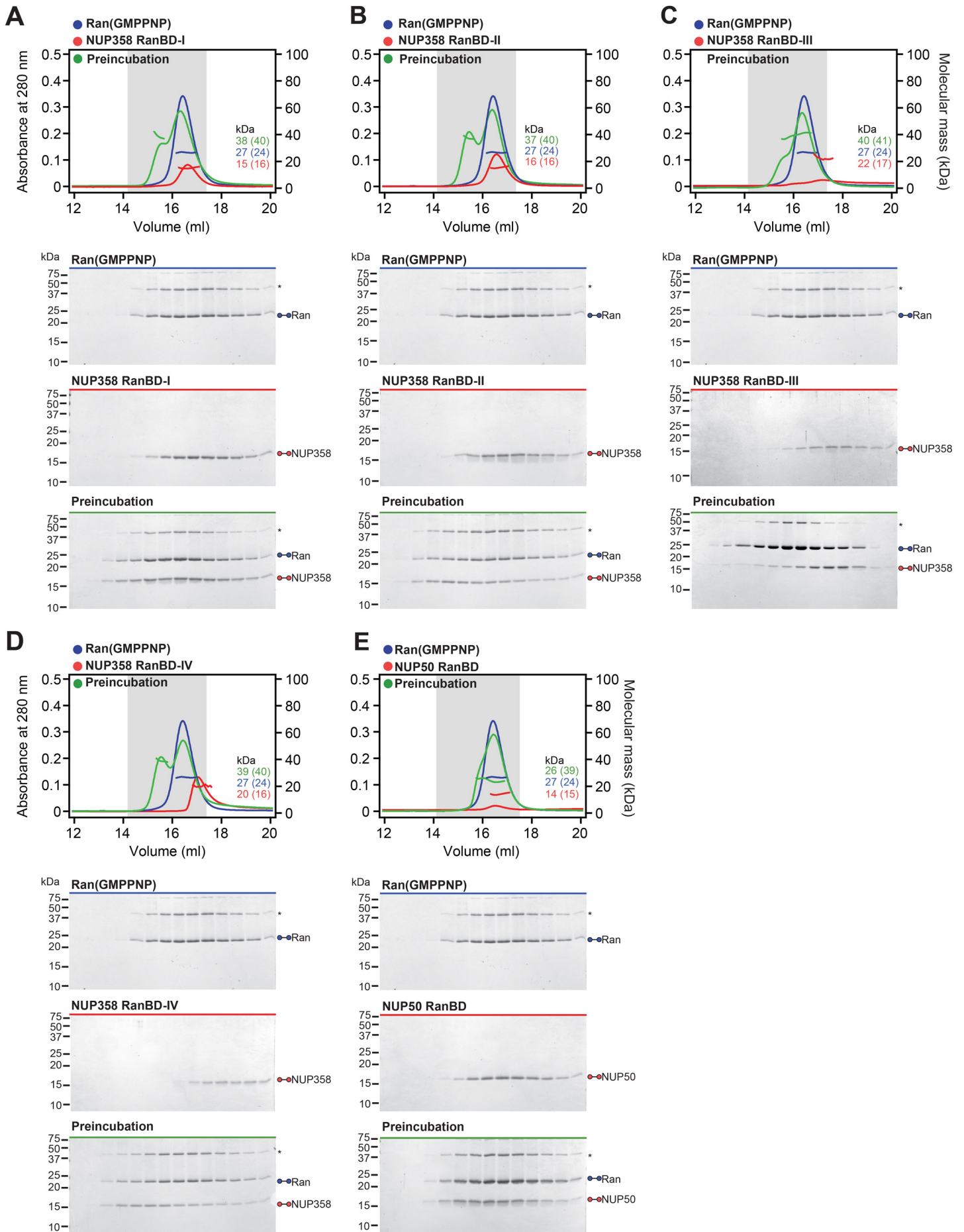


Fig. S54. Biochemical analysis of the Ran interaction with NUP358/NUP50 RanBDs. (A-E) SEC-MALS interaction analyses of Ran(GMPPNP) with (A) NUP358^{RanBD-I}, (B) NUP358^{RanBD-II}, (C) NUP358^{RanBD-III}, (D) NUP358^{RanBD-IV}, and (E) NUP50^{RanBD}. SEC profiles of RanBDs (blue) and Ran(GMPPNP) red are shown individually and after their preincubation (green). Measured molecular masses are indicated, with the respective theoretical masses shown in parentheses. Gray boxes indicate fractions resolved on SDS-PAGE gels and visualized by Coomassie brilliant blue staining. Asterisks indicate oligomeric Ran species, arising from boiling in SDS-loading dye.

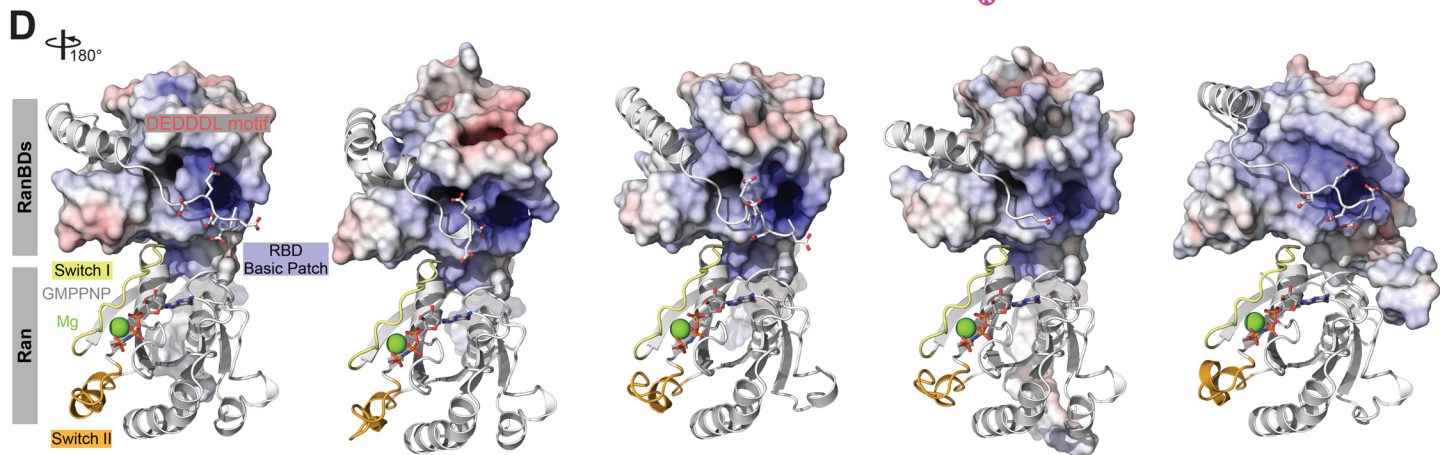
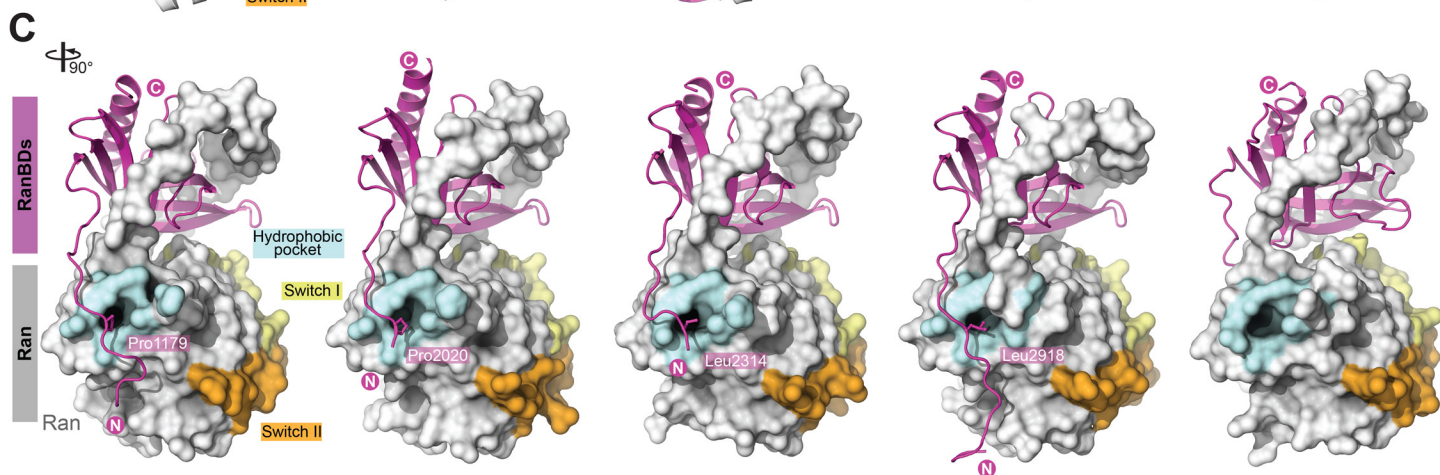
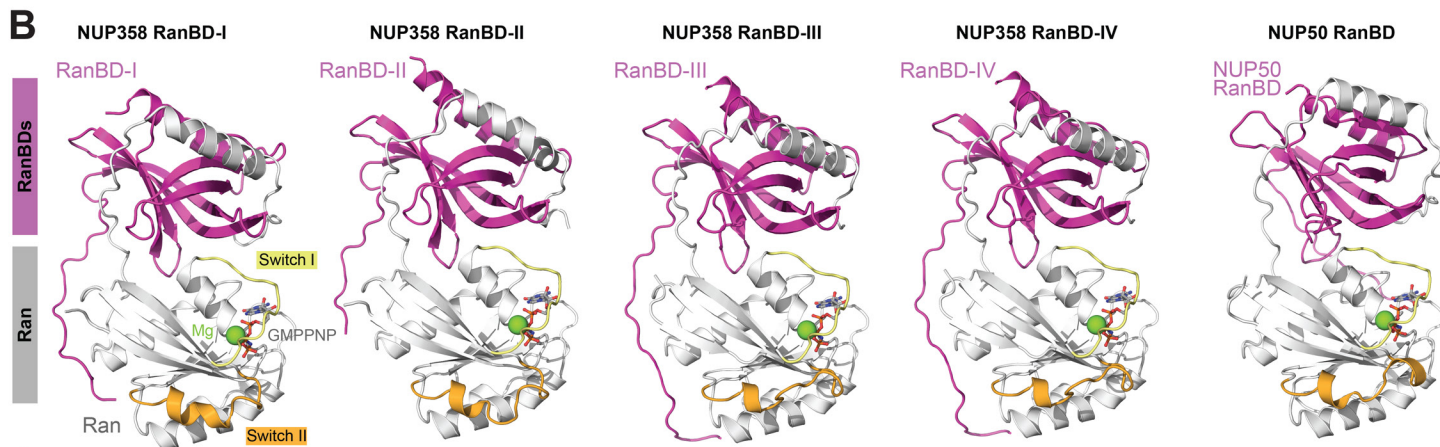
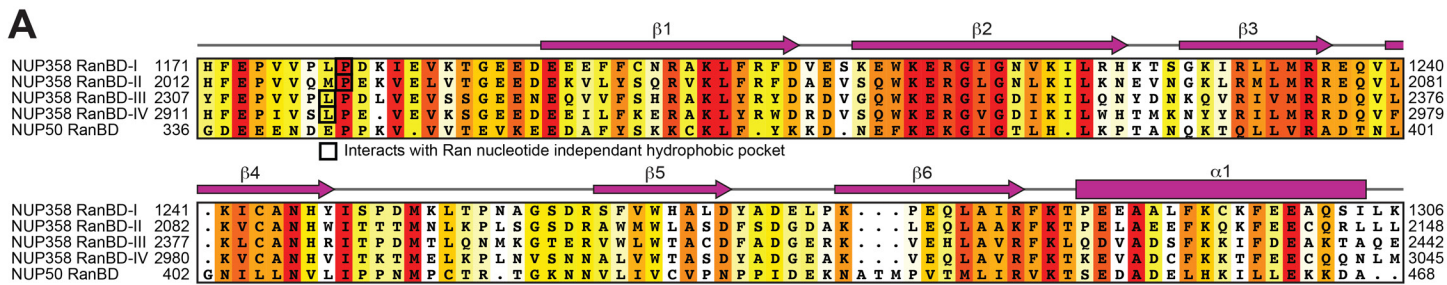
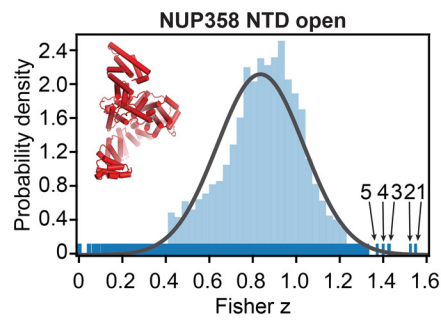
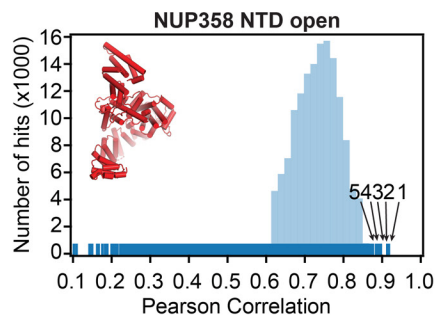
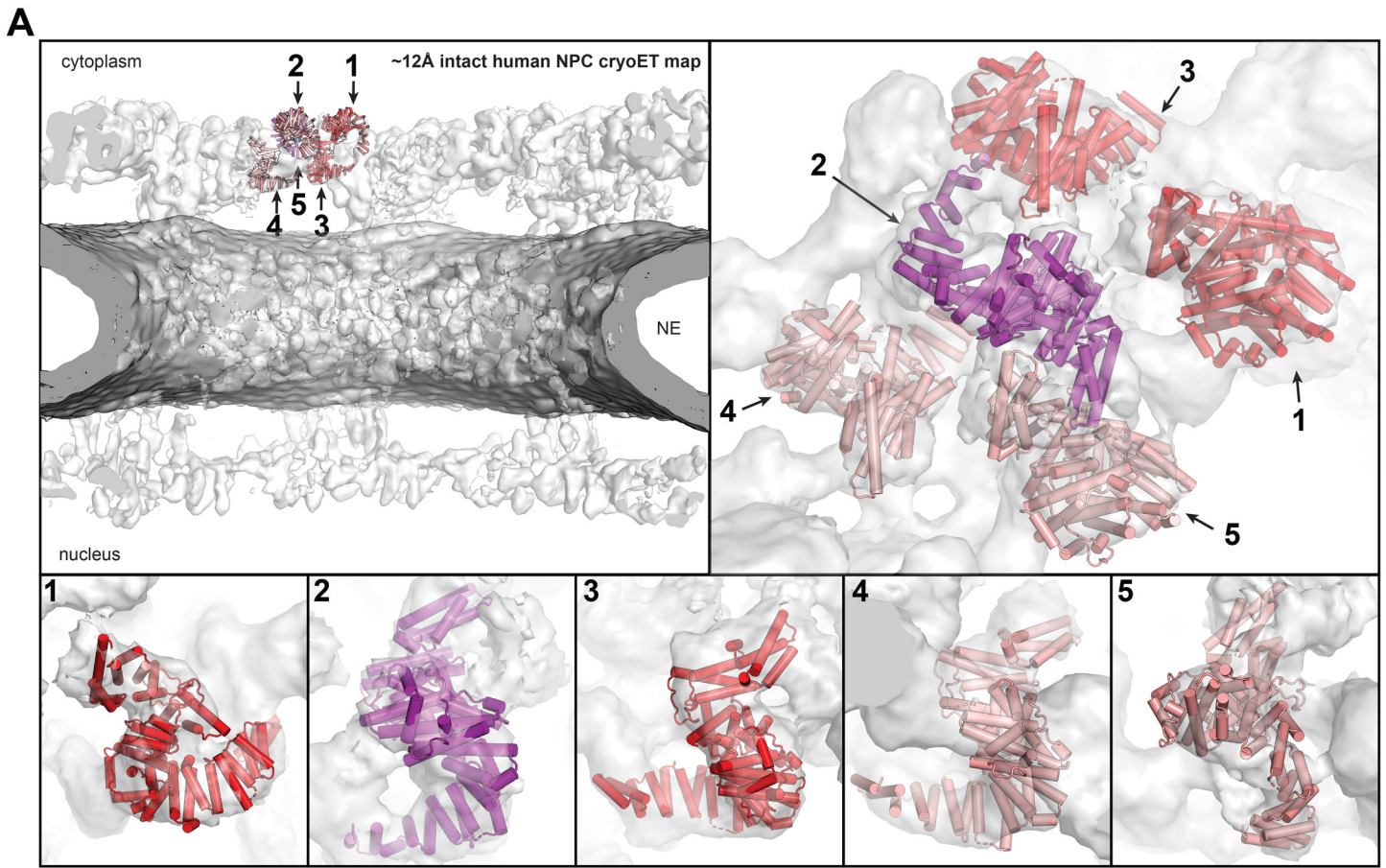
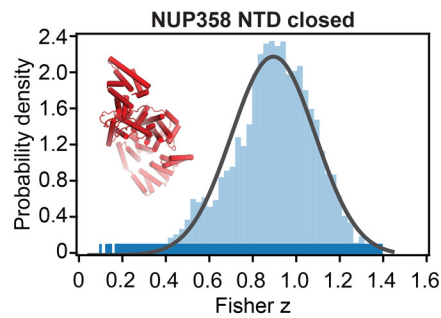
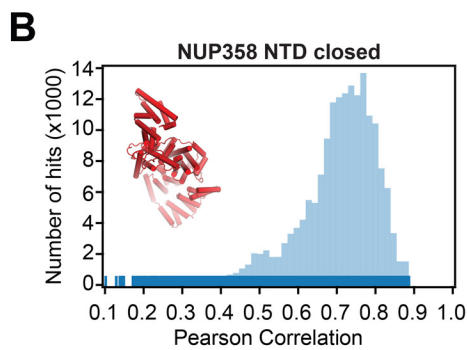


Fig. S55. Crystal structures of NUP358/NUP50^{RanBD}•Ran(GMPPNP). (A) Sequence alignment of the NUP358/NUP50 RanBD, colored according to the BLOSUM62 weighting algorithm from white (less than 40% similarity), through yellow (60% similarity), to red (100% identity). The secondary structure is indicated above the sequences as rectangles (α -helices), arrows (β -strands), and lines (unstructured regions). (B) Co-crystal structures of the five NUP358/NUP50^{RanBD}•Ran(GMPPNP) complexes shown in cartoon representation. (C) 90°-rotated views of all five complexes illustrating the location of Ran's nucleotide-independent hydrophobic pocket that accommodates a hydrophobic residue of all four NUP358^{RanBD}, an interaction not observed in the NUP50^{RanBD} complex. (D) 180°-rotated views of all five complexes highlighting the interaction of the DEDDDL motif of Ran with the basic patch found on each RanBD. The RanBD surface representation is colored according to electrostatic potential from red (-10 k_BT/e) to blue (+10 k_BT/e).



Cryo-ET map fitting statistics

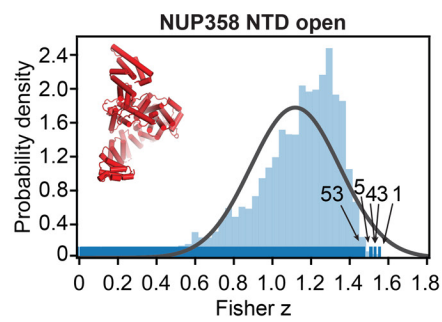
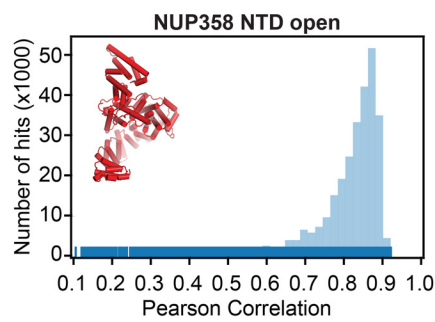
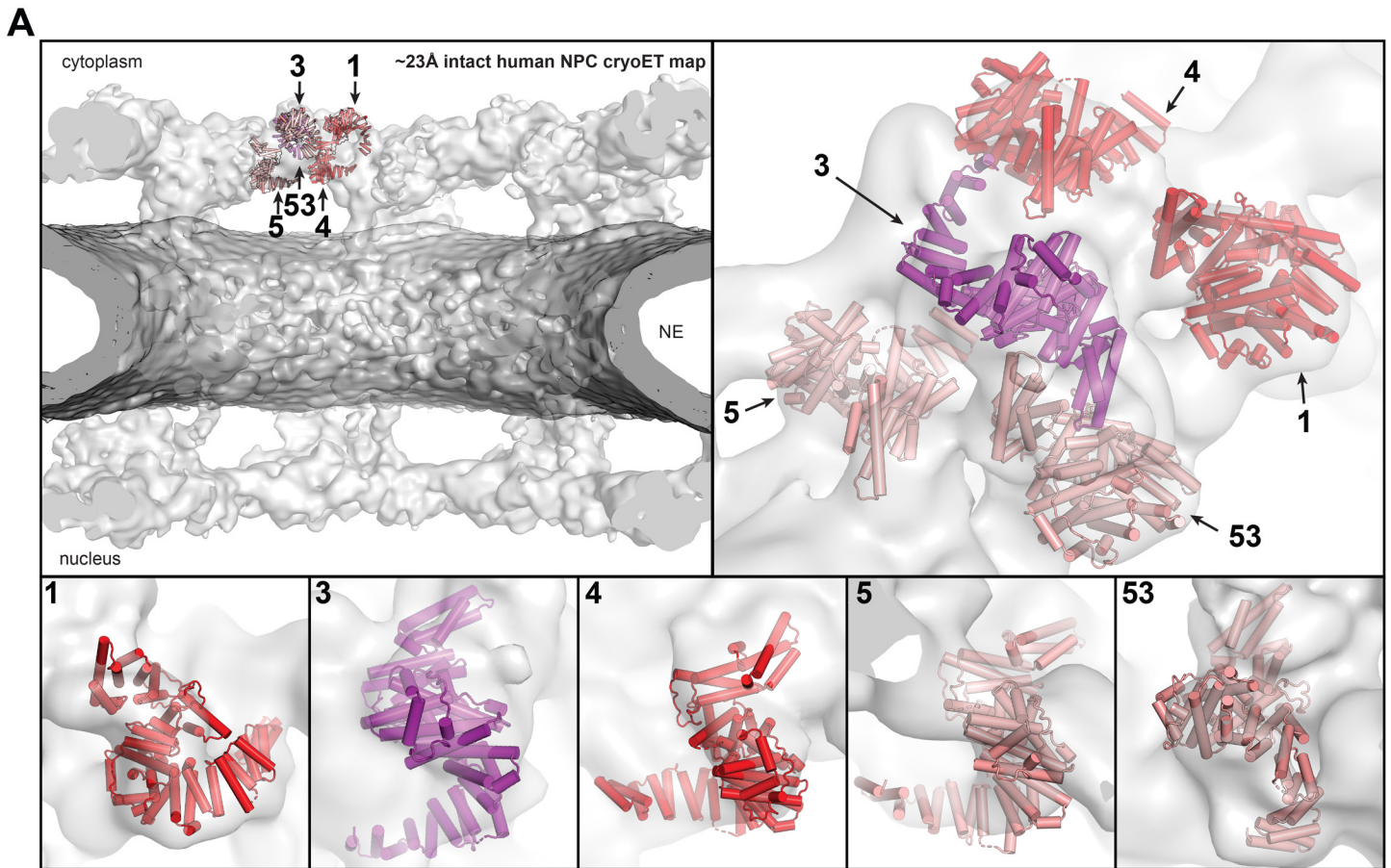
| solution rank | Pearson correlation | Fisher z | p-value |
|---------------|---------------------|----------|---------|
| 1 | 0.913 | 1.54 | 1.7 e-4 |
| 2 | 0.909 | 1.52 | 2.6 e-4 |
| 3 | 0.892 | 1.43 | 1.5 e-3 |
| 4 | 0.891 | 1.43 | 1.5 e-3 |
| 5 | 0.890 | 1.40 | 2.3 e-3 |



Cryo-ET map fitting statistics

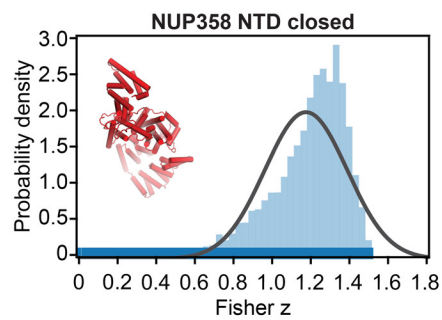
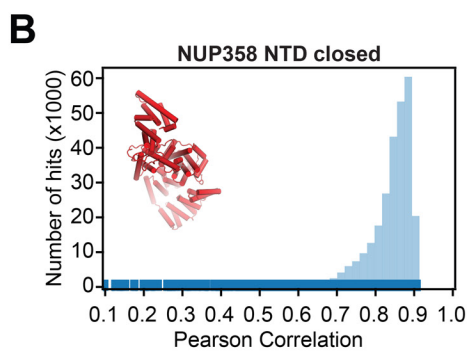
| solution rank | Pearson correlation | Fisher z | p-value |
|---------------|---------------------|----------|---------|
| 1 | 0.882 | 1.38 | 4.9 e-3 |
| 2 | 0.880 | 1.38 | 5.6 e-3 |
| 3 | 0.878 | 1.37 | 6.2 e-3 |
| 4 | 0.877 | 1.36 | 6.7 e-3 |
| 5 | 0.875 | 1.35 | 7.6 e-3 |

Fig. S56. Docking of the NUP358^{NTD} structure into an ~12Å cryo-ET map of the intact human NPC. (A) The open conformation NUP358^{NTD} crystal structure was quantitatively docked into the ~12 Å sub-tomogram averaged cryo-ET map of the intact human NPC (46). Placed unique solutions are shown in cartoon representation with their rank indicated, whereas the cryo-ET map is rendered as a transparent isosurface. Solutions are viewed from a central cross-section of the intact NPC (*left*), from a closeup view from above the cytoplasmic face (*right*), or individually (*bottom*). Isosurfaces of the nuclear envelope and the NPC are colored dark and light gray, respectively. Rug plots (blue) and histograms (light blue) of Pearson correlation scores and derived Fisher z scores, fit with a normalized Gaussian curve (black), from a global search with 1 million random initial placements, are shown. Arrows and corresponding numbers indicate the rank of accepted solutions. A table summary of the accepted solutions fitting statistics, along with one-tailed p-values calculated from the Fisher z score distribution, is shown. (B) The same analysis as in (A) was applied to the closed conformation NUP358^{NTD} crystal structure. Unlike with the open conformation, the docking solutions identified for the closed conformation of NUP358^{NTD} crystal structure did not segregate to high confidence.



Cryo-ET map fitting statistics

| solution rank | Pearson correlation | Fisher z | p-value |
|---------------|---------------------|----------|---------|
| 1 | 0.915 | 1.56 | 0.029 |
| 3 | 0.909 | 1.52 | 0.044 |
| 4 | 0.908 | 1.52 | 0.044 |
| 5 | 0.908 | 1.52 | 0.045 |
| 53 | 0.894 | 1.44 | 0.090 |



Cryo-ET map fitting statistics

| solution rank | Pearson correlation | Fisher z | p-value |
|---------------|---------------------|----------|---------|
| 1 | 0.909 | 1.52 | 0.055 |
| 2 | 0.907 | 1.51 | 0.061 |
| 3 | 0.906 | 1.50 | 0.064 |
| 4 | 0.906 | 1.50 | 0.066 |
| 5 | 0.905 | 1.50 | 0.066 |

Fig. S57. Docking of the NUP358^{NTD} structure into an ~23Å cryo-ET map of the intact human NPC. (A) The open conformation NUP358^{NTD} crystal structure was quantitatively docked into the ~23 Å sub-tomogram averaged cryo-ET map of the intact human NPC (44). Placed unique solutions are shown in cartoon representation with their rank indicated, whereas the cryo-ET map is rendered as a transparent isosurface. Solutions are viewed from a central cross-section of the intact NPC (*left*), from a closeup view from above the cytoplasmic face (*right*), or individually (*bottom*). Isosurfaces of the nuclear envelope and the NPC are colored dark and light gray, respectively. Rug plots (blue) and histograms (light blue) of Pearson correlation scores and derived Fisher z scores, fit with a normalized Gaussian curve (black), from a global search with 1 million random initial placements, are shown. Arrows and corresponding numbers indicate the rank of accepted solutions. A table summary of the accepted solutions fitting statistics, along with one-tailed p-values calculated from the Fisher z score distribution, is shown. (B) The same analysis as in (A) was applied to the closed conformation NUP358^{NTD} crystal structure. Unlike with the open conformation, the docking solutions identified for the closed conformation of NUP358^{NTD} crystal structure did not segregate to high confidence.

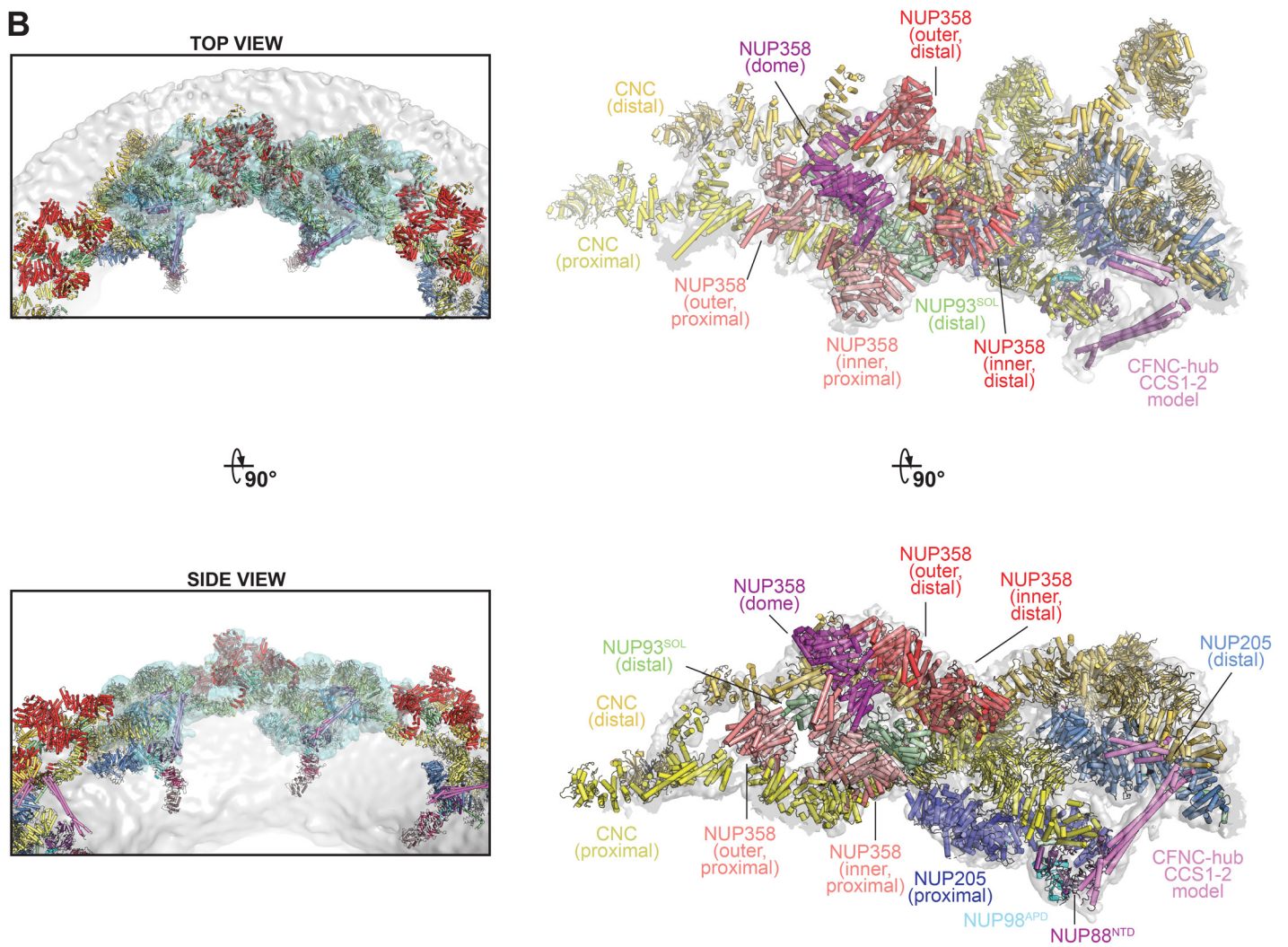
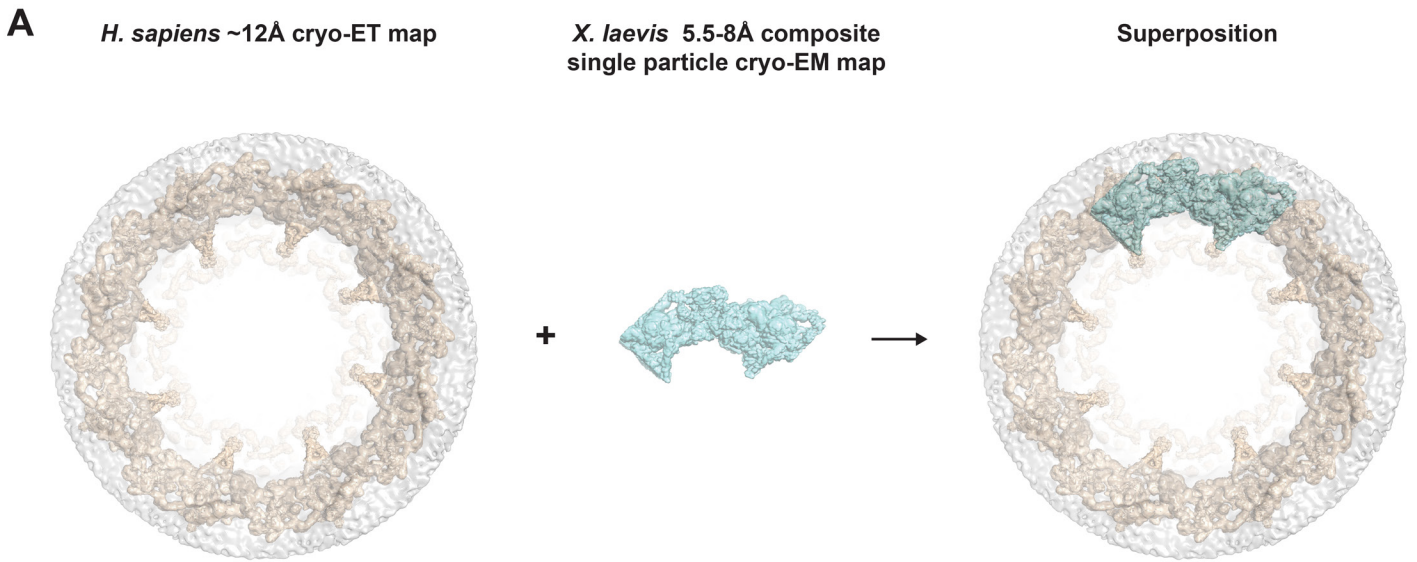
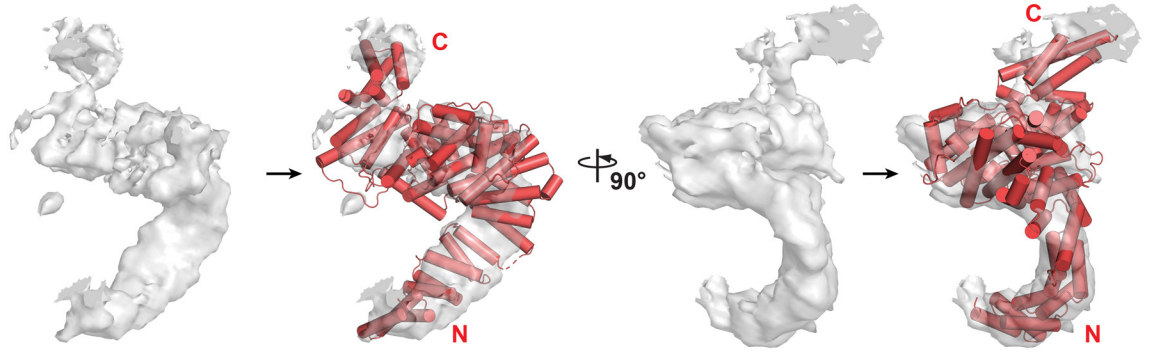
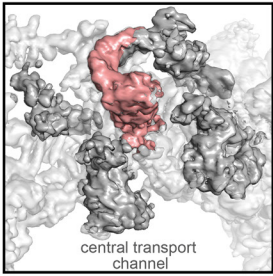
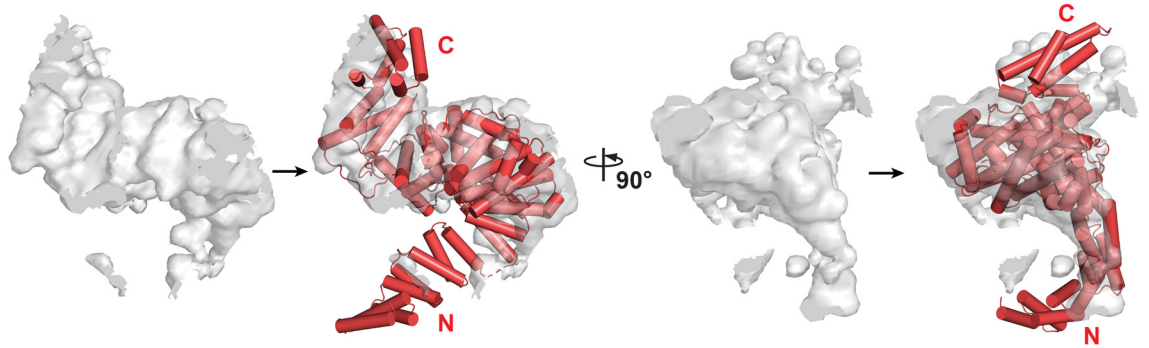
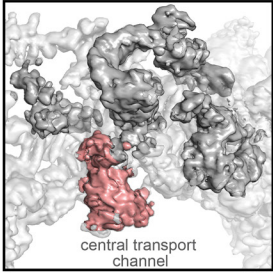


Fig. S58. Docking of the CF nups into the anisotropic composite single particle cryo-EM map of the *X. laevis* cytoplasmic face protomer. (A) (A) An anisotropic ~ 8 Å composite single particle cryo-EM map of the *X. laevis* cytoplasmic face protomer (light cyan; EMD-0909) (45) was superposed to the ~ 12 Å cryo-ET map of the intact human NPC (wheat; EMD-14322) (46). Maps and nuclear envelope (gray) are rendered as isosurfaces. (B) The superposition of the two maps placed the docked cytoplasmic outer ring and cytoplasmic face asymmetric nup structures, shown in cartoon representation, into the composite single particle cryo-EM map of the *X. laevis* cytoplasmic face protomer (*left*). The fit of the structures was subsequently locally optimized against the fully explained *X. laevis* cryo-EM map (*right*).

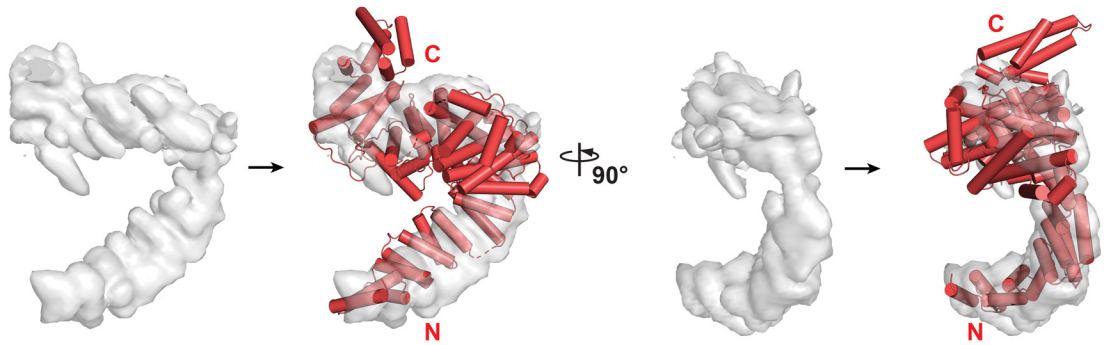
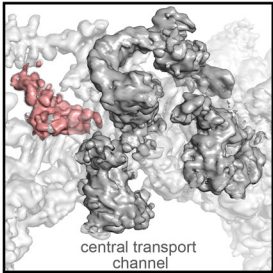
**NUP358
dome**



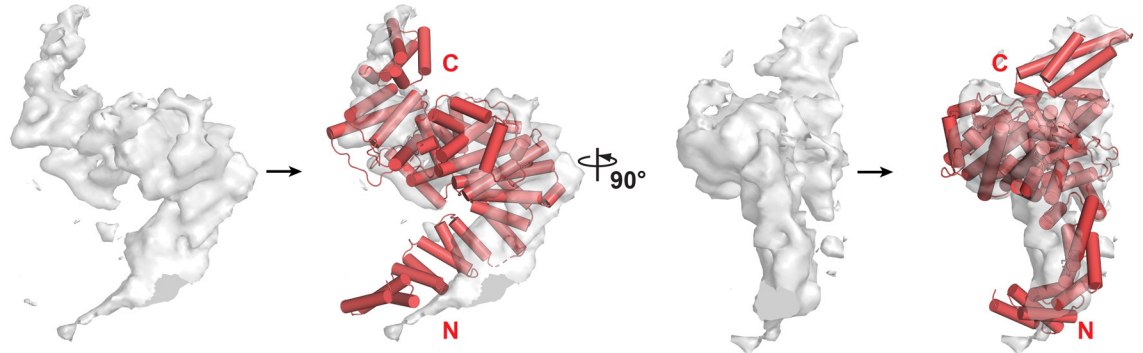
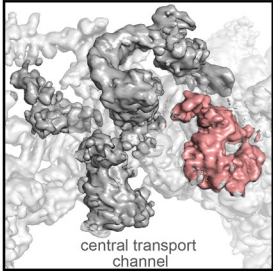
**NUP358
proximal inner**



**NUP358
proximal outer**



**NUP358
distal inner**



**NUP358
distal outer**

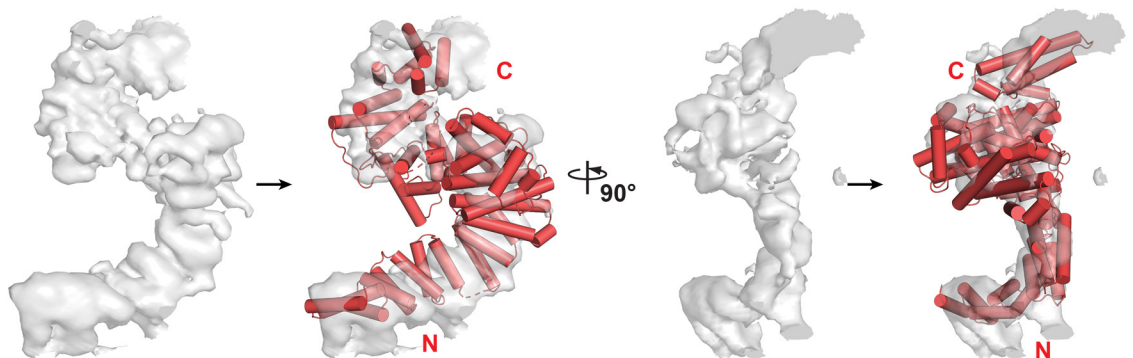
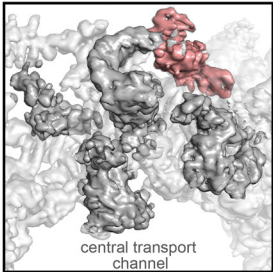


Fig. S59. Identifying five NUP358^{NTD} copies in the *X. laevis* cytoplasmic face protomer. The NUP358^{NTD} open conformation crystal structure was globally placed by superposition of the ~12 Å cryo-ET map of the intact human NPC and locally rigid body refined at five positions (*left*) in the ~7 Å region of an anisotropic composite single particle cryo-EM map of the *X. laevis* cytoplasmic face protomer (light cyan; EMD-0909) (45). Two orthogonal views (*middle* and *right*) of carved out cryo-EM density rendered as transparent isosurfaces are shown superposed to NUP358^{NTD} structures in cartoon representation.

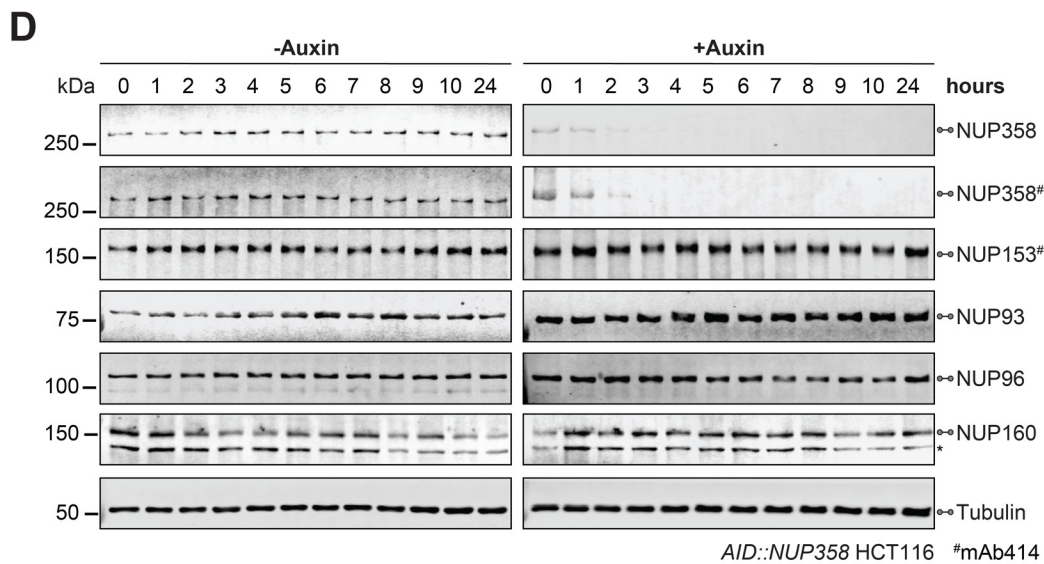
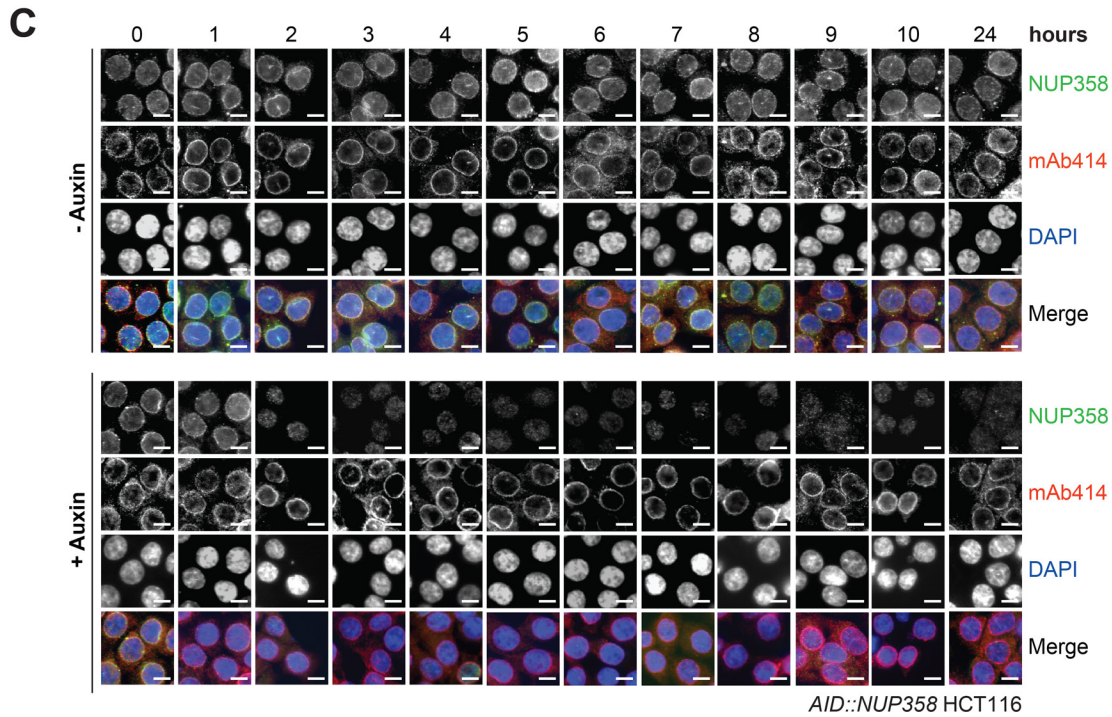
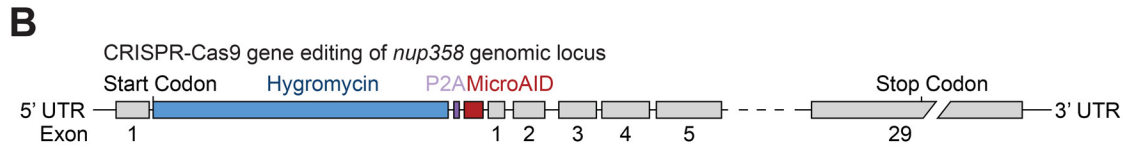
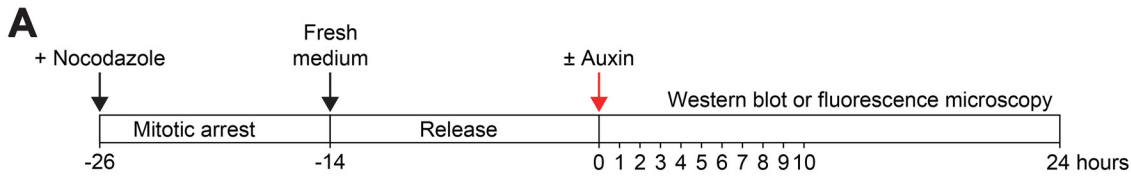
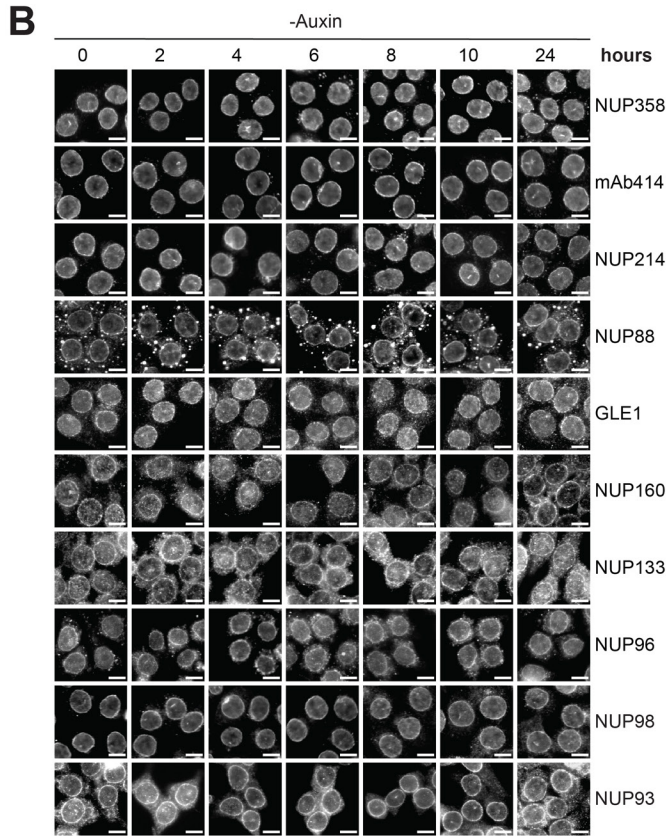
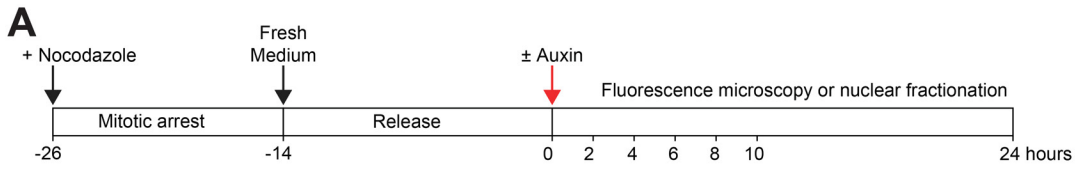
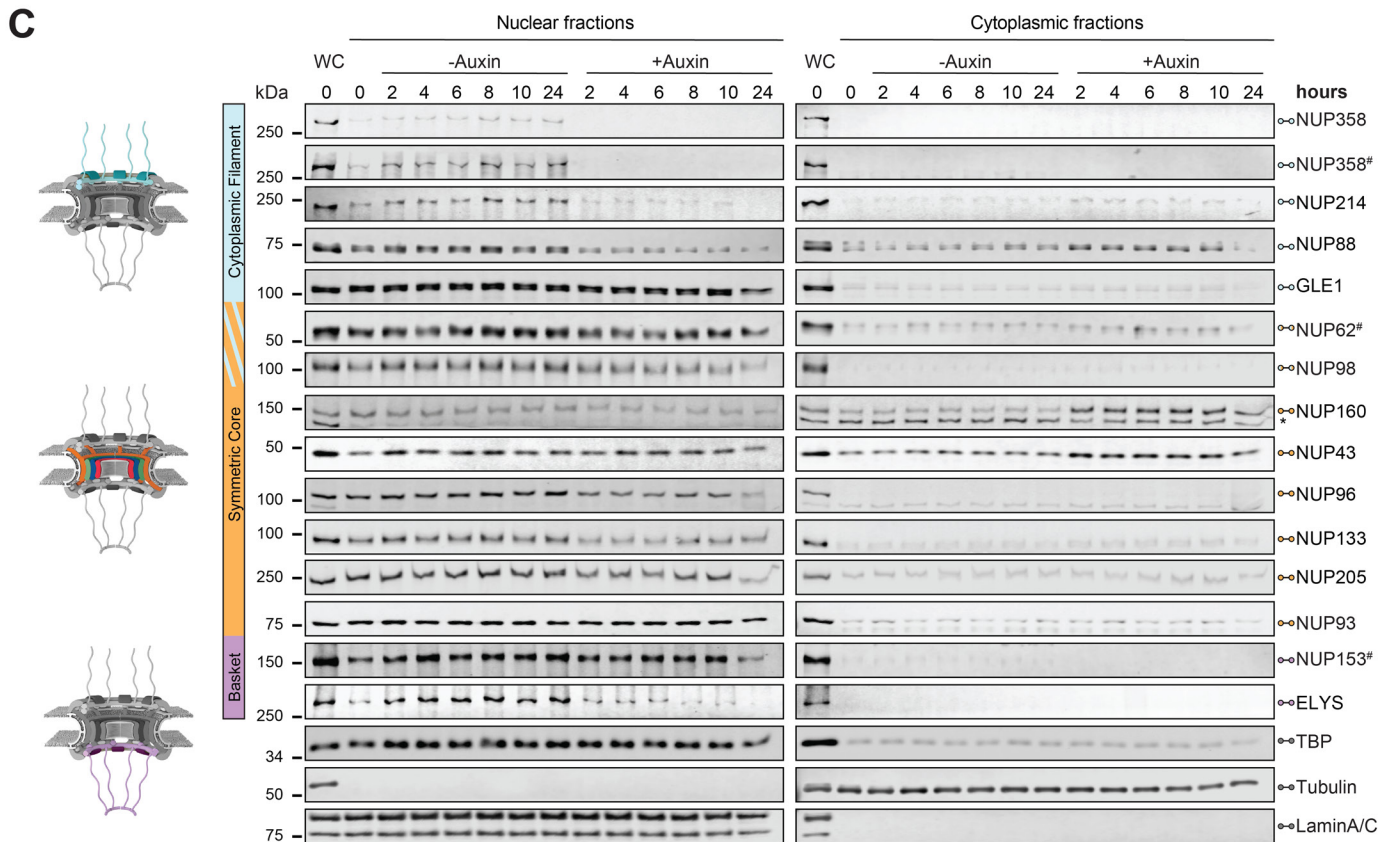


Fig. S60. Validation of auxin-induced NUP358 degradation in *AID::NUP358* HCT116 cells. (A) Experimental timeline. (B) Schematic representation of CRISPR/Cas9-mediated genomic tagging of *nup358* alleles. (C) Time-resolved subcellular localization analysis of AID-tagged NUP358 by immunofluorescence microscopy upon auxin treatment. The mAb414 antibody (red) and DAPI (blue) staining were used as a reference for the nuclear envelope and nucleus, respectively. Scale bars are 10 μm . (D) Time-resolved western blot analysis of AID-tagged NUP358 expression levels upon auxin treatment. The specificity of auxin induced NUP358 depletion was assessed by the indicated antibodies. Asterisks indicate a nonspecific band detected by the anti-NUP160 antibody. Control cells were not treated with auxin.



AID::NUP358 HCT116



AID::NUP358 HCT116

#mAb414

Fig. S61. Time-resolved localization analysis of endogenous nups in *AID::NUP358* HCT116 cells. (A) Experimental timeline. (B) Time-resolved subcellular localization analysis by immunofluorescence microscopy of endogenous nups in synchronized *AID::NUP358* HCT116 cells without auxin treatment, as a control for Fig. 5A. (C) Western blot analysis of nup levels in cytoplasmic and nuclear fractions of synchronized *AID::NUP358* HCT116 cells upon auxin-induced NUP358 depletion, according to the experimental timeline outlined in (A). Control cells were not treated with auxin. A whole cell extract (WC) control is included in the first lane of each blot. Colored regions in the schematics indicate nup locations within the NPC (*left*). Asterisk indicates a non-specific band. mAb414 antibody recognizes nups containing FG repeats including NUP62, NUP153, NUP214, and NUP358. Scale bars are 10 μm .

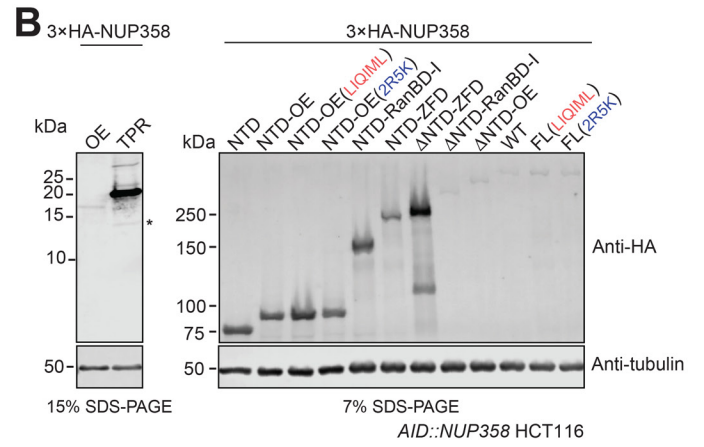
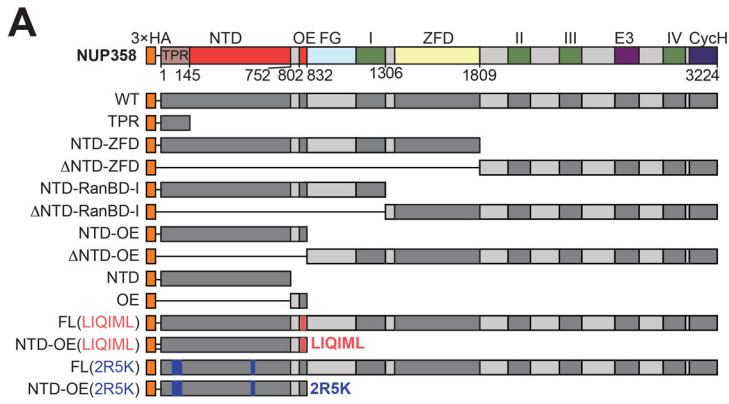


Fig. S62. Expression levels of 3×HA-tagged NUP358 variants in *AID::NUP358*HCT116 cells. (A) Schematics indicating the domain boundaries of the transfected N-terminally 3×HA-tagged NUP358 variants. (B) Western blot expression analysis of the 3×HA-NUP358 variants in *AID::NUP358*HCT116 cells (corresponding to localization in [Fig. 5B](#)).

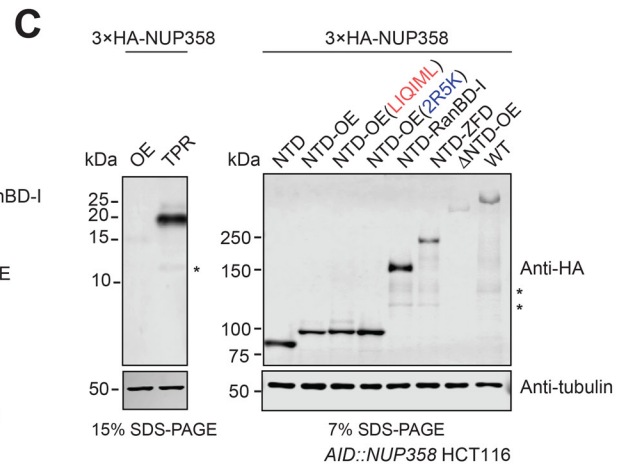
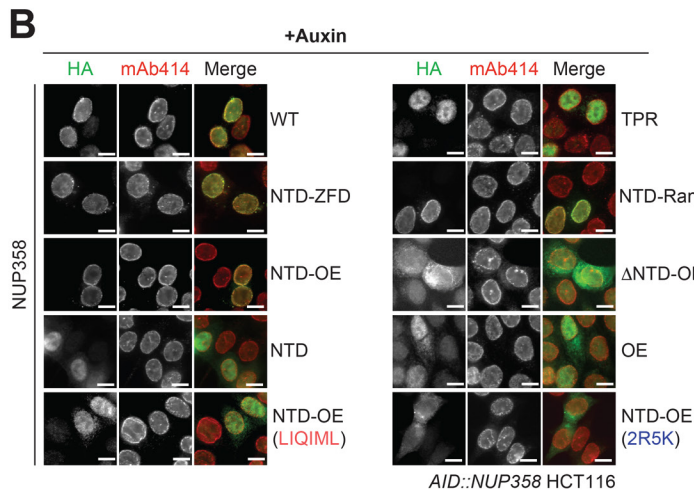
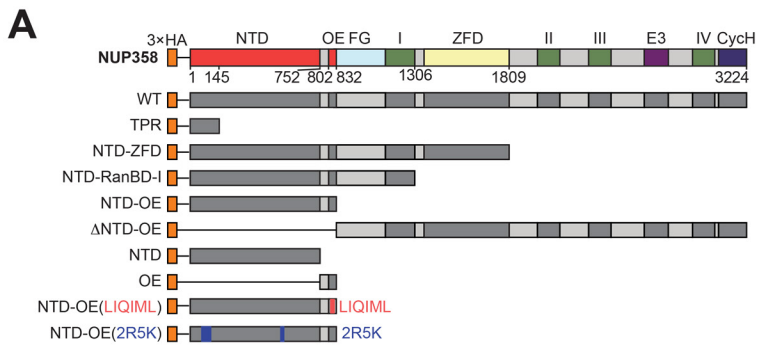


Fig. S63. Localization analysis of 3×HA-tagged NUP358 variants in NUP358 depleted cells. (A) Schematics indicating the domain boundaries of the transfected N-terminally 3×HA-tagged NUP358 variants. (B) Immunofluorescence microscopy localization analysis of 3×HA-NUP358 variants in *AID::NUP358* HCT116 cells after 3 hours of auxin treatment. mAb414 antibody staining was used as reference for the nuclear envelope. Scale bars are 10 μm. (C) Western blot expression analysis of 3×HA-tagged NUP358 variants in *AID::NUP358* HCT116 cells after 3 hours of auxin treatment.

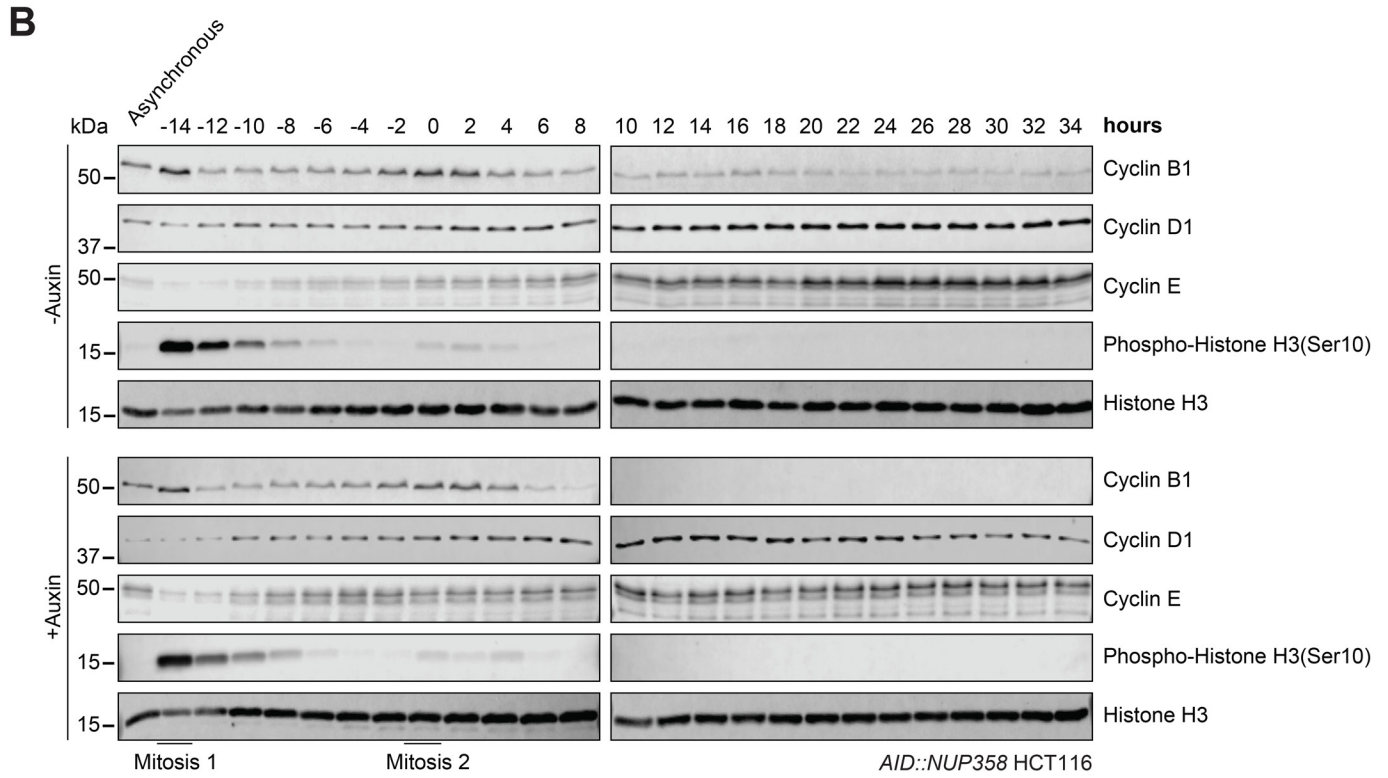
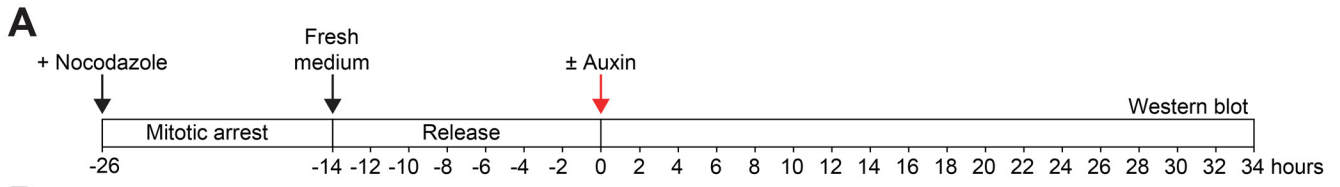


Fig. S64. Analysis of the cell cycle in nocodazole synchronized *AID::NUP358* HCT116 cells. (A) Experimental timeline. (B) Time resolved western blot analysis of the indicated cell cycle markers in *AID::NUP358* HCT116 cells post release from nocodazole block, establishing an ~14 hour cell cycle. Histone H3 serves as a loading control.

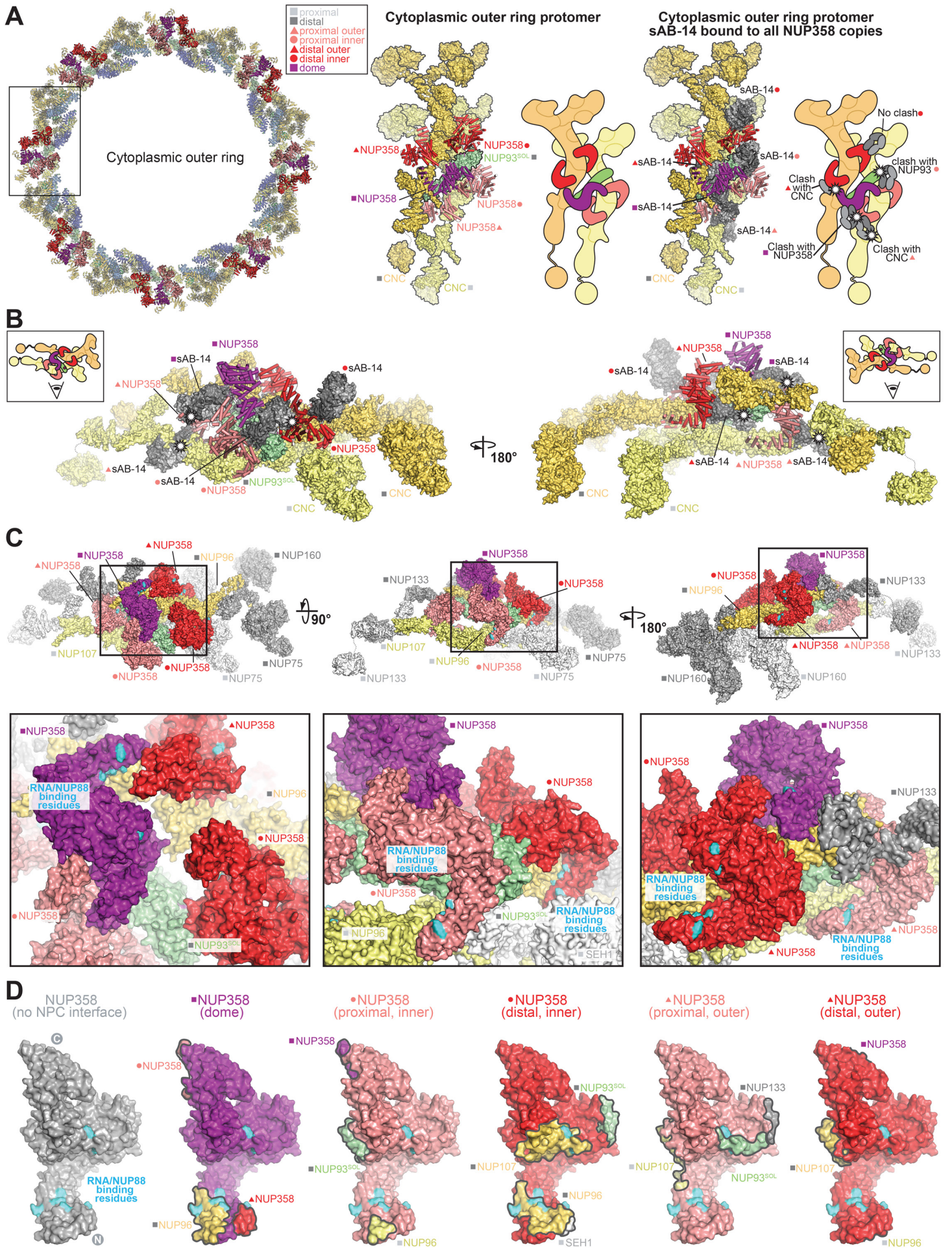


Fig. S65. Accessibility of sAB-14 and RNA/NUP88^{NTD} binding sites in NPC-attached NUP358^{NTD}. (A) Top view of the cytoplasmic face of the human NPC with NUP358^{NTD} docked (*left*). A closeup view of the region from the inset indicates a single spoke protomer with tandem-arranged CNCs (distal, gold; proximal, pale yellow), and distal NUP93^{SOL} (pale green) shown in surface representation, as well as five NUP358^{NTD} copies (salmon, red, and purple) shown as cartoons (*middle*). An equivalent protomer is shown with NUP358^{NTD}•sAB-14 crystal structures superposed to the docked NUP358^{NTD} copies. The sAB-14 heavy chain (light gray) and light chain (dark gray) are shown in surface representation. White stars indicate potential clashes that would occur if sAB-14 bound to a given NPC-attached NUP358^{NTD}. Schematics are shown to facilitate the interpretation of the rendered cartoons and surfaces. Distal and proximal positions are labeled according to the legend. (B) Two side views orthogonal to the cytoplasmic face protomer superposed with NUP358^{NTD}•sAB-14 in (A). (C) Three views of a surface representation of the cytoplasmic face protomer with closeup views of the regions in the insets. Residues identified as involved in RNA and NUP88^{NTD} binding by surface mutagenesis of NUP358^{NTD} are colored cyan. (D) Surface representation (gray) of NUP358^{NTD} with RNA/NUP88^{NTD}-binding residues colored cyan (*left*). Five NUP358^{NTD} copies found at the five unique positions in the cytoplasmic face protomer and colored accordingly (salmon, red, and purple) are shown in the same orientation, with RNA/NUP88^{NTD}-binding residues colored cyan, and surface patches colored according to the color assigned to the interfacing nup.

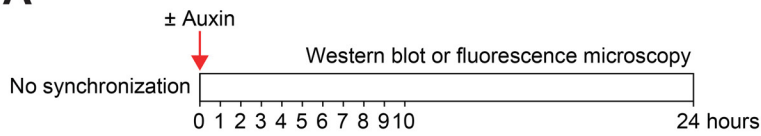
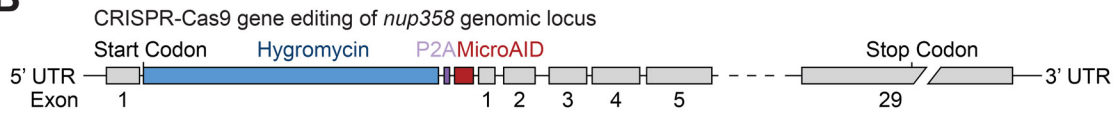
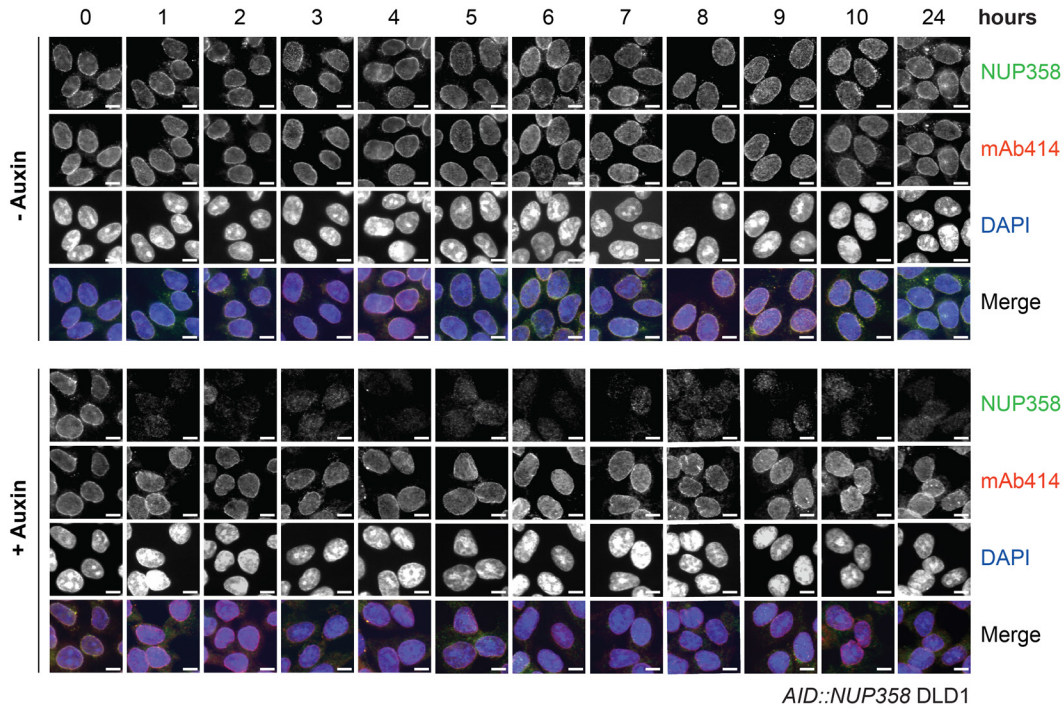
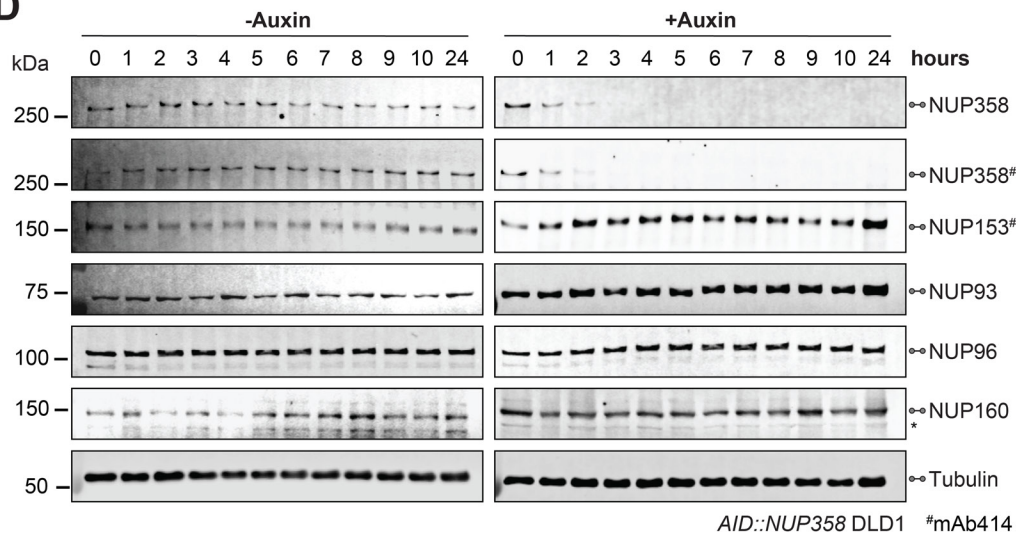
A**B****C****D**

Fig. S66. Validation of auxin-induced NUP358 degradation in *AID::NUP358* DLD1 cells. (A) Experimental timeline. (B) Schematic representation of CRISPR/Cas9-mediated genomic tagging of *nup358* alleles. (C) Time-resolved subcellular localization analysis of AID-tagged NUP358 by immunofluorescence microscopy upon auxin treatment. The mAb414 antibody (red) and DAPI (blue) staining were used as a reference for the nuclear envelope and nucleus, respectively. Scale bars are 10 μm . (D) Time-resolved western blot analysis of AID-tagged NUP358 expression levels upon auxin treatment. The specificity of auxin induced NUP358 depletion was assessed by the indicated antibodies. Asterisks indicate a nonspecific band detected by the anti-NUP160 antibody. Control cells were not treated with auxin.

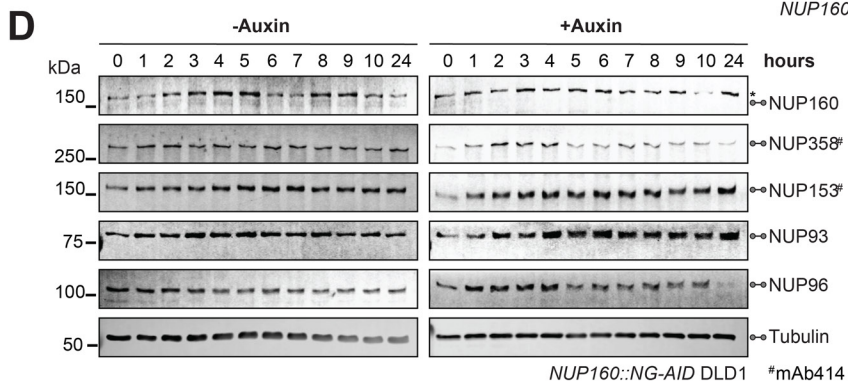
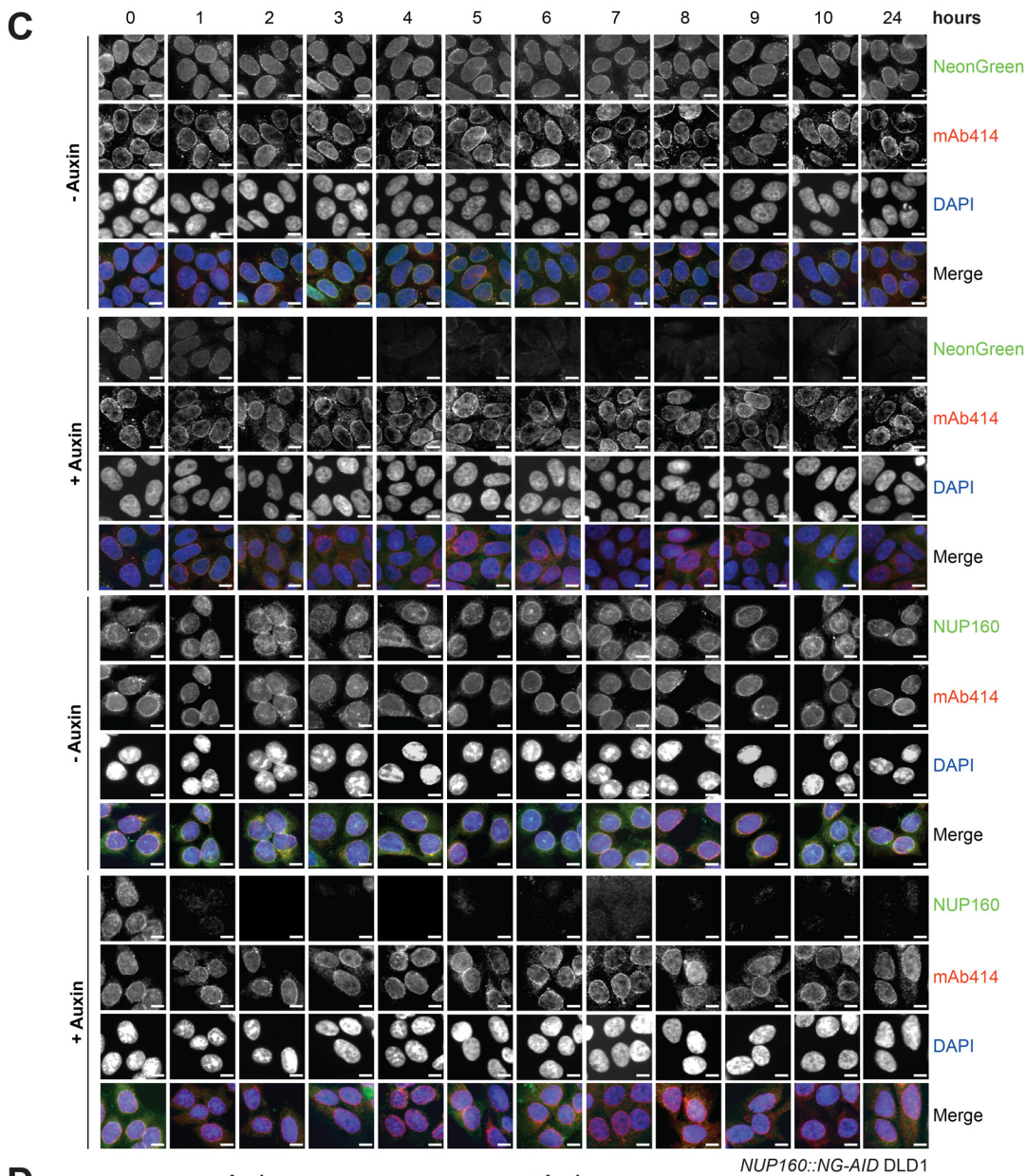
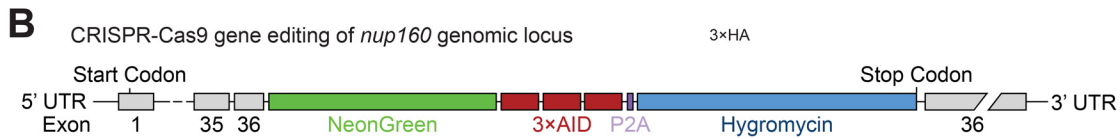
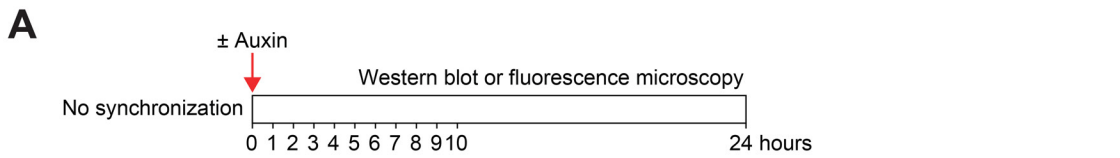


Fig. S67. Validation of auxin-induced NUP160 degradation in *NUP160::NG-AID* DLD1 cells. (A) Experimental timeline. (B) Schematic representation of CRISPR/Cas9-mediated genomic tagging of *nup160* alleles. (C) Time-resolved subcellular localization analysis of NeonGreen (NG)-AID-tagged NUP160 by immunofluorescence microscopy upon auxin treatment. The NG-AID-tagged NUP160 was detected by an anti-NUP160 antibody (green) or NeonGreen fluorescence (green). The mAb414 antibody (red) and DAPI (blue) staining were used as a reference for the nuclear envelope and nucleus, respectively. Scale bars are 10 μm . (D) Time-resolved western blot analysis of NG-AID-tagged NUP160 expression levels upon auxin treatment. The specificity of auxin induced NUP160 depletion was assessed by the indicated antibodies. Asterisks indicate a nonspecific band detected by the anti-NUP160 antibody. Control cells were not treated with auxin.

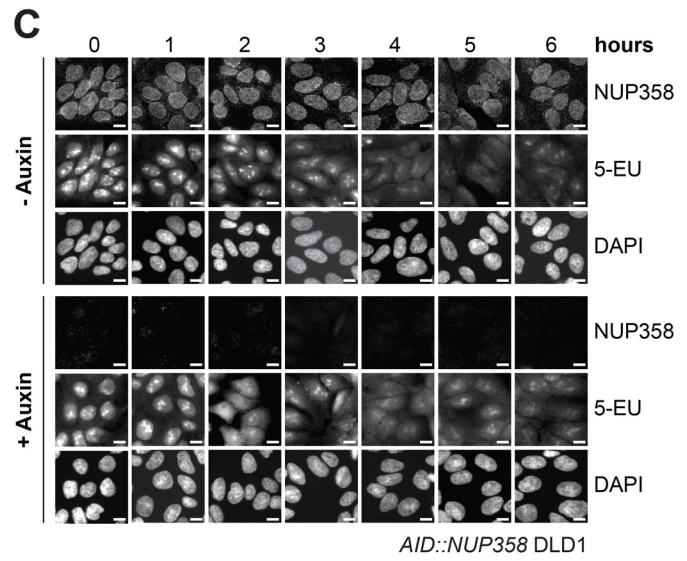
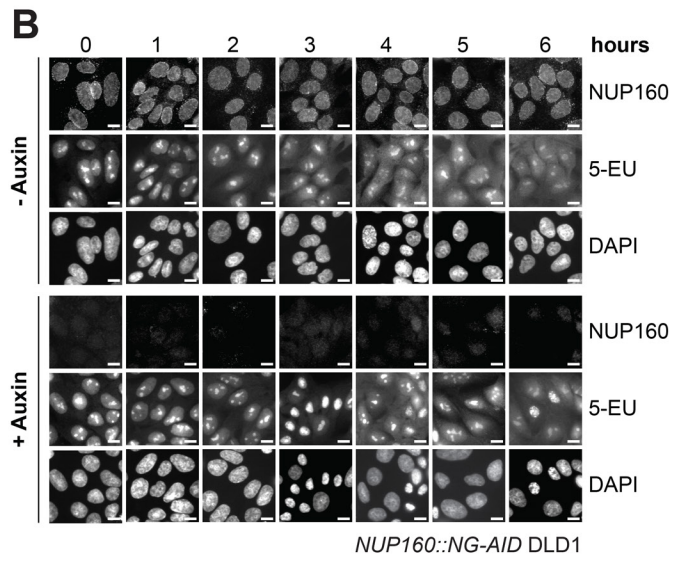
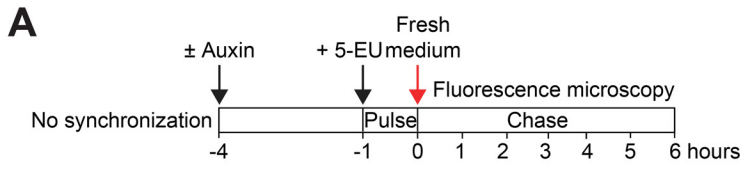


Fig. S68. Time-resolved analysis of nuclear RNA retention in NUP160/NUP358 depleted DLD1 cells. (A) Experimental timeline. (B, C) Time-resolved fluorescence microscopy analysis of RNA nuclear retention in (B) *NUP160::NG-AID* or (C) *AID::NUP358* DLD1 cells upon auxin treatment. Nascent RNA was metabolically pulse-labeled with 5-ethynyl uridine (5-EU) and its subcellular localization determined by Alexa Fluor 594 azide conjugation and fluorescence microscopy at the indicated time points. Scale bars are 10 μm .

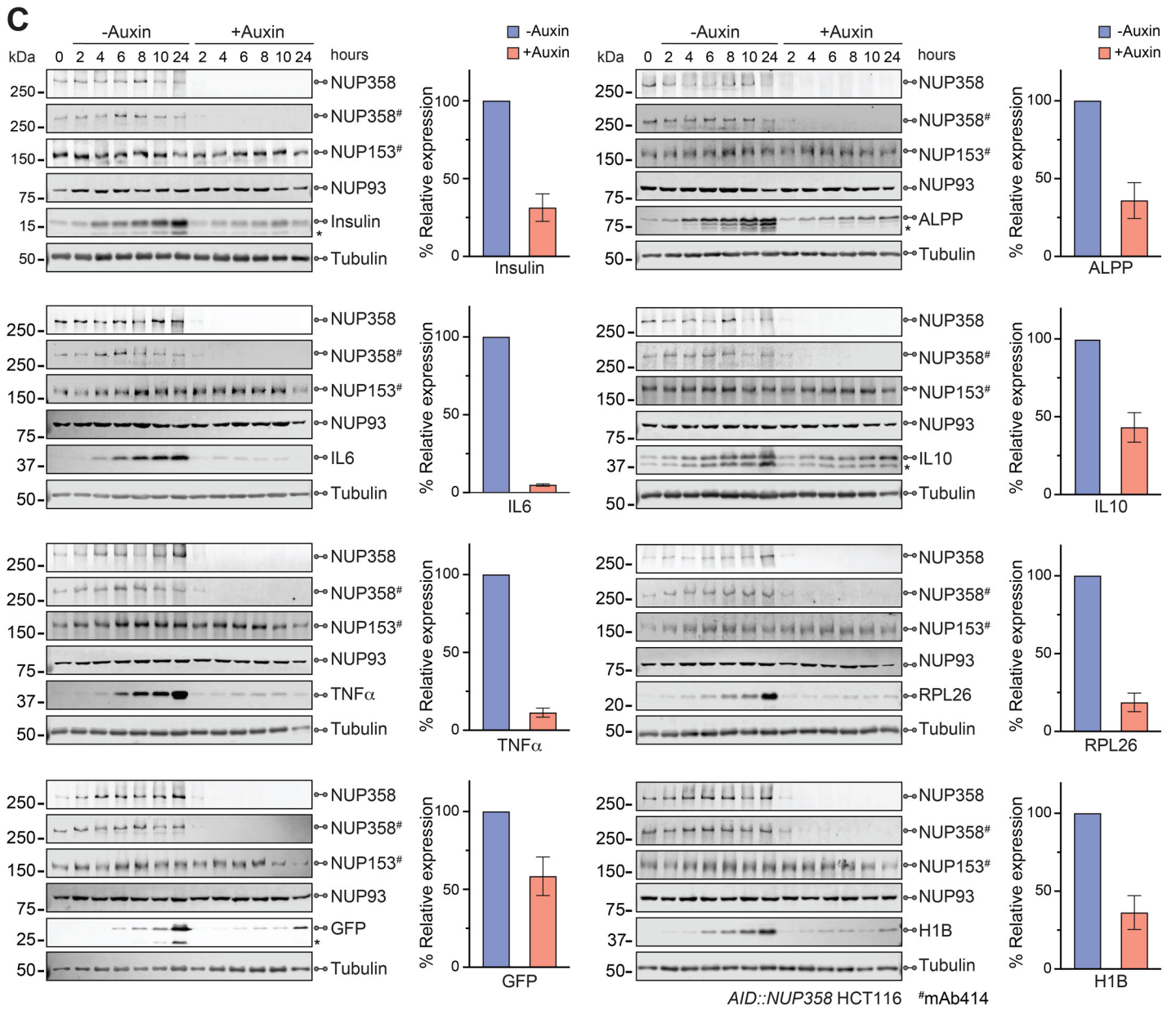
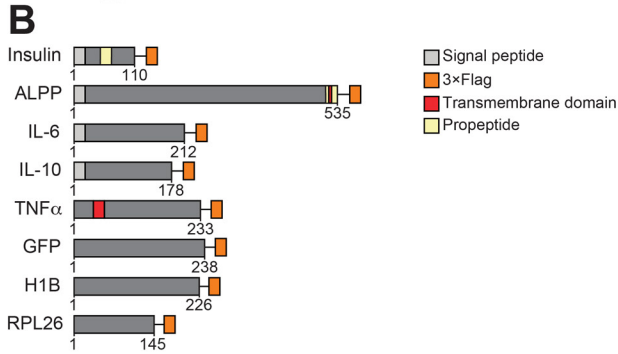
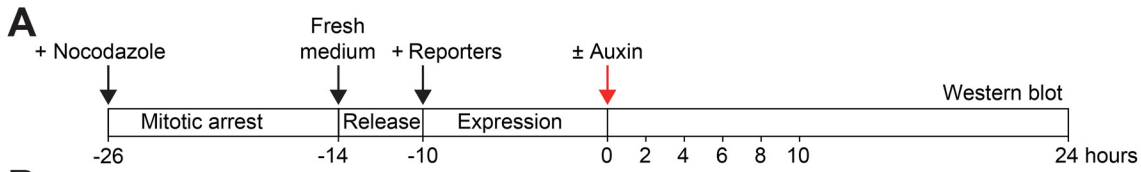


Fig. S69. Depletion of NUP358 reduces reporter protein expression. (A) Experimental timeline. (B) Domain structures of the transfected C-terminally 3×FLAG-tagged reporters. (C) Time-resolved western blot expression analysis of the 3×FLAG-tagged reporter proteins in synchronized *AID::NUP358* HCT116 cells upon auxin-induced NUP358 depletion. Control cells were not treated with auxin. Quantitated reporter expression in auxin-treated cells was normalized to expression in control cells, at the 10-hour timepoint. Experiments were performed in triplicate, and the mean with the associated standard error reported. Asterisks indicate degradation bands detected by the anti-FLAG antibody.

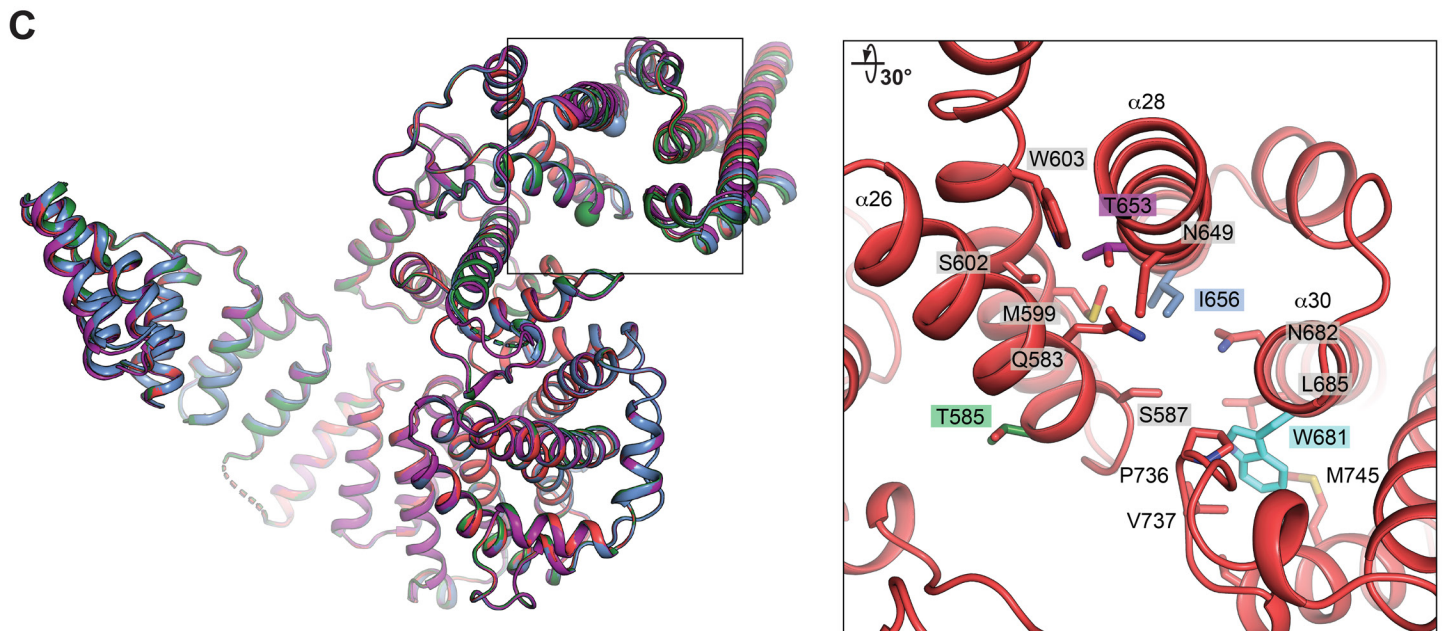
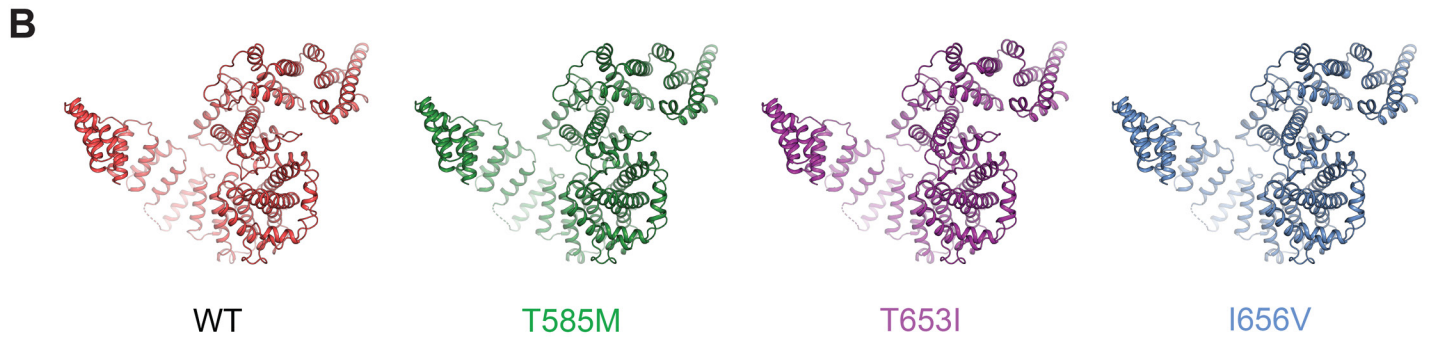
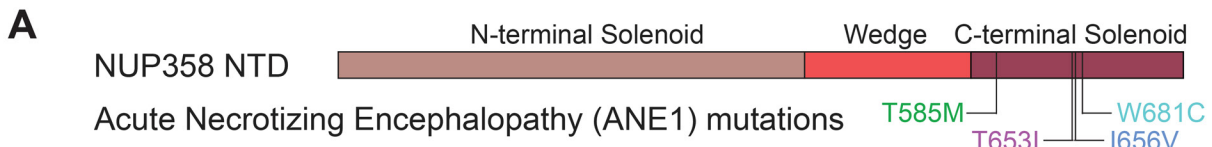


Fig. S70. Structural analysis of NUP358^{NTD} containing ANE1 mutations (A) NUP358^{NTD} domain architecture with location of ANE1 mutations indicated. (B) Structures of wildtype NUP358^{NTD} and three distinct ANE1 mutants (T585M, T653I, or I656V) shown individually and (C) superposed in cartoon representation. A magnified view of the inset region shows the local environment of the four ANE1-associated mutation sites (*right*).

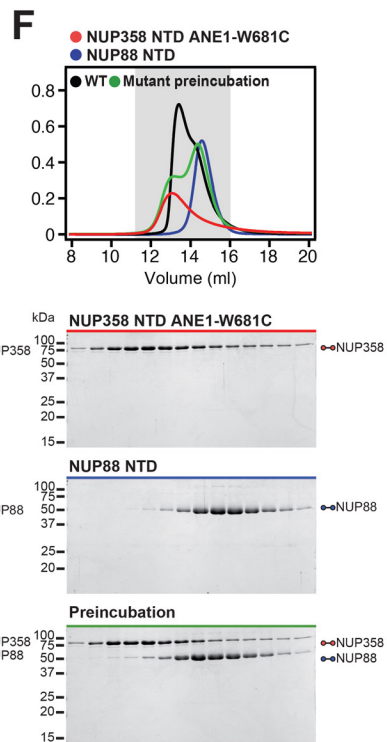
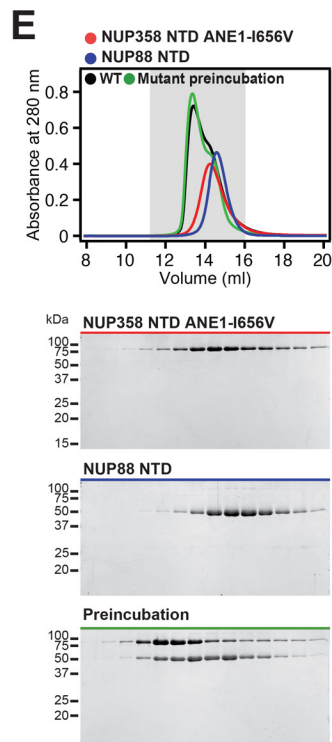
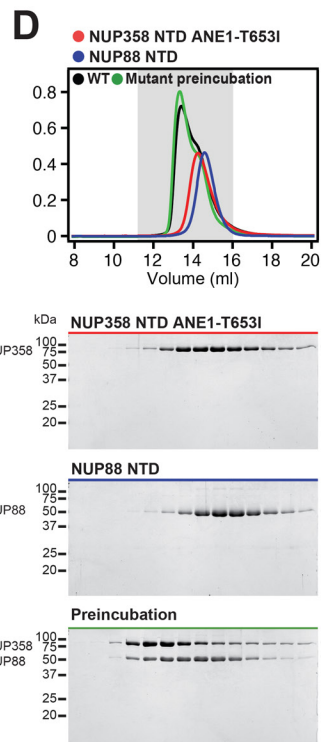
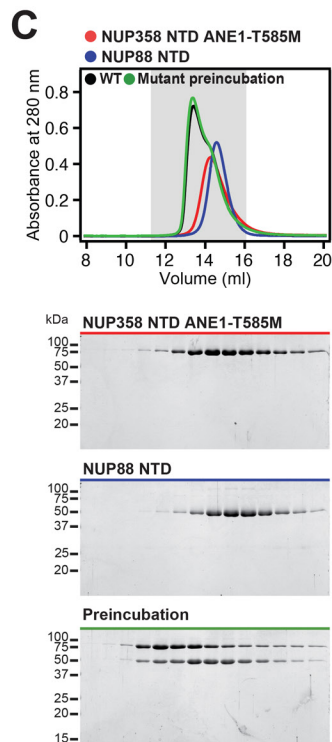
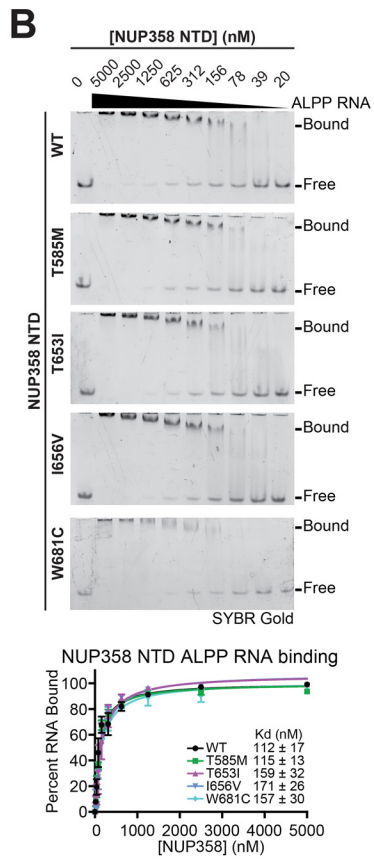
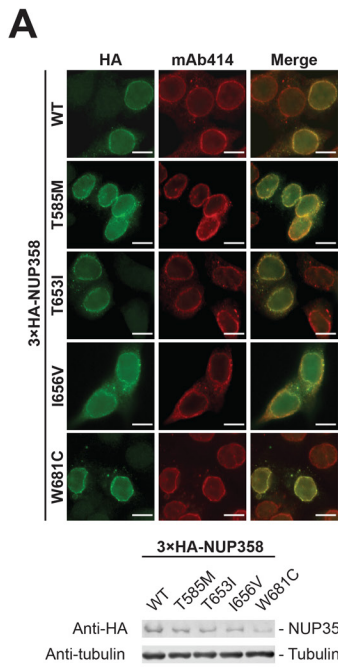


Fig. S71. Characterization of NUP358 ANE1 mutants localization and interaction analysis with NUP88^{NTD} and ALPP^{SSCR} RNA. (A) Subcellular localization analysis by immunofluorescence microscopy of N-terminally 3×HA-tagged NUP358 ANE1 mutants in *AID::NUP358* HCT116 cells. The mAb414 antibody (red) staining was used as a reference for the nuclear envelope. Scale bars are 10 μm. Expression of NUP358 mutants was verified by western blot of whole cell extracts. (B) EMSA titrations of NUP358^{NTD} variants against ALPP^{SSCR} RNA visualized with SYBR Gold stain. Representative titrations of triplicate are shown. Triplicate EMSA experiments are plotted with mean values and standard errors. Apparent dissociation constants (K_D) were estimated by fitting single-site binding models to the data. (C-F) SEC interaction analysis of NUP88^{NTD} with (C) NUP358^{NTD} T585M, (D) NUP358^{NTD} T653I, (E) NUP358^{NTD} I656V, (F) and NUP358^{NTD} W681C. SEC profiles of NUP358^{NTD} variants (red) and NUP88^{NTD} (blue) are shown individually and after their preincubation (green). Preincubation with wildtype NUP358^{NTD} shown in black for reference. SEC profiles were obtained using a Superdex 200 10/300 GL column. Gray boxes indicate fractions resolved on SDS-PAGE gels and visualized by Coomassie brilliant blue staining.

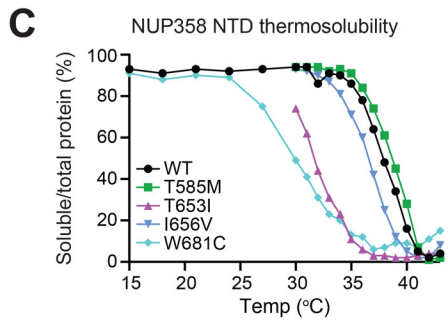
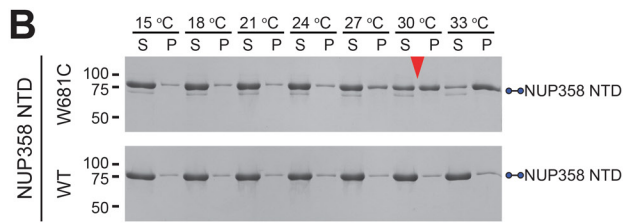
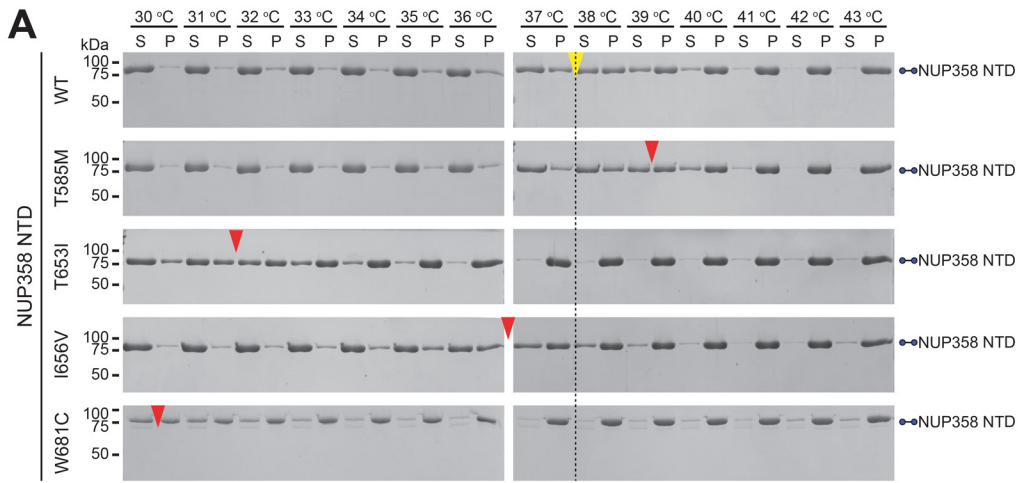


Fig. S72. Thermosolubility assay of NUP358 harboring ANE1 mutants. (A) Wildtype and NUP358^{NTD} mutants associated with ANE1 (T585M, T653I, I656V, and W681C) were incubated for 20 minutes at the indicated temperatures prior to centrifugation. Pelleted (P) and soluble (S) fractions were analyzed by SDS-PAGE and visualized by Coomassie brilliant blue staining. (B) Lower temperature range thermosolubility pelleting assay for highly unstable NUP358^{NTD} W681C and wildtype Nup358^{NTD}. Red arrows indicate 50% solubility temperature for NUP358^{NTD} ANE1 mutants. For reference, a yellow arrow indicates 50% solubility temperature of wildtype NUP358^{NTD}. (C) Quantitation of thermosolubility pelleting assay of wildtype and ANE1 mutant purified NUP358^{NTD}, ratio of soluble over total protein is plotted for each temperature.

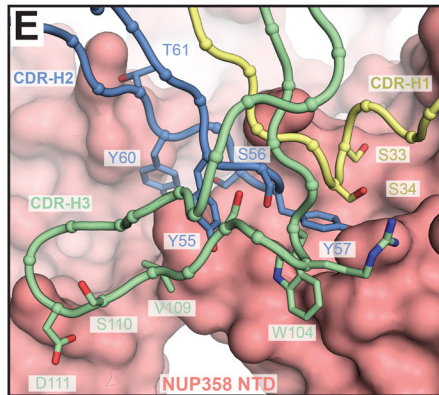
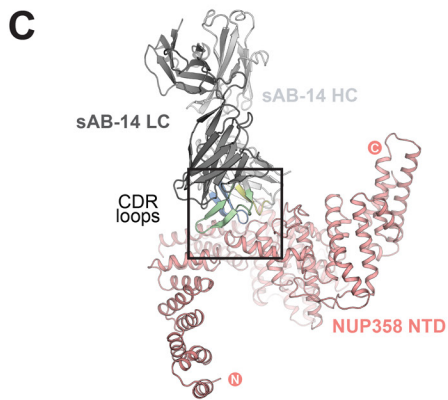
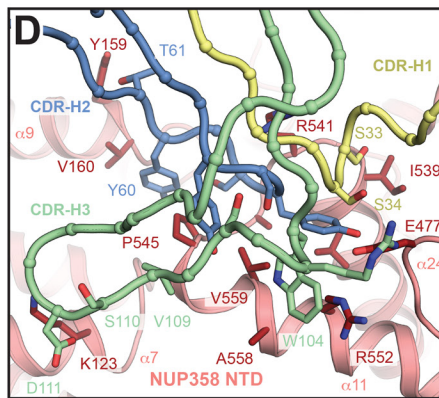
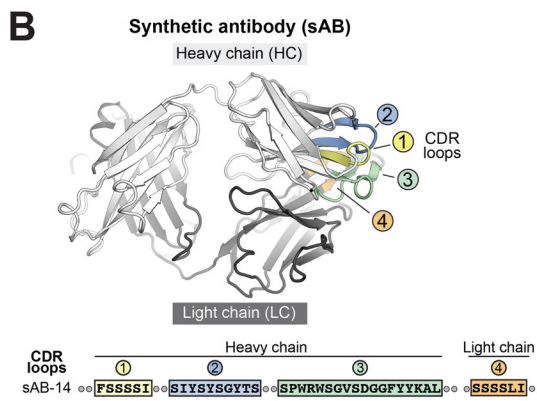
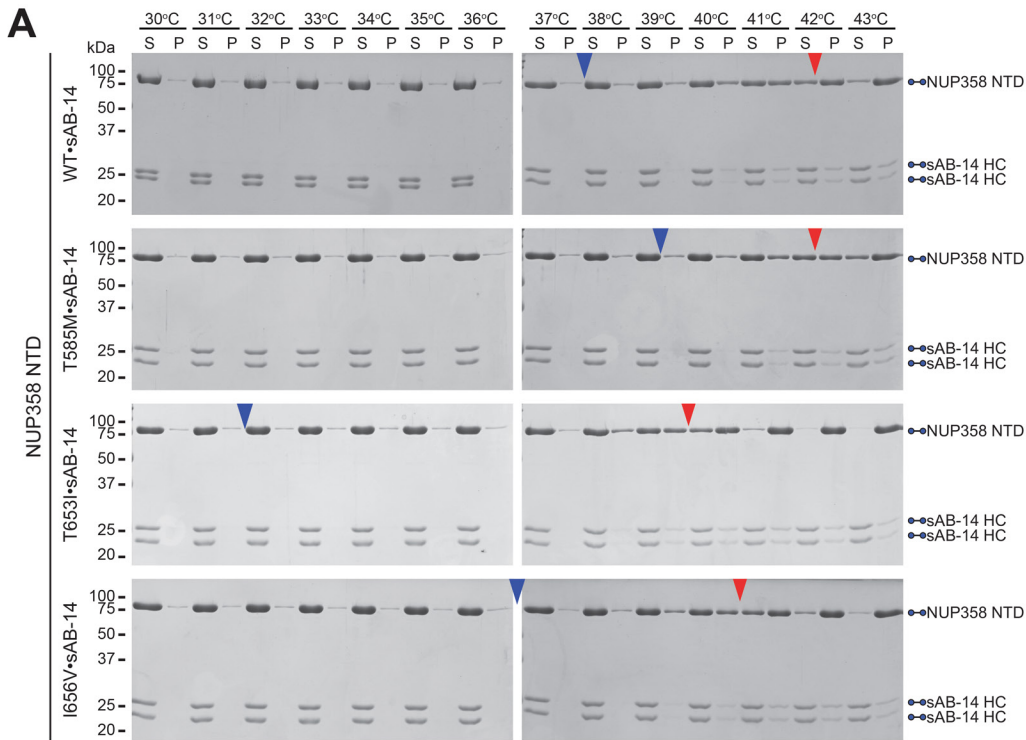


Fig. S73. Thermosolubility of NUP358^{NTD} ANE1 mutations is increased by sAB-14 binding. (A) Thermosolubility assay of NUP358 harboring ANE1 mutants (T585M, T653I, I656V) in the presence of sAB-14. Wildtype NUP358^{NTD} and mutants associated with ANE1 were pre-complexed with sAB-14 and purified by SEC prior to performing the protein thermosolubility pelleting assay. Complexes were incubated at the indicated temperatures for 20 minutes prior to centrifugation. Pelleted (P) and soluble (S) fractions were analyzed by SDS-PAGE and visualized by Coomassie brilliant blue staining. The 50% solubility temperature for proteins in isolation and in presence of sAB-14 are indicated by blue and red arrows, respectively. (B) sAB-14 structure shown in cartoon representation. The sequences of the four complementarity determining region (CDR) loops are provided and their location in the structure indicated. (C) Structure of NUP358^{NTD}•sAB-14 shown in cartoon representation. The sAB-14 binding site is located on the convex surface of NUP358^{NTD} at the interface between the N-terminal solenoid and central wedge domain. The inset indicates the region magnified in panels (D) and (E). (D) Magnified view of the sAB-14-NUP358^{NTD} interface, illustrating the tight interactions formed by the four sAB-14 CDR loops with an exposed hydrophobic patch on the NUP358^{NTD} surface. (E) Magnified view as (D) with NUP358^{NTD} shown in surface representation highlighting the shape complementarity of the sAB-14 CDR loops.

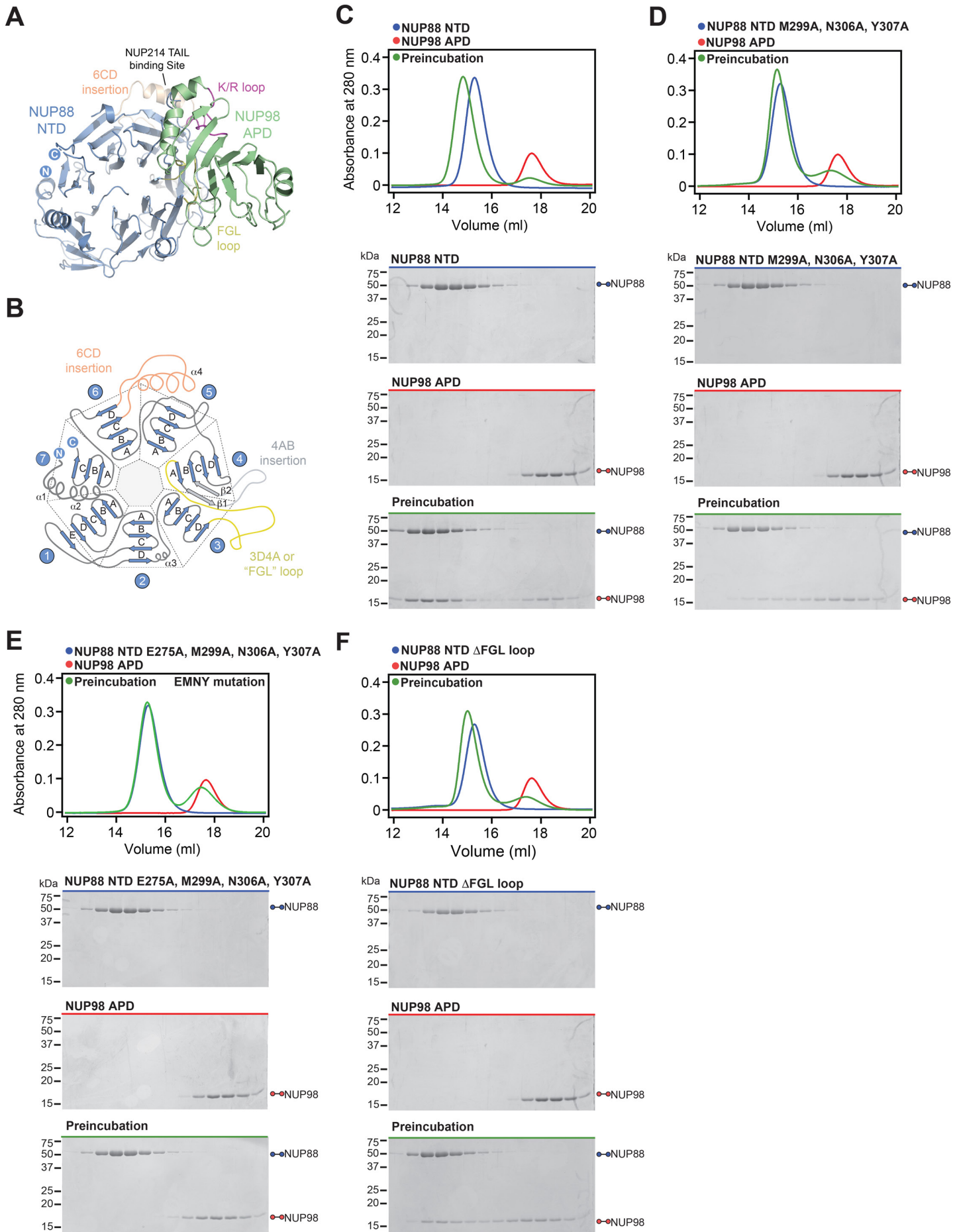
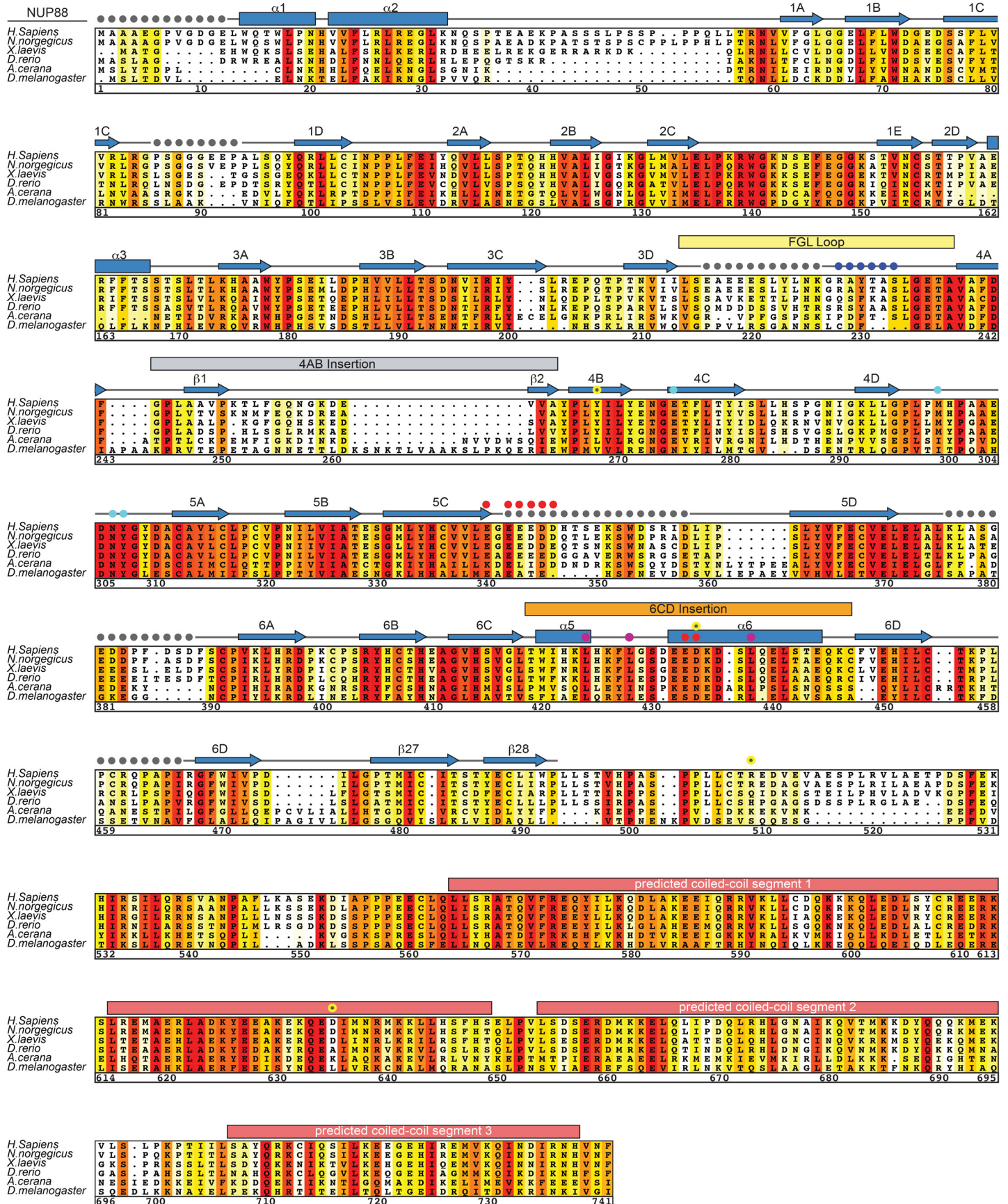


Fig. S74. Mutational analysis of the NUP88^{NTD}-Nup98^{APD} interaction. (A) Cartoon representation of the NUP88^{NTD}•NUP98^{APD} crystal structure. (B) Schematic of the seven-bladed NUP88^{NTD} β -propeller domain, indicating prominent loop insertions. (C-F) SEC interaction analyses of NUP98^{APD} with (C) wildtype NUP88^{NTD}, (D) the NUP88^{NTD} M2999A/N306A/Y307A mutant, (E) the NUP88^{NTD} E275A/M2999A/N306A/Y307A mutant, and (F) the NUP88^{NTD} Δ FGL-loop mutant. SEC profiles of wildtype and mutant NUP88^{NTD} (blue) and NUP98^{APD} (red) are shown individually and after their preincubation (green). SEC profiles were obtained using a Superdex 200 10/300 GL column. Gray boxes indicate fractions resolved on SDS-PAGE gels and visualized by Coomassie brilliant blue staining.



- fetal akinesia deformation sequence (FADS) associated mutation sites
- LLL mutation (NUP214 interaction)
- 5E3D mutation (NUP358 interaction)
- ΔFGL mutation (NUP98 interaction)
- EMNY mutation (NUP98 interaction)
- unresolved

Fig. S75. Multispecies sequence alignment of NUP88. Sequences of NUP88 from six species were aligned and colored according to similarity using the BLOSUM62 matrix from white (less than 40% similarity), through yellow (60% similarity), to red (100% identity). The numbering is according to the *H. sapiens* protein. For NUP88^{NTD}, the secondary structure is indicated above the sequences as rectangles (α -helices), arrows (β -strands), and lines (unstructured regions). Unresolved residues are indicated by gray dots. For NUP88^{CTD}, the secondary structure elements were predicted by JPred4 (146). Residues of sequence variations associated with fetal akinesia deformation sequence disease (93) are indicated by yellow dots. Residues substituted by alanine in the NUP88NTD 5E3D, LLL, and EMNY combination mutants are indicated by red, magenta, and cyan dots, respectively. Residues removed in the Δ FGL loop mutation are indicated by blue dots.

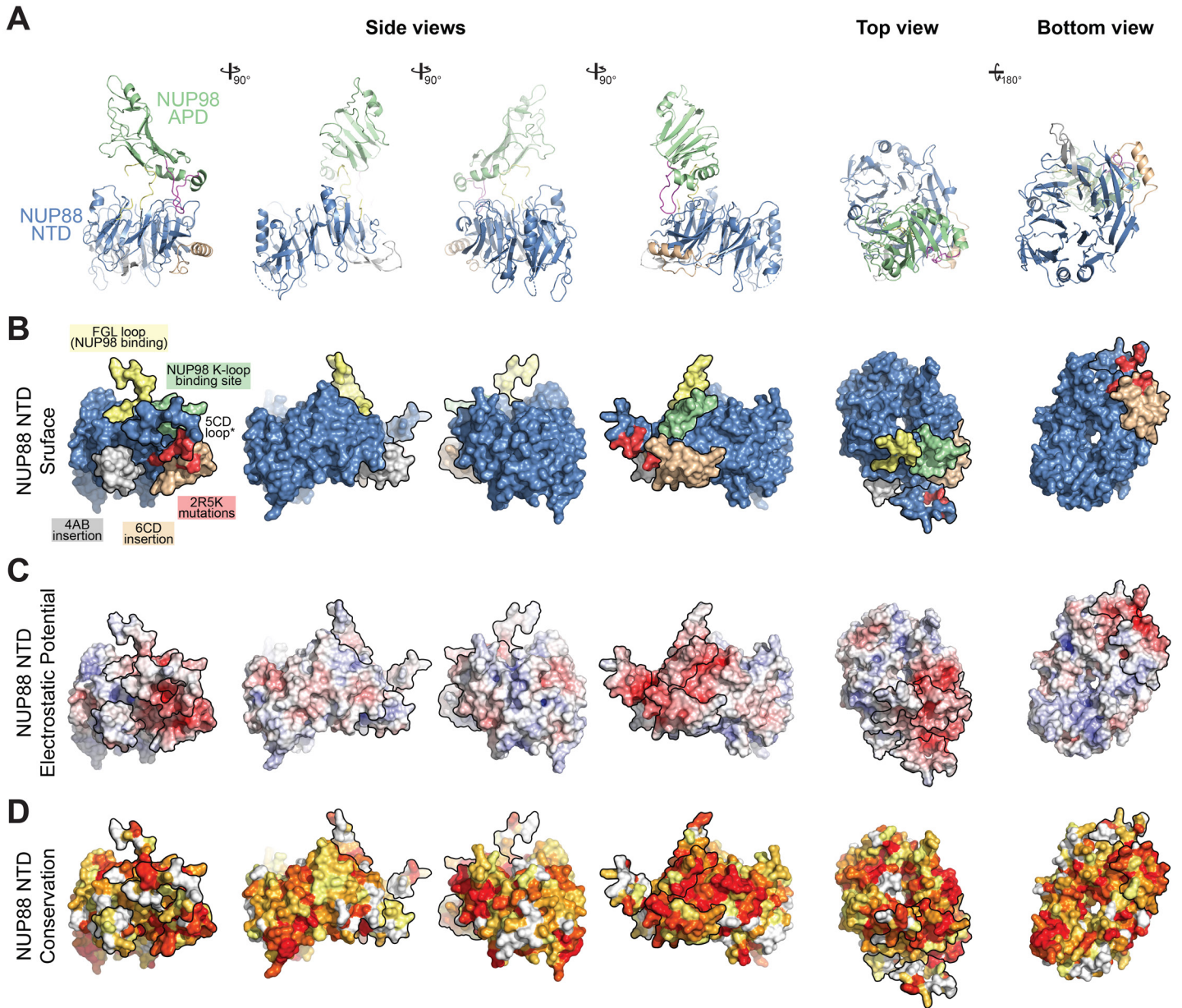


Fig. S76. Surface properties of NUP88^{NTD}. (A) Cartoon representation of the NUP88^{NTD}•NUP98^{APD} crystal structure. (B) Surface representation of NUP88^{NTD} colored as in (A). The binding site of NUP98 (green) and the approximate location of the residues of the 2R5K combination mutant (yellow), which are located in the unresolved 5CD loop and abolish NUP358NTD binding, are indicated. (C) Surface representation colored according to electrostatic potential from red (-10 k_BT/e) to blue (+10 k_BT/e). (D) Surface representation colored according to sequence identity based on the alignment in [fig. S75](#). The NUP98^{APD} binding site is strongly negatively charged.

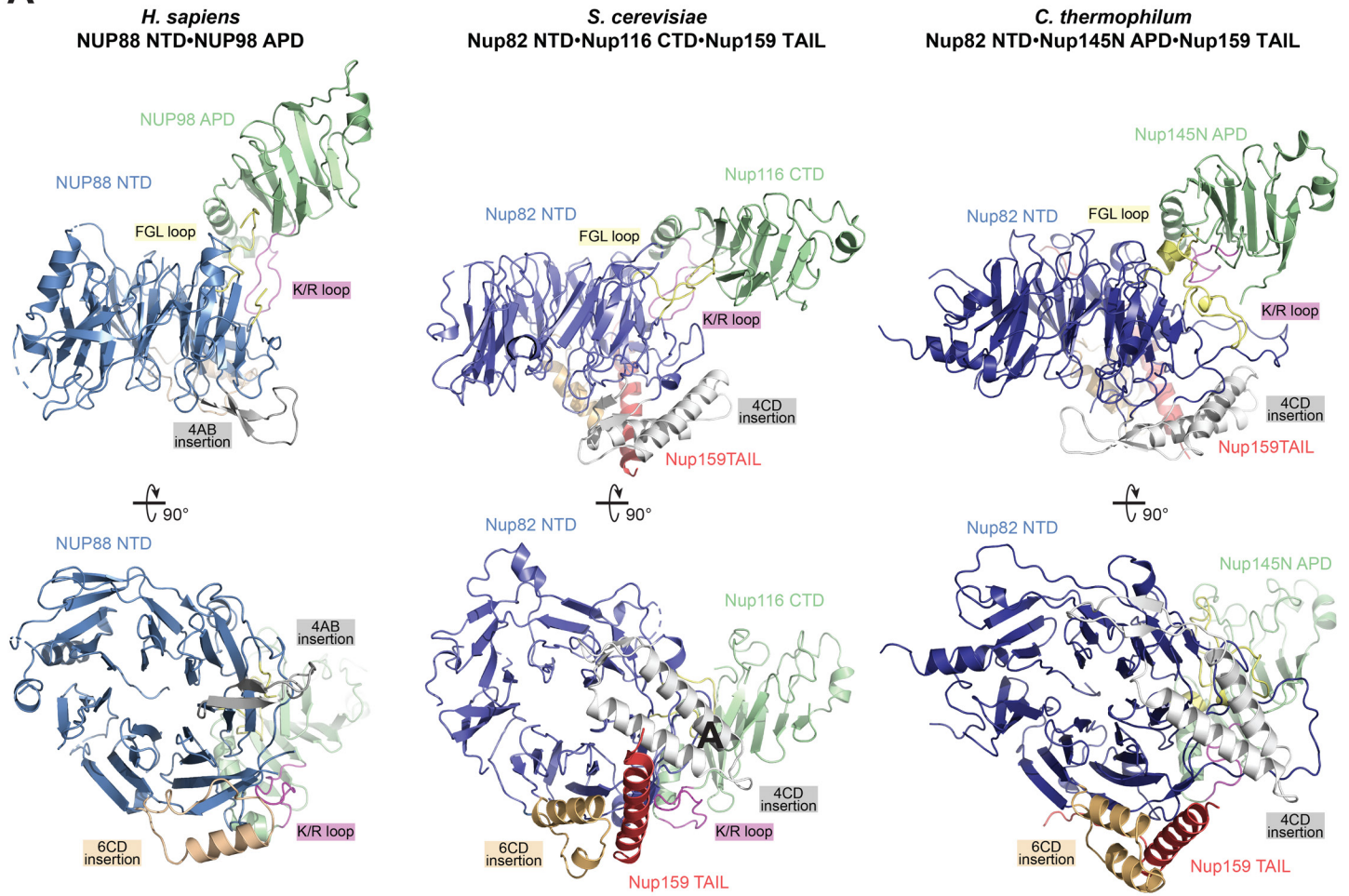
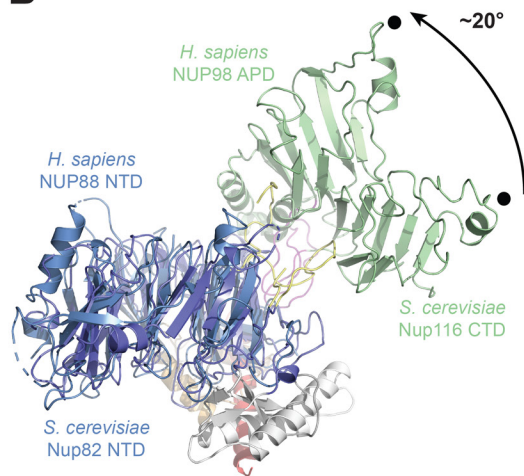
A**B**

Fig. S77. Evolutionary conservation of the NUP88^{NTD}•NUP98^{APD}•NUP214^{TAIL} architecture. (A) Cartoon representations of the NUP88^{NTD}•NUP98^{APD} co-crystal structure and the previously determined crystal structures of *S. cerevisiae* Nup82^{NTD}•Nup116^{CTD}•Nup159^{TAIL} (PDB ID 3PBP) (59) and *C. thermophilum* Nup82^{NTD}•Nup145N^{APD}•Nup159^{TAIL} (PDB ID 5CWW) (11), illustrating the evolutionary conservation of the NUP88/Nup82 FGL, 6CD, and 4AB/4CD loops and the NUP98/Nup116/Nup145N K/R loop (*top*). 90°-rotated views of all three complexes illustrating the location of the NUP88/Nup82^{NTD} 6CD, and 4AB/4CD loop insertions that form the evolutionarily conserved binding site for NUP214/Nup159^{TAIL} (*bottom*). (D) Superposition of *H. sapiens* and *S. cerevisiae* structures indicating the ~20° rotation of NUP98^{APD}/Nup116^{CTD}.

NUP214(ΔFG)

Sequence alignment for NUP214(ΔFG) residues 470-525. Species: H.sapiens, M.musculus, X.laueis, O.latipes, C.intestinalis, C.elegans, A.mellifera, D.melanogaster.

Sequence alignment for NUP214(ΔFG) residues 526-576. Species: H.sapiens, M.musculus, X.laueis, O.latipes, C.intestinalis, C.elegans, A.mellifera, D.melanogaster.

Sequence alignment for NUP214(ΔFG) residues 577-627. Species: H.sapiens, M.musculus, X.laueis, O.latipes, C.intestinalis, C.elegans, A.mellifera, D.melanogaster.

Sequence alignment for NUP214(ΔFG) residues 628-683. Species: H.sapiens, M.musculus, X.laueis, O.latipes, C.intestinalis, C.elegans, A.mellifera, D.melanogaster.

Sequence alignment for NUP214(ΔFG) residues 684-738. Species: H.sapiens, M.musculus, X.laueis, O.latipes, C.intestinalis, C.elegans, A.mellifera, D.melanogaster.

Sequence alignment for NUP214(ΔFG) residues 739-797. Species: H.sapiens, M.musculus, X.laueis, O.latipes, C.intestinalis, C.elegans, A.mellifera, D.melanogaster. Includes predicted coiled-coil segment 1.

Sequence alignment for NUP214(ΔFG) residues 798-851. Species: H.sapiens, M.musculus, X.laueis, O.latipes, C.intestinalis, C.elegans, A.mellifera, D.melanogaster. Includes predicted coiled-coil segment 2.

Sequence alignment for NUP214(ΔFG) residues 852-910. Species: H.sapiens, M.musculus, X.laueis, O.latipes, C.intestinalis, C.elegans, A.mellifera, D.melanogaster. Includes predicted coiled-coil segment 3.

Sequence alignment for NUP214(ΔFG) residues 911-965. Species: H.sapiens, M.musculus, X.laueis, O.latipes, C.intestinalis, C.elegans, A.mellifera, D.melanogaster. Includes predicted alpha-helix regions.

Fig. S78. Multispecies sequence alignment of NUP214. Sequences of NUP214 from eight species were aligned and colored according to similarity using the BLOSUM62 matrix from white (less than 40% similarity), through yellow (60% similarity), to red (100% identity). The numbering is according to the *H. sapiens* protein. For NUP214^{NTD}, the secondary structure is indicated above the sequences as rectangles (α -helices, magenta), arrows (β -strands, magenta), and lines (unstructured regions, gray) and was derived from the previously reported crystal structure (PDB ID 2OIT) (54). The secondary structure elements of the structurally uncharacterized C-terminal coiled-coil region is indicated as rectangles (α -helices, blue) and was determined with JPred4 (146). The C-terminal ~1,100-residue FG-repeat region was omitted.

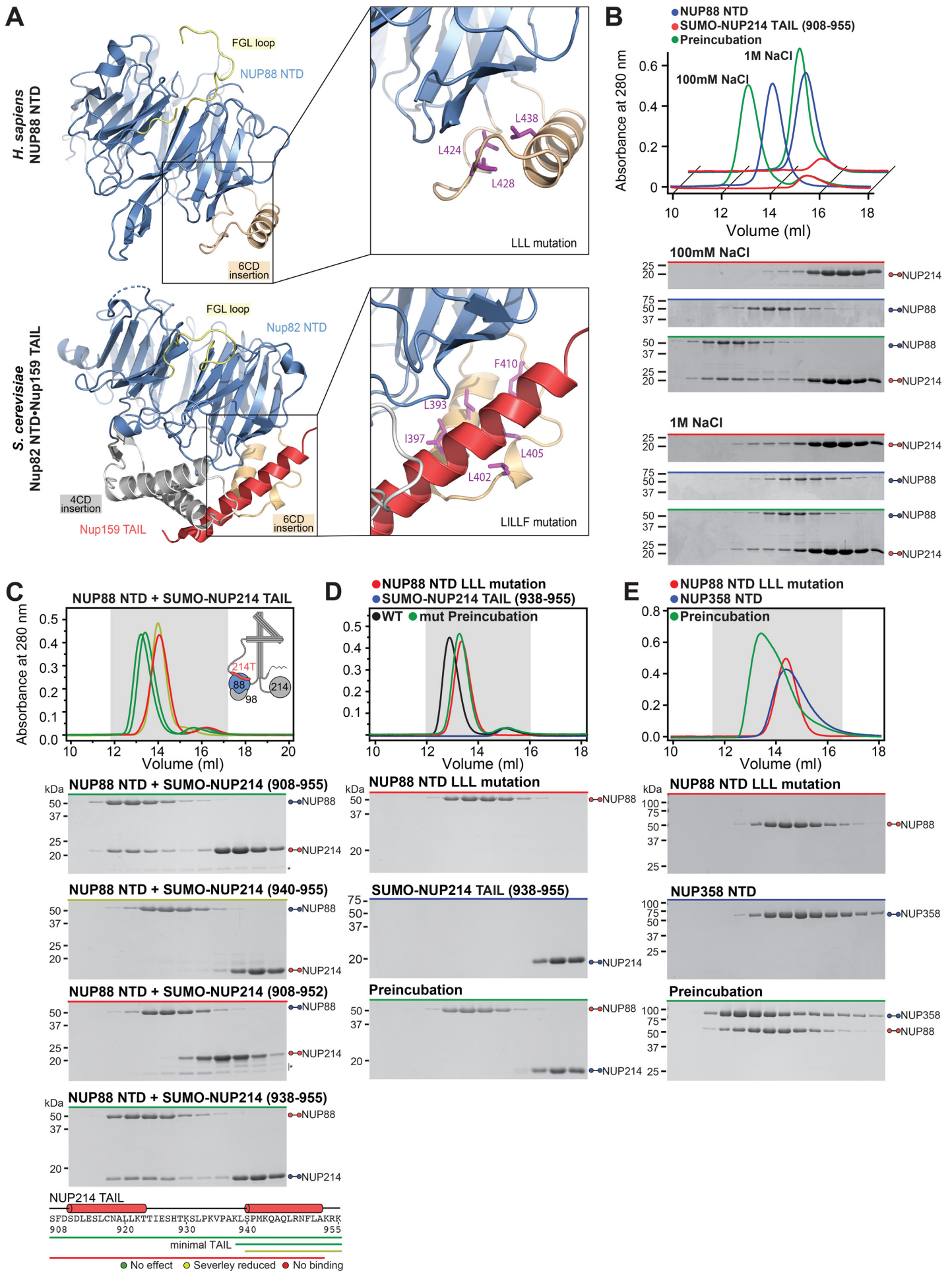


Fig. S79. Evolutionary conservation of NUP214 TAIL binding site on NUP88^{NTD}. (A) Cartoon representation of *H. sapiens* NUP88^{NTD}•NUP98^{APD} and *S. cerevisiae* Nup82^{NTD}•Nup159^{TAIL}•Nup116^{CTD} (PDB ID 3PBP) (59), colored according to Fig. 6H. The insets indicate the location of the Nup82^{NTD}•Nup159^{TAIL} interface and the corresponding region in NUP88^{NTD} that are magnified on the right. The five scNup82^{NTD} residues of the previously identified LILLF (L393A, I397A, L402A, L405A, and F410A) combination mutant, located in the 6CD loop (59), and the corresponding three residues (L424, L428, and L438) of NUP88^{NTD} are shown in ball-and-stick representation (purple). For clarity, NUP98^{APD} Nup116^{CTD} have been omitted. (B) SEC interaction analysis of NUP88^{NTD} with SUMO-tagged NUP214^{TAIL} in buffers containing 100 mM or 1 M NaCl, establishing the salt-stable nature of the interaction. (C) SEC interaction analysis of NUP88^{NTD} with the indicated SUMO-tagged NUP214^{TAIL} truncations, identifying a minimal NUP214^{TAIL} fragment (minimal TAIL; residues 938-955), which is sufficient for NUP88^{NTD} binding. Summary of truncation mapping of minimal NUP214^{TAIL} fragment binding NUP88^{NTD} (*bottom*). (D) SEC interaction analyses of SUMO-tagged NUP214^{minimal TAIL} with wildtype NUP88^{NTD} and the NUP88^{NTD} LLL (L424A, L428A, and L438A) combination mutant. The NUP88^{NTD} LLL mutation abolishes the NUP214^{minimal TAIL} interaction, identifying the NUP214^{minimal TAIL} binding site on the NUP88^{NTD} surface and suggesting a binding mode that is evolutionarily conserved from yeast to human. (E) SEC interaction analysis of the NUP88^{NTD} LLL combination mutant with NUP358^{NTD}, demonstrating that the NUP88^{NTD} LLL mutation does not affect the NUP358^{NTD} interaction. SEC profiles were obtained using a Superdex 200 10/300 GL column. Gray boxes indicate fractions resolved on SDS-PAGE gels and visualized by Coomassie brilliant blue staining.

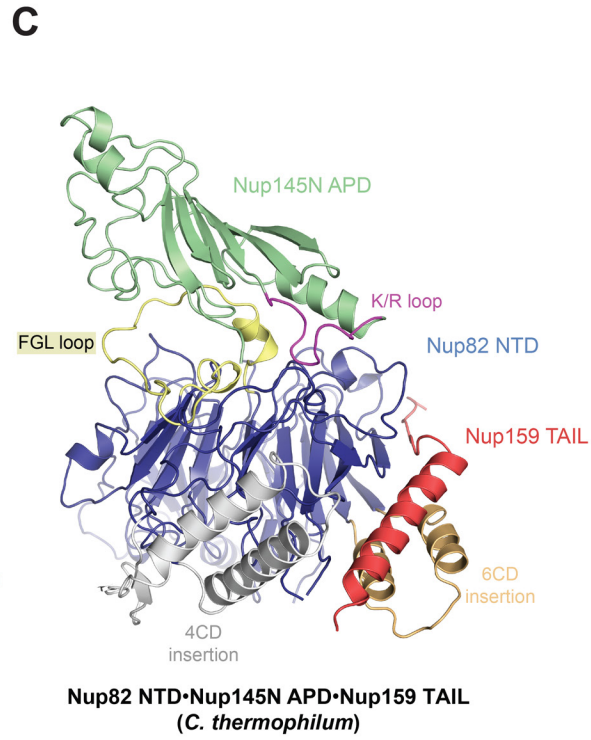
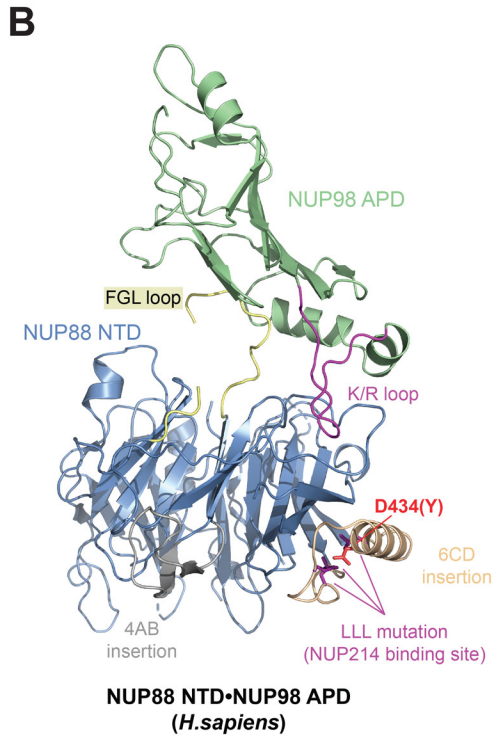
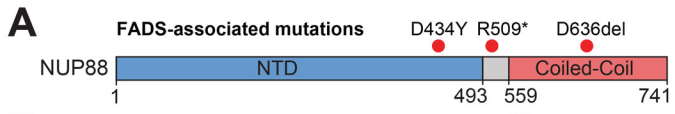
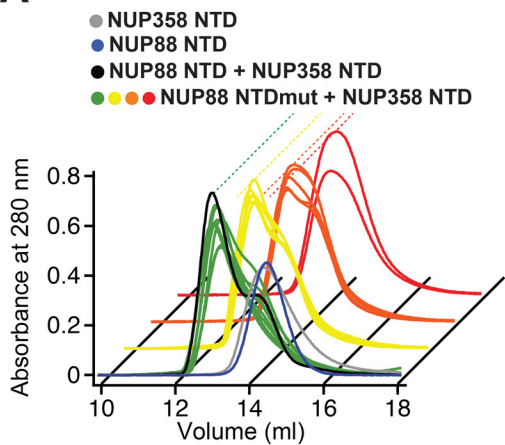


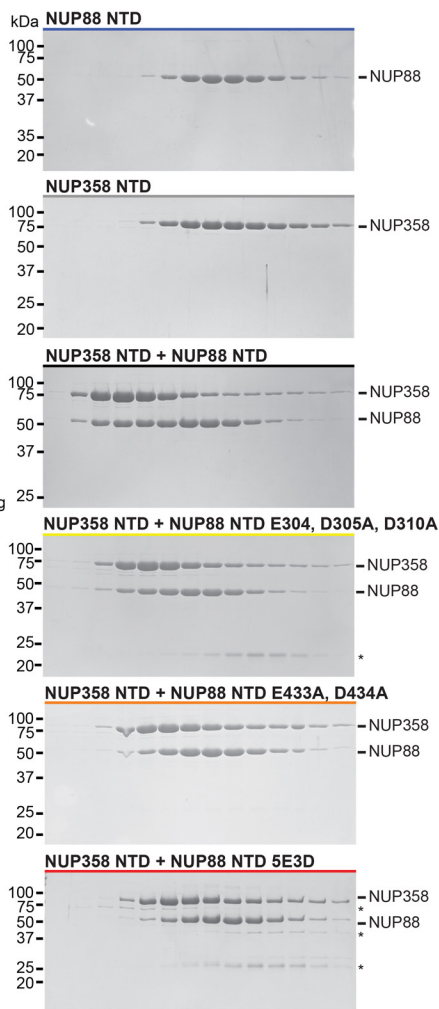
Fig. S80. FADS-associated NUP88 D434Y mutation is located at the NUP214^{TAIL} binding site. (A) NUP88 domain architecture indicating locations of the three mutations associated with fetal akinesia deformation sequence (FADS) (93). The D434Y mutant is located in the 6CD loop insertion of NUP88^{NTD}, directly adjacent to the identified NUP214^{TAIL} binding site (L424, L428, and L438). The nonsense mutation R509* truncates the C-terminal coiled-coil domain, whereas the single residue deletion of D636 falls within the predicted coiled-coil domain. (B) Co-crystal structure of NUP88^{NTD}•NUP98^{APD} is shown in cartoon representation and colored according to Fig 9, indicating the location of D434 and the adjacent L424, L428 and L438 of the LLL mutation of NUP88^{NTD}. (C) Crystal structure of *C. thermophilum* Nup82^{NTD}•Nup145N^{APD}•Nup159^{TAIL} (PDB ID 5CWW) (11) shown in cartoon representation, illustrating the involvement of the 6CD loop of Nup159^{NTD} in anchoring Nup159^{TAIL}.

A



| Location | NUP88 mutation | NUP358 binding |
|----------------------------|--|----------------|
| L1 | D10A, E12A | ● |
| α2-1A | E29A, E38A, E40A | ● |
| 1BC/1CD | E74A, E75A, E91A, E92A | ● |
| 3D4A | E216A, E218A, E219A, E220A | ● |
| 3D4A/4AB insertion | E236A, E272A, E275A | ● |
| 4D5A | E304A, D305A, D310A | ● |
| 5BC/5D6A | E329A, E370A, E372A | ● |
| 5CD | E340A, E342A, E343A, E344A, D345A, D346A | ● |
| 5CD | E340A, E342A, E343A | ● |
| 5CD | E343A, E344A | ● |
| 5CD | E344A, D345, D346A | ● |
| 5CD | E350A, D354A, D358A | ● |
| 5D6A | E381A, D382A, D383A | ● |
| 6CD insertion-A | D431A, E432A, E433A, D434A | ● |
| 6CD insertion-B | D431A, E432A | ● |
| 6CD insertion-C | E433A, D434A | ● |
| 6CD insertion-D | D433A | ● |
| 6CD insertion-E | D434A | ● |
| 6CD insertion-F | D434Y | ● |
| 6CD insertion-G | D436A, E440A, E444A | ● |
| 5CD + 6CD insertion | E340A, E342A, E343A, E344A, D345A, D346A, D431A, E432A, E433A, D434A | ● |
| 5CD + 6CD insertion (5E3D) | E340A, E342A, E343A, E344A, D345A, D346A, E433A, D434A | ● |

Effect on Binding: ● No effect ● Mild ● Moderate ● Severe



B

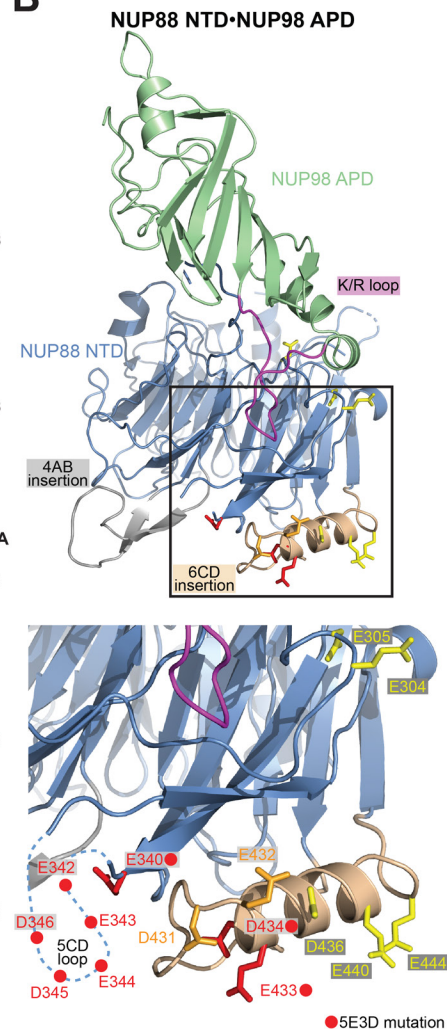


Fig. S81. Identification of the NUP88^{NTD} 5E3D mutation interrupting NUP358^{NTD} binding. (A) SEC interaction analyses of the indicated NUP88^{NTD} mutants with NUP358^{NTD}. Stacked preincubation curves are shown grouped by effect category; no effect (green, front), mild effect (yellow), moderate effect (orange), and severe effect (red) on NUP358^{NTD} binding. SDS-PAGE gels of representative preincubation peak fractions are shown. **(B)** Structure of NUP88^{NTD}•NUP98^{APD} shown in cartoon representation. Residues that affect NUP358^{NTD} binding are shown in ball-and-stick representation. The inset marks the location of the mutation that affects NUP358^{NTD} binding. A dashed line indicates the approximate location of the unresolved acidic 5CD loop. Red circles indicate alanine substitutions in the 5E3D mutant.

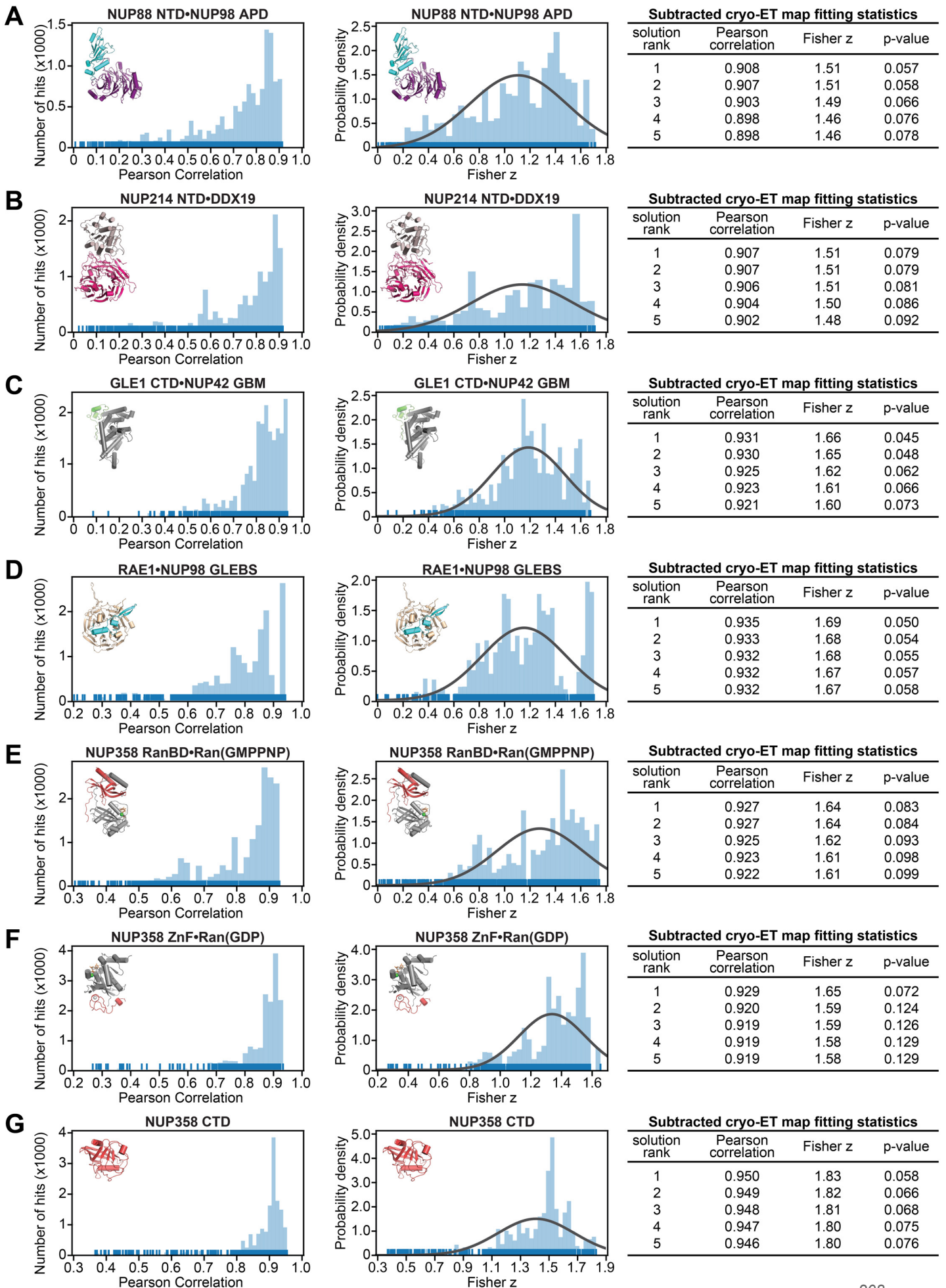


Fig. S82. Quantitative docking searches for CF subunits. Resolution-matched densities simulated from the crystal structures of **(A)** NUP88^{NTD}•NUP98^{APD}, **(B)** NUP214^{NTD}•DDX19 (PDB ID 3FMO) (55), **(C)** GLE1^{CTD}•NUP42^{GBM} (PDB ID 6B4F) (63), **(D)** RAE1•NUP98^{GLEBS} (PDB ID 3MMY) (57), **(E)** NUP358^{RanBD-II}•Ran, **(F)** NUP358^{ZnF3}•Ran, and **(G)** NUP358^{CTD} (PDB ID 4I9Y) (129) were quantitatively docked into the ~12 Å sub-tomogram averaged cryo-ET map of the intact human NPC (EMD-14322) (46) from which cryo-ET density corresponding to all placed nucleoporins was subtracted. Rug plots (blue) and histograms (light blue) of Pearson correlation scores (*left*) and derived Fisher z scores fit with a normalized Gaussian curve (black) from a global search with 1 million random initial placements (*middle*) are shown. A tabular summary of the solutions fitting statistics, along with one-tailed p-values calculated from the Fisher z score distribution, is shown (*right*). No docking solution segregated to high confidence.

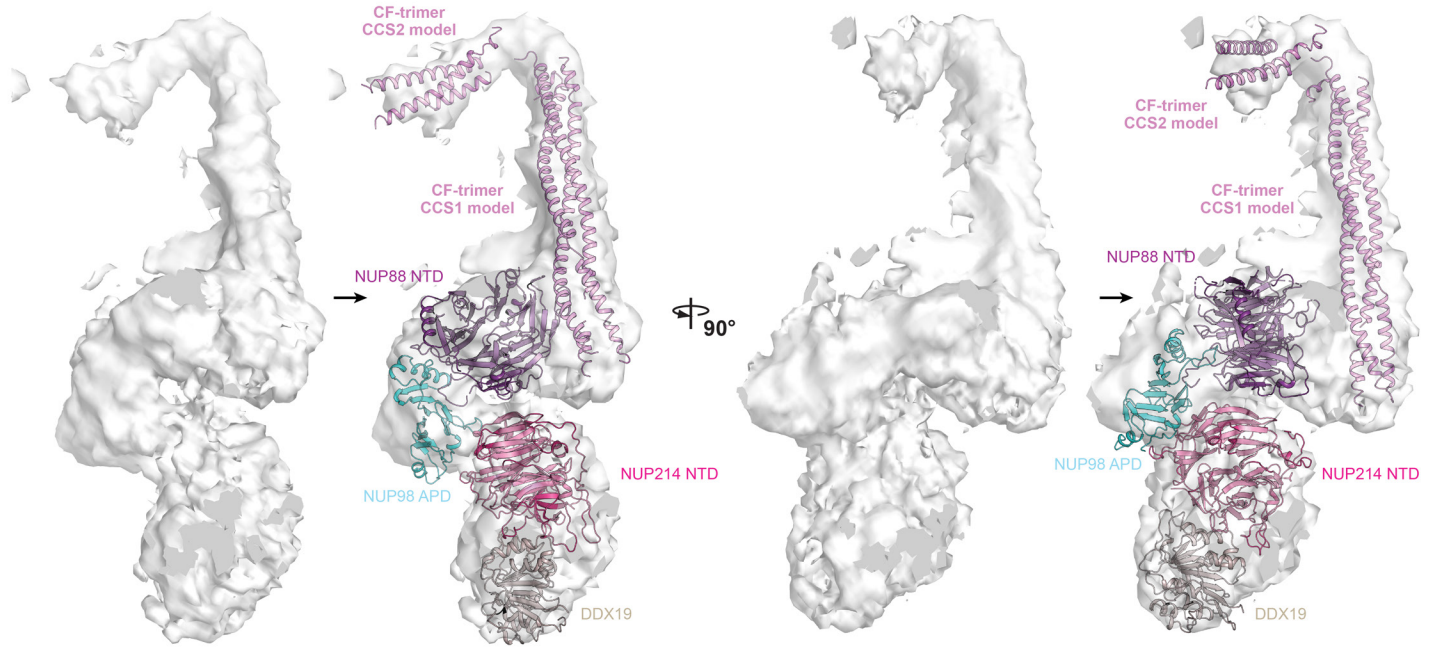
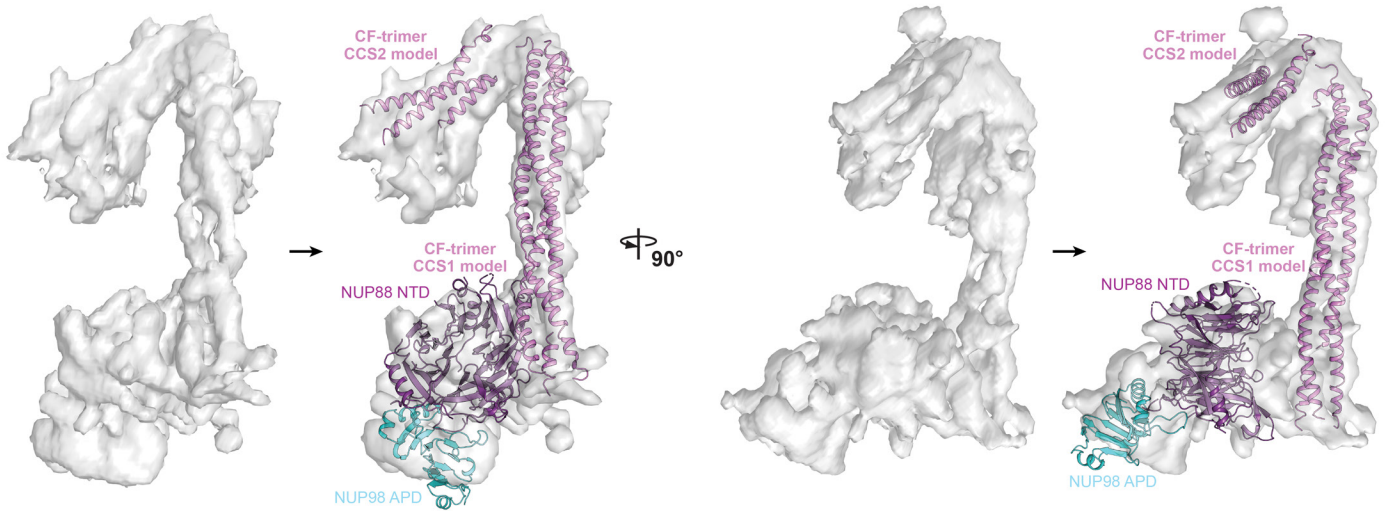
A***H. sapiens* cryo-ET CF-complex density****B*****X. laevis* cryo-EM map CF-complex density**

Fig. S83. Docking and modeling of the *H. sapiens* and *X. laevis* CFNC complex. The CFNC complex was modeled by manually docking and rigid body refining structures against **(A)** the ~12 Å cryo-ET map of the intact human NPC (EMD-14322) (46) and **(B)** a ~8 Å region of the anisotropic composite single particle cryo-EM map of the *X. laevis* cytoplasmic outer ring protomer (EMD-0909) (45). In lieu of an experimental structure of the CFNC-hub coiled-coils, poly-alanine models of the CFNC-hub coiled-coil segments CCS1 and CCS2 (pink) were derived from the *X. laevis* NUP54•NUP58•NUP62 (PDB ID 5C3L) (10) and *C. thermophilum* Nup49•Nup57•Nsp1 (PDB ID 5CWS) (11) complexes and fit into the tube-like densities. NUP88^{NTD}•NUP98^{APD} (purple and cyan) was placed in a disk-like density at the base of the long CFNC-hub^{CCS1} structure. The dumbbell-shaped density assigned to NUP214^{NTD}•DDX19 (bright pink and umber) in the human ~12 Å cryo-ET map was not present in the ~8 Å region of the anisotropic composite single particle cryo-EM map of the *X. laevis* cytoplasmic outer ring protomer. Cryo-EM and cryo-ET densities were carved out from larger maps for illustrative purposes and rendered as gray isosurface. Structures and models are shown as cartoons.

Cytoplasmic cluster II density

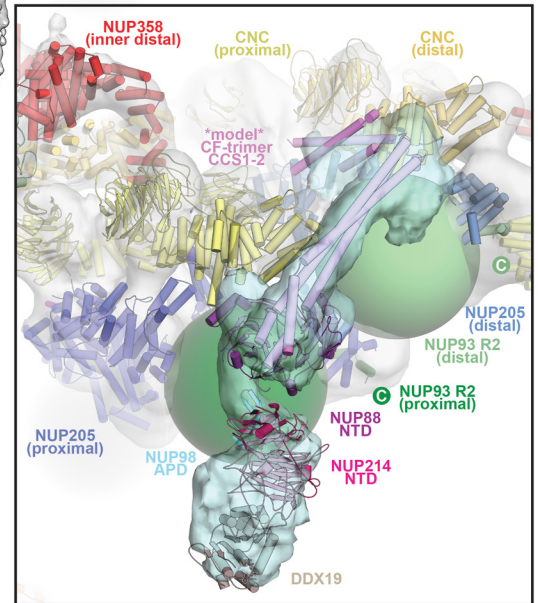
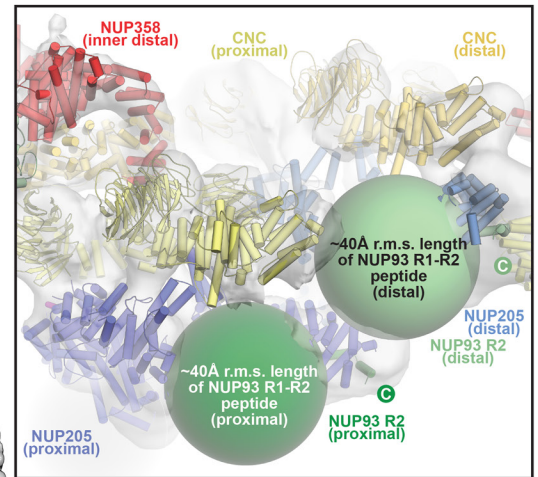
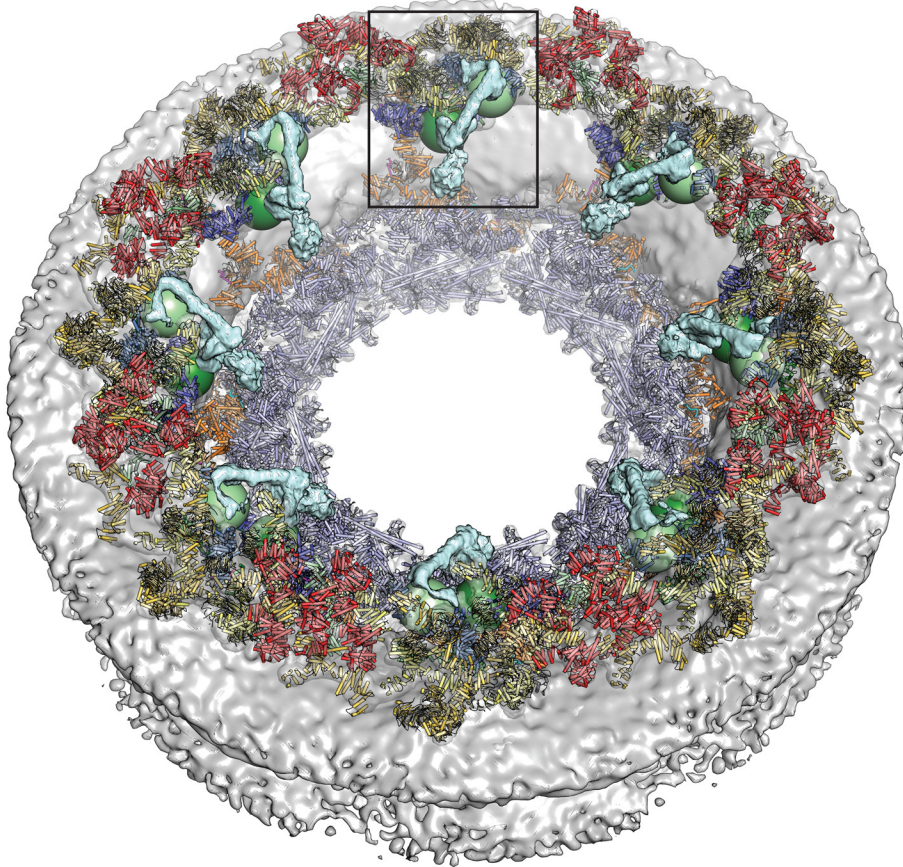


Fig. S84. NUP93^{R1-R2} peptide can span the distance between NUP205 and the CFNC-hub binding sites. Composite structure of the human NPC shown as cartoon. The nuclear envelope (gray) and unassigned density cluster II, corresponding to the CFNC (cyan), are shown as isosurfaces (*left*). Root mean square (r.m.s.) end-to-end length estimates for the NUP93^{R1-R2} peptide that links the NUP93^{R2} region that binds to NUP205 and the NUP93^{R1} region that binds to the CFNC-hub, are shown as spheres (proximal, green; distal, pale green). Magnified view of the region in the inset box shown in the absence (*right top*) and presence (*right bottom*) of the unassigned density cluster II and the CFNC-hub model docked in it. The distal NUP93^{R1} region is expected in the vicinity of CFNC-hub coiled-coil segments CCS1, CCS2, and likely of the unresolved CCS3.

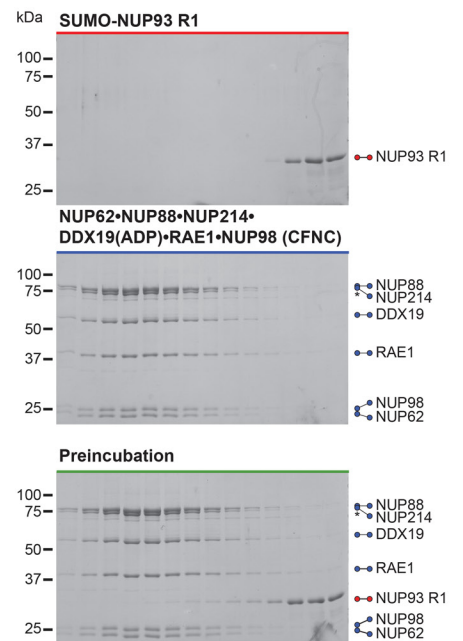
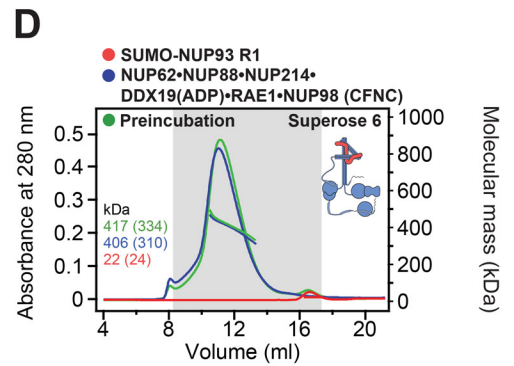
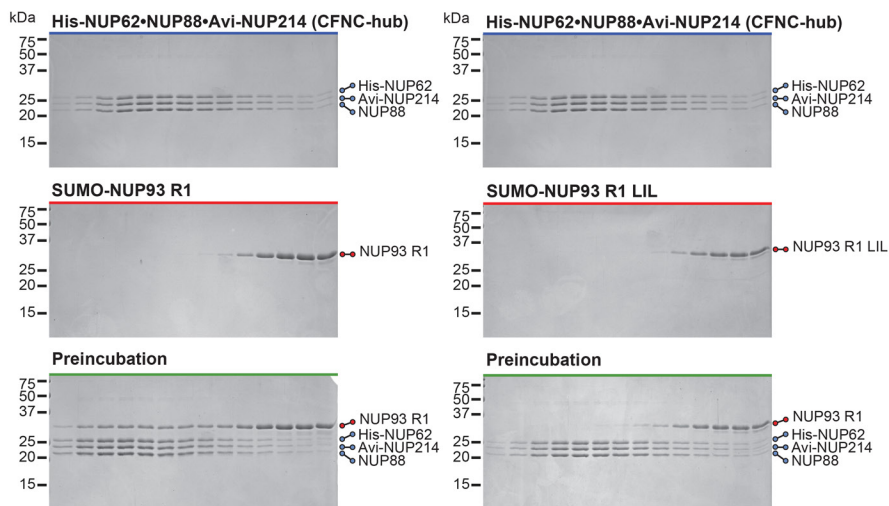
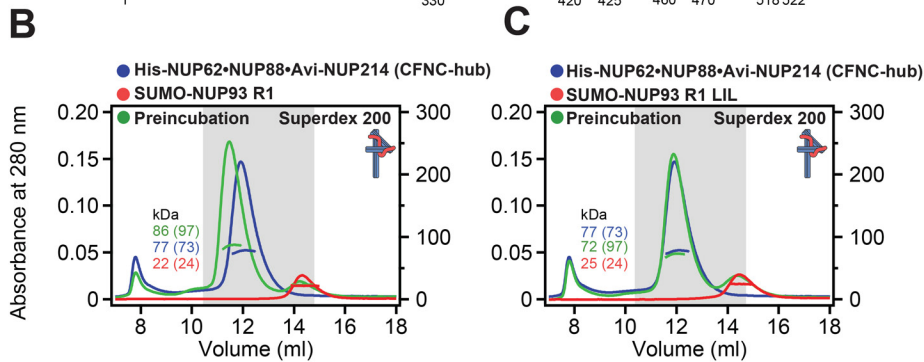
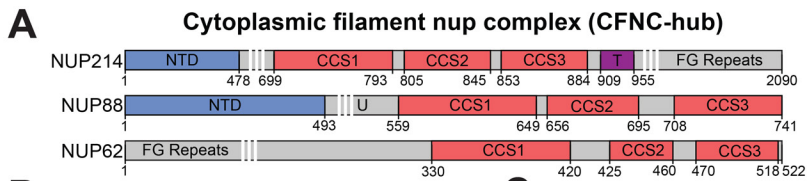


Fig. S85. NUP93 anchors the human CFNC to the NPC. (A) Domain architectures of NUP214, NUP88, and NUP62 showing the predicted coiled-coil segments, CCS1, CCS2, and CSCS3, which form the CFNC-hub. **(B)** SEC-MALS interaction analysis of the human CFNC-hub with SUMO-NUP93^{R1}, demonstrating the formation of a stable stoichiometric complex. **(C)** SEC-MALS interaction analyses of the human CFNC-hub with the NUP93^{R1} LIL combination mutant, which we identify in the accompanying manuscript to abolish the interaction with the NUP54•NUP58•NUP62 channel nup hetero-trimer (CNT) (42), showing that the NUP93^{R1} LIL mutant also abolishes the interaction with the human CFNC-hub. To resolve the three stoichiometric protein bands of the human CFNC-hub by SDS-PAGE, NUP62^{CCS1-3} and NUP214^{CCS1-3} were tagged with His₆-PreScission- and Avi-tag sequence overhangs, respectively. SEC interactions with the untagged proteins yielded identical results. **(D)** SEC-MALS interaction analysis of NUP93^{R1} with human hetero-hexameric CFNC. SEC-MALS profiles of nups and nup complexes are shown individually (blue and red) and after their preincubation (green). SEC profiles were obtained using a Superdex 200 10/300 GL or a Superose 6 10/300 GL column, as indicated. Measured molecular masses are indicated, with the respective theoretical masses shown in parentheses. Inset schematics display tested protein samples colored to match the corresponding chromatogram trace. Gray boxes indicate fractions resolved on SDS-PAGE gels and visualized by Coomassie brilliant blue staining.

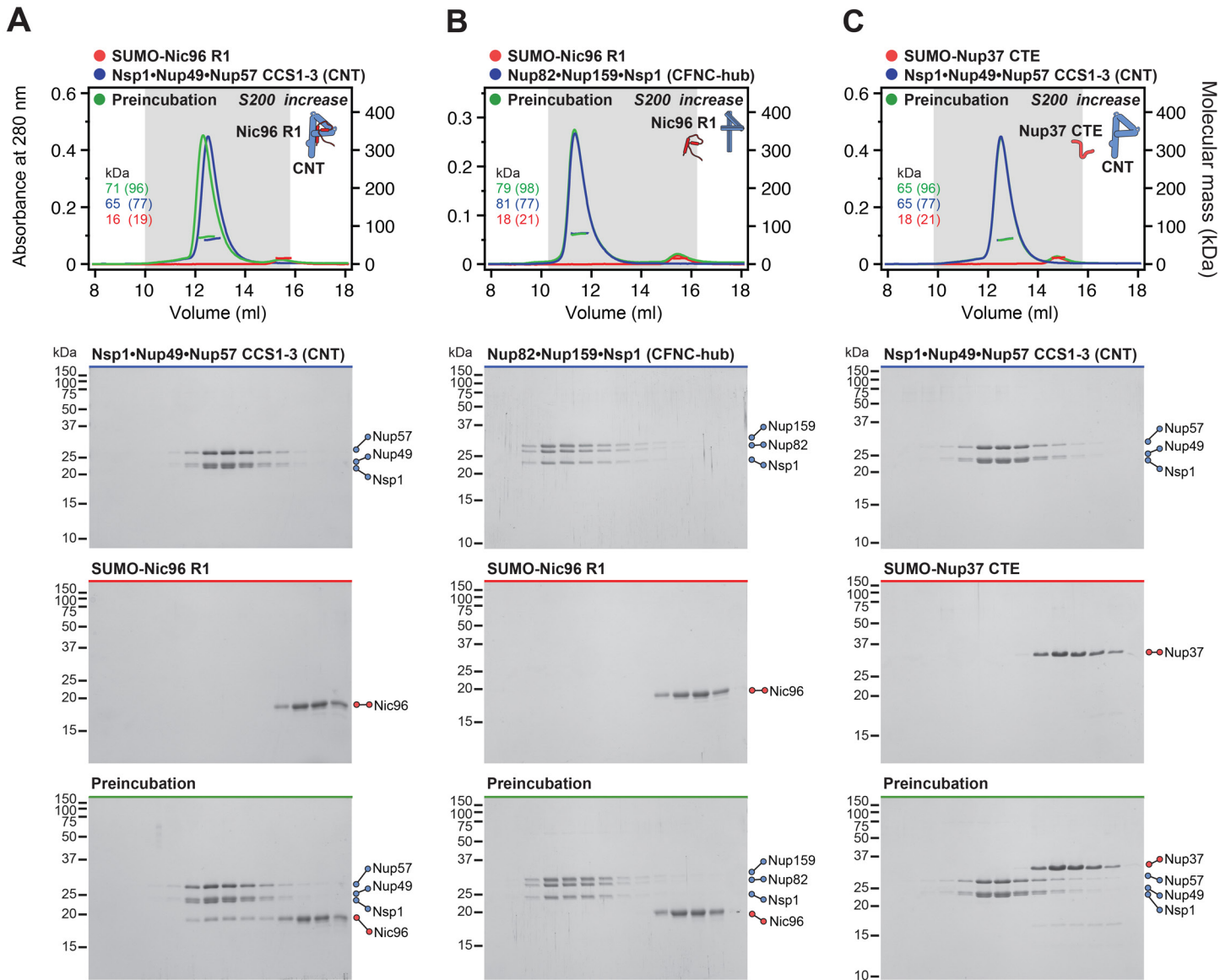


Fig. S86. Nic96 and Nup37 assembly sensors possess binding specificity for CNT and CFNC-hub. SEC-MALS interaction analyses of (A) SUMO-Nic96^{R1} with CNT, (B) SUMO-Nic96^{R1} with CFNC-hub, and (C) SUMO-Nup37^{CTE} with CNT. Whereas Nup37^{CTE} exclusively binds the CFNC-hub, Nic96^{R1} exclusively binds to the CNT, and not vice versa. SEC profiles of nups or nup complexes are shown individually (blue and red) and after their preincubation (green). SEC profiles were obtained using a Superdex 200 Increase 10/300 GL column. Measured molecular masses are indicated, with the respective theoretical masses shown in parentheses. Inset schematics display tested protein samples shaded to match corresponding chromatogram trace. Gray boxes indicate fractions resolved on SDS-PAGE gels and visualized by Coomassie brilliant blue staining.

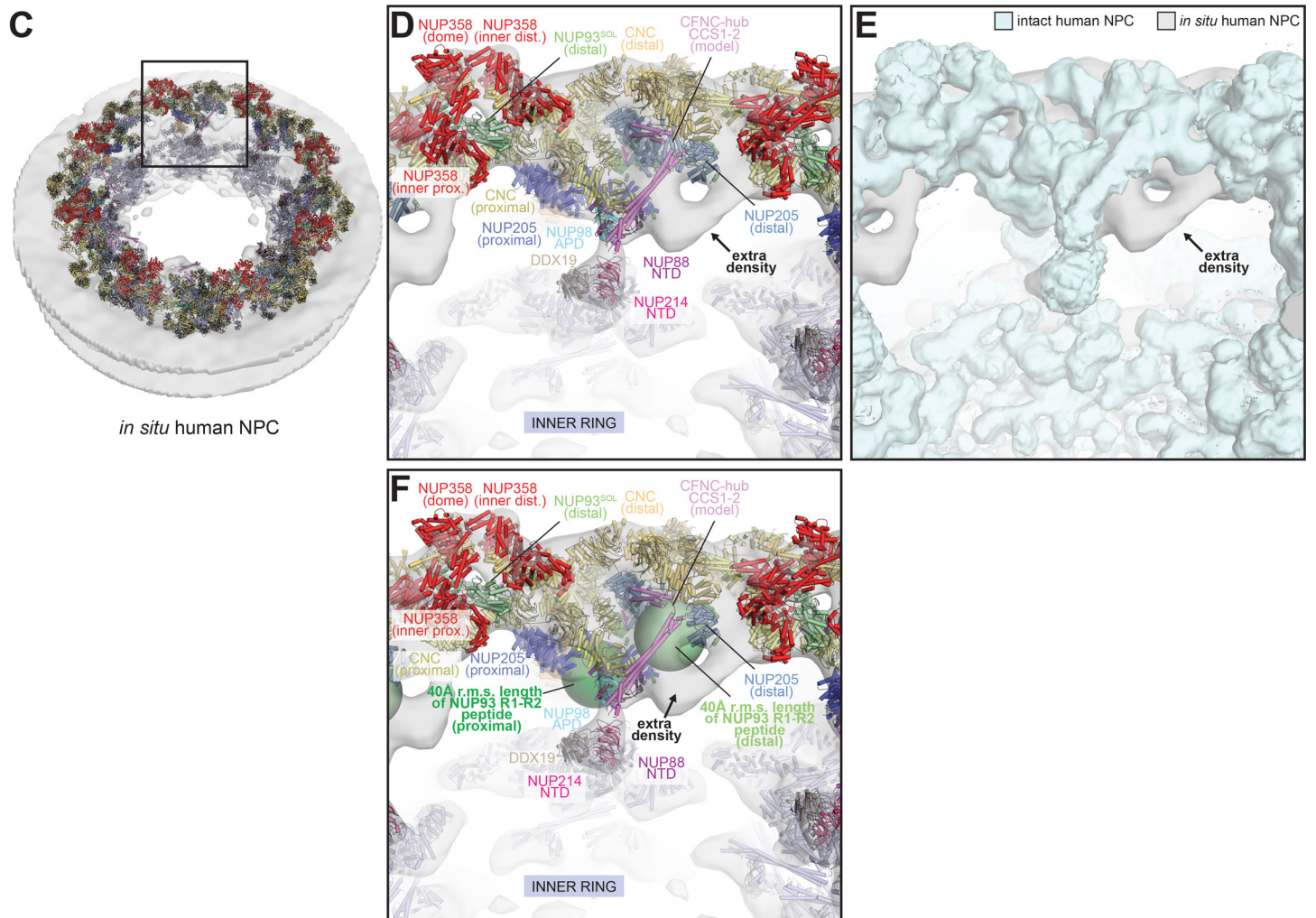
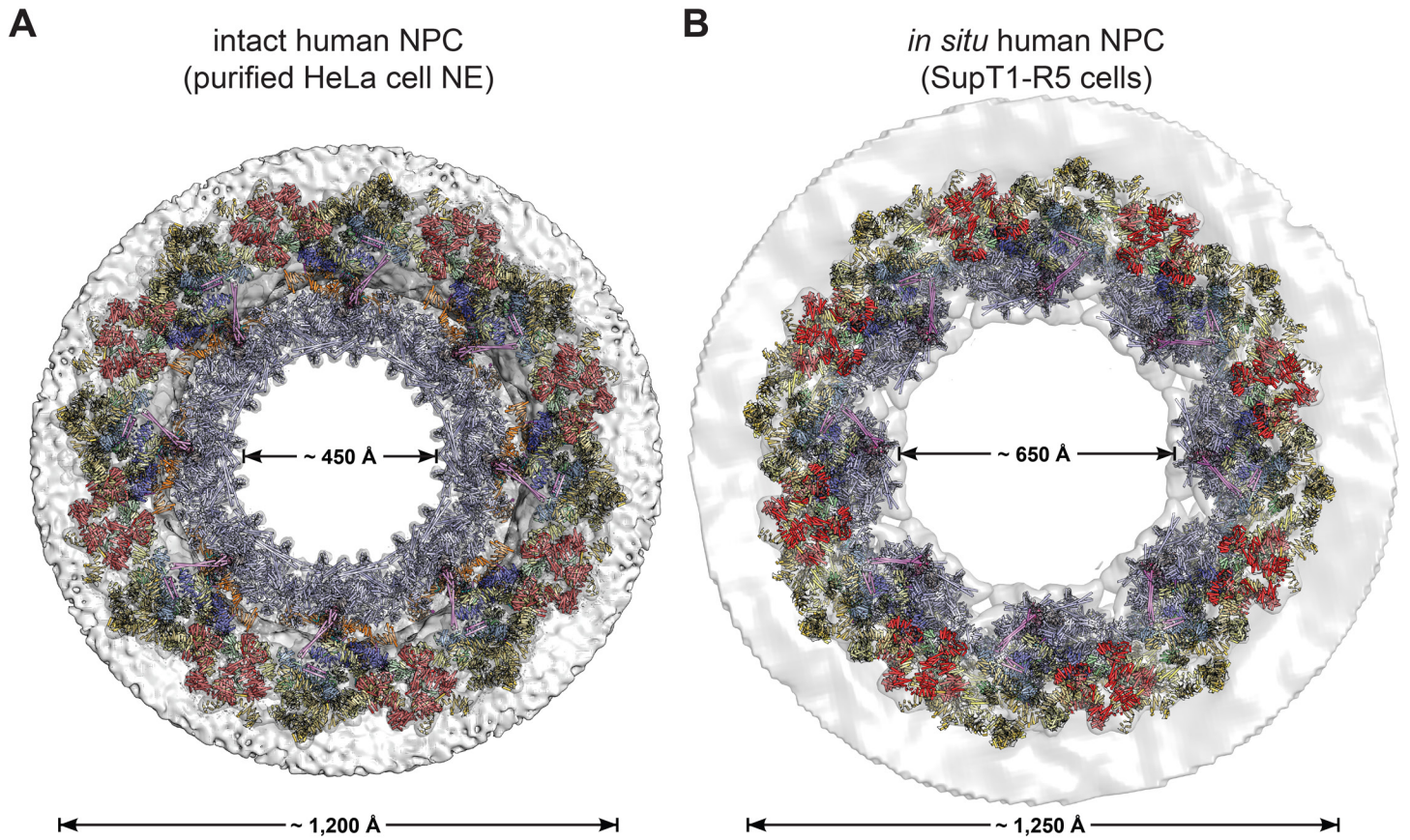
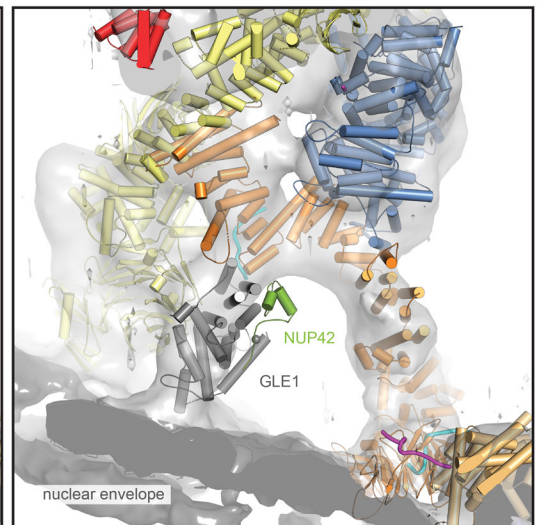
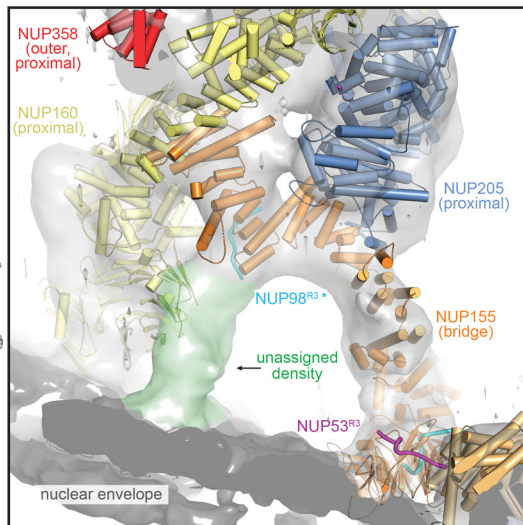
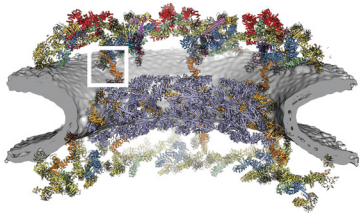
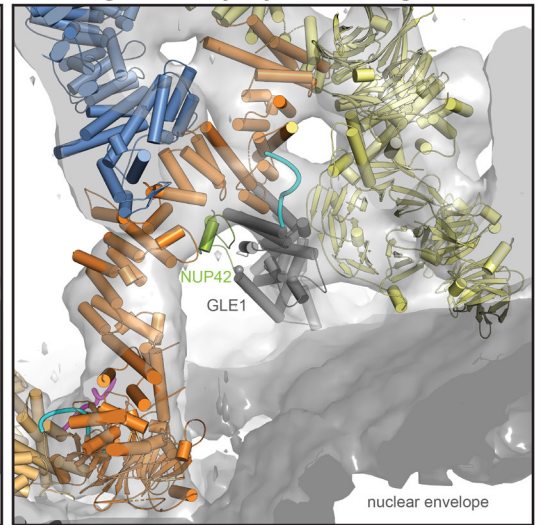
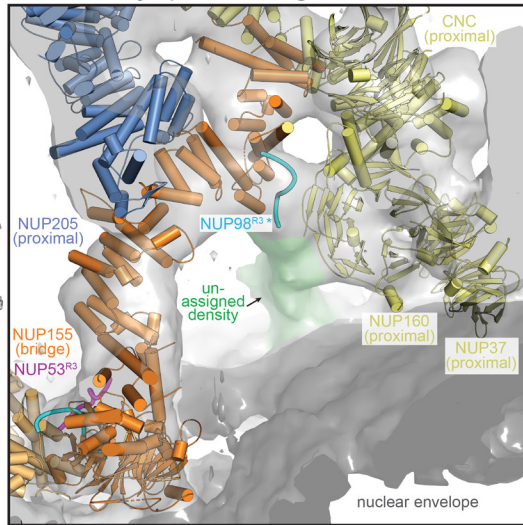
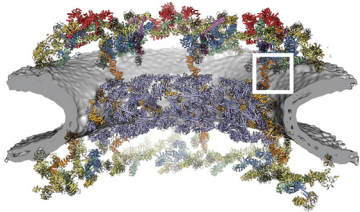


Fig. S87. Additional density in unassigned density cluster II from dilated *in situ* human NPC. (A, B) Comparison of the cytoplasmic face of (A) the constricted human NPC imaged in purified HeLa cell nuclear envelopes and (B) the dilated human NPC imaged *in situ* in SupT1-R5 cells. Outer and inner ring spoke subcomplexes from the composite NPC structure built into the constricted ~ 12 Å cryo-ET sub-tomogram averaged human NPC map (EMD-14322) (46) were manually docked and locally fit as rigid units in the dilated *in situ* ~ 37 Å cryo-ET sub-tomogram averaged human NPC map (EMD-11967) (95). The composite NPC structures are shown as cartoons and superposed to isosurfaces of the constricted and dilated NPCs (gray). (C) A 60°-rotated overview of the dilated human NPC. The inset box indicates the region magnified in the following panels. (D) Magnified view of the docked structures and model of the CFNC-hub (lacking CCS3) are shown as cartoons superposed to the cryo-ET map of the dilated human NPC rendered as gray isosurface. (E) Magnified view of the cryo-ET map of the dilated human NPC (gray), superposed to the cryo-ET map of the constricted human NPC (cyan). Whereas the density of the constricted human NPC is entirely explained by the composite structure, additional unexplained density adjacent to the assigned CFNC-hub is observed in the map of the dilated human NPC (black arrow). (F) Magnified view as in panel (D) with green spheres indicating the root mean square (r.m.s) end-to-end length estimates for the NUP93^{R1-R2} peptide connector, which links NUP93^{R2}•NUP205 with the NUP93^{R1}•CFNC-hub (proximal, green; distal, pale green). The unassigned rod-shaped density of the cryo-ET map of the dilated human NPC is in close proximity to NUP205•NUP93^{R2}, suggesting that the unexplained additional density may accommodate a second CFNC copy. The composite structures in all figure panels are colored according to Fig. 6.

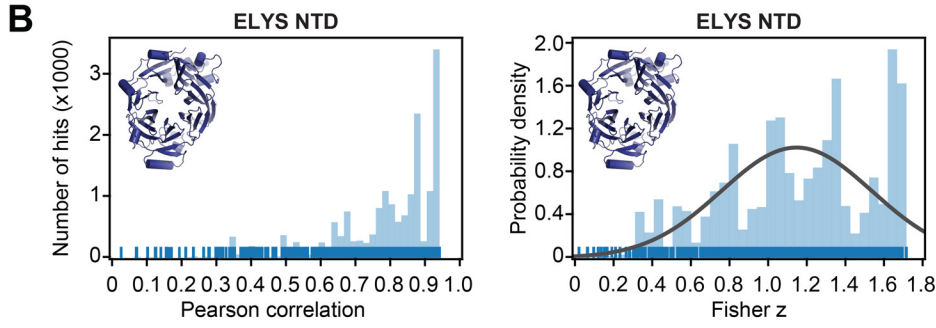
Unassigned density adjacent to the cytoplasmic bridge NUP155

Suggested placement of GLE1•NUP42 in unassigned density adjacent to bridge NUP155



* competitive with GLE1 NTD binding

Fig. S88. Suggested placement of GLE1^{CTD}•NUP42. Overview of the composite structure of the human NPC (*left*). The inset boxes indicate regions magnified in the middle and right panels, harboring unassigned cytoplasmic density directly adjacent to the bridging NUP155 molecules in the ~12 Å cryo-ET map of the intact human NPC (EMD-14322) (46). Magnified views illustrating the globular shape and environment of the cytoplasmic unexplained density (green) shown from the front and the back (*middle*). As previously proposed (63), the manually placed GLE1^{CTD}•NUP42 structure (PDB ID 6B4F) accounts for the unexplained density and is consistent with previous biochemical analyses showing that GLE1^{NTD} and NUP98^{R3} bind to NUP155 in a mutually exclusive fashion (*right*). GLE1^{CTD}•NUP42 is shown in cartoon representation and colored in dark gray and green. The quantitatively docked nups in close proximity to the unassigned density are shown in cartoon representation and colored according to Fig. 6. Cryo-ET densities corresponding to protein and nuclear envelope are rendered as gray and dark gray isosurfaces, respectively.



Subtracted cryo-ET map fitting statistics

| solution rank | Pearson correlation | Fisher z | p-value |
|---------------|---------------------|----------|---------|
| 1 | 0.936 | 1.71 | 0.072 |
| 2 | 0.933 | 1.68 | 0.080 |
| 3 | 0.933 | 1.68 | 0.081 |
| 4 | 0.933 | 1.68 | 0.082 |
| 5 | 0.932 | 1.67 | 0.085 |

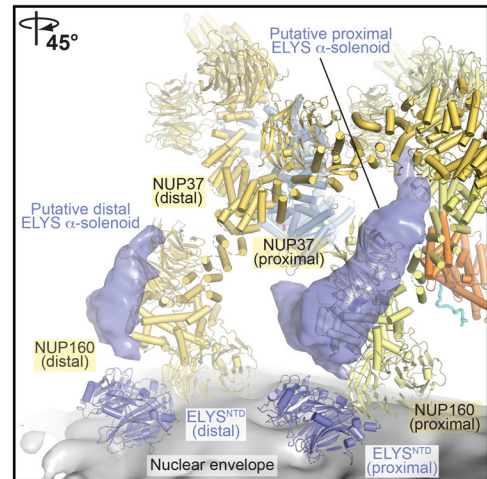
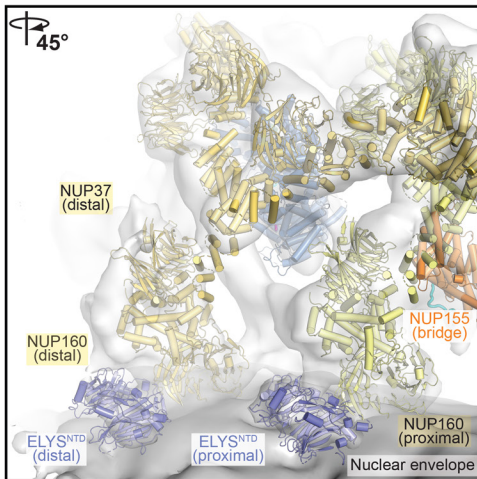
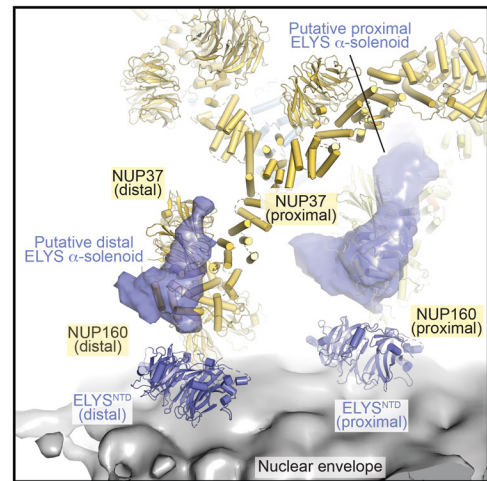
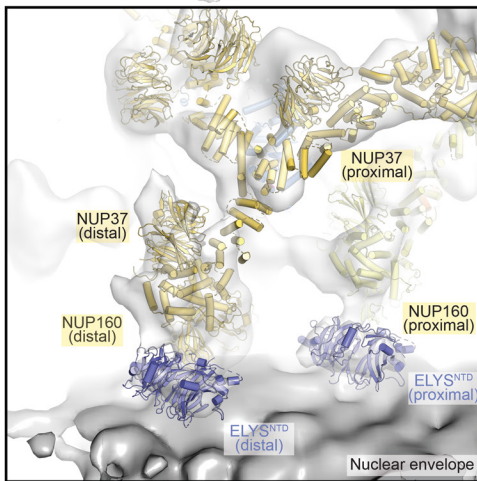
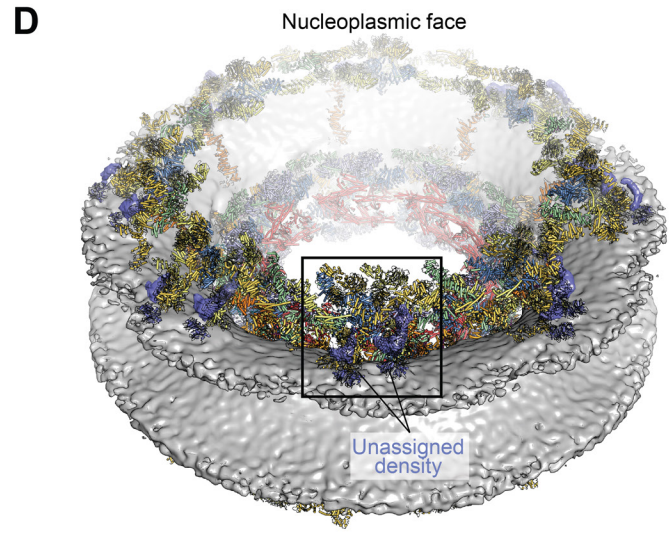
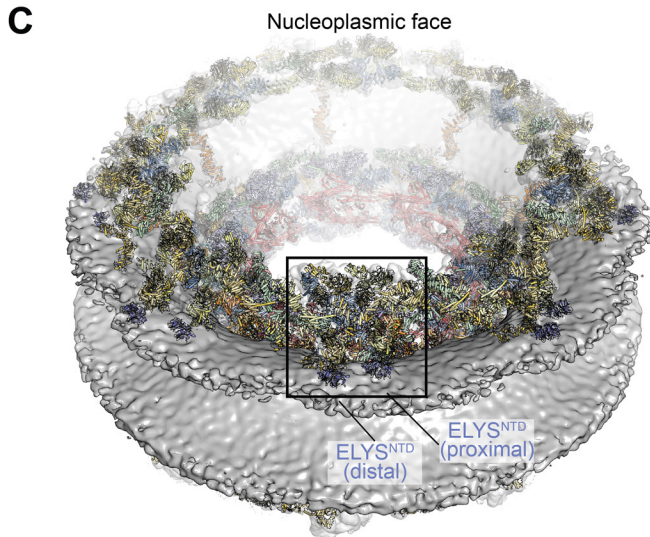


Fig. S89. ELYS placement on nuclear face of the NPC. (A) Domain architecture of human ELYS with residue numbers indicated. The AT-hook and RRK motifs interact with chromatin (147, 148). (B) Resolution-matched densities simulated from the *M. musculus* ELYS^{NTD} crystal structure (PDB ID 4I0O) (25) were quantitatively docked into the ~12 Å sub-tomogram averaged cryo-ET map of the intact human NPC (EMD-14322) (46) from which cryo-ET density corresponding to all placed nups was subtracted. Rug plots (blue) and histograms (light blue) of Pearson correlation scores (*left*) and derived Fisher z scores fit with a normalized Gaussian curve (black) from a global search with 1 million random initial placements are shown (*middle*). A tabular summary of the solutions fitting statistics, along with one-tailed p-values calculated from the Fisher z score distribution (*right*). No docking solution segregated to high confidence. (C) Two magnified views (*middle and bottom*) of the region in the inset box (*top*), showing the placement of ELYS^{NTD} copies into disk-shaped density adjacent to nuclear proximal and distal NUP160 copies and the nuclear envelope. Docked structures are shown in cartoon representation. Cryo-ET densities corresponding to protein and nuclear envelope are rendered as gray and dark gray isosurfaces, respectively. (D) Views as in (C), with unexplained crescent-shaped densities suggested to correspond to the ELYS α -solenoid domain rendered as isosurface (dark blue).

Table S1. Materials and reagents

| REAGENT or RESOURCE | SOURCE | IDENTIFIER |
|---|------------------------------|-------------------|
| <i>C. thermophilum</i> and <i>H. sapiens</i> nucleoporin cDNAs | | |
| Nup82 | This study | N/A |
| Nup159 | This study | N/A |
| Nsp1 | (11) | N/A |
| Dbp5 | (63) | N/A |
| Nup145N | (11) | N/A |
| Gle1 | This study | N/A |
| Gle2 | This study | N/A |
| Nup42 | (63) | N/A |
| Nic96 | (11) | N/A |
| Nup120 | (38) | N/A |
| Nup37 | (38) | N/A |
| Elys | (38) | N/A |
| Nup85 | (38) | N/A |
| Sec13 | (38) | N/A |
| Nup145C | (38) | N/A |
| Nup84 | (38) | N/A |
| Nup133 | (38) | N/A |
| NUP358 | (76) | N/A |
| NUP88 | Open Biosystems | MHS6278-202826062 |
| NUP214 | (54) | N/A |
| NUP62 | Open Biosystems | MHS6278-202806024 |
| NUP98 | Gift, Beatriz Fontoura (103) | N/A |
| RAE1 | (57) | N/A |
| DDX19 | (55) | N/A |
| GLE1 | (63) | N/A |
| NUP42 | Gift, Susan Wente (104) | N/A |
| NUP155 | Gift, Susan Wente (104) | N/A |
| GFP | (89) | N/A |
| H1B | (89) | N/A |
| Insulin | (89) | N/A |
| ALPP | DNASU | HsCD00641203 |
| IL6 | DNASU | HsCD00001047 |
| IL10 | DNASU | HsCD00001333 |
| RPL26 | Horizon | MHS6278-20280 |
| TNF α | DNASU | HsCD00001318 |
| Molecular biology reagents | | |
| SV Total RNA Isolation System | Promega | Cat# Z3100 |
| Superscript-III Reverse Transcriptase | Invitrogen | Cat# 18080044 |
| PfuUltra II Fusion HotStart DNA Polymerase | Agilent Technologies | Cat# 600674 |
| Phusion High-Fidelity DNA Polymerase | New England Biolabs | Cat# M0530L |
| Ascl | New England Biolabs | Cat# R0558L |
| BamHI | New England Biolabs | Cat# R0136L |
| EcoRI | New England Biolabs | Cat# R0101L |
| HindIII | New England Biolabs | Cat# R0104L |
| KpnI | New England Biolabs | Cat# R0142L |
| NcoI | New England Biolabs | Cat# R0193L |
| NdeI | New England Biolabs | Cat# R0111L |
| NotI | New England Biolabs | Cat# R0189L |
| Sall | New England Biolabs | Cat# R0138L |
| SmaI | New England Biolabs | Cat# R0141L |
| SbfI | New England Biolabs | Cat# R3642L |
| XhoI | New England Biolabs | Cat# R0146L |
| T4 DNA Ligase | New England Biolabs | Cat# M0202L |
| QIAquick PCR Purification Kit | Qiagen | Cat# 28104 |

| REAGENT or RESOURCE | SOURCE | IDENTIFIER |
|---|--------------------------|---------------------|
| QIAquick Miniprep Kit | Qiagen | Cat# 27104 |
| NucleoSpin buffer | Clontech Laboratories | Cat# 740953 |
| ViaFect transfection reagent | Promega | Cat# E4982 |
| Nucleic acid miniprep columns | VitaScientific | Cat# DBOC50009 |
| Agarose | Invitrogen | Cat# 16500500 |
| Bacterial and <i>C. thermophilum</i> culture reagents | | |
| Dextrin heptahydrate | Fisher BioReagents | Cat# BP9725-5 |
| Peptone | Fisher BioReagents | Cat# BP9726-5 |
| Yeast extract | Fisher BioReagents | Cat# BP9727-5 |
| Luria-Bertani (LB) media | Fisher BioReagents | Cat# BP9723-5 |
| 2×YT media | Fisher BioReagents | Cat# BP97435 |
| Isopropyl-β-D-thiogalactopyranoside (IPTG) | Gold Biotechnology | Cat# 12481C-1KG |
| Ampicillin | Gold Biotechnology | Cat# A-301-100 |
| Kanamycin | Gold Biotechnology | Cat# K-120-100 |
| Chloramphenicol | Gold Biotechnology | Cat# C-105-100 |
| Dipotassium hydrogen phosphate trihydrate | Macron | Cat# 7088-06 |
| Iron (III) sulfate | Sigma-Aldrich | Cat# 307718 |
| Magnesium sulfate | Sigma-Aldrich | Cat# M2643 |
| Seleno-L-methionine (SeMet) | TCL | Cat# S0442 |
| Insect cell culture reagents | | |
| 5-bromo-3-indolyl-β-D-galactopyranoside (BluoGal) | Sigma-Aldrich | Cat# 97753-82-7 |
| SF-900 III SFM (1x) | Gibco | Cat# 12658-019 |
| ESF 921 insect cell culture medium | Expression Systems | Cat# 96-001-01 |
| Production boost additive | Expression Systems | Cat# 95-006-100 |
| Cellfectin II reagent | Gibco | Cat# 10362-100 |
| Protein purification reagents / general chemicals | | |
| TRIS (trometamol, 2-amino-2-(hydroxymethyl)-1,3-propanediol) | Sigma-Aldrich | Cat# 93362 |
| MES (2-(N-morpholino)ethanesulfonic acid) | Gold Biotechnology | Cat# M-090-500 |
| Sodium chloride | Sigma-Aldrich | Cat# 71376-5KG |
| Potassium phosphate | Sigma-Aldrich | Cat# 60353-1KG |
| Zinc chloride | Fluka | Cat# 96468 |
| Magnesium chloride | Fluka | Cat# 63068 |
| Imidazole | Sigma-Aldrich | Cat# 56750 |
| Glutathione | Sigma-Aldrich | Cat# G4251 |
| Glycerol | Fisher Scientific | Cat# BP229-1 |
| 2-Mercaptoethanol (β-ME) | Sigma-Aldrich | Cat# M6250 |
| Dithiothreitol (DTT) | Gold Biotechnology | Cat# DTT100 |
| Aprotinin from bovine lung | Sigma-Aldrich | Cat# A6279 |
| Phenylmethylsulfonyl fluoride (PMSF) | Gold Biotechnology | Cat# P-470-50 |
| EDTA-free protease inhibitor cocktail | Roche | Cat# A32965 |
| DNase I | Sigma-Aldrich | Cat# D4527 |
| Inositol hexaphosphate (IP ₆) | Sigma-Aldrich | Cat# P8810-25G |
| GMPPNP (5'-guanosine-(β,γ-imido)-triphosphate) | Jena Bioscience | Cat# NU-401-50 |
| AMPPNP (Adenosine 5'-(β,γ-imido)-triphosphate lithium salt hydrate) | Sigma-Aldrich | Cat# A2647 |
| Biotin | Pierce | Cat# 21335 |
| Ethylenediaminetetraacetic acid (EDTA) | Sigma-Aldrich | Cat# 03620-1KG |
| Ethanol | Sigma-Aldrich | Cat# 459844 |
| Alkaline phosphatase | Roche | Cat# 10 567 744 001 |
| Ubl-specific protease 1(ULP1) | Invitrogen | Cat# 12588018 |
| PreScission protease (Pres) | Sigma-Aldrich | Cat# GE27-0843-01 |
| Tabaco etch virus protease (TEV) | Sigma-Aldrich | Cat# T4455 |
| Synthetic antibodies reagents | | |
| M13-KO7 helper phage | New England Biolabs | Cat# N0315S |
| 96 well high binding microlon plates | Greiner Bio-one | Cat# 655081 |
| Neutravidin | Thermo Fisher Scientific | Cat# 34021 |
| Streptavidin MagneSphere | Promega | Cat# Z548C |

| REAGENT or RESOURCE | SOURCE | IDENTIFIER |
|---|---------------------|-------------------|
| 3,3',5,5'-tetramethylbenzidine (TMB) substrate | Pierce | Cat# 34021 |
| BSA | Sigma-Aldrich | Cat# A9418-100G |
| Tween-20 | Anatrace | Cat# T1003 |
| SDS-PAGE reagents | | |
| 40% Acrylamide/Bis solution (37.5:1) | Bio-Rad | Cat# 1610148 |
| TEMED | Bio-Rad | Cat# 161-0801 |
| Glycine | Gold Biotechnology | Cat# G-630-5 |
| Sodium dodecyl sulfate | Sigma-Aldrich | Cat# L3771-1KG |
| Ammonium persulfate | Sigma-Aldrich | Cat# 09913-100g |
| Tricine | Gold Biotechnology | Cat# T-870-1 |
| Acetic acid | Sigma-Aldrich | Cat# 695092 |
| Brilliant Blue R | Sigma-Aldrich | Cat# B7920-50G |
| LLPS interaction assay reagents | | |
| Bodipy (boron-dipyrromethene) FL NHS Ester (succinimidyl ester) | Invitrogen | Cat# D2184 |
| 7-Hydroxycoumarin-3carboxylic acid NHS ester (succinimidyl ester) | Sigma-Aldrich | Cat# 55156 |
| Alexa Fluor 647 NHS Ester (succinimidyl ester) | Invitrogen | Cat# A37573 |
| Sodium bicarbonate | Sigma-Aldrich | Cat# S5761 |
| RNA reagents | | |
| T7 RNA polymerase | Invitrogen | Cat# AM1334 |
| T4 polynucleotide kinase | New England Biolabs | Cat# M0201L |
| Calf intestinal alkaline phosphatase | New England Biolabs | Cat# M0290 |
| Inorganic pyrophosphatase from baker's yeast | Sigma-Aldrich | Cat# I1643 |
| Uridine 5'-Triphosphate trisodium salt | Sigma-Aldrich | Cat# U6625 |
| Cytidine 5'-Triphosphate disodium salt | Sigma-Aldrich | Cat# C1506 |
| Guanosine 5'-Triphosphate sodium salt | Sigma-Aldrich | Cat# G8877 |
| Adenosine 5'-Triphosphate disodium salt | Sigma-Aldrich | Cat# A7699 |
| ³² P γ-ATP (3000Ci/mmol, 10mCi/ml) | Perkin Elmer | Cat# BLU002A250UC |
| Acid-phenol:chloroform:IAA (125:124:1) | Life technologies | cat# AM9722 |
| Spermidine-HCl | Sigma-Aldrich | Cat# 85578 |
| SUPERase-In | Invitrogen | Cat# AM2694 |
| SYBR Gold stain | Invitrogen | Cat# 1730968 |
| 10 x NEB Buffer 4 | New England Biolabs | Cat# B7004S |
| 10 x PNK Buffer | New England Biolabs | Cat# B0201S |
| Zeba Spin Desalting Columns | Thermo Scientific | Cat# 89882 |
| Crystallization reagents | | |
| Ammonium sulfate | MP Bio | Cat# 808211 |
| Bicine | Sigma-Aldrich | Cat# 14871 |
| Bis-TRIS | Sigma-Aldrich | Cat# 14879 |
| Citric acid | Sigma-Aldrich | Cat# 27487 |
| HEPES | Sigma-Aldrich | Cat# 54457-250G-F |
| Magnesium formate | Fluka | Cat# 793 |
| PEG 2,000 MME | Sigma-Aldrich | Cat# 202509 |
| PEG 3,350 | Sigma-Aldrich | Cat# 88276 |
| PEG 4,000 | Sigma-Aldrich | Cat# 95904-1kG-F |
| Potassium sodium tartrate tetrahydrate | Sigma-Aldrich | Cat# S6170 |
| Sodium acetate | Sigma-Aldrich | Cat# S3272 |
| Sodium citrate | Sigma-Aldrich | Cat# 71405 |
| Sodium formate | Sigma-Aldrich | Cat# 71539 |
| Succinic acid | Sigma-Aldrich | Cat# 14079 |
| 100% glycerol | Sigma-Aldrich | Cat# 49767 |
| 100% Ethylene glycol | Fluka | Cat# 03750 |
| Paratone oil | Hampton Research | Cat# HR2-043 |
| Cell culture reagents | | |
| McCoy's 5A medium | ATCC | Cat# 30-2007 |
| Dulbecco's Modified Eagle Medium (DMEM) | Gibco | Cat# 11965-092 |
| Fetal bovine serum (FBS) | Gibco | Cat# 16000044 |

| REAGENT or RESOURCE | SOURCE | IDENTIFIER |
|---|--------------------------|---------------------------------------|
| Penicillin and streptomycin | Gibco | Cat# 15140-122 |
| Hygromycin | Gibco | Cat# 10687010 |
| 0.25% trypsin/0.05% EDTA | Gibco | Cat# 25200-056 |
| Lipofectamine 2000 | Sigma-Aldrich | Cat# 25988-63-0 |
| Opti-MEM | Gibco | Cat# 3185-062 |
| Poly-L-lysine | Sigma-Aldrich | Cat# P8920 |
| Paraformaldehyde | Polysciences | Cat# 04018 |
| TritonX-100 | Thermo-Fisher | Cat# 041092 |
| Saponin | Sigma-Aldrich | Cat# 47036-50G-F |
| Nocodazole | Sigma-Aldrich | Cat# M1404-10MG |
| 3-Indoleacetic acid (auxin) | Sigma-Aldrich | Cat# I3750 |
| DMSO | Sigma-Aldrich | Cat# D2650-5 x 5ML |
| Sucrose | Sigma-Aldrich | Cat# 821721 |
| Calcium dichloride | Sigma-Aldrich | Cat# 529575 |
| Superblock Blocking Buffer | Thermo-Fisher | Cat# 37517 |
| Immobilon P transfer membrane | Millipore | Cat# IPVH00010 |
| Click-iT RNA Alexa Fluor 594 Imaging Kits | Invitrogen | Cat# C10330 |
| Commercial crystallization screens | | |
| Crystal Screen | Hampton Research | Cat# HR2-110 |
| Crystal Screen 2 | Hampton Research | Cat# HR2-112 |
| Index Screen | Hampton Research | Cat# HR2-144 |
| PEG/Ion Screen | Hampton Research | Cat# HR2-126 |
| PEG/Ion 2 Screen | Hampton Research | Cat# HR2-098 |
| ProPlex Screen | Molecular Dimensions | Cat# BN043 |
| PEGs Suite | Qiagen | Cat# 130704 |
| PEGs II Suite | Qiagen | Cat# 130716 |
| Antibodies | | |
| Rat monoclonal anti-NUP98 | Abcam | Cat# ab50610; RRID:AB_881769 |
| Rabbit polyclonal anti-NUP214 | Abcam | Cat# ab70497; RRID:AB_1269607 |
| Rabbit polyclonal anti-GLE1 | Abcam | Cat# ab96007; RRID:AB_10678755NUP |
| Rabbit monoclonal Anti-LaminA/C | Abcam | Cat# ab108595; RRID:AB_10866185 |
| Mouse monoclonal anti-TBP | Abcam | Cat# ab51841; RRID:AB_945758 |
| Rabbit polyclonal anti-NUP358 | Bethyl Laboratories | Cat# A301-797A; RRID:AB_1211503 |
| Rabbit polyclonal anti-NUP96 | Bethyl Laboratories | Cat# A301-784A; RRID:AB_1211487 |
| Rabbit polyclonal anti-NUP133 | Bethyl Laboratories | Cat# A302-386A; RRID:AB_1907269 |
| Mouse monoclonal mAb414 antibody | BioLegend | Cat# 902907; RRID:AB_2734672 |
| Mouse monoclonal anti-HA | BioLegend | Covance Cat# MMS-101P; RRID:AB_231467 |
| Mouse monoclonal anti-Phospho-Histone H3 (Ser10) | Millipore | Cat# 05-806; RRID:AB_310016 |
| Mouse monoclonal anti-Histone H3 | Millipore | Cat# 05-499; RRID:AB_309763 |
| Mouse monoclonal anti-NUP88 | Santa Cruz Biotechnology | Cat# sc-365868; RRID:AB_10842170 |
| Mouse monoclonal anti-NUP93 | Santa Cruz Biotechnology | Cat# sc-374399; RRID:AB_10990113 |
| Mouse monoclonal anti-CyclinB1 | Santa Cruz Biotechnology | Cat# sc-245; RRID:AB_627338) |
| Mouse monoclonal anti-CyclinD1 | Santa Cruz Biotechnology | Cat# sc-8396; RRID:AB_627344 |
| Mouse monoclonal anti-CyclinE | Santa Cruz Biotechnology | Cat# sc-247; RRID:AB_627357 |
| Rabbit polyclonal anti-NUP160 | St John's Lab | Cat# STJ94576 |
| Mouse monoclonal anti-FLAG | Sigma-Aldrich | Cat# F1804; RRID:AB_262044 |
| Mouse monoclonal anti-Tubulin | Sigma-Aldrich | Cat# T6199; RRID:AB_477583 |
| Rabbit anti-NUP43 | Gift, Valerie Doye (149) | N/A |
| Rabbit anti-NUP205 | Gift, Ulrike Kutay (150) | N/A |
| Rabbit anti-ELYS | Gift, Iain Mattaj (151) | N/A |
| Mouse monoclonal anti-HA, Alexa Fluor 488 | Invitrogen | Cat#A-21287; RRID:AB_2535829 |
| Mouse monoclonal anti-M13 phage coat protein, HRP | Invitrogen | Cat# MA5-36126 |
| Donkey anti-Rabbit IgG(H+L), Alexa Fluor 488 | Invitrogen | Cat# A-21206; RRID:AB_2535792 |
| Goat anti-Mouse IgG(H+L), Alexa Fluor 568 | Invitrogen | Cat# A-11004; RRID:AB_2534072 |
| Goat anti-Rat IgG (H+L), Alexa Fluor 488 | Invitrogen | Cat# A-11006; RRID:AB_2534074 |
| IRDye 800CW Goat anti-Mouse IgG | LI-COR | P/N 925-32210; RRID: AB_2687825 |
| IRDye 800CW Goat anti-Rat IgG | LI-COR | P/N 926-32219; RRID: AB_2721932 |

| REAGENT or RESOURCE | SOURCE | IDENTIFIER |
|--|-------------------|--|
| IRDye 800CW Goat anti-Rabbit IgG | LI-COR | P/N 926-32211; RRID: AB_2651127 |
| Software | | |
| DALI protein structure comparison server | (78) | http://ekhidna2.biocenter.helsinki.fi/dali/ |
| XDS | (116) | https://xds.mr.mpg.de/ |
| DIALS | (117) | http://dials.github.io/ |
| RESOLVE | (123) | http://resolve.lanl.gov/ |
| COOT | (125) | http://www2.mrc-lmb.cam.ac.uk/personal/pemsley/cool/ |
| PHENIX | (126) | http://phenix-online.org/ |
| MolProbity | (127) | http://molprobity.biochem.duke.edu/ |
| Fiji | (138) | http://imagej.net/software/fiji/ |
| ALSCRIPT | (140) | http://www.cryst.bbk.ac.uk/CCSG/info/software/prot-sequ/alscript/alscript.html |
| ASTRA 6 | Wyatt Technology | http://www.wyatt.com/products/software/astra.html |
| ClustalX | (139) | http://www.clustal.org/clustal2/ |
| Chimera fitmap tool | (128) | http://www.cgl.ucsf.edu/chimera/ |
| CRISPR Design Tools | (135) | http://crispr.mit.edu:8079 http://figshare.com/articles/CRISPR_Design_Tool/1117899 |
| Prism | GraphPad Software | http://www.graphpad.com/scientific-software/prism/ |
| PYMOLE | Schrödinger | http://pymol.org/2/ |
| IGOR Pro | WaveMetrics | http://www.wavemetrics.com/ |
| Adobe illustrator | Adobe | http://www.adobe.com/products/illustrator.html |
| Adobe photoshop | Adobe | http://www.adobe.com/products/photoshop.html |
| Expression vectors | | |
| pET24a | Addgene | Cat# 69749-3 |
| pET28a-SUMO | (106) | N/A |
| pET28a-SUMO-Avi | This study | N/A |
| pET28a-His-PreS-Avi | (27) | N/A |
| pET28a-His-PreS-Avi-SUMO | This study | N/A |
| pET28a-PreS | (105) | N/A |
| pGEX-6P1 | GE Healthcare | Cat# 28-9546-48 |
| pETDuet1 | Novagen | Cat# 71146-3 |
| pETDuet1-SUMO | This study | N/A |
| pETDuet1-SUMO2 | This study | N/A |
| pETDuet1-SUMO-Avi | This Study | N/A |
| pET-MCN | (107) | N/A |
| pET-MCN-SUMO | (11) | N/A |
| pET-MCN-PreS | This study | N/A |
| pcDNA3.1 | Invitrogen | Cat# V79020 |
| pX330 | Addgene | Cat# 42230 |
| pRH2.2 | Sidhu Lab (108) | N/A |
| pFastBac-HTB | Invitrogen | Cat# 10360014 |
| pFastBac-Dual | Invitrogen | Cat# 10712024 |
| Columns and resins | | |
| HiLoad 16/60 Superdex 200 PG | GE Healthcare | N/A |
| HiLoad 16/60 Superdex 75 PG | GE Healthcare | N/A |
| Superdex 200 10/300 GL | GE Healthcare | N/A |
| Superdex 75 10/300 GL | GE Healthcare | N/A |
| Superdex 200 Increase 10/300 GL | GE Healthcare | N/A |
| Superose 6 10/300 GL | GE Healthcare | N/A |
| HiTrap Q HP | GE Healthcare | N/A |
| HiTrap SP HP | GE Healthcare | N/A |
| MonoQ 10/100 GL | GE Healthcare | N/A |
| HiTrap Heparin HP | GE Healthcare | N/A |
| HiPrep 26/20 Desalting | GE Healthcare | N/A |
| HiTrap Desalting 5 mL | GE Healthcare | N/A |
| HiTrap MabSelect SuRe | GE Healthcare | N/A |
| Glutathione Sepharose 4 fast flow | GE Healthcare | Cat# 17-5132-02 |
| Ni-NTA agarose | Qiagen | Cat# 30230 |

| REAGENT or RESOURCE | SOURCE | IDENTIFIER |
|--|----------------------|---------------|
| Cell lines | | |
| HCT116 ^{AID::NUP358} | This study | N/A |
| DLD1 ^{AID::NUP358} | This study | N/A |
| DLD1 ^{NUP160::NG-AID} | This study | N/A |
| <i>E. coli</i> BL21-CodonPlus (DE3)-RIL | Agilent Technologies | Cat# 230245 |
| <i>E. coli</i> Max Efficiency DH5 α | Invitrogen | Cat# 18258012 |
| <i>E. coli</i> XL1-Blue cells | Agilent Technologies | Cat# 200249 |
| <i>E. coli</i> BL21-Gold | Agilent Technologies | Cat# 230130 |
| DH10Bac cells | Gibco | Cat# 10361012 |
| <i>T. ni</i> Hi5 cells | Gibco | Cat# B5502 |
| <i>S. frugiperda</i> Sf9 cells | Gibco | Cat# 11496015 |
| <i>C. thermophilum</i> strain | Gift, Ed Hurt (152) | DSM-1495 |

Table S2. Bacterial expression constructs and conditions

| # | Protein | Residues | Expression vector | Restriction sites 5', 3' | N-terminal overhang | C-terminal overhang | Expression conditions |
|-----|---------------------------------------|--|-----------------------|------------------------------|-------------------------------------|---------------------|-----------------------|
| 1 | NUP88 | 1-741 | pET28a-SUMO | BamHI, NotI | S | AAALEHHHHHH | 18 °C, 18 hours |
| 2* | NUP88 NTD | 1-493 | pET28a-SUMO | BamHI, NotI | S | none | 18 °C, 18 hours |
| 3 | NUP62 NUP214 | 317-522 (1-450)-(699-955) | pETDuet1-SUMO2 | NcoI, NotI NdeI, XhoI | S S | none none | 18 °C, 18 hours |
| 4 | NUP62 | 317-522 | pET28a-PreS | NdeI, XhoI | MGSSHHHHHHSS GLEVLFGQGP | none | 18 °C, 18 hours |
| 5 | NUP214 CCS1-3 NUP88 CCS1-3 | 699-888 559-741 | pETDuet1-SUMO | BamHI, NotI NdeI/XhoI | S none | none none | 18 °C, 18 hours |
| 6 | AVI-NUP214 CCS1-3 NUP88 CCS1-3 | 699-888 559-741 | pETDuet1-SUMO- Avi | BamHI, NotI Nde, XhoI | SSGLNDIFEAQKIE WHEGSAGGSGGS M | none none | 18 °C, 18 hours |
| 7 | NUP98 GLEBS-APD | (157-213)-GSGSGSHM- (715-863) | pET28a-PreS | NdeI, XhoI | GPHM | none | 18 °C, 18 hours |
| 8* | NUP98 APD | 715-863 | pET28a-PreS | NdeI, XhoI | GPHM | none | 18 °C, 18 hours |
| 9 | DDX19 | 1-479 | pET28a-PreS | NdeI, NotI | none | none | 18 °C, 18 hours |
| 10 | DDX19 E243Q | 1-479 E243Q | pET28a-PreS | NdeI, NotI | GPHM | none | 18 °C, 18 hours |
| 11 | GLE1 CTD NUP42 GBM | 382-698 379-423 | pETDuet1-PreS | NdeI, XhoI BamHI, NotI | M GPSGS | none none | 18 °C, 18 hours |
| 12 | NUP42 ZnF | 2-26 | pET28a-SUMO | BamHI, XhoI | S | none | 37 °C, 2 hours |
| 13 | NUP214 NTD | 1-450 | pET28a-PreS | NdeI, NotI | GPHM | none | 18 °C, 18 hours |
| 14 | SUMO-NUP214 TAIL | 908-955 | pET28a-SUMO | BamHI, NotI | none | none | 18 °C, 18 hours |
| 15 | SUMO-NUP214 (908-952) | 908-952 | pET28a-SUMO | BamHI, NotI | none | none | 18 °C, 18 hours |
| 16 | SUMO-NUP214 (938-955) | 938-955 | pET28a-SUMO | BamHI, NotI | none | none | 18 °C, 18 hours |
| 17 | SUMO-NUP214 (940-955) | 940-955 | pET28a-SUMO | BamHI, NotI | none | none | 18 °C, 18 hours |
| 18 | NUP155 CTD | 870-1391 | pET28a-PreS | NdeI, NotI | GPHM | none | 18 °C, 18 hours |
| 19 | SUMO-NUP93 R1 | 2-93 | pET28a-SUMO | BamHI, NotI | S | none | 18 °C, 18 hours |
| 20 | SUMO-NUP93 R1 LIL | 2-93 L33A, I36A, L43A | pET28a-SUMO | BamHI, NotI | S | none | 18 °C, 18 hours |
| 21* | NUP358 NTD | 1-752 I599M | pET28a-SUMO | BamHI, NotI | S | none | 18 °C, 18 hours |
| 22 | NUP358 OE | 802-832 | pET28a-SUMO | BamHI, NotI | S | none | 18 °C, 18 hours |
| 23* | NUP358 OE | 805-832 | pET28a-SUMO | BamHI, NotI | S | none | 18 °C, 18 hours |
| 24 | NUP358 NTD-OE | 1-832 I599M | pET28a-SUMO | BamHI, NotI | S | AAALEHHHHHH | 18 °C, 18 hours |
| 25 | NUP358 OE LIQIML | 802-832 L811A, I814A, Q817A, I821A, M825A, L828A | pET28a-SUMO | BamHI, NotI | S | none | 18 °C, 18 hours |
| 26 | NUP358 NTD-OE LIQIML | 1-832 I599M L811A, I814A, Q817A, I821A, M825A, L828A | pET28a-SUMO | BamHI, NotI | S | AAALEHHHHHH | 18 °C, 18 hours |
| 27 | NUP358 TPR | 1-145 | pGEX-6P1 | BamHI, NotI | GPLGS | none | 18 °C, 18 hours |
| 28 | NUP358 NTD ΔTPR | 145-752 I599M | pET28a-SUMO | BamHI, NotI | S | none | 18 °C, 18 hours |
| 29 | NUP358 1-673 | 1-673 I599M | pET28a-SUMO | BamHI, NotI | S | none | 18 °C, 18 hours |
| 30* | NUP358 145-673 | 145-673 I599M | pET28a-SUMO | BamHI, NotI | S | none | 18 °C, 18 hours |
| 31* | AVI-NUP358 145-673 | 145-673 | pET28a-SUMO-Avi | BamHI, NotI | SSGLNDIFEAQKIE WHEGSAGGSGGS | none | 18 °C, 18 hours |
| 32* | NUP358 RBD-I | 1171-1306 | pGEX-6P1 | BamHI, NotI | GPLGS | none | 18 °C, 18 hours |
| 33* | NUP358 RBD-II | 2012-2148 | pGEX-6P1 | BamHI, NotI | GPLGS | none | 18 °C, 18 hours |
| 34* | NUP358 RBD-III | 2309-2444 | pGEX-6P1 | BamHI, NotI | GPLGS | none | 18 °C, 18 hours |
| 35 | NUP358 RBD-IV | 2911-3045 | pGEX-6P1 | BamHI, NotI | GPLGS | none | 18 °C, 18 hours |
| 36* | NUP358 RBD-IV | 2911-3045 W2962Q, H2963N, T2964Y, M2965D, K2966N, N2967K, Y2968Q, Y2969V | pGEX-6P1 | BamHI, NotI | GPLGS | none | 18 °C, 18 hours |
| 37 | NUP358 ZnF1 | 1343-1380 | pGEX-6P1 | BamHI, NotI | GPLGS | none | 37 °C, 2 hours |
| 38* | NUP358 ZnF2 | 1416-1443 | pGEX-6P1 | BamHI, NotI | GPLGS | none | 37 °C, 2 hours |
| 39* | NUP358 ZnF3 | 1471-1507 | pGEX-6P1 | BamHI, NotI | GPLGS | none | 37 °C, 2 hours |
| 40* | NUP358 ZnF4 | 1535-1571 | pGEX-6P1 | BamHI, NotI | GPLGS | none | 37 °C, 2 hours |
| 41* | NUP358 ZnF5/6 | 1607-1634 | pGEX-6P1 | BamHI, NotI | GPLGS | none | 37 °C, 2 hours |
| 42* | NUP358 ZnF7 | 1716-1752 | pGEX-6P1 | BamHI, NotI | GPLGS | none | 37 °C, 2 hours |
| 43* | NUP358 ZnF8 | 1774-1809 | pGEX-6P1 | BamHI, NotI | GPLGS | none | 37 °C, 2 hours |
| 44 | NUP358 ZnF1 ΔNTE | 1352-1380 | pGEX-6P1 | BamHI, NotI | GPLGS | none | 37 °C, 2 hours |
| 45 | NUP358 ZnF2 ΔNTE | 1416-1443 | pGEX-6P1 | BamHI, NotI | GPLGS | none | 37 °C, 2 hours |
| 46 | NUP358 ZnF3 ΔNTE | 1480-1507 | pGEX-6P1 | BamHI, NotI | GPLGS | none | 37 °C, 2 hours |
| 47 | NUP358 ZnF4 ΔNTE | 1480-1507 | pGEX-6P1 | BamHI, NotI | GPLGS | none | 37 °C, 2 hours |
| 48 | NUP358 ZnF5/6 ΔNTE | 1607-1634 | pGEX-6P1 | BamHI, NotI | GPLGS | none | 37 °C, 2 hours |
| 49 | NUP358 ZnF7 ΔNTE | 1725-1752 | pGEX-6P1 | BamHI, NotI | GPLGS | none | 37 °C, 2 hours |
| 50 | NUP358 ZnF8 ΔNTE | 1782-1809 | pGEX-6P1 | BamHI, NotI | GPLGS | none | 37 °C, 2 hours |
| 51 | NUP358 ZFD | 1343-1890 | pGEX-6P1 | BamHI, NotI | GPLGS | none | 37 °C, 2 hours |
| 52 | NUP358 CTD | 3062-3224 | pET28a-PreS | NdeI, NotI | GPHM | none | 18 °C, 18 hours |
| 53 | NUP358 NTD (R2E/R3E) | 1-752 I599M | pET28a-SUMO | BamHI, NotI | S | none | 18 °C, 18 hours |

| # | Protein | Residues | Expression vector | Restriction sites 5', 3' | N-terminal overhang | C-terminal overhang | Expression conditions |
|-----|--|-------------|-------------------|--------------------------|---------------------|---------------------|-----------------------|
| 54 | NUP358 NTD (R2A/R3A) | 1-752 I599M | pET28a-SUMO | BamHI, NotI | S | none | 18 °C, 18 hours |
| 55 | NUP358 NTD (K5E) | 1-752 I599M | pET28a-SUMO | BamHI, NotI | S | none | 18 °C, 18 hours |
| 56 | NUP358 NTD (K5A) | 1-752 I599M | pET28a-SUMO | BamHI, NotI | S | none | 18 °C, 18 hours |
| 57 | NUP358 NTD (R10E) | 1-752 I599M | pET28a-SUMO | BamHI, NotI | S | none | 18 °C, 18 hours |
| 58 | NUP358 NTD (R10A) | 1-752 I599M | pET28a-SUMO | BamHI, NotI | S | none | 18 °C, 18 hours |
| 59 | NUP358 NTD (K23E) | 1-752 I599M | pET28a-SUMO | BamHI, NotI | S | none | 18 °C, 18 hours |
| 60 | NUP358 NTD (K23A) | 1-752 I599M | pET28a-SUMO | BamHI, NotI | S | none | 18 °C, 18 hours |
| 61 | NUP358 NTD (K25E) | 1-752 I599M | pET28a-SUMO | BamHI, NotI | S | none | 18 °C, 18 hours |
| 62 | NUP358 NTD (K25A) | 1-752 I599M | pET28a-SUMO | BamHI, NotI | S | none | 18 °C, 18 hours |
| 63 | NUP358 NTD (K28E) | 1-752 I599M | pET28a-SUMO | BamHI, NotI | S | none | 18 °C, 18 hours |
| 64 | NUP358 NTD (K28A) | 1-752 I599M | pET28a-SUMO | BamHI, NotI | S | none | 18 °C, 18 hours |
| 65 | NUP358 NTD (K28E/R58E) | 1-752 I599M | pET28a-SUMO | BamHI, NotI | S | none | 18 °C, 18 hours |
| 66 | NUP358 NTD (K34E) | 1-752 I599M | pET28a-SUMO | BamHI, NotI | S | none | 18 °C, 18 hours |
| 67 | NUP358 NTD (K34A) | 1-752 I599M | pET28a-SUMO | BamHI, NotI | S | none | 18 °C, 18 hours |
| 68 | NUP358 NTD (K40E) | 1-752 I599M | pET28a-SUMO | BamHI, NotI | S | none | 18 °C, 18 hours |
| 69 | NUP358 NTD (K40A) | 1-752 I599M | pET28a-SUMO | BamHI, NotI | S | none | 18 °C, 18 hours |
| 70 | NUP358 NTD (K34A/K40A) | 1-752 I599M | pET28a-SUMO | BamHI, NotI | S | none | 18 °C, 18 hours |
| 71 | NUP358 NTD (K34A/K40A/K61A/R64A) | 1-752 I599M | pET28a-SUMO | BamHI, NotI | S | none | 18 °C, 18 hours |
| 72 | NUP358 NTD (K34A/K40A/R58A/K61A/R64A) | 1-752 I599M | pET28a-SUMO | BamHI, NotI | S | none | 18 °C, 18 hours |
| 73 | NUP358 NTD 2R5K (K34A/K40A/R58A/K61A/R64A/K500A/K502A) | 1-752 I599M | pET28a-SUMO | BamHI, NotI | S | none | 18 °C, 18 hours |
| 74 | NUP358 NTD (K40E/K61E/R64E) | 1-752 I599M | pET28a-SUMO | BamHI, NotI | S | none | 18 °C, 18 hours |
| 75 | NUP358 NTD (K40A/K61A/R64A) | 1-752 I599M | pET28a-SUMO | BamHI, NotI | S | none | 18 °C, 18 hours |
| 76 | NUP358 NTD (K40A/R58A/K61A/R64A) | 1-752 I599M | pET28a-SUMO | BamHI, NotI | S | none | 18 °C, 18 hours |
| 77 | NUP358 NTD (K40A/R58A/K61A/R64A/H303A) | 1-752 I599M | pET28a-SUMO | BamHI, NotI | S | none | 18 °C, 18 hours |
| 78 | NUP358 NTD (K46/K47E) | 1-752 I599M | pET28a-SUMO | BamHI, NotI | S | none | 18 °C, 18 hours |
| 79 | NUP358 NTD (K47A) | 1-752 I599M | pET28a-SUMO | BamHI, NotI | S | none | 18 °C, 18 hours |
| 80 | NUP358 NTD (R58E) | 1-752 I599M | pET28a-SUMO | BamHI, NotI | S | none | 18 °C, 18 hours |
| 81 | NUP358 NTD (R58A) | 1-752 I599M | pET28a-SUMO | BamHI, NotI | S | none | 18 °C, 18 hours |
| 82 | NUP358 NTD (K61E) | 1-752 I599M | pET28a-SUMO | BamHI, NotI | S | none | 18 °C, 18 hours |
| 83 | NUP358 NTD (K61A) | 1-752 I599M | pET28a-SUMO | BamHI, NotI | S | none | 18 °C, 18 hours |
| 84 | NUP358 NTD (R64E) | 1-752 I599M | pET28a-SUMO | BamHI, NotI | S | none | 18 °C, 18 hours |
| 85 | NUP358 NTD (R64A) | 1-752 I599M | pET28a-SUMO | BamHI, NotI | S | none | 18 °C, 18 hours |
| 86 | NUP358 NTD (K61E/R64E) | 1-752 I599M | pET28a-SUMO | BamHI, NotI | S | none | 18 °C, 18 hours |
| 87 | NUP358 NTD (K61A/R64A) | 1-752 I599M | pET28a-SUMO | BamHI, NotI | S | none | 18 °C, 18 hours |
| 88 | NUP358 NTD (K78E) | 1-752 I599M | pET28a-SUMO | BamHI, NotI | S | none | 18 °C, 18 hours |
| 89 | NUP358 NTD (R84E/R85E) | 1-752 I599M | pET28a-SUMO | BamHI, NotI | S | none | 18 °C, 18 hours |
| 90 | NUP358 NTD (K94E) | 1-752 I599M | pET28a-SUMO | BamHI, NotI | S | none | 18 °C, 18 hours |
| 91 | NUP358 NTD (K94A) | 1-752 I599M | pET28a-SUMO | BamHI, NotI | S | none | 18 °C, 18 hours |
| 92 | NUP358 NTD (K99E) | 1-752 I599M | pET28a-SUMO | BamHI, NotI | S | none | 18 °C, 18 hours |
| 93 | NUP358 NTD (K106E) | 1-752 I599M | pET28a-SUMO | BamHI, NotI | S | none | 18 °C, 18 hours |
| 94 | NUP358 NTD (R113E) | 1-752 I599M | pET28a-SUMO | BamHI, NotI | S | none | 18 °C, 18 hours |
| 95 | NUP358 NTD (R113A) | 1-752 I599M | pET28a-SUMO | BamHI, NotI | S | none | 18 °C, 18 hours |
| 96 | NUP358 NTD (K115E) | 1-752 I599M | pET28a-SUMO | BamHI, NotI | S | none | 18 °C, 18 hours |
| 97 | NUP358 NTD (R120E) | 1-752 I599M | pET28a-SUMO | BamHI, NotI | S | none | 18 °C, 18 hours |
| 98 | NUP358 NTD (K123E) | 1-752 I599M | pET28a-SUMO | BamHI, NotI | S | none | 18 °C, 18 hours |
| 99 | NUP358 NTD (K133E) | 1-752 I599M | pET28a-SUMO | BamHI, NotI | S | none | 18 °C, 18 hours |
| 100 | NUP358 NTD (K133A) | 1-752 I599M | pET28a-SUMO | BamHI, NotI | S | none | 18 °C, 18 hours |
| 101 | NUP358 NTD (K135E) | 1-752 I599M | pET28a-SUMO | BamHI, NotI | S | none | 18 °C, 18 hours |
| 102 | NUP358 NTD (K135A) | 1-752 I599M | pET28a-SUMO | BamHI, NotI | S | none | 18 °C, 18 hours |
| 103 | NUP358 NTD (K149E) | 1-752 I599M | pET28a-SUMO | BamHI, NotI | S | none | 18 °C, 18 hours |
| 104 | NUP358 NTD (R161E) | 1-752 I599M | pET28a-SUMO | BamHI, NotI | S | none | 18 °C, 18 hours |
| 105 | NUP358 NTD (R161A) | 1-752 I599M | pET28a-SUMO | BamHI, NotI | S | none | 18 °C, 18 hours |
| 106 | NUP358 NTD (R170E) | 1-752 I599M | pET28a-SUMO | BamHI, NotI | S | none | 18 °C, 18 hours |
| 107 | NUP358 NTD (R170A) | 1-752 I599M | pET28a-SUMO | BamHI, NotI | S | none | 18 °C, 18 hours |
| 108 | NUP358 NTD (R176E) | 1-752 I599M | pET28a-SUMO | BamHI, NotI | S | none | 18 °C, 18 hours |
| 109 | NUP358 NTD (K179E/R180E) | 1-752 I599M | pET28a-SUMO | BamHI, NotI | S | none | 18 °C, 18 hours |
| 110 | NUP358 NTD (K179A) | 1-752 I599M | pET28a-SUMO | BamHI, NotI | S | none | 18 °C, 18 hours |
| 111 | NUP358 NTD (R180A) | 1-752 I599M | pET28a-SUMO | BamHI, NotI | S | none | 18 °C, 18 hours |
| 112 | NUP358 NTD (K182E) | 1-752 I599M | pET28a-SUMO | BamHI, NotI | S | none | 18 °C, 18 hours |
| 113 | NUP358 NTD (K182A) | 1-752 I599M | pET28a-SUMO | BamHI, NotI | S | none | 18 °C, 18 hours |
| 114 | NUP358 NTD (R193E) | 1-752 I599M | pET28a-SUMO | BamHI, NotI | S | none | 18 °C, 18 hours |
| 115 | NUP358 NTD (R198E) | 1-752 I599M | pET28a-SUMO | BamHI, NotI | S | none | 18 °C, 18 hours |
| 116 | NUP358 NTD (R198A) | 1-752 I599M | pET28a-SUMO | BamHI, NotI | S | none | 18 °C, 18 hours |
| 117 | NUP358 NTD (K212E) | 1-752 I599M | pET28a-SUMO | BamHI, NotI | S | none | 18 °C, 18 hours |
| 118 | NUP358 NTD (K212A) | 1-752 I599M | pET28a-SUMO | BamHI, NotI | S | none | 18 °C, 18 hours |

| # | Protein | Residues | Expression vector | Restriction sites 5', 3' | N-terminal overhang | C-terminal overhang | Expression conditions |
|------|--------------------------------|-------------|-------------------|--------------------------|---------------------|---------------------|-----------------------|
| 119 | NUP358 NTD (K225E) | 1-752 I599M | pET28a-SUMO | BamHI, NotI | S | none | 18 °C, 18 hours |
| 120 | NUP358 NTD (K225A) | 1-752 I599M | pET28a-SUMO | BamHI, NotI | S | none | 18 °C, 18 hours |
| 121 | NUP358 NTD (R229E) | 1-752 I599M | pET28a-SUMO | BamHI, NotI | S | none | 18 °C, 18 hours |
| 122 | NUP358 NTD (R250E) | 1-752 I599M | pET28a-SUMO | BamHI, NotI | S | none | 18 °C, 18 hours |
| 123 | NUP358 NTD (R256E) | 1-752 I599M | pET28a-SUMO | BamHI, NotI | S | none | 18 °C, 18 hours |
| 124 | NUP358 NTD (K270E) | 1-752 I599M | pET28a-SUMO | BamHI, NotI | S | none | 18 °C, 18 hours |
| 125 | NUP358 NTD (K286E) | 1-752 I599M | pET28a-SUMO | BamHI, NotI | S | none | 18 °C, 18 hours |
| 126 | NUP358 NTD (K286A) | 1-752 I599M | pET28a-SUMO | BamHI, NotI | S | none | 18 °C, 18 hours |
| 127 | NUP358 NTD (K299E) | 1-752 I599M | pET28a-SUMO | BamHI, NotI | S | none | 18 °C, 18 hours |
| 128 | NUP358 NTD (H303A) | 1-752 I599M | pET28a-SUMO | BamHI, NotI | S | none | 18 °C, 18 hours |
| 129 | NUP358 NTD (R310E) | 1-752 I599M | pET28a-SUMO | BamHI, NotI | S | none | 18 °C, 18 hours |
| 130 | NUP358 NTD (R328E) | 1-752 I599M | pET28a-SUMO | BamHI, NotI | S | none | 18 °C, 18 hours |
| 131 | NUP358 NTD (K330E/K332E) | 1-752 I599M | pET28a-SUMO | BamHI, NotI | S | none | 18 °C, 18 hours |
| 132 | NUP358 NTD (K335E) | 1-752 I599M | pET28a-SUMO | BamHI, NotI | S | none | 18 °C, 18 hours |
| 133 | NUP358 NTD (R363E/K365E) | 1-752 I599M | pET28a-SUMO | BamHI, NotI | S | none | 18 °C, 18 hours |
| 134 | NUP358 NTD (K370E) | 1-752 I599M | pET28a-SUMO | BamHI, NotI | S | none | 18 °C, 18 hours |
| 135 | NUP358 NTD (K379E) | 1-752 I599M | pET28a-SUMO | BamHI, NotI | S | none | 18 °C, 18 hours |
| 136 | NUP358 NTD (K396E) | 1-752 I599M | pET28a-SUMO | BamHI, NotI | S | none | 18 °C, 18 hours |
| 137 | NUP358 NTD (R412E) | 1-752 I599M | pET28a-SUMO | BamHI, NotI | S | none | 18 °C, 18 hours |
| 138 | NUP358 NTD (R421E) | 1-752 I599M | pET28a-SUMO | BamHI, NotI | S | none | 18 °C, 18 hours |
| 139 | NUP358 NTD (R428E) | 1-752 I599M | pET28a-SUMO | BamHI, NotI | S | none | 18 °C, 18 hours |
| 140 | NUP358 NTD (R454E/K458E) | 1-752 I599M | pET28a-SUMO | BamHI, NotI | S | none | 18 °C, 18 hours |
| 141 | NUP358 NTD (K455E) | 1-752 I599M | pET28a-SUMO | BamHI, NotI | S | none | 18 °C, 18 hours |
| 142 | NUP358 NTD (R470E) | 1-752 I599M | pET28a-SUMO | BamHI, NotI | S | none | 18 °C, 18 hours |
| 143 | NUP358 NTD (K500E/K502E) | 1-752 I599M | pET28a-SUMO | BamHI, NotI | S | none | 18 °C, 18 hours |
| 144 | NUP358 NTD (K500A/K502A) | 1-752 I599M | pET28a-SUMO | BamHI, NotI | S | none | 18 °C, 18 hours |
| 145 | NUP358 NTD (K521E) | 1-752 I599M | pET28a-SUMO | BamHI, NotI | S | none | 18 °C, 18 hours |
| 146 | NUP358 NTD (R527E/K529E) | 1-752 I599M | pET28a-SUMO | BamHI, NotI | S | none | 18 °C, 18 hours |
| 147 | NUP358 NTD (R527A/K529A) | 1-752 I599M | pET28a-SUMO | BamHI, NotI | S | none | 18 °C, 18 hours |
| 148 | NUP358 NTD (R541E/K542E) | 1-752 I599M | pET28a-SUMO | BamHI, NotI | S | none | 18 °C, 18 hours |
| 149 | NUP358 NTD (R550E/R552E) | 1-752 I599M | pET28a-SUMO | BamHI, NotI | S | none | 18 °C, 18 hours |
| 150 | NUP358 NTD (R563) | 1-752 I599M | pET28a-SUMO | BamHI, NotI | S | none | 18 °C, 18 hours |
| 151 | NUP358 NTD (K567E) | 1-752 I599M | pET28a-SUMO | BamHI, NotI | S | none | 18 °C, 18 hours |
| 152 | NUP358 NTD (K584E) | 1-752 I599M | pET28a-SUMO | BamHI, NotI | S | none | 18 °C, 18 hours |
| 153 | NUP358 NTD (R596E) | 1-752 I599M | pET28a-SUMO | BamHI, NotI | S | none | 18 °C, 18 hours |
| 154 | NUP358 NTD (R601) | 1-752 I599M | pET28a-SUMO | BamHI, NotI | S | none | 18 °C, 18 hours |
| 155 | NUP358 NTD (K614E) | 1-752 I599M | pET28a-SUMO | BamHI, NotI | S | none | 18 °C, 18 hours |
| 156 | NUP358 NTD (K607E K608E) | 1-752 I599M | pET28a-SUMO | BamHI, NotI | S | none | 18 °C, 18 hours |
| 157 | NUP358 NTD (K617E/K618E/K619E) | 1-752 I599M | pET28a-SUMO | BamHI, NotI | S | none | 18 °C, 18 hours |
| 158 | NUP358 NTD (K631E) | 1-752 I599M | pET28a-SUMO | BamHI, NotI | S | none | 18 °C, 18 hours |
| 159 | NUP358 NTD (K675E) | 1-752 I599M | pET28a-SUMO | BamHI, NotI | S | none | 18 °C, 18 hours |
| 160 | NUP358 NTD (K690E) | 1-752 I599M | pET28a-SUMO | BamHI, NotI | S | none | 18 °C, 18 hours |
| 161 | NUP358 NTD (R689E/K690E) | 1-752 I599M | pET28a-SUMO | BamHI, NotI | S | none | 18 °C, 18 hours |
| 162 | NUP358 NTD (K708E) | 1-752 I599M | pET28a-SUMO | BamHI, NotI | S | none | 18 °C, 18 hours |
| 163 | NUP358 NTD (R712E) | 1-752 I599M | pET28a-SUMO | BamHI, NotI | S | none | 18 °C, 18 hours |
| 164 | NUP358 NTD (R715E) | 1-752 I599M | pET28a-SUMO | BamHI, NotI | S | none | 18 °C, 18 hours |
| 165 | NUP358 NTD (K713E/K720E) | 1-752 I599M | pET28a-SUMO | BamHI, NotI | S | none | 18 °C, 18 hours |
| 166 | NUP358 NTD (K720E) | 1-752 I599M | pET28a-SUMO | BamHI, NotI | S | none | 18 °C, 18 hours |
| 167 | NUP358 NTD (K733E K734E) | 1-752 I599M | pET28a-SUMO | BamHI, NotI | S | none | 18 °C, 18 hours |
| 168 | NUP358 NTD (K743E) | 1-752 I599M | pET28a-SUMO | BamHI, NotI | S | none | 18 °C, 18 hours |
| 169• | NUP358 NTD (D140M) | 1-752 I599M | pET28a-SUMO | BamHI, NotI | S | none | 18 °C, 18 hours |
| 170• | NUP358 NTD (D152M) | 1-752 I599M | pET28a-SUMO | BamHI, NotI | S | none | 18 °C, 18 hours |
| 171• | NUP358 NTD (I171M) | 1-752 I599M | pET28a-SUMO | BamHI, NotI | S | none | 18 °C, 18 hours |
| 172• | NUP358 NTD (I322M) | 1-752 I599M | pET28a-SUMO | BamHI, NotI | S | none | 18 °C, 18 hours |
| 173• | NUP358 NTD (I427M) | 1-752 I599M | pET28a-SUMO | BamHI, NotI | S | none | 18 °C, 18 hours |
| 174• | NUP358 NTD (I453M) | 1-752 I599M | pET28a-SUMO | BamHI, NotI | S | none | 18 °C, 18 hours |
| 175• | NUP358 NTD (I539M) | 1-752 I599M | pET28a-SUMO | BamHI, NotI | S | none | 18 °C, 18 hours |
| 176• | NUP358 NTD (I559M) | 1-752 I599M | pET28a-SUMO | BamHI, NotI | S | none | 18 °C, 18 hours |
| 177• | NUP358 NTD (I615M) | 1-752 I599M | pET28a-SUMO | BamHI, NotI | S | none | 18 °C, 18 hours |
| 178• | NUP358 NTD (I626M) | 1-752 I599M | pET28a-SUMO | BamHI, NotI | S | none | 18 °C, 18 hours |
| 179• | NUP358 NTD (I652M) | 1-752 I599M | pET28a-SUMO | BamHI, NotI | S | none | 18 °C, 18 hours |
| 180• | NUP358 NTD (L401M) | 1-752 I599M | pET28a-SUMO | BamHI, NotI | S | none | 18 °C, 18 hours |
| 181• | NUP358 NTD (D693M) | 1-752 I599M | pET28a-SUMO | BamHI, NotI | S | none | 18 °C, 18 hours |
| 182• | NUP358 NTD (N709M) | 1-752 I599M | pET28a-SUMO | BamHI, NotI | S | none | 18 °C, 18 hours |
| 183• | NUP358 NTD (Q137M) | 1-752 I599M | pET28a-SUMO | BamHI, NotI | S | none | 18 °C, 18 hours |
| 184• | NUP358 NTD (T92M) | 1-752 I599M | pET28a-SUMO | BamHI, NotI | S | none | 18 °C, 18 hours |
| 185• | NUP358 NTD (V668M) | 1-752 I599M | pET28a-SUMO | BamHI, NotI | S | none | 18 °C, 18 hours |
| 186* | NUP358 NTD ANE1 T585M | 1-752 I599M | pET28a-SUMO | BamHI, NotI | S | none | 18 °C, 18 hours |
| 187* | NUP358 NTD ANE1 T653I | 1-752 I599M | pET28a-SUMO | BamHI, NotI | S | none | 18 °C, 18 hours |
| 188* | NUP358 NTD ANE1 I656V | 1-752 I599M | pET28a-SUMO | BamHI, NotI | S | none | 18 °C, 18 hours |

| # | Protein | Residues | Expression vector | Restriction sites 5', 3' | N-terminal overhang | C-terminal overhang | Expression conditions |
|------|---|-------------------------------------|-------------------|---------------------------|--------------------------|---------------------|-----------------------|
| 189 | NUP358 NTD ANE1 W681C | 1-752 I599M | pET28a-SUMO | BamHI, NotI | S | none | 18 °C, 18 hours |
| 190• | NUP358 145-673 (I652M) | 145-673 I599M | pET28a-SUMO | BamHI, NotI | S | none | 18 °C, 18 hours |
| 191• | NUP358 145-673 (I615M) | 145-673 I599M | pET28a-SUMO | BamHI, NotI | S | none | 18 °C, 18 hours |
| 192• | NUP358 145-673 (L401M) | 145-673 I599M | pET28a-SUMO | BamHI, NotI | S | none | 18 °C, 18 hours |
| 193• | NUP358 145-673 (I169M) | 145-673 I599M | pET28a-SUMO | BamHI, NotI | S | none | 18 °C, 18 hours |
| 194• | NUP358 145-673 (L385M) | 145-673 I599M | pET28a-SUMO | BamHI, NotI | S | none | 18 °C, 18 hours |
| 195• | NUP358 145-673 (I372M) | 145-673 I599M | pET28a-SUMO | BamHI, NotI | S | none | 18 °C, 18 hours |
| 196 | NUP88 NTD (D10A/E12A) | 1-493 | pET28a-SUMO | BamHI, NotI | S | none | 18 °C, 18 hours |
| 197 | NUP88 NTD (E29A, E38A, E40A) | 1-493 | pET28a-SUMO | BamHI, NotI | S | none | 18 °C, 18 hours |
| 198 | NUP88 NTD (E236A, E272A, E275) | 1-493 | pET28a-SUMO | BamHI, NotI | S | none | 18 °C, 18 hours |
| 199 | NUP88 NTD (E304A/D305/ D310A) | 1-493 | pET28a-SUMO | BamHI, NotI | S | none | 18 °C, 18 hours |
| 200 | NUP88 NTD (E340A/E342A/E343/ E344A/ D345A/D346A) | 1-493 | pET28a-SUMO | BamHI, NotI | S | none | 18 °C, 18 hours |
| 201 | NUP88 NTD (E350A/E354A/E358A) | 1-493 | pET28a-SUMO | BamHI, NotI | S | none | 18 °C, 18 hours |
| 202 | NUP88 NTD (E381A/D382A/D383A) | 1-493 | pET28a-SUMO | BamHI, NotI | S | none | 18 °C, 18 hours |
| 203 | NUP88 NTD (D436A/E440A/E444A) | 1-493 | pET28a-SUMO | BamHI, NotI | S | none | 18 °C, 18 hours |
| 204 | NUP88 NTD (E216A/E218A/E219A/E220A) | 1-493 | pET28a-SUMO | BamHI, NotI | S | none | 18 °C, 18 hours |
| 205 | NUP88 NTD (E74A/E75A/E91A/E92A) | 1-493 | pET28a-SUMO | BamHI, NotI | S | none | 18 °C, 18 hours |
| 206 | NUP88 NTD (E329A/E370A/E372A) | 1-493 | pET28a-SUMO | BamHI, NotI | S | none | 18 °C, 18 hours |
| 207 | NUP88 NTD (D434Y) | 1-493 | pET28a-SUMO | BamHI, NotI | S | none | 18 °C, 18 hours |
| 208 | NUP88 NTD (D434A) | 1-493 | pET28a-SUMO | BamHI, NotI | S | none | 18 °C, 18 hours |
| 209 | NUP88 NTD (E433A) | 1-493 | pET28a-SUMO | BamHI, NotI | S | none | 18 °C, 18 hours |
| 210 | NUP88 NTD (E340A/E342A/E343A/E344A/ D345A/D346A/D431A/E432A/ E433A/D434A) | 1-493 | pET28a-SUMO | BamHI, NotI | S | none | 18 °C, 18 hours |
| 211 | NUP88 NTD (E340A/E342A/E343A) | 1-493 | pET28a-SUMO | BamHI, NotI | S | none | 18 °C, 18 hours |
| 212 | NUP88 NTD (E344A/D345A/D346A) | 1-493 | pET28a-SUMO | BamHI, NotI | S | none | 18 °C, 18 hours |
| 213 | NUP88 NTD (D431A/E432A) | 1-493 | pET28a-SUMO | BamHI, NotI | S | none | 18 °C, 18 hours |
| 214 | NUP88 NTD (E433A/D434A) | 1-493 | pET28a-SUMO | BamHI, NotI | S | none | 18 °C, 18 hours |
| 215 | NUP88 NTD (E343A/E344A) | 1-493 | pET28a-SUMO | BamHI, NotI | S | none | 18 °C, 18 hours |
| 216 | NUP88 NTD (E340A/E342A/E343A/E344A/ D345A/D346A/E433A/D434A) | 1-493 | pET28a-SUMO | BamHI, NotI | S | none | 18 °C, 18 hours |
| 217 | NUP88 NTD LLL | 1-493 L424A, L428A, L438A | pET28a-SUMO | BamHI, NotI | S | none | 18 °C, 18 hours |
| 218 | NUP88 NTD MNY | 1-493 M299A, N306A, Y307A | pET28a-SUMO | BamHI, NotI | S | none | 18 °C, 18 hours |
| 219 | NUP88 NTD EMNY | 1-493 E275A, M299A, N306A, Y307A | pET28a-SUMO | BamHI, NotI | S | none | 18 °C, 18 hours |
| 220 | NUP88 NTD ΔFGL loop | 1-493 Δ228-233 | pET28a-SUMO | BamHI, NotI | S | none | 18 °C, 18 hours |
| 221 | TAP P15 | 117-554 1-140 | pET-MCN-SUMO | BamHI, NotI NdeI, XhoI | S none | none none | 18 °C, 18 hours |
| 222* | RAN | 1-216 | pET28a-SUMO | BamHI, NotI | S | none | 18 °C, 18 hours |
| 223 | RAN Q69L | 1-216 Q69L | pET28a-SUMO | BamHI, NotI | S | none | 18 °C, 18 hours |
| 224* | RAN F35S | 1-216 | pET28a-SUMO | BamHI, NotI | S | none | 18 °C, 18 hours |
| 225* | Thrombin Ran F35 | 1-216 | pET28a | NdeI, NotI | MGSSHHHHHHSS GLVPRGSS | none | 18 °C, 18 hours |
| 226* | NUP50 RBD | 336-468 | pET28a-SUMO | BamHI, NotI | S | none | 18 °C, 18 hours |
| 227* | sAB14-LC sAB14-HC | 1-217 1-263 | pRH2.2 | HindIII, SalI | none | none | 37 °C, 2 hours |
| 228* | mNup153 ZnF1 | 649-687 | pGEX-6P1 | BamHI, NotI | GPLGS | none | 37 °C, 2 hours |
| 229* | mNup153 ZnF2 | 713-749 | pGEX-6P1 | BamHI, NotI | GPLGS | none | 37 °C, 2 hours |
| 230* | mNup153 ZnF3 | 781-817 | pGEX-6P1 | BamHI, NotI | GPLGS | none | 37 °C, 2 hours |
| 231* | mNup153 ZnF4 | 839-874 | pGEX-6P1 | BamHI, NotI | GPLGS | none | 37 °C, 2 hours |
| 232 | mNup153 ZnF1ΔNTE | 659-687 | pGEX-6P1 | BamHI, NotI | GPLGS | none | 37 °C, 2 hours |
| 233 | mNup153 ZnF2ΔNTE | 723-749 | pGEX-6P1 | BamHI, NotI | GPLGS | none | 37 °C, 2 hours |
| 234 | mNup153 ZnF3ΔNTE | 791-817 | pGEX-6P1 | BamHI, NotI | GPLGS | none | 37 °C, 2 hours |

| # | Protein | Residues | Expression vector | Restriction sites 5', 3' | N-terminal overhang | C-terminal overhang | Expression conditions |
|-----|-----------------------------|----------------------------|------------------------------|---|---------------------------------------|----------------------|-----------------------|
| 235 | mNup153 ZnF4ΔNTE | 848-874 | pGEX-6P1 | BamHI, NotI | GPLGS | none | 37 °C, 2 hours |
| 236 | Nup82 | 1-882 | pET28a-SUMO | BamHI, NotI | S | AAALEHHHHHH | 18 °C, 18 hours |
| 237 | Nup82 NTD | 1-595 | pET28a-PreS | NdeI, NotI | GPHM | none | 18 °C, 18 hours |
| 238 | Nup82 CCS1 | 661-784 | pET28a-SUMO | BamHI, XhoI | S | none | 18 °C, 18 hours |
| 239 | Nup82 CCS2-3 | 793-882 | pET28a-SUMO | BamHI, XhoI | S | none | 18 °C, 18 hours |
| 240 | Nup82 CCS1-3 | 661-882 | pET28a-SUMO | BamHI, XhoI | S | none | 18 °C, 18 hours |
| 241 | Nup159 CCS1-3 | 1109-1367 | pET28a-SUMO | BamHI, NotI | S | none | 18 °C, 18 hours |
| 242 | Nup159 NTD | 1-444 | pET28a-SUMO | BamHI, XhoI | S | none | 18 °C, 18 hours |
| 243 | Nup159 CCS1 | 1109-1259 | pET28a-SUMO | BamHI, XhoI | S | none | 18 °C, 18 hours |
| 244 | Nup159 CCS2-3 | 1262-1381 | pET28a-SUMO | BamHI, NotI | S | none | 18 °C, 18 hours |
| 245 | Nsp1 CCS1 | 467-557 | pET28a-SUMO | BamHI, XhoI | S | none | 18 °C, 18 hours |
| 246 | Nsp1 CCS2-3 | 569-674 | pET28a-SUMO | BamHI, XhoI | S | none | 18 °C, 18 hours |
| 247 | Nsp1 CCS1-3 | 467-678 | pET28a-SUMO | BamHI, XhoI | S | none | 18 °C, 18 hours |
| 248 | Nsp1 Nup159 | 467-678 1-456 1109-1481 | pETDuet1 | NcoI, NotI NdeI, XhoI | none M | none none | 18 °C, 18 hours |
| 249 | Nsp1 Nup82 CCS1-3 | 467-678 661-879 | pETDuet1 | NcoI, NotI NdeI, XhoI | none M | none none | 18 °C, 18 hours |
| 250 | Nsp1 Nup82ΔNTD | 467-678 661-879 | pETDuet1 | NcoI, NotI NdeI, XhoI | none M | none HHHHHH | 18 °C, 18 hours |
| 251 | Nsp1 Nup159ΔNTD | 467-678 1109-1367 | pETDuet-SUMO | BamHI, NotI NdeI/XhoI | M S | none none | 18 °C, 18 hours |
| 252 | Nup159 TAIL | 1440-1481 | pET28a-SUMO | BamHI, NotI | S | none | 18 °C, 18 hours |
| 253 | Nup159ΔTAIL | 1-456 1109-1367 | pET28a-SUMO | BamHI, NotI | S | AAALEHHHHHH | 18 °C, 18 hours |
| 254 | Nup145N GLEBS-APD | 171-221 868-994 | pET28a-SUMO | BamHI, NotI | S | none | 23 °C, 18 hours |
| 255 | Nup145N APD | 868-994 | pET28a-PreS | NdeI, XhoI | GPHM | none | 23 °C, 18 hours |
| 256 | Nup145N GLEBS | 171-221 | pET28a-SUMO | BamHI, NotI | S | none | 18 °C, 18 hours |
| 257 | Dbp5 | 1-477 | pET-MCN-SUMO | BamHI, NotI | S | none | 18 °C, 18 hours |
| 258 | Gle1 | 1-478 | pET28a-PreS | NdeI, NotI | GPHM | none | 37 °C, 3 hours |
| 259 | Gle1 CTD | 216-478 | pET28a-PreS | NdeI, NotI | GPHM | none | 37 °C, 3 hours |
| 260 | Gle1 NTD | 1-216 | pET28a-SUMO | BamHI, NotI | S | none | 18 °C, 18 hours |
| 261 | Nup42 GBM | 494-558 | pETDuet-PreS | NdeI, NotI | MGSSHHHHHSS GLEGGSGPSGS | None | 30 °C, 3 hours |
| 262 | Nup120 | 1-1262 | pET28a-SUMO | BamHI, NotI | S | none | 37 °C, 2 hours |
| 263 | Elys | 1-299 | pET-MCN-SUMO | BamHI, NotI | S | none | 37 °C, 2 hours |
| 264 | Nup37 | 1-751 | pET-MCN-SUMO | BamHI, NotI | S | none | 37 °C, 2 hours |
| 265 | Nup37 ΔCTE | 1-692 | pET-MCN-SUMO | BamHI, NotI | S | none | 37 °C, 2 hours |
| 266 | Nup120 Nup37 NTD ELYS | 1-1262 1-610 1-299 | pET-MCN-SUMO | NdeI, BamHI NdeI, BamHI BamHI, NotI | GPHMHHHHHH Q S | none none none | 37 °C, 2 hours |
| 267 | SUMO-Nup37 CTE | 693-751 | pET28a-SUMO | BamHI, NotI | S | none | 18 °C, 18 hours |
| 268 | AVI-SUMO-Nup37 CTE | 693-751 | pET28a-His-PreS- Avi-SUMO | BamHI, NotI | GPLMSGLNDIFEA QKIEWHEGSAGGS GHM | none | 18 °C, 18 hours |
| 269 | SUMO-Nup37 (723-751) | 723-751 | pET28a-SUMO | BamHI, NotI | S | none | 18 °C, 18 hours |
| 270 | SUMO-Nup37 (728-751) | 728-751 | pET28a-SUMO | BamHI, NotI | S | none | 18 °C, 18 hours |
| 271 | SUMO-Nup37 (693-746) | 693-746 | pET28a-SUMO | BamHI, NotI | S | none | 18 °C, 18 hours |
| 272 | SUMO-Nup37 (693-741) | 693-741 | pET28a-SUMO | BamHI, NotI | S | none | 18 °C, 18 hours |
| 273 | SUMO-Nup37 (693-736) | 693-736 | pET28a-SUMO | BamHI, NotI | S | none | 18 °C, 18 hours |
| 274 | Nup85 | 230-1169 | pET24a | NdeI, BamHI | MGHHHHHH | none | 37 °C, 2 hours |
| 275 | Nup85 NTE | 1-230 | pET28a-PreS | NdeI, BamHI | M | none | 18 °C, 18 hours |
| 276 | Nup84 | 1-939 | pET24a | NdeI, BamHI | MGHHHHHH | none | 18 °C, 18 hours |
| 277 | Nup133 | 1-1364 | pET-MCN-SUMO | BamHI, NotI | S | none | 18 °C, 18 hours |
| 278 | Nup133 ΔNTE | 105-1364 | pET-MCN-SUMO | BamHI, NotI | S | none | 18 °C, 18 hours |
| 279 | Nup133 NTE | 1-114 | pET28a-SUMO | BamHI, NotI | S | none | 18 °C, 18 hours |
| 280 | Sec13-Nup145C | 1-309 1-800 | pET-MCN-PreS | NdeI, NotI | GPHM | none | 30 °C, 3 hours |
| 281 | Sec13-Nup145C ΔNTE | 1-309 272-800 | pET-MCN-PreS | NdeI, NotI | GPHM | none | 30 °C, 3 hours |
| 282 | Nup145C NTE | 1-272 | pET28a-SUMO | BamHI, NotI | S | AAALEHHHHHH | 18 °C, 18 hours |
| 283 | AVI-SUMO-Nup145C NTE | 2-272 | pET28a-His-PreS- Avi-SUMO | BamHI, NotI | GPLMSGLNDIFEA QKIEWHEGSAGGS GHM | none | 18 °C, 18 hours |
| 284 | Nup49 | 246-470 | pET28a-SUMO | BamHI, NotI | S | none | 18 °C, 18 hours |
| 285 | Nsp1 Nup57 | 467-674 74-319 | pETDuet1 | NcoI, NotI NdeI, XhoI | none M | none none | 18 °C, 18 hours |
| 286 | Nic96 R1 | 139-180 | pET28a-SUMO | BamHI, NotI | S | none | 18 °C, 18 hours |

Constructs #8 (60), #9, #10, #11, #18, #258, and #260 (63), #27 (76), #52 (129), #237, #254, #257, #286, #287, and #288 (11), and #264, #265, #268, #276, #278, #279, and #280 (38) were previously reported.

* Constructs that were used for crystallization

Constructs that were used for sAB and MB selection

• Constructs that were used for ascertaining sequence register by Se-Met labeling

Table S3. Baculovirus/insect cell expression constructs and conditions

| # | Protein | Residues | Expression vector | Restriction sites 5', 3' | N-terminal overhang | C-terminal overhang | Expression conditions |
|-----|---------------------|------------------|-------------------|----------------------------|---------------------|---------------------|-----------------------|
| 287 | RAE1 | 1-368 | pFastBac-Dual | SmaI, KpnI | none | HHHHHHH | Described in methods |
| 288 | RAE1 NUP98 GLEBS | 1-368 157-213 | pFastBac-Dual | SmaI, KpnI BamHI, EcoRI | none | HHHHHHH | Described in methods |
| 289 | Gle2 | 1-357 | pFastBac-HTB | BamHI, XhoI | GAMGS | none | Described in methods |

Constructs #287 and #288 were reported previously in (57).

Table S4. Mammalian cell expression constructs

| Name | Protein | Residues (Mutations) | Vector | Restriction sites 5', 3' | N-terminal tag | C-terminal tag |
|-----------------|--------------|---|-------------------|--------------------------|----------------|----------------|
| WT | NUP358 | 1-3224 | pcDNA3.1-3×HA | BamHI, NotI | 3×HA | none |
| TPR | NUP358 | 1-145 | pcDNA3.1-3×HA | BamHI, NotI | 3×HA | none |
| NTD-ZFD | NUP358 | 1-1809 | pcDNA3.1-3×HA | BamHI, NotI | 3×HA | none |
| ΔNTD-ZFD | NUP358 | 1810-3224 | pcDNA3.1-3×HA | BamHI, NotI | 3×HA | none |
| NTD-RanBD-I | NUP358 | 1-1306 | pcDNA3.1-3×HA | BamHI, NotI | 3×HA | none |
| ΔNTD-RanBD-I | NUP358 | 1308-3224 | pcDNA3.1-3×HA | BamHI, NotI | 3×HA | none |
| NTD-OE | NUP358 | 1-832 | pcDNA3.1-3×HA | BamHI, NotI | 3×HA | none |
| ΔNTD-OE | NUP358 | 833-3224 | pcDNA3.1-3×HA | BamHI, NotI | 3×HA | none |
| NTD | NUP358 | 1-752 | pcDNA3.1-3×HA | BamHI, NotI | 3×HA | none |
| OE | NUP358 | 753-832 | pcDNA3.1-3×HA | BamHI, NotI | 3×HA | none |
| FL (LIQIML) | NUP358 | 1-3224 (L811A, I814A, Q817A, I828A, M825A, L828A) | pcDNA3.1-3×HA | BamHI, NotI | 3×HA | none |
| NTD-OE (LIQIML) | NUP358 | 1-832 (L811A, I814A, Q817A, I828A, M825A, L828A) | pcDNA3.1-3×HA | BamHI, NotI | 3×HA | none |
| FL (2R5K) | NUP358 | 1-3224 (K34A, K40A, R58A, K61A, R64A, K500A, K502A) | pcDNA3.1-3×HA | BamHI, NotI | 3×HA | none |
| NTD-OE (2R5K) | NUP358 | 1-832 (K34A, K40A, R58A, K61A, R64A, K500A, K502A) | pcDNA3.1-3×HA | BamHI, NotI | 3×HA | none |
| T585M | NUP358 | 1-3224 (T585M) | pcDNA3.1-3×HA | BamHI, NotI | 3×HA | none |
| T653I | NUP358 | 1-3224 (T653I) | pcDNA3.1-3×HA | BamHI, NotI | 3×HA | none |
| I656V | NUP358 | 1-3224 (I656V) | pcDNA3.1-3×HA | BamHI, NotI | 3×HA | none |
| W681C | NUP358 | 1-3224 (W681C) | pcDNA3.1-3×HA | BamHI, NotI | 3×HA | none |
| Insulin | Insulin | 1-110 | pcDNA3.1-3×C-FLAG | Kpn1/Kpn1 | none | 3×FLAG |
| ALPP | ALPP | 1-535 | pcDNA3.1-3×C-FLAG | Kpn1/Kpn1 | none | 3×FLAG |
| IL6 | IL6 | 1-184 | pcDNA3.1-3×C-FLAG | Kpn1/Kpn1 | none | 3×FLAG |
| IL10 | IL10 | 1-145 | pcDNA3.1-3×C-FLAG | Kpn1/Kpn1 | none | 3×FLAG |
| RPL26 | RPL26 | 1-145 | pcDNA3.1-3×C-FLAG | Kpn1/Kpn1 | none | 3×FLAG |
| GFP | GFP | 1-239 | pcDNA3.1-3×C-FLAG | Kpn1/Kpn1 | none | 3×FLAG |
| H1B | H1B | 1-219 | pcDNA3.1-3×C-FLAG | Kpn1/Kpn1 | none | 3×FLAG |
| TNF α | TNF α | 1-233 | pcDNA3.1-3×C-FLAG | Kpn1/Kpn1 | none | 3×FLAG |

3×HA: N-MYPYDVPDYAGGGYPYDVPDYAGGGYPYDVPDYA-C

3×FLAG: N-MDYKDHDGDYKDHDIDYKDDDDK-C

Table S5. Protein purification protocols

| Protein(s) | Expression constructs | Purification step | Buffer A | Buffer B |
|---------------------------------------|---------------------------|--|--|--|
| NUP62•NUP88•NUP214 | Co-expression (# 1 and 3) | 1. Ni-NTA 2. Dialysis/Cleavage 3. Mono Q 4. Superose 6 10/300 GL | 1. Ni-A1, 5 mM β -ME, 5% glycerol 2. IEX-A1, pH 8.0, 5 mM DTT, 5% glycerol / ULP1 3. IEX-A1, pH 8.0, 5 mM DTT, 5% glycerol 4. SEC-A, 5 mM DTT, 5% Glycerol | 1. Ni-B1, 5 mM β -ME, 5% glycerol 2. N/A 3. IEX-B1, pH 8.0, 5 mM DTT, 5% glycerol 4. N/A |
| NUP88 NTD Wild-type and mutants | Individual (#2, 196-220) | 1. Ni-NTA 2. HiPrep 26/20 Desalting/Cleavage 3. HiTrap Q HP 4. HiLoad Superdex 200 16/60 PG | 1. Ni-A1, 5 mM β -ME 2. IEX-A1, pH 8.0, 5 mM β -ME / ULP1 3. IEX-A1, pH 8.0, 1 mM DTT 4. SEC-A, 1 mM DTT | 1. Ni-B1, 5 mM β -ME 2. N/A 3. IEX-B1, pH 8.0, 1 mM DTT 4. N/A |
| NUP62•NUP88•NUP214 CCS1-3 | Co-expression (#4 and 5) | 1. Ni-NTA 2. HiPrep 26/20 Desalting 3. HiTrap Q HP 4. HiLoad Superdex 200 16/60 PG 5. Cleavage 6. MonoQ | 1. Ni-A1, 5 mM β -ME 2. IEX-A1, pH 8.0, 5 mM DTT 3. IEX-A1, pH 8.0, 5 mM DTT 4. SEC-A, 5 mM DTT 5. N/A 6. IEX-A1, pH 8.0, 5 mM DTT | 1. Ni-B1, 5 mM β -ME 2. N/A 3. IEX-B1, pH 8.0, 5 mM DTT 4. N/A 5. N/A 6. IEX-B1, pH 8.0, 5 mM DTT |
| NUP62•NUP88•AVI- NUP214 CCS1-3 | Co-expression (#4 and 6) | 1. Ni-NTA 2. HiPrep 26/20 Desalting 3. HiTrap Q HP 4. HiLoad Superdex 200 16/60 PG 5. Cleavage 6. MonoQ | 1. Ni-A1, 5 mM β -ME 2. IEX-A1, pH 8.0, 5 mM DTT 3. IEX-A1, pH 8.0, 5 mM DTT 4. SEC-A, 5 mM DTT 5. N/A 6. IEX-A1, pH 8.0, 5 mM DTT | 1. Ni-B1, 5 mM β -ME 2. N/A 3. IEX-B1, pH 8.0, 5 mM DTT 4. N/A 5. N/A 6. IEX-B1, pH 8.0, 5 mM DTT |
| NUP98 GLEBS-APD | Individual (#7) | 1. Ni-NTA 2. Dialysis/Cleavage 3. Ni-NTA 4. HiTrap Q HP 5. HiLoad Superdex 75 16/60 PG | 1. Ni-A1, 5 mM β -ME 2. IEX-A1, pH 8.0, 5 mM β -ME / Pres 3. Ni-A2, 5 mM β -ME 4. IEX-A1, pH 8.0, 5 mM DTT 5. SEC-A, 5 mM DTT | 1. Ni-B1, 5 mM β -ME 2. N/A 3. Ni-B1, 5 mM β -ME 4. IEX-B1, pH 8.0, 5 mM DTT 5. N/A |
| NUP98 APD | Individual (#8) | 1. Ni-NTA 2. Dialysis/Cleavage 3. Ni-NTA 4. HiTrap Q HP 5. HiLoad Superdex 75 16/60 PG | 1. Ni-A1, 5 mM β -ME 2. IEX-A1, pH 8.0, 5 mM β -ME / Pres 3. Ni-A2, 5 mM β -ME 4. IEX-A1, pH 8.0, 5 mM DTT 5. SEC-A, 5 mM DTT | 1. Ni-B1, 5 mM β -ME 2. N/A 3. Ni-B1, 5 mM β -ME 4. IEX-B1, pH 8.0, 5 mM DTT 5. N/A |
| DDX19 | Individual (#9) | 1. Ni-NTA 2. Dialysis/Cleavage 3. Ni-NTA 4. HiTrap Q HP 5. HiLoad Superdex 200 16/60 PG | 1. Ni-A1, 5 mM β -ME, 5% glycerol 2. IEX-A1, pH 8.0, 5 mM β -ME, 5% glycerol / Pres 3. Ni-A2, 5 mM β -ME, 5% glycerol 4. IEX-A1, pH 8.0, 5 mM DTT, 5% glycerol 5. SEC-A, 5 mM DTT, 5% glycerol | 1. Ni-B1, 5 mM β -ME, 5% glycerol 2. N/A 3. Ni-B1, 5 mM β -ME, 5% glycerol 4. IEX-B1, pH 8.0, 5 mM DTT, 5% Glycerol 5. N/A |
| DDX19 E243Q | Individual (#10) | 1. Ni-NTA 2. Dialysis/Cleavage 3. Ni-NTA 4. HiTrap Q HP 5. HiLoad Superdex 200 16/60 PG | 1. Ni-A1, 5 mM β -ME, 5% glycerol 2. IEX-A1, pH 8.0, 5 mM β -ME, 5% glycerol / Pres 3. Ni-A2, 5 mM β -ME, 5% glycerol 4. IEX-A1, pH 8.0, 5 mM DTT, 5% glycerol 5. SEC-A, 5 mM DTT, 5% glycerol | 1. Ni-B1, 5 mM β -ME, 5% glycerol 2. N/A 3. Ni-B1, 5 mM β -ME, 5% glycerol 4. IEX-B1, pH 8.0, 5 mM DTT, 5% Glycerol 5. N/A |
| GLE1 CTD•NUP42 GBM | Co-expression (#11) | 1. Ni-NTA 2. Dialysis/Cleavage 3. Ni-NTA 4. HiTrap Heparin HP 5. HiLoad Superdex 200 16/60 PG | 1. Ni-A1, 5 mM β -ME 2. IEX-A1, pH 8.0, 5 mM β -ME / Pres 3. Ni-A2, 5 mM β -ME 4. IEX-A1, pH 8.0, 5 mM DTT 5. SEC-A, 5 mM DTT | 1. Ni-B1, 5 mM β -ME 2. N/A 3. Ni-B1, 5 mM β -ME 4. IEX-B1, pH 8.0, 5 mM DTT 5. N/A |
| SUMO-NUP42 ZnF | Individual (#12) | 1. Ni-NTA 2. HiPrep 26/20 Desalting 3. HiTrap Q HP 4. HiLoad Superdex 75 16/60 PG | 1. Ni-A1, 5 mM β -ME 2. IEX-A1, pH 8.0, 5 mM DTT 3. IEX-A1, pH 8.0, 5 mM DTT 4. SEC-A, 5 mM DTT | 1. Ni-B1, 5 mM β -ME 2. N/A 3. IEX-B1, pH 8.0, 5 mM DTT 4. N/A |
| NUP214 NTD | Individual (#13) | 1. Ni-NTA 2. Dialysis/Cleavage 3. Ni-NTA 4. HiTrap Q HP 5. HiLoad Superdex 200 16/60 PG | 1. Ni-A1, 5 mM β -ME 2. IEX-A1, pH 8.0, 5 mM β -ME / Pres 3. Ni-A2, 5 mM β -ME 4. IEX-A1, pH 8.0, 5 mM DTT 5. SEC-A, 5 mM DTT | 1. Ni-B1, 5 mM β -ME 2. N/A 3. Ni-B1, 5 mM β -ME 4. IEX-B1, pH 8.0, 5 mM DTT 5. N/A |
| SUMO-NUP214TAIL WT and truncations | Individual (#14-17) | 1. Ni-NTA 2. HiPrep 26/20 Desalting 3. HiTrap SP HP 4. HiLoad Superdex 75 16/60 PG | 1. Ni-A1, 5 mM β -ME 2. IEX-A1, pH 8.0, 5 mM DTT 3. IEX-A1, pH 8.0, 5 mM DTT 4. SEC-A, 5 mM DTT | 1. Ni-B1, 5 mM β -ME 2. N/A 3. IEX-B1, pH 7.0, 5 mM DTT 4. N/A |
| NUP155 CTD | Individual (#18) | 1. Ni-NTA 2. HiPrep 26/20 Desalting/Cleavage 3. Ni-NTA 4. HiTrap Q HP 5. HiLoad Superdex 200 16/60 PG | 1. Ni-A1, 5 mM β -ME, 5% glycerol 2. IEX-A1, pH 8.0, 5 mM β -ME, 5% glycerol / Pres 3. Ni-A2, 5 mM β -ME, 5% glycerol 4. IEX-A1, pH 8.0, 5 mM DTT, 5% glycerol 5. SEC-B, 5 mM DTT, 5% glycerol | 1. Ni-B1, 5 mM β -ME, 5% glycerol 2. N/A 3. Ni-B1, 5 mM β -ME, 5% glycerol 4. IEX-B1, pH 8.0, 5 mM DTT, 5% Glycerol 5. N/A |
| NUP93 R1 Wildtype and mutants | Individual (#19-20) | 1. Ni-NTA 2. HiPrep 26/20 Desalting/Cleavage 3. HiTrap Q HP 4. HiLoad Superdex 200 16/60 PG | 1. Ni-A1, 5 mM β -ME 2. IEX-A1, pH 8.0, 5 mM DTT / ULP1 3. IEX-A1, pH 8.0, 5 mM DTT 4. SEC-C, 5 mM DTT | 1. Ni-B1, 5 mM β -ME 2. N/A 3. IEX-B1, pH 8.0, 5 mM DTT 4. N/A |
| SUMO-NUP93 R1 | Individual (#19) | 1. Ni-NTA 2. HiPrep 26/20 Desalting 3. HiTrap Q HP 4. HiLoad Superdex 200 16/60 PG | 1. Ni-A1, 5 mM β -ME 2. IEX-A1, pH 8.0, 5 mM DTT 3. IEX-A1, pH 8.0, 5 mM DTT 4. SEC-C, 5 mM DTT | 1. Ni-B1, 5 mM β -ME 2. N/A 3. IEX-B1, pH 8.0, 5 mM DTT 4. N/A |
| NUP358NTD Wild-type and mutants | Individual (#21, 53-189) | 1. Ni-NTA 2. HiPrep 26/20 Desalting/Cleavage 3. HiTrap Q HP 4. HiLoad Superdex 200 16/60 PG | 1. Ni-A1, 5 mM β -ME 2. IEX-A1, pH 8.0, 5 mM β -ME / ULP1 3. IEX-A1, pH 8.0, 1 mM DTT 4. SEC-A, 1 mM DTT | 1. Ni-B1, 5 mM β -ME 2. N/A 3. IEX-B1, pH 8.0, 1 mM DTT 4. N/A |
| NUP358 OE and OE LIQIML | Individual (#22, 23, 25) | 1. Ni-NTA 2. HiPrep 26/20 Desalting/Cleavage 3. Ni-NTA 4. HiTrap Q HP 5. HiLoad Superdex 200 16/60 PG | 1. Ni-A1, 5 mM β -ME 2. IEX-A1, pH 8.0, 5 mM β -ME / Pres 3. Ni-A2, 5 mM β -ME 4. IEX-A1, pH 8.0, 5 mM DTT 5. SEC-A, 5 mM DTT | 1. Ni-B1, 5 mM β -ME 2. N/A 3. Ni-B1, 5 mM β -ME 4. IEX-B1, pH 8.0, 5 mM DTT 5. N/A |

| Protein(s) | Expression constructs | Purification step | Buffer A | Buffer B |
|--------------------------------|-------------------------------|---|---|---|
| NUP358 NTD-OE | Individual (#24) | 1. Ni-NTA 2. HiPrep 26/20 Desalting/Cleavage 3. HiLoad Superdex 200 16/60 PG 4. HiLoad Superdex 200 16/60 PG | 1. Ni-A1, 5 mM β -ME 2. SEC-E, 5mM DTT / ULP1 3. SEC-E, 5mM DTT 4. SEC-E, 5mM DTT | 1. Ni-B1, 5 mM β -ME 2. N/A 3. N/A 4. N/A |
| NUP358 NTD-OE LIQIML mutant | Individual (#26) | 1. Ni-NTA 2. HiPrep 26/20 Desalting/Cleavage 3. HiTrap Q HP 4. HiLoad Superdex 200 16/60 PG | 1. Ni-A1, 5 mM β -ME 2. IEX-A1, pH 8.0, 5 mM β -ME / ULP1 3. IEX-A1, pH 8.0, 1 mM DTT 4. SEC-A, 1 mM DTT | 1. Ni-B1, 5 mM β -ME 2. N/A 3. IEX-B1, pH 8.0, 1 mM DTT 4. N/A |
| NUP358 TPR | Individual (#27) | 1. GST Affinity 2. Dialysis/Cleavage 3. GST Affinity 4. HiTrap Q HP 5. HiLoad Superdex 75 16/60 PG | 1. GST-A, 5 mM DTT 2. IEX-A1, pH 8.0, 5 mM DTT / Pres 3. IEX-A1, pH 8.0, 5 mM DTT 4. IEX-A1, pH 8.0, 5 mM DTT 5. SEC-A, 5 mM DTT | 1. GST-B, 5 mM DTT 2. N/A 3. GST-B, 5 mM DTT 4. IEX-B1, pH 8.0, 5 mM DTT 5. N/A |
| NUP358 NTD Δ TPR | Individual (#28) | 1. Ni-NTA 2. HiPrep 26/20 Desalting/Cleavage 3. HiTrap Q HP 4. HiLoad Superdex 200 16/60 PG | 1. Ni-A1, 5 mM β -ME 2. IEX-A1, pH 8.0, 5 mM β -ME / ULP1 3. IEX-A1, pH 8.0, 1 mM DTT 4. SEC-A, 1 mM DTT | 1. Ni-B1, 5 mM β -ME 2. N/A 3. IEX-B1, pH 8.0, 1 mM DTT 4. N/A |
| NUP358 1-673 | Individual (#29) | 1. Ni-NTA 2. HiPrep 26/20 Desalting/Cleavage 3. HiTrap Q HP 4. HiLoad Superdex 200 16/60 PG | 1. Ni-A1, 5 mM β -ME 2. IEX-A1, pH 8.0, 5 mM β -ME / ULP1 3. IEX-A1, pH 8.0, 1 mM DTT 4. SEC-A, 1 mM DTT | 1. Ni-B1, 5 mM β -ME 2. N/A 3. IEX-B1, pH 8.0, 1 mM DTT 4. N/A |
| NUP358 145-673 | Individual (#30, 190-195) | 1. Ni-NTA 2. HiPrep 26/20 Desalting/Cleavage 3. HiTrap Q HP 4. HiLoad Superdex 200 16/60 PG | 1. Ni-A1, 5 mM β -ME 2. IEX-A1, pH 8.0, 5 mM β -ME / ULP1 3. IEX-A1, pH 8.0, 1 mM DTT 4. SEC-A, 1 mM DTT | 1. Ni-B1, 5 mM β -ME 2. N/A 3. IEX-B1, pH 8.0, 1 mM DTT 4. N/A |
| AVI-NUP358 145-673 | Individual (#31) | 1. Ni-NTA 2. HiPrep 26/20 Desalting/Cleavage 3. HiTrap Q HP 4. HiLoad Superdex 200 16/60 PG | 1. Ni-A1, 5 mM β -ME 2. IEX-A1, pH 8.0, 5 mM β -ME / ULP1 3. IEX-A1, pH 8.0, 1 mM DTT 4. SEC-A, 1 mM DTT | 1. Ni-B1, 5 mM β -ME 2. N/A 3. IEX-B1, pH 8.0, 1 mM DTT 4. N/A |
| NUP358 RBD | Individual (#32-36) | 1. GST Affinity 2. Dialysis/Cleavage 3. GST Affinity 4. HiTrap Q HP 5. HiLoad Superdex 75 16/60 PG | 1. GST-A, 5 mM DTT 2. IEX-A1, pH 8.0, 5 mM DTT / Pres 3. IEX-A1, pH 8.0, 5 mM DTT 4. IEX-A1, pH 8.0, 5 mM DTT 5. SEC-A, 5 mM DTT | 1. GST-B, 5 mM DTT 2. N/A 3. GST-B, 5 mM DTT 4. IEX-B1, pH 8.0, 5 mM DTT 5. N/A |
| NUP358 ZnFs | Individual (#37-50) | 1. GST Affinity 2. Dialysis/Cleavage 3. GST Affinity 4. HiTrap Q HP 5. HiLoad Superdex 75 16/60 PG | 1. GST-A, 5 mM DTT 2. IEX-A1, pH 8.0, 5 mM DTT / Pres 3. IEX-A1, pH 8.0, 5 mM DTT 4. IEX-A1, pH 8.0, 5 mM DTT 5. SEC-A, 5 mM DTT | 1. GST-B, 5 mM DTT 2. N/A 3. GST-B, 5 mM DTT 4. IEX-B1, pH 8.0, 5 mM DTT 5. N/A |
| NUP358 ZFD | Individual (#51) | 1. GST Affinity 2. Dialysis/Cleavage 3. GST Affinity 4. HiTrap Q HP 5. HiLoad Superdex 200 16/60 PG | 1. GST-A, 5 mM DTT 2. IEX-A1, pH 8.0, 5 mM DTT / Pres 3. IEX-A1, pH 8.0, 5 mM DTT 4. IEX-A1, pH 8.0, 5 mM DTT 5. SEC-A, 5 mM DTT | 1. GST-B, 5 mM DTT 2. N/A 3. GST-B, 5 mM DTT 4. IEX-B1, pH 8.0, 5 mM DTT 5. N/A |
| NUP358 CTD | Individual (#52) | 1. Ni-NTA 2. HiPrep 26/20 Desalting/Cleavage 3. Ni-NTA 4. HiLoad Superdex 75 16/60 PG | 1. Ni-A1, 5 mM β -ME 2. IEX-A1, pH 8.0, 5 mM β -ME / Pres 3. Ni-A2, 5 mM β -ME 4. SEC-A, 5 mM DTT | 1. Ni-B1, 5 mM β -ME 2. N/A 3. Ni-B1, 5 mM β -ME 4. N/A |
| P15 TAP | Co-expression (# 221) | 1. Ni-NTA 2. HiPrep 26/20 Desalting/Cleavage 3. Ni-NTA 4. HiTrap Heparin 5. HiLoad Superdex 200 16/60 PG | 1. Ni-A1, 5 mM β -ME 2. IEX-A1, pH 8.0, 5 mM β -ME / ULP1 3. Ni-A2, 5 mM β -ME 4. IEX-A1, pH 8.0, 5 mM DTT 5. SEC-F, 5 mM DTT | 1. Ni-B1, 5 mM β -ME 2. N/A 3. Ni-B1, 5 mM β -ME 4. IEX-B1, pH 8.0, 5 mM DTT 5. N/A |
| Ran Wild-type and mutants | Individual (#222-224) | 1. Ni-NTA 2. HiPrep 26/20 Desalting/Cleavage 3. Ni-NTA 4. HiTrap Q HP 5. HiLoad Superdex 75 16/60 PG | 1. Ni-A1, 5 mM β -ME 2. IEX-A1, pH 8.0, 5 mM β -ME / ULP1 3. Ni-A2, 5 mM β -ME 4. IEX-A1, pH 8.0, 5 mM DTT 5. SEC-A, 5 mM DTT | 1. Ni-B1, 5 mM β -ME 2. N/A 3. Ni-B1, 5 mM β -ME 4. IEX-B1, pH 8.0, 5 mM DTT 5. N/A |
| Thrombin Ran F35S | Individual (#225) | 1. Ni-NTA 2. HiPrep 26/20 Desalting 3. HiTrap Q HP 4. HiLoad Superdex 200 16/60 PG | 1. Ni-A1, 5 mM β -ME 2. IEX-A1, pH 8.0, 5 mM β -ME 3. IEX-A1, pH 8.0, 1 mM DTT 4. SEC-A, 1 mM DTT | 1. Ni-B1, 5 mM β -ME 2. N/A 3. IEX-B1, pH 8.0, 1 mM DTT 4. N/A |
| NUP50 RanBD | Individual (#226) | 1. Ni-NTA 2. HiPrep 26/20 Desalting/Cleavage 3. Ni-NTA 4. HiTrap Q HP 5. HiLoad Superdex 75 16/60 PG | 1. Ni-A1, 5 mM β -ME 2. IEX-A1, pH 8.0, 5 mM β -ME / ULP1 3. Ni-A2, 5 mM β -ME 4. IEX-A1, pH 8.0, 5 mM DTT 5. SEC-A, 5 mM DTT | 1. Ni-B1, 5 mM β -ME 2. N/A 3. Ni-B1, 5 mM β -ME 4. IEX-B1, pH 8.0, 5 mM DTT 5. N/A |
| sAB14 | Individual (#227) | Detailed description in SI methods | | |
| mNUP153 ZnFs | Individual (#228-235) | 1. GST Affinity 2. Dialysis/Cleavage 3. GST Affinity 4. HiTrap Q HP 5. HiLoad Superdex 75 16/60 PG | 1. GST-A, 5 mM DTT 2. IEX-A1, pH 8.0, 5 mM DTT / Pres 3. IEX-A1, pH 8.0, 5 mM DTT 4. IEX-A1, pH 8.0, 5 mM DTT 5. SEC-A, 5 mM DTT | 1. GST-B, 5 mM DTT 2. N/A 3. GST-B, 5 mM DTT 4. IEX-B1, pH 8.0, 5 mM DTT 5. N/A |
| Nup82•Nsp1•Nup159 | Co-expression (#236 and 248) | 1. Ni-NTA 2. HiPrep 26/20 Desalting /Cleavage 3. MonoQ 10/100 GL 4. Superose 6 10/300 GL | 1. Ni-A3, 5 mM β -ME 2. IEX-A3, pH 8.0, 5 mM DTT / ULP1 3. IEX-A3, pH 8.0, 5 mM DTT 4. SEC-C, pH 8.0, 5 mM DTT | 1. Ni-B3, 5 mM β -ME 2. N/A 3. IEX-B2, pH 8.0, 5 mM DTT 4. N/A |
| Nup82•Nsp1•Nup159 Δ NTD | Co-expression (#236 and 251) | 1. Ni-NTA 2. HiPrep 26/20 Desalting /Cleavage 3. MonoQ 10/100 GL 4. Superose 6 10/300 GL | 1. Ni-A3, 5 mM β -ME 2. IEX-A3, pH 8.0, 5 mM DTT / ULP1 3. IEX-A3, pH 8.0, 5 mM DTT 4. SEC-C, pH 8.0, 5 mM DTT | 1. Ni-B3, 5 mM β -ME 2. N/A 3. IEX-B2, pH 8.0, 5 mM DTT 4. N/A |
| Nup82 NTD•Nup159 TAIL | Co-expression (# 237 and 252) | 1. Ni-NTA 2. Dialysis/Cleavage 3. Ni-NTA 4. MonoQ 10/100 GL 5. HiLoad Superdex 200 16/60 PG | 1. Ni-A3, 5 mM β -ME 2. Ni-A4, 5 mM β -ME / ULP1 / PreS 3. Ni-A4, 5 mM β -ME 4. IEX-A2, pH 8.0, 5 mM DTT 5. SEC-C, pH 8.0, 5 mM DTT | 1. Ni-B3, 5 mM β -ME 2. N/A 3. Ni-B3, 5 mM β -ME 4. IEX-B2, pH 8.0, 5 mM DTT 5. N/A |

| Protein(s) | Expression constructs | Purification step | Buffer A | Buffer B |
|--|---|---|---|---|
| Nup82•Nup159•Nsp1 CCS1 | Co-lysis (#238, 243, and 245) | 1. Ni-NTA 2. Desalting/Cleavage 3. Ni-NTA 4. HiTrap Q HP 5. HiLoad Superdex 200 16/60 PG | 1. Ni-A3, 5 mM β-ME 2. Ni-A4, 5 mM β-ME / ULP1 3. Ni-A4, 5 mM β-ME 4. IEX-A2, pH 8.0, 5 mM DTT 5. SEC-C, pH 8.0, 5 mM DTT | 1. Ni-B3, 5 mM β-ME 2. N/A 3. Ni-B3, 5 mM β-ME 4. IEX-B2, pH 8.0, 5 mM DTT 5. N/A |
| Nup82•Nup159•Nsp1 CCS2-3 | Co-lysis (#239, 244, and 246) | 1. Ni-NTA 2. HiPrep 26/20 Desalting/Cleavage 3. Ni-NTA 4. HiTrap S HP 5. HiLoad Superdex 200 16/60 PG | 1. Ni-A3, 5 mM β-ME 2. Ni-A4, 5 mM β-ME / ULP1 3. Ni-A4, 5 mM β-ME 4. IEX-A2, pH 8.0, 5 mM DTT 5. SEC-C, pH 8.0, 5 mM DTT | 1. Ni-B3, 5 mM β-ME 2. N/A 3. Ni-B3, 5 mM β-ME 4. IEX-B2, pH 8.0, 5 mM DTT 5. N/A |
| Nup82•Nsp1•Nup159 CFNC-hub | Co-expression (#241 and 249) | 1. Ni-NTA 2. HiPrep 26/20 Desalting/Cleavage 3. HiTrap Q HP 4. HiLoad Superdex 200 16/60 PG | 1. Ni-A3, 5 mM β-ME 2. IEX-A3, pH 8.0, 5 mM DTT / ULP1 3. IEX-A3, pH 8.0, 5 mM DTT 4. SEC-C, pH 8.0, 5 mM DTT | 1. Ni-B3, 5 mM β-ME 2. N/A 3. IEX-B2, pH 8.0, 5 mM DTT 4. N/A |
| Nup159 NTD | Individual (#242) | 1. Ni-NTA 2. HiPrep 26/20 Desalting/Cleavage 3. Ni-NTA 4. HiTrap Q HP 5. HiLoad Superdex 200 16/60 PG | 1. Ni-A3, 5 mM β-ME 2. Ni-A4, 5 mM β-ME / ULP1 3. Ni-A4, 5 mM β-ME 4. IEX-A2, pH 8.0, 5 mM DTT 5. SEC-C, pH 8.0, 5 mM DTT | 1. Ni-B3, 5 mM β-ME 2. N/A 3. Ni-B3, 5 mM β-ME 4. IEX-B2, pH 8.0, 5 mM DTT 5. N/A |
| Nup82ΔNTD•Nsp1•Nup159ATAIL | Co-expression (#250 and 253) | 1. Ni-NTA 2. HiPrep 26/20 Desalting/Cleavage 3. MonoQ 10/100 GL 4. Superose 6 10/300 GL | 1. Ni-A3, 5 mM β-ME 2. IEX-A3, pH 8.0, 5 mM DTT / ULP1 3. IEX-A3, pH 8.0, 5 mM DTT 4. SEC-C, pH 8.0, 5 mM DTT | 1. Ni-B3, 5 mM β-ME 2. N/A 3. IEX-B2, pH 8.0, 5 mM DTT 4. N/A |
| Nup145N GLEBS-APD | Individual (#254) | 1. Ni-NTA 2. HiPrep 26/20 Desalting/Cleavage 3. Ni-NTA 4. HiTrap SP HP 5. HiLoad Superdex 200 16/60 PG | 1. Ni-A3, 5 mM β-ME 2. Ni-A4, 5 mM β-ME / ULP1 3. Ni-A4, 5 mM β-ME 4. IEX-A2, pH 6.5, 5 mM DTT 5. SEC-C, pH 8.0, 5 mM DTT | 1. Ni-B3, 5 mM β-ME 2. N/A 3. Ni-B3, 5 mM β-ME 4. IEX-B2, pH 6.5, 5 mM DTT 5. N/A |
| Nup145N APD | Individual (#255) | 1. Ni-NTA 2. Dialysis/Cleavage 3. Ni-NTA 4. HiTrap SP HP 5. HiLoad Superdex 200 16/60 PG | 1. Ni-A3, 5 mM β-ME 2. Ni-A4, 5 mM β-ME / PreS 3. Ni-A4, 5 mM β-ME 4. IEX-A2, pH 6.5, 5 mM DTT 5. SEC-C, pH 8.0, 5 mM DTT | 1. Ni-B3, 5 mM β-ME 2. N/A 3. Ni-B3, 5 mM β-ME 4. IEX-B2, pH 6.5, 5 mM DTT 5. N/A |
| Nup145N GLEBS | Individual (#256) | 1. Ni-NTA 2. HiPrep 26/20 Desalting/Cleavage 3. Ni-NTA 4. HiTrap Q HP 5. HiLoad Superdex 200 16/60 PG | 1. Ni-A3, 5 mM β-ME 2. Ni-A4, 5 mM β-ME / ULP1 3. Ni-A4, 5 mM β-ME 4. IEX-A2, pH 8.0, 5 mM DTT 5. SEC-C, pH 8.0, 5 mM DTT | 1. Ni-B3, 5 mM β-ME 2. N/A 3. Ni-B3, 5 mM β-ME 4. IEX-B2, pH 8.0, 5 mM DTT 5. N/A |
| Dbp5 | Individual (#257) | 1. Ni-NTA 2. HiPrep 26/20 Desalting/Cleavage 3. HiTrap Q HP 4. HiLoad Superdex 200 16/60 PG | 1. Ni-A3, 5 mM β-ME 2. IEX-A2, pH 8.0, 5 mM DTT / ULP1 3. IEX-A2, pH 8.0, 5 mM DTT 4. SEC-C, pH 8.0, 5 mM DTT | 1. Ni-B3, 5 mM β-ME 2. N/A 3. IEX-B2, pH 8.0, 5 mM DTT 4. N/A |
| Gle1•Nup42 GBM | Co-expression (#258 and 261) | 1. Ni-NTA 2. Dialysis/Cleavage 3. HiTrap SP HP 4. HiLoad Superdex 200 16/60 PG | 1. Ni-A3, 5 mM β-ME 2. IEX-A3, pH 8.0, 5 mM DTT / ULP1 3. IEX-A3, pH 6.5, 5 mM DTT 4. SEC-C, pH 8.0, 5 mM DTT | 1. Ni-B3, 5 mM β-ME 2. N/A 3. IEX-B2, pH 8.0, 5 mM DTT 4. N/A |
| Gle1 CTD•Nup42 GBM | Co-expression (#259 and 261) | 1. Ni-NTA 2. Dialysis/Cleavage 3. HiTrap SP HP 4. HiLoad Superdex 200 16/60 PG | 1. Ni-A3, 5 mM β-ME 2. IEX-A3, pH 8.0, 5 mM DTT / ULP1 3. IEX-A3, pH 6.5, 5 mM DTT 4. SEC-C, pH 8.0, 5 mM DTT | 1. Ni-B3, 5 mM β-ME 2. N/A 3. IEX-B2, pH 8.0, 5 mM DTT 4. N/A |
| Gle1 NTD | Individual (# 260) | 1. Ni-NTA 2. HiPrep 26/20 Desalting/Cleavage 3. HiTrap Q HP 4. HiLoad Superdex 200 16/60 PG | 1. Ni-A3, 5 mM β-ME 2. IEX-A2, pH 8.0, 5 mM DTT / ULP1 3. IEX-A2, pH 8.0, 5 mM DTT 4. SEC-C, pH 8.0, 5 mM DTT | 1. Ni-B3, 5 mM β-ME 2. N/A 3. IEX-B2, pH 8.0, 5 mM DTT 4. N/A |
| Nup120 Nup37 Elys Nup85 | Co-expression (# 262 and 264) co-lysis with (# 263 and 274) | 1. Ni-NTA 2. Dialysis/Cleavage 3. HiTrap Q HP 4. HiLoad Superdex 200 16/60 PG | 1. Ni-A3, 5 mM β-ME 2. IEX-A4, pH 8.0, 5 mM DTT / ULP1 3. IEX-A4, pH 8.0, 5 mM DTT 4. SEC-D, 5 mM DTT | 1. Ni-B1, 5 mM β-ME, 5 % glycerol 2. N/A 3. IEX-B2, pH 8.0, 5 mM DTT 4. N/A |
| Nup120 Nup37ΔCTE Elys Nup85 | Co-expression (# 266 and 274) | 1. Ni-NTA 2. Dialysis/Cleavage 3. HiTrap Q HP 4. HiLoad Superdex 200 16/60 PG | 1. Ni-A3, 5 mM β-ME 2. IEX-A4, pH 8.0, 5 mM DTT / ULP1 3. IEX-A4, pH 8.0, 5 mM DTT 4. SEC-D, 5 mM DTT | 1. Ni-B1, 5 mM β-ME, 5 % glycerol 2. N/A 3. IEX-B2, pH 8.0, 5 mM DTT 4. N/A |
| Nup37 | Individual (#264) | 1. Ni-NTA 2. HiPrep 26/20 Desalting/Cleavage 3. Ni-NTA 4. MonoQ 10/100 GL 5. HiLoad Superdex 200 16/60 PG | 1. Ni-A3, 5 mM β-ME 2. Ni-A4, 5 mM β-ME / ULP1 3. Ni-A4, 5 mM β-ME 4. IEX-A2, pH 8.0, 5 mM DTT 5. SEC-C, pH 8.0, 5 mM DTT | 1. Ni-B3, 5 mM β-ME 2. N/A 3. Ni-B3, 5 mM β-ME 4. IEX-B2, pH 8.0, 5 mM DTT 5. N/A |
| Nup37ΔCTE | Individual (#265) | 1. Ni-NTA 2. HiPrep 26/20 Desalting/Cleavage 3. Ni-NTA 4. MonoQ 10/100 GL 5. HiLoad Superdex 200 16/60 PG | 1. Ni-A3, 5 mM β-ME 2. Ni-A4, 5 mM β-ME / ULP1 3. Ni-A4, 5 mM β-ME 4. IEX-A2, pH 8.0, 5 mM DTT 5. SEC-C, pH 8.0, 5 mM DTT | 1. Ni-B3, 5 mM β-ME 2. N/A 3. Ni-B3, 5 mM β-ME 4. IEX-B2, pH 8.0, 5 mM DTT 5. N/A |
| SUMO-Nup37 CTE wildtype and truncation | Individual (#267, 269-273) | 1. Ni-NTA 2. Dialysis 3. HiTrap Q HP 4. HiLoad Superdex 75 16/60 PG | 1. Ni-A3, 5 mM β-ME 2. Ni-A4, 5 mM β-ME 3. IEX-A2, pH 8.0, 5 mM DTT 4. SEC-C, pH 8.0, 5 mM DTT | 1. Ni-B3, 5 mM β-ME 2. N/A 3. IEX-B2, pH 8.0, 5 mM DTT 4. N/A |
| AVI-SUMO-Nup37 CTE | Individual (#268) | 1. Ni-NTA 2. HiPrep 26/20 Desalting 3. HiTrap Q HP 4. HiLoad Superdex 75 16/60 PG | 1. Ni-A3, 5 mM β-ME 2. Ni-A4, 5 mM β-ME 3. IEX-A2, pH 8.0, 5 mM DTT 4. SEC-C, pH 8.0, 5 mM DTT | 1. Ni-B3, 5 mM β-ME 2. N/A 3. IEX-B2, pH 8.0, 5 mM DTT 4. N/A |

| Protein(s) | Expression constructs | Purification step | Buffer A | Buffer B |
|----------------------------|-------------------------------|---|---|---|
| Nup85 NTE | Individual (#275) | 1. Ni-NTA 2. Dialysis/Cleavage 3. Ni-NTA 4. HiTrap Q HP 5. HiLoad Superdex 200 16/60 PG | 1. Ni-A3, 5 mM β -ME 2. Ni-A4, 5 mM β -ME / PreS 3. Ni-A4, 5 mM β -ME 4. IEX-A2, pH 8.0, 5 mM DTT 5. SEC-C, pH 8.0, 5 mM DTT | 1. Ni-B3, 5 mM β -ME 2. N/A 3. Ni-B3, 5 mM β -ME 4. IEX-B2, pH 8.0, 5 mM DTT 5. N/A |
| Nup84•Nup133 | Co-expression (#276-277) | 1. Ni-NTA 2. HiPrep 26/20 Desalting/Cleavage 3. MonoQ 10/100 GL 4. HiLoad Superdex 200 16/60 PG | 1. Ni-A3, 5 mM β -ME 2. IEX-A3, pH 8.0, 5 mM DTT / ULP1 3. IEX-A3, pH 8.0, 5 mM DTT 4. SEC-D, pH 8.0, 5 mM DTT | 1. Ni-B3, 5 mM β -ME 2. N/A 3. IEX-B2, pH 8.0, 5 mM DTT 4. N/A |
| Nup84•Nup133 Δ NTE | Co-expression (#276 and 278) | 1. Ni-NTA 2. HiPrep 26/20 Desalting/Cleavage 3. MonoQ 10/100 GL 4. HiLoad Superdex 200 16/60 PG | 1. Ni-A3, 5 mM β -ME 2. IEX-A3, pH 8.0, 5 mM DTT / ULP1 3. IEX-A3, pH 8.0, 5 mM DTT 4. SEC-D, pH 8.0, 5 mM DTT | 1. Ni-B3, 5 mM β -ME 2. N/A 3. IEX-B2, pH 8.0, 5 mM DTT 4. N/A |
| Nup133 NTE | Individual (#279) | 1. Ni-NTA 2. Dialysis/Cleavage 3. Ni-NTA 4. HiTrap SP HP 5. HiLoad Superdex 75 16/60 PG | 1. Ni-A3, 5 mM β -ME 2. Ni-A4, 5 mM β -ME / PreS 3. Ni-A4, 5 mM β -ME 4. IEX-A2, pH 6.5, 5 mM DTT 5. SEC-C, pH 8.0, 5 mM DTT | 1. Ni-B3, 5 mM β -ME 2. N/A 3. Ni-B3, 5 mM β -ME 4. IEX-B2, pH 6.5, 5 mM DTT 5. N/A |
| Sec13-Nup145C | Individual (#280) | 1. Ni-NTA 2. Dialysis/Cleavage 3. Ni-NTA 4. MonoQ 10/100 GL 5. HiLoad Superdex 200 16/60 PG | 1. Ni-A3, 5 mM β -ME 2. Ni-A4, 5 mM β -ME / PreS 3. Ni-A4, 5 mM β -ME 4. IEX-A2, pH 8.0, 5 mM DTT 5. SEC-C, pH 8.0, 5 mM DTT | 1. Ni-B3, 5 mM β -ME 2. N/A 3. Ni-B3, 5 mM β -ME 4. IEX-B2, pH 8.0, 5 mM DTT 5. N/A |
| Sec13-Nup145C Δ NTE | Individual (#281) | 1. Ni-NTA 2. Dialysis/Cleavage 3. Ni-NTA 4. MonoQ 10/100 GL 5. HiLoad Superdex 200 16/60 PG | 1. Ni-A3, 5 mM β -ME 2. Ni-A4, 5 mM β -ME / PreS 3. Ni-A4, 5 mM β -ME 4. IEX-A2, pH 8.0, 5 mM DTT 5. SEC-C, pH 8.0, 5 mM DTT | 1. Ni-B3, 5 mM β -ME 2. N/A 3. Ni-B3, 5 mM β -ME 4. IEX-B2, pH 8.0, 5 mM DTT 5. N/A |
| Nup145C NTE | Individual (#282) | 1. Ni-NTA 2. HiPrep 26/20 Desalting/Cleavage 3. HiTrap Q HP 4. Ni-NTA 5. HiLoad Superdex 200 16/60 PG | 1. Ni-A3, 5 mM β -ME 2. Ni-A4, 5 mM β -ME / ULP1 3. IEX-A2, pH 8.0, 5 mM β -ME 4. IEX-A2, pH 8.0, 5 mM β -ME 5. SEC-C, pH 8.0, 5 mM DTT | 1. Ni-B3, 5 mM β -ME 2. N/A 3. IEX-B2, pH 8.0, 5 mM DTT 4. Ni-B3, 5 mM β -ME 5. N/A |
| AVI-SUMO-Nup145C NTE | Individual (#283) | 1. Ni-NTA 2. HiPrep 26/20 Desalting 3. HiTrap Q HP 5. HiLoad Superdex 200 16/60 PG | 1. Ni-A3, 5 mM β -ME 2. IEX-A2, pH 8.0, 5 mM β -ME 3. IEX-A2, pH 8.0, 5 mM β -ME 5. SEC-C, pH 8.0, 5 mM DTT | 1. Ni-B3, 5 mM β -ME 2. N/A 3. IEX-B2, pH 8.0, 5 mM DTT 5. N/A |
| Nup49•Nup57•Nsp1 | Co-expression (# 284 and 285) | 1. Ni-NTA 2. HiPrep 26/20 Desalting/Cleavage 3. Ni-NTA 4. MonoQ 10/100 GL 5. HiLoad Superdex 200 16/60 PG | 1. Ni-A3, 5 mM β -ME 2. HiPrep 26/20 Desalting / ULP1 3. Ni-A3, 5 mM β -ME 4. IEX-A2, pH 8.0, 5 mM DTT 5. SEC-C, pH 8.0, 5 mM DTT | 1. Ni-B3, 5 mM β -ME 2. N/A 3. Ni-B3, 5 mM β -ME 4. IEX-B2, pH 8.0, 5 mM DTT 5. N/A |
| Nic96 R1 | Individual (#286) | 1. Ni-NTA 2. HiPrep 26/20 Desalting 3. HiTrap Q HP 4. HiLoad Superdex 75 16/60 PG | 1. Ni-A3, 5 mM β -ME 2. IEX-A3, pH 8.0, 5 mM DTT 3. IEX-A3, pH 8.0, 5 mM DTT 4. SEC-C, 5 mM DTT | 1. Ni-B3, 5 mM β -ME 2. N/A 3. IEX-B2, pH 8.0, 5 mM DTT 4. N/A |
| RAE1 | Individual (#287) | 1. Ni-NTA 2. Dialysis/Cleavage 3. HiTrap SP HP 4. HiLoad Superdex 75 16/60 PG | 1. Ni-A1, 5 mM β -ME 2. IEX-A3, pH 8.0, 5 mM DTT/TEV 3. IEX-A3, pH 6.5, 5 mM DTT 4. SEC-D, 5 mM DTT | 1. Ni-B1, 5 mM β -ME 2. N/A 3. IEX-B1, pH 6.50, 5 mM DTT 4. N/A |
| RAE1•NUP98GLEBS | Co-expression (#288) | 1. Ni-NTA 2. Dialysis/Cleavage 3. HiTrap SP HP 4. HiLoad Superdex 75 16/60 PG | 1. Ni-A1, 5 mM β -ME 2. IEX-A3, pH 8.0, 5 mM DTT/TEV 3. IEX-A3, pH 6.5, 5 mM DTT 4. SEC-D, 5 mM DTT | 1. Ni-B1, 5 mM β -ME 2. N/A 3. IEX-B1, pH 6.5, 5 mM DTT 4. N/A |
| Gle2 | Individual (#289) | 1. Ni-NTA 2. Dialysis/Cleavage 3. HiTrap SP HP 4. HiLoad Superdex 75 16/60 PG | 1. Ni-A1, 5 mM β -ME 2. IEX-A3, pH 8.0, 5 mM DTT/TEV 3. IEX-A3, pH 6.5, 5 mM DTT 4. SEC-D, 5 mM DTT | 1. Ni-B1, 5 mM β -ME 2. N/A 3. IEX-B1, pH 6.50, 5 mM DTT 4. N/A |

Ni-A1: 20 mM TRIS (pH 8.0), 500 mM NaCl, 20 mM imidazole
 Ni-A2: 20 mM TRIS (pH 8.0), 100 mM NaCl, 20 mM imidazole
 Ni-A3: 20 mM TRIS (pH 8.0), 500 mM NaCl, 20 mM imidazole, 5% (v/v) glycerol
 Ni-A4: 20 mM TRIS (pH 8.0), 100 mM NaCl, 20 mM imidazole, 5% (v/v) glycerol
 Ni-B1: 20 mM TRIS (pH 8.0), 500 mM NaCl, 500 mM imidazole
 Ni-B2: 20 mM TRIS (pH 8.0), 100 mM NaCl, 500 mM imidazole
 Ni-B3: 20 mM TRIS (pH 8.0), 500 mM NaCl, 500 mM imidazole, 5% (v/v) glycerol
 GST-A: 20 mM TRIS (pH 8.0), 300 mM NaCl
 GST-B: 20 mM TRIS (pH 8.0), 300 mM NaCl, 20 mM glutathione
 IEX-A1: 20 mM TRIS (pH 8.0), 100 mM NaCl
 IEX-A2: 20 mM TRIS (pH 8.0), 100 mM NaCl, 5% (v/v) glycerol
 IEX-A3: 20 mM TRIS (pH 8.0), 150 mM NaCl, 5% (v/v) glycerol
 IEX-A4: 20 mM TRIS (pH 8.0), 200 mM NaCl, 5% (v/v) glycerol
 IEX-B1: 20 mM TRIS, 2.0 M NaCl
 IEX-B2: 20 mM TRIS, 2.0 M NaCl, 5% (v/v) glycerol
 SEC-A: 20 mM TRIS (pH 8.0), 100 mM NaCl
 SEC-B: 20 mM TRIS (pH 8.0), 200 mM NaCl
 SEC-C: 20 mM TRIS (pH 8.0), 100 mM NaCl, 5% (v/v) glycerol
 SEC-D: 20 mM TRIS (pH 8.0), 200 mM NaCl, 5% (v/v) glycerol
 SEC-E: 20 mM TRIS (pH 8.0), 350 mM NaCl
 SEC-F: 20 mM TRIS (pH 8.0), 150 mM NaCl

Table S6. SEC-MALS analysis

| Figure(s) | Nucleoporin or nucleoporin complex | Experimental mass (kDa) | Theoretical mass (kDa) | Stoichiometry | Buffer |
|----------------------|---|-------------------------------------|------------------------------|--|---------------------------------|
| Fig. 1D Fig. S4A | Nup82•Nup159•Nsp1 Gle2•Nup145N GLEBS-APD Dbp5 Preincubation | 202 60 47 283 | 211 62 53 326 | equimolar equimolar n/a equimolar | SEC-A |
| Fig. 1E Fig. S20A | Nup82•Nup159•Nsp1•Dbp5•Nup145N•Gle2 (CFNC) Gle1•Nup42 GBM +IP ₆ Preincubation | 258 62 275 | 326 68 394 | equimolar equimolar equimolar | SEC-A 200 μM IP ₆ |
| Fig. 1F Fig. S23A | Nup82•Nup159•Nsp1•Dbp5•Nup145N•Gle2 (CFNC) Nup120•Nup37•Elys•Nup85•Sec13•Nup145C•Nup84•Nup133ΔNTE(CNC) Gle1•Nup42 GBM +IP ₆ Preincubation | 255 791 63 1163 | 326 730 68 1124 | equimolar equimolar equimolar equimolar | SEC-A 200 μM IP ₆ |
| Fig. S4B | Nup82ΔNTD•Nup159ΔTAIL•Nsp1 Dbp5 Preincubation | 119 51 153 | 125 52 177 | equimolar n/a equimolar | SEC-A |
| Fig. S4C | Nup82•Nup159ΔNTD•Nsp1 Dbp5 Preincubation | 141 51 137 | 150 52 202 | equimolar n/a no interaction | SEC-A |
| Fig. S4D | Nup82•Nup159ΔNTD•Nsp1 Gle2•Nup145N GLEBS-APD Preincubation | 141 60 182 | 150 62 212 | equimolar equimolar equimolar | SEC-A |
| Fig. S4E | Nup82ΔNTD•Nup159ΔTAIL•Nsp1 Gle2•Nup145N GLEBS-APD Preincubation | 119 60 121 | 125 62 187 | equimolar equimolar no interaction | SEC-A |
| Fig. S5A | Nup82•Nup159•Nsp1 (CFNC-hub) Nup159 NTD•Dbp5 Preincubation | 81 80 75 | 77 100 177 | equimolar equimolar no interaction | SEC-A |
| Fig. S5B | Nup82•Nup159•Nsp1 (CFNC-hub) Gle2•Nup145N GLEBS Preincubation | 81 38 76 | 77 47 124 | equimolar equimolar no interaction | SEC-A |
| Fig. S5C | Nup82•Nup159•Nsp1 (CFNC-hub) Nup82 NTD•Nup145N APD•Nup159 TAIL Preincubation | 81 57 75 | 77 85 162 | equimolar equimolar no interaction | SEC-A |
| Fig. S5D | Nup82•Nup159•Nsp1 (CFNC-hub) Nup159 NTD•Dbp5 Nup82 NTD•Nup145N APD•Nup159 TAIL Gle2•Nup145N GLEBS Preincubation | 80 82 61 43 79/80/60/40 | 77 100 85 47 309 | equimolar equimolar equimolar equimolar no interaction | SEC-A |
| Fig. S8A | Nup82•Nup159•Nsp1•Dbp5•Nup145N•Gle2 (CFNC) Nup120•Nup37•Elys•Nup85•Sec13•Nup145C•Nup84•Nup133ΔNTE Preincubation | 275 734 1016 | 326 730 1056 | equimolar equimolar equimolar | SEC-A |
| Fig. S8B | Nup159 NTD•Dbp5 Nup120•Nup37•Elys•Nup85•Sec13•Nup145C•Nup84•Nup133ΔNTE Preincubation | 88 765 762 | 100 730 830 | equimolar equimolar no interaction | SEC-A |
| Fig. S8C | Gle2•Nup145N GLEBS Nup120•Nup37•Elys•Nup85•Sec13•Nup145C•Nup84•Nup133ΔNTE Preincubation | 42 765 779 | 47 730 777 | equimolar equimolar no interaction | SEC-A |
| Fig. S8D | Nup82 NTD•Nup145N APD•Nup159 TAIL Nup120•Nup37•Elys•Nup85•Sec13•Nup145C•Nup84•Nup133ΔNTE Preincubation | 63 765 780 | 85 730 815 | equimolar equimolar no interaction | SEC-A |
| Fig. S8E | Nup82•Nup159•Nsp1 (CFNC-hub) Nup120•Nup37•Elys•Nup85•Sec13•Nup145C•Nup84•Nup133ΔNTE Preincubation | 76 765 819 | 77 730 806 | equimolar equimolar equimolar | SEC-A |
| Fig. S9A | Nup82•Nup159•Nsp1 (CFNC-hub) Nup133 NTE Preincubation | 81 26 87 | 77 26 98 | equimolar n/a no interaction | SEC-A |
| Fig. S9B | Nup82•Nup159•Nsp1 (CFNC-hub) Nup85 NTE Preincubation | 83 23 83 | 77 24 101 | equimolar n/a no interaction | SEC-A |
| Fig. S9C | Nup82•Nup159•Nsp1 (CFNC-hub) Nup145C NTE Preincubation | 82 28 87 | 77 30 107 | equimolar n/a weak interaction | SEC-A |
| Fig. S9D | Nup82•Nup159•Nsp1 (CFNC-hub) SUMO-Nup37 CTE Preincubation | 81 19 87 | 77 21 98 | equimolar n/a equimolar | SEC-A |
| Fig. S10A | Nup82•Nup159•Nsp1 (CFNC-hub) Nup37 Preincubation | 81 74 143 | 77 80 157 | equimolar n/a equimolar | SEC-A |

| Figure(s) | Nucleoporin or nucleoporin complex | Experimental mass (kDa) | Theoretical mass (kDa) | Stoichiometry | Buffer |
|-----------|--|--|---|--|---|
| Fig. S10B | Nup82•Nup159•Nsp1 (CFNC-hub) Nup37ΔCTE Preincubation | 81 66 81 | 77 64 141 | equimolar n/a no interaction | SEC-A |
| Fig. S10C | Nup82•Nup159•Nsp1 (CFNC-hub) Nup120•Nup37ΔCTE•Elys•Nup85•Sec13-Nup145C•Nup84•Nup133ΔNTE Preincubation | 76 756 737 | 77 712 789 | equimolar equimolar no interaction | SEC-A |
| Fig. S11A | Nup82•Nup159•Nsp1•Dbp5•Nup145N•Gle2 (CFNC) Nup120•Nup37ΔCTE•Elys•Nup85•Sec13-Nup145C•Nup84•Nup133ΔNTE Preincubation | 275 792 905 | 326 712 1037 | equimolar equimolar weak interaction | SEC-A |
| Fig. S11B | Nup82•Nup159•Nsp1•Dbp5•Nup145N•Gle2 (CFNC) Nup120•Nup37•Elys•Nup85•Sec13-Nup145CΔNTE•Nup84•Nup133ΔNTE Preincubation | 275 711 942 | 326 699 1024 | equimolar equimolar equimolar | SEC-A |
| Fig. S11C | Nup82•Nup159•Nsp1•Dbp5•Nup145N•Gle2 (CFNC) Nup120•Nup37ΔCTE•Elys• Nup85•Sec13-Nup145CΔNTE•Nup84•Nup133ΔNTE Preincubation | 275 724 829 | 326 683 1008 | equimolar equimolar weak interaction | SEC-A |
| Fig. S12A | Nup82•Nup159•Nsp1 (CFNC-hub) Nup120•Nup37•Elys•Nup85 Preincubation | 76 424 553 | 77 360 437 | equimolar equimolar equimolar | SEC-A |
| Fig. S12B | Nup82•Nup159•Nsp1 (CFNC-hub) Sec13-Nup145C Preincubation | 76 118 120 | 77 124 201 | equimolar equimolar weak interaction | SEC-A |
| Fig. S12C | Nup82•Nup159•Nsp1 (CFNC-hub) Nup84•Nup133ΔNTE Preincubation | 76 226 183 | 77 246 323 | equimolar equimolar no interaction | SEC-A |
| Fig. S12D | Nup82•Nup159•Nsp1 (CFNC-hub) Sec13-Nup145CΔNTE Preincubation | 78 98 80 | 77 93 170 | equimolar equimolar no interaction | SEC-A |
| Fig. S13A | Nup82•Nup159•Nsp1 Nup120•Nup37ΔCTE•Elys• Nup85•Sec13-Nup145CΔNTE•Nup84•Nup133ΔNTE Preincubation | 201 724 719 | 211 683 894 | equimolar equimolar no interaction | SEC-A |
| Fig. S13B | Nup82•Nup159•Nsp1 Nup120•Nup37ΔCTE•Elys• Nup85•Sec13-Nup145CΔNTE•Nup84•Nup133ΔNTE Dbp5 Preincubation | 201 724 53 733 | 211 683 53 947 | equimolar equimolar n/a no interaction | SEC-A |
| Fig. S13C | Nup82•Nup159•Nsp1 Nup120•Nup37ΔCTE•Elys• Nup85•Sec13-Nup145CΔNTE•Nup84•Nup133ΔNTE Nup145N APD Preincubation | 201 724 15 721 | 211 683 15 909 | equimolar equimolar n/a no interaction | SEC-A |
| Fig. S13D | Nup82•Nup159•Nsp1 Nup120•Nup37ΔCTE•Elys• Nup85•Sec13-Nup145CΔNTE•Nup84•Nup133ΔNTE Gle2•Nup145N GLEBS-APD Preincubation | 201 724 59 846 | 211 683 62 956 | equimolar equimolar n/a weak interaction | SEC-A |
| Fig. S16A | Nup82•Nup159•Nsp1 (CFNC-hub) 100 mM NaCl SUMO-Nup37 CTE 100 mM NaCl Preincubation 100 mM NaCl Preincubation 200 mM NaCl Preincubation 300 mM NaCl Preincubation 500 mM NaCl Preincubation 1000 mM NaCl | 78 17 87 84 83 82 80 | 77 21 98 98 98 98 98 | equimolar n/a equimolar equimolar equimolar equimolar equimolar | SEC-A 100 mM NaCl 200 mM NaCl 300 mM NaCl 500 mM NaCl 1000 mM NaCl |
| Fig. S16B | Nup82•Nup159•Nsp1 (CFNC-hub) 100 mM NaCl Nup145C NTE 100 mM NaCl Preincubation 100 mM NaCl Preincubation 200 mM NaCl Preincubation 300 mM NaCl Preincubation 500 mM NaCl Preincubation 1000 mM NaCl | 78 17 84 80 80 77 79 | 77 28 105 105 105 105 105 | equimolar n/a weak interaction weak interaction weak interaction weak interaction weak interaction | SEC-A 100 mM NaCl 200 mM NaCl 300 mM NaCl 500 mM NaCl 1000 mM NaCl |
| Fig. S16C | Nup82•Nup159•Nsp1 (CFNC-hub) SUMO-Nup37 CTE Nup145C NTE Preincubation | 79 19 27 87 | 77 21 30 107/98 | equimolar n/a n/a equimolar | SEC-A |
| Fig. S17A | Nup82•Nup159•Nsp1•Dbp5•Nup145N•Gle2 (CFNC) SUMO-Nup37 CTE Preincubation | 264 20 283 | 326 21 347 | equimolar equimolar equimolar | SEC-A |
| Fig. S17B | Nup82•Nup159•Nsp1•Dbp5•Nup145N•Gle2 (CFNC) Nup145C NTE Preincubation | 264 29 289 | 326 30 394 | equimolar equimolar weak interaction | SEC-A |

| Figure(s) | Nucleoporin or nucleoporin complex | Experimental mass (kDa) | Theoretical mass (kDa) | Stoichiometry | Buffer |
|-----------|--|--|------------------------------------|---|---------------------------------|
| Fig. S19B | Nup82•Nup159•Nsp1•Dbp5•Nup145N•Gle2 (CFNC) Gle1•Nup42 GBM -IP ₆ Preincubation | 275 71 277 | 326 68 394 | equimolar equimolar weak interaction | SEC-A 200 μM IP ₆ |
| Fig. S19C | Nup82•Nup159•Nsp1•Dbp5•Nup145N•Gle2 (CFNC) Gle1 NTD Preincubation | 258 33 271 | 326 23 349 | equimolar n/a weak interaction | SEC-A |
| Fig. S19D | Nup82•Nup159•Nsp1•Dbp5•Nup145N•Gle2 (CFNC) Gle1 CTD•Nup42 GBM -IP ₆ Preincubation | 264 43 275 | 326 44 370 | equimolar equimolar no interaction | SEC-A 200 μM IP ₆ |
| Fig. S19E | Nup82•Nup159•Nsp1•Dbp5•Nup145N•Gle2 (CFNC) Gle1 CTD•Nup42 GBM +IP ₆ Preincubation | 258 43 258 | 326 44 370 | equimolar equimolar no interaction | SEC-A 200 μM IP ₆ |
| Fig. S20A | Dbp5 Gle1•Nup42 GBM +IP ₆ Preincubation | 45 63 62 | 53 68 121 | n/a equimolar weak interaction | SEC-C 200 μM IP ₆ |
| Fig. S20B | Nup159 NTD•Dbp5 Gle1•Nup42 GBM +IP ₆ Preincubation | 83 63 62 | 100 68 168 | equimolar equimolar weak interaction | SEC-A 200 μM IP ₆ |
| Fig. S20C | Dbp5 Gle1 CTD•Nup42 GBM +IP ₆ Preincubation | 45 40 50 | 53 44 97 | n/a equimolar weak interaction | SEC-A 200 μM IP ₆ |
| Fig. S20D | Nup159 NTD•Dbp5 Gle1 CTD•Nup42 GBM +IP ₆ Preincubation | 83 40 81 | 100 44 144 | equimolar equimolar weak interaction | SEC-A 200 μM IP ₆ |
| Fig. S21A | Nup159 NTD•Dbp5 Gle1•Nup42 GBM Preincubation | 82 65 80 | 100 68 168 | equimolar equimolar no interaction | SEC-A |
| Fig. S21B | Gle2•Nup145N GLEBS Gle1•Nup42 GBM Preincubation | 43 65 63 | 47 68 115 | equimolar equimolar no interaction | SEC-A |
| Fig. S21C | Nup82 NTD•Nup145N APD•Nup159 TAIL Gle1•Nup42 GBM Preincubation | 61 65 63 | 85 68 115 | equimolar equimolar no interaction | SEC-A |
| Fig. S21D | Nup82•Nup159•Nsp1 (CFNC-hub) Gle1•Nup42 GBM Preincubation | 79 65 78 | 77 68 145 | equimolar equimolar no interaction | SEC-A |
| Fig. S21E | Nup82•Nup159•Nsp1 (CFNC-hub) Nup159 NTD•Dbp5 Gle1•Nup42 GBM Gle2•Nup145N GLEBS Nup82 NTD•Nup145N APD•Nup159 TAIL Preincubation | 79 83 65 40 60 80/82/72/42/60 | 77 100 68 68 47 145 | equimolar equimolar equimolar equimolar equimolar no interaction | SEC-A |
| Fig. S23B | Nup82•Nup159•Nsp1•Dbp5•Nup145N•Gle2 (CFNC) Nup120•Nup37•Elys•Nup85•Sec13•Nup145C•Nup84•Nup133ΔNTE Gle1•Nup42 GBM -IP ₆ Preincubation | 275 734 71 2002-1273 | 326 730 68 1124 | equimolar equimolar equimolar equimolar monomer/dimer | SEC-A 200 μM IP ₆ |
| Fig. S23C | Nup82•Nup159•Nsp1•Dbp5•Nup145N•Gle2 (CFNC) Nup120•Nup37•Elys•Nup85•Sec13•Nup145C•Nup84•Nup133ΔNTE Gle1 CTD•Nup42 GBM -IP ₆ Preincubation | 275 775 53 1625 | 326 730 44 1100 | equimolar equimolar equimolar equimolar | SEC-A 200 μM IP ₆ |
| Fig. S23D | Nup82•Nup159•Nsp1•Dbp5•Nup145N•Gle2 (CFNC) Nup120•Nup37•Elys•Nup85•Sec13•Nup145C•Nup84•Nup133ΔNTE Gle1 NTD Preincubation | 275 775 21 1625 | 326 730 23 1100 | equimolar equimolar n/a weak interaction | SEC-A |
| Fig. S24A | Gle1•Nup42 GBM -IP ₆ Nup120•Nup37•Elys•Nup85•Sec13•Nup145C•Nup84•Nup133ΔNTE Preincubation | 67 765 822 | 68 730 798 | equimolar equimolar equimolar | SEC-A 200 μM IP ₆ |
| Fig. S24B | Gle1•Nup42 GBM +IP ₆ Nup120•Nup37•Elys•Nup85•Sec13•Nup145C•Nup84•Nup133ΔNTE Preincubation | 67 765 736 | 68 730 798 | equimolar equimolar no interaction | SEC-A 200 μM IP ₆ |
| Fig. S25A | Gle1 NTD -IP ₆ Nup120•Nup37•Elys•Nup85•Sec13•Nup145C•Nup84•Nup133ΔNTE Preincubation | 22 743 716 | 23 730 753 | equimolar equimolar no interaction | SEC-A 200 μM IP ₆ |
| Fig. S25B | Gle1 CTD•Nup42 GBM -IP ₆ Nup120•Nup37•Elys•Nup85•Sec13•Nup145C•Nup84•Nup133ΔNTE Preincubation | 57 743 672 | 44 730 774 | equimolar equimolar equimolar | SEC-A 200 μM IP ₆ |
| Fig. S25C | Gle1 CTD•Nup42 GBM +IP ₆ Nup120•Nup37•Elys•Nup85•Sec13•Nup145C•Nup84•Nup133ΔNTE Preincubation | 40 743 683 | 44 730 774 | equimolar equimolar no interaction | SEC-A 200 μM IP ₆ |

| Figure(s) | Nucleoporin or nucleoporin complex | Experimental mass (kDa) | Theoretical mass (kDa) | Stoichiometry | Buffer |
|----------------------|---|-------------------------|------------------------|--|---|
| Fig. 2C Fig. S29A | NUP62•NUP88•NUP214 (CFNC-hub) DDX19 (ADP) RAE1•NUP98 Preincubation | 216 51 57 337 | 188 54 67 310 | equimolar n/a equimolar equimolar | SEC-A |
| Fig. S30A | NUP358 NTD NUP88 NTD Preincubation | 89 49 118 | 86 54 140 | n/a n/a weak interaction | SEC-B |
| Fig. S30B | NUP358 NTD NUP88 NTD•NUP98 APD Preincubation | 89 65 95 | 86 72 158 | n/a equimolar weak interaction | SEC-B |
| Fig. S30C | NUP358 NTD NUP88 NTD•NUP98 APD•NUP214 TAIL Preincubation | 106 71 94 | 86 77 163 | n/a equimolar weak interaction | SEC-B |
| Fig. S30D | NUP358 NTD NUP88 NTD•NUP214 TAIL Preincubation | 106 56 123 | 86 60 146 | n/a equimolar weak interaction | SEC-B |
| Fig. S30E | NUP358 NTD NUP98 APD Preincubation | 89 19 93 | 86 17 103 | n/a n/a no interaction | SEC-B |
| Fig. S30F | NUP358 NTD SUMO-NUP214 TAIL Preincubation | 93 23 92 | 86 17 103 | n/a n/a no interaction | SEC-B |
| Fig. S30G | NUP358 NTD NUP214 NTD Preincubation | 93 48 76 | 86 50 136 | n/a n/a no interaction | SEC-B |
| Fig. S30H | NUP358 NTD NUP62•NUP88•NUP214 (CFNC-hub) Preincubation | 93 69 88 | 86 69 155 | n/a equimolar no interaction | SEC-B |
| Fig. S30I | NUP358 NTD DDX19 (ADP) Preincubation | 99 51 72 | 86 54 140 | n/a n/a no interaction | SEC-B 2 mM MgCl ₂ |
| Fig. S30J | NUP358 NTD DDX19 E243Q (AMPPNP) Preincubation | 99 51 101 | 86 54 140 | n/a n/a no interaction | SEC-B 2 mM MgCl ₂ |
| Fig. S30K | NUP358 NTD GLE1 CTD•NUP42 GBM Preincubation | 96 39 95 | 86 42 128 | n/a equimolar no interaction | SEC-B |
| Fig. S30L | NUP358 NTD SUMO-NUP42 ZnF Preincubation | 99 17 100 | 86 17 103 | n/a n/a no interaction | SEC-B 2 mM MgCl ₂ 1 μM ZnCl ₂ |
| Fig. S30M | NUP358 NTD RAE1•NUP98 GLEBS Preincubation | 92 46 95 | 86 48 134 | n/a equimolar no interaction | SEC-B |
| Fig. S30N | NUP358 NTD NUP358 OE Preincubation | 99 9 92 | 86 3.6 89.5 | n/a n/a no interaction | SEC-B |
| Fig. S31A | NUP358 OE NUP88 NTD Preincubation | 10 52 52 | 3.6 55 58.6 | n/a n/a no interaction | SEC-B |
| Fig. S31B | NUP358 OE NUP98 APD Preincubation | 11 18 17 | 3.6 17 20.6 | n/a n/a no interaction | SEC-B |
| Fig. S31C | NUP358 OE SUMO-NUP214 TAIL Preincubation | 10 23 21 | 3.6 17 20.6 | n/a n/a no interaction | SEC-B |
| Fig. S31D | NUP358 OE NUP214 NTD Preincubation | 10 48 48 | 3.6 50 53.6 | n/a n/a no interaction | SEC-B |
| Fig. S31E | NUP358 OE NUP62•NUP88•NUP214 (CFNC-hub) Preincubation | 10 69 69 | 3.6 69 72.6 | n/a n/a no interaction | SEC-B |
| Fig. S31F | NUP358 OE DDX19 (ADP) Preincubation | 10 51 51 | 3.6 54 57.6 | n/a n/a no interaction | SEC-B 2 mM MgCl ₂ |
| Fig. S31G | NUP358 OE DDX19 E243Q (AMPPNP) Preincubation | 10 51 53 | 3.6 54 57.6 | n/a n/a no interaction | SEC-B 2 mM MgCl ₂ |
| Fig. S31H | NUP358 OE GLE1 CTD•NUP42 GBM Preincubation | 10 39 39 | 3.6 42 45.6 | n/a equimolar no interaction | SEC-B |

| Figure(s) | Nucleoporin or nucleoporin complex | Experimental mass (kDa) | Theoretical mass (kDa) | Stoichiometry | Buffer |
|-----------|--|-------------------------|------------------------|------------------------------------|---|
| Fig. S31I | NUP358 OE SUMO-NUP42 ZnF Preincubation | 10 17 17 | 3.6 17 20.6 | n/a n/a no interaction | SEC-B |
| Fig. S31J | NUP358 OE RAE1•NUP98 GLEBS Preincubation | 10 46 46 | 3.6 48 51.6 | n/a equimolar no interaction | SEC-B |
| Fig. S32A | NUP88 NTD NUP98 APD Preincubation | 49 19 71 | 54 17 72 | n/a n/a equimolar | SEC-B |
| Fig. S32B | NUP88 NTD NUP214 TAIL Preincubation | 52 23 71 | 55 17 72 | n/a n/a equimolar | SEC-B |
| Fig. S32C | NUP88 NTD NUP214 NTD Preincubation | 51 48 50 | 55 50 105 | n/a n/a no interaction | SEC-B |
| Fig. S32D | NUP88 NTD NUP62•NUP88•NUP214 (CFNC-hub) Preincubation | 51 69 68 | 55 69 124 | n/a equimolar no interaction | SEC-B |
| Fig. S32E | NUP88 NTD DDX19 (ADP) Preincubation | 51 51 53 | 55 54 109 | n/a n/a no interaction | SEC-B 2 mM MgCl ₂ |
| Fig. S32F | NUP88 NTD DDX19 E243Q (AMPPNP) Preincubation | 51 51 56 | 55 54 109 | n/a n/a no interaction | SEC-B 2 mM MgCl ₂ |
| Fig. S32G | NUP88 NTD GLE1 CTD•NUP42 GBM Preincubation | 51 39 50 | 55 42 97 | n/a equimolar no interaction | SEC-B |
| Fig. S32H | NUP88 NTD SUMO-NUP42 ZnF Preincubation | 51 17 51 | 55 17 72 | n/a n/a no interaction | SEC-B 2 mM MgCl ₂ 1 μM ZnCl ₂ |
| Fig. S32I | NUP88 NTD RAE1•NUP98 GLEBS Preincubation | 52 46 52 | 55 48 115 | n/a equimolar no interaction | SEC-B |
| Fig. S33A | NUP98 APD SUMO-NUP214 TAIL Preincubation | 17 21 21 | 17 17 34 | n/a n/a no interaction | SEC-B |
| Fig. S33B | NUP98 APD NUP214 NTD Preincubation | 17 48 47 | 17 50 67 | n/a n/a no interaction | SEC-B |
| Fig. S33C | NUP98 APD NUP62•NUP88•NUP214 (CFNC-hub) Preincubation | 17 69 67 | 17 69 86 | n/a equimolar no interaction | SEC-B |
| Fig. S33D | NUP98 APD DDX19 (ADP) Preincubation | 17 51 51 | 17 54 71 | n/a n/a no interaction | SEC-B 2 mM MgCl ₂ |
| Fig. S33E | NUP98 APD DDX19 E243Q (AMPPNP) Preincubation | 17 52 52 | 17 54 71 | n/a n/a no interaction | SEC-B 2 mM MgCl ₂ |
| Fig. S33F | NUP98 APD GLE1 CTD•NUP42 GBM Preincubation | 17 40 52 | 17 42 59 | n/a equimolar no interaction | SEC-B |
| Fig. S33G | NUP98 APD SUMO-NUP42 ZF Preincubation | 19 17 17 | 17 17 34 | n/a n/a no interaction | SEC-B 2 mM MgCl ₂ 1 μM ZnCl ₂ |
| Fig. S33H | NUP98 APD NUP155 CTD Preincubation | 17 57 57 | 17 60 77 | n/a n/a no interaction | SEC-B |
| Fig. S33I | NUP98 APD RAE1•NUP98 GLEBS Preincubation | 17 46 44 | 17 48 65 | n/a equimolar no interaction | SEC-B |
| Fig. S34A | SUMO-NUP214 TAIL NUP214 NTD Preincubation | 23 48 48 | 17 50 65 | n/a n/a no interaction | SEC-B |
| Fig. S34B | SUMO-NUP214 TAIL NUP62•NUP88•NUP214 (CFNC-hub) Preincubation | 21 69 70 | 17 69 86 | n/a equimolar no interaction | SEC-B |
| Fig. S34C | SUMO-NUP214 TAIL DDX19 (ADP) Preincubation | 21 51 51 | 17 54 71 | n/a n/a no interaction | SEC-B 2 mM MgCl ₂ |

| Figure(s) | Nucleoporin or nucleoporin complex | Experimental mass (kDa) | Theoretical mass (kDa) | Stoichiometry | Buffer |
|-----------|--|-------------------------|------------------------|--|---|
| Fig. S34D | SUMO-NUP214 TAIL DDX19 E243Q (AMPPNP) Preincubation | 17 51 50 | 17 54 71 | n/a n/a no interaction | SEC-B 2 mM MgCl ₂ |
| Fig. S34E | SUMO-NUP214 TAIL GLE1 CTD•NUP42 GBM Preincubation | 21 40 24 | 17 42 59 | n/a equimolar no interaction | SEC-B |
| Fig. S34F | SUMO-NUP214 TAIL SUMO-NUP42 ZnF Preincubation | 21 17 21 | 17 17 34 | n/a n/a no interaction | SEC-B 2 mM MgCl ₂ 1 μM ZnCl ₂ |
| Fig. S34G | SUMO-NUP214 TAIL RAE1•NUP98 GLEBS Preincubation | 20 46 24 | 17 48 65 | n/a equimolar no interaction | SEC-B |
| Fig. S35A | NUP214 NTD NUP62•NUP88•NUP214 (CFNC-hub) Preincubation | 48 69 69 | 50 69 119 | n/a equimolar no interaction | SEC-B |
| Fig. S35B | NUP214 NTD DDX19 (ADP) Preincubation | 48 51 99 | 50 54 119 | n/a n/a equimolar | SEC-B 2 mM MgCl ₂ |
| Fig. S35C | NUP214 NTD DDX19 E243Q (AMPPNP) Preincubation | 48 51 98 | 50 54 119 | n/a n/a equimolar | SEC-B 2 mM MgCl ₂ |
| Fig. S35D | NUP214 NTD GLE1 CTD•NUP42 GBM Preincubation | 48 40 47 | 50 42 92 | n/a equimolar no interaction | SEC-B |
| Fig. S35E | NUP214 NTD SUMO-NUP42 ZnF Preincubation | 48 17 47 | 50 17 67 | n/a n/a no interaction | SEC-B 2 mM MgCl ₂ 1 μM ZnCl ₂ |
| Fig. S35F | NUP214 NTD RAE1•NUP98 GLEBS Preincubation | 47 46 47 | 50 48 92 | n/a equimolar no interaction | SEC-B |
| Fig. S36A | NUP62•NUP88•NUP214 (CFNC-hub) DDX19 (ADP) Preincubation | 69 51 69 | 69 54 123 | equimolar n/a no interaction | SEC-B 2 mM MgCl ₂ |
| Fig. S36B | NUP62•NUP88•NUP214 (CFNC-hub) DDX19 E243Q (AMPPNP) Preincubation | 69 51 71 | 69 54 123 | equimolar n/a no interaction | SEC-B 2 mM MgCl ₂ |
| Fig. S36C | NUP62•NUP88•NUP214 (CFNC-hub) GLE1 CTD•NUP42 GBM Preincubation | 69 40 69 | 69 42 111 | equimolar equimolar no interaction | SEC-B |
| Fig. S36D | NUP62•NUP88•NUP214 (CFNC-hub) SUMO-NUP42 ZnF Preincubation | 69 16 77 | 69 17 86 | equimolar n/a no interaction | SEC-B 2 mM MgCl ₂ 1 μM ZnCl ₂ |
| Fig. S36E | NUP62•NUP88•NUP214 (CFNC-hub) RAE1•NUP98 GLEBS Preincubation | 69 46 69 | 69 48 117 | equimolar equimolar no interaction | SEC-B |
| Fig. S37A | DDX19 (ADP) GLE1 CTD•NUP42 GBM Preincubation | 51 69 58 | 54 42 96 | n/a equimolar weak interaction | SEC-B 2 mM MgCl ₂ |
| Fig. S37B | DDX19 E243Q (AMPPNP) GLE1 CTD•NUP42 GBM Preincubation | 51 40 59 | 54 42 96 | n/a equimolar weak interaction | SEC-B 2 mM MgCl ₂ |
| Fig. S37C | DDX19 (APD) SUMO-NUP42 ZnF Preincubation | 53 17 53 | 54 17 71 | n/a n/a no interaction | SEC-B 2 mM MgCl ₂ 1 μM ZnCl ₂ |
| Fig. S37D | DDX19 E243Q (AMPPNP) SUMO-NUP42 ZnF Preincubation | 48 17 53 | 54 17 71 | n/a n/a no interaction | SEC-B 2 mM MgCl ₂ 1 μM ZnCl ₂ |
| Fig. S37E | DDX19 (ADP) RAE1•NUP98 GLEBS Preincubation | 52 46 52 | 54 48 102 | n/a equimolar no interaction | SEC-B 2 mM MgCl ₂ |
| Fig. S37F | DDX19 E243Q (AMPPNP) RAE1•NUP98 GLEBS Preincubation | 52 46 53 | 54 48 102 | n/a equimolar no interaction | SEC-B 2 mM MgCl ₂ |
| Fig. S38A | GLE1 CTD•NUP42 GBM SUMO-NUP42 ZnF Preincubation | 41 17 24 | 42 17 59 | equimolar n/a no interaction | SEC-B 2 mM MgCl ₂ 1 μM ZnCl ₂ |
| Fig. S38B | GLE1 CTD•NUP42 GBM RAE1•NUP98 GLEBS Preincubation | 40 46 45 | 42 48 90 | equimolar equimolar no interaction | SEC-B |

| Figure(s) | Nucleoporin or nucleoporin complex | Experimental mass (kDa) | Theoretical mass (kDa) | Stoichiometry | Buffer |
|----------------------|---|---|--|---|---|
| Fig. S39A | SUMO-NUP42 ZnF RAE1-NUP98 GLEBS Preincubation | 16 47 29 | 17 48 65 | n/a equimolar no interaction | SEC-B 2 mM MgCl ₂ 1 μM ZnCl ₂ |
| Fig. 3B Fig. S41B | NUP358 NTD 2 μM 100 mM NaCl NUP358 NTD 5 μM 100 mM NaCl NUP358 NTD 10 μM 100 mM NaCl NUP358 NTD 20 μM 100 mM NaCl NUP358 NTD 30 μM 100 mM NaCl | 94 92 95 102 142 | 86 86 86 86 86 | monomer monomer monomer monomer monomer/dimer | SEC-B |
| Fig. 3B Fig. S41C | NUP358 NTD 2 μM 350 mM NaCl NUP358 NTD 5 μM 350 mM NaCl NUP358 NTD 10 μM 350 mM NaCl NUP358 NTD 20 μM 350 mM NaCl NUP358 NTD 30 μM 350 mM NaCl | 81 82 81 82 84 | 86 86 86 86 86 | monomer monomer monomer monomer monomer | SEC-C |
| Fig. 3B Fig. S41D | NUP358 NTDΔTPR 2 μM 100 mM NaCl NUP358 NTDΔTPR 5 μM 100 mM NaCl NUP358 NTDΔTPR 10 μM 100 mM NaCl NUP358 NTDΔTPR 20 μM 100 mM NaCl NUP358 NTDΔTPR 30 μM 100 mM NaCl NUP358 NTDΔTPR 50 μM 100 mM NaCl | 68 67 67 69 69 70 | 69 69 69 69 69 69 | monomer monomer monomer monomer monomer monomer | SEC-B |
| Fig. 3B Fig. S41E | NUP358 NTDΔTPR 2 μM 350 mM NaCl NUP358 NTDΔTPR 5 μM 350 mM NaCl NUP358 NTDΔTPR 10 μM 350 mM NaCl NUP358 NTDΔTPR 20 μM 350 mM NaCl NUP358 NTDΔTPR 30 μM 350 mM NaCl NUP358 NTDΔTPR 50 μM 350 mM NaCl | 65 66 67 68 68 68 | 69 69 69 69 69 69 | monomer monomer monomer monomer monomer monomer | SEC-C |
| Fig. 3C Fig. S41A | NUP358 NTD-OE (1-832) 2 μM 350 mM NaCl NUP358 NTD-OE (1-832) 5 μM 350 mM NaCl NUP358 NTD-OE (1-832) 10 μM 350 mM NaCl | 396 435 449 | 97 97 97 | tetramer tetramer/pentamer tetramer/pentamer | SEC-C |
| Fig. 3G Fig. S42B | NUP358 OE 150 μM 100 mM NaCl NUP358 OE 375 μM 100 mM NaCl NUP358 OE 750 μM 100 mM NaCl NUP358 OE 1500 μM 100 mM NaCl | 8.1 10.4 11.6 12.5 | 3.8 3.8 3.8 3.8 | dimer dimer/trimer trimer trimer/tetramer | SEC-B |
| Fig. 3G Fig. S42C | NUP358 OE 150 μM 350 mM NaCl NUP358 OE 375 μM 350 mM NaCl NUP358 OE 750 μM 350 mM NaCl NUP358 OE 1500 μM 350 mM NaCl | 9.7 11.2 12 12.7 | 3.8 3.8 3.8 3.8 | dimer/trimer trimer trimer/tetramer trimer/tetramer | SEC-C |
| Fig. 3G Fig. S42D | NUP358 OE LIQIML 150 μM 100 mM NaCl NUP358 OE LIQIML 375 μM 100 mM NaCl NUP358 OE LIQIML 750 μM 100 mM NaCl NUP358 OE LIQIML 1500 μM 100 mM NaCl | 3.4 3.4 3.4 3.4 | 3.8 3.8 3.8 3.8 | monomer monomer monomer monomer | SEC-B |
| Fig. 3G Fig. S42E | NUP358 OE LIQIML 150 μM 350 mM NaCl NUP358 OE LIQIML 375 μM 350 mM NaCl NUP358 OE LIQIML 750 μM 350 mM NaCl NUP358 OE LIQIML 1500 μM 350 mM NaCl | 3.1 3.5 3.4 3.3 | 3.8 3.8 3.8 3.8 | monomer monomer monomer monomer | SEC-C |
| Fig. S42F | NUP358 NTD-OE (1-832) LIQIML 1 μM 100 mM NaCl NUP358 NTD-OE (1-832) LIQIML 2 μM 100 mM NaCl NUP358 NTD-OE (1-832) LIQIML 5 μM 100 mM NaCl NUP358 NTD-OE (1-832) LIQIML 10 μM 100 mM NaCl | 112 118 123 138 | 96 96 96 96 | monomer/dimer monomer/dimer monomer/dimer monomer/dimer | SEC-B |
| Fig. S42G | NUP358 NTD-OE (1-832) LIQIML 1 μM 350 mM NaCl NUP358 NTD-OE (1-832) LIQIML 2 μM 350 mM NaCl NUP358 NTD-OE (1-832) LIQIML 5 μM 350 mM NaCl NUP358 NTD-OE (1-832) LIQIML 10 μM 350 mM NaCl NUP358 NTD-OE (1-832) LIQIML 20 μM 350 mM NaCl NUP358 NTD-OE (1-832) LIQIML 30 μM 350 mM NaCl NUP358 NTD-OE (1-832) LIQIML 50 μM 350 mM NaCl | 90 92 91 93 95 97 102 | 96 96 96 96 96 96 96 | monomer monomer monomer monomer monomer monomer monomer | SEC-C |
| Fig. S54A | Ran (GMPPNP) NUP358 RBD-I Preincubation | 27 15 38 | 24 16 40 | n/a n/a equimolar | SEC-B 2 mM MgCl ₂ |
| Fig. S54B | Ran (GMPPNP) NUP358 RBD-II Preincubation | 27 16 37 | 24 16 40 | n/a n/a equimolar | SEC-B 2 mM MgCl ₂ |
| Fig. S54C | Ran (GMPPNP) NUP358 RBD-III Preincubation | 27 22 40 | 24 17 41 | n/a n/a equimolar | SEC-B 2 mM MgCl ₂ |
| Fig. 3J Fig. S54D | Ran (GMPPNP) NUP358 RBD-IV Preincubation | 27 20 39 | 24 16 40 | n/a n/a equimolar | SEC-B 2 mM MgCl ₂ |
| Fig. S54E | Ran (GMPPNP) NUP50 RBD Preincubation | 27 14 26 | 24 15 39 | n/a n/a equimolar | SEC-B 2 mM MgCl ₂ |

| Figure(s) | Nucleoporin or nucleoporin complex | Experimental mass (kDa) | Theoretical mass (kDa) | Stoichiometry | Buffer |
|----------------------|---|-------------------------|------------------------|------------------------------------|--------|
| Fig. 6F Fig. S85D | NUP62•NUP88•NUP214•DDX19 (ADP)•RAE1•NUP98 SUMO-NUP93 R1 Preincubation | 406 22 417 | 310 24 334 | equimolar n/a equimolar | SEC-A |
| Fig. 6F Fig. S85B | His-NUP62•NUP88•AVI-NUP214 CFNC-hub SUMO-NUP93 R1 Preincubation | 77 22 86 | 73 24 97 | equimolar n/a equimolar | SEC-A |
| Fig. 6F Fig. S85C | His-NUP62•NUP88•AVI-NUP214 CFNC-hub SUMO-NUP93 R1 LIL Preincubation | 77 23 72 | 73 24 97 | equimolar n/a no interaction | SEC-A |
| Fig. S86A | Nsp1•Nup49•Nup57 CCS1-3 (CNT) SUMO-Nic96 R1 Preincubation | 65 16 71 | 77 19 97 | equimolar n/a equimolar | SEC-A |
| Fig. S86B | Nup82•Nup159•Nsp1 CFNC-hub SUMO-Nic96 R1 Preincubation | 81 18 79 | 77 21 98 | equimolar n/a no interaction | SEC-A |
| Fig. S86C | Nsp1•Nup49•Nup57 CCS1-3 (CNT) SUMO-Nup37 CTE Preincubation | 65 18 65 | 77 21 96 | equimolar n/a no interaction | SEC-A |

SEC-A: 20 mM TRIS (pH 8.0), 100 mM NaCl, 5% (v/v) glycerol, 5 mM DTT

SEC-B: 20 mM TRIS (pH 8.0), 100 mM NaCl, 5 mM DTT

SEC-C: 20 mM TRIS (pH 8.0), 350 mM NaCl, 5 mM DTT

Table S7. Crystallization and cryoprotection conditions

| Protein(s) | Concentration | Crystallization condition | Cryo protection condition |
|---|---------------|--|---------------------------|
| NUP358 145-673 | 20 mg/ml | 0.1 M HEPES (pH 7.0) 0.8 M succinic acid (pH 7.0) 1% (w/v) PEG 2,000 MME | 20% (v/v) ethylene glycol |
| NUP358 145-673 SeMet | 20 mg/ml | 0.1 M HEPES (pH 7.0) 0.8 M succinic acid (pH 7.0) 1% (w/v) PEG 2,000 MME | 20% (v/v) ethylene glycol |
| NUP358 NTD*sAB-14 | 5 mg/ml | 0.1 M sodium citrate (pH 4.6) 0.15 M sodium acetate 3% (w/v) PEG 4,000 | 25% (v/v) ethylene glycol |
| NUP358 NTD*sAB-14 SeMet | 5 mg/ml | 0.1 M sodium citrate (pH 4.6) 0.15 M sodium acetate 3% (w/v) PEG 4,000 | 25% (v/v) ethylene glycol |
| NUP358 NTD*sAB-14 T585M | 5 mg/ml | 0.1 M sodium citrate (pH 4.9) 0.15 M sodium acetate 2.5% (w/v) PEG 4,000 | 20% (v/v) ethylene glycol |
| NUP358 NTD*sAB-14 T653I | 5 mg/ml | 0.1 M sodium citrate (pH 4.5) 0.15 M sodium acetate 4% (w/v) PEG 4,000 | 20% (v/v) ethylene glycol |
| NUP358 NTD*sAB-14 I656V | 5 mg/ml | 0.1 M sodium citrate (pH 4.6) 0.15 M sodium acetate 3.5% (w/v) PEG 4,000 | 20% (v/v) ethylene glycol |
| NUP358 NTD*sAB-14 (D140M/I599M), (I322M/I599M), (I427M/I599M), (I453M/I599M), (I539M/I599M), (I615M/I599M), (I626M/I599M), (I652M/I599M), (L401M/I599M), (N709M/I599M), (Q137M/I599M), (T92M/I599M), (V668M/I599M) SeMet | 5 mg/ml | 0.1 M sodium citrate (pH 4.9) 0.15 M sodium acetate 2.5% (w/v) PEG 4,000 | 20% (v/v) ethylene glycol |
| NUP358 NTD*sAB-14 I152M I599M SeMet | 5 mg/ml | 0.1 M sodium citrate (pH 4.5) 0.15 M sodium acetate 4% (w/v) PEG 4,000 | 20% (v/v) ethylene glycol |
| NUP358 NTD*sAB-14 D693M I599M SeMet | 5 mg/ml | 0.1 M sodium citrate (pH 4.7) 0.15 M sodium acetate 4% (w/v) PEG 4,000 | 20% (v/v) ethylene glycol |
| NUP358 NTD*sAB-14 I171M I599M SeMet | 5 mg/ml | 0.1 M sodium citrate (pH 4.4) 0.15 M sodium acetate 2.5% (w/v) PEG 4,000 | 20% (v/v) ethylene glycol |
| NUP358 NTD*sAB-14 I559M I599M SeMet | 5 mg/ml | 0.1 M sodium citrate (pH 4.7) 0.15 M sodium acetate 6% (w/v) PEG 4,000 | 20% (v/v) ethylene glycol |
| NUP358 OE | 20 mg/ml | 0.1 M citric acid (pH 3.5) 2 M ammonium sulfate | 20% (v/v) ethylene glycol |
| NUP358 ZnF2•Ran(GDP) F35S | 15 mg/ml | 0.1M Bis-TRIS (pH 6.4) 17 % (w/v) PEG 3,350 | 20% (v/v) glycerol |
| NUP358 ZnF2•Ran(GDP) F35S (Thrombin) | 15 mg/ml | 0.1 M Bis-TRIS (pH 6.5) 21% (w/v) PEG 3350 | 20% (v/v) glycerol |
| NUP358 ZnF3•Ran(GDP) F35S (Thrombin) | 15 mg/ml | 0.1 M Bis-TRIS (pH 6.5) 19% (w/v) PEG 3350 | 20% (v/v) glycerol |
| NUP358 ZnF4•Ran(GDP) F35S (Thrombin) | 30 mg/ml | 0.1 M Bis-TRIS (pH 6.5) 18 % (w/v) PEG 3,350 | 20% (v/v) glycerol |
| NUP358 ZnF5/6•Ran(GDP) F35S (Thrombin) | 30 mg/ml | 0.1 M Bis-TRIS (pH 6.5) 19 % (w/v) PEG 3,350 | 20% (v/v) glycerol |
| NUP358 ZnF7•Ran(GDP) F35S (Thrombin) | 15 mg/ml | 0.1 M Bis-TRIS (pH 6.5) 19% (w/v) PEG 3350 | 20% (v/v) glycerol |
| NUP358 ZnF8•Ran(GDP) F35S (Thrombin) | 15 mg/ml | 0.1 M Bis-TRIS (pH 6.7) 19% (w/v) PEG 3350 | 20% (v/v) glycerol |
| mNUP153 ZnF1•Ran(GDP) F35S | 15 mg/ml | 0.1 M Bis-TRIS (pH 6.0) 22 % (w/v) PEG 3,350 | 20% (v/v) glycerol |
| mNUP153 ZnF2•Ran(GDP) F35S | 15 mg/ml | 0.1 M Bis-TRIS (pH 6.3) 19 % (w/v) PEG 3,350 | 20% (v/v) glycerol |
| mNUP153 ZnF3•Ran(GDP) F35S | 10 mg/ml | 0.1 M Bis-TRIS (pH 7.0) 20 % (w/v) PEG 3,350 | 20% (v/v) glycerol |
| mNUP153 ZnF4•Ran(GDP) F35S | 15 mg/ml | 0.1 M Bis-TRIS (pH 6.2) 22 % (w/v) PEG 3,350 | 20% (v/v) glycerol |
| mNUP153 ZnF1•Ran(GDP) F35S (Thrombin) | 15 mg/ml | 0.1 M Bis-TRIS (pH 6.5) 20% (w/v) PEG 3350 | 20% (v/v) glycerol |
| mNUP153 ZnF2•Ran(GDP) F35S (Thrombin) | 15 mg/ml | 0.1 M Bis-TRIS (pH 6.5) 19% (w/v) PEG 3350 | 20% (v/v) glycerol |
| mNUP153 ZnF3•Ran(GDP) F35S (Thrombin) | 15 mg/ml | 0.1 M Bis-TRIS (pH 6.5) 19% (w/v) PEG 3350 | 20% (v/v) glycerol |
| mNUP153 ZnF4•Ran(GDP) F35S (Thrombin) | 15 mg/ml | 0.1 M Bis-TRIS (pH 6.5) 19% (w/v) PEG 3350 | 20% (v/v) glycerol |

| Protein(s) | Concentration | Crystallization condition | Cryo protection condition |
|--------------------------------------|----------------------|--|----------------------------------|
| NUP358 RanBD-I•Ran(GMPPNP) | 8 mg/ml | 0.2 M potassium sodium tartrate tetrahydrate 20 % (w/v) PEG 3,350 | 20% (v/v) glycerol |
| NUP358 RanBD-II•Ran(GMPPNP) | 20 mg/ml | 0.125 M magnesium formate 15 % (w/v) PEG 3,350 | 20% (v/v) ethylene glycol |
| NUP358 RanBD-III•Ran(GMPPNP) | 5 mg/ml | 0.2 M sodium formate 20 % (w/v) PEG 3,350 | 25% (v/v) ethylene glycol |
| NUP358 RanBD-IV QNYDNKQV•Ran(GMPPNP) | 3.5 mg/ml | 0.1 M HEPES (pH 7.0) 0.1 M ammonium sulfate 20 % (w/v) PEG 3,350 | 25% (v/v) glycerol |
| NUP50 RanBD•Ran(GMPPNP) | 20 mg/ml | 0.1 M HEPES (pH 7.5) 0.2 M ammonium sulfate 25 % (w/v) PEG 3,350 | 20% (v/v) ethylene glycol |
| NUP88 NTD•NUP98 APD | 15 mg/ml | 0.1 M TRIS (pH 8.3) 0.22 M NaCl 20% (w/v) PEG 4000 | Paratone-N |

Table S8. X-ray crystallographic analysis of NUP358¹⁴⁵⁻⁶⁷³

| Data collection | | | | |
|---|----------------------------------|----------------------------------|----------------------------------|----------------------------------|
| Protein 1 | NUP358 ¹⁴⁵⁻⁶⁷³ | NUP358 ¹⁴⁵⁻⁶⁷³ | NUP358 ¹⁴⁵⁻⁶⁷³ | NUP358 ¹⁴⁵⁻⁶⁷³ |
| | Wildtype | Wildtype | Wildtype | Wildtype |
| PDB code | 7MNJ | | | |
| Synchrotron ^a | SSRL | SSRL | SSRL | SSRL |
| Beamline | BL 12-2 | BL 12-2 | BL 12-2 | BL 12-2 |
| Space group | P4 ₃ 2 ₁ 2 | P4 ₃ 2 ₁ 2 | P4 ₃ 2 ₁ 2 | P4 ₃ 2 ₁ 2 |
| Cell parameters | | | | |
| <i>a</i> (Å) | 133.5 | 136.4 | 136.6 | 136.3 |
| <i>b</i> (Å) | 133.5 | 136.4 | 136.6 | 136.3 |
| <i>c</i> (Å) | 286.9 | 289.6 | 289.6 | 288.9 |
| α (°) | 90.0 | 90.0 | 90.0 | 90.0 |
| β (°) | 90.0 | 90.0 | 90.0 | 90.0 |
| γ (°) | 90.0 | 90.0 | 90.0 | 90.0 |
| | <i>Native</i> | <i>Se peak</i> | <i>Se inflection</i> | <i>Se remote</i> |
| Wavelength (Å) | 1.03320 | 0.97920 | 0.97940 | 0.95370 |
| Resolution (Å) | 30.0 – 3.8 | 30.0 – 4.2 | 30.0 – 4.3 | 30.0 – 4.4 |
| <i>R</i> _{merge} (%) ^b | 8.7 (149) | 13.7 (176) | 14.3 (164) | 16.2 (196) |
| <i>R</i> _{meas} (%) ^b | 9.0 (155) | 14.3 (183) | 14.9 (170) | 16.8 (205) |
| <i>R</i> _{pim} (%) ^b | 2.4 (43.6) | 3.9 (49.3) | 4.0 (46.2) | 4.6 (58.6) |
| <i>CC</i> _{1/2} (%) ^b | 99.9 (93.5) | 100.0 (84.5) | 100.0 (85.6) | 100.0 (75.5) |
| <i><I> / <σI></i> ^b | 18.3 (2.1) | 15.6 (2.3) | 15.3 (2.5) | 14.1 (1.9) |
| Completeness (%) ^b | 100.0 (98.8) | 100.0 (100.0) | 100.0 (100.0) | 100.0 (100.0) |
| No. observations ^b | 654,682 (60,258) | 517,269 (52,138) | 481,005 (47,613) | 444,858 (40,060) |
| No. unique reflections ^{b,c} | 26,310 (2,545) | 20,692 (2,008) | 19,360 (1,872) | 17,981 (1,752) |
| Redundancy ^b | 24.9 (23.7) | 25.0 (26.0) | 24.8 (25.4) | 24.7 (22.9) |
| Wilson B factor (Å ²) | 155 | 171 | 172 | 182 |
| Refinement | | | | |
| Resolution (Å) | 30.0 – 3.8 | | | |
| No. reflections total | 26,172 | | | |
| No. reflections test set | 1,292 (4.9%) | | | |
| <i>R</i> _{work} / <i>R</i> _{free} (%) | 20.8 / 24.2 | | | |
| No. atoms | 12,695 | | | |
| Protein | 12,695 | | | |
| Ligand/ion | 0 | | | |
| Water | 0 | | | |
| <i>B</i> -factors (Å ²) | 210 | | | |
| Protein | 210 | | | |
| Ligand/ion | - | | | |
| Water | - | | | |
| R.m.s. deviations | | | | |
| Bond lengths (Å) | 0.002 | | | |
| Bond angles (°) | 0.4 | | | |
| Ramachandran plot^d | | | | |
| Favored (%) | 98.3 | | | |
| Additionally allowed (%) | 1.7 | | | |
| Outliers (%) | 0 | | | |

^a SSRL, Stanford Synchrotron Radiation Lightsource^b Highest-resolution shell is shown in parentheses^c Friedel pairs were merged^d As determined by MolProbity (127)

Table S9. X-ray crystallographic analysis of NUP358¹⁴⁵⁻⁶⁷³ seleno-L-methionine mutations

| Data collection | | | | | | | |
|---|----------------------------------|----------------------------------|----------------------------------|----------------------------------|----------------------------------|----------------------------------|----------------------------------|
| Protein | NUP358 ¹⁴⁵⁻⁶⁷³ | NUP358 ¹⁴⁵⁻⁶⁷³ | NUP358 ¹⁴⁵⁻⁶⁷³ | NUP358 ¹⁴⁵⁻⁶⁷³ | NUP358 ¹⁴⁵⁻⁶⁷³ | NUP358 ¹⁴⁵⁻⁶⁷³ | NUP358 ¹⁴⁵⁻⁶⁷³ |
| | I652M | I615M/I599M | I599M | L401M/I599M | I169M/I481M | L385M/I599M | I372M/I599M |
| Synchrotron ^a | SSRL | APS | SSRL | SSRL | SSRL | SSRL | APS |
| Beamline | BL 12-2 | 23 ID-D | BL 12-2 | BL 12-2 | BL 12-2 | BL 12-2 | 23 ID-D |
| Space group | P4 ₃ 2 ₁ 2 | P4 ₃ 2 ₁ 2 | P4 ₃ 2 ₁ 2 | P4 ₃ 2 ₁ 2 | P4 ₃ 2 ₁ 2 | P4 ₃ 2 ₁ 2 | P4 ₃ 2 ₁ 2 |
| Cell parameters | | | | | | | |
| <i>a</i> (Å) | 133.6 | 135.6 | 134.0 | 136.2 | 133.8 | 133.1 | 135.5 |
| <i>b</i> (Å) | 133.6 | 135.6 | 134.0 | 136.2 | 133.8 | 133.1 | 135.5 |
| <i>c</i> (Å) | 291.3 | 289.8 | 288.3 | 291.6 | 291.5 | 286.8 | 289.6 |
| α (°) | 90.0 | 90.0 | 90.0 | 90.0 | 90.0 | 90.0 | 90.0 |
| β (°) | 90.0 | 90.0 | 90.0 | 90.0 | 90.0 | 90.0 | 90.0 |
| γ (°) | 90.0 | 90.0 | 90.0 | 90.0 | 90.0 | 90.0 | 90.0 |
| | <i>Se peak</i> | <i>Se peak</i> | <i>Se peak</i> | <i>Se peak</i> | <i>Se peak</i> | <i>Se peak</i> | <i>Se peak</i> |
| Wavelength (Å) | 0.97910 | 0.97936 | 0.97950 | 0.97920 | 0.97950 | 0.97920 | 0.97936 |
| Resolution (Å) | 30.0 – 4.5 | 30.0 – 5.2 | 30.0 – 6.3 | 30.0 – 6.3 | 30.0 – 4.7 | 30.0 – 5.5 | 30.0 – 5.0 |
| <i>R</i> _{merge} (%) ^b | 24.3 (389) | 28.9 (502) | 27.6 (258) | 16.9 (527) | 18.3 (153) | 19.3 (375) | 27.5 (518) |
| <i>R</i> _{meas} (%) ^b | 24.8 (396) | 29.6 (513) | 28.3 (264) | 17.2 (539) | 19.0 (159) | 19.6 (383) | 28.1 (529) |
| <i>R</i> _{plim} (%) ^b | 4.7 (76.1) | 6.1 (106) | 6.0 (56.1) | 3.3 (110) | 5.2 (44.5) | 3.8 (72.6) | 5.8 (109) |
| <i>CC</i> _{1/2} (%) ^b | 99.9 (60.3) | 99.9 (73.2) | 99.7 (86.8) | 99.9 (70.5) | 99.9 (89.4) | 99.9 (72.6) | 100.0 (71.2) |
| $\langle I \rangle / \langle \sigma \rangle$ ^b | 15.3 (1.6) | 16.0 (1.3) | 11.7 (1.4) | 20.7 (1.3) | 9.7 (1.0) | 19.3 (1.9) | 16.8 (1.3) |
| Completeness (%) ^b | 100.0 (100.0) | 100.0 (100.0) | 100.0 (100.0) | 99.0 (88.3) | 100.0 (100.0) | 100.0 (99.8) | 100.0 (100.0) |
| No. observations ^b | 833,414 (77,052) | 469,578 (46,501) | 232,212 (23,396) | 299,622 (23,303) | 350,720 (33,574) | 437,310 (43,864) | 527,226 (52,764) |
| No. unique reflections ^{b,c} | 16,277 (1,572) | 10,962 (1,061) | 6,065 (589) | 6,259 (549) | 14,414 (1,405) | 8,883 (857) | 12,270 (1,196) |
| Redundancy ^b | 51.2 (49.0) | 42.8 (43.8) | 38.3 (39.7) | 47.9 (42.4) | 24.3 (23.9) | 49.2 (51.2) | 43.0 (44.1) |
| Wilson B factor (Å ²) | 225 | 246 | 308 | 440 | 214 | 317 | 238 |

^a SSRL, Stanford Synchrotron Radiation Lightsource; APS, Advanced Photon Source^b Highest-resolution shell is shown in parentheses^c Friedel pairs were merged

Table S10. X-ray crystallographic analysis of NUP358^{NTD} and NUP358^{NTD} ANE1 mutants

| Data collection | | | | |
|---|-------------------------|-------------------------|-------------------------|-------------------------|
| Protein 1 | NUP358 ¹⁻⁷⁵² | NUP358 ¹⁻⁷⁵² | NUP358 ¹⁻⁷⁵² | NUP358 ¹⁻⁷⁵² |
| | Wildtype | ANE1 T585M | ANE1 T653I | ANE1 I656V |
| Protein 2 | sAB-14 | sAB-14 | sAB-14 | sAB-14 |
| PDB code | 7MNL | 7MNM | 7MNN | 7MNO |
| Synchrotron ^a | APS | APS | SSRL | SSRL |
| Beamline | 23 ID-B | 23 ID-B | BL 12-2 | BL 12-2 |
| Space group | P6 ₅ 22 | P6 ₅ 22 | P6 ₅ 22 | P6 ₅ 22 |
| Cell parameters | | | | |
| <i>a</i> (Å) | 161.4 | 160.4 | 161.5 | 161.6 |
| <i>b</i> (Å) | 161.4 | 160.4 | 161.5 | 161.6 |
| <i>c</i> (Å) | 644.7 | 642.2 | 647.4 | 645.4 |
| α (°) | 90.0 | 90.0 | 90.0 | 90.0 |
| β (°) | 90.0 | 90.0 | 90.0 | 90.0 |
| γ (°) | 120.0 | 120.0 | 120.0 | 120.0 |
| | <i>Native</i> | <i>Native</i> | <i>Native</i> | <i>Native</i> |
| Wavelength (Å) | 1.03314 | 1.03318 | 0.97946 | 1.03317 |
| Resolution (Å) | 20.0 – 3.95 | 30.0 – 4.7 | 30.0 – 6.7 | 30.0 – 6.7 |
| R_{merge} (%) ^b | 37.9 (588) | 58.6 (482) | 77.9 (638) | 55.4 (322) |
| R_{meas} (%) ^b | 38.4 (596) | 59.4 (488) | 78.3 (641) | 56.2 (326) |
| R_{pim} (%) ^b | 6.0 (95.1) | 9.4 (77.8) | 7.7 (62.1) | 9.1 (52.9) |
| $CC_{1/2}$ (%) ^b | 99.9 (45.5) | 99.9 (58.6) | 99.6 (67.5) | 99.3 (62.1) |
| $\langle I \rangle / \langle \sigma \rangle$ ^b | 10.3 (1.0) | 6.6 (1.1) | 11.0 (1.5) | 8.5 (1.6) |
| Completeness (%) ^b | 99.2 (99.8) | 99.6 (100.0) | 98.9 (100.0) | 98.6 (98.9) |
| No. observations ^b | 1,772,720 (176,902) | 1,037,121 (182,414) | 955,034 (275,234) | 348,970 (95,598) |
| No. unique reflections ^{b,c} | 44,627 (4,585) | 26,575 (4,697) | 9,674 (2,677) | 9,487 (2,593) |
| Redundancy ^b | 39.7 (38.6) | 39.0 (38.8) | 98.7 (102.8) | 36.8 (36.9) |
| Wilson B factor (Å ²) | 181 | 295 | 549 | 398 |
| Refinement | | | | |
| Resolution (Å) | 20.0 – 3.95 | 30.0 – 4.7 | 30.0 – 6.7 | 30.0 – 6.7 |
| No. reflections total | 44,483 | 26,442 | 9,591 | 9,417 |
| No. reflections test set | 2,213 (5.0%) | 1,304 (4.9%) | 456 (4.8%) | 445 (4.7%) |
| $R_{\text{work}} / R_{\text{free}}$ (%) | 19.2 / 24.1 | 20.4 / 25.4 | 21.7 / 26.3 | 20.5 / 25.4 |
| No. atoms | 17,358 | 17,453 | 17,499 | 17,474 |
| Protein | 17,358 | 17,453 | 17,499 | 17,474 |
| Ligand/ion | 0 | 0 | 0 | 0 |
| Water | 0 | 0 | 0 | 0 |
| <i>B</i> -factors (Å ²) | 204 | 246 | 331 | 317 |
| Protein | 204 | 246 | 331 | 317 |
| Ligand/ion | - | - | - | - |
| Water | - | - | - | - |
| R.m.s. deviations | | | | |
| Bond lengths (Å) | 0.002 | 0.002 | 0.003 | 0.002 |
| Bond angles (°) | 0.5 | 0.5 | 0.6 | 0.6 |
| Ramachandran plot^d | | | | |
| Favored (%) | 98.7 | 98.3 | 98.4 | 98.3 |
| Additionally allowed (%) | 1.3 | 1.7 | 1.6 | 1.7 |
| Outliers (%) | 0 | 0 | 0 | 0 |

^aSSRL, Stanford Synchrotron Radiation Lightsource; APS, Advanced Photon Source^bHighest-resolution shell is shown in parentheses^cFriedel pairs were merged^dAs determined by MolProbity (127)

Table S11. X-ray crystallographic analysis of NUP358^{NTD} seleno-L-methionine mutations

| Data collection | | | | | | | | | |
|---|-------------------------|-------------------------|-------------------------|-------------------------|-------------------------|-------------------------|-------------------------|-------------------------|-------------------------|
| Protein 1 | NUP358 ¹⁻⁷⁵² | NUP358 ¹⁻⁷⁵² | NUP358 ¹⁻⁷⁵² | NUP358 ¹⁻⁷⁵² | NUP358 ¹⁻⁷⁵² | NUP358 ¹⁻⁷⁵² | NUP358 ¹⁻⁷⁵² | NUP358 ¹⁻⁷⁵² | NUP358 ¹⁻⁷⁵² |
| Protein 2 | sAB-14 | sAB-14 | sAB-14 | sAB-14 | sAB-14 | sAB-14 | sAB-14 | sAB-14 | sAB-14 |
| D140M/I599M | D152M/I599M | D693M/I599M | I171M/I599M | I322M/I599M | I427M/I599M | I453M/I599M | I539M/I599M | I559M/I599M | |
| Protein 2 | sAB-14 | sAB-14 | sAB-14 | sAB-14 | sAB-14 | sAB-14 | sAB-14 | sAB-14 | sAB-14 |
| Synchrotron ^a | APS | APS | SSRL | APS | SSRL | SSRL | SSRL | SSRL | SSRL |
| Beamline | 23 ID-B | 23 ID-B | BL 12-2 | 23 ID-D | BL 12-2 | BL 12-2 | BL 12-2 | BL 12-2 | BL 12-2 |
| Space group | P6 ₅ 22 | P6 ₅ 22 | P6 ₅ 22 | P6 ₅ 22 | P6 ₅ 22 | P6 ₅ 22 | P6 ₅ 22 | P6 ₅ 22 | P6 ₅ 22 |
| Cell parameters | | | | | | | | | |
| <i>a</i> (Å) | 160.2 | 161.0 | 160.5 | 160.6 | 160.9 | 161.8 | 160.4 | 161.9 | 160.8 |
| <i>b</i> (Å) | 160.2 | 161.0 | 160.5 | 160.6 | 160.9 | 161.8 | 160.4 | 161.9 | 160.8 |
| <i>c</i> (Å) | 639.9 | 644.0 | 643.7 | 641.9 | 642.7 | 645.4 | 642.9 | 646.4 | 643.7 |
| α (°) | 90.0 | 90.0 | 90.0 | 90.0 | 90.0 | 90.0 | 90.0 | 90.0 | 90.0 |
| β (°) | 90.0 | 90.0 | 90.0 | 90.0 | 90.0 | 90.0 | 90.0 | 90.0 | 90.0 |
| γ (°) | 120.0 | 120.0 | 120.0 | 120.0 | 120.0 | 120.0 | 120.0 | 120.0 | 120.0 |
| | <i>Se peak</i> | <i>Se peak</i> | <i>Se peak</i> | <i>Se peak</i> | <i>Se peak</i> | <i>Se peak</i> | <i>Se peak</i> | <i>Se peak</i> | <i>Se peak</i> |
| Wavelength (Å) | 0.97923 | 0.97922 | 0.97910 | 0.97937 | 0.97944 | 0.97921 | 0.97920 | 0.97929 | 0.97949 |
| Resolution (Å) | 30.0 – 6.0 | 30.0 – 7.0 | 30.0 – 4.7 | 30.0 – 7.5 | 30.0 – 5.7 | 30.0 – 6.3 | 30.0 – 5.3 | 30.0 – 4.25 | 30.0 – 4.3 |
| <i>F</i> _{merge} (%) ^b | 35.1 (268) | 47.9 (256) | 30.3 (323) | 45.5 (115) | 42.1 (345) | 40.9 (247) | 30.8 (305) | 37.5 (389) | 49.3 (365) |
| <i>F</i> _{meas} (%) ^b | 35.7 (271) | 48.6 (260) | 30.7 (327) | 46.6 (118) | 42.7 (350) | 41.5 (250) | 31.3 (309) | 38.0 (394) | 49.9 (370) |
| <i>R</i> _{pim} (%) ^b | 6.0 (44.6) | 8.0 (42.0) | 4.9 (51.4) | 9.9 (24.2) | 6.9 (55.0) | 6.7 (39.4) | 5.3 (51.1) | 6.0 (61.4) | 7.9 (59.0) |
| <i>CC</i> _{1/2} (%) ^b | 99.7 (77.2) | 99.3 (76.7) | 99.9 (62.6) | 98.4 (90.9) | 99.7 (63.5) | 99.5 (77.9) | 99.8 (78.8) | 99.8 (62.3) | 99.8 (65.8) |
| $\langle I \rangle / \langle \sigma \rangle$ ^b | 9.5 (1.9) | 7.3 (1.8) | 12.3 (1.6) | 6.0 (3.0) | 9.8 (1.6) | 10.2 (2.1) | 11.9 (1.7) | 9.7 (1.4) | 8.6 (1.5) |
| Completeness (%) ^b | 99.1 (99.6) | 98.7 (100.0) | 99.4 (99.1) | 98.4 (100.0) | 99.1 (99.4) | 99.0 (99.9) | 98.8 (98.9) | 99.7 (99.7) | 99.7 (99.8) |
| No. observations ^b | 440,163 | 303,958 | 1,020,322 | 145,273 | 572,998 | 430,299 | 630,389 | 1,411,824 | 1,352,239 |
| | (129,500) | (86,803) | (184,556) | (43,416) | (166,519) | (125,907) | (151,852) | (173,500) | (173,737) |
| No. unique reflections ^{b,c} | 13,015 | 8,352 | 26,547 | 6,820 | 15,278 | 11,444 | 18,541 | 36,253 | 34,750 |
| | (3,602) | (2,310) | (4,651) | (1,890) | (4,225) | (3,181) | (4,290) | (4,269) | (4,507) |
| Redundancy ^c | 33.8 (36.0) | 36.4 (37.6) | 38.4 (39.7) | 21.3 (23.0) | 37.5 (39.4) | 37.6 (39.6) | 34.0 (35.4) | 38.9 (40.6) | 38.9 (38.5) |
| Wilson B factor (Å ²) | 387 | 662 | 324 | 516 | 359 | 364 | 349 | 238 | 242 |

^a SSRL, Stanford Synchrotron Radiation Lightsource; APS, Advanced Photon Source^b Highest-resolution shell is shown in parentheses^c Friedel pairs were merged

Table S12. X-ray crystallographic analysis of NUP358^{NTD} seleno-L-methionine mutations

| Data collection | | | | | | | | |
|---|--|--|--|--|--|--|---------------------------------------|--|
| Protein 1 | NUP358 ¹⁻⁷⁵² I615M/I599M | NUP358 ¹⁻⁷⁵² I626M/I599M | NUP358 ¹⁻⁷⁵² I652M/I599M | NUP358 ¹⁻⁷⁵² L401M/I599M | NUP358 ¹⁻⁷⁵² N709M/I599M | NUP358 ¹⁻⁷⁵² Q137M/I599M | NUP358 ¹⁻⁷⁵² T92M/I599M | NUP358 ¹⁻⁷⁵² V668M/I599M |
| Protein 2 | sAB-14 | sAB-14 | sAB-14 | sAB-14 | sAB-14 | sAB-14 | sAB-14 | sAB-14 |
| Synchrotron ^a | SSRL | SSRL | SSRL | SSRL | SSRL | SSRL | SSRL | SSRL |
| Beamline | BL 12-2 | BL 12-2 | BL 12-2 | BL 12-2 | BL 12-2 | BL 12-2 | BL 12-2 | BL 12-2 |
| Space group | P6 ₅ 22 | P6 ₅ 22 | P6 ₅ 22 | P6 ₅ 22 | P6 ₅ 22 | P6 ₅ 22 | P6 ₅ 22 | P6 ₅ 22 |
| Cell parameters | | | | | | | | |
| <i>a</i> (Å) | 160.5 | 160.5 | 160.8 | 161.3 | 161.6 | 161.2 | 160.9 | 160.2 |
| <i>b</i> (Å) | 160.5 | 160.5 | 160.8 | 161.3 | 161.6 | 161.2 | 160.9 | 160.2 |
| <i>c</i> (Å) | 650.7 | 645.1 | 645.8 | 644.2 | 636.4 | 645.2 | 648.1 | 647.1 |
| α (°) | 90.0 | 90.0 | 90.0 | 90.0 | 90.0 | 90.0 | 90.0 | 90.0 |
| β (°) | 90.0 | 90.0 | 90.0 | 90.0 | 90.0 | 90.0 | 90.0 | 90.0 |
| γ (°) | 120.0 | 120.0 | 120.0 | 120.0 | 120.0 | 120.0 | 120.0 | 120.0 |
| | <i>Se peak</i> | <i>Se peak</i> | <i>Se peak</i> | <i>Se peak</i> | <i>Se peak</i> | <i>Se peak</i> | <i>Se peak</i> | <i>Se peak</i> |
| Wavelength (Å) | 0.97947 | 0.97949 | 0.97951 | 0.97929 | 0.97922 | 0.97922 | 0.97949 | 0.97910 |
| Resolution (Å) | 30.0 – 6.5 | 30.0 – 6.4 | 30.0 – 5.8 | 30.0 – 5.8 | 30.0 – 5.9 | 30.0 – 6.5 | 30.0 – 5.6 | 30.0 – 4.5 |
| <i>F</i> _{merge} (%) ^b | 38.6 (263) | 35.3 (203) | 44.5 (245) | 39.2 (332) | 36.6 (289) | 32.3 (210) | 39.8 (329) | 36.5 (323) |
| <i>F</i> _{meas} (%) ^b | 39.1 (266) | 35.8 (206) | 45.6 (250) | 39.7 (336) | 37.1 (291) | 33.0 (215) | 40.3 (334) | 37.0 (327) |
| <i>F</i> _{pim} (%) ^b | 6.3 (43.5) | 5.8 (33.2) | 9.9 (52.0) | 6.4 (52.9) | 6.2 (47.8) | 6.4 (41.3) | 6.4 (52.0) | 5.8 (50.2) |
| <i>CC</i> _{1/2} (%) ^b | 99.6 (75.2) | 99.7 (81.9) | 99.3 (67.0) | 99.7 (65.3) | 99.6 (66.8) | 99.6 (7.6) | 99.7 (72.4) | 99.9 (67.8) |
| $\langle I \rangle / \langle \sigma \rangle$ ^b | 9.9 (1.9) | 10.4 (2.3) | 5.8 (1.5) | 10.0 (1.5) | 9.2 (1.8) | 8.9 (1.9) | 9.3 (1.6) | 10.7 (1.6) |
| Completeness (%) ^b | 98.7 (98.9) | 98.8 (99.2) | 99.2 (99.6) | 98.9 (99.1) | 99.1 (100.0) | 99.0 (100.0) | 99.3 (99.9) | 99.3 (99.9) |
| No. observations ^b | 385,426 (105,437) | 397,949 (111,545) | 300,981 (90,375) | 539,571 (156,204) | 481,226 (138,712) | 270,195 (75,397) | 613,880 (178,204) | 1,180,062 (177,326) |
| No. unique reflections ^{b,c} | 10,447 (2,890) | 10,815 (2,968) | 14,546 (4,014) | 14,449 (3,971) | 13,790 (3,819) | 10,376 (2,885) | 16,129 (4,450) | 30,272 (4,318) |
| Redundancy ^b | 36.9 (36.5) | 36.8 (37.6) | 20.7 (22.5) | 37.3 (39.3) | 34.9 (36.3) | 26.0 (26.1) | 38.1 (40.0) | 39.0 (41.1) |
| Wilson B factor (Å ²) | 366 | 448 | 334 | 419 | 414 | 479 | 356 | 268 |

^a SSRL, Stanford Synchrotron Radiation Lightsource^b Highest-resolution shell is shown in parentheses^c Friedel pairs were merged

Table S13. X-ray crystallographic analysis of NUP358^{OE}

| Data collection | | |
|---|------------------------------|------------------------------|
| Protein 1 | NUP358 ⁸⁰⁵⁻⁸³² OE | NUP358 ⁸⁰⁵⁻⁸³² OE |
| Stoichiometry | 4 | 4 |
| PDB code | 7MNK | |
| Synchrotron ^a | SSRL | SSRL |
| Beamline | BL 12-2 | BL 12-2 |
| Space group | I422 | I422 |
| Cell parameters | | |
| <i>a</i> (Å) | 99.9 | 99.9 |
| <i>b</i> (Å) | 99.9 | 99.9 |
| <i>c</i> (Å) | 60.2 | 60.2 |
| α (°) | 90.0 | 90.0 |
| β (°) | 90.0 | 90.0 |
| γ (°) | 90.0 | 90.0 |
| | <i>Native</i> | <i>S peak</i> |
| Wavelength (Å) | 0.90000 | 1.30000 |
| Resolution (Å) | 30.0 – 1.1 | 20.0 – 1.45 |
| R_{merge} (%) ^b | 6.0 (295) | 5.2 (16.2) |
| R_{meas} (%) ^b | 6.3 (308) | 5.4 (17.9) |
| R_{pim} (%) ^b | 1.7 (86.8) | 1.5 (7.5) |
| $CC_{1/2}$ (%) ^b | 100.0 (55.3) | 100.0 (98.9) |
| $\langle I \rangle / \langle \sigma I \rangle$ ^b | 24.1 (1.1) | 27.0 (9.5) |
| Completeness (%) ^b | 100.0 (99.9) | 99.9 (87.4) |
| No. observations ^b | 1,558,137 (144,840) | 51,021 (2,360) |
| No. unique reflections ^{b,c} | 61,560 (6,077) | 26,904 (1,123) |
| Redundancy ^b | 25.3 (23.8) | 1.9 (1.9) |
| Wilson B factor (Å ²) | 14 | 11 |
| Refinement | | |
| Resolution (Å) | 30.0 – 1.1 | |
| No. reflections total | 61,541 | |
| No. reflections test set | 2,090 (3.4%) | |
| $R_{\text{work}} / R_{\text{free}}$ (%) | 15.5 / 16.7 | |
| No. atoms | 1,487 | |
| Protein | 1,294 | |
| Ligand/ion | 55 | |
| Water | 138 | |
| <i>B</i> -factors (Å ²) | 23 | |
| Protein | 21 | |
| Ligand/ion | 49 | |
| Water | 36 | |
| R.m.s. deviations | | |
| Bond lengths (Å) | 0.012 | |
| Bond angles (°) | 1.3 | |
| Ramachandran plot^d | | |
| Favored (%) | 100.0 | |
| Additionally allowed (%) | 0 | |
| Outliers (%) | 0 | |

^a SSRL, Stanford Synchrotron Radiation Lightsource^b Highest-resolution shell is shown in parentheses^c Friedel pairs were merged^d As determined by MolProbity (127)

Table S14. X-ray crystallographic analysis of NUP358 ZnF•Ran(GDP) complexes

| Data collection | | | | | | | |
|---|---|---|----------------------------------|-----------------------------|---|-----------------------------|----------------------------------|
| Protein 1 | Ran(GDP) F35S | Ran(GDP) F35S | Ran(GDP) F35S | Ran(GDP) F35S | Ran(GDP) F35S | Ran(GDP) F35S | Ran(GDP) F35S |
| N-terminal tag | None | His ₆ -thrombin | His ₆ -thrombin | His ₆ -thrombin | His ₆ -thrombin | His ₆ -thrombin | His ₆ -thrombin |
| Protein 2 | NUP358 ¹⁴⁰⁷⁻¹⁴⁴³ | NUP358 ¹⁴⁰⁷⁻¹⁴⁴³ | NUP358 ¹⁴⁷¹⁻¹⁵⁰⁷ | NUP358 ¹⁵³⁵⁻¹⁵⁷¹ | NUP358 ¹⁵⁹⁸⁻¹⁶³⁴ | NUP358 ¹⁷¹⁶⁻¹⁷⁵² | NUP358 ¹⁷⁷⁴⁻¹⁸⁰⁹ |
| | ZnF2 | ZnF2 | ZnF3 | ZnF4 | ZnF5 ^e | ZnF7 | ZnF8 |
| PDB code | 7MNP | 7MNQ | 7MNR | 7MNS | 7MNT | 7MNU | 7MNV |
| Synchrotron ^a | SSRL | SSRL | APS | SSRL | APS | SSRL | SSRL |
| Beamline | BL12-2 | BL12-2 | 23 ID-B | BL12-2 | 23 ID-B | BL12-2 | BL12-2 |
| Space group | P2 ₁ 2 ₁ 2 ₁ | P2 ₁ 2 ₁ 2 ₁ | P2 ₁ 2 ₁ 2 | P6 ₅ 22 | P2 ₁ 2 ₁ 2 ₁ | P6 ₅ 22 | P2 ₁ 2 ₁ 2 |
| Cell parameters | | | | | | | |
| <i>a</i> (Å) | 60.2 | 59.8 | 59.6 | 92.5 | 53.0 | 92.7 | 60.5 |
| <i>b</i> (Å) | 79.8 | 78.7 | 80.2 | 92.5 | 94.3 | 92.7 | 80.5 |
| <i>c</i> (Å) | 108.8 | 56.3 | 54.8 | 194.8 | 108.2 | 196.0 | 58.3 |
| α (°) | 90.0 | 90.0 | 90.0 | 90.0 | 90.0 | 90.0 | 90.0 |
| β (°) | 90.0 | 90.0 | 90.0 | 90.0 | 90.0 | 90.0 | 90.0 |
| γ (°) | 90.0 | 90.0 | 90.0 | 120.0 | 90.0 | 120.0 | 90.0 |
| | <i>Zn remote</i> | <i>Zn peak</i> | <i>Zn peak</i> | <i>Zn peak</i> | <i>Zn peak</i> | <i>Zn peak</i> | <i>Zn peak</i> |
| Wavelength (Å) | 1.03317 | 1.28291 | 1.28238 | 1.28210 | 1.28283 | 1.28275 | 1.28247 |
| Resolution (Å) | 30.0 – 2.05 | 30.0 – 2.05 | 30.0 – 1.8 | 30.0 – 2.1 | 30.0 – 2.45 | 30.0 – 2.0 | 30.0 – 1.8 |
| <i>R</i> _{merge} (%) ^b | 11.5 (132) | 9.4 (192) | 7.8 (98.6) | 17.2 (224) | 11.0 (317) | 15.5 (221) | 10.8 (174) |
| <i>R</i> _{meas} (%) ^b | 12.6 (147) | 10.2 (210) | 9.2 (124) | 17.9 (232) | 11.4 (329) | 16.4 (235) | 11.7 (189) |
| <i>R</i> _{pim} (%) ^b | 5.2 (63.9) | 3.9 (83.7) | 4.9 (74.6) | 4.8 (62.0) | 3.1 (88.6) | 5.4 (79.6) | 4.5 (73.7) |
| <i>CC</i> _{1/2} (%) ^b | 99.9 (74.1) | 99.9 (60.3) | 99.8 (57.5) | 99.9 (66.4) | 99.9 (54.1) | 99.9 (63.2) | 99.9 (58.5) |
| $\langle I \rangle / \langle \sigma \rangle$ ^b | 12.5 (1.6) | 13.9 (1.2) | 13.7 (1.3) | 21.2 (1.8) | 21.8 (1.6) | 14.0 (1.4) | 14.0 (1.2) |
| Completeness (%) ^b | 99.4 (95.3) | 99.4 (95.6) | 99.7 (95.8) | 100.0 (99.9) | 100.0 (100.0) | 100.0 (100.0) | 99.6 (96.4) |
| No. observations ^b | 326,611 (28,669) | 215,148 (17,443) | 153,861 (9,866) | 754,508 (73,905) | 524,547 (52,237) | 584,705 (55,080) | 341,183 (31,307) |
| No. unique reflections ^{b,c} | 33,217 (3,140) | 17,126 (1,596) | 24,915 (2,354) | 29,596 (2,860) | 20,617 (2,020) | 34,531 (3,346) | 26,934 (2,561) |
| Redundancy ^b | 10.9 (9.1) | 12.6 (10.9) | 6.2 (4.2) | 25.5 (25.8) | 25.4 (25.9) | 16.9 (16.5) | 12.7 (12.2) |
| Wilson B factor (Å ²) | 30 | 40 | 23 | 32 | 66 | 31 | 25 |
| Refinement | | | | | | | |
| Resolution (Å) | 30.0 – 2.05 | 30.0 – 2.05 | 30.0 – 1.8 | 30.0 – 2.1 | 30.0 – 2.45 | 30.0 – 2.0 | 30.0 – 1.8 |
| No. reflections total | 33,084 | 17,055 | 24,867 | 29,526 | 20,568 | 34,459 | 26,877 |
| No. reflections test set | 1,614 (4.9%) | 891 (5.2%) | 1,230 (5.0%) | 1,477 (5.0%) | 1,019 (5.0%) | 1,784 (5.2%) | 1,422 (5.3%) |
| <i>R</i> _{work} / <i>R</i> _{free} (%) | 19.4 / 23.1 | 19.0 / 20.9 | 16.0 / 19.6 | 17.5 / 20.3 | 21.2 / 25.7 | 20.2 / 22.4 | 15.9 / 18.6 |
| No. atoms | 4,194 | 2,009 | 2,173 | 2,234 | 3,882 | 2,157 | 2,181 |
| Protein | 3,868 | 1,914 | 1,931 | 2,045 | 3,795 | 1,931 | 1,945 |
| Ligand/ion | 60 | 30 | 30 | 30 | 60 | 30 | 36 |
| Water | 266 | 65 | 212 | 159 | 27 | 196 | 200 |
| <i>B</i> -factors (Å ²) | 45 | 65 | 37 | 48 | 98 | 45 | 40 |
| Protein | 46 | 66 | 37 | 48 | 99 | 45 | 40 |
| Ligand/ion | 34 | 51 | 26 | 34 | 84 | 32 | 35 |
| Water | 42 | 54 | 40 | 51 | 75 | 48 | 43 |
| R.m.s. deviations | | | | | | | |
| Bond lengths (Å) | 0.002 | 0.002 | 0.011 | 0.004 | 0.003 | 0.002 | 0.009 |
| Bond angles (°) | 0.6 | 0.6 | 1.1 | 0.7 | 0.6 | 0.6 | 0.9 |
| Ramachandran plot^d | | | | | | | |
| Favored (%) | 97.7 | 98.3 | 98.7 | 98.3 | 98.3 | 98.3 | 97.9 |
| Additionally allowed (%) | 2.3 | 1.7 | 1.3 | 1.7 | 1.7 | 1.7 | 2.1 |
| Outliers (%) | 0 | 0 | 0 | 0 | 0 | 0 | 0 |

^a SSRL, Stanford Synchrotron Radiation Lightsource; APS, Advanced Photon Source^b Highest-resolution shell is shown in parentheses^c Friedel pairs were merged^d As determined by MolProbity (127)^e Primary sequence of NUP358 ZnF5 is identical to ZnF6¹⁶⁵⁷⁻¹⁶⁹³

Table S15. X-ray crystallographic analysis of NUP153 ZnF•Ran(GDP) complexes

| Data collection | | | | | | | | | |
|---|-----------------------------------|-----------------------------------|-----------------------------------|-----------------------------------|-----------------------------------|-----------------------------------|---|-----------------------------------|-----------------------------------|
| Protein 1 | Ran(GDP) F35S | Ran(GDP) F35S | Ran(GDP) F35S | Ran(GDP) F35S | Ran(GDP) F35S | Ran(GDP) F35S | Ran(GDP) F35S | Ran(GDP) F35S | Ran(GDP) F35S |
| N-terminal tag | None | His ₆ -thrombin | None | His ₆ -thrombin | None | None | His ₆ -thrombin | None | His ₆ -thrombin |
| Protein 2 | NUP153 ZnF1 ⁶⁴⁹⁻⁶⁸⁷ | NUP153 ⁶⁵¹⁻⁶⁸⁷ ZnF1 | NUP153 ⁷¹³⁻⁷⁴⁹ ZnF2 | NUP153 ⁷¹³⁻⁷⁴⁹ ZnF2 | NUP153 ⁷⁸¹⁻⁸¹⁷ ZnF3 | NUP153 ⁷⁸¹⁻⁸¹⁷ ZnF3 | NUP153 ⁷⁸¹⁻⁸¹⁷ ZnF3 | NUP153 ⁸³⁸⁻⁸⁷⁴ ZnF4 | NUP153 ⁸³⁸⁻⁸⁷⁴ ZnF4 |
| PDB code | 7MO1 | | 7MO2 | | 7MO3 | 7MO4 | | 7MO5 | |
| Synchrotron ^a | SSRL | SSRL | SSRL | SSRL | SSRL | SSRL | SSRL | SSRL | APS |
| Beamline | BL12-2 | BL12-2 | BL12-2 | BL12-2 | BL12-2 | BL12-2 | BL12-2 | BL12-2 | 23 ID-B |
| Space group | P2 ₁ 2 ₁ 2 | P2 ₁ 2 ₁ 2 | P2 ₁ | P2 ₁ 2 ₁ 2 | P2 ₁ | P2 ₁ | P2 ₁ 2 ₁ 2 ₁ | P2 ₁ 2 ₁ 2 | P2 ₁ 2 ₁ 2 |
| Cell parameters | | | | | | | | | |
| <i>a</i> (Å) | 60.3 | 60.0 | 58.1 | 61.0 | 69.0 | 67.7 | 61.1 | 59.8 | 60.2 |
| <i>b</i> (Å) | 79.6 | 79.8 | 60.4 | 79.7 | 62.6 | 61.2 | 80.8 | 80.1 | 78.7 |
| <i>c</i> (Å) | 55.1 | 54.8 | 79.4 | 57.7 | 70.6 | 69.8 | 114.4 | 54.5 | 54.8 |
| α (°) | 90.0 | 90.0 | 90.0 | 90.0 | 90.0 | 90.0 | 90.0 | 90.0 | 90.0 |
| β (°) | 90.0 | 90.0 | 90.1 | 90.0 | 105.1 | 104.0 | 90.0 | 90.0 | 90.0 |
| γ (°) | 90.0 | 90.0 | 90.0 | 90.0 | 90.0 | 90.0 | 90.0 | 90.0 | 90.0 |
| | <i>Zn remote</i> | <i>Zn peak</i> | <i>Zn remote</i> | <i>Zn peak</i> | <i>Zn remote</i> | <i>Zn remote</i> | <i>Zn peak</i> | <i>Zn remote</i> | <i>Zn peak</i> |
| Wavelength (Å) | 1.03317 | 1.28272 | 1.03317 | 1.28272 | 1.03317 | 0.97946 | 1.28272 | 1.03317 | 1.28279 |
| Resolution (Å) | 30.0 – 1.6 | 30.0 – 1.6 | 30.0 – 1.65 | 30.0 – 1.9 | 30.0 – 2.05 | 30.0 – 2.4 | 30.0 – 1.6 | 30.0 – 1.55 | 30.0 – 1.85 |
| <i>R</i> _{merge} (%) ^b | 7.8 (172) | 5.8 (89.8) | 7.3 (108) | 8.6 (161) | 4.7 (169) | 7.9 (135) | 5.1 (116) | 6.8 (173) | 6.7 (134) |
| <i>R</i> _{meas} (%) ^b | 8.1 (179) | 6.3 (97.8) | 7.9 (119) | 9.4 (176) | 5.5 (198) | 8.6 (146) | 5.5 (126) | 7.4 (187) | 7.3 (148) |
| <i>R</i> _{pim} (%) ^b | 3.0 (49.8) | 2.4 (38.0) | 3.0 (48.1) | 3.6 (68.4) | 2.8 (101) | 3.3 (55.2) | 2.1 (49.1) | 2.8 (71.1) | 2.8 (61.5) |
| <i>CC</i> _{1/2} (%) ^b | 100.0 (65.3) | 99.9 (87.3) | 99.9 (49.3) | 99.9 (77.8) | 99.9 (57.8) | 99.8 (75.1) | 100.0 (74.3) | 99.9 (58.8) | 99.9 (63.5) |
| $\langle I \rangle / \langle \sigma \rangle$ ^b | 19.0 (1.5) | 24.6 (2.9) | 13.8 (1.5) | 13.5 (1.2) | 15.7 (1.1) | 11.3 (1.3) | 23.2 (2.0) | 15.3 (2.3) | 20.1 (1.7) |
| Completeness (%) ^b | 100.0 (99.5) | 99.0 (97.5) | 98.5 (96.6) | 99.9 (99.4) | 93.2 (93.7) | 98.6 (98.5) | 99.0 (97.1) | 99.9 (99.9) | 100.0 (100.0) |
| No. observations ^b | 467,759 (22,144) | 445,449 (42,096) | 444,419 (18,540) | 282,478 (27,077) | 247,248 (24,296) | 145,075 (14,427) | 961,259 (88,740) | 498,936 (50,078) | 291,124 (23,395) |
| No. unique reflections ^{b,c} | 35,851 (1,762) | 35,072 (3,423) | 65,381 (3,167) | 22,744 (2,221) | 34,158 (3,415) | 21,520 (2,104) | 74,712 (7,263) | 38,670 (50,078) | 22,891 (2,238) |
| Redundancy ^b | 13.0 (12.6) | 6.7 (6.4) | 68 (5.9) | 12.4 (12.2) | 7.2 (7.1) | 6.7 (6.9) | 12.9 (12.2) | 12.9 (13.1) | 12.7 (10.5) |
| Wilson B factor (Å ²) | 21 | 23 | 21 | 38 | 49 | 63 | 23 | 21 | 31 |
| Refinement | | | | | | | | | |
| Resolution (Å) | 30.0 – 1.6 | | 30.0 – 1.65 | | 30.0 – 2.05 | | 30.0 – 2.4 | | 30.0 – 1.55 |
| No. reflections total | 35,806 | | 65,364 | | 34,076 | | 21,484 | | 38,623 |
| No. reflections test set | 1,756 (4.9%) | | 3,284 (5.0%) | | 1,626 (4.8%) | | 1081 (4.4%) | | 1,871 (4.8%) |
| <i>R</i> _{work} / <i>R</i> _{free} (%) | 15.1 / 17.5 | | 21.1 / 24.1 | | 20.4 / 22.8 | | 21.4 / 23.7 | | 16.2 / 19.0 |
| No. atoms | 2,235 | | 4,320 | | 4,004 | | 3,914 | | 2,176 |
| Protein | 1,983 | | 3,832 | | 3,861 | | 3,828 | | 1,918 |
| Ligand/ion | 30 | | 60 | | 60 | | 60 | | 30 |
| Water | 222 | | 428 | | 83 | | 26 | | 228 |
| <i>B</i> -factors (Å ²) | 35 | | 38 | | 89 | | 98 | | 36 |
| Protein | 35 | | 38 | | 90 | | 98 | | 35 |
| Ligand/ion | 23 | | 29 | | 64 | | 79 | | 24 |
| Water | 39 | | 37 | | 65 | | 75 | | 40 |
| R.m.s. deviations | | | | | | | | | |
| Bond lengths (Å) | 0.013 | | 0.012 | | 0.013 | | 0.012 | | 0.013 |
| Bond angles (°) | 1.2 | | 0.9 | | 0.9 | | 0.8 | | 1.2 |
| Ramachandran plot^d | | | | | | | | | |
| Favored (%) | 97.8 | | 97.7 | | 97.7 | | 97.9 | | 97.9 |
| Additionally allowed (%) | 2.2 | | 2.3 | | 2.3 | | 2.1 | | 2.1 |
| Outliers (%) | 0.0 | | 0.0 | | 0.0 | | 0.0 | | 0.0 |

^aSSRL, Stanford Synchrotron Radiation Lightsource; APS, Advanced Photon Source^bHighest-resolution shell is shown in parentheses^cFriedel pairs were merged^dAs determined by MolProbity (127)

Table S16. X-ray crystallographic analysis of NUP358/50 RanBD•Ran(GMPPNP) complexes

| Data collection | | NUP358 ¹¹⁷¹⁻¹³⁰⁶ RanBD1 | NUP358 ²⁰¹¹⁻²¹⁴⁸ RanBD2 | NUP358 ²³⁰⁹⁻²⁴⁴³ RanBD3 | NUP358 ²⁹¹¹⁻³⁰⁴⁵ RanBD4 | NUP50 ³³⁷⁻⁴⁶⁸ RanBD |
|---|------------------|---|---|------------------------------------|---|---|
| Protein 1 | Wildtype | Wildtype | Wildtype | Wildtype | WHTMKNYQ/ONYDNKQV | Wildtype |
| Protein 2 | Ran(GMPPNP) | Ran(GMPPNP) | Ran(GMPPNP) | Ran(GMPPNP) | Ran(GMPPNP) | Ran(GMPPNP) |
| PDB code | 7MNV | 7MNX | 7MNY | 7MNZ | 7MO0 | 7MO0 |
| Synchrotron ^a | APS | SSRL | APS | SSRL | APS | APS |
| Beamline | 23 ID-B | BL 12-2 | 23 ID-B | BL 12-2 | 23 ID-D | 23 ID-D |
| Space group | I222 | P2 ₁ 2 ₁ 2 ₁ | P2 ₁ 2 ₁ 2 ₁ | P3 ₁ | P2 ₁ 2 ₁ 2 ₁ | P2 ₁ 2 ₁ 2 ₁ |
| Cell parameters | | | | | | |
| <i>a</i> (Å) | 137.4 | 94.2 | 110.2 | 142.7 | 66.6 | 66.6 |
| <i>b</i> (Å) | 137.8 | 134.0 | 136.0 | 142.7 | 73.2 | 73.2 |
| <i>c</i> (Å) | 172.9 | 182.5 | 158.8 | 96.7 | 152.9 | 152.9 |
| α (°) | 90.0 | 90.0 | 90.0 | 90.0 | 90 | 90 |
| β (°) | 90.0 | 90.0 | 90.0 | 90.0 | 90 | 90 |
| γ (°) | 90.0 | 90.0 | 90.0 | 120.0 | 90 | 90 |
| | <i>Native</i> | <i>Native</i> | <i>Native</i> | <i>Native</i> | <i>Se peak</i> | <i>Se peak</i> |
| Wavelength (Å) | 1.00000 | 0.97946 | 1.00000 | 1.03317 | 0.97942 | 0.97942 |
| Resolution (Å) | 30.0 – 2.40 | 30.0 – 2.4 | 30.0 – 2.70 | 30.0 – 2.35 | 30.0 – 2.45 | 30.0 – 2.45 |
| <i>F</i> _{merge} (%) ^b | 28.6 (268) | 16.1 (230) | 21.7 (174) | 14.1 (165) | 11.0 (251) | 11.0 (251) |
| <i>F</i> _{meas} (%) ^b | 30.8 (288) | 17.4 (251) | 23.4 (188) | 15.8 (185) | 11.9 (271) | 11.9 (271) |
| <i>R</i> _{pim} (%) ^b | 11.5 (106) | 6.6 (98.8) | 8.8 (70.9) | 6.9 (84.1) | 4.5 (102) | 4.5 (102) |
| <i>CC</i> _{1/2} (%) ^b | 99.7 (47.0) | 99.7 (54.7) | 99.6 (69.9) | 99.8 (59.9) | 99.8 (55.2) | 99.8 (55.2) |
| $\langle I \rangle / \langle \sigma \rangle$ ^b | 6.7 (1.3) | 9.7 (1.1) | 8.4 (1.5) | 12.4 (1.8) | 15.3 (1.1) | 15.3 (1.1) |
| Completeness (%) ^b | 99.8 (98.2) | 98.8 (96.9) | 100.0 (99.8) | 99.9 (99.8) | 100.0 (99.6) | 100.0 (99.6) |
| No. observations ^b | 880,269 (87,689) | 1,189,731 (107,541) | 900,779 (88,275) | 935,004 (86,810) | 369,132 (36,629) | 369,132 (36,629) |
| No. unique reflections ^{b,c} | 64,146 (6,219) | 89,794 (8,716) | 66,178 (6,497) | 91,578 (9,170) | 28,242 (2,762) | 28,242 (2,762) |
| Redundancy ^b | 13.7 (14.1) | 13.2 (12.3) | 7.1 (7.0) | 10.2 (9.5) | 13.1 (13.3) | 13.1 (13.3) |
| Wilson B factor (Å ²) | 36 | 46 | 44 | 44 | 56 | 56 |
| Refinement | | | | | | |
| Resolution (Å) | 30.0 – 2.4 | 30.0 – 2.4 | 30.0 – 2.7 | 30.0 – 2.35 | 30.0 – 2.45 | 30.0 – 2.45 |
| No. reflections total | 64,143 | 89,660 | 66,076 | 91,515 | 28,183 | 28,183 |
| No. reflections test set | 3,185 (5.0%) | 2,353 (2.6%) | 3,310 (5.0%) | 4,426 (4.8%) | 2,618 (4.9%) | 2,618 (4.9%) |
| <i>R</i> _{work} / <i>R</i> _{free} (%) | 20.2 / 24.1 | 19.2 / 23.0 | 21.4 / 26.2 | 18.3 / 22.5 | 21.2 / 23.9 | 21.2 / 23.9 |
| No. atoms | 11,709 | 16,979 | 16,688 | 17,360 | 5,503 | 5,503 |
| Protein | 11,177 | 16,397 | 16,223 | 16,669 | 5,369 | 5,369 |
| Ligand/ion | 132 | 198 | 198 | 270 | 71 | 71 |
| Water | 400 | 384 | 267 | 473 | 63 | 63 |
| <i>B</i> -factors (Å ²) | 56 | 69 | 76 | 60 | 78 | 78 |
| Protein | 56 | 70 | 77 | 61 | 79 | 79 |
| Ligand/ion | 45 | 47 | 50 | 42 | 67 | 67 |
| Water | 44 | 55 | 53 | 51 | 59 | 59 |
| R.m.s. deviations | | | | | | |
| Bond lengths (Å) | 0.004 | 0.004 | 0.003 | 0.002 | 0.004 | 0.004 |
| Bond angles (°) | 0.7 | 0.7 | 0.6 | 0.5 | 0.7 | 0.7 |
| Ramachandran plot^d | | | | | | |
| Favored (%) | 98.3 | 98.1 | 98.0 | 97.5 | 98.0 | 98.0 |
| Additionally allowed (%) | 1.7 | 1.9 | 2.0 | 2.5 | 2.0 | 2.0 |
| Outliers (%) | 0 | 0 | 0 | 0 | 0 | 0 |

^aSSRL, Stanford Synchrotron Radiation Lightsource; APS, Advanced Photon Source^bHighest-resolution shell is shown in parentheses^cFriedel pairs were merged^dAs determined by MolProbity (127)

Table S17. X-ray crystallographic analysis of NUP88^{NTD}•NUP98^{APD}

| Data collection | |
|---|------------------------------|
| Protein 1 | NUP88 ¹⁻⁴⁹³ NTD |
| Protein 2 | NUP98 ⁷³²⁻⁸⁸⁰ APD |
| PDB code | 7MNI |
| Synchrotron ^a | APS |
| Beamline | 23 ID-B |
| Space group | P1 |
| Cell parameters | |
| <i>a</i> (Å) | 59.8 |
| <i>b</i> (Å) | 72.1 |
| <i>c</i> (Å) | 73.0 |
| α (°) | 92.5 |
| β (°) | 103.7 |
| γ (°) | 100.4 |
| | <i>Native</i> |
| Wavelength (Å) | 1.00003 |
| Resolution (Å) | 20.0 – 2.0 |
| <i>R</i> _{merge} (%) ^b | 13.1 (98.4) |
| <i>R</i> _{meas} (%) ^b | 14.3 (116) |
| <i>R</i> _{pim} (%) ^b | 5.6 (60.4) |
| <i>CC</i> _{1/2} (%) ^b | 99.6 (51.3) |
| <i><I> / <σI></i> ^b | 7.5 (1.3) |
| Completeness (%) ^b | 97.8 (96.6) |
| No. observations ^b | 456,229 (16,182) |
| No. unique reflections ^{b,c} | 76,633 (4,472) |
| Redundancy ^c | 6.0 (3.6) |
| Wilson B factor (Å ²) | 36 |
| Refinement | |
| Resolution (Å) | 20.0 – 2.0 |
| No. reflections total | 76,489 |
| No. reflections test set | 3,639 (4.8%) |
| <i>R</i> _{work} / <i>R</i> _{free} (%) | 17.5 / 20.8 |
| No. atoms | 9,442 |
| Protein | 9,024 |
| Ligand/ion | 0 |
| Water | 418 |
| <i>B</i> -factors (Å ²) | 56 |
| Protein | 56 |
| Ligand/ion | - |
| Water | 49 |
| R.m.s. deviations | |
| Bond lengths (Å) | 0.002 |
| Bond angles (°) | 0.5 |
| Ramachandran plot^d | |
| Favored (%) | 98.7 |
| Additionally allowed (%) | 1.3 |
| Outliers (%) | 0.09 |

^aAPS, Advanced Photon Source

^bHighest-resolution shell is shown in parentheses

^cFriedel pairs were merged

^dAs determined by MolProbity (127)

Table S18. Inventory of experimental nup structures in the composite structure of the human NPC

| Human nup or nup complex | Experimental structure | PDB ID | References |
|--|---|--------|------------|
| CNC (SEC13•NUP96•SEH1•NUP75•NUP160•NUP107•NUP84•NUP133•NUP37•NUP43) | <i>S. cerevisiae</i> CNC-hexamer (Sec13•Nup145C•Seh1•Nup85•Nup120•Nup84 ^{NTD}) | 4XMM | (27) |
| | <i>H. sapiens</i> NUP107 ^{CTD} •NUP133 | 3I4R | (20) |
| | <i>H. sapiens</i> NUP133 ^{NTD} | 1XKS | (14) |
| | <i>H. sapiens</i> NUP43 | 4I79 | (26) |
| | <i>H. sapiens</i> NUP37 | 4FHM | (24) |
| NUP155•NUP98 ^{R3} •NUP53 ^{R3} | <i>C. thermophilum</i> Nup170 ^{NTD} •Nup53 ^{R3} | 5HAX | (38) |
| | <i>C. thermophilum</i> Nup170 ^{CTD} | 5HAY | (38) |
| | <i>C. thermophilum</i> Nup170 ^{CTD} | 5HAZ | (38) |
| | <i>C. thermophilum</i> Nup170 ^{CTD} •Nup145N ^{R3} | 5HB0 | (38) |
| | <i>C. thermophilum</i> Nup170 ^{SOL} | 5HB1 | (38) |
| NUP93 ^{SOL} •NUP53 ^{R2} | <i>H. sapiens</i> NUP93 ^{SOL} •NUP53 ^{R2} | 7MW0 | (42) |
| NUP205•NUP93 ^{R2} •NUP98 ^{R1} •NUP53 ^{R1} | <i>C. thermophilum</i> Nup192 ^{NTD} | 4KNH | (37) |
| | <i>C. thermophilum</i> Nup192 ^{ΔHead} •Nic96 ¹⁸⁷⁻³⁰¹ | 7MVT | (42) |
| | <i>C. thermophilum</i> Nup192•Nic96 ^{R2} •Nup145N ^{R1} •Nup53 ^{R1} | 7MVV | (42) |
| NUP188•NUP93 ^{R2} •NUP98 ^{R2} | <i>C. thermophilum</i> Nup188•Nic96 ^{R2} •Nup145N ^{R2} | 7MVZ | (42) |
| CNT•NUP93 ^{R1} (NUP62•NUP58•NUP54•NUP93 ^{R1}) | <i>C. thermophilum</i> CNT•Nic96 ^{R1} (Nsp1•Nup49•Nup57•Nic96 ^{R1}) | 5CWS | (11) |
| | <i>X. laevis</i> NUP54 ferredoxin-like domain | 5C2U | (10) |
| NUP53 ^{RRM} | <i>H. sapiens</i> NUP53 ^{RRM} | 4LIR | N/A |
| NUP88 ^{NTD} •NUP98 ^{APD} | <i>H. sapiens</i> NUP88 ^{NTD} •NUP98 ^{APD} | 7MNI | This study |
| NUP214 ^{NTD} •DDX19 | <i>H. sapiens</i> NUP214 ^{NTD} •DDX19 | 3FMO | (54) |
| CFNC-hub model | <i>C. thermophilum</i> CNT•Nic96 ^{R1} (Nsp1•Nup49•Nup57•Nic96 ^{R1}) | 5CWS | (11) |
| | <i>X. laevis</i> CNT (NUP62•NUP58•NUP54) | 5C3L | (10) |
| GLE1 ^{CTD} •NUP42 ^{GBM} | <i>H. sapiens</i> GLE1 ^{CTD} •NUP42 ^{GBM} | 6B4F | (63) |
| ELYS ^{NTD} | <i>M. musculus</i> ELYS ^{NTD} | 4I0O | (25) |
| NUP358 ^{NTD} | <i>H. sapiens</i> NUP358 ^{NTD} | 7MNL | This study |
| NUP358 ^{OE} | <i>H. sapiens</i> NUP358 ^{OE} | 7MNK | This study |
| NUP358 ^{ZnF2} •Ran(GDP) | <i>H. sapiens</i> NUP358 ^{ZnF2} •Ran(GDP) | 7MNP | This study |
| NUP358 ^{ZnF3} •Ran(GDP) | <i>H. sapiens</i> NUP358 ^{ZnF3} •Ran(GDP) | 7MNR | This study |
| NUP358 ^{ZnF4} •Ran(GDP) | <i>H. sapiens</i> NUP358 ^{ZnF4} •Ran(GDP) | 7MNS | This study |
| NUP358 ^{ZnF5/6} •Ran(GDP) | <i>H. sapiens</i> NUP358 ^{ZnF5/6} •Ran(GDP) | 7MNT | This study |
| NUP358 ^{ZnF7} •Ran(GDP) | <i>H. sapiens</i> NUP358 ^{ZnF7} •Ran(GDP) | 7MNU | This study |
| NUP358 ^{ZnF8} •Ran(GDP) | <i>H. sapiens</i> NUP358 ^{ZnF8} •Ran(GDP) | 7MNV | This study |
| NUP358 ^{RanBD-I} •Ran(GMPPNP) | <i>H. sapiens</i> NUP358 ^{RanBD-I} •Ran(GMPPNP) | 7MNW | This study |
| NUP358 ^{RanBD-II} •Ran(GMPPNP) | <i>H. sapiens</i> NUP358 ^{RanBD-II} •Ran(GMPPNP) | 7MNX | This study |
| NUP358 ^{RanBD-III} •Ran(GMPPNP) | <i>H. sapiens</i> NUP358 ^{RanBD-III} •Ran(GMPPNP) | 7MNY | This study |
| NUP358 ^{RanBD-IV} •Ran(GMPPNP) | <i>H. sapiens</i> NUP358 ^{RanBD-IV} •Ran(GMPPNP) | 7MNZ | This study |
| NUP358 ^{E3} •SUMO-RanGAP•UBC9 | <i>H. sapiens</i> NUP358 ^{E3} •SUMO-RanGAP•UBC9 | 1Z5S | (153) |
| NUP358 ^{CTD} | <i>H. sapiens</i> NUP358 ^{CTD} | 4I9Y | (129) |

Supplemental References

1. A. Hoelz, E. W. Debler, G. Blobel, The structure of the nuclear pore complex. *Annu. Rev. Biochem.* **80**, 613-643 (2011).
2. D. H. Lin, A. Hoelz, The Structure of the Nuclear Pore Complex (An Update). *Annu. Rev. Biochem.* **88**, 725-783 (2019).
3. B. Hampoelz, A. Andres-Pons, P. Kastiris, M. Beck, Structure and Assembly of the Nuclear Pore Complex. *Annu. Rev. Biophys.* **48**, 515-536 (2019).
4. K. E. Knockenhauer, T. U. Schwartz, The Nuclear Pore Complex as a Flexible and Dynamic Gate. *Cell* **164**, 1162-1171 (2016).
5. M. L. Yarbrough, M. A. Mata, R. Sakthivel, B. M. Fontoura, Viral subversion of nucleocytoplasmic trafficking. *Traffic* **15**, 127-140 (2014).
6. A. Kohler, E. Hurt, Gene regulation by nucleoporins and links to cancer. *Mol. Cell* **38**, 6-15 (2010).
7. A. Cook, F. Bono, M. Jinek, E. Conti, Structural biology of nucleocytoplasmic transport. *Annu. Rev. Biochem.* **76**, 647-671 (2007).
8. R. A. Pumroy, G. Cingolani, Diversification of importin-alpha isoforms in cellular trafficking and disease states. *Biochem. J.* **466**, 13-28 (2015).
9. Y. M. Chook, K. E. Suel, Nuclear import by karyopherin-betas: recognition and inhibition. *Biochim. Biophys. Acta* **1813**, 1593-1606 (2011).
10. H. Chug, S. Trakhanov, B. B. Hulsmann, T. Pleiner, D. Gorlich, Crystal structure of the metazoan Nup62*Nup58*Nup54 nucleoporin complex. *Science* **350**, 106-110 (2015).
11. T. Stuwe, C. J. Bley, K. Thierbach, S. Petrovic, S. Schilbach, D. J. Mayo, T. Perriches, E. J. Rundlet, Y. E. Jeon, L. N. Collins, F. M. Huber, D. H. Lin, M. Paduch, A. Koide, V. Lu, J. Fischer, E. Hurt, S. Koide, A. A. Kossiakoff, A. Hoelz, Architecture of the fungal nuclear pore inner ring complex. *Science* **350**, 56-64 (2015).
12. J. Fischer, R. Teimer, S. Amlacher, R. Kunze, E. Hurt, Linker Nups connect the nuclear pore complex inner ring with the outer ring and transport channel. *Nat. Struct. Mol. Biol.* **22**, 774-781 (2015).
13. A. E. Hodel, M. R. Hodel, E. R. Griffis, K. A. Hennig, G. A. Ratner, S. Xu, M. A. Powers, The three-dimensional structure of the autoproteolytic, nuclear pore-targeting domain of the human nucleoporin Nup98. *Mol. Cell* **10**, 347-358 (2002).
14. I. C. Berke, T. Boehmer, G. Blobel, T. U. Schwartz, Structural and functional analysis of Nup133 domains reveals modular building blocks of the nuclear pore complex. *J. Cell Biol.* **167**, 591-597 (2004).
15. K. C. Hsia, P. Stavropoulos, G. Blobel, A. Hoelz, Architecture of a coat for the nuclear pore membrane. *Cell* **131**, 1313-1326 (2007).
16. S. G. Brohawn, N. C. Leksa, E. D. Spear, K. R. Rajashankar, T. U. Schwartz, Structural evidence for common ancestry of the nuclear pore complex and vesicle coats. *Science* **322**, 1369-1373 (2008).
17. T. Boehmer, S. Jeudy, I. C. Berke, T. U. Schwartz, Structural and functional studies of Nup107/Nup133 interaction and its implications for the architecture of the nuclear pore complex. *Mol. Cell* **30**, 721-731 (2008).
18. E. W. Debler, Y. Ma, H. S. Seo, K. C. Hsia, T. R. Noriega, G. Blobel, A. Hoelz, A fence-like coat for the nuclear pore membrane. *Mol. Cell* **32**, 815-826 (2008).
19. N. C. Leksa, S. G. Brohawn, T. U. Schwartz, The structure of the scaffold nucleoporin Nup120 reveals a new and unexpected domain architecture. *Structure* **17**, 1082-1091 (2009).
20. J. R. R. Whittle, T. U. Schwartz, Architectural nucleoporins Nup157/170 and Nup133 are structurally related and descend from a second ancestral element. *J. Biol. Chem.* **284**, 28442-28452 (2009).

21. H. S. Seo, Y. Ma, E. W. Debler, D. Wacker, S. Kutik, G. Blobel, A. Hoelz, Structural and functional analysis of Nup120 suggests ring formation of the Nup84 complex. *Proc. Natl. Acad. Sci. U.S.A.* **106**, 14281-14286 (2009).
22. S. G. Brohawn, T. U. Schwartz, Molecular architecture of the Nup84-Nup145C-Sec13 edge element in the nuclear pore complex lattice. *Nat. Struct. Mol. Biol.* **16**, 1173-1177 (2009).
23. V. Nagy, K. C. Hsia, E. W. Debler, M. Kampmann, A. M. Davenport, G. Blobel, A. Hoelz, Structure of a trimeric nucleoporin complex reveals alternate oligomerization states. *Proc. Natl. Acad. Sci. U.S.A.* **106**, 17693-17698 (2009).
24. S. Bilokapic, T. U. Schwartz, Molecular basis for Nup37 and ELY5/ELYS recruitment to the nuclear pore complex. *Proc. Natl. Acad. Sci. U.S.A.* **109**, 15241-15246 (2012).
25. S. Bilokapic, T. U. Schwartz, Structural and functional studies of the 252 kDa nucleoporin ELYS reveal distinct roles for its three tethered domains. *Structure* **21**, 572-580 (2013).
26. C. Xu, Z. Li, H. He, A. Wernimont, Y. Li, P. Loppnau, J. Min, Crystal structure of human nuclear pore complex component NUP43. *FEBS Lett.* **589**, 3247-3253 (2015).
27. T. Stuwe, A. R. Correia, D. H. Lin, M. Paduch, V. T. Lu, A. A. Kossiakov, A. Hoelz, Nuclear pores. Architecture of the nuclear pore complex coat. *Science* **347**, 1148-1152 (2015).
28. K. Kelley, K. E. Knockenhauer, G. Kabachinski, T. U. Schwartz, Atomic structure of the Y complex of the nuclear pore. *Nat. Struct. Mol. Biol.* **22**, 425-431 (2015).
29. A. Hoelz, J. S. Glavy, M. Beck, Toward the atomic structure of the nuclear pore complex: when top down meets bottom up. *Nat. Struct. Mol. Biol.* **23**, 624-630 (2016).
30. K. H. Bui, A. von Appen, A. L. DiGuilio, A. Ori, L. Sparks, M. T. Mackmull, T. Bock, W. Hagen, A. Andres-Pons, J. S. Glavy, M. Beck, Integrated structural analysis of the human nuclear pore complex scaffold. *Cell* **155**, 1233-1243 (2013).
31. N. Handa, M. Kukimoto-Niino, R. Akasaka, S. Kishishita, K. Murayama, T. Terada, M. Inoue, T. Kigawa, S. Kose, N. Imamoto, A. Tanaka, Y. Hayashizaki, M. Shirouzu, S. Yokoyama, The crystal structure of mouse Nup35 reveals atypical RNP motifs and novel homodimerization of the RRM domain. *J. Mol. Biol.* **363**, 114-124 (2006).
32. S. Jeudy, T. U. Schwartz, Crystal structure of nucleoporin Nic96 reveals a novel, intricate helical domain architecture. *J. Biol. Chem.* **282**, 34904-34912 (2007).
33. N. Schrader, P. Stelter, D. Flemming, R. Kunze, E. Hurt, I. R. Vetter, Structural basis of the nic96 subcomplex organization in the nuclear pore channel. *Mol. Cell* **29**, 46-55 (2008).
34. H. S. Seo, B. J. Blus, N. Z. Jankovic, G. Blobel, Structure and nucleic acid binding activity of the nucleoporin Nup157. *Proc. Natl. Acad. Sci. U.S.A.* **110**, 16450-16455 (2013).
35. P. Sampathkumar, S. J. Kim, P. Upla, W. J. Rice, J. Phillips, B. L. Timney, U. Pieper, J. B. Bonanno, J. Fernandez-Martinez, Z. Hakhverdyan, N. E. Ketaren, T. Matsui, T. M. Weiss, D. L. Stokes, J. M. Sauder, S. K. Burley, A. Sali, M. P. Rout, S. C. Almo, Structure, dynamics, evolution, and function of a major scaffold component in the nuclear pore complex. *Structure* **21**, 560-571 (2013).
36. K. R. Andersen, E. Onischenko, J. H. Tang, P. Kumar, J. Z. Chen, A. Ulrich, J. T. Liphardt, K. Weis, T. U. Schwartz, Scaffold nucleoporins Nup188 and Nup192 share structural and functional properties with nuclear transport receptors. *Elife* **2**, e00745 (2013).
37. T. Stuwe, D. H. Lin, L. N. Collins, E. Hurt, A. Hoelz, Evidence for an evolutionary relationship between the large adaptor nucleoporin Nup192 and karyopherins. *Proc. Natl. Acad. Sci. U.S.A.* **111**, 2530-2535 (2014).
38. D. H. Lin, T. Stuwe, S. Schilbach, E. J. Rundlet, T. Perriches, G. Mobbs, Y. Fan, K. Thierbach, F. M. Huber, L. N. Collins, A. M. Davenport, Y. E. Jeon, A. Hoelz, Architecture of the symmetric core of the nuclear pore. *Science* **352**, aaf1015 (2016).
39. J. Kosinski, S. Mosalaganti, A. von Appen, R. Teimer, A. L. DiGuilio, W. Wan, K. H. Bui, W. J. Hagen, J. A. Briggs, J. S. Glavy, E. Hurt, M. Beck, Molecular architecture of the inner ring scaffold of the human nuclear pore complex. *Science* **352**, 363-365 (2016).

40. S. J. Kim, J. Fernandez-Martinez, I. Nudelman, Y. Shi, W. Zhang, B. Raveh, T. Herricks, B. D. Slaughter, J. A. Hogan, P. Upla, I. E. Chemmama, R. Pellarin, I. Echeverria, M. Shivaraju, A. S. Chaudhury, J. Wang, R. Williams, J. R. Unruh, C. H. Greenberg, E. Y. Jacobs, Z. Yu, M. J. de la Cruz, R. Mironska, D. L. Stokes, J. D. Aitchison, M. F. Jarrold, J. L. Gerton, S. J. Ludtke, C. W. Akey, B. T. Chait, A. Sali, M. P. Rout, Integrative structure and functional anatomy of a nuclear pore complex. *Nature* **555**, 475-482 (2018).
41. M. Allegretti, C. E. Zimmerli, V. Rantos, F. Wilfling, P. Ronchi, H. K. H. Fung, C. W. Lee, W. Hagen, B. Turonova, K. Karius, M. Bormel, X. Zhang, C. W. Muller, Y. Schwab, J. Mahamid, B. Pfander, J. Kosinski, M. Beck, In-cell architecture of the nuclear pore and snapshots of its turnover. *Nature* **586**, 796-800 (2020).
42. S. Petrovic, D. Samanta, T. Perriches, C. J. Bley, K. Thierbach, B. Brown, S. Nie, G. W. Mobbs, T. A. Stevens, X. Liu, G. P. Tomaleri, L. Schaus, A. Hoelz, Architecture of the linker-scaffold in the nuclear pore. *Accompanying Manuscript*, (2022).
43. M. Stewart, Polyadenylation and nuclear export of mRNAs. *J. Biol. Chem.* **294**, 2977-2987 (2019).
44. A. von Appen, J. Kosinski, L. Sparks, A. Ori, A. L. DiGuilio, B. Vollmer, M. T. Mackmull, N. Banterle, L. Parca, P. Kastritis, K. Buczak, S. Mosalaganti, W. Hagen, A. Andres-Pons, E. A. Lemke, P. Bork, W. Antonin, J. S. Glavy, K. H. Bui, M. Beck, In situ structural analysis of the human nuclear pore complex. *Nature* **526**, 140-143 (2015).
45. G. Huang, Y. Zhang, X. Zhu, C. Zeng, Q. Wang, Q. Zhou, Q. Tao, M. Liu, J. Lei, C. Yan, Y. Shi, Structure of the cytoplasmic ring of the *Xenopus laevis* nuclear pore complex by cryo-electron microscopy single particle analysis. *Cell Res.* **30**, 520-531 (2020).
46. S. Mosalaganti, A. Obarska-Kosinska, M. Siggel, B. Turonova, C. E. Zimmerli, K. Buczak, F. H. Schmidt, E. Margiotta, M.-T. Mackmull, W. Hagen, G. Hummer, M. Beck, J. Kosinski, Artificial intelligence reveals nuclear pore complexity. *bioRxiv*, 2021.2010.2026.465776 (2021).
47. P. Grandi, S. Emig, C. Weise, F. Hucho, T. Pohl, E. C. Hurt, A novel nuclear pore protein Nup82p which specifically binds to a fraction of Nsp1p. *J. Cell Biol.* **130**, 1263-1273 (1995).
48. S. M. Bailer, S. Siniossoglou, A. Podtelejnikov, A. Hellwig, M. Mann, E. Hurt, Nup116p and nup100p are interchangeable through a conserved motif which constitutes a docking site for the mRNA transport factor gle2p. *EMBO J.* **17**, 1107-1119 (1998).
49. N. Belgareh, C. Snay-Hodge, F. Pasteau, S. Dagher, C. N. Cole, V. Doye, Functional characterization of a Nup159p-containing nuclear pore subcomplex. *Mol. Biol. Cell* **9**, 3475-3492 (1998).
50. C. Schmitt, C. von Kobbe, A. Bachi, N. Pante, J. P. Rodrigues, C. Boscheron, G. Rigaut, M. Wilm, B. Seraphin, M. Carmo-Fonseca, E. Izaurralde, Dbp5, a DEAD-box protein required for mRNA export, is recruited to the cytoplasmic fibrils of nuclear pore complex via a conserved interaction with CAN/Nup159p. *EMBO J.* **18**, 4332-4347 (1999).
51. A. K. Ho, T. X. Shen, K. J. Ryan, E. Kiseleva, M. A. Levy, T. D. Allen, S. R. Wente, Assembly and preferential localization of Nup116p on the cytoplasmic face of the nuclear pore complex by interaction with Nup82p. *Mol. Cell. Biol.* **20**, 5736-5748 (2000).
52. C. S. Weirich, J. P. Erzberger, J. M. Berger, K. Weis, The N-terminal domain of Nup159 forms a beta-propeller that functions in mRNA export by tethering the helicase Dbp5 to the nuclear pore. *Mol. Cell* **16**, 749-760 (2004).
53. A. R. Alcazar-Roman, E. J. Tran, S. Guo, S. R. Wente, Inositol hexakisphosphate and Gle1 activate the DEAD-box protein Dbp5 for nuclear mRNA export. *Nat. Cell Biol.* **8**, 711-716 (2006).
54. J. Napetschnig, G. Blobel, A. Hoelz, Crystal structure of the N-terminal domain of the human protooncogene Nup214/CAN. *Proc. Natl. Acad. Sci. U.S.A.* **104**, 1783-1788 (2007).

55. J. Napetschnig, S. A. Kassube, E. W. Debler, R. W. Wong, G. Blobel, A. Hoelz, Structural and functional analysis of the interaction between the nucleoporin Nup214 and the DEAD-box helicase Ddx19. *Proc. Natl. Acad. Sci. U.S.A.* **106**, 3089-3094 (2009).
56. H. von Moeller, C. Basquin, E. Conti, The mRNA export protein DBP5 binds RNA and the cytoplasmic nucleoporin NUP214 in a mutually exclusive manner. *Nat. Struct. Mol. Biol.* **16**, 247-254 (2009).
57. Y. Ren, H. S. Seo, G. Blobel, A. Hoelz, Structural and functional analysis of the interaction between the nucleoporin Nup98 and the mRNA export factor Rae1. *Proc. Natl. Acad. Sci. U.S.A.* **107**, 10406-10411 (2010).
58. B. Montpetit, N. D. Thomsen, K. J. Helmke, M. A. Seeliger, J. M. Berger, K. Weis, A conserved mechanism of DEAD-box ATPase activation by nucleoporins and InsP6 in mRNA export. *Nature* **472**, 238-242 (2011).
59. K. Yoshida, H. S. Seo, E. W. Debler, G. Blobel, A. Hoelz, Structural and functional analysis of an essential nucleoporin heterotrimer on the cytoplasmic face of the nuclear pore complex. *Proc. Natl. Acad. Sci. U.S.A.* **108**, 16571-16576 (2011).
60. T. Stuwe, L. S. von Borzyskowski, A. M. Davenport, A. Hoelz, Molecular basis for the anchoring of proto-oncoprotein Nup98 to the cytoplasmic face of the nuclear pore complex. *J. Mol. Biol.* **419**, 330-346 (2012).
61. M. Gaik, D. Flemming, A. von Appen, P. Kastritis, N. Mucke, J. Fischer, P. Stelter, A. Ori, K. H. Bui, J. Bassler, E. Barbar, M. Beck, E. Hurt, Structural basis for assembly and function of the Nup82 complex in the nuclear pore scaffold. *J. Cell Biol.* **208**, 283-297 (2015).
62. R. Teimer, J. Kosinski, A. von Appen, M. Beck, E. Hurt, A short linear motif in scaffold Nup145C connects Y-complex with pre-assembled outer ring Nup82 complex. *Nat. Commun.* **8**, 1107 (2017).
63. D. H. Lin, A. R. Correia, S. W. Cai, F. M. Huber, C. A. Jette, A. Hoelz, Structural and functional analysis of mRNA export regulation by the nuclear pore complex. *Nat. Commun.* **9**, 2319 (2018).
64. J. Fernandez-Martinez, S. J. Kim, Y. Shi, P. Upla, R. Pellarin, M. Gagnon, I. E. Chemmama, J. Wang, I. Nudelman, W. Zhang, R. Williams, W. J. Rice, D. L. Stokes, D. Zenklusen, B. T. Chait, A. Sali, M. P. Rout, Structure and Function of the Nuclear Pore Complex Cytoplasmic mRNA Export Platform. *Cell* **167**, 1215-1228 e1225 (2016).
65. C. S. Weirich, J. P. Erzberger, J. S. Flick, J. M. Berger, J. Thorner, K. Weis, Activation of the DExD/H-box protein Dbp5 by the nuclear-pore protein Gle1 and its coactivator InsP6 is required for mRNA export. *Nat. Cell Biol.* **8**, 668-676 (2006).
66. J. Enninga, D. E. Levy, G. Blobel, B. M. Fontoura, Role of nucleoporin induction in releasing an mRNA nuclear export block. *Science* **295**, 1523-1525 (2002).
67. D. Forler, G. Rabut, F. D. Ciccarelli, A. Herold, T. Kocher, R. Niggeweg, P. Bork, J. Ellenberg, E. Izaurralde, RanBP2/Nup358 provides a major binding site for NXF1-p15 dimers at the nuclear pore complex and functions in nuclear mRNA export. *Mol. Cell. Biol.* **24**, 1155-1167 (2004).
68. S. Hutten, R. H. Kehlenbach, Nup214 is required for CRM1-dependent nuclear protein export in vivo. *Mol. Cell. Biol.* **26**, 6772-6785 (2006).
69. M. Hamada, A. Haeger, K. B. Jeganathan, J. H. van Ree, L. Malureanu, S. Walde, J. Joseph, R. H. Kehlenbach, J. M. van Deursen, Ran-dependent docking of importin-beta to RanBP2/Nup358 filaments is essential for protein import and cell viability. *J. Cell Biol.* **194**, 597-612 (2011).
70. B. Quan, H. S. Seo, G. Blobel, Y. Ren, Vesiculoviral matrix (M) protein occupies nucleic acid binding site at nucleoporin pair (Rae1 * Nup98). *Proc. Natl. Acad. Sci. U.S.A.* **111**, 9127-9132 (2014).

71. J. Wu, M. J. Matunis, D. Kraemer, G. Blobel, E. Coutavas, Nup358, a cytoplasmically exposed nucleoporin with peptide repeats, Ran-GTP binding sites, zinc fingers, a cyclophilin A homologous domain, and a leucine-rich region. *J. Biol. Chem.* **270**, 14209-14213 (1995).
72. N. Yokoyama, N. Hayashi, T. Seki, N. Pante, T. Ohba, K. Nishii, K. Kuma, T. Hayashida, T. Miyata, U. Aebi, et al., A giant nucleopore protein that binds Ran/TC4. *Nature* **376**, 184-188 (1995).
73. M. P. Rout, J. D. Aitchison, A. Suprpto, K. Hjertaas, Y. Zhao, B. T. Chait, The yeast nuclear pore complex: composition, architecture, and transport mechanism. *J. Cell Biol.* **148**, 635-651 (2000).
74. J. M. Cronshaw, A. N. Krutchinsky, W. Zhang, B. T. Chait, M. J. Matunis, Proteomic analysis of the mammalian nuclear pore complex. *J. Cell Biol.* **158**, 915-927 (2002).
75. J. Joseph, M. Dasso, The nucleoporin Nup358 associates with and regulates interphase microtubules. *FEBS Lett.* **582**, 190-196 (2008).
76. S. A. Kassube, T. Stuwe, D. H. Lin, C. D. Antonuk, J. Napetschnig, G. Blobel, A. Hoelz, Crystal structure of the N-terminal domain of Nup358/RanBP2. *J. Mol. Biol.* **423**, 752-765 (2012).
77. M. Paduch, A. Koide, S. Uysal, S. S. Rizk, S. Koide, A. A. Kossiakoff, Generating conformation-specific synthetic antibodies to trap proteins in selected functional states. *Methods* **60**, 3-14 (2013).
78. L. Holm, Using Dali for Protein Structure Comparison. *Methods Mol. Biol.* **2112**, 29-42 (2020).
79. B. Hampoelz, A. Schwarz, P. Ronchi, H. Bragulat-Teixidor, C. Tischer, I. Gaspar, A. Ephrussi, Y. Schwab, M. Beck, Nuclear Pores Assemble from Nucleoporin Condensates During Oogenesis. *Cell* **179**, 671-686 e617 (2019).
80. N. R. Yaseen, G. Blobel, Two distinct classes of Ran-binding sites on the nucleoporin Nup-358. *Proc. Natl. Acad. Sci. U.S.A.* **96**, 5516-5521 (1999).
81. S. Nakielny, S. Shaikh, B. Burke, G. Dreyfuss, Nup153 is an M9-containing mobile nucleoporin with a novel Ran-binding domain. *EMBO J.* **18**, 1982-1995 (1999).
82. T. Guan, R. H. Kehlenbach, E. C. Schirmer, A. Kehlenbach, F. Fan, B. E. Clurman, N. Arnheim, L. Gerace, Nup50, a nucleoplasmically oriented nucleoporin with a role in nuclear protein export. *Mol. Cell. Biol.* **20**, 5619-5630 (2000).
83. M. M. Higa, S. L. Alam, W. I. Sundquist, K. S. Ullman, Molecular characterization of the Ran-binding zinc finger domain of Nup153. *J. Biol. Chem.* **282**, 17090-17100 (2007).
84. N. Schrader, C. Koerner, K. Koessmeier, J. A. Bangert, A. Wittinghofer, R. Stoll, I. R. Vetter, The crystal structure of the Ran-Nup153ZnF2 complex: a general Ran docking site at the nuclear pore complex. *Structure* **16**, 1116-1125 (2008).
85. J. R. Partridge, T. U. Schwartz, Crystallographic and biochemical analysis of the Ran-binding zinc finger domain. *J. Mol. Biol.* **391**, 375-389 (2009).
86. A. Ori, N. Banterle, M. Iskar, A. Andres-Pons, C. Escher, H. Khanh Bui, L. Sparks, V. Solis-Mezarino, O. Rinner, P. Bork, E. A. Lemke, M. Beck, Cell type-specific nuclear pores: a case in point for context-dependent stoichiometry of molecular machines. *Mol. Syst. Biol.* **9**, 648 (2013).
87. D. Salina, P. Enarson, J. B. Rattner, B. Burke, Nup358 integrates nuclear envelope breakdown with kinetochore assembly. *J. Cell Biol.* **162**, 991-1001 (2003).
88. P. D. Pereira, A. Serra-Caetano, M. Cabrita, E. Bekman, J. Braga, J. Rino, R. Santus, P. L. Filipe, A. E. Sousa, J. A. Ferreira, Quantification of cell cycle kinetics by EdU (5-ethynyl-2'-deoxyuridine)-coupled-fluorescence-intensity analysis. *Oncotarget* **8**, 40514-40532 (2017).

89. K. Mahadevan, H. Zhang, A. Akef, X. A. Cui, S. Gueroussov, C. Cenik, F. P. Roth, A. F. Palazzo, RanBP2/Nup358 potentiates the translation of a subset of mRNAs encoding secretory proteins. *PLoS Biol.* **11**, e1001545 (2013).
90. C. V. Heath, C. S. Copeland, D. C. Amberg, V. Del Priore, M. Snyder, C. N. Cole, Nuclear pore complex clustering and nuclear accumulation of poly(A)⁺ RNA associated with mutation of the *Saccharomyces cerevisiae* RAT2/NUP120 gene. *J. Cell Biol.* **131**, 1677-1697 (1995).
91. D. E. Neilson, M. D. Adams, C. M. Orr, D. K. Schelling, R. M. Eiben, D. S. Kerr, J. Anderson, A. G. Bassuk, A. M. Bye, A. M. Childs, A. Clarke, Y. J. Crow, M. Di Rocco, C. Dohna-Schwake, G. Dueckers, A. E. Fasano, A. D. Gika, D. Giannis, M. P. Gorman, P. J. Grattan-Smith, A. Hackenberg, A. Kuster, M. G. Lentschig, E. Lopez-Laso, E. J. Marco, S. Mastroyianni, J. Perrier, T. Schmitt-Mechelke, S. Servidei, A. Skardoutsou, P. Uldall, M. S. van der Knaap, K. C. Goglin, D. L. Tefft, C. Aubin, P. de Jager, D. Hafler, M. L. Warman, Infection-triggered familial or recurrent cases of acute necrotizing encephalopathy caused by mutations in a component of the nuclear pore, RANBP2. *Am. J. Hum. Genet.* **84**, 44-51 (2009).
92. K. Sell, K. Storch, G. Hahn, M. A. Lee-Kirsch, G. Ramantani, S. Jackson, D. Neilson, M. von der Hagen, U. Hehr, M. Smitka, Variable clinical course in acute necrotizing encephalopathy and identification of a novel RANBP2 mutation. *Brain Dev.* **38**, 777-780 (2016).
93. E. Bonnin, P. Cabochette, A. Filosa, R. Juhlen, S. Komatsuzaki, M. Hezwani, A. Dickmanns, V. Martinelli, M. Vermeersch, L. Supply, N. Martins, L. Pirenne, G. Ravenscroft, M. Lombard, S. Port, C. Spillner, S. Janssens, E. Roets, J. Van Dorpe, M. Lammens, R. H. Kehlenbach, R. Ficner, N. G. Laing, K. Hoffmann, B. Vanhollebeke, B. Fahrenkrog, Biallelic mutations in nucleoporin NUP88 cause lethal fetal akinesia deformation sequence. *PLoS Genet.* **14**, e1007845 (2018).
94. S. G. Regmi, H. Lee, R. Kaufhold, B. Fichtman, S. Chen, V. Aksenova, E. Turcotte, A. Harel, A. Arnaoutov, M. Dasso, The Nuclear Pore Complex consists of two independent scaffolds. *bioRxiv*, 2020.2011.2013.381947 (2020).
95. V. Zila, E. Margiotta, B. Turonova, T. G. Muller, C. E. Zimmerli, S. Mattei, M. Allegretti, K. Borner, J. Rada, B. Muller, M. Lusic, H. G. Krausslich, M. Beck, Cone-shaped HIV-1 capsids are transported through intact nuclear pores. *Cell* **184**, 1032-1046 e1018 (2021).
96. A. P. Schuller, M. Wojtynek, D. Mankus, M. Tatli, R. Kronenberg-Tenga, S. G. Regmi, P. V. Dip, A. K. R. Lytton-Jean, E. J. Brignole, M. Dasso, K. Weis, O. Medalia, T. U. Schwartz, The cellular environment shapes the nuclear pore complex architecture. *Nature* **598**, 667-671 (2021).
97. M. Hamed, B. Caspar, S. A. Port, R. H. Kehlenbach, A nuclear export sequence promotes CRM1-dependent targeting of the nucleoporin Nup214 to the nuclear pore complex. *J. Cell Sci.* **134**, (2021).
98. T. C. Walther, H. S. Pickersgill, V. C. Cordes, M. W. Goldberg, T. D. Allen, I. W. Mattaj, M. Fornerod, The cytoplasmic filaments of the nuclear pore complex are dispensable for selective nuclear protein import. *J. Cell Biol.* **158**, 63-77 (2002).
99. E. Onischenko, J. H. Tang, K. R. Andersen, K. E. Knockenhauer, P. Vallotton, C. P. Derrer, A. Kralt, C. F. Mugler, L. Y. Chan, T. U. Schwartz, K. Weis, Natively Unfolded FG Repeats Stabilize the Structure of the Nuclear Pore Complex. *Cell* **171**, 904-917 e919 (2017).
100. L. Miorin, T. Kehrer, M. T. Sanchez-Aparicio, K. Zhang, P. Cohen, R. S. Patel, A. Cupic, T. Makio, M. Mei, E. Moreno, O. Danziger, K. M. White, R. Rathnasinghe, M. Uccellini, S. Gao, T. Aydililo, I. Mena, X. Yin, L. Martin-Sancho, N. J. Krogan, S. K. Chanda, M. Schotsaert, R. W. Wozniak, Y. Ren, B. R. Rosenberg, B. M. A. Fontoura, A. Garcia-Sastre, SARS-CoV-2 Orf6 hijacks Nup98 to block STAT nuclear import and antagonize interferon signaling. *Proc. Natl. Acad. Sci. U.S.A.* **117**, 28344-28354 (2020).

101. C. J. Bley, S. Nie, G. W. Mobbs, S. Petrovic, A. T. Gres, X. Liu, S. Mukherjee, S. Harvey, F. M. Huber, D. H. Lin, B. Brown, A. W. Tang, E. J. Rundlet, A. R. Correia, S. Chen, S. R. Regmi, T. A. Stevens, C. A. Jette, M. Dasso, A. Patke, A. F. Palazzo, A. A. Kossiakoff, A. Hoelz, Architecture of the cytoplasmic face of the nuclear pore, Version 1.0, CaltechDATA (2021). doi: 10.22002/D1.2209.
102. N. Kellner, J. Schwarz, M. Sturm, J. Fernandez-Martinez, S. Griesel, W. Zhang, B. T. Chait, M. P. Rout, U. Kuck, E. Hurt, Developing genetic tools to exploit *Chaetomium thermophilum* for biochemical analyses of eukaryotic macromolecular assemblies. *Sci. Rep.* **6**, 20937 (2016).
103. B. M. Fontoura, G. Blobel, M. J. Matunis, A conserved biogenesis pathway for nucleoporins: proteolytic processing of a 186-kilodalton precursor generates Nup98 and the novel nucleoporin, Nup96. *J. Cell Biol.* **144**, 1097-1112 (1999).
104. F. Kendirgi, D. J. Rexer, A. R. Alcazar-Roman, H. M. Onishko, S. R. Wentz, Interaction between the shuttling mRNA export factor Gle1 and the nucleoporin hCG1: a conserved mechanism in the export of Hsp70 mRNA. *Mol. Biol. Cell* **16**, 4304-4315 (2005).
105. A. Hoelz, A. C. Nairn, J. Kuriyan, Crystal structure of a tetradecameric assembly of the association domain of Ca²⁺/calmodulin-dependent kinase II. *Mol. Cell* **11**, 1241-1251 (2003).
106. E. Mossessova, C. D. Lima, Ulp1-SUMO crystal structure and genetic analysis reveal conserved interactions and a regulatory element essential for cell growth in yeast. *Mol. Cell* **5**, 865-876 (2000).
107. C. Romier, M. Ben Jelloul, S. Albeck, G. Buchwald, D. Busso, P. H. N. Celie, E. Christodoulou, V. De Marco, S. van Gerwen, P. Knipscheer, J. H. Lebbink, V. Notenboom, A. Poterszman, N. Rochel, S. X. Cohen, T. Unger, J. L. Sussman, D. Moras, T. K. Sixma, A. Perrakis, Co-expression of protein complexes in prokaryotic and eukaryotic hosts: experimental procedures, database tracking and case studies. *Acta Crystallogr. D Biol. Crystallogr.* **62**, 1232-1242 (2006).
108. S. Mukherjee, S. K. Erramilli, M. Ammirati, F. J. D. Alvarez, K. F. Fennell, M. D. Purdy, B. M. Skrobek, K. Radziwon, J. Coukos, Y. Kang, P. Dutka, X. Gao, X. Qiu, M. Yeager, H. Eric Xu, S. Han, A. A. Kossiakoff, Synthetic antibodies against BRIL as universal fiducial marks for single-particle cryoEM structure determination of membrane proteins. *Nat. Commun.* **11**, 1598 (2020).
109. S. Doublet, Preparation of selenomethionyl proteins for phase determination. *Methods Enzymol.* **276**, 523-530 (1997).
110. I. R. Vetter, C. Nowak, T. Nishimoto, J. Kuhlmann, A. Wittinghofer, Structure of a Ran-binding domain complexed with Ran bound to a GTP analogue: implications for nuclear transport. *Nature* **398**, 39-46 (1999).
111. P. J. Wyatt, Multiangle light scattering: The basic tool for macromolecular characterization. *Instrum. Sci. Technol.* **25**, 1-18 (1997).
112. K. Sabath, M. L. Staubli, S. Marti, A. Leitner, M. Moes, S. Jonas, INTS10-INTS13-INTS14 form a functional module of Integrator that binds nucleic acids and the cleavage module. *Nat. Commun.* **11**, 3422 (2020).
113. K. R. Miller, A. Koide, B. Leung, J. Fitzsimmons, B. Yoder, H. Yuan, M. Jay, S. S. Sidhu, S. Koide, E. J. Collins, T cell receptor-like recognition of tumor in vivo by synthetic antibody fragment. *PLoS One* **7**, e43746 (2012).
114. S. Mukherjee, M. Ura, R. J. Hoey, A. A. Kossiakoff, A New Versatile Immobilization Tag Based on the Ultra High Affinity and Reversibility of the Calmodulin-Calmodulin Binding Peptide Interaction. *J. Mol. Biol.* **427**, 2707-2725 (2015).
115. Z. Otwinowski, W. Minor, Processing of X-ray diffraction data collected in oscillation mode. *Methods Enzymol.* **276**, 307-326 (1997).
116. W. Kabsch, Xds. *Acta Crystallogr. D Biol. Crystallogr.* **66**, 125-132 (2010).

117. G. Winter, D. G. Waterman, J. M. Parkhurst, A. S. Brewster, R. J. Gildea, M. Gerstel, L. Fuentes-Montero, M. Vollmar, T. Michels-Clark, I. D. Young, N. K. Sauter, G. Evans, DIALS: implementation and evaluation of a new integration package. *Acta Crystallogr. D Struct. Biol.* **74**, 85-97 (2018).
118. P. R. Evans, G. N. Murshudov, How good are my data and what is the resolution? *Acta Crystallogr. D Biol. Crystallogr.* **69**, 1204-1214 (2013).
119. A. J. McCoy, R. W. Grosse-Kunstleve, P. D. Adams, M. D. Winn, L. C. Storoni, R. J. Read, Phaser crystallographic software. *J. Appl. Crystallogr.* **40**, 658-674 (2007).
120. C. Vonrhein, E. Blanc, P. Roversi, G. Bricogne, Automated structure solution with autoSHARP. *Methods Mol. Biol.* **364**, 215-230 (2007).
121. G. M. Sheldrick, A short history of SHELX. *Acta Crystallogr. A.* **64**, 112-122 (2008).
122. R. W. Grosse-Kunstleve, P. D. Adams, Substructure search procedures for macromolecular structures. *Acta Crystallogr. D Biol. Crystallogr.* **59**, 1966-1973 (2003).
123. T. C. Terwilliger, Maximum-likelihood density modification. *Acta Crystallogr. D Biol. Crystallogr.* **56**, 965-972 (2000).
124. M. D. Winn, C. C. Ballard, K. D. Cowtan, E. J. Dodson, P. Emsley, P. R. Evans, R. M. Keegan, E. B. Krissinel, A. G. Leslie, A. McCoy, S. J. McNicholas, G. N. Murshudov, N. S. Pannu, E. A. Potterton, H. R. Powell, R. J. Read, A. Vagin, K. S. Wilson, Overview of the CCP4 suite and current developments. *Acta Crystallogr. D Biol. Crystallogr.* **67**, 235-242 (2011).
125. P. Emsley, B. Lohkamp, W. G. Scott, K. Cowtan, Features and development of Coot. *Acta Crystallogr. D Biol. Crystallogr.* **66**, 486-501 (2010).
126. D. Liebschner, P. V. Afonine, M. L. Baker, G. Bunkoczi, V. B. Chen, T. I. Croll, B. Hintze, L. W. Hung, S. Jain, A. J. McCoy, N. W. Moriarty, R. D. Oeffner, B. K. Poon, M. G. Prisant, R. J. Read, J. S. Richardson, D. C. Richardson, M. D. Sammito, O. V. Sobolev, D. H. Stockwell, T. C. Terwilliger, A. G. Urzhumtsev, L. L. Videau, C. J. Williams, P. D. Adams, Macromolecular structure determination using X-rays, neutrons and electrons: recent developments in Phenix. *Acta Crystallogr. D Struct. Biol.* **75**, 861-877 (2019).
127. C. J. Williams, J. J. Headd, N. W. Moriarty, M. G. Prisant, L. L. Videau, L. N. Deis, V. Verma, D. A. Keedy, B. J. Hintze, V. B. Chen, S. Jain, S. M. Lewis, W. B. Arendall, 3rd, J. Snoeyink, P. D. Adams, S. C. Lovell, J. S. Richardson, D. C. Richardson, MolProbity: More and better reference data for improved all-atom structure validation. *Protein Sci.* **27**, 293-315 (2018).
128. E. F. Pettersen, T. D. Goddard, C. C. Huang, G. S. Couch, D. M. Greenblatt, E. C. Meng, T. E. Ferrin, UCSF Chimera--a visualization system for exploratory research and analysis. *J. Comput. Chem.* **25**, 1605-1612 (2004).
129. D. H. Lin, S. Zimmermann, T. Stuwe, E. Stuwe, A. Hoelz, Structural and functional analysis of the C-terminal domain of Nup358/RanBP2. *J. Mol. Biol.* **425**, 1318-1329 (2013).
130. P. J. Flory, M. Volkenstein, Statistical mechanics of chain molecules. *Biopolymers* **8**, 699-700 (1969).
131. T. H. Evers, E. M. van Dongen, A. C. Faesen, E. W. Meijer, M. Merckx, Quantitative understanding of the energy transfer between fluorescent proteins connected via flexible peptide linkers. *Biochemistry* **45**, 13183-13192 (2006).
132. K. Thierbach, A. von Appen, M. Thoms, M. Beck, D. Flemming, E. Hurt, Protein interfaces of the conserved Nup84 complex from *Chaetomium thermophilum* shown by crosslinking mass spectrometry and electron microscopy. *Structure* **21**, 1672-1682 (2013).
133. T. Waldman, K. W. Kinzler, B. Vogelstein, p21 is necessary for the p53-mediated G1 arrest in human cancer cells. *Cancer Res.* **55**, 5187-5190 (1995).
134. T. Knutsen, H. M. Padilla-Nash, D. Wangsa, L. Barenboim-Stapleton, J. Camps, N. McNeil, M. J. Difilippantonio, T. Ried, Definitive molecular cytogenetic characterization of 15 colorectal cancer cell lines. *Genes Chromosomes Cancer* **49**, 204-223 (2010).

135. L. Cong, F. A. Ran, D. Cox, S. Lin, R. Barretto, N. Habib, P. D. Hsu, X. Wu, W. Jiang, L. A. Marraffini, F. Zhang, Multiplex genome engineering using CRISPR/Cas systems. *Science* **339**, 819-823 (2013).
136. K. C. Yau, A. Arnaoutov, V. Aksenova, R. Kaufhold, S. Chen, M. Dasso, RanBP1 controls the Ran pathway in mammalian cells through regulation of mitotic RCC1 dynamics. *Cell Cycle* **19**, 1899-1916 (2020).
137. A. Patke, P. J. Murphy, O. E. Onat, A. C. Krieger, T. Ozcelik, S. S. Campbell, M. W. Young, Mutation of the Human Circadian Clock Gene CRY1 in Familial Delayed Sleep Phase Disorder. *Cell* **169**, 203-215 e213 (2017).
138. J. Schindelin, I. Arganda-Carreras, E. Frise, V. Kaynig, M. Longair, T. Pietzsch, S. Preibisch, C. Rueden, S. Saalfeld, B. Schmid, J. Y. Tinevez, D. J. White, V. Hartenstein, K. Eliceiri, P. Tomancak, A. Cardona, Fiji: an open-source platform for biological-image analysis. *Nat. Methods* **9**, 676-682 (2012).
139. F. Jeanmougin, J. D. Thompson, M. Gouy, D. G. Higgins, T. J. Gibson, Multiple sequence alignment with Clustal X. *Trends Biochem. Sci.* **23**, 403-405 (1998).
140. G. J. Barton, ALSCRIPT: a tool to format multiple sequence alignments. *Protein Eng.* **6**, 37-40 (1993).
141. N. A. Baker, D. Sept, S. Joseph, M. J. Holst, J. A. McCammon, Electrostatics of nanosystems: application to microtubules and the ribosome. *Proc. Natl. Acad. Sci. U.S.A.* **98**, 10037-10041 (2001).
142. P. Grandi, N. Schlaich, H. Tekotte, E. C. Hurt, Functional interaction of Nic96p with a core nucleoporin complex consisting of Nsp1p, Nup49p and a novel protein Nup57p. *EMBO J.* **14**, 76-87 (1995).
143. F. E. Loughlin, R. E. Mansfield, P. M. Vaz, A. P. McGrath, S. Setiyaputra, R. Gamsjaeger, E. S. Chen, B. J. Morris, J. M. Guss, J. P. Mackay, The zinc fingers of the SR-like protein ZRANB2 are single-stranded RNA-binding domains that recognize 5' splice site-like sequences. *Proc. Natl. Acad. Sci. U.S.A.* **106**, 5581-5586 (2009).
144. F. E. Loughlin, P. J. Lukavsky, T. Kazeeva, S. Reber, E. M. Hock, M. Colombo, C. Von Schroetter, P. Pauli, A. Clery, O. Muhlemann, M. Polymenidou, M. D. Ruepp, F. H. Allain, The Solution Structure of FUS Bound to RNA Reveals a Bipartite Mode of RNA Recognition with Both Sequence and Shape Specificity. *Mol Cell* **73**, 490-504 e496 (2019).
145. J. Kuhlmann, I. Macara, A. Wittinghofer, Dynamic and equilibrium studies on the interaction of Ran with its effector, RanBP1. *Biochemistry* **36**, 12027-12035 (1997).
146. A. Drozdetskiy, C. Cole, J. Procter, G. J. Barton, JPred4: a protein secondary structure prediction server. *Nucleic Acids Res.* **43**, W389-394 (2015).
147. W. Kobayashi, Y. Takizawa, M. Aihara, L. Negishi, H. Ishii, H. Kurumizaka, Structural and biochemical analyses of the nuclear pore complex component ELYS identify residues responsible for nucleosome binding. *Commun Biol* **2**, 163 (2019).
148. P. J. Gillespie, G. A. Khoudoli, G. Stewart, J. R. Swedlow, J. J. Blow, ELYS/MEL-28 chromatin association coordinates nuclear pore complex assembly and replication licensing. *Curr Biol* **17**, 1657-1662 (2007).
149. M. Zuccolo, A. Alves, V. Galy, S. Bolhy, E. Formstecher, V. Racine, J. B. Sibarita, T. Fukagawa, R. Shiekhattar, T. Yen, V. Doye, The human Nup107-160 nuclear pore subcomplex contributes to proper kinetochore functions. *EMBO J.* **26**, 1853-1864 (2007).
150. J. Mansfeld, S. Guttinger, L. A. Hawryluk-Gara, N. Pante, M. Mall, V. Galy, U. Haselmann, P. Muhlhauser, R. W. Wozniak, I. W. Mattaj, U. Kutay, W. Antonin, The conserved transmembrane nucleoporin NDC1 is required for nuclear pore complex assembly in vertebrate cells. *Mol. Cell* **22**, 93-103 (2006).
151. C. Franz, R. Walczak, S. Yavuz, R. Santarella, M. Gentzel, P. Askjaer, V. Galy, M. Hetzer, I. W. Mattaj, W. Antonin, MEL-28/ELYS is required for the recruitment of nucleoporins to

- chromatin and postmitotic nuclear pore complex assembly. *EMBO Rep.* **8**, 165-172 (2007).
152. S. Amlacher, P. Sarges, D. Flemming, V. van Noort, R. Kunze, D. P. Devos, M. Arumugam, P. Bork, E. Hurt, Insight into structure and assembly of the nuclear pore complex by utilizing the genome of a eukaryotic thermophile. *Cell* **146**, 277-289 (2011).
 153. D. Reverter, C. D. Lima, Insights into E3 ligase activity revealed by a SUMO-RanGAP1-Ubc9-Nup358 complex. *Nature* **435**, 687-692 (2005).